Biological Magnetic Resonance 23

Biomedical EPR- Part A:
Free Radicals, Metals, Medicine, and Physiology

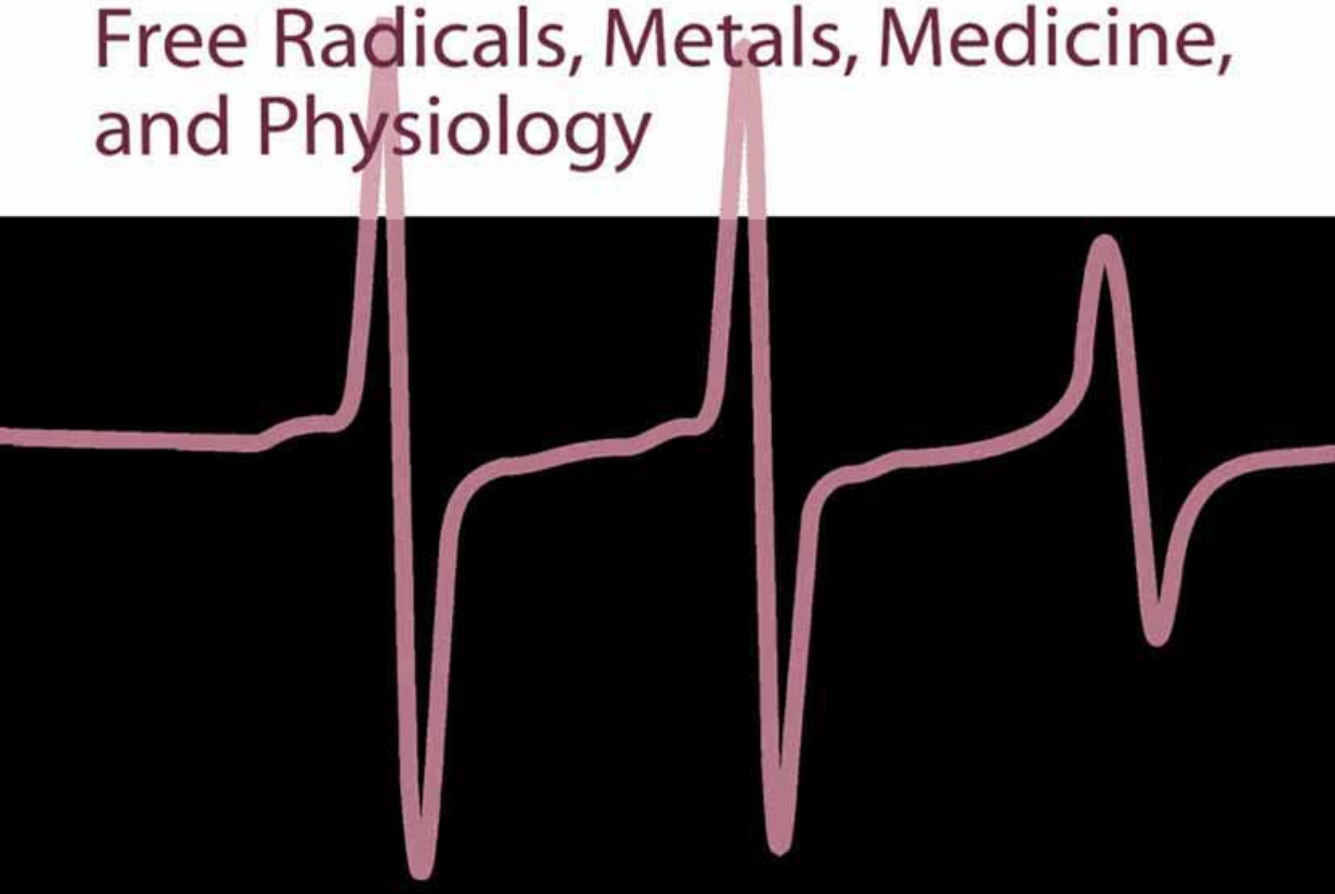

Sandra S. Eaton
Gareth R. Eaton
Lawrence J. Berliner

Biological Magnetic Resonance

Volume 23

Biomedical EPR, Part A: Free Radicals, Metals, Medicine, and Physiology

Biological Magnetic Resonance

Volume 23

Biomedical EPR, Part A: Free Radicals, Metals, Medicine, and Physiology

Edited by

Sandra R. Eaton
University of Denver
Denver, Colorado

Gareth R. Eaton
University of Denver
Denver, Colorado

and

Lawrence J. Berliner
University of Denver
Denver, Colorado

KLUWER ACADEMIC PUBLISHERS
NEW YORK, BOSTON, DORDRECHT, LONDON, MOSCOW

eBook ISBN: 0-306-48556-7
Print ISBN: 0-306-48506-0

Created in the United States of America

Visit Springer's eBookstore at: http://ebooks.kluweronline.com
and the Springer Global Website Online at: http://www.springeronline.com

Dedication:

To the students whom we hope to stimulate to become the next generation of biomedical EPR researchers.

Contributors

William E. Antholine • National Biomedical EPR Center, Medical College of Wisconsin, 8701 Watertown Plank Road, Milwaukee, WI 53226

Riccardo Basosi • Department of Chemistry, University of Siena, Siena, Italy

Helmut Beinert • University of Wisconsin, Institute for Enzyme Research and Department of Biochemistry, College of Agriculter and Life Sciences, Madison, Wisconsin, USA

Lawrence J. Berliner •Department of Chemistry and Biochemistry, University of Denver, Denver, CO 80208

Michael J. Colaneri • Department of Chemistry and Physics, State University of New York at Old Westbury, Old Westbury, New York 11568

Peter L. Gutierrez • Greenebaum Cancer Center, University of Maryland Medical School, Baltimore, MD USA

Howard J. Halpern • Department of Radiation and Cellular Oncology, University of Chicago, Chicago, Illinois 60637

Neil Hogg • National Biomedical EPR Center, Department of Biophysics, Medical College of Wisconsin, Milwaukee, Wisconsin 53226

Maria B. Kadiiska • Free Radical Metabolite Section, Laboratory of Pharmacology and Chemistry, National Institute of Environmental Health Sciences, National Institutes of Health, Research Triangle Park, North Carolina 27709

Balaraman Kalyanaraman • Biophysics Research Institute, Medical College of Wisconsin, Milwaukee, WI USA 53226

Nadeem Khan • Department of Diagnostic Radiology, Dartmouth Medical School, Hanover, New Hampshire 03755

Agnes Keszler • National Biomedical EPR Center, Department of Biophysics, Medical College of Wisconsin, Milwaukee, Wisconsin 53226

Murali C. Krishna • Radiation Biology Branch, Center for Cancer Research, National Cancer Institute, National Institutes of Health, Bethesda, MD

Giovanni Della Lunga • Department of Chemistry, University of Siena, Siena, Italy

Pavel Martásek • Department of Biochemistry, University of Texas Health Science Center, San Antonio, Texas 78284

Ronald P. Mason • Free Radical Metabolite Section, Laboratory of Pharmacology and Chemistry, National Institute of Environmental Health Sciences, National Institutes of Health, Research Triangle Park, North Carolina 27709

Jack Peisach • Department of Physiology and Biophysics, Albert Einstein College of Medicine, 1300 Morris Park Avenue, Bronx, New York 10461

Przemyslaw M. Plonka • Department of Biophysics, Faculty of Biotechnology, Jagiellonian University, 30-387 Krakow, Poland

Rebecca Pogni • Department of Chemistry, University of Siena, Siena, Italy

Tadeusz Sarna • Department of Biophysics, Faculty of Biotechnology, Jagiellonian University, Krakow, Poland

Witold K. Subczynski • National Biomedical EPR Center, Department of Biophysics, Medical College of Wisconsin, Milwaukee, Wisconsin 53226

Sankaran Subramanian • Radiation Biology Branch, Center for Cancer Research, National Cancer Institute, National Institutes of Health, Bethesda, MD

Harold M. Swartz • Department of Diagnostic Radiology, Dartmouth Medical School, Hanover, New Hampshire 03755

Alexander N. Tikhonov • Department of Biophysics, Faculty of Physics, M. V. Lomonosov Moscow State University, Moscow, 119899, Russia

Jeannette Vásquez-Vivar • Biophysics Research Institute, Medical College of Wisconsin, Milwaukee, Wisconsin 53226

PREFACE

There has not been an attempt to cover the full scope of biological EPR in a single volume since *Biological Applications of Electron Spin Resonance* edited by Swartz, Bolton, and Borg in 1972. In three decades there have been enormous changes in the field. Our original plan for one volume expanded into two. A stimulus for an updated book at this time was the 70th birthday of James S. Hyde (May 20, 2002), one of the leaders in the development of EPR instrumentation and methodology applied to biological problems. To symbolically tie this book to Jim Hyde's efforts, we choose the title "Biomedical EPR", which is the name of the NIH-funded National Biomedical EPR Center founded by Harold Swartz and James Hyde at the Medical College of Wisconsin in 1975. This Center has been funded continuously since then, and has been a focal point of new developments and applications in biomedical research. Many of the authors of chapters in this book have been close associates of Jim Hyde, and several have been long-term members of the Advisory Committee of the Center.

There is a long history underlying most of the topics in these books. Some of this history was surveyed in *Foundations of Modern EPR,* edited by Eaton, Eaton, and Salikhov (1998). It is helpful to keep in mind that theoretical and experimental studies of spin relaxation preceded the development of EPR and NMR. The early work of Waller and of Gorter, for example, focused on spin relaxation (see *Foundations of Modern EPR*). Long development periods, and indirect paths from initial concept to biomedical application are the norm. Even new instrumentation or methodology developments, with few exceptions, require of the order of 10 to 15 years from "invention" to general application. No one could have predicted that the attempt to make a better measurement of the deuterium magnetic moment would lead to functional magnetic resonance imaging (fMRI), and if such a prediction had been made, it would have been dismissed as ridiculous. Those who sponsor research, and nurture researchers, enrich humanity by not demanding proof of relevance. We each pursue goals that inspire us, and hope that they will be of benefit. This book is part of a story as it unfolds.

Contributors were asked to make this book more "pedagogical" than "review." The goal is a multi-author introduction to biomedical EPR with up-to-date examples, explanations, and applications, pointing toward the future. Thus, the book is aimed not just at readers who are EPR experts, but at biomedical researchers seeking to learn whether EPR technology and methodology will be useful to solve their biomedical problems. The derivation and explanation of the underlying theory and methodology for many of the topics presented would require separate books. The authors

were asked to keep the background and theory to a minimum, referring whenever possible to other texts and reviews to lead the reader to additional information. The referencing in most chapters is thus to be tutorial and helpful, rather than to be comprehensive or to reflect priority of discovery. There is a focus on papers with a biological orientation. Thus, for example, although the fact that oxygen in solution broadens CW EPR spectra has been known since 1959 (see the chapter by Hauser and Brunner in *Foundations of Modern EPR*), the citations in the oxymetry chapter in this book to biologically relevant literature about oxygen broadening start about twenty years later. The perspective in each chapter is presented from the viewpoint of people involved in cutting-edge research.

Chapters, including our own, were peer-reviewed, usually by at least two referees in addition to the editors. We thank the referees for their assistance in improving the pedagogy of the chapters. The editors have added cross references between chapters.

In these volumes, we did not include some topics that had been reviewed recently. Spin Labeling I (1976) and II (1979), and the two volumes in this series that are successors to these, volumes 8 (1989) and 14 (1998), emphasize nitroxyl radicals. Volume 13 (1993) emphasizes paramagnetic metals, especially in enzymes, and transient EPR and spin trapping. Volume 18 (2004) describes *in vivo* EPR. Volume 19 (2000) is about measuring distances between unpaired electrons. Volume 21 of the Biological Magnetic Resonance series includes chapters on instrumentation (Bender), sensitivity (Rinard, Quine, Eaton, and Eaton), and a survey of low-frequency spectrometers (Eaton and Eaton). Other chapters of interest can be found in the list of contents of related prior volumes, at the end of each of these volumes. Some volumes in the series Metal Ions in Biological Systems, edited by Sigel focus on EPR. See, for example, Volume 22 (*ENDOR, EPR, and Electron Spin Echo for Probing Coordination Spheres,* 1987).

Although the focus of this book is on biomedical applications of EPR, and the examples used in this book therefore are largely from the biomedical field, an analogous treatise could focus on materials science, traditional small-molecule chemistry, or solid state physics. There are, of course, unifying theoretical, instrumental, and experimental methodologies that cross disciplinary applications. EPR has the great power of specificity for unpaired electron spins, and as Jim has said more than once, "there are spins everywhere."

Biological applications of EPR encompass measuring metal ion environments in proteins at liquid helium temperature and measuring NO production in living animals. The variety of technologies and methodologies required is so wide that a researcher who is expert in one may be almost

unaware of another. The landscape is rich and the horizons extend as far as we can see. These two volumes, which should be read as a single treatise, have the goal of helping biomedical researchers see a little further.

Some potential users will need a more extensive basic introduction to EPR. The reader unfamiliar with EPR may want to start with the Introduction to the chapter by Subramanian and Krishna in Part B (Volume 24), which includes a concise survey of the basic principles of EPR. The Swartz, Bolton and Borg book (1972) mentioned above also is a good place to start. Among the several complete texts on EPR, those by Carrington and McLachlan (1967), by Weil, Bolton and Wertz (1994), and by Atherton (1993) are particularly appropriate for beginners who have a good physical chemistry background. Eaton and Eaton (1997) present an introduction to CW and pulsed EPR, with an emphasis on practical experimental aspects for the novice. Experimental and instrumental aspects of EPR are treated in Fraenkel (1959) and Reiger (1972), but the two major and most highly recommended sources are Alger (1968) and Poole (1967, 1983). Jim Hyde also wrote a brief summary of instrumental aspects of EPR (1995). It is hoped that some readers will enjoy learning some of the historical background of the field. Some of the chapters in this book provide a glimpse, and Foundations of Modern EPR (1998) captures the thinking of pioneers in the field on the occasion of the 50^{th} anniversary of the discovery.

Pictures of experimental EPR spectra beyond those in these books may help the reader's understanding. Many spectra are reproduced in the texts cited above, and in Yen (1969), McGarvey (1966), Goodman and Raynor (1970), Drago (1992), Gerson (1970), and Gerson and Huber (2003). Some early reviews of spin labeling remain very useful introductions to the fundamentals of CW EPR of nitroxyl radical line shapes (Griffith and Wagoner, 1969; Jost, Wagoner, and Griffith, 1971; Jost and Griffith, 1972; Gaffney, 1974).

There is not enough space in these two volumes to teach the underlying principles of pulsed EPR in depth, nor to illustrate the wide range of applications. Readers are directed to several other books for more on these topics: Kevan and Swartz (1979), Keijzers et al. (1989), Hoff (1989), Kevan and Bowman (1990), Dikanov and Tsvetkov (1992), Schweiger and Jeschke (2000), and Berliner, Eaton, and Eaton, (2000) (volume 19 in this series).

For those readers unfamiliar with the practical methodology of EPR, it is reasonable to ask "how long will it take to run an EPR spectrum?" The answer depends strongly on what one wants to learn from the sample, and can range from a few minutes to many weeks. Even the simple question, are there any unpaired electrons present, may take quite a bit of effort to answer, unless one already knows a lot about the sample. Column fractions of a nitroxyl-spin-labeled polymer can be monitored for radicals about as fast as

the samples can be put in the spectrometer. This is an example of an application that could be automated. On the other hand, the spins may have relaxation times so long that they are difficult to observe without saturation or so short that they cannot be observed except at very low temperature where the relaxation times become long enough (e.g., Co(II) in many environments). If one wants to know the concentration of Co(II) in a sample, need for quantitative sample preparation, accurate cryogenic temperature control, careful background subtraction, and skillful setting of instrument parameters lead to a rather time-consuming measurement.

Other reasonable questions include "how much will this cost?" and "how/where can I do this?" EPR measurements require a significant investment in instrumentation, but spectrometer systems are available from several vendors. The largest manufacturers, Bruker BioSpin EPR Division, and JEOL, market general-purpose spectrometers intended to fulfil most analytical needs. The focus is on X-band (ca. 9-10 GHz) continuous wave (CW) spectrometers, with a wide variety of resonators to provide for many types of samples. Accessories facilitate control of the sample temperature from <4K to ca. 700 K. Magnets commonly range from 6-inch to 12-inch pole face diameters. Smaller, table-top spectrometers are available from Bruker, JEOL, and Resonance Instruments. Some of these have permanent magnets and sweep coils for applications that focus on spectra near g = 2, and others have electromagnets permitting wide field sweeps. Bruker makes one small system optimized for quantitation of organic radicals and defect centers, such as for dosimetry. Bruker and JEOL market pulsed, time-domain spectrometers as well as CW spectrometers. Bruker and JEOL market spectrometers for frequencies lower than X-band, which are useful for study of lossy samples. Bruker markets high-frequency (95 GHz), high-field EPR spectrometers that require superconducting magnets, not electromagnets.

Volume 23 begins with an appreciation of the contributions that Jim Hyde made to biomedical EPR, with some historical perspective by Helmut Beinert and Harold Swartz of the mutual stimulation of Jim, the NIH Research Resource "Center" funding program, and the collaborations it spawned.

Among the common analytical tools available to those who study the properties of matter, whether biological or non-biological, ESR has the special feature that it is very sensitive to the anisotropy of the environment of the unpaired electron. The CW EPR spectral line shape is strongly influence by motions that are of the order of the anisotropies in hyperfine couplings and in g-values. Electron spin relaxation times are also sensitive to molecular motions. These effects give rise to the ability to measure rates

and anisotropies of molecular motions, and stimulate the extensive field of spin labeling. One of the first physical parameters of spin labels to be exploited, the incomplete averaging of anisotropic g and hyperfine values, remains central to many uses of nitroxyl spin probes and spin labels. Freed (volume 24 chapter 9) explores the motions reported in great detail by nitroxyl EPR spectra. The saturation transfer technique developed by Jim Hyde and Larry Dalton (1979) is crucial to learning about the dynamics of biological membranes (Marsh et al., volume 24 chapter 11, and Beth and Husted, chapter 12). Beth and Husted show the sensitivity of Q-band (ca. 35 GHz) and W-band (ca. 95 GHz) EPR for analyzing complex anisotropic rotational dynamics, and emphasize the utility of global analysis of spectra obtained at two or more microwave frequencies. Basosi in volume 23 chapter 13 illustrates the kinds of information that can be learned about motions of metal ions.

There are contributions to the CW lines shape and some relaxation properties from electron-nuclear and electron-electron couplings. The dipolar part of the interaction is the basis for distance measurements. Electron-electron distance measurements were the topic of Volume 19 in this series (Berliner, Eaton, and Eaton, 2000), and the Eatons have presented a concise summary of this topic in chapter 8, and in Eaton and Eaton (2002). Because the electron dipole is larger than the nuclear dipoles, EPR measures distances that are larger than the distances measured by NMR. Multiple resonance techniques provide more detail about the spin environment than do "normal" EPR techniques. ENDOR is a very important tool for resolving hyperfine structure. ENDOR of species in frozen glassy solutions is described by Mustafi and Makinen in volume 24 chapter 4 and ENDOR of radicals in fluid solution is described by Gerson and Gescheidt in chapter 5. Next, Lowell Kispert (chapter 6) describes CW, pulsed, and multiquantum ELDOR as ways of probing electron-electron spin-spin interactions.

Many fundamental studies are directly relevant to biomedical science, but the goal of it all is to understand function and malfunction of living systems. It is important to perceive the relevance to human studies of early explorations in plants, for example. The chapter on free radicals and medicine (volume 23 chapter 3) surveys many of the motivations for investigating free radical phenomena. We thank Hal Swartz for coordinating the several contributors to this chapter, and for writing the introduction that give his overall perspective on this important area of science. How far we have come toward studies of animals and humans is reflected by several chapters. Hal Swartz and Nadeem Khan in volume 23 chapter 9 discuss the achievements to date and future possibilities in EPR spectroscopy of function *in vivo*. Depending on your point of view, Hal's perspective could be described as realistic or pessimistic. Maybe some reader will be

stimulated to demonstrate clinical importance of tools that Hal says are unlikely to have major application. The major focus of research for *in vivo* EPR is the development of methodology to measure O_2 concentrations for medical purposes. Modern instrumentation facilitates a new focus on measurement of relaxation times, and use of relaxation properties to measure O_2, distances, etc. (see, for example, volume 24 chapters 1 and 8 by Eaton and Eaton). Benjamin Williams and Howard Halpern in volume 23 chapter 11 and Sankaran Subramanian and Murali Krishna in chapter 12 describe the fundamentals *in vivo* EPR spectroscopy and imaging by CW and pulsed low frequency EPR, respectively. Both of these chapters relate to measurement of O_2 in vivo. Oximetry is also the topic of the very detailed chapter 10 by Subczynski and Swartz.

Reactive free radicals, including superoxide (see volume 23 chapter 4 by Vásquez-Vivar, Martásek, and Kalyanaraman), are studied by the spin-trapping technique. In chapter 5 Ron Mason and Maria Kadiiska describe trapping of reactive radicals *in vivo,* with *ex vivo* detection of the EPR signal. Then, in chapter 6 Keszler and Hogg demonstrate linear regression analysis of multiple spin-trapped spectra to obtain kinetic information.

Application of EPR to understanding complex biological systems is illustrated by the examples of melanin (Sarna and Plonka, volume 23, chapter 7) and photosynthesis (Tikhanov and Subczynski, chapter 8).

As is emphasized in the introductory perspectives by Beinert and Swartz, many of Jim Hyde's contributions were innovations in instrumentation. The tight coupling to biomedical applications, first via visitors to Varian Associates and then with his colleagues at the Medical College and visitors to the National Biomedical ESR Center, focused Jim's instrumentation and methodology development on biomedical problems. Saturation recovery (Eaton and Eaton, volume 24 chapter 1) is applied in several biological investigations, including the oximetry measurements mentioned above. Loop-gap resonators (volume 24 chapter 2 by Rinard and Eaton) were the enabling technology for some of the recent developments in stopped-flow and rapid mixing EPR (Scholes, volume 24, chapter 3) and for the ability to study small spin-labeled protein samples, which gave the impetus to rapid application of site-directed spin labeling (Feix and Klug, Volume 24 chapter 10). In volume 24, chapter 13, Jim presents a perspective on the role of instrumentation in biomedical research. One of the trends foreseen, increased use of computer capability for fast digitization and post-processing, is illustrated by volume 24 chapter 7 (Hyde et al.). Having all frequencies in a magnetic resonance spectrometer phase-locked to a single master oscillator, then using fast digital detection and time-locked

subsampling permits, for example, study of multiple harmonics of the field modulated signal.

We thank the authors for contributing to this book, and we also thank the many anonymous referees whose attention to both large and small matters helped improve the chapters. Beverly Ventura, Biophysics Research Institute, Medical College of Wisconsin, helped several authors with grammar and layout of their chapters. The final formatting of all chapters was done by one of the editors (SSE). We add special thanks to Hal Swartz, whose recruitment of Jim Hyde from Varian to the Medical College of Wisconsin set the stage for much of what is presented in these books, and who somehow could not say no to repeated entreaties to write on yet another topic. He ended up writing the introductory chapter on the background of Jim Hyde and the ESR Center in Milwaukee, and three chapters covering *in vivo* spectroscopy, oximetry, and free radicals in medicine. The last of these was a major effort, since we persuaded him to take contributions from many co-authors and assemble them into the overall chapter, which was probably more work than just writing it all himself!

Overall, even though we introduced these two books as a successor to the Swartz, Bolton, and Borg 1972 book, these books are still just a preface to the future of biomedical applications of EPR.

S. S. Eaton
G. R. Eaton
L. J. Berliner
Denver, Colorado

REFERENCES

Alger, R. S. (1968) *Electron Paramagnetic Resonance: Techniques and Applications,* Wiley-Interscience.

Atherton, N. M. (1993) *Principles of Electron Spin Resonance.* Ellis Horwood PTR Prentice Hall, London. This book has a strong emphasis on hyperfine interactions and ENDOR.

Carrington, A. and McLachlan, A. D. (1967) *Introduction to Magnetic Resonance,* Harper and Row, 1967. This book provides a parallel treatment of NMR and EPR.

Dikanov, S. A., and Tsvetkov, Yu. D. (1992) *Electron Spin Echo Envelope Modulation (ESEEM) Spectroscopy.* CRC Press, Boca Raton, FL.

Drago, R. S. (1992) *Physical Methods for Chemists,* 2nd ed. Saunders, Orlando, FL.

Eaton, S. S., and Eaton, G. R., (1997) Electron Paramagnetic Resonance, in *Analytical Instrumentation Handbook,* G. W. Ewing, ed., Marcel Dekker, 2nd ed., 767-862. The third edition will be published in 2004.

Eaton, G. R., Eaton, S. S., and Salikhov, K., eds., (1998) *Foundations of Modern EPR,* World Scientific Publishing, Singapore.

Eaton S. S. and G. R. Eaton, Electron Paramagnetic Resonance Techniques for Measuring Distances in Proteins, in *Structures and Mechanisms: from Ashes to Enzymes,* ACS Symposium Series 827, American Chemical Society, Washington, D. C., 2002, 321-339.

Fraenkel, G. K., (1959) Paramagnetic Resonance Absorption, in *Technique of Organic Chemistry,* Vol. I, Part IV, 3rd. ed., Chapter XLII, pp. 2801-2872. This is an old article, but it contains much valuable information not readily available elsewhere.

Gaffney, B. J. (1974) Spin Label Measurements in Membranes. *Methods Enzymol.* **32**, 161-198.

Gerson, F. (1970) *High Resolution E.S.R. Spectroscopy.* Verlag Chemie, Weinheim.

Gerson, F. and Huber, W. (2003) *Electron Spin Resonance Spectroscopy of Organic Radicals.* Wiley-VCH, Weinheim.

Goodman, B. A. and Raynor, J. B. Raynor, Electron Spin Resonance of Transition Metal Complexes, in *Advances in Inorganic Chemistry and Radiochemistry,* vol 13, 1970.

Griffith, O. H. and Waggoner, A. S. (1969) Nitroxide free Radicals: Spin Labels for Probing Biomolecular Structure. *Acct. Chem. Res.* **2**, 17-24.

Hausser, K. H. and Brunner, H. (1998) The Effect of Concentration and Oxygen in EPR Chapter H.2 in *Foundations of Modern EPR,* edited by Eaton, G. R., Eaton, S. S., and Salikhov, K. M., World Scientific, Singapore.

Hoff, A. J., ed., (1989) *Advanced EPR : Applications in Biology and Biochemistry.* Elsevier, Amsterdam.

Hyde, J. S., and Dalton, L. R. (1979) Saturation-Transfer Spectroscopy, in *Spin Labeling II: Theory and Applications.* L. J. Berliner, ed., Academic Press, New York.

Hyde, J. S. (1995) Electron Paramagnetic Resonance. Chapter 13 in *Handbook of Microwave Technology,* Volume 2, Ishii, T. K., ed., Academic Press.

Jost, P., Waggoner, A. S., and Griffith, O. H. (1971) Spin Labeling and Membrane Structure, in *Structure and Function of Biological Membranes,* Rothfield, L., ed., Academic Press, New York.

Jost, P. and Griffith, O. H. (1972) Electron Spin Resonance and the Spin Labeling Method. *Methods in Pharmacology* **2**, 223-276.

Keijzers, C. P., Reijerse, E. J., and Schmidt, J. (1989) *Pulsed EPR: A New Field of Applications.* North Holland, Amsterdam.

Kevan, L. and Schwartz, R. N. (1979) *Time Domain Electron Spin Resonance.* Wiley, New York.

Kevan, L. and Bowman, M. K. (1990) *Modern Pulsed and Continuous-Wave Electron Spin Resonance.* Wiley, New York.

McGarvey, B. R. (1966), Electron Spin Resonance of Transition Metal Complexes, in *Transition Metal Chemistry,* vol. 3, R. L. Carlin, ed., Marcel Dekker.

Poole, C. P., Jr. (1967, 1983) *Electron Spin Resonance: A Comprehensive Treatise on Experimental Techniques,* Wiley-Interscience, 1967. Second edition, Wiley, 1983. Note that both editions should be consulted. Especially for the topics of microwave components the coverage is more extensive in the first edition than in the second edition.

Rieger, P. H. (1972) Electron Spin Resonance, in *Techniques of Chemistry,* Vol. 1, Part III A, pp. 499-598.

Schweiger, A., and Jeschke, G. (2001) *Principles of Pulse Electron Paramagnetic Resonance.* Oxford University Press, Oxford.

Sigel, A., and Sigel, H., eds. (1999) *Interrelations between Free Radicals and Metal Ions in Life Processes.* Marcel Dekker, New York.

Swartz, H. M., Bolton, J. R., and Borg, D. C. (1972) *Biological Applications of Electron Spin Resonance.* Wiley

Weil, J. A., Bolton, J. R., and Wertz, J. E. (1994) *Electron Paramagnetic Resonance: Elementary Theory and Practical Applications.* Wiley, New York.

Yen, T. F. (1969) *Electron Spin Resonance of Metal Complexes,* Plenum.

Contents

Section III. In Vivo EPR and Physiology

Chapter 9

EPR Spectroscopy of Function *In Vivo:* Origins, Achievements, And Future Possibilities

Harold M. Swartz and Nadeem Khan

Chapter 10

EPR Oximetry in Biological and Model Samples

Witold K. Subczynski and Harold M. Swartz

Chapter 11

***In vivo* EPR Imaging**

Chapter 12

Time-Domain Radio Frequency EPR Imaging

Section IV. Metals

Chapter 13

Copper Biomolecules in Solution

Riccardo Basosi, Giovanni Della Lunga, Rebecca Pogni

Chapter 14

Low Frequency EPR of Cu^{2+} in Proteins

William E. Antholine

Chapter 15

Electron Spin-Echo Envelope Modulation Studies Of ^{14}N In Biological Systems

Michael J. Colaneri and Jack Peisach

Biological Magnetic Resonance

Volume 23

Biomedical EPR, Part A: Free Radicals, Metals, Medicine, and Physiology

I

James S. Hyde and Biomedical EPR

Chapter 1

Introduction

Helmut Beinert
University of Wisconsin, Institute for Enzyme Research, Madison, Wisconsin, USA

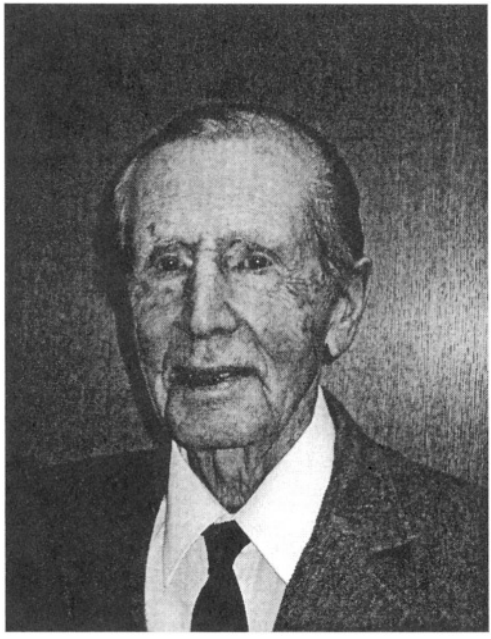

Figure 1. Helmut Beinert. Photograph taken during a visit to the Milwaukee EPR Center, a few months before his 89th birthday. Photograph courtesy of Karen Hyde.

As the editors say in the preface, there has been no comprehensive volume on biological EPR for almost 30 years. Yet, since then this field has

expanded profusely. In my specialty alone, namely Fe-S proteins, where EPR is one of the principal tools, two whole volumes have appeared in "Advances in Inorganic Chemistry" (Vol. 38 and 47), and a third is underway; and these do not include other metal proteins such as those containing Cu, Ni, Mo or W. For other topics touching on the EPR field, such as nitric oxides for instance, a specific journal has been started, or an "Oxygen Society" for oxygen and its reduction products. Moreover, many applications of EPR methods in the medical sciences have been explored and introduced. Thus, an even moderately comprehensive new treatise would have to fill many volumes. We have, therefore, urged our authors to include references to recent treatises on sub-fields - such as the ones I am citing above, to provide a background of literature in areas that cannot be exhaustively dealt with in the present volume. Understandably, after 30 years, the planed volume will have quite a different face. Problems discussed in the 1972 volume may have been solved, others may have vanished from the scene as irrelevant. On the other hand, our capabilities have grown enormously thanks to the ongoing research and development in instrumentation, methodology and the consequently advanced understanding of the phenomena observed.

Many clever minds have been involved in the development of EPR to what it is today, as it is obvious from the volume published to commemorate the 50th anniversary of Zavoiski's demonstration of the phenomenon of EPR (Eaton et al., 1998); however there is barely a single person who has had as much impact and influence on the practice of EPR by the general user physicist or biomedical scientist than Jim Hyde; thus, it seems fitting that the forthcoming volume be dedicated to Jim to his 70th birthday. In his 16 years at Varian Associates, where he had become product manager soon after acquiring his PhD from MIT, Jim and his collaborators have made EPR manageable and practical even for the non-specialist, have developed accessories such as special cavities, sample holders and flat cells for room temperature work, and have educated the users in their "EPR at Work" bulletins, which are still useful today, and have given us numerous practical hints. No wonder that, in 1975, the community of users was stunned by the message that Varian was withdrawing from the EPR field altogether. Many asked the question whether this would mean that Jim's expertise, inventiveness and enthusiasm for improving and extending EPR capabilities might be lost forever, as there was no other manufacturer in sight in the USA that could have taken over Jim and his task. Fortunately, at this point, another talent came into the picture, which, to the community's delight, was able to turn the tide, namely Harold Swartz's organizational and diplomatic talent and skills. He succeeded in winning Jim for the fledgling ESR Center at Milwaukee's Medical College of Wisconsin, which has since flourished

and developed into a unique, national EPR facility, generously supported by the NIH and known worldwide in EPR circles. Thus, with little interruption, Jim could continue to follow his ideas about extending the capabilities of EPR. A time-domain spectrometer was built to determine relaxation times; multi-frequency stations were set up; the necessity for magnetic field modulation was eliminated by introduction of multiquantum EPR; bimodal cavities for X and Q band were built for ELDOR; as alternative to cavities, which pose many restrictions on sample size and shape, the loop-gap resonator (LGR) was developed for several frequencies; data output and recording was radically streamlined by introducing time-locked sub-sampling (TLSS), which allows one to acquire, in a single sweep, all in- and out-of-phase harmonics; and viable alternatives to the rare and expensive klystrons were built.

As not every investigator can afford having all the accessories and modifications in his lab or the know-how to use them, the ESR Center is open for visitors, who have been coming in regularly from this country and all parts of the world. The development of commercial versions of spectrometers is a laborious, expensive and slow process. Thus, modifications in these instruments to accommodate progress in design and capabilities is not lightly undertaken. The innovations developed at the Center can, therefore, not be expected to instantly appear in instruments on the market. It may take years. However, this should not detract from the merit of having the principles of these improvements established, their feasibility proven and any complications resolved and having this documented in the literature.

With a salute to Jim Hyde, master of microwaves, inventor, innovator and optimizer, at his 70th birthday, the EPR community hopes that Jim will be able to contribute for many more years to the joint good of EPR spectroscopy and of those who benefit from its practice and applications.

REFERENCES

Eaton, G. R., Eaton, S. S., Salikhov, K. M. (1998). *Foundations of Modern EPR,* World Scientific, Singapore.

Chapter 2

An Incomplete History of Jim Hyde and the EPR Center at MCW

Harold M. Swartz[1] (with important contributions by Bill Antholine, Lowell Kispert, Balaraman Kalyanaraman, and Helmut Beinert, plus input by Jim Hyde)
[1]*Department of Radiology, Dartmouth Medical School, Hanover, New Hampshire 03755*

Abstract: The contributions of James Hyde to biomedical EPR are reviewed.

1. INTRODUCTION

Hal Swartz had overall responsibility for this chapter and the other authors provided invaluable input, but cannot be held accountable for the way that this chapter has been finalized. Any significant omissions or errors should be attributed to Hal. Bill provided additional information on the development of the research in metal ions, Raman provided similar input on the development of the free radical program, Lowell Kispert contributed much of the information on Jim's activities before Jim came to MCW from the viewpoint of a post-doctoral student at Varian, and Helmut Beinert provided many important insights on the founding of the Center and its subsequent course. Jim has provided invaluable information, insights, and corrections on the chapter.

2. JIM HYDE BEFORE THE ESTABLISHMENT OF THE NATIONAL BIOMEDICAL EPR CENTER

Jim obtained his B.S. from MIT in physics in 1954. His Ph.D. degree, also from MIT, was in solid state physics. His research home was the

Laboratory for Insulation Research directed by Prof. A. R. von Hippel. This was an interdisciplinary laboratory based in the Department of Electrical Engineering, with graduate students from a number of different departments. It is interesting to note that the laboratories in which Jim worked at Varian and MCW were organized in a somewhat similar manner.

During the course of his dissertation research, Jim designed and built a 24 GHz superheterodyne EPR spectrometer with a transmission cavity, a bucking arm in the signal pathway, and an AC Pound AFC. Two papers from his research dissertation were published in *Physical Review* that contributed to the understanding of rapid passage effects in EPR (Hyde, 1960 a, b).

In 1959, which was post Sputnik, Jim found job hunting easy, receiving firm offers from Bell Labs, Texas Instruments, Hughes Aircraft, and Varian. Varian had entered the EPR field and had decided to make another appointment and fortunately, Jim chose Varian. He never considered the possibility of taking a postdoctoral position and preparing for an academic career.

Jim's career prior to coming to the Medical College of Wisconsin was primarily as a physical scientist whose talents were well recognized as highly innovative in new technological concepts. He also helped develop the leading EPR instruments in the world. Many interesting aspects of this phase of his career are described in the chapter on EPR at Varian: 1954-1974 in "Foundations of Modern EPR" (Hyde, 1998). Jim is generally considered to be the guiding force behind the high quality of the EPR instruments made by Varian. The clearest indication of their quality is the fact that more than 25 years after Varian stopped producing these instruments, many experienced EPR spectroscopists feel that the existing Varian instruments still have cutting edge sensitivity and are more reliable than any other commercial instrument. The start and successful initial course of the National Biomedical EPR Center at MCW was based largely on Jim's accomplishments prior to coming to Milwaukee.

In 1964, Varian initiated a postdoctoral program to train the next generation of EPR instrumentalists. Their general plan was to support one postdoc each in three areas of instrumentation in EPR. This was an important program to the future health of EPR, as it exposed future EPR spectroscopists to the highest quality of research and the expectation that somehow it could be done better. Between 1965 and 1974, nine postdocs in EPR spectroscopy rotated through Varian, where they took advantage of the equipment and experience provided by Jim and his colleagues. This was a time when many groundbreaking discoveries in magnetic resonance were achieved, often with the very active and productive involvement of the post-docs.

In 1966, Lowell Kispert became Jim Hyde's second postdoc, and Lowell's recollections provide an excellent glimpse into the environment that Jim and Varian provided at this crucial time in the development of EPR: "My training included having an office next door to Richard Ernst, who was working on research for which he was later awarded a Nobel Prize. Nearby were Ray Freeman and his incredible artwork based on various NMR results, forever making fundamental discoveries as if it was the typical thing to do. In between was Jim Hyde, always with groundbreaking ideas, thinking outside the box. It was like discoveries by the hour. The excitement was tremendous. To help out with any instrument problems, Jim Hyde supervised an electrical engineer named Jim and a technician named Jim. I had to always be on my toes to determine "which Jim."

In 1967, Jim Hyde helped put on a Varian instrument show in Moscow, which was made feasible by the interest and efforts of the famous Russian scientist V.V. Voevodskii. The idea for the Moscow exhibition began in Palo Alto, California, where Prof Voevodskii had been hosted by Harden McConnell. The discussion laid the foundations for the Varian exhibit in Moscow, the first exhibit of this type ever held in Russia, and which helped to establish Varian spectrometers as the instruments of choice on the other side of the "iron curtain." Upon returning, Jim told amusing stories of a fellow by the name of Wojciech Froncisz, who used the Varian E-3 day and night – whenever it was not being shown – to carry out research for his M.Sc.* Even then, I found Jim had a certain feeling of what was right to do – even though hard to explain. I wonder if he knew then that he was setting the stage for the future of EPR, decades later, in the development of the loop gap resonator? Before I arrived, he had duplicated the Fessenden *in situ* radiolysis experiment by borrowing for a short time (two weeks) the medical linear accelerator and test pit from the radiation division. The *in situ* experiment worked perfectly. Unfortunately, the radiation division demanded the return of their equipment! It took almost two years of research to realize that Jim's first guess on equipment needs were correct – bits and pieces stuck together from others left over from various departments had serious problems that took considerable study to correct. As a postdoc under Jim's guidance, you were constantly being exposed to new territory – with a 'yes we can solve this interesting problem...' it was solved – onto the next problem. You didn't have to read the literature – we were creating it."

* (Wojciech later became perhaps Jim's closest colleague, teaming with him in the development of loop gap resonators and a number of other important developments. In reviewing this chapter, Wojciech noted, "I benefited a lot collaborating with Jim. He really has the ability to sense what is important. That happened with the loop-gap resonator. I made a first resonator when he was away from the lab. When he returned I presented the results to him and he immediately realized the potential of the new resonator. That happened many times with Jim with many different things.")

Before coming to MCW, Jim had had some very significant involvement in applications of EPR to biology that set the stage for his desire to do more of this. Anders Ehrenberg invited Jim to present a paper at the 2nd International Conference on Magnetic Resonance in Biological Systems held in Stockholm in 1966 (Hyde, 1966), attracted by the ideas in the 1964 publication by Hyde and Maki (1964) demonstrating ENDOR in the liquid phase. This meeting was pivotal in directing Jim's interest towards biomedical research. Ehrenberg made it possible for one of his associates, L. E. G. Eriksson, to spend a few months at Varian, which resulted in the first paper on ENDOR in an unordered solid (Hyde *et al.,* 1968), followed by the first paper on ENDOR in a protein (Ehrenberg *et al.,* 1968). Jim spent a sabbatical half year in Ehrenberg's laboratory in Stockholm in 1970 and a paper resulted on the EPR relaxation of slowly moving flavin radicals (Hyde *et al.,* 1970). In turn, this study of EPR relaxation in systems undergoing slow rotational diffusion led directly to the discovery by Hyde and Dalton of saturation transfer spectroscopy in 1972 (Hyde and Dalton, 1972). It was this work that caught the attention of Prof. Harden McConnell, who suggested that it be the topic of Ph.D. dissertation research for David D. Thomas. Anders Ehrenberg must have been following this work closely, for he later made a suggestion that collaboration be established with John Gergely of the Boston Biomedical Research Institute, who was interested in the dynamics of supramolecular complexes during muscle contraction. A paper in *Proceedings of the National Academy of Sciences* communicated by McConnell established the utility of saturation transfer in spin labeled myosin (Thomas *et al.,* 1975). Thomas did a postdoctoral fellowship with Gergely that established the foundations of his scientific career. In retrospect, Ehrenberg's high level of scientific foresight seems astonishing. He profoundly affected the careers of both Jim Hyde and David Thomas.

Jim continued to participate in the biannual Magnetic Resonance in Biological Systems conferences, attending them all from 1966 to 1998. Initially, this series had a high level of EPR input, but in later years, NMR became increasingly dominant. Jim fought a rear-guard battle, usually serving on the International Scientific Program committee and doing what he could for EPR. The culmination of this effort took place in 1988 when he, Chien Ho (Carnegie-Mellon University), and John L. Markley (University of Wisconsin) co-chaired the 13th meeting in this series in Madison, Wisconsin. Lectures by H. Beinert, H.M. McConnell, D.D. Thomas, B. Kalyanaraman, B.M. Hoffman, W.L. Hubbell, J. Peisach, S. Schreier, G. Feher, and J.H. Freed created a dynamic EPR ambience. A special high point was the plenary finale by R.R. Ernst: "Advances in NMR and ESR Pulse Methodology for Biological Applications." Jim takes some credit for the title – he and Ernst had been colleagues at Varian.

3. ESTABLISHING THE CENTER

The National Biomedical EPR Center originated through a fortuitous combination of several factors. The most important was Jim's decision that he would like to leave industry and go to academia, where he could pursue his ideas and interests without the constraints that are intrinsic to being in industry. The availability of the "P41" centers from NIH was another major factor, which provided a mechanism for funding a technology-centered initiative. Other important factors included my own interests in biomedical applications of EPR, the environment at the Medical College of Wisconsin, and the opportunity for Jim and me to connect so that we could pursue this type of research together. The latter was perhaps the most random of the factors, and therefore will be considered first.

My first one-on-one interaction with Jim came several years before the Center was established, during a visit to Varian for a workshop. Previously, I had known Jim only through published materials from Varian and the scientific literature. During one of the workshops, Jim asked to meet with me. He had been developing a technique that he called saturation-transfer, potentially an idea with limited applications. But he was convinced otherwise and wanted to talk to a real biologist to get ideas about how it could be applied usefully to a broader range of important problems. He was disappointed to find out that his concept of biology and mine had little in common. For Jim at that time, the quintessential biological object was a macromolecule – preferably one that would readily crystallize. For me, of course, I thought that single-celled organisms were the most simple biological units. In retrospect, it was perhaps that clear gap in our perception of biology that enabled us, years later, to become the "odd couple" that started the National Biomedical EPR Center in Milwaukee. We met again through meetings that we both attended, especially the International Biophysics Congress in Moscow in 1972 and then, more extensively, at a Gordon Conference that I organized in June, 1974, to consider controversial areas in magnetic resonance, especially in relation to cancer. This was a time when Raymond Damadian was making some very controversial claims about the ability to specifically diagnose the presence of cancer through characteristic changes in NMR relaxation times, and several scientists were espousing theories of carcinogenesis based on free radicals. The premise for having the meeting was simple, and in retrospect, very naive. We would bring together the scientists on both sides of the controversy along with a "truth squad" of well-recognized experts in magnetic resonance theory and instrumentation. By having everyone together at the same time, and with the input of technical experts who had no prior intellectual stake in the controversy and who could detect problems

arising from technical factors, truth and consensus would emerge! Jim was a member of the "truth squad," and during the course of the conference, we had a number of opportunities to get to know each other better.

I had come to MCW in 1969. Initially recruited from Walter Reed Army Hospital as a radiation biologist to provide support for the radiation oncology program that was part of Radiology, I established an EPR facility as the cornerstone of this research. Bill Antholine was the first postdoc recruited, and he remains a cornerstone of an important aspect of the research program of the Center. Shortly before I arrived, MCW had become an independent medical school, leaving Marquette University in order to relieve them of the potential financial burden of a medical school. This provided the medical faculty with an opportunity to develop unfettered by the constraints of the rest of a university. It also had important implications for the future of the EPR Center, because it provided both an entrepreneurial attitude and a minimally organized structure for support services. While the latter had some disadvantages, it also meant that we could establish administrative/support procedures that facilitated our goals.

The impetus for the Center began with a telephone conversation a few months after the Gordon Conference, in which we discussed Jim's desire to channel his increasing interest in biological applications of EPR into full time research. This meant leaving Varian and, ideally, obtaining an appointment to the faculty of a medical school. This push to leave Varian was accompanied by an increasing perception by Jim, which certainly was correct, that Varian was rapidly losing interest in commercial production of EPR spectrometers. After some preliminary discussion that included identification of the Biotechnology Research Resource Program at what is now called NCRR as the most viable funding source, we decided that we should meet in person and do some concrete planning. In December of 1974, near the end of the month, I travelled from Milwaukee to northern California. There, in Jim's office, we laid out plans for the initial funding application. We used our complementary skills and interests to fashion a proposal.

We were aided in this process by a courageous decision by the acting head of Radiology at MCW, Jerry Scanlon. The chairman, Jim Youker, was on sabbatical leave, but had told Jerry that he should act as if he were really in charge. I came to Jerry with the potentially outrageous statement that, prior to the site visit, it was essential that we offer Jim a firm appointment in Radiology. I argued that it was absolutely clear that the proposal would be funded. To our pleasant surprise, he agreed, and committed the department to appoint Jim and guarantee his salary. The Radiology department at that time brought in large amounts of money from clinical practice, which it was allowed to control, allowing Jerry more freedom to make decisions like this.

(This model of medical schools, in which the Dean has no real power, is now a historical footnote!)

Before completing the grant application, we had to find a site for the Center, and in this we were aided by a shared vision that workable space was what was needed, while beauty and modern facilities were luxuries that we could bypass. So our initial site was an old house-like structure (about 100 years old) that had once been used as part of the tuberculosis hospital. The building had had a succession of increasingly less prestigious occupants, finally being abandoned even by the radiological techs as too primitive to be used as a dormitory or office. In addition to space, it had another superb feature: it was symmetrical, so we could bypass the question of who got the better office space. Ours were equally dismal, each consisting of a room that formerly had been an enclosed (sort of) porch. The rest of the building was equally symmetrical and "grand." The upper porches became the conference room and the electronics shop. The many bathrooms (with two exceptions, which were kept functional) became storage areas. There were four large rooms that became the four spectrometer stations. There was initial concern as to whether the floors could handle the weight of the magnets, but with the use of metal plates to spread out the load, it was decided that the structure would hold.

The proposal was funded after a somewhat traumatic site visit. I suspect that it was Helmut Beinert's comments during the site visit that saved the day, making the point that in Jim, we had a priceless asset for the development and application of EPR to biological studies. At the time, Helmut was well known in biologically-oriented EPR circles, through his success in using EPR to study enzymes, particularly iron- and copper-containing enzymes, and related proteins. He was also known as distinguished participant and lecturer at the Varian EPR-workshops, which were very popular.

Helmut had set up a well-equipped and versatile facility at the Enzyme Institute of the University of Wisconsin, which attracted many collaborators from the U.S. and abroad. At the time, he also was a member (later chairman), of the NIH Study Section on Biophysics and Biophysical Chemistry. He held one of the rare Career Awards from NIH. Thus, there were always friends of his in study and site visit groups and his opinion was not without influence. When the Center was funded, quite appropriately, Helmut Beinert was invited to become chairman of the Advisory Committee of the Center.

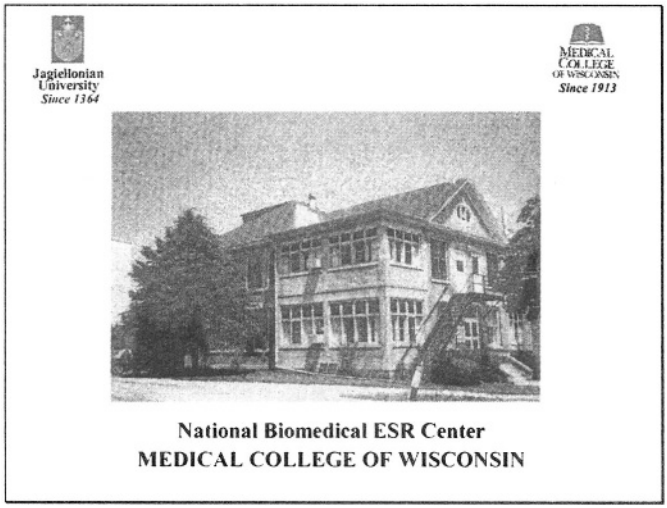

We also were spared having to make a choice as to who would be the P.I., because although it was clear that Jim had the far superior credentials as an EPR spectroscopist, I had the essential credentials for NIH, an M.D. with a biomedical Ph.D.

The award made it possible to appoint a staff scientist. In response to our ad, an outstanding application came from Dr. Christopher C. Felix, together with an enthusiastic letter from his Ph.D. mentor at Washington University, Sam Weissman. Chris knew how to operate every instrument, and also exhibited organizational and administrative skills. He is now Scientific Administrator of the Department of Biophysics.

Success in the early days was aided by a serendipitous connection that we established with the Department of Biophysics of the Jagiellonian University in Krakow. Through a series of events that is not necessary to cover here, we had obtained a pipeline to a rich reservoir of talent, knowledge, and energy that continues to flourish to this day. It was and continues to be a great source of strength to the EPR Center, and also has been a major source of productive collaborators and collaborations for the two subsequent centers that I have established at Illinois and then at Dartmouth. The total number of joint publications with these collaborators, directly involving the Center in Milwaukee, is now about 300!

The Center was initially funded for three years instead of the usual five, probably because of a desire to see how well it would work out. This seemed reasonable, because Jim was in a new environment and we had not worked together previously. The science and the partnership flourished and we were confident that the competing renewal would go well. The site visit for the competing renewal was, in fact, quite successful in terms of both the score and the narrative. But, we did not receive the official notice on the

decision as to the funding. We began contacting the division of NIH that administered the P41 programs. At first they responded with reassurances, but noted that bureaucratic delays were inevitable. Then they stopped receiving or returning our calls, and the funding period was drawing to a close. Finally, we managed to find out what was the problem. The administrators of the program had grossly failed to manage their finances and found themselves facing more financial obligations for ongoing centers than they had funds in their budget. Their solution appeared to be to go into denial, just sitting and hoping that somehow all the problems would go away if they ignored them!

Our response was to obtain as much advice as possible and then initiate an action plan. We rapidly settled on a two-pronged approach. We would go to Washington, where we would attempt to get the funding for the whole P41 program increased (via contacts with the very powerful congressional delegation from Wisconsin) and we also would seek additional sources of direct grant support from NIH for our Center. Remarkably, both parts of the strategy worked. We talked with the powerful congressman who represented the Milwaukee area (Clement J. Zablocki) and members of his staff, as well as the staff of both senators from Wisconsin (Gaylord Nelson and William Proxmire). They were instrumental in getting the appropriation for the biotechnology program increased, so that with a short pause, we received the funding recommended by the site visit team. We also were successful in getting immediate support in the form of an additional grant from NIGMS through the biophysical sciences program. The net result of our labors was a substantial increase in the overall funding for the Center along with a diversification of our support base. We emerged with a much more sophisticated understanding of NIH and Congress, which probably has enhanced both of our careers.

Shortly after the successful efforts for the renewal of the Center funding, two events occurred that had major implications for the future directions of the Center and Jim's career. The first was that I began to explore opportunities for leadership positions in medical schools. This eventually resulted in my departure in 1980 to become Associate Dean at the University of Illinois College of Medicine, providing Jim with the opportunity for full leadership of the Center. I continued to be associated with the Center; for the next two years I continued my research program by commuting every other week from Champagne, Illinois, to Milwaukee, Wisconsin, for three days of intense research on Friday through Sunday. I also served, and still serve, as a member of the advisory committee for the Center.

The second event was the emergence of clinical applications of NMR. Jim and I were asked to consult with the leadership of the Department of Radiology at MCW about potential applications for this new technique.

Although we were initially cautious in our estimates of the clinical potential of NMR, we eventually became convinced of its strong possibilities and facilitated the development of a very strong program at MCW. Most of the development occurred after I left for the University of Illinois. Jim was closely involved and eventually became a leading scientist in this field, especially in fMRI. The leadership role of MCW in clinical NMR (MRI) was facilitated by a close working relationship with General Electric, whose principal NMR manufacturing facility was established in Milwaukee. This also turned out to be an excellent vehicle for enhancing the development of a strong academic radiology program at MCW, aided in no small measure by Jim's increasing involvement in this research. As a consequence, Jim became a leader in the field of MRI, became a prominent member of the leading professional organization in the field (Society for Magnetic Resonance in Medicine, SMRM), and ultimately was a recipient of their highest award for scientific achievement. (I actually preceded Jim in being involved formally in SMRM, being elected to the board of trustees as the sole representative for the EPR side of magnetic resonance when the society was founded. I remained on the board as a member for ten years, including several years as Secretary.) Jim actively participated in some of the scientific aspects that preceded the formation of the SMRM and soon became an important part of the formal structure of the Society.

The ESR Center now has had more than 28 years of continuous funding. Jim and I started, and Jim has continuously improved, a recipe that enabled the National Biomedical EPR Center to be funded for the long term. Its core consists of technology development plus applications, which can be divided into spin labels, free radicals, and metals. These have been pursued in concert with other types of grants that utilize the strong base provided by the Center and help to drive the advancement of the technology.

The program on spin labels began with an independent R01 grant entitled "Nitroxide Radical Spin Label Methods," for which Jim was the P.I. This unambiguously strove to obtain excellent data on the magnetic characteristics of nitroxides and their interactions. The initial draft, however, was certainly not in the NIH style, so I helped to revise it into the expected format. This was just the type of successful complementary interactions that made the partnership successful. The grant was funded on the first try and led a number of excellent publications. It was renewed a number of times (total length, 25 years) with excellent scores, including a prestigious "merit" award that provided 10 years of funding without competitive review. Scientific highlights of this work include: i) establishing the field of spin label oximetry, ii) providing methodological advances, particularly loop gap resonators, that served as a basis for Wayne

Hubbell's development of site-directed spin labelling, iii) continued development of saturation transfer spectroscopy, and iv) multiquantum EPR.

The program on free radicals had two aspects initially: i) the possible role of free radicals in disease, especially cancer, and ii) melanin. While the studies on free radicals in cancer produced a number of papers, most of them served to demonstrate that the role of free radicals in cancer was quite limited. While this was a very important contribution to the field, it also meant that this line of research was inherently self-limiting and so it has not continued as an important aspect of the Center.

On the other hand, the studies on melanin have persisted and developed into important new areas of research that are one of the major strengths of the Center. The initial studies with melanins took advantage of the fact that melanin contains a number of stable free radicals that provide excellent tools for understanding the interactions of this complex molecule, mostly by serving as probe molecules to follow biophysical parameters but also with some important aspects of chemical reactivity. From the beginning, the experiments with melanin involved close collaborations with colleagues from the Jagiellonian University in Krakow, Poland. These studies began with me, but Jim soon became involved and helped to lead the collaboration into other very productive paths. This aspect began shortly after Jim came to Milwaukee, when he struck up a conversation with Tadeusz Sarna (who was the first young visiting scientist from Krakow) that led to a paper in *Science* (Sarna *et al.,* 1976). It was an auspicious beginning. These interactions grew and grew, expanding into many different aspects of the research at the EPR Center as well as at Illinois and Dartmouth. Collaborations with colleagues from Krakow continue to be a very important source of productivity at the Center.

Melanin free radical research initiated by Swartz, Hyde, and Sarna led to several "spin-off research programs on oxy radical spin-trapping and ortho-semiquinone (imine) spin stabilization that flourished under the direction of Roger Sealy. Sealy, Swartz, Felix, Sarna, and Kalyanaraman were largely responsible for applying the "spin-stabilization" technique to detecting ortho-semiquinones in biological and photobiological systems. Spin label oximetry was another area of research that grew out of the melanin photochemistry studies. Ching-San (Monty) Lai, Swartz and Hyde applied this technique to measure oxygen consumption during cell respiration. Thus these three areas, spin-stabilization, spin-trapping, and spin label oximetry, became the "bread and butter" of the biological free radical programs, ranging from photodynamic research to free radical metabolism of xenobiotics, to detection of oxy radicals in ischemia and to reperfusion and other diseases under the direction of Kalyanaraman. Joy Joseph, a synthetic organic chemist, joined the Center in 1984. Syntheses of new spin labels

(N-14 and N-15 labeled) and novel spin traps that form more persistent superoxide adducts, and nitric oxide traps became possible. Neil Hogg, a physical chemist and specialist in nitric oxide and peroxynitrite reaction kinetics, joined the Biophysics Research Institute in 1992. Neil provided expertise in the kinetics of nitric oxide and oxy radical reactions. With the inception of the Free Radical Research Institute in 2000, the ESR Center is enabling new and novel research techniques for clinical researchers in several diseases, including vascular dysfunction, inflammation, cancer, and neurodegeneration.

The program on the EPR of metals began with Bill Antholine. Initially, he was the only one in the Center with a principal background in the EPR of metals, but this area of research has continued to the present and has developed into an important component. Bill's initial studies had a strong connection to the free radical program, both in regard to the interaction of melanin with metal ions and the evaluation of the role of free radicals in cancer. Because the EPR Center budget only covered about 25% of the funding for this area, in the mid 1970s Bill also joined Dave Petering's group, a bioinorganic group across town at the University of Wisconsin-Milwaukee interested in cupric complexes of known antitumor agents. This connection has continued throughout the lifetime of the Center and has resulted in a number of significant contributions to the literature. One of the aims of the first proposal for the EPR Center was development of a high-sensitivity, low-frequency bridge (2-4 GHz, "S-band"). This aim had not been viewed favorably by the initial review group, and funds for it were deleted. Our interest in it persisted, however, because of its potential value for the study of metals, especially when the hyperfine was obscured by "g-strain" due to the superimposition of spectra from metal ions with different orientations, as is common in many preparations of metal-containing biomolecules. Therefore, we persisted with development of a low-frequency spectrometer, and it has been an extremely productive aspect of the Center. It also was the conceptual first step in another important aspect of the Center, multifrequency EPR spectroscopy.

The S-band bridge was designed and personally constructed by Wojciech during his first visit to the Center in 1978. A feature was an octave bandwidth from 2-4 GHz. A rectangular cavity with dimensions 18.5 × 7.2 × 3.4 cm was designed by Jim, resonating in the TE_{104} mode at 3.78 GHz and the TE_{102} mode at 2.62 GHz. Thus, a single sample could be examined at two microwave frequencies (Froncisz *et al.,* 1979). This huge resonator provided the direct motivation for development of loop gap resonators that required a more reasonable amount of sample (Froncisz and Hyde, 1982). Octave bandwidth bridges in the frequency ranges of 0.5 to 1, 1 to 2, 2 to 4

and 4 to 8 GHz were subsequently developed, which served as a unique capability of the Center.

Application of low-field EPR to metal ions resulted in close cooperation with a number of outstanding scientists in the field of metal ions in biology. The group at Illinois, headed by Linn Belford, had a leading role in the development and application of simulation programs that exploited the power of low-frequency EPR. In 1982, Froncisz and Hyde published the first loop gap resonator paper and a paper on the frequency dependence of line widths for cupric complexes. These papers provided the basis for applications, not only for cupric complexes of known antitumor agents, but also for cupric sites, first in low molecular weight cupric complexes and then in enzymes (see chapter by Antholine). John Pilbrow of Monash University, Australia, spent a year's sabbatical with Jim Hyde. This was a wonderful year, in which everyone concentrated on studying copper EPR. Because of the availability of low-frequency spectrometers at the Center, Ricardo Basosi of the University of Siena spent a sabbatical year with Jim Hyde and was frequently heard inquiring in a loud voice "where is Billlll?" Papers concerned with line shapes and second order shifts of lines from cupric complexes as a function of frequency followed (see ch. 13, this volume).

Then Helmut Beinert retired from the University of Wisconsin. Helmut had the ambiguous luck to be born in late 1913, which spared him from being drafted into Hitler's army 20 years later, but, according to Wisconsin law, also prevented him from taking advantage of a new law that allowed professors to stay in office beyond age 70, if their birthday was after December 1913. Betty Sue Masters, who was then chair of the Biochemistry Department at MCW and who had collaborated with Helmut, came up with the idea of attracting him to the College. With Jim's support, she persuaded the Dean to invite Helmut to join the College as a Distinguished Scholar in Residence. In 1985, Helmut became a member of the MCW Biochemistry Department along with his trusted collaborator of many years, Dr. Mary Claire Kennedy. In 1989, when the new building that was to house the EPR Center was completed, Jim offered Helmut and Mary Claire generous space in the new facility. In return, the two brought biochemical know-how, experience, and equipment for anaerobic and rapid freezing techniques, spectrophotometry, or microanalyses, to the Center. Helmut returned to Madison in 1994.

Helmut's arrival at MCW was the beginning of the work at the Center on low-temperature EPR of metals, particularly the Fe-S cluster signal in aconitase. Helmut brought Peter Kroneck of the University of Konstanz, Germany, to the Center. S-band (3.4 GHz) and C-band (4.5 GHz) EPR were used to support a model based on a mixed valence [Cu (1.5+)...Cu (1.5+)] EPR signal in nitrous oxide reductase and in cytochrome *c* oxidase (see

chapter by Antholine), which resulted in recognition of a new type of copper in enzymes, i.e. purple copper. Just as envisioned by Jim, the base for this work was provided by low-frequency EPR and the loop gap resonator.

The EPR Center has always employed professional electrical engineers for instrument development, since it was felt that a high degree of reliability was required for multi-user instruments. Jorg E. Forrer, on leave from the ETH in Zurich, spent three years at the Center in the early days designing a high speed digital receiver for use in saturation recovery EPR. For many years, this was the finest instrument in the world for this purpose. It enabled Jim's student, J. J. Yin, to develop the foundation for saturation recovery of spin labels. Jorg hired Joseph J. Ratke to assist him, and Joe in turn hired Theodore G. Camenisch. These latter two engineers have continued to serve the Center for almost a quarter of a century. Their contributions are particularly evident in the chapter on digital detection (vol. 24, ch. 7). Engineers from Poland made substantial contributions, including numerous papers on loop gap resonators co-authored by Tadeusz Oles, a paper on a novel AFC by Hyde and Gajdzinski (1988), and a paper by Lesniewski and Hyde on a 19 GHz bridge (1990). Robert A. Strangeway pursued both an M.S. and Ph.D. at Marquette University in Milwaukee, with Jim serving as co-advisor. Bob is currently Professor of Electrical Engineering at Milwaukee School of Engineering (MSOE). His work with Jim, which continues on a part time basis, provides a foundation for an understanding of microwave phase noise in EPR. Recently Richard Mett, also on the faculty of MSOE, has helped to develop a program of research at the Center based on finite element modeling of electromagnetic fields in EPR resonators in the presence of a sample. Jim attributes his success in EPR instrumentation in considerable measure to the engineers with whom he has worked.

Early on, Jim became interested in patent activity. He was awarded 14 United States Patents while at Varian, and the total has since increased to 31. Of these, nine involve cavity resonators, five involve loop gap resonators, and six are related to resonators for MRI. Thus, about two-thirds of his patents involve sample resonators for magnetic resonance, and innovation in this area has been a focus throughout his career.

It has long been apparent that resonators can be divided into two categories – distributed circuit such as cavities, where the inductance and capacitance of the structure are not readily apparent and it is more convenient to speak of microwave fields, and lumped circuit resonators, otherwise known as RLC (resistance, inductance, and capacitance) resonant circuits. The wavelength is about the same as the cavity dimensions for distributed circuits, and is much larger than the circuit dimensions for RLC resonators. The discovery with Wojciech of loop gap resonators was seminal – structures for EPR usage that were intermediate between the

classical limits of lumped and distributed circuit resonators (see ch. 2 in vol. 24 by Rinard and Eaton). In the earliest days of MRI, Jim realized that the ratio of the MRI sample size (for example, a person) to the wavelength was about the same as for an EPR loop gap resonator. Microwave EPR structures should, in principle, scale to the lower frequency and larger sample size of MRI. This was the enabling idea that led to the MRI resonator patents, numerous papers, and the first grant at MCW in MRI.

The RF coil development program at MCW expanded into gradient coils, which led to expertise in the high-speed imaging technique known as echo planar imaging, EPI, which led to functional magnetic resonance imaging, fMRI. One of the earliest publications in fMRI was co-authored by Jim, and initiatives on cognition and the human brain have continued to expand at MCW. Jim directs a Program Project on fMRI of the brain funded by the National Institute of Mental Health. In recent years, he has devoted his time about 50:50 between EPR and fMRI. There have been several crossovers in technology between these fields in addition to loop gap resonators. Perhaps the most important was the transfer of digital detection methods from MRI to EPR, which is the subject ch. 7 in vol. 24. Analogies between the microwave resonators of EPR and the RF resonators of MRI continue to be identified. Other analogies, Jim reports, have been made between these fields in management of data storage and in signal processing.

The external funding and prestige of the Center made it a "star" at MCW from its initial funding. This status was continuously enhanced by success in getting other grants funded. This has resulted in attracting unusually strong institutional support, eventually including baseline financial support for Jim, in part to be symmetrical with that already provided to me. Another important aspect in the growth of the Center was the development of a graduate program that became a real academic strength for MCW. This, in turn, brought excellent students into the Center and expanded the contacts of the faculty of the Center as well as the rest of MCW. Under Jim's leadership, the graduate initiative eventually became a formal, separate Graduate Program in Biophysics at MCW. The Biophysics Research Institute achieved department status in early 2003. These are unusual and important developments that have enhanced the research processes and the reputation of the Center. While some of these were put in motion when I was at MCW, development and institutionalization of the graduate program and the recognition as a department were accomplished after my departure.

In summary, Jim's role in the success of the National Biomedical EPR Center and its role in the success of Jim Hyde are inexorably linked. The interaction has clearly been synergistic, and many individuals and programs have benefited enormously from the events that have occurred at MCW related to Jim's presence.

4. REFERENCES

Ehrenberg, A., Eriksson, L. E. G., and Hyde, J. S. (1968). Electron-nuclear double resonance from flavin free radicals in NADPH dehydrogenase ("old yellow enzyme"), *Biochim. Biophys. Acta*. **167**, 482-484.

Froncisz, W. and Hyde, J. S. (1982). The loop-gap resonator: a new microwave lumped circuit esr sample structure. *J. Magn. Reson.* **47**, 515-521.

Froncisz, W., Scholes, C. P., Hyde, J. S., Wei, Y.-H., King, T. E., Shaw, R. W., and Beinert, H. (1979). Hyperfine structure resolved by 2 to 4 GHz EPR of Cytochrome *c* Oxidase. *J. Biol. Chem.* **254**, 7482-7484.

Hyde, J.S. (1960a). Magnetic resonance and rapid passage in irradiated LiF, *Phys. Rev.* **119**, 1483-1492.

Hyde, J.S. (1960b). Saturation of the magnetic resonance absorption in dilute inhomogenously broadened systems, *Phys. Rev.* **119**, 1492-1495.

Hyde, J. S. (1966). Electron nuclear double resonance using an intense nuclear radio frequency field, *Proceedings: Magn. Reson. in Biol. Systems* 2nd International Conference, 63-84.

Hyde, J.S. (1998). EPR at Varian: 1954-1974, in *Foundations of Modern EPR* (Book), World Scientific Publishing, Singapore/New Jersey/London. S. Eaton, G. Eaton, and K. Salikhov (Eds.), 695-716.

Hyde, J. S. and Dalton, L. (1972). Very slowly tumbling spin labels: adiabatic rapid passage, *Chem. Phys. Lett.* **16**, 568-572.

Hyde, J. S. and Maki, A. H. (1964). Electron nuclear double resonance (E.N.D.O.R.) of a free radical in solution, *J. Chem. Phys.* **40**, 3117-3118.

Hyde, J.S., Eriksson, L.E.G., and Ehrenberg, A. (1970). EPR relaxation of slowly moving flavin radicals: "anomalous" saturation, *Biochim. Biophys. Acta* **222**, 688-692.

Hyde, J. S. and Gajdzinski, J. (1988). EPR automatic frequency control circuit with field effect transistor (FET) microwave amplification. *Rev. Sci. Instrum.* **59,** 1352-1356.

Hyde, J. S., Rist, G. H., and Eriksson, L. E. G. (1968). ENDOR of methyl, matrix and α protons in amorphous and polycrystalline matrices, *J. Phys. Chem.* **72**, 4269-4276.

Lesniewski, P. and Hyde, J. S. (1990). Phase noise reduction of a 19 GHz veractor-tuned Gunn oscillator for electron paramagnetic resonance spectroscopy. *Rev. Sci. Instrum.* **61,** 2248-2250.

Sarna, T., Hyde, J.S., and Swartz, H.M. (1976). Ion-exchange in melanin: and electron spin resonance study with lanthanide probes, *Science* **192**, 1132-1134.

Thomas, D. D., Seidel, J. C., Hyde, J. S., and Gergely, J. (1975). Motion of subfragment-1 in myosin and its supramolecular complexes: saturation transfer electron paramagnetic resonance, *Proc. Natl. Acad. Sci. USA* **72**,1729-1733.

II

Biological Free Radicals and Medicine

Chapter 3

Free Radicals and Medicine

[1]H.M. Swartz, [2]R. P. Mason, [3]N. Hogg, [3]B. Kalyanaraman, [4]T. Sarna, [4]P.M. Plonka, [4]M. Zareb, [5]P. L. Gutierrez and [6]L. J. Berliner

[1]Dartmouth Medical School, Hanover, NH USA; [2]NIH/NIEHS, Research Triangle Park, NC, USA; [3]Medical College of Wisconsin, Milwaukee, WI USA; [4]Jagiellonian University, Krakow, Poland; [5]Greenebaum Cancer Center, University of Maryland Medical School, Baltimore, MD USA; [6]University of Denver, Denver, CO USA

Abstract: EPR has been employed in attempts to understand the basis of specific pathophysiologies in which free radicals have a postulated role. Examples described include pulmonary free radical damage, free radicals and sickle cell disease, free radicals in amyotrophic lateral sclerosis, melanin and free radicals and the potential role of oxidative stress in the induction of cancer. The final section of the chapter describes the use of NMR as the spectroscopic measure of spin-trapped radicals, after they have reacted further to form diamagnetic species.

1. INTRODUCTION

This chapter is a joint effort that aims to provide an illustrative view of the current understanding of the relationship between free radicals and disease. This is a vast subject and while EPR has an important role in its study, the role of EPR is far from dominant. Therefore, instead of trying to provide a comprehensive review of the role of free radicals in medicine, we have chosen to provide an overview through some general remarks, followed by more detailed considerations of several illustrative examples in which EPR has been employed in attempts to understand the basis of specific pathophysiologies in which free radicals have a postulated role. The first author has drafted the overview section and the primary author(s) for each specific section are indicated in those sections. The terms EPR and ESR are used in accordance with the preference of the authors of each section.

1.1 Theoretical Considerations for Expecting Links Between Free Radicals and Medicine

The theoretical basis for expecting free radicals to be related to disease has evolved over the years. Initially the hypothesized links between free radicals and disease were based on loosely reasoned considerations that because free radicals are so reactive, and cells are so well organized, that the occurrence of free radicals *in vivo* would likely lead to disease. This type of reasoning became somewhat more focused on the role of free radicals in cancer (Swartz, 1979). The current status of concepts of the role of free radicals in cancer is illustrated in the section drafted by Gutierrez.

The next phase of theories potentially linking free radicals and disease was based on the specific potential of free radicals to initiate strong oxidizing reactions. The fundamental rationale comes from the fact that living organisms include many highly oxidizable components, yet usually require the presence of oxygen in order to carry out basic metabolic functions. Interest in these aspects became greatly increased with the discovery of the natural occurrence of large amounts of superoxide dismutases in both the blood and cells. Subsequently a role of free radicals in almost every conceivable disease has been proposed on various theoretical grounds related to the potential for uncontrolled oxidations. Such theories have general support by observations that the extent of many pathologies can be modified by changing the availability of superoxide (especially by modifying the activity of superoxide dismutases) or the strongly oxidizing functions of macrophages. But the observations did not provide rigorous proof of causality, and the chemical reactions through which the superoxide caused the observed effects has remained obscure.

Until very recently, it has been assumed that the damage caused by free radicals occurred because of direct reactions with key molecules, damaging sufficient numbers of the key molecules to alter function. This has been puzzling when looked at critically, because when considering the specific free radicals that are expected to be involved, it has been difficult to construct plausible reaction schemes that would account for the observed effects. The hydroxyl radical and closely related species (e.g. the perferyl radical), are so reactive that they must be generated on or immediately adjacent to the target molecules, because their diffusion distance is usually the distance to the next molecule. Therefore it would take very special circumstances for such radicals to be important in a disease. On the other hand, the superoxide radical is so unreactive that it is difficult to understand how it can lead to the very profound effects that clearly are associated with excess or inappropriate production of superoxide.

Because of recent advances in molecular biology, however, it now seems reasonable to expect that within the next few years we will have, finally, an adequate theoretical basis for understanding the roles of free radicals in biology. Then it will be much more feasible to develop methods to control or ameliorate the undesirable processes that they can cause.

The keys to the potential of much more effective progress have been the discoveries that oxidizing species and the amount of oxygen can have profound effects on gene activation and cell signaling. This has, finally, provided a potentially satisfactory mechanism for understanding the association of free radicals (and other oxidizing species) with pathophysiology. It has become clear that there are a large number of activators and modulators of genes and cytokines that respond to the presence of oxidizing species. Currently the understanding of the role of free radicals and other oxidizing species in cell signaling is still at an early stage, but rapid progress is likely as the cascades of effectors that are activated or inactivated by the amount of oxidizing species and/or oxygen are delineated. It seems likely that in many cases the origin of the free radicals will be from inappropriate responses of the naturally occurring defense systems, mediated through cell signaling. The old paradigm of deleterious actions of free radicals occurring through direct damage from the free radicals is likely to be applicable only in exceptional circumstances (e.g. ionizing radiation). Thus the experimental approaches in which roles of free radicals are likely to be important aspects for understanding probably will be in the arena of molecular biology, and the role of EPR in these studies may be critical. This is perhaps even more exciting than the vague postulates of free radicals being "bad" and leading to disease, because the responses of cells to the presence of oxidizing species are probably very fundamental properties of cellular systems. These mechanisms have enabled life to evolve in an environment with an abundant potential for deleterious oxidations, due to an atmosphere that is 20% oxygen. With this understanding, the value of EPR and related techniques to follow free radical reactions is likely to increase, as the techniques are applied in experiments that are more appropriately framed.

It is not surprising then, that recently theories suggesting links between free radicals and pathophysiological, physiological, and therapeutic processes have become more specific, linked to specific intermediates and/or specific cell signaling pathways. These are areas where it seems more likely that important and useful links will be found. EPR is likely to have an important role in elucidating what already has been shown to be a very complex set of processes.

1.2 Conceptual Approaches for EPR Experiments on Links Between Free Radicals and Medicine

Initially investigators sought evidence for the role of free radicals in disease by direct observations with EPR, reasoning that there should be increased amounts of free radicals in the related diseases. In general increases were not found, although in a few cases in studies of cancer some unexpected EPR signals were seen (Swartz, 1986). As noted in the review, more thorough consideration of this approach leads to the conclusion that even if free radicals are involved, there are seldom specific reasons for there to be increased amounts of free radicals that can be detected by EPR. The role of free radicals could be critical but transient. And even if there was a continuing role of free radicals, the more reactive that they are, the less likely it would be that they could be detected directly by conventional EPR spectroscopy. Hence it is not surprising that there has been little concrete evidence for a general link between the amount of free radicals and pathological or physiological processes.

Subsequently EPR has been used more specifically to detect free radical intermediates associated with a wide range of physiological, pathophysiological, and therapeutic processes that are potentially related to medicine. These studies have ranged from serially observing tissues in which tumors are expected to development in models of carcinogenesis, to looking for free radical intermediates in drugs. The more specific the hypothesis and the rationale for anticipating the occurrence of free radicals, the more likely it is that such approaches will be productive. In virtually all situations, it is unlikely that measurements of free radicals will be sufficient to test a hypothesis or reach a firm conclusion pertinent to a disease or its treatment. Appropriate additional studies, including tests of factors that may affect the amount or type of free radicals usually will be needed. The later sections of this chapter provide some illustrative examples of studies in which the role of free radicals in disease have been studied under appropriately rigorous conditions.

1.2.1 Experimental approaches for studying links between free radicals and medicine in experimental animals

A wide and effective range of approaches have been used for studies in animal models relevant to clinical medicine. The available approaches are quite wide because unlike the situation in human subjects, there is much less concern about the long term effects of materials that are administered to carry out the studies and/or the invasiveness of the approach. Recently, as described in much more detail in ch. 9 on *in vivo* studies it has become

possible to carry out studies in intact animals as well as in model systems and cells.

Sometimes it is possible to have direct detection of free radicals, if they occur in high enough concentrations and have sufficient stability. This approach is especially applicable when substantial amounts of a substance are administered, such as with therapeutic drugs or toxins. The occurrence of free radical intermediates of drugs is among the most likely situations where direct observations with EPR are likely to be productive. Sometimes it may be possible to have sufficient amounts of radicals to observe them directly in aqueous systems under physiological conditions, including normal temperatures for the organism (Fujii et al., 1994; Mader et al., 1995). Often this will not provide sufficient sensitivity and rapid freezing will be required. While the use of frozen samples often results in the loss of resolvable structure in the EPR spectrum, the ability to have a much larger sample (because of the much lower dielectric loss in ice, the sample volume can be much larger) and the enhanced sensitivity of lower temperatures usually result in very significant increases in sensitivity versus aqueous samples.

For most studies, however, it is likely that there will be a need to employ spin trapping or other techniques to observe the free radicals. Several different experimental approaches using spin traps have been successfully employed with cells and experimental animals including:

a) *use of model systems (in vitro).* This is the most widely used approach. The concentration of spin traps can be made as high as needed when live organisms are not used. When the studies are carried out in cell systems careful attention has to be paid to effects of the spin traps on the cells (toxicity) and effects of the cells on the spin adducts (stability of the adduct) (Khan et al., 2003).
b) *ex vivo approaches in which the trapping occurs in vivo and samples are obtained for study in vitro.* This approach has been used productively, especially by Mason and colleagues (ch. 5). It involves the administration of the spin trap to the animal and then obtaining samples through biopsies or removal of biological fluids. It can provide excellent evidence for the occurrence of free radical reactions *in vivo,* but considerable care is needed to avoid artifacts or misleading results. The potential problems include loss of spin adducts during the extraction steps and generation of spin adducts during the processing of the samples.
c) *direct spin trapping in vivo with measurements made directly in the organism under physiological conditions.* In principle this is a very desirable approach, providing direct evidence without intervening processing steps and, also, the potential to provide kinetic data under physiological conditions. This approach, however, has lower sensitivity than *ex vivo* methods, because the latter can study the samples at X-band

or even higher frequencies, while direct *in vivo* studies require the use of L-band or even lower frequencies, with the consequent power sensitivity of such frequencies. Both *ex vivo* and direct *in vivo* approaches share the problem of potential instability of the spin adducts, which often are converted to non-paramagnetic products in the presence of functioning cells (Khan and Swartz, 2002; Timmins et al., 1999).

d) *spin trapping using combined NMR and EPR.* This is a new approach whose utility has not been fully evaluated. In principle it provides a means to use the widespread availability of *in vivo* NMR, and that is very attractive. The section by Berliner in this chapter provides an excellent summary of this approach.

e) *indirect assays based on reactions of free radicals with nitroxides or other paramagnetic labels.* This has been especially advocated by Utsumi's group, using the rate of disappearance of nitroxides. While in principle this could be a very productive approach, there are some potential fundamental limitations because of the non-specificity of the observed parameter.

1.3 Experimental Approaches for Studying Links Between Free Radicals and Medicine in Human Subjects

In the near future it may be possible to develop techniques for studies in human subjects. The potential limiting factors for such studies include the technical problems of carrying out EPR measurements in human subjects and, for techniques that involve the administration of spin traps or other substances, the complex and difficult process for obtaining permission to administer substances to human subjects (Swartz, 2003). These also are discussed in some detail in ch. 9. Here we will briefly summarize those aspects that are especially pertinent to measurements of free radicals in human subjects.

The technical problems for using EPR in human subjects revolve around accommodating the human body in the system and obtaining sufficient sensitivity. The geometric constraints can readily be overcome and at least one specifically designed whole body clinical EPR spectrometer already is in operation. This is at Dartmouth where a conventional but large-sized permanent magnet has been specifically built by Sumitomo Special Metals for the facility. It provides a 400 gauss field with a gap that can accommodate human subjects on a cart, or sitting or standing within the gap of the magnet.

For studies in which the direct observable is a free radical form of a drug, etc., the only potential limitations are the sensitivity that can be achieved and

the pertinence of the radical to the processes under investigation. Unfortunately, there appears to be a very limited number of drugs or toxins that generate sufficient amounts of free radicals to be observed directly.

All other approaches, e.g. spin traps, interactions with nitroxides, require the administration of a compound. This adds the requirement that the administered compound has been demonstrated to be safe for use in humans. This is potentially a very limiting aspect, because of the time and expense involved in obtaining the data for achieving such clearance.

There are a few drugs that may be of use that already have been cleared for use in human subjects. In particular, one of the usual EPR responsive trapping agents for nitric oxide, the dithiocarbamates, have been approved for use in humans as chelators of potentially toxic metals and as the alcohol avoidance agent ("antabuse").

There are some possibilities for the approval of some spin trapping agents and nitroxides as the result of initiatives to use them as therapeutic agents. The nitrone spin traps are being evaluated for use in humans because they appear to have potential therapeutic benefits, probably through their effects on the induction of nitric oxide synthesizing enzymes. The nitroxides have been put forth as potential therapeutic agents for the dismutation of superoxide and/or as protective gents against damage by ionizing radiation. If these initiatives result in the approval of nitrones or nitroxides for use in humans, then it would be much more feasible to obtaining permission to use them as spin trapping agents in humans.

2. PULMONARY FREE RADICAL DAMAGE (R. MASON)

2.1 Chemical Toxicants

2.1.1 Paraquat

The herbicide paraquat serves as a model for investigating free radical-mediated pulmonary toxicity because it has no known metabolism other than the free radical metabolism. In microsomal systems, the enzymatic reduction of paraquat to its cation radical is catalyzed by the flavoenzyme NADPH-cytochrome P-450 reductase. The paraquat radical is stable in the absence of oxygen. In the presence of oxygen, paraquat is re-formed, and superoxide is generated in a catalytic fashion with no net change occurring to the paraquat molecule. This process has been termed futile metabolism (Mason 1979, 1982). The mechanism of paraquat poisoning in man is a superoxide-mediated toxicity that is completely analogous to the herbicide mode of

action. The lung is the site of injury by paraquat because it accumulates there (Rose and Smith, 1977). The energy-dependent uptake of paraquat and the subsequent free radical formation are cell-specific. Paraquat free radical formation occurs with clara cells and alveolar type 2 cells, but not with alveolar macrophages (Horton et al., 1986). Diquat, morfamquat, and other bipyridylium compounds do not affect the lung as seriously, but these compounds do cause liver damage and are reduced by rat hepatocytes to their respective radical cations (DeGray et al., 1991).

2.1.2 Nitrofurantoin

In early investigations of the mechanism of rat hepatic mitochondria! and microsomal nitroreductase (Mason and Holtzman, 1975 a), ESR and kinetic evidence demonstrated that the first step in these nitroreductase reactions is the transfer of a single electron to nitro compounds to give the corresponding nitro anion free radical. For instance, in the case of nitrofurantoin, the interaction of the free electron with the nitrogens and protons gives a complex hyperfine pattern that has been analyzed to demonstrate that the free radical is simply nitrofurantoin plus an extra electron (Rao et al., 1987, 1988a). Nitrofurantoin increased the NADPH-supported oxygen consumption by pulmonary microsomes sevenfold over the basal rate, and this stimulation was partially reversed by superoxide dismutase. The presence of superoxide anion radical strongly suggested reductase under aerobic conditions (Mason and Holtzman, 1975b). As expected, the disproportionation of hydrogen peroxide by catalase also decreased the nitrofurantoin-stimulated oxygen uptake.

The effect of superoxide dismutase and catalase on the nitrofurantoin-stimulated oxygen consumption by microsomes is consistent with the formation of nitroaromatic anion radicals under aerobic conditions and with the rapid air oxidation of these radical intermediates, which results in the catalytic generation of superoxide and the well-known oxygen inhibition of nitroreductases. The nitrofurantoin-catalyzed reduction of oxygen to superoxide and the hydrogen peroxide that forms from this superoxide may be responsible for some of the toxic manifestations that occur during nitrofurantoin therapy (Mason and Holtzman, 1975b). For instance, the occasional cases of pulmonary edema and fibrosis caused by nitrofurantoin therapy are similar to the effects of paraquat poisoning. Subsequent work with animal models supported this proposal (Peterson et al., 1982; Boyd et al., 1979). Boyd and coworkers (1979) have shown that the acute toxicity of nitrofurantoin is markedly increased by vitamin E deficiency, an oxygen-enriched atmosphere, or a diet high in highly polyunsaturated fats. Further studies by Peterson and colleagues (1982) showed that decreasing the

activity of selenium-dependent glutathinone peroxidase in 8-day-old chicks enhanced the acute toxicity of nitrofurantoin.

2.1.3 Smoke-Mediated Free Radicals

Both cigarette smoke and the smoke from burning buildings form free radicals even after combustion stops. Both the *in vitro* effects of this smoke and the use of ESR in these studies have been extensively reviewed (Pryor 1992). Smoke inhalation by rabbits formed unidentified PBN radical adducts in plasma (Yamaguchi et al., 1992; Murphy et al., 1991). Cotton smoke formed radical adduct concentrations similar to those caused by 2.5 atm of oxygen (Yamaguchi et al., 1992). Formation of a burst of PBN radical adducts by a brief exposure to cigarette smoke required pretreatment by bacterial endotoxin (Murphy et al., 1991).

2.1.4 Ozone

The spin trapping technique detected free radicals produced *in vivo* by ozone exposure (Kennedy et al., 1992). When rats were exposed for 2 hr to either 0, 0.5, 1.0, 1.5, or 2.0 ppm ozone with 8% CO_2 to increase their respiratory rate, a six-line 4-POBN/radical spin adduct signal was detected by ESR in lipid extracts from lungs of rats treated with 4-POBN. Only a weak signal was observed from rats exposed to 0 ppm ozone (air with CO_2 only). A correlation was observed between the radical adduct concentration and the lung weight/body weight ratio, an index of lung damage. These results demonstrate that ozone induces the production of free radicals in rat lungs during inhalation exposure and that radical production may be involved in the induction of pulmonary toxicity by ozone.

2.1.5 Asbestos

It has been postulated that the *in vivo* toxicity of asbestos results from its catalysis of free radical generation. We examined *in vivo* radical production using ESR and the spin trap 4-POBN; 180 day-old rats were intratracheally instilled with either 500 μg crocidolite asbestos or saline. Twenty-four hours later, histologic examination revealed a neutrophilic inflammatory response. ESR spectroscopy of the chloroform extract from lungs exposed to asbestos gave a spectrum consistent with a carbon-centered radical adduct, while those spectra from lungs instilled with saline revealed a much weaker signal. This same radical formation persisted and, even one month after instillation, could be detected in the lungs of rats exposed to asbestos.

2.1.6 Oil Fly Ash Particles

Exposure to air pollution particles can be associated with increased human morbidity and mortality. Lung exposure to oil fly ash (an emission source air pollution particle) causes *in vivo* free radical production as evidenced by ESR analysis of chloroform extract from lungs of animals exposed to oil fly ash, which gave a spectrum consistent with a carbon-centered radical adduct (Kadiiska et al., 1997). This signal was also reproduced by instilling animals with the soluble fraction of the oil fly ash, which contains soluble metal compounds. The same signal was observed after instillation of either a mixture of vanadium, nickel, and iron sulfates or $VOSO_4$ alone, metals which are prevalent in oil fly ash. Therefore, this generation of free radicals appears to be associated with the soluble metals in the oil fly ash.

2.2 Biological Toxins

2.2.1 Lipopolysaccharide

Intratracheal instillation of lipopolysaccharides (LPS) activates alveolar macrophages and infiltration of neutrophils, causing lung injury/acute respiratory distress syndrome. Free radicals are a special focus as the final causative molecules in the pathogenesis of lung injury caused by LPS. *In vivo* free radical production by rats was detected after intratracheal instillation of LPS. ESR spectroscopy of lipid extract from lungs exposed to LPS for 6 h gave a spectrum consistent with that of a POBN/carbon-centered radical adduct tentatively assigned as a product of lipid peroxidation. To further investigate the mechanism of LPS-initiated free radical generation, rats were pretreated with the phagocytic toxicant $GdCl_3$, which significantly decreased the production of radical adducts with a corresponding decrease in neutrophil infiltration. NADPH oxidase knockout mice completely blocked phagocyte-mediated, ESR-detectable radical production in this model of acute lung injury, demonstrating that superoxide formation by NADPH oxidase is the root cause of this free radical formation.

3. FREE RADICALS AND SICKLE CELL DISEASE (N. HOGG)

There has been a long association between sickle-cell disease and the formation of oxidants from the partial reduction of molecular oxygen. In general this association has focused on either the deposition of redox active

iron as a mediator of biomolecule oxidation, or on accelerated autoxidation of HbS as opposed to HbA, leading to enhanced superoxide formation. In both cases increased oxidative stress in sickle cell disease results in the oxidation of biological macromolecules which contributes to the pathogenesis of the disease (Hebbel et al., 1982; Klings et al., 2001; Natta et al., 1992; Repka and Hebbel, 1991; Schacter, 1986; Sheng et al., 1998) of free radicals and oxidants in the control of vascular function (as opposed to oxidative damage).

Endothelial dysfunction, which is most often indicated by loss of endothelial-dependent relaxation, can be regarded as a disease of altered free radical balance. For example the scavenging of nitric oxide by superoxide has long been thought to be contributing factor to hypertension and it is becoming apparent that this same mechanism may be responsible for altered endothelial signaling in atherosclerosis, diabetes, and other cardiovascular pathologies, and may also be a control mechanism of normal cardiovascular responses such as the modulating effects of shear stress on vessel relaxation. Recently two nitric oxide scavengers have been identified in the lumen of patients with sickle cell disease.

The first of these, xanthine oxidase, has long been understood to be a physiological source of superoxide, however, the recently discovered elevation of vessel wall xanthine oxdase may be an important component of endothelial dysfunction in sickle cell disease. Aslan et al. (2001) have demonstrated that liver injury in both sickle-cell patients and a mouse sickle cell model can result in the release of xanthine oxidase into the blood stream. Accumulation and/or uptake of this enzyme by the vascular endothelium can lead to enhanced superoxide production and impairment of endothelium-dependent relaxation.

Another molecule that has only recently been implicated as a nitric oxide scavenger in sickle cell disease is plasma hemoglobin. A major paradox of nitric oxide function has been the presence of high (10 mM) concentrations of hemoglobin in the vascular lumen. Calculations have clearly shown that this level of hemoglobin should preclude nitric oxide radical from having any appreciable steady-state concentration in the vessel wall. This paradox has been recently addressed by the discovery that compartmentalized hemoglobin reacts with nitric oxide at significantly slower rates (up to 1000 times) than cell-free hemoglobin. The effects of increased levels of cell-free hemoglobin on vascular function have only recently been realized. As recently demonstrated by Reiter et al. (2002), the levels of plasma cell free hemoglobin are substantially elevated in patients with sickle cell disease, averaging 4 μM and as high as 20 μM. The hemoglobin appears to be in the ferrous form as the plasma from sickle cell patients exhibits a greater ability to scavenged nitric oxide. Measurements of blood flow in the forearm

indicate that plasma hemoglobin can severely limit nitric oxide-dependent vasodilation. An important corollary of these studies is that pharmacologically administered nitric oxide (for example by inhalation) can act to 'scavenge the scavenger' by oxidizing plasma hemoglobin to its met or ferric (Fe^{III}) derivative. Ferric hemoglobin then has limited ability to scavenge peripheral nitric oxide, thus potentially restoring NO bioavailablility. The level of methemoglobin in plasma (as demonstrated by electron paramagnetic resonance spectroscopy) is increased when sickle-cell patients inhale nitric oxide, together with the level of nitrosylhemoglobin (Reiter et al., 2002). Cell-free hemoglobin circulating through the pulmonary circulation is a much more amenable target for nitric oxide therapy than guanylyl cyclase and it may be the case that the effects of nitric oxide inhalation in other clinical conditions are at least in part mediated through plasma hemoglobin oxidation. It is interesting to speculate that the ability of hydroxyurea, recently identified as an NO congener, to relieve sickle cell disease may also be at least in part related to its ability to oxidize hemoglobin in the extracellular compartment (Glover et al., 1999; Huang et al., 2002; Jiang et al., 1997).

4. FREE RADICALS IN MOTOR NEURON DISEASE OR AMYOTROPHIC LATERAL SCLEROSIS (ALS) (B. KALYANARAMAN)

4.1 Motor Neuron Disease

Motor neuron disease or ALS (also known as Lou Gehrig's disease) is a fatal illness that progressively causes the degeneration of the nerve cells that control the muscles, paralyzing the body but sparing the mind (Price et al., 1994). Approximately 10% of ALS cases are familial with the rest being sporadic. The genetic defect in familial ALS (FALS) has now been linked to *Sod 1,* the gene encoding the cytosolic Cu, Zn, superoxide dismutase (SOD1) (Brown, 1995, 1998). At present, approximately 70 or so missense FALS mutations in *Sod 1* at 26 different amino acid positions have been identified. The mechanisms by which FALS-linked *Sod 1* mutants cause selective degeneration of motor neurons of the spinal cord, brain stem, and cerebral cortex remain unclear (Brown, 1995, 1998). Of the various mechanisms proposed, the hypothesis suggesting that the FALS-linked mutants acquired a cytotoxic "gain-in-function" has found increased acceptance (Brown, 1998). The "gain-in-function" of *Sod 1* mutants had been postulated to arise from an increased peroxidase or hydroxyl radical activity. The EPR technique has played a key role in identifying the

structure of the oxidant formed from the peroxidase activity of SOD 1 (Singh et al., 1998).

4.2 Bicarbonate-dependent Increased Peroxidase Activity -- Role of Carbonate Anion Radical

Nearly 30 years ago, Hodgson and Fridovich demonstrated that the copper-bound hydroxyl radical ($SOD\text{-}Cu_2^{+}\text{-}{}^{\cdot}OH$), a putative oxidant generated in the reaction between SOD1 and H_2O_2, could oxidize several anionic ligands (e. g., formate, azide, and nitrite anion) (Hodgson and Fridovich, 1975). In addition to these anions, several other molecules (which are too bulky to find access to the active site of Cu, Zn and SOD) were also oxidized. These experiments were performed in a bicarbonate buffer.

The x-ray crystal structure of SOD1 indicates that access to the active site is via a narrow channel that restricts the entry of large molecules. However, a relatively small anion like HCO_3^- could reach the active site of SOD1 and undergo oxidation to the carbonate anion radical ($CO_3^{\cdot-}$) by $SOD\text{-}Cu^{2+}\text{-}{}^{\cdot}OH$. $CO_3^{\cdot-}$ is a diffusible oxidant that could leave the active site and cause oxidation of various substrates in free solution. Bicarbonate thus effectively exports oxidation from the sterically hindered active site to large molecules in bulk solution (Liochev and Fridovich, 1999). This model which gives a new perspective on the peroxidative mechanism of SOD1, is pivotal for explaining the published discrepancies in spin trapping reports using SOD1 and FALS SOD1 mutants (Goss et al., 1999; Zhang et al., 2002).

4.3 Reaction between Nitrones and Carbonate Anion Radical Causes Hydroxylation

Evidence for increased peroxidase activity from FALS SOD1 mutants (e. g., A4V with alanine substituted by valine at amino acid 4, G93A with glycine replaced by alanine at amino acid 93) was first obtained by monitoring the oxidation of nitrone spin trap 5, 5'-dimethyl-1-pyrroline N-oxide (DMPO) to its hydroxylated adduct (DMPO-OH) (Wideau-Pazos et al., 1996). The EPR spectrum of DMPO-OH is characterized by an equivalent hyperfine interaction (=15 G) from the nitroxide nitrogen and the β–hydrogen atom. Investigators attributed the formation of DMPO-OH to trapping of hydroxyl radical (see Zhang et al., 2000 for references). Significant differences in DMPO-OH signal intensity were observed between the wild type SOD1 and FALS mutant SODs. However, the fact

that bicarbonate was needed for DMPO-OH formation in this system has been previously ignored.

We reinvestigated the mechanism of formation of DMPO-OH using oxygen-17 labeled water and hydrogen peroxide. Results from these experiments unambiguously demonstrated that nearly all of the oxygen in DMPO-OH originated from water. We proposed that either a nucleophilic addition of ^{17}O-labeled H_2O to the DMPO-carbonate radical intermediate or an addition of $[^{17}O]$-H_2O to the DMPO cation radical intermediate.

Independent evidence for the intermediacy of $CO_3^{\cdot}$ was obtained from photolysis studies using the pentammine carbonate complex of Co (III). The UV photolysis of this cobalt complex has been shown to generate the authentic $CO_3^{\cdot}$ radical. This system yielded the same type of radical adducts in the presence of substrates (e. g., azide, ethanol, and formate) as detected in the $SOD1/H_2O_2/HCO_3^-$ system (Zhang et al., 2000, 2002).

Bicarbonate-dependent peroxidase activity of SOD1 was found to be responsible for hydroxylation and oxidation of azulenyl nitrone to an aldehyde. Aldehyde formation was attributed to trapping of hydroxyl radicals by the azulenyl nitrone (Gurney et al., 1998). Recently, we showed that in the absence of bicarbonate, oxidation of azulenyl nitrone to azulenyl aldehyde was negligible in phosphate buffers containing SOD1, H_2O_2, and the chelator DTPA (Zhang et al., 2002). Photolysis of solutions containing the cobalt complex that generates the carbonate radical anion and azulenyl nitrone yielded azulenyl aldehyde. Based on these results, we proposed that $CO_3^{\cdot}$ is responsible for $SOD1/H_2O_2/HCO_3^-$ mediated oxidation of azulenyl nitrone. Bicarbonate-dependent SOD1 peroxidase activity is, thus, inhibitable by nitrones. Bicarbonate-dependent SOD1 peroxidase activity was shown to be higher in FALS mutants (Brown, 1995, 1998).

4.4 Nitrones as Therapeutic Drugs in ALS Animal Models

The first *in vivo* spin trapping evidence for increased free radical formation was provided using the SOD1-G93A transgenic mouse model for FALS (Gurney et al., 1998). The investigators found that when azulenyl nitrone was administered to the nontransgenic, wild-type transgenic, and mutant transgenic mice of different ages (30, 60, and 90 days), increased levels of azulenyl aldehyde were detected in spinal cord extracts of mutant mice but not in transgenic wild-type and nontransgenic mice. Concomitantly, azulenyl nitrone treatment prolonged the survival of FALS overexpressing mice.

More recently, it was shown that treatment of mutant G93A-SOD1 transgenic mice with nitrone trap DMPO significantly delayed paralysis and

prolonged survival (Li et al., 2002). However, DMPO-derived products were not analyzed. In conclusion, *in vitro* and *in vivo* experiments suggest that nitrone spin traps can potentially mitigate oxidative stress in FALS mutant overexpressing cells and mice and protect against progressive motor neuron death.

5. MELANIN, FREE RADICALS, AND PATHOPHYSIOLOGY (T. SARNA, P. PLONKA AND M. ZAREB)

Melanins are virtually the only naturally occurring stable free radicals in mammals. EPR spectroscopy can be used as a unique non-destructive tool for studying melanin in *in vitro* in cultivated cells (Pilas and Sarna, 1985; Cieszka et al., 1995; Hill et al., 1997), in isolated tissues and organs *ex vivo* (Enochs et al., 1993a; Slominski et al., 1994; Plonka et al., 2002), and even under *in vivo* conditions (Lukiewicz and Sarna, 1972; Katsuda et al., 1990). The putative function of the pigment is protection against light-induced damage, perhaps mediated by free-radical damage (Woods et al., 1999).

The interactions of melanin probably involve both radical and non-radical aspects of the quinone-hydroquinone equilibria that underlie many of its properties (Sarna and Swartz, 1993). Because of their redox activity and ability to bind charged materials, including metal ions and drugs, melanins potentially can affect many physiological, pathophysiological, and therapeutic processes (Enochs et al., 1994; Larsson, 1993; Mars and Larsson, 1999). In addition, due to the high reactivity of some of the intermediates, melanin synthesis has also been linked to cytotoxicity (Halaban and Lerner, 1977; Pawelek and Lerner, 1978).

Because of these complex and diverse properties, the study of melanins with EPR has been a large and productive field that has pertinence to the subject of this chapter: free radicals and medicine. As an example of such studies, we consider here two aspects in which the ESR Center at the Medical College of Wisconsin has been especially involved, ocular melanins and neuromelanins.

Specialized cells that synthesize melanin in humans are found not only in the skin epidermis and in the hair follicles, they are also present in the eye, ear and in restricted regions of the brain (Boissy, 1998). Although populations of these extracutaneous melanin-synthesizing cells have some morphological and functional similarities to the various cutaneous melanocytes, it is expected that significant differences between extracutaneous and cutaneous melanocytes should exist (Boissy, 1998). Melanin synthesis usually occurs in specific organelles, the melanosomes,

and is controlled by specialized enzymes (Orlow, 1998; Boissy, 1998; Pawelek and Chakraborty, 1998), but the formation of neuromelanin (NM) in dopaminergic and noradrenergic neurons of the substantia nigra (SN) and locus coeruleus (LC), appears to be enzyme-independent and the neuromelanin granules show significant similarities to inactivated lysosomes (Barden and Brizzee, 1987).

5.1 Ocular Melanin

In primates, two different cell types are involved in ocular melanogenesis – melanocytes of the uveal tract and neuroepithelial cells of the retinal pigment epithelium (RPE). All true melanocytes, including ocular melanocytes, originate from the neural crest; in contrast, the RPE cells are derived from neuroepithelial cells of the developing forebrain of the embryo (Noden, 1991; Mann, 1964). Both types of the melanin-synthesizing cells of the eye express melanocyte-specific proteins (Boissy, 1998).

Allthough biological functions of ocular melanin have not been unambiguously determined, a growing body of experimental evidence and epidemiological data suggest that both the iridial (uveal) and RPE melanin may have important photoprotective and antioxidant properties (Sarna, 1992; Sarna and Różanowska, 1994). Clearly, ocular pigmentation, particularly in the uveal tract, protects the retina from overexposure by absorbing and scattering the impinging light. Melanin in the choroid and RPE contributes to visual acuity by preventing light reflection from the fundus. It has long been recognized that the severity of the visual abnormalities in albinism correlates with the degree of hypopigmentation (Kinnear et al., 1985). However, even with corrective tinted lenses that help photophobia and, in a minor way, vision by increasing contrast, the results in albinos are rather disappointing (Taylor, 1978). It has been postulated that the albino visual system may represent a case of arrested development (Wilson et al., 1988). Thus, melanin synthesis in the RPE appears to be of crucial importance for normal development of the visual system of an organism, and the presence of RPE is not only responsible for the maintenance of the neural retina but also for its successful embronic development and organization (Boissy et al., 1993; Raymond and Jackson, 1995).

Age-related macular degeneration (AMD) is the major cause of late onset blindness in developed countries (Evans and Wormald, 1996; Klein et al., 1992). There is currently no established etiology that could serve as a basis for preventive medicine and no cure for this disease. Light can damage photoreceptor cells in the mammalian retina (Organisciak and Sarna, 2001; Rapp, 1995; Ham et al., 1980) and population-based studies indicate an association between advanced AMD and a patients' exposure to blue or

visible light over the preceding 20 years (Cruickshanks et al., 1993; McCarty and Taylor, 1999; Taylor et al., 1992). The primary lesion in AMD may occur in the RPE (Zarbin, 1998) and result from oxidative damage (Beatty et al., 2000; Cai et al., 2000).

Due to the close structural and functional association between the RPE and photoreceptors, it is generally agreed that any oxidative damage to the RPE, which causes RPE dysfunction, could contribute to the photoreceptor degeneration that characterizes AMD. Thus, the antioxidant status of the RPE may be a key factor in determining the tissue's health, and the health of the photoreceptors that the RPE supports. An RPE antioxidant that may be particularly relevant when photic stress is implicated in tissue damage is the light-absorbing pigment melanin (Sarna, 1992). It has been postulated that RPE melanin can protect the RPE from oxidative stress by sequestering redox active metal ions, quenching electronically excited states of certain photosensitizing dye molecules and by scavenging reactive free radicals (Sarna et al., 1998; Rozanowska et al., 1999). Significantly, melanin content of the human eye seems to be inversely correlated with the incidence of AMD (Weiter et al., 1985; Young, 1988), and the risk of suffering from AMD is about 40 times higher in whites than in blacks (Pauleikhoff and Holz, 1996), even though the inter-racial differences in the amount of ocular melanin mainly concern the uveal pigmentation. However, it is important to realize that antioxidant abilities of melanin may change with age. Indeed, a recent EPR study has shown that the amount of RPE melanin decreases by a factor of 2.5 between the first and ninth decade of life (Sarna et al., 2002). In an independent study, the melanin content of RPE melanosomes from human donors of different age was analyzed by EPR after drying the pigment granules (Bilinska et al., 2002). Surprisingly, the content of melanin, when normalized to a single pigment granule, was found independent of age. On the other hand, RPE melanosomes from younger individuals could contain significantly higher percentage of strongly bound water, that those from older individuals (Bilinska et al., 2002). RPE melanosomes from older human donors exhibit increased photoreactivity: they induce faster oxygen photouptake and accumulation of superoxide anion spin adducts (Rozanowska et al., 2002). Thus with age, RPE melanin may contribute to oxidative stress in the outer retina both as a result of a decreased antioxidant efficiency and an increased aerobic photoreativity. Interestingly, W-band EPR spectroscopy may provide a sensitive measure for differentiating RPE melanin from human donors of different age and monitoring possible chemical changes of the melanin that are likely to be aggravated with aging (Rozanowska et al., 1993). In this preliminary study a striking pattern in the changes of magnetic parameters of melanin radicals with age was observed. Although the molecular nature of these changes is

not yet understood, they may result from life-long oxidative modifications of the RPE melanin.

Neuromelanin (NM) is an insoluble brown-black or greyish in appearance pigment that accumulates with age in the midbrain of primates, most notably of humans (Van Woert et al., 1966). Based on standard histochemical tests and various physicochemical analysis, including EPR spectroscopy, NM has been classified as a true melanin (Barden and Brizzee, 1987; Enochs et al., 1993b). Characteristic degradation products of NM indicate that this melanin has chemical properties similar to both eumelanins and pheomelanins (Odh et al., 1994). It appears that the synthesis of NM occurs via oxidative polymerization of dopamine and its sulfur containing derivatives. As a synthetic model of NM, a polymer obtained by autooxidation of dopamine and cysteine is often used (Shima et al., 1997). Biological functions of NM remain unknown. Unlike cutaneous and ocular melanins, neuromelanin is never exposed to environmental light. Therefore, no photoprotective role of NM is likely.

It has been postulated that under normal physiological conditions NM may have a cytoprotective function by the sequestration of redox-active metal ions (Swartz et al., 1992; Zareba et al., 1995; Korytowski et al., 1995). On the other hand, the presence of NM may also be responsible for the vulnerability of pigmented neurons observed in Parkinson's disease (PD). This neurological disorder is characterized clinically by akinesia, rigidity, and tremor (Stern, 1990). Histological analysis of Parkinsonian brains shows extensive degeneration of the pigmented dopaminergic neurons of the substantia nigra. In PD, the neuromelanin containing cells of the SN appear to be more vulnerable to degeneration than the non-pigmented neurons. However, there seems to be no strict correlation between the vulnerability of the neurons and their melanin content (Kastner et al., 1992).

The formation of NM in the human brain, probably is a by-product of oxidative metabolism of dopamine, known to occur at high rate in catecholaminergic neurons of the SN and LC. While both autooxidative reactions and enzymatic oxidation of dopamine are accompanied by the generation of hydrogen peroxide, the former process can also lead to the formation of potentially cytotoxic semiquinones and quinones (Cohen, 1983; 1989; Graham 1984). Therefore, the dopaminergic neurons of the SN and LC are intrinsically at risk of oxidative stress. Despite the presence of antioxidative mechanisms in catecholaminergic neurons for maintaining their neurotransmitters in a reduced state, the system is not perfect and some semiquinones and quinones may escape from reduction and randomly form products that cannot be catabolized and gradually accumulate in lysosomes, eventually becoming neuromelanin granules (Enochs et al., 1994). It can be argued that when formed, NM can exert its antioxidant action by binding of

advantitious multivalent metal ions, such as iron and copper (Swartz et al., 1992). There is evidence that SN neurons in patients with PD exhibit an elevated level of oxidative stress (Jenner, 1991). Thus the ratio of reduced to oxidized glutathione is decreased in Parkinsonian brains, compared to normal brains (Riederer et al., 1989; Sofic et al., 1992).

In addition, a decreased level of polyunsaturated fatty acids and increased levels of malondialdehyde, a product of lipid peroxidation, were found in PD brains (Dexter et al., 1989). Whether these changes are the cause of the disease or they result from an increased dopamine turnover in the remaining neurons of a PD patient, remains unclear.

One of the most important properties of NM that may determine its biological functions is the ability of NM to bind metal ions (Enochs et al., 1993b). High levels of metal ions, particularly iron; were found in the human SN (Zecca and Swartz, 1993; Gerlach et al., 1995; Shima et al., 1997). Although ferritin is known to be responsible for accumulation of iron in many tissues, it is believed that in SN iron is bound to NM (Jellinger et al., 1992; Zecca and Swartz, 1993; Gerlach et al., 1995). Indeed, recent measurements suggest that ferritin is not present in SN neurons (Moos, 2000), which implies that neuromelanin may be a key buffering system for iron in pigmented neurons (Zecca et al., 2002).

The antioxidant efficiency of neuromelanin was studied in model systems. The study has clearly shown that the yield of hydroxyl radicals generated via iron ion-catalyzed free radical decomposition of hydrogen peroxide dramatically decreased in the presence of synthetic NM (Zareba et al., 1995). Both synthetic and natural NMs were able to inhibit peroxidation of lipids induced by iron/ascorbate or thermolabile azo-compounds (Korytowski et al., 1995). A hypothesis, about the role of NM in the multifactioral etiology of PD was proposed by Enochs et al. (1994): oxidative degradation of NM that can occur with aging or as a result of an intense or chronic oxidative stress in the pigmented neurons of SN could, via positive feed-back mechanism, further increase the level of the oxidative stress. Oxidatively modified NM is expected to have a decreased binding affinity for iron and other metal ions. It would, therefore, not only bind fewer metal ions compared to “native” NM, but even raise the cytoplasmic level of potentially cytotoxic species by release of the accumulated ones.

6. FREE RADICALS AND CANCER- POTENTIAL ROLES OF OXIDATIVE STRESS IN THE INDUCTION OF CANCER (P. L. GUTIERREZ)

The genetic basis of human cancer has been well documented. Widespread genomic instability is a hallmark of tumor cells (Jeong, 2003; Nowell, 1976). An average of about 1/3 of all tumor types appear to exhibit a genomic instability manifested by subtle nucleotide sequence alternations that activate proto-oncogenes or inactivate tumor suppressor genes. Chromosomal rearrangements are likely to be a result of aberrant recombination repair that occurs during normal cellular mitotic growth (Przybytkowski, 2003; Friedberg, 1985; Friedberg et al., 1995; Kucherlapati and Smith, 1988). A very large number of genes has been identified as tumor promoter genes or tumor suppressor genes (Cheng, 2003; Stanbridge, 1990; Weiberg, 1989). As far back as 1993, genetic analysis of tumor cells has suggested that between 6 to 12 of these genes are altered during the development of a tumor (Renan, 1993). The number of altered genes far exceeds the number of mutations that would be predicted by the spontaneous mutation rate in human cells. Of the several theories to account for this discrepancy, the "mutator hypothesis" for tumorigenesis has gained much attention (Loeb, 1991, 1994). In this hypothesis, an early spontaneous mutation in one of many genes that maintain the genetic information in chromosomes becomes altered. This leads to genetic instability, or a mutator phenotype, either by accumulation of replicative errors or by gross chromosome rearrangement. A higher-than-normal mutation rate then leads to the combination of mutations in genes that regulate growth, invasion, or metastasis. Post-replication mismatch repair systems enhance the fidelity of DNA replication by correction of replicative errors. It has recently been shown that mutations in mismatch repair genes are associated with cancers (e.g. Jeong, 2003; Worrillow, 2003).

Oxidative stress caused by reactive oxygen species (ROS) can lead to genomic instability. Oxygen is metabolized inside the cell by a series of one electron reductions with the generation of reactive and potentially damaging ROS which include superoxide radical anion, H_2O_2, and the hydroxyl radical (Halliwell and Gutteridge, 1989). A pro-oxidant status in the cell can lead to the accumulation of ROS. Humans are exposed to substantial amounts of oxidative stress from a variety of sources. Halliwell has estimated levels of up to $100\ \mu M\ H_2O_2$ in the urine of individuals ingesting such foods as instant coffee (Long et al., 1999a,b).

Oxygen and its metabolites are known to function as intracellular signals, playing a role in apoptosis (Butts et al, 2003; Liu et al., 2003; Barr and Tomei, 1994; Buttke and Sandstrom, 1994,1995; Corcoran et al., 1994;

Davies, 1995; Forrest et al., 1994; Greenspan and Aruma, 1994; Hockenbery, 1995; Sandstrom et al., 1994) as well as in the stimulation of cell growth via the induction of a number of transcriptional activation factors such as *c-fos, c-jun, egr*-1, NF-κB and metabolizing enzymes (Anderson et al., 1994; Burdon, 1995; Crawford et al., 1988; Curran and Morgan, 1995; Janknecht et al., 1995; Khan and Wilson, 1995; Koong et al., 1994 a,b; Chen and Giaccia, 1994; Nose et al., 1991; Piechaczyk et al., 1994; Remade et al., 1995; Schreck et al., 1991; Xanthoudakis and Curran, 1994; Xanthoudakis et al., 1994; Yao et al., 1994; Lambert et al., 1994; Vile et al., 1994; Firth et al., 1994). ROS are believed to play a causative role in the degenerative diseases of aging including cancer (Ames and Shigenaga, 1993; Ames et al., 1993; Peterszegi et al., 2003; Cantuti-Castelvetri et al., 2003). Endogenously, activated neutrophils and macrophages generate large quantities of NO, O_2^-, H_2O_2, OCl^- as part of the inflammatory response (Chanock et al., 1994; Densen et al., 1995, Ginsburg and Kohen, 1995; Laskin and Pendino, 1995), and a variety of other normal cells can also be stimulated to produce low levels of superoxide and hydrogen peroxide (Burdon, 1995). Ames has estimated that one third of the cancers in developing countries can be attributed to chronic infections (Ames et al., 1993). When oxidative stress due to these reactive species from whatever source exceeds the capacity of the defense systems of the cells to intercept and neutralize them (i.e. pro-oxidant status), toxicity (Mytar et al., 1999), genomic instability and mutations in cells result. For example, tumor promoters stimulate the production of reactive oxygen species which may play a critical role in the progression to malignancy (Beckman et al., 1994; Gopalakrishna et al., 1994; Hu et al., 1995; Marnett and Ji, 1994; Lin and Shih, 1994; Panandiker et al., 1994). Also, an African green monkey kidney cell line (CV-1) transfected with the H_2O_2-generating enzyme peroxisomal fatty acyl-CoA oxidase. When exposed to the enzyme substrate linoleic acid for 2-6 weeks, 4% of the cells became tumorigenic (Chu et al., 1995).

ROS targets are many, including membranes and proteins. The most critical potentially carcinogenic targets of ROS are probably deoxynucleotides and DNA, which generate in DNA 7,8-dihydro-8-hydroxy-2'-deoxyguanine (8-OHdG), 7,8-dihydro-8-hydroxy-2'-deoxyadenine (8-OHdA), 2,6-diamino-4-hydroxy-5-formamidopyrimidine (Fapy-G), and 4,6-diamino-5-formamidopyrimidine (Fapy-A) (Bertoncini and Meneghini, 1995; Breen and Murphy, 1995; Dizdaroglu, 1993; Feig et al., 1994; Giese et al., 1995; Halliwell and Aruoma, 1991; Steenken, 1989). Guanine is the most easily oxidized of the nucleic acid bases (an electron-loss center created in a system containing the four nucleic acid bases will eventually migrate to guanine) (Steenken, 1989). The keto and enol forms of this damaged guanine are found in equilibrium. Thus, the interchangeable

use of 8-oxodG and 8-OHdG found in the literature. We will use the 8-oxoG terminology in this discussion. Since the last step in formation of 8-oxoG and 8-oxoA is an oxidation while the last step in the formation of Fapy-G and Fapy-A is a reduction (Breen and Murphy, 1995; Steenken, 1989), it has been suggested that 8-oxoG formation is favored under the more oxidizing (pro-oxidant) conditions found in cancer cells (Malins et al., 2003; Malins, 1993; Malins et al., 1993), or alternatively, that a pro-oxidant condition exists in cells destined to become malignant favoring the accumulation of 8-oxoG. For instance, the DNA of hepatitis B virus infected mouse liver cells destined to become tumorigenic had elevated levels of 8-oxoG (Hagen et al., 1994). Whatever the reason, 8-oxoG is considered to be a major stable product generated by ROS attack on DNA and it is excreted in the urine of humans where it is used as a biological marker of *in vivo* oxidative DNA damage (Halliwell, 1993; Shigenaga et al., 1994).

The formation of 8-oxoG in DNA, if not repaired, leads to misincorporation of dA opposite to the 8-oxoG lesion. The misincorporated dA leads to an A/8-oxoG mispair resulting in G·C → T·A transversions Moriya, 1993; Cheng et al., 1992; Moriya et al., 1991). The A/8-oxo G mispair also interferes with DNA-processing enzymes such as methylases (Weitzman et al., 1994) and restriction enzymes (Turk and Weitzman, 1995). It is interesting to note that G·C → T·A transversions occur frequently as mutations of the p53 tumor suppressor gene in human lung, breast, and liver cancers (e.g. Hollstein et al., 1991). More importantly, in p53, H_2O_2 induces a G to T transversion at both G-residues of codon 249 (AGG) and a C to A transversion at codon 250 (CCC) (Hussain et al., 1994).

In order to minimize the deleterious effects of reactive oxygen species, all aerobic organisms possess extensive defense systems. The primary defense is achieved by decomposing superoxide and hydrogen peroxide, which thus minimizes the formation of the ensuing hydroxyl radical (·OH). This primary antioxidant defense system includes various enzymatic and nonenzymatic mechanisms such as superoxide dismutase, catalase, glutathione peroxidase, and ascorbic acid (e.g. Halliwell and Gutteridge, 1989). In addition, although controversial, data indicate that BCL-2, the antiapoptotic protein also has antioxidant powers (Amstad et al., 2001). The reactive oxygen species that escape from the primary defense system have a significant chance of damaging DNA. Several repair enzymes in both prokaryotes and eukaryotes have been shown to remove 8-oxoG residues from DNA providing a secondary line of defense. The mammalian repair enzyme hOGG1, the human homolog of the yeast OGG1 is able to repair C/8-oxoG DNA damage back to CG in cells due to its 8-oxoG glycosylase /AP lyase activity (Gu et al., 2001; Aburatani et al., 1987; Arai et al., 1997; Friedberg et al., 1995; Hazra et al., 1998; Nash et al., 1996; Radicella et al.,

1997; Ramotar and Demple, 1993; Roldan-Arjona et al., 1997; Shibutani et al., 1991; Van der Kemp et al., 1996). The mammalian MTH1 enzyme, like the E. Coli MutT homolog eliminates 8-oxodGTP damage from the deoxynucleotide pool (Maki and Sekiguchi, 1992). Based on sequence homology with yeast OGG1, hOOG1 has been cloned (Aburatani et al., 1997; Arai et al., 1997; Lu et al., 1997; Radicella et al., 1997; Roland-Arjona et al., 1997; Rosenquist et al., 1997; Shibutani et al., 1991). If the 8-oxoG lesion is not removed by the hOGG1 protein before DNA replication, then misincorporation of dA opposite to the 8-oxoG lesion occurs (Hazra et al., 1998; Moriya et al., 1991; Nghiem et al., 1988; Shibutani et al., 1991). The mammalian hMYH enzyme, like E. Coli MutY, removes this misincorporated adenine from an A/8-oxoG mispair, with the formation of C/8-oxoG, which is then a substrate for hOGG1. This is considered the third level of defense (Au et al., 1989; McGoldrick et al., 1995; Slupska et al., 1996; Tsai-Wu et al., 1991; Yeh et al., 1991). The MutY gene has been cloned and sequenced (Boiteux et al., 1987; Michaels et al., 1990; Michaels et al., 1991; Slupska et al., 1996). In addition, it has been shown that expression of the *E. coli* MutM gene which expresses Fpg, an enzyme with the same activity as hOGG1 in mammalian cells, reduces the mutagenicity of X-rays (Laval, 1994). Furthermore, germ line mutations in human genes *h*MSH2, or *h*MLH1, which express proteins with the ability to correct DNA mismatches and misalignments lead to genetic instability in microsatellite repeat sequences in hereditary nonpolyposis colon cancer (Jeong et al., 2003; Bronner et al., 1994; Papadopoulos et al., 1994), It thus seems likely that the hOGG1/hMYH repair pathways are linked to protection against certain cancers.

An elevation of oxidative modifications in DNA has recently been reported in human cancers of the breast, prostate (Malins and Haimanot, 1991; Malins et al., 1993, Malins et al., 2003) and other tissues (LePage et al., 2000; Olinski et al., 1992). The 8-oxoG lesion has been suggested to be a putative link to cancer development (Malins et al., 2003; Malins, 1993) and a predictor for breast cancer (Malins et al., 1995). This modification occurs by the attack of hydroxyl radicals that arise from H_2O_2 mediated by trace metal ions such as Fe^{2+} and Cu^{+} (Luo et al., 1994). Since H_2O_2 diffuses readily across the nuclear membrane, hydroxyl radicals are formed near DNA and modify it by attacking the purine and pyrimidine bases (Meneghini and Martins, 1993). Breast cancer is not commonly associated with pre-existing chronic inflammatory conditions, unlike bowel cancer where a causal relationship between ulcerative colitis and bowel cancer has been suggested (Weitzman and Gordon, 1990). Breast lesions (benign or malignant) are, however, commonly infiltrated with macrophages, which lead to oxidative stress. This in turn could lead to the progression of some

cells from benign to malignant and/or facilitate the transformation to a more aggressive metastatic tumor. There are a number of tumorigenic cell lines including one from breast that chronically elaborate large quantities of H_2O_2 (Szatrowski and Nathan, 1991) that can lead to chromosome mutations and cancer (Emerit, 1994). In addition, the most lethal form of locally advanced breast cancer is termed inflammatory breast cancer due to the acute inflammatory changes observed in patients with this type of malignancy (Jaiyesimi et al., 1992). As mentioned above, humans are exposed to considerable oxidative stress as judged by measurements of up to 100 μM H_2O_2 in urine (Long et al., 1999a,b). These levels vary with a normal diet. Halliwell concluded that urine contains "autooxidizable proteins" which upon exposure to oxygen result in the generation of O_2^- to generate H_2O_2 (Long et al., 1999a). Exposing cells to H_2O_2 can shift the cell to a pro-oxidant state, which facilitates ROS damage to a variety of targets. We have shown this to be true in the benign human breast epithelial cell line MCF-10A (Gu et al., 2001). MCF-10A is a spontaneously immortalized human breast cell line, which has characteristics of human breast epithelium such as: lack of tumorigenicity in nude mice and lack of anchorage independent growth (Soule et al., 1990). We treated these cells with 450 μM H_2O_2 5 separate time after allowing for growth (P5 line) or gradually at 50 μM H_2O_2 increments until reaching μM H_2O_2 (GP line). The peroxide decay and the concomitant production of OH radicals was measured by EPR using DMPO as mentioned earlier in this chapter (Figure 1).

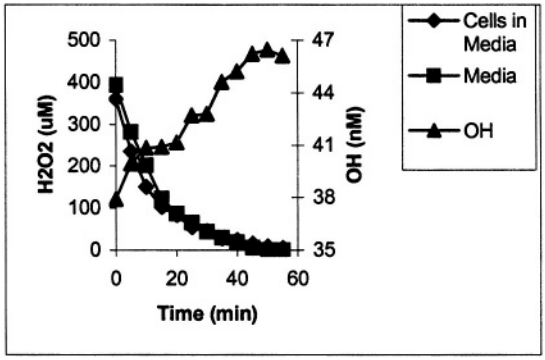

Figure 1 Hydrogen peroxide decay with concomitant formation of hydroxyl radicals. A colorimetric assay was used in the detection of hydrogen peroxide and DMPO/EPR in the detection of hydroxyl radicals.

After exposure to hydrogen peroxide, the cells became resistant to this oxidant and went on to exhibit different degrees of some of them being able to grow in immunodeficient mice (GP line). This transformation towards malignancy can be related to the cell's ability to bypass apoptosis to ensure survival, cell cycle anomalies modulated by oxidative stress-induceable

genes and the lack of repair of 8-oxoG in DNA (Gu et al., 2001). With respect to the latter damage, the role of hOGG1 and hMYH repair enzymes in mammalian tumor progression is to maintain genetic stability by avoiding G·C → T·A transversions. This is based on the work on *E. coli* MutY and MutM gene mutants. Cells with a single mutation in these genes are moderate mutators; however, cells with a double mutation in MutY and MutM genes have mutation rates three orders of magnitude higher than the wild-type cells (Nghiem et al., 1988; Cabrera et al., 1988). Overexpression of these genes will reduce the transversion mutations in tumor promoter genes or tumor suppressor genes and thus reduce the risk of tumorigenesis. Thus, if indeed the role of 8-oxoG in breast cancer tumorigenesis is established, one application to the treatment of cancer would be elevating the enzymes that repair such lesion over the endogenous levels present in healthy tissue.

With respect to cell responses to H_2O_2, we found that H_2O_2 induced p53 in MCF-10A but not in the H_2O_2-transformed line P5. In addition, all transformed lines overexpress BCL-2 when compared to MCF-10A (data not shown). It has been recently shown that the transfection of MCF-10A cells with the BCL-2 gene resulted in a 5 fold increase in BCL-2 protein expression over the parental MCF-10A line (Upadhyay et al., 1995) and that apoptosis did not occur in the transfectants at concentrations of 500 μM H_2O_2. In contrast, this concentration of H_2O_2 induced apoptosis in the parental non-transfected line (Upadhyay et al., 1995). This H_2O_2-induced apoptosis in MCF-10A cells is p53 dependent (Upadhyay et al., 1995).

7. USING NMR AND EPR WITH SPIN TRAPS (L. J. BERLINER)

The other contributors to this book have presented excellent approaches and examples to the use of EPR for observing radical species in biological systems. However, there are many further potential applications that currently cannot be done because of limited radical concentration or stability. This section describes alternate approaches to overcoming some of these obstacles, combining the two magnetic modalities that Jim Hyde has used so productively, often in combination with the use of spin traps. Spin traps have the potential advantages of being able to accumulate ("trap") highly reactive radicals that could not be otherwise observed directly, due to sensitivity limits and kinetic considerations. This is clearly the case for the hydroxyl radical, $\bullet OH^{\cdot}$, which may be directly observed only by fast freeze quenching at liquid nitrogen temperatures and quickly undergo secondary radical reactions and interconversions. Obviously, quickly immersing a

mouse into liquid nitrogen negates an *in vivo* experiment! Many of the applications, successes and pitfalls of *in vivo* spin trapping are reviewed in this volume by Mason (ch. 5). A major problem that is difficult to overcome is the tendency of the living cell to reduce radicals; consequently, the nitroxyl product of a nitrone radical adduct is normally bioreduced to the diamagnetic hydroxylamine. This section discusses potential alternatives utilizing NMR as the ultimate spectroscopic probing method. It also considers the use of more conventional NMR techniques to further characterize the spin traps and their metabolism.

7.1 NMR Spin Trapping

Many years ago Selinsky et al. (1989) suggested the use of ^{19}F NMR to study free radical reactions with fluorinated spin traps. They monitored organic free radical reactions in the test tube by both EPR and NMR. In later work outlined below, this technique was coined as "NMR spin trapping." The success of this approach depends on the following:

1. Do the diamagnetic (decomposition or transformed) products of a spin trap adduct accumulate to sufficient levels for detection by NMR?
2. Does the resultant NMR spectrum allow extrapolation back to a specific radical adduct?

The definition encompasses not only the spin trap chemistry described below, but also "MRI spin trapping" described in the last section below, in which the T_1 weighted NMR images of water protons are measured in the presence of stable, paramagnetic, biologically generated radical adducts or complexes. The enhanced relaxation of the water protons at the site of the radicals effectively 'localizes' the site of radical generation.

7.1.1 Phosphorus containing nitrone spin traps DEPMPO

Tordo and coworkers (Frejaville et al., 1995) described a series of nitrone spin traps, based initially on DEPMPO (5-diethoxyphosphoryl-5-methyl-1-pyrroline-N-oxide), a phosphorus containing analog of DMPO (2,2-dimethyl-pyrroline-N-oxide). The advantages were that oxygen radical adducts of this trap showed a somewhat longer half life compared with DMPO. Despite these improvements, the in-vivo "stability" of paramagnetic spin trap adducts is sharply reduced relative to stable nitroxyl radicals, probably due to biological reduction of the resulting nitroxide to the hydroxylamine, but perhaps also by other destructive chemical processes.

It seems prudent to take advantage of the phosphorus moiety of DEPMPO by utilizing ^{31}P-NMR to probe its chemistry during and after radical reactions to understand the pathways of its radical adduct

degradation. As described below, a series of biologically relevant DEPMPO adduct reaction products for •OH and $•O_2^-$, as well as methyl radical ($•CH_3$) and hydroxymethyl radical ($•CH_2OH$) were characterized by ^{31}P-NMR.

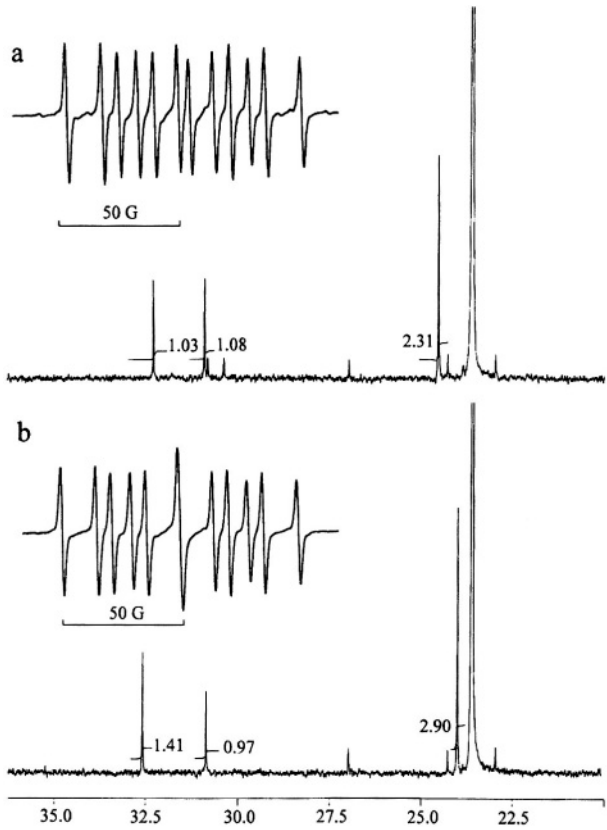

Figure 2 ^{31}P-NMR and ESR spectra of DEPMPO/·CH_3 and DEPMPO/·CH_2OH reaction products. a) ^{31}P-NMR spectra obtained from 0.1 M DEPMPO in 0.1 M cacodylate buffer, 20 mM DTPA, pH 7.0, 10% DMSO, detected 2 h after addition of 5 mM $FeSO_4$ and 5 mM H_2O_2 at T=300K. *Inset:* corresponding ESR spectra observed at 10 min; b) the same reactions but in the presence of 10% methanol instead of DMSO. *Inset:* corresponding ESR spectra observed at 10 min.. Experimental spectra were in a good agreement with simulations using the calculated parameters a_N = 14.56 G, a_H = 21.8 G, a_P = 46.95 G for DEPMPO/·CH_3 and a_N = 14.5 G, a_H = 20.7 G, a_P = 49.95 for DEPMPO/·CH_2OH adducts, which are in agreement with literature data. From Khramtsov et al. (1999) with permission.

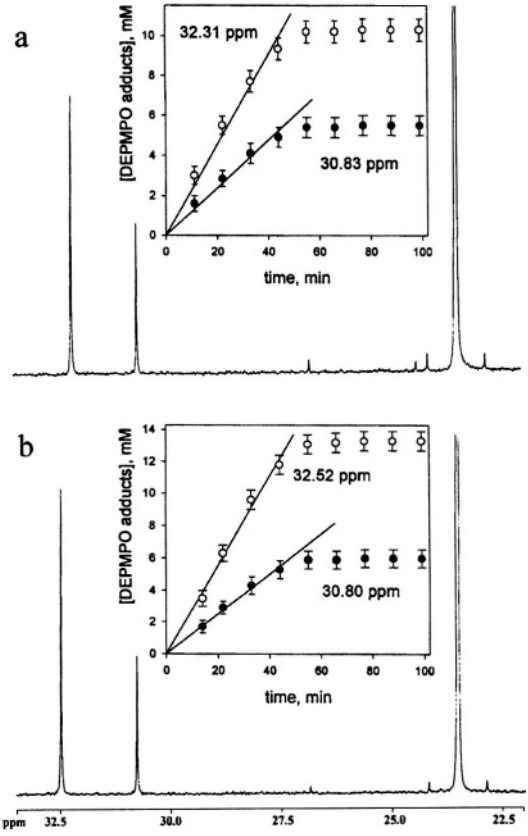

Figure 3. Quantitative determination of DEPMPO/·OH using ESR and NMR. Filled squares: concentration of DEPMPO adduct from the double integrated ESR spectrum; open circles: concentration calculated from the integral intensity of the ^{31}P-NMR peak at 27.05 ppm; filled circles: the same integral intensities of the ^{31}P-NMR peak multiplied by 2.0 to reflect the mechanism in Scheme B. The bent curve was calculated proposing bimolecular decay of DEPMPO-OH from initial concentration equaling the concentration of Fenton reagents ($[FeSO_4] = [H_2O_2]$) with the rate constant k_d=15.8 $M^{-1}s^{-1}$ (namely $[DEPMPO\text{-}OH] = [H_2O_2]/([H_2O_2]\cdot k_d\cdot t + 1)$, where t=10 min. was the time at which the EPR spectra were obtained). The straight line was inserted as a guide to evaluate how closely the experimental data reflected a 1:1 stoichiometry between hydroxyl radical produced and product formed. Note that both the ESR data (at concentrations lower than 50 mM) and the adjusted NMR data show a linear concentration dependence on the Fenton concentration reagents. From Khramtsov et al. (1999) with permission.

7.1.1.1 DEPMPO

The reaction of DEPMPO with radical, R• as shown in Scheme A, emphasizes the fact that two stereoisomers are obtained since the spin trap contains an asymmetric center (yielding, in effect, two pairs of EPR spectra). However, the radical signals decay within two hours, yielding the ^{31}P NMR spectra depicted in Figure 2. For example, in Figure 2a (DEPMPO/·CH_3), there is evidence of several new, unique ^{31}P peaks at 24.54 ppm with additional peaks at 30.83 and 32.52 ppm. (A small 'DEPMPO/•OH' resonance at 27.05 ppm also occurs since the reaction conditions involve Fenton •OH chemistry (Khramtsov et al., 1999).

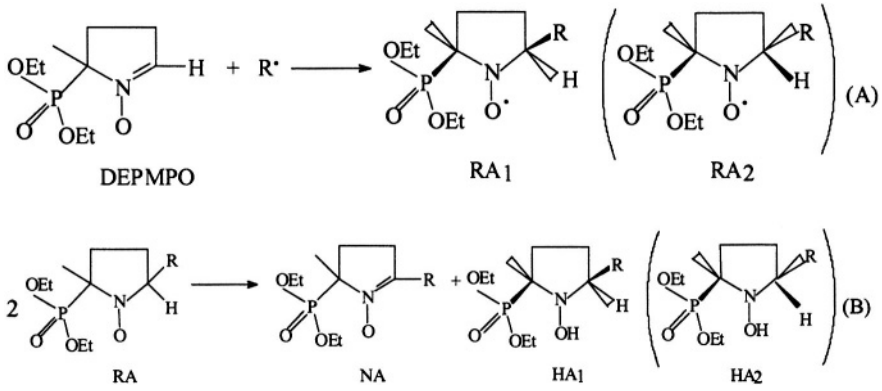

These peaks originate from bimolecular disproportionation chemistry as outlined in Scheme B, where *both* reaction products were diamagnetic: a new nitrone (NA) and the hydroxylamine of the spin adducts, HA_1 and HA_2. This accounts for the three ^{31}P NMR peaks, one of which is 50% total intensity, two of which are 25% each (the ratio depends slightly on the stereospecificity of the initial radical addition). Since the concentrations of spin trap adduct are significantly lower *in vivo,* disproportionation would not be appreciable; however, *direct reduction* of the DEPMPO adduct to the hydroxylamines HA_1 and HA_2 is highly facile. Hence, when ascorbic acid was added to the radical reaction system, direct conversion to HA_1 and HA_2 occurred. Consequently the two new ^{31}P lines at 32.31 and 30.83 ppm reflected the direct "history" of spin adduct formation of the methyl radical adduct of DEPMPO and its subsequent disproportionation or *in vivo* bioreduction.

At high concentrations the bimolecular decay of the DEPMPO/•OH EPR adduct spectrum reaction is relatively rapid. The adduct remains for only a few minutes unless balanced by extremely high steady state levels of new radical production (Liu et al., 1999; Timmins et al., 1999). As shown in Figure 3, the maximum intensity of the new ^{31}P line at 27.05 ppm never

exceeded 50% of the theoretical yield of the diamagnetic product from an •OH adduct. Scheme C suggests that the nitrone product of disproportionation (depicted in Scheme B) is in tautomeric equilibrium with the more stable N-hydroxypyrrolidone, NA-OH, to which the ^{31}P NMR line at 27.05 ppm was attributed. In addition, as shown in the scheme, the hydroxylamine can spontaneously eliminate H_2O, regenerating DEPMPO. Similar results were found with superoxide radical where, in fact, the ^{31}P NMR peaks were identical to those observed after reaction with •OH, suggesting a conversion of DEPMPO/•O_2^- to DEPMPO/•OH (or transformation of their diamagnetic products). *In vivo,* however, this is unlikely to be important because the local concentrations of spin adduct are unlikely to high.

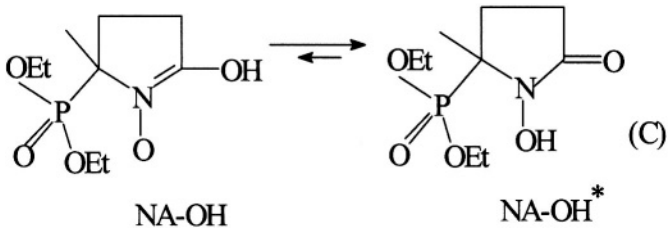

7.1.2 Fluorine containing nitrone spin traps – FDMPO

From a sensitivity viewpoint, nitrones that contain trifluoromethyl groups might be more promising than those containing other stable isotopes. This was borne out with new spin trap, FDMPO (4-hydroxy-5,5-dimethyl–2-trifluoro methylpyrroline-1-oxide). The parent nitrone yields a single NMR resonance at –66.0 ppm, which yields a net ten-fold higher sensitivity than with ^{31}P NMR of DEPMPO.

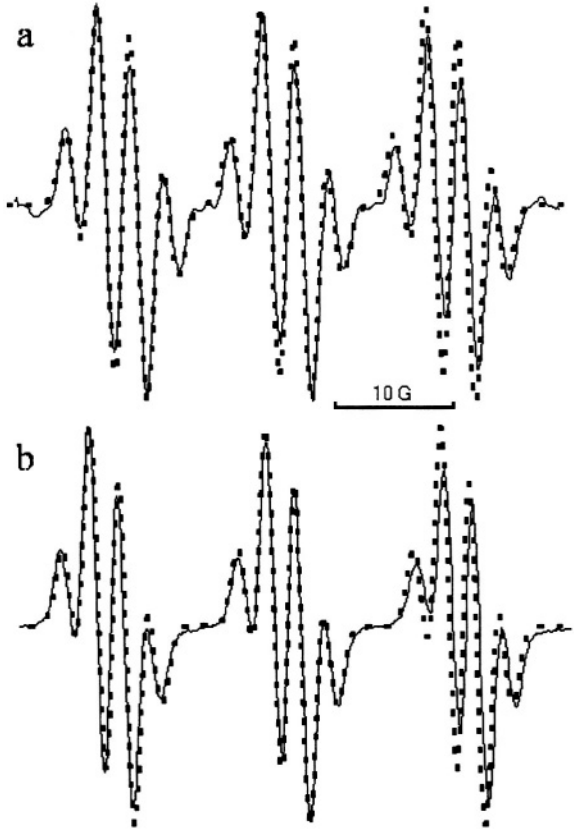

Figure 4. X-band ESR spectra of FDMPO spin adducts with ·OH (a) and ·CH_2OH (b). Spectra were obtained in 0.1 M K-phosphate buffer, pH 7.0, 2 mM DTPA, 0.1 mM H_2O_2, 50 mM FDMPO, after addition of 0.1 mM $FeSO_4$ solution, and in 10% (v/v) methanol (b). Spectrometer settings were: microwave power 20 mW; modulation amplitude, 0.63 G; sweep time, 1 min. The dotted lines are calculated spectra. From Khramtsov et al. (2001) with permission.

Figure 4 shows simulated and observed EPR spectra for the •OH and •CH_2OH adducts, respectively (Khramtsov et al., 2001). The EPR signals were stable for over a day since bimolecular decay (as noted in Scheme B) is much less probable with the absence of an alpha proton. In order to observe the products by ^{19}F NMR, it was necessary to reduce the paramagnetic adduct(s) with ascorbic acid. However, despite the significantly increased *in vitro* stability of the paramagnetic adducts, it is likely that bioreduction would occur fairly rapidly. Figure 5 depicts ^{19}F results for the •CH_3 adduct of FDMPO in a system containing ascorbate. The inset shows the precursor EPR spectrum.

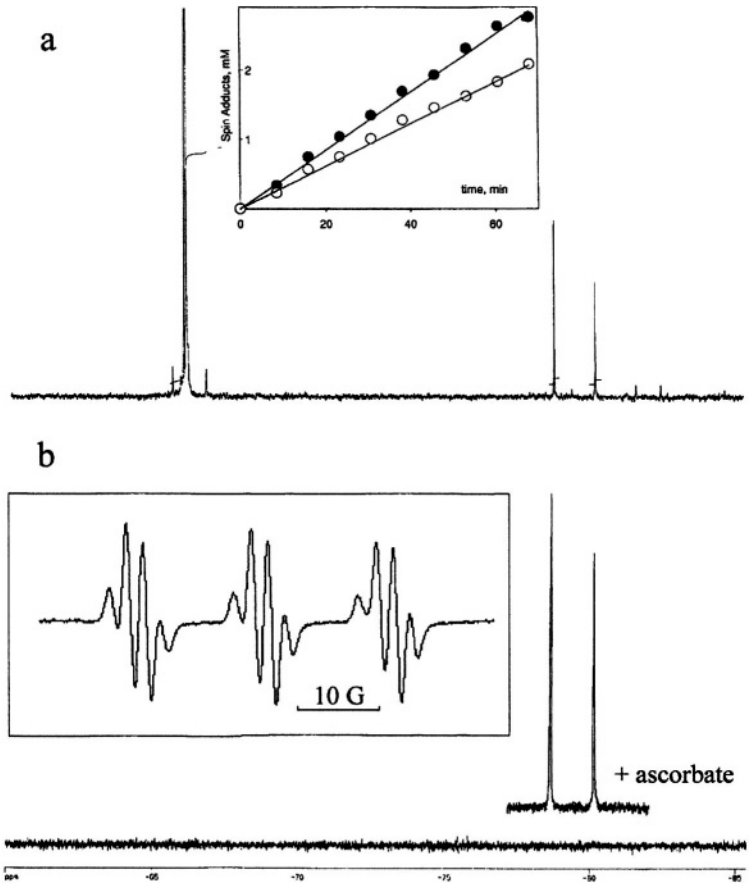

Figure 5. ^{19}F-NMR spectra of FDMPO/CH_3 adduct products: (a) in a Fenton "iron recycling" system in 0.1 M K-phosphate buffer, pH 7.0, 2 mM DTPA, 20 mM H_2O_2, 50 mM FDPMPO, 10% v/v of DMSO, 20 mM of ascorbate, 30 min after addition of 0.5 mM FeSO4 solution; number of scans, 208; *inset:* kinetics of product accumulation. The symbols (•) and (o) denote integral intensities of the 19P-NMR peaks of reduced FPMPO/·CH_3 products at –78.6 ppm and–80.0 ppm, respectively; (b) 19F-NMR spectra of 3 mM of FDMPO/CH_3, synthesized in Scheme B, in 0.1 M phosphate buffer, pH 7.0, before and after addition of 10 mM ascorbate; number of scans, 120; inset: EPR spectrum of 0.1 mM FDMPO/CH_3 adduct; spectrometer settings were microwave power 20 mW; modulation amplitude, 0.63 G; sweep time, 1 min. From Khramtsov et al. (2001) with permission.

The •O_2^- adduct gave identical NMR spectra to that with •OH. However, overall, the fluorine containing spin traps are less likely to undergo destructive metabolism assuming toxicity levels will not be a major problem. Overall the reactivity of FDMPO was comparable to that of DMPO as

measured by competitive kinetics. Consequently, the trifluoromethyl NMR spin traps have greater potential than traps containing other stable isotopes.

7.1.3 Carbon-13 containing nitrone spin traps [Methyl-^{13}C]-

The remaining biological isotope, ^{13}C, is at *ca* 1% natural abundance. In order to distinguish a particular molecule of interest, one must synthesize it enhanced with ^{13}C. In a novel application by Bose-Bsau et al. (2001). [Methyl-$^{13}C_3$]-2-methyl-2-nitrosopropane (MNP) was employed, in the presence of H_2O_2, as an NMR spin trap for tyrosyl radical in met-myoglobin. Relatively stable paramagnetic adducts were detectable by EPR; however, the direct identification and characterization of the final adduct on the protein and the specific chemistry involved was possible only after reduction of the paramagnetic adduct by ascorbate and the use of 2D high resolution NMR to assign the relevant Tyr residue and the chemistry of the modification. Previous spin trapping studies on myoglobin had shown the presence of tyrosyl radicals that could be trapped with MNP (Barr et al., 1996), but the EPR results were ambiguous as to which residue was preferentially labeled. These recent results were definitive in identifying Tyr 103 in equine myoglobin and that the adduct formation occurs at the C-3 carbon of the amino acid. Figure 6 depicts the reaction scheme that most likely occurs. In addition, the ^{13}C-^{1}H HMQC-NOESY studies identified the nearby protons of Phe 106.

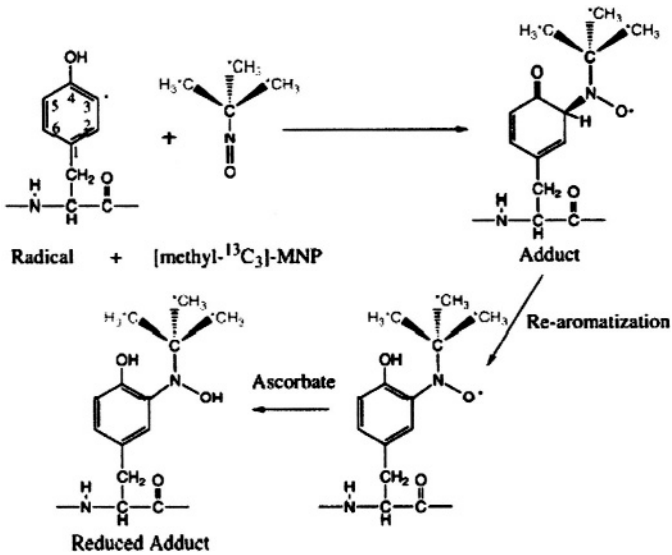

Figure 6. Scheme 1. Adduct formation at Tyrosine C-3, rearomatization, and reduction by ascorbate to the hydroxyl amine. From Bose-Bsau et al. (2001 with permission).

7.1.4 MRI Spin Trapping

The direct localization and imaging of free radical distributions is much more challenging with EPR due both to aspects of stability discussed above as well as linewidth limitations. Despite almost three orders of magnitude higher sensitivity (eg, a free electron vs a proton) the much broader linewidths usually encountered in EPR places limitations on both resolution and overall sensitivity. There are additionally other limits to distinguishing tissue boundaries with radical distributions; these are simply more difficult to visualize by EPR. On the other hand, MRI, which is a mature, commercialized technology, offers exquisite anatomical resolution based on the protons of water (i.e. 100 M). Several physical aspects, such as nuclear relaxation times, diffusion rates, oxygen magnetic susceptibility effects, etc., allow multifaceted approaches to EPR and MRI image resolution. On the other hand, paramagnetic compounds serve as excellent contrast agents in MRI by inducing proton (nuclear) relaxation enhancement from rapidly exchanging water molecules. Consequently, MRI spin trapping potentially allows visualization of free radical biology at the site of its generation, by using the spin adducts as "contrast agents".

7.1.5 Nitric Oxide (NO)

NO may be 'spin trapped' with dithiocarbamate compounds and Fe(II), which form a stoichiometric 2:1 complex for axial coordination of NO. The water soluble trap, MGD, forms the $(MGD)_2Fe(II)$ NO complex where a diagnostic EPR spectrum is found with septic shock mice (which has been almost the sole example with sufficient sensitivity *in vivo).* Recently Kaneko et al. (2002) demonstrated *in vivo* observations of NO in the brain of epileptic mice models. The relaxivity of this complex is relatively frequency independent for both T_1 and T_2 at 20 and 85 MHz, respectively. Uncomplexed MGD, Fe(II) or $(MGD)_2$-Fe(II) show essentially negligible relaxivity while the $(MGD)_2Fe(II)$ NO complex yields appreciable relaxation enhancement (Fujii et al., 1999). Consequently, in MRI measurements, only the NO complex will yield image contrast enhancement, frequently at the site of NO generation. As shown in Figure 7, 1.5T T_1-weighted MRI images of septic-shock rats showed increased enhancement in the liver with time. This was suppressed by injecting the animals with a specific iNOS inhibitor, L-NMMA. Consequently, both the localization and "biochemistry" of NO generation can be visualized at high-resolution *in vivo.*

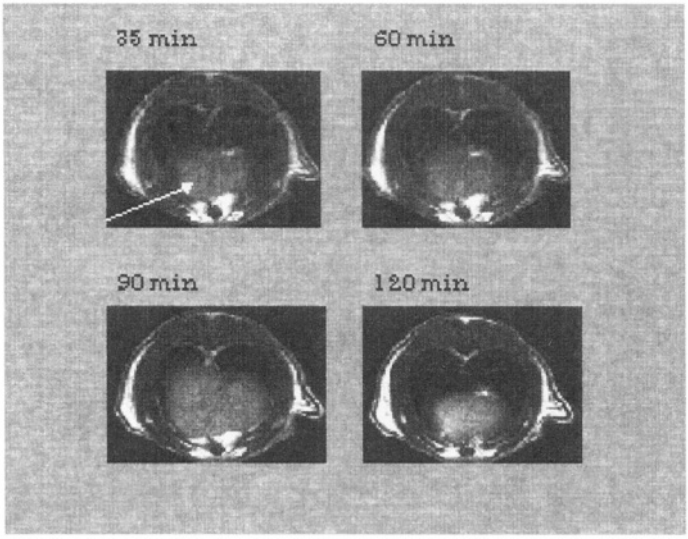

Figure 7. Transverse T_1-weighted MR images of the liver in LPS-doped rats. MR images were measured at the times indicated for two different slices of the liver. Six hours after LPS injection, the NO spin-trap (3 ml of $(MGD)_2$-Fe(II), MGD: 100 mM, Fe: 20 mM) was administered i.p. The slice thickness was 2 mm, and each slice was separated by 1 mm. The image enhancement was drastically reduced upon treatment with the NOS inhibitor, L-NMMA. Adapted from Fujii et al. (1999) with permission.

7.2 Prospects for the Future

Most of the new approaches outlined here are still in their infancy. The future, however, looks promising Feasibility studies have been quite successful. Most of the stable isotopes incorporated in the spin traps described above are easily resolvable in the presence of other biological milieu. Sensitivity is particularly promising with ^{19}F NMR, a technique that has never been exploited to its full capacity *in vivo.*

Of particular note is the use of paramagnetic relaxation enhanced MRI. The power of paramagnetic contrast agents to MRI has been proven time and again. Several sophisticated pulse sequences exist which take advantage of small susceptibility/relaxation effects. In addition, the development of new, targeted paramagnetic spin traps and spin probes promise to provide the requisite localization. The ability to observe biological radical production at the site of generation offers the ultimate advantage in diagnosis.

8. SUMMARY AND CONCLUSIONS

There clearly are many areas in which free radicals are intrinsically involved in both physiology and pathophysiology. There also are many situations where the involvement of free radicals is minimal or not significant. EPR spectroscopy, combined with thoughtful experimental approaches can be a powerful method for resolving many of the questions that arise regarding the role of free radicals in disease. The National Biomedical ESR Center at MCW has had, and will continue to have an important role in providing critical EPR spectroscopy tools and original experimental results that will provide an understanding of the role of free radicals in disease. There appear to be sufficient important problems to make this a productive field for many years.

REFERENCES

Aburatani, H., Yoshitaka, H., Ishida, T., Takashima, R., Matsuba, C., Kodama, T., Takao, M., Yasui, A., Yomamoto, K., Asano, M., Fukasawa, K., Yoshinari, T., Inoue, H., Ohtsuka, E. and Nishimura, S. (1997) Cloning and characterization of mammalian 8-hydroxyguanine-specific DNA glycosylase/apurinic, apyrimidinic lyase, a functional mutM homologue. *Canc. Res.* **57**, 2151-2156.

Ames, B.N. and Shigenaga, M.K. (1993) Oxidants are a major contributor to cancer and aging, in *DNA and Free Radicals* (B. Halliwell and O.I. Aruoma, eds.) pp. 1-18, Ellis Horwood: New York.

Ames, B.N., Shigenaga, M.K. and Hagen, T.M. (1993) Oxidants, antioxidants, and the degenerative diseases of aging. *Proc. Natl. Acad. Sci. USA* **90,** 7915-7922.

Anderson, M.T., Staal, F.J.T., Gitler, C., Herzenberg, L.A. and Herzenberg, L.A. (1994) Separation of oxidant-initiated and redox-regulated steps in the NF-κB signal transduction pathway. *Proc. Natl. Acad. Sci. USA* **91,** 11527-11531.

Arai, K., Morishita, K., Shinmura, K., Kehno, T.., Kim, R.-S., Nohmi, T., Toniwaki, M., Ohwada, S. and Yokota, J. (1997) Cloning of a human homolog of the yeast OGG1 gene that is involved in the repair of oxidative DNA damage. *Oncogene* **14,** 2857-2861.

Amstad, P. A., Liu, H., Ichimiya, M., Berezesky, I.K., Trump. B.F., Buhimschi, I.A. and Gutierrez, P.L. (2001) BCL-2 is involved in preventing oxidant-induced cell death and in decreasing oxygen radical production. *Redox Report* **6**, 351-362.

Aslan, M., Ryan, T. M., Adker, B., Townes, T. M., Parks, D. A., Thompson, J. A., Tousson, A., Gladwin, M. T., Patel, R. P., Tarpey, M. M., Batinic-Haberle, I., White, C. R., and Freeman, B. A. (2001) Oxygen radical inhibition of nitric oxide-dependent vascular function in sickle cell disease, *Proc.Natl.Acad.Sci.*U.S.A. **98,** 15215-15220.

Au, K.G., Clark, S., Miller, J.H. and Modrich, P. (1989) *Escherichia coli mutY* gene encodes an adenine glycosylase active on G/A mispairs. *Proc. Natl. Acad. Sci. USA* **86,** 8877-8881.

Barden H. and Brizzee, K. R. (1987) The histochemistry of lipofuscin and neuromelanin. In Aloj-Totaro, E., Glees, R., and Pisanti, E. A., eds, *Advances in the Biosciences,* **64,** Pergamon Press, Oxford, 339-392.

Barr, D. P., Gunther, M. R., Deterding, L. J.,Tomer, K. B. and Mason, R.P. (1996). ESR spin trapping of a protein-derived tyrosyl radical from the reaction of *cytochrome c* with hydrogen peroxide. *J. Biol. Chem.* **271**, 15498-15503.

Barr, P.J. and Tomei, L.D. (1994) Apoptosis and its role in human disease. *Biotechnology* **12**, 487-493.

Beatty, S., Koh, H., Phil, M., Henson, D., and Boulton, M. (2000) The role of oxidative stress in the pathogenesis of age-related macular degeneration. *Surv. Ophthalmol.* **45**, 115-134.

Beckman, J.K., Bagheri, F., Ji, C., Blair, I.A. and Marnett, L.J. (1994) Phospholipid peroxidation in tumor promoter-exposed mouse skin. *Carcinogenesis* **15**, 2937-2944.

Bertoncini, C.R.A. and Meneghini, R. (1995) DNA strand breaks produced by oxidative stress in mammalian cells exhibit 3'-phosphoglycolate termini. *Nucleic Acids Res.* **23**,2995-3002.

Boiteux, S., O'Connor, T.R. and Laval, J. (1987) Formamidopyrimidine-DNA glycosylase of *Escherichia coli:* cloning and sequencing of the fpg structural gene and overproduction of the protein. *The EMBO J.* **6**, 3177-3183.

Bilinska, B., Pilawa, B., Zawada, Z., Wylegala, E., Wilczok, T., Dontsov, A. E., Sakina, N. L., Ostrovsky, M. A., and Ilyasova, V. B. (2002) Electron spin resonance investigations of human retinal pigment epithelium melanosomes from young and old donors. *Spectrochim. Acta A* **58**, 2257-2264.

Boissy, R. E. (1998) Chapter 4. Extracutaneous Melanocytes. In Nordlund, J. J., Boissy, R. E., Hearing, V. J., King, R. A., and Ortonne, J.-P., eds., *The Pigmentary System. Physiology and Patophysiology.* Oxford University Press, New York-Oxford, 59-73.

Boissy, R. E., Boissy, Y. L., Krakowsky, J. M., Lamoreux, M. L., Lingrel, J. B., and Nordlund, J. J. (1993) Ocular pathology in mice with a transgenic insertion at the microphthalmia locus. *J. Submicrosc. Cytol. Pathol.* **25**, 319-332.

Bose-Basu, B. Derose, E. F. Chen, Y-R Mason, R. P. and London R. E. (2001) Protein NMR spin trapping with **[methyl-^{13} C_3]-MNP:** application to the tyrosyl radical of equine myoglobin *Free Rad. Biol. Med.* **31**, 383–390 .

Boyd, M.R., Catignani, G.L., Sasame, H.A., Mitchell, J.R., and Stiko, A.W.. (1979) Acute pulmonary injury in rats by nitrofurantoin and modification by vitamin E, dietary fat, and oxygen. *Am. Rev. Respir. Dis.* **120**, 93-99.

Breen, A.P. and Murphy, J.A. (1995) Reactions of oxyl radicals with DNA. *Free Radical Biology and Medicine* **18**, 1033-1077.

Bronner, C.E., Baker, S.M., Morrison, P.T., Warren, G., Smith, L.G Lescoe, M.K., Kane, M., Earabino, C., Lipford, J., Lindblom, A., Tannergard, P., Bollag, R.J., Godwin, A.R., Ward, D.C., Nordenskjold, M., Fishel, R., Kolodner, R. and Liskay, R.M. (1994) Mutation in the DNA mismatch repair gene homologue hMLHI is associated with hereditary non-polyposis colon cancer. *Nature (London)* **368**, 258-261.

Brown, R. H. Jr. (1995) Amyotrophic lateral sclerosis: recent insights from genetics and transgenic mice. *Cell* **80**, 687-692.

Brown, R. H. Jr. (1998) SOD1 aggregates in ALS: cause, correlate, or consequence? *Nature Med.* **4**, 1362-1364.

Burdon, R.H. (1995) Superoxide and hydrogen peroxide in relation to mammalian cell proliferation. *Free Radical Biology and Medicine* **18**, 775-794.

Buttke, T.M. and Sandstrom, P.A. (1995) Redox regulation of programmed cell death in lymphocytes. *Free Rad. Res.* **22**, 389-397.

Buttke, T.M. and Sandstrom, P.A. (1994) Oxidative stress as a mediator of apoptosis. *Immunology Today* **15**, 7-10.

Butts, B.D., Kwei, K.A., Bowden G.T. and Briehl M.M. (2003) Elevated basal reactive oxygen species and phospho-Akt in murine keratinocytes resistant to ultraviolet B-induced apoptosis. *Mol. Carcinog.* **37,**149-157.

Cabrera, M., Nghiem, Y. and Miller, J.H. (1988) *mutM,* a second mutator locus in *Escherichia coli* that generates G·Ç →T·A transversions. *J. Bacteriol.* **170,** 5405-5407.

Cai, J., Nelson, K. C., Wu, M., Sternberg, Jr, P., and Jones, D. P. (2000) Oxidative damage and protection of the RPE. *Prog. Retin. Eye. Res.* **19,** 205-221.

Cantuti-Castelvetri, I., Shukitt-Hale B. and Joseph J.A. (2003) Dopamine neurotoxicity: age-dependent behavioral and histological effects. *Neurobiol. Aging* **24,** 697-706.

Chanock, S.L., Benna, J. E., Smith, R.M. and Babior, B.M. (1994) The Respiratory burst oxidase. *J. Biol. Chem.* **269,** 24519-24522.

Cheng, K.C., Cahill, D.S., Kasai, H., Nishimura, S. And Loeb, L.A. (1992) 8-hydroxyguanine, an abundant form of oxidative DNA damage causes G → T and A → C substitutions. *J. Biol. Chem.* **267,** 166-172.

Cheng, Y., Ko J.M., Lung, H.L., Lo, P.H., Stanbridge, E.J. and Lung, M.L. (2003) Monochromosome transfer provides functional evidence for growth-suppressive genes on chromosome 14 in nasopharyngeal carcinoma. *Genes Chromsom. Cancer* **37,** 359-368.

Chu, S., Huang, Q., Alvares, K., Yeldandi, A.V., Rao, M.S. and Reddy, J.K. (1995) Transformation of mammalian cells by overexpressing H_2O_2-generating peroxisomal fatty acyl-CoA oxidase. *Proc. Natl. Acad. Sci. USA* **92**, 7080-7084.

Cieszka, K. A., Hill, H. Z., Hill, G. J., and Plonka, P. M. (1995) Growth and pigmentation in genetically related S91 Cloudman melanoma cell lines treated with IBMX and MSH. *Exp. Dermatol.* **4**,192-198.

Cohen, G. (1989) Monoamine oxidase and oxidative stress at dopaminergic synapses. *J. Neural. Transm.* **32**, Suppl, 229-238.

Cohen, G. (1983) The pathobiology of Parkinson's disease: biochemical aspects of dopamine neuron senescence. *J. Neural. Transm.* **19**, Suppl., 89-103.

Corcoran, G.B., Fix, L., Jones, D.P., Moslen, M.T., Nicotera, P. Oberhammer, F.A. and Buttyan, R. (1994) Apoptosis: molecular control point in toxicity. *Toxicol. Appl. Pharmacol.* **128**, 169-181.

Crawford, D., Zbinden, I., Amstad, P. and Cerutti, P. (1988) Oxidant stress induces the proto-oncogenes *c-fos* and *c-myc* in mouse epidermal cells. *Oncogene* **3**,27-32.

Cruickshanks, K. J., Klein, R., and Klein, B. E. (1993) Sunlight and age-related macular degeneration. The beaver dam eye study. *Arch. Ophthalmol.* **111**, 514-518.

Curran, T and Morgan, J.I. (1995) Fos: An immediate-early transcription factor in neurons. *J. Neurobiology* **26**, 403-412.

Davies, A.M. (1995) The Bcl-2 family of proteins, and the regulation of neuronal survival. *Trends Neurosci.* **18**, 355-358.

Densen, P., Clark, R.A. and Nauseef, W.M. (1995) in Principles and *Practice of Infectious Diseases,* 4th ed. (G.L. Mandell, J.E. Bennett and R. Dolin, eds.) Churchill Livingstone: New York.

DeGray, J.A., Rao, D.N.R., and Mason, R.P. (1991) Reduction of paraquat and related bipyridylium compounds to free radical metabolites by rat hepatocytes. *Arch. Biochem. Biophys.* **289**,145-152.

Dexter, T. D., Carter, C. J., Wells, F. R., Javoy-Agid, F., Agid,Y., Lees, A., Jenner, P., and Marsden, C. D. (1989) Basal lipid peroxidation in substantia nigra is increased in Parkinson's disease. *J. Neurochem.* **52**, 381-389.

Dizdaroglu, M. (1993) Chemistry of free radical damage to DNA and nucleoproteins, in *DNA and Free Radicals* (B. Halliwell and O.I. Aruoma, eds.) pp. 19-40, Ellis Horwood: New York.

Emerit, I. (1994) Reactive oxygen species, chromosome mutation, and cancer: Possible role of clastogenic factors in carcinogenesis. *Free Rad. Biol, Med.* **16,** 99-109.

Enochs, W. S., Nilges, M. J., and Swartz, H. M. (1993a) A standardized test for the identification and characterization of melanins using electron paramagnetic resonance (EPR) spectroscopy. *Pigment Cell Res.* **6**, 91-99.

Enochs, W. S., Nilges, M. J., and Swartz, H. M. (1993b) Purified human neuromelanin, synthetic dopamine melanin as a potential model pigment, and the normal human substantia nigra: characterization by electron paramagnetic resonance spectroscopy. *J. Neurochem.* **61,** 68-79.

Enochs, W. S., Sarna, T., Zecca, L., Riley, P. A., and Swartz, H. M. (1994) The roles of neuromelanin, binding of metal ions, and oxidative cytotoxicity in the pathogenesis of Parkinson's disease: a hypothesis. *J. Neural. Transm. [P-D Sect]* **7**, 83-100.

Evans, J. and Wormald, R. (1996) Is the incidence of registrable age-related macular degeneration increasing? *Brit. J. Ophthalmol.* **80,** 9-14.

Feig, D., Sowers, L.C. and Loeb, L.A. (1994) Reverse chemical mutagenesis: Identification of the mutagenic lesions resulting from reactive oxygen species-mediated damage to DNA. *Proc. Natl. Acad. Sci. USA* **91**, 6609-6613.

Finkelstein, E., Rosen, G.M. and Rauckman, E.J. (1980) Spin trapping of superoxide and hydroxyl radical: practical aspects. *Arch. Biochem. Biophys.* **200,** 1-16.

Firth, J.D., Ebert, B.L., Pugh, C.W. and Ratcliffe, P.J. (1994) Oxygen-regulated control elements in the phosphoglycerate kinase 1 and lactate dehydrogenase A genes: Similarities with the erythropoietin 3' enhancer. *Proc. Natl. Acad. Sci. USA* **91**, 6496-6500.

Forrest, V.J., Kang, Y.-H., McClain, D.E., Robinson, D.H. and Ramakrishnan, N. (1994) Oxidative stress-induced apoptosis prevented by trolox. *Free Rad. Biol. Med.* **16,** 675-684.

Friedberg, E. C. (1985) DNA repair. W.H. Freemann, New York, N.Y.

Friedberg, E.C., Walker, G.C. and Siede, W. (1995) *DNA Repair and Mutagenesis* pp.157-161, American Society for Microbiology: Washington, D.C.

Frejaville C., Karoui H., Tuccio B., Le Moigne F., Culcasi M., Pietri S., Lauricella R. and Tordo P. (1995) 5-(Diethoxyphosphoryl)-5-methyl-1-pyrroline -oxide: a new efficient phosphorylated nitrone for the *in vitro* and *in vivo* spin trapping of oxygen-centered radicals. *J. Med. Chem.* **38**, 258-265.

Fujii, H., Zhao, B., Koscielniak, J. and Berliner, Lawrence J. (1994) *In vivo* EPR studies of the metabolic fate of nitrosobenzene in the mouse. *Magn. Reson. Med.* **31**, 77-80.

Fujii, H., Wan, X., Zhong, J.,Berliner, L. J. and Yoshikawa, K. (1999) *In vivo* imaging of spin-trapped nitric oxide in rats with septic shock: MRI spin trapping. *Magn. Reson. Med.* **42**, 235-239.

Ghio, A.J., Kadiiska, M.B., Xiang, Q-H., and Mason, R.P. (1998) *In vivo* evidence of free radical formation after asbestos instillation: an ESR spin trapping investigation. *Free Rad. Biol. Med.* **24**, 11-17.

Giese, B., Beyrich-Graf, X., Erdmann. P., Petretta, M. and Schwitter, U. (1995) The chemistry of single-stranded 4'-DNA radicals: influence of the radical precursor on anaerobic and aerobic strand cleavage. *Chem. Biol.* **2,** 367-375.

Ginsburg, I and Kohen, R. (1995) Cell damage in inflammatory and infectious sites might involve a coordinated "cross-talk" among oxidants, microbial haemolysins and ampiphiles, cationic proteins, phospholipases, fatty acids, proteinases and cytokines (an overview). *Free Rad. Res.* **22**, 489-517.

Gerlach, M., Trautwein, A. X., Zecca, L., Youdim, M. B. H., and Riederer, P. (1995) Mossbauer spectroscopic studies of purified human neuromelanin isolated from the substantia nigra. *J. Neurochem.* **65**, 923-926.

Glover, R. E., Ivy, E. D., Orringer, E. P., Maeda, H., and Mason, R. P. (1999) Detection of nitrosyl hemoglobin in venous blood in the treatment of sickle cell anemia with hydroxyurea. *Mol.Pharmacol.* **55**, 1006-1010.

Gopalakrishna, R., Chen, Z.-H. and Gundimeda, U. (1994) Tobacco smoke tumor promoters, catechol and hydroquinone, induce oxidative regulation of protein kinase C and influence invasion and metastasis of lung carcinoma cells. *Proc. Natl. Acad. Sci. USA* **91**, 12233-12237.

Goss, S. P. A., Singh, R. J., and Kalyanaraman, B. (1999) Bicarbonate enhances the peroxidase activity of Cu, Zn-superoxide dismutase. *J. Biol. Chem.* **274**, 28233-28239.

Greenspan, H.C. and Aruoma, O.I. (1994) Oxidative stress and apoptosis in HIV infection: a role for plant-derived metabolites with synergistic antioxidant activity. *Immunology Today* **15**, 209-213.

Graham, D. G. (1984) Catecholamine toxicity: a proposal for the molecular pathogenesis of manganese neurotoxicity and Parkinson's disease. *Neurotoxicology* **5**, 83-96.

Gurney, M. E., Lui, R., Althaus, J. S., Hall, E. D., and Becker, D. A. (1998) Mutant Cu, Zn,-superoxide dismutase in motor neuron disease. *J. Inherit. Metab. Disease* **21**, 587-597.

Gu, Y., Deasai, T., Gutierrez, P.L. and Lu, A-L (2001) Alteration of DNA base excision repair enzymes hMYH and hOGG1 in hydrogen peroxide resistant transformed human breast cells. *Med. Sci. Monit.* **7**, 861-868.

Halaban, R. and Lerner, A. B. (1977) Tyrosinase and inhibition of proliferation of melanoma cells and fibroblasts. *Exp. Cell Res.* **108,** 119-125.

Halliwell, B. (1993) Oxidative DNA damage: meaning and measurement, in *DNA and Free Radicals* (B. Halliwell and O.I. Aruoma, eds.) pp.67-82 Ellis Horwood: New York.

Halliwell, B. and Aruoma, O.I. (1991) DNA damage by oxygen-derived species. Its mechanism and measurement in mammalian systems. *FEBS Letters* **281**, 9-19.

Halliwell, B. and Gutteridge, J.M.C. (1989) *Free Radicals in Biology and Medicine,* 2nd edition. Oxford University Press: New York.

Hagen, T.M., Huang, S., Curnutte, J., Fowler, P., Martinez, V., Wehr, C.M., Ames, B.N. and Chisari, F.V. (1994) Extensive oxidative DNA damage in hepatocytes of transgenic mice with chronic active hepatitis destined to develop hepatocellular carcinoma. *Proc. Natl. Acad. Sci. USA* **91**, 12808-12812.

Ham, Jr, W. T., Ruffolo, Jr, J. J., Mueller, H. A., and Guerry, 3rd., D. (1980) The nature of retinal radiation damage: dependence on wavelength, power level and exposure time. *Vision Res.* **20**, 1105-1111.

Hazra, T.K., Izumi, T., Maidt, L., Floyd, R.A. and Mitra, S. (1998) The presence of two distinct 8-oxoguanine repair enzymes in human cells: their potential complementary roles in preventing mutation. *Nucleic Acids Res.* **26**, 5116-5122.

Hebbel, R. P., Eaton, J. W., Balasingam, M., and Steinberg, M. H. (1982) Spontaneous oxygen radical generation by sickle erythrocytes. *J. Clin. Invest.* **70**, 1253-1259.

Hill, H. Z., Hill, G. J., Cieszka, K., Plonka, P. M., Mitchell, D. L, Meyehoffer, M. F., Xin, P., and Boissy, R. E. (1997) Comparative action spectrum for ultraviolet light killing of mouse melanocytes from different genetic coat color backgrounds. *Photochem. Photobiol.* **65**, 983-989.

Hockenbery, D.M. (1995) bcl-2, a novel regulator of cell death. *BioEssays* **17**, 631-638.

Hodgson, E. K., and Fridovich, I. (1975) The Interaction of bovine erythrocyte superoxide dismutase with hydrogen peroxide: inactivation of the enzyme. *Biochemistry* **14**, 5294-5298.

Hollstein, M., Sidransky, D., Vogelstein, B. and Harris, C.C. (1991) p53 Mutations in human cancers. *Science* **253**, 49-53.

Horton, J.K., Brigelius, R., Mason, R.P., and Bend, J.R. (1986) Paraquat uptake into freshly isolated rabbit lung epithelial cells and its reduction to the paraquat radical under anaerobic conditions. *Mol. Pharmacol.* **29**, 484-488.

Hu, J., Engman, L. and Cotgreave, I.A. (1995) Redox-active chalcogen-containing glutathione peroxidase mimetics and antioxidants inhibit tumor promoter-induced downregulation of gap junctional intercellular communication between WB-F344 liver epithelial cells. *Carcinogenesis* **16**, 1815-1824.

Huang, J., Hadimani, S. B., Rupon, J. W., Ballas, S. K., Kim-Shapiro, D. B., and King, S. B. (2002) Iron nitrosyl hemoglobin formation from the reactions of hemoglobin and hydroxyurea, *Biochemistry* **41**, 2466-2474.

Hussain, S.P., Aguilar, F., Amstad, P. And Cerutti, P. (1994) Oxy-radical induced mutagenesis of hotspot codons 248 and 249 of the human p53 gene. *Oncogene* **9**, 2277-2281.

Janknecht, R., Cahill, M.A. and Nordheim, A. (1995) Signal integration at the c-*fos* promoter. *Carcinogenesis* **16**, 443-450.

Jaiyesimi, I.A., Buzdar, A.U., and Hortobagyi, G., Inflammatory Breass Cancer: A Review (1992) *J. Clin. Oncol.* **10**, 1014-1024.

Jellinger, K., Kienzl, E., Rumpelmair, G., Riederer, P., Stachelberger, H., Ben-Shachar, D., and Youdim, M. B. H. (1992) Iron-melanin complex in substantia nigra of parkinsonian brains:an X-ray microanalysis. *J. Neurochem.* **59**, 1168-1171.

Jenner, P. (1991) Oxidative stress as a cause of Parkinson's disease. *Acta Neurol. Scand.* **84**, Suppl., 6-15.

Jeong, S.Y., Shin, K.H., Shin, J.H., Ku, J.L., Shin Y.K., Park, S.Y., Kim, W. H., and Park, J.G. (2003) Microsatellite instability and mutations in DNA mismatch repair genes in sporadic colorectal cancer. *Dis Colon Rectum* **46,** 1069-1077.

Jiang, J., Jordan, S. J., Barr, D. P., Gunther, M. R., Maeda, H., and Mason, R. P. (1997) *Mol. Pharmacol.* **52,** 1081-1086.

Kadiiska, M.B., Mason, R.P., Dreher, K.L., Costa, D.L., and Ghio, A.J. (1997) *In vivo* evidence of free radical formation in the rat lung after exposure to an emission source air pollution particle. *Chem. Res. Toxicol.* **10**, 1104-1108.

Kaneko, K., Itoh, K., Berliner, L.J., Miyasaka, K. and Fujii, H. (2002) Consequences of nitric oxide generation in epileptic-seizure rodent models as studied by *in vivo* EPR, *Magn. Reson. Med.* **48**, 1051-1056.

Kastner, A., Hirsh, E., Lejenne, O., Javoy-Agid, F., and Agid, Y. (1992) Is the vulnerability of neurons in the substantia nigra of patients with Parkinson's disease related to their neuromelanin content? *J. Neurochem.* **59**, 1080-1089.

Katsuda, H., Kobayashi, T., Saito, H., Matsunaga, T., and Ikeya, M. (1990) Electron spin resonance imaging of mouse B16 melanoma. *Chem. Pharm. Bull. Tokyo* 38, 2838-2840.

Kennedy, C.H., Hatch, G.E., Slade, R., and Mason, R.P. (1992) Application of the EPR spin trapping technique to the detection of radicals produced *in vivo* during inhalation exposure of rats to ozone. *Toxicol. Appl. Pharmacol.* **114**, 41-46.

Khan, N. and Swartz, H.M.(2002) Measurements of *in vivo* parameters pertinent to ROS/RNS using EPR spectroscopy. *Mol. and Cell. Biochem.* **234/235,** 341-357.

Khan, A.U. and Wilson, T. (1995) Reactive oxygen species as cellular messengers. *Chemistry and Biology* **2**, 437-445.

Khan, N., Wilmot, C.M., Rosen, G.M., Demidenko, E., Sun, J., Joseph, J., O'Hara, J., Kalyanaraman, B., and Swartz, H.M. (2003) Spin traps: *in vitro* toxicity and stability of readical adducts. *Free Rad. Biol. Med.* **11**, 1473-1481.

Khramtsov, V.V., Berliner, L. J. and Clanton T.L. (1999) NMR Spin Trapping: detection of free radical adducts using a phosphorus containing nitrone spin trap. *Magn. Reson. Med.* **42**, 228-234 (1999).

Khramtsov, V.V., Reznikov, V.A., Berliner L.J., Litkin, A.K., Grigor'ev, LA. and Clanton T.L. (2001). NMR spin trapping: detection of free radical reactions using a new fluorinated DMPO analog, *Free Rad. Biol. Med.* **30**, 1099-1107.

Klings, E. S. and Farber, H. W. (2001) Role of free radicals in the pathogenesis of acute chest syndrome in sickle cell disease. *Respir. Res.* **2**, 280-285.

Kinnear, P. E., Jay, B., and Witkop, Jr., C. J. (1985) Albinism. *Surv. Ophthalmol.* **30**, 75-101.

Klein, R., Klein, B. E., and Linton, K. L. (1992) Prevalence of age-related maculopathy. The beaver dam eye Study. *Ophthalmol.* **99**, 933-943.

Koong, A.C., Chen, E.Y. and Giaccia, A.J. (1994a) Hypoxia causes the activation of nuclear factor κB through the phosphorylation of κBα on tyrosine residues. *Cancer Res.* **54**, 1425-1430.

Koong, A.C., Chen, E.Y., Mivechi, N.F., Denko, N.C., Stambrook, P. and Giaccia, A.J. (1994b) Hypoxia Activation of nuclear factor κB is mediated by a *Ras* and *Raf* signaling pathway and does not involve MAP Kinase (ERK1 or ERK2). *Cancer Res.* **54**, 5273-5279.

Korytowski, W., Sarna, T., and Zaręba M. (1995) Antioxidant action of neuromelanin: the inhibitory effect on lipid peroxidation. *Arch. Biochem. Biophys.* **319**, 142-148.

Kucherlapati, R. and G. R. Smith. (1988) *Genetic Recombination.* American Society for Microbiology, Washington, D.C.

Lambert, J.R., Bilanchone, V.W. and Cumsky, M.G. (1994) The ORD1 gene encodes a transcription factor involved in oxygen regulation and is identical to IXR1, a gene that confers cisplatin sensitivity to *Saccharomyces cerevisiae. Proc. Natl. Acad. Sci. USA* **91**, 7345-7349.

Larsson, B. S. (1993) Interaction between chemicals and melanin. *Pigment Cell Res.* **6**, 127-133.

Laskin, D.L. and Pendino, K.J. (1995) Macrophages and inflammatory mediators in tissue injury. *Annu. Rev. Pharmacol. Toxicol.* **35**, 655-677.

Laval, F. (1994) Expression of the *E. coli fpg* gene in mammalian cells reduces the mutagenicity of xrays. *Nucleic Acids Res.* **22**, 4943-4946.

Le Page, F., Kwoh, E. E., Avrustskaya, A., Leadon, S. A., Sarasin, A. and Cooper, P. K. (2000) Transcription coupled repair of 8-oxoguanine: requirement for XPG, TFIIH, and CSB and implications for Cockayne syndrom. *Cell* **101**, 159-171.

Liochev, S. I., and Fridovich, I. (1999) On the role of bicarbonate in peroxidations catalyzed by Cu, Zn, superoxide dismutase. *Free Rad. Biol. Med.* **27**, 1444-1447.

Lin, J.-K. and Shih, C.-A. (1994) Inhibitory effect of curcumin on xanthine dehydrogenase/oxidase induced by phorbol-12-myristate-13-acetate in NIH3T3 cells. Carcinogenesis **15**, 1717-1721.

Liu, R., Li, B., Flanagan, W., Oberley, L. W., Gozal, D., and Qiu, M. (2002) Increased mitochondrial antioxidative activity or decreased oxygen free radical propagation prevent mutant SODl-mediated motor neuron cell death and increased amyotrophic lateral sclerosis-like transgenic mouse survival. *J. Neurochem.* **80**, 488-500.

Liu, K.J. Miyake, M. Panz, T. and Swartz, H.M. (1999) Evaluation of DEPMPO as a spin trapping agent in biological systems. *Free Rad. Biol Med.* **26**, 714-721.

Liu, H., Yuan, L., Yang X. and Wang, K. (2003) La(3+), Gd(3+) and Yb(3+) induced changes in mitochondrial structure, membrane permeability, cytochrome c release and intracellular ROS level. *Chem. Biol. Interactions* **146**, 27-37.

Loeb, L. A. (1991) Mutator phenotype may be required for multistage carcinogenesis. *Cancer Res.* **51**, 3075-3079.

Loeb, L. A. (1994) Microsatellite instability: marker of a mutator phenotype in cancer. *Cancer Res.* **54**, 5059-5063.

Long, L.H., Evans, P.J., Halliwell, B. (1999a) Hydrogen peroxide in human urine: implications for antioxidant defense and redox regulation. *Biochem. Biophys. Res. Commun.* **262**, 605-609.

Long, L.H., Lan, A.N., Hsuan, F.T., and Halliwell, B. (1999b) Generation of hydrogen peroxide by "antioxidant" beverages and the effect of milk addition. Is cocoa the best beverage? *Free Radio. Res.* **1**, 67-71.

Lukiewicz S. And Sarna T. (1972) Electron spin resonance studies on living cells. III. Development of single individuals in *Triturus alpestris. Folia Histochemica et Cytochemica* **10**, 137-150.

Luo, Y., Han, Z., Chin, S.M. and Linn, S. (1994) Three chemically distinct types of oxidants formed by iron-mediated Fenton reactions in the presence of DNA. *Proc. Natl. Acad. Sci. USA* **91**, 12438-12442.

Lu, R., Nash, H.M. and Verdine, G.L. (1997) A mammalian DNA repair enzyme that excises oxidatively damaged oxoguanine maps to a locus frequently lost in lung cancer. *Curr.Biol.* **7**, 397-407.

Mader, K., Bacic, G. and Swartz, H.M. *In vivo* detection of anthralin-derived free radicals in the skin of hairless mice by low-frequency electron paramagnetic resonance spectroscopy. *J. Invest. Derm.* **104**, 514-517.

Maki, H. and Sekiguchi, M. (1992) MutT protein specifically hydrolyzes a potent mutagenic substrate for DNA synthesis. *Nature* (London) **355**, 273-275.

Malins, D.C. (1993) Identification of hydroxyl radical-induced lesions in DNA as structure biomarkers with a putative link to cancer development. *J. Toxicol. and Environmental Health* **40**, 247-261.

Malins, D.C. and Haimanot, R. (1991) Major alterations in the nucleotide structure of DNA in cancer of the female breast. *Cancer Res.* **51**, 5430-5432.

Malins, D.C., Holmes, E.H., Polissar, N.L. and Gunselman, S.J. (1993) The etiology of breast cancer: Characteristic alterations in hydroxyl radical-induced DNA bas lesions during oncogenesis with potential for evaluating incidence risk. *Cancer* **71**, 3036-3043.

Malins D.C., Johnson, P.M., Barker, E.A., Polissaer, N.L., Wheeler, T.M. and Anderson, K.M. (2003) Cancer-related changes in prostate DNA as men age early identification of metastasis in primary prostate tumors. *Proc. Natl. Acad. Sci. USA* **100**, 5401-5406.

Malins, D.C., Polissar, N.L., Nishikida, K., Holmes, E.H., Gardner. H.S. and Gunselman, S.J. (1995) The Etiology and Prediction of Breast Cancer. *Cancer* **75**, 503-517.

Mann, I. C. (1964) *The Development of the Human Eye.* **2nd** ed., Grune & Stratton, New York.

Marnett, L.J. and Ji, C. (1994) Modulation of oxidant formation in mouse skin *in vivo* by tumor-promoting phorbol esters. *Cancer Res.* **54**, 1886s-1889s.

Mars, U. and Larsson, B. S. (1999) Pheomelanin as a binding site for drugs and chemicals. *Pigment Cell Res.* **12**, 266-274.

Mathieu, C. Mercier, A. Witt, D. Debmkowski, L. Tordo and P. Beta (1997). Phosphorylated nitroxides in the pyrrolidine series: reduction by ascorbate. *Free Radic. Biol. Med.* **22**, 803 -806.

Mason, R.P. (1979) Free radical metabolites of foreign compounds and their texicological significance. In *Reviews in Biochemical Toxicology,* (E. Hodgson, J.R. Bend, R.M. Philpot, Eds.), vol. 1. New York: Elsevier, pp. 151-200.

Mason, R.P. (1982) Free radical intermediates in the metabolism of toxic chemicals. In: W.A. Pryor, ed. *Free Radicals in Biology,* vol. V. New York: Academic Press, pp. 161-222.

Mason, R.P. and Holtzman, J.L. (1975a) The mechanism of microsomal and mitochondrial nitroreductase. Electron spin resonance evidence for nitroaromatic free radical intermediates. *Biochemistry* **14**, 1626-1632.

Mason, R.P. and Holtzman, J.L. (1975b) The role of catalytic superoxide formation in the O_2 inhibition of nitroreductase. *Biochem. Biophys. Res. Commun.* **67**, 1267-1274.

McCarty, C. and Taylor, H. R. (1999) Light and risk for age-related eye diseases. In Taylor, A., ed., *Nutritional and Environmental Influences on the Eye.* CRC Press, Boca Raton, 135-150.

McGoldrick, J.P., Yeh, Y.-C, Solomon, M., Essigmann, J.M. and Lu, A.-L. (1995) Characterization of a mammalian homolog of the *Escherichia coli* MutY Mismatch *Repair Protein* **15**, 989-996.

Meneghini, R. and Martins, E.L. (1993) Hydrogen peroxide and DNA damage, in *DNA and Free Radicals* (B. Halliwell and O.I. Aruoma, eds.) pp. 83-94 Ellis Horwood: New York.

Michaels, M.L., Pham, L., Cruz, C. and Miller, J.H. (1991) MutM, a protein that prevents G:C to T:A transversions, is formamidopyrimidine-DNA glycosylase. *Nucleic Acids Res.***19**, 3629-3632.

Michaels, M.L., Pham, L., Nghiem, Y., Cruz, C. and Miller, J.H. (1990) MutY, an adenine glycosylase active on G:A mispairs, has homology to endonuclease III. *Nucleic Acids Res.* **18**, 3841-3845.

Moriya M. (1993) Single-stranded shuttle phagemid for mutagenesis studies in mammalian cells: 8-Oxoguanine in DNA induces targeted G-C transversions in simian kidney cells. *Proc. Natl. Acad. Sci. USA* **90**, 1122-1126.

Moriya, M., Ou, C., Bodepudi, V., Johnson, F., Takeshita, M. and Grollman, A.P. (1991) Site-specific mutagenesis using a gapped duplex vector: a study of translesion synthesis past 8-oxodeoxyguanosine in *E. coli. Mutation Res.* **254**, 281-288.

Moos, T. (2000) Absence of ferritin protein in substantia nigra pars compacta neurons. A reappraisal to the role of iron in Parkinson disease pathogenesis. *Mov. Disord.* **15,** [Suppl.], 319.

Murphy, P.G., Myers, D.S., Webster, N.R., Jones, J.G., and Davies, M.J. (1991) Direct detection of free radical generation in an *in vivo* model of acute lung injury. *Free Rad. Res. Commun.* **15**, 167-176.

Mytar, B., Siedlar, M., Woloszyn, M., Ruggiero, I., Pyrjma, J., Zembala, M. (1999) Induction of reactive oxygen intermediates in human monocytes by tumor cells and their role in spontaneous monocyte cytotoxicity. *Br. J. Cancer* **79**, 737-743.

Nash, H.M., Bruner, S.D., Scharer, O.D., Kawate, T., Addona, T.A., Spooner, E., Lanes, W.S. and Verdine, G.L. (1996) Cloning of yeast 8-oxoguanine DNA glycosylase reveals the existence of a base-excision DNA-repair protein superfamily. *Curr. Biol.* **5**, 968-980.

Natta, C. L., Tatum, V. L., and Chow, C. K. (1992) Antioxidant status and free radical-induced oxidative damage of sickle erythrocytes. *Ann. N. Y. Acad. Sci.* **669**, 365-367.

Nghiem, Y., Cabrera, M., Cupples, C.G. and Miller, J.H. (1988) The *mutY* gene: a mutator locus in *Escherichia coli* that generates G:C to T:A transversions. *Proc. Natl. Acad. Sci. USA* **85**, 2709-2713.

Noden D. M. (1991) Vertebrate craniofacial development: the relation between ontogenic process and morphological outcome. *Brain Behav. Evol.* **38**, 190-225.

Nose, K., Shibanuma, M., Kikuchi, K., Kageyama, H., Sakiyama, S. and Kuroki, T. (1991) Transcriptional activation of early-response genes by hydrogen peroxide in a mouse osteoblastic cell line. *Eur. J. Biochem.* **201**, 99-106.

Nowell, P. C. (1976) The clonal evolution of tumor cell populations. *Science* **194**, 23-28.

Olinski, R., Zastawny, T., Budzbon, J., Skokowski, J., Zegarski, W. and Dizdaroglu, M. (1992) DNA base modifications in chromatin of human cancerous tissues. *FEBS* **309**, 193-198.

Odh, G., Carstam, R., Paulson, J., Wittbjer, A., Rosengren, E., and Rorsman, H. (1994) Neuromelanin of the human substantia nigra: a mixed-type melanin. *J. Neurochem.* **62,** 2030–2036.

Organisciak, D. T. and Sarna, T. (2001) Genetic-, age- and light-induced degeneration of the retina and retinal pigment epithelium. In Coohill, T. P. and Valenzeno, D. P., eds, *Photobiology for the 21st Century,* Valdenmar Publishing Company, Overland Park, KS, 81-100.

Orlow, S. J. (1998) Chapter 6. The Biogenesis of Melanosomes. In Nordlund, J. J., Boissy, R. E., Hearing, V. J., King, R. A., and Ortonne, J.-P., eds., *The Pigmentary System. Physiology and Patophysiology.* Oxford University Press, New York-Oxford, 97-106.

Panandiker, A., Maru, G.B. and Rao, K.V.K. (1994) Dose-response effects of malachite green on free radical formation, lipid peroxidation and DNA damage in Syrian hamster embryo cells and their modulation by antioxidants. *Carcinogenesis* **15**, 2445-2448.

Papadopoulos, N. Nicolaides, N.C., Wei, Y.-F., Ruben, S.M., Carter, K.C., Rosen, C.A., Haseltine, W.A., Fleischmann, R.K., Graser, C.M., Adams, M.D., Venter, J.C., Hamilton, S.R., Petersen, G.M., Watson, P., Lynch, H.T., Peltomaki, P., Mecklin, J.-P., Chapelle, A. de la, Kinzler, K.W. and Vogelstein, B. (1994) Mutation of a mutL homolog in hereditary colon cancer. *Science* **263**, 1625-1629.

Pauleikhoff, D. and Holz, F. G. (1996) Age-related macular degeneration. 1. Epidemiology, pathogenesis and differential diagnosis. *Ophthalmologie* **93**, 299-315.

Pawelek, J. M. and Chakraborty, A. K. (1998) Chapter 28. The Enzymology of melanogenesis. In Nordlund, J. J., Boissy, R. E., Hearing, V. J., King, R. A., and Ortonne, J.-P., eds., *The Pigmentary System. Physiology and Pathophysiology.* Oxford University Press, New York-Oxford, 391-400.

Pawelek, J. M. and Lerner, A. B. (1978) 5,6-Dihydroxyindole is a melanin precursor showing potent cytotoxicity. *Nature* **276**, 626-628.

Peterson, F.J., Combs, G.F., Jr., Holtzman, J.L., and Mason, R.P. (1982) Effect of selenium and vitamin E deficiency on nitrofurantoin toxicity in the chick. *J. Nutr.* **112**, 1741-1746.

Peterszegi, G., Isnard, N., Robert, A.M. and Robert L. (2003) Studies on skin aging. Preparation and properties of fucose-rich oligo-and polysaccharides. Effect on fibroblast proliferation and survival. *Biomed. Pharmacother.* **57**, 187-194.

Piechaczyk, M. and Blanchard, J.-M. (1994) c-*fos* proto-oncogene regulation and function. *Critical Reviews in Oncology/Hematology* **17**, 93-131.

Pietri, S.; Liebgott, T.; Frejaville, C.; Tordo, P.; and Culcasi, M. Nitrone spin traps and their pyrrolidine analogs in myocardial reperfusion injury: hemodynamic and ESR implications. (1998) *Eur. J. Biochem.* **254**, 256–265.

Pilas, B. and Sarna, T. (1985) Quantitative determination of melanin in pigmented cells by electron spin resonance spectroscopy. In Bagnara, J., Klaus S. N., Paul, E., and Schartl M., eds., *Pigment Cells 1985. Biological, Molecular and Clinical Aspects of Pigmentation. Proceedings of the XIIth International Pigment Cell Conference Giessen, Federal Republic of Germany,* University of Tokyo Press, Tokyo, 97-103.

Plonka, P. M., Slominski, A. T, Pajak, S., and Urbanska, K. (2003) Transplantable melanomas in gerbils (Meriones unguiculatus). II – melanogenesis. *Exp. Dermatol.* **12**, in press.

Price, D. L., Cleveland, D. W., and Koliatsos, V. E. (1994) Motor neuron disease and animal models. *Neurobiol.Dis.***1**, 3-11.

Pryor, W.A. (1992) Biological effects of cigarette smoke, wood smoke, and the smoke from plastics: the use of electron spin resonance. *Free Rad. Biol. Med.* **13,** 659-676.

Przybytkowski, E., Girouard, S., Allard, B., Lamarre, L. and Basik, M. (2003) Widespread bimodal intrachromosomal genomic instability in sporadic breast cancers associated with 13q allelic imbalance. *Cancer Res.* **63,** 4588-4593.

Radicella, J.P., Dherin, C., Desmaz., Fox, M.S. and Boiteux, S. (1997) Cloning and characterization of hOGG1, a human homolog of the OGG1 gene of saccharomyces cerevisiae. *Proc. Natl. Acad. Sci. USA* **94,** 8010-8015.

Ramotar, D. and Demple, B. (1993) Enzymes that repair oxidative damage to DNA, in *DNA and Free Radicals* (B. Halliwell and O.I. Aruoma, eds.) pp. 165-192 Ellis Horwood: New York.

Rao, D.N.R., Harman, L., Motten, A., Schreiber, J., and Mason, R.P. (1987) Generation of radical anions of nitrofurantoin, misonidazole, and metronidazole by ascorbate. *Arch. Biochem. Biophys.* **255**, 419-427.

Rao, D.N.R., Jordan, S., and Mason, R.P. (1988a) Generation of nitro radical anions of some 5-nitrofurans, and 2- and 5-nitroimidazoles by rat hepatocytes. *Biochem. Pharmacol,* **37**, 2907-2913.

Rapp, L. M. (1995) Chapter 32. Retinal phototoxicity. In Chang, L. W. and Dyer, R. S., eds, *Handbook of Neurotoxicology,* Marcel Dekker, New York, 963-1003.

Raymond, S. M. and Jackson, I. J. (1995) The retinal pigmented epithelium is required for development and maintenance of the mouse neural retina. *Curr. Biol.* **5**, 1286-1295.

Reiter, C. D., Wang, X., Tanos-Santos, J. E., Hogg, N., Cannon III, R. O., Schechter, A., and Gladwin, M. T. (2002) Cell-free hemoglobin limits nitric oxide bioavailability in sickle-cell disease. *Nature Medicine* **8**: 1383-1389.

Remacle, J., Raes, M., Toussaint, O., Renard, P. and Rao, G. (1995) Low levels of reactive oxygen species as modulators of cell function. *Mutation Research* **316,** 103-122.

Renan, M. J. (1993) How many mutations are required for tumorgenesis? Implications from human cancer data. *Mol. Carcinogen* **7**, 139-146.

Repka, T. and Hebbel, R. P. (1991) Hydroxyl radical formation by sickle erythrocyte membranes: role of pathologic iron deposits and cytoplasmic reducing agents. *Blood* **78**, 2753-2758.

Riederer, P., Sofic, E., Raush, W., Shmidt, B., Reynolds, G. P., Jellinger, K., and Youdim, M. B. H. (1989) Transition metals, ferritin, glutathione, and ascorbic acid in parkinsonian brains. *J. Neurochem.* **52**, 515-520.

Roldan-Arjona, T., Wei, Y., Carter, K.C., Klungland, A., Anselmino, C., Wang, R., Augustus, M. and Lindahl, T. (1997) Molecular cloning and functional expression of a human cDNA encoding the antimutator enzyme 8-hydroxyguanine-DNA glycosylase. *Proc. Natl. Acad. Sci. USA* **84**, 8016-8020.

Rose, M.S. and Smith, L.L. (1977) Tissue uptake of paraquat and diquat. *Gen. Pharmacol.* **8**, 173-176.

Rosenquist, T.A., Zharkov, D.O. and Grollman, A.P. (1997) Cloning and characterization of a mammalian 8-oxoguanine DNA glycosylase. *Proc. Natl. Acad. Sci. USA* **94**, 7429-7434.

Roubaud, V. Sankakarpandi, S. Kuppusamy, P. Tordo, P. and Zweier, J. (1997) Quantitative measurement of superoxide generation using the spin trap 5-(Diethoxyphoshporyl)-5-methyl-1-pyrroline-*N*-oxide. *Analytical Biochemistry* **247**, 404 - 411.

Rozanowska, M., Korytowski, W., Rozanowski, B., Skumatz, C., Boulton, M. E., Burke, J. M., and Sarna, T. (2002) Photoreactivity of aged human RPE melanosomes: a comparison with lipofuscin. *Invest. Ophthalmol. Vis. Sci.* **43**, 2088-2096.

Rozanowska, M., Kukulski, T., Burke, J., Nilges, M., Pilas, B., Korytowski, W., and Sarna, T. (1993) OR7 - Photooxidation of retinal pigment melanin – a model for melanin aging. *Pigment Cell Res.* **6**, 272-273.

Rozanowska, M., Sarna, T., Land, E. J., and Truscott, T. G. (1999) Free radical scavenging properties of melanin interaction of eu- and pheo-melanin models with reducing and oxidising radicals. *Free Rad. Biol. Med.* **26**, 518-525.

Sandstrom, P.A., Mannie, M.D. and Buttke, T.M. (1994) Inhibition of activation-induced death in T cell hybridoma by thiol antioxidants: oxidative stress as a mediator of apoptosis. *J. Leukocyte Biol.* **55**, 221-226.

Sarna, T. (1992) Properties and function of the ocular melanin--a photobiophysical view. *J Photochem. Photobiol. B* **12**, 215-258.

Sarna T. and Swartz H. M. (1993) Interactions of melanin with oxygen (and related species). In Scott G. ed, *Atmospheric Oxidation and Antioxidants vol. III,* Elsevier, 129-169.

Sarna, T., Burke, J. M., Korytowski, W., Rozanowska, M., Skumatz, C. M. B., Zareba, A., and Zareba, M. (2003) Loss of melanin in human RPE with aging. *Exp. Eye Res.* **76**, 89-98.

Sarna, T., and Rozanowska, M. (1994) Photobiology of the Eye. In Jori, G., Pottier, RH, Rodgers, M. A. J., and Truscott, T. G., eds., *Photobiology in Medicine, NATO ASI Series, Series A: Life Sciences* **272**, Plenum Press (in cooperation with NATO Scientific Affairs Division), New York-London, 125-141.

Sarna, T., Rozanowska, M., Zareba, M., Korytowski, W., and Boulton, M. (1998). Retinal melanin and lipofuscin: possible role in photoprotection and phototoxicity of human RPE. In Hoenigsmann, H., Knoblerl R. M., Trautinger, F., and Jori, G., eds., *Landmarks in Photobiology. Proceedings of the* 12^{th} *International Congress of Photobiology,* OEMF spa, Milano, 418-421.

Sato, K., Kadiiska, M.B., Ghio, A.J., Corbett, J., Fann, Y.C., Holland, S.M., Thurman, R.G., and Mason, R.P. (2002) *In vivo* lipid-derived free radical formation by NADPH oxidase in acute lung injury induced by lipopolysaccharide: a model for ARDS. *FASEB J.* **16,** 1713-1720.

Schacter, L. P. (1986) Generation of superoxide anion and hydrogen peroxide by erythrocytes from individuals with sickle trait or normal hemoglobin. *Eur. J. Clin. Invest.* **16**, 204-210

Schreck, R., Rieber, P. and Baeuerle, P.A. (1991) Reactive oxygen intermediates as apparently widely used messengers in the activation of the NF-κB transcription factor and HIV-1. EMBO J. **10**, 2247-2258.

Selinsky, B.S., Levy, L.A., Motten, A.G., and London RE. (1989). Development of fluorinated, NMR-active spin traps for studies of free radical chemistry. *J. Magn. Reson* **81**, 57-67.

Sheng, K., Shariff, M., and Hebbel, R. P. (1998) Comparative oxidation of hemoglobins A and S. *Blood* **91**, 3467-3470.

Shibutani, S., Takeshita, M. and Grollman, A.P. (1991) Insertion of specific bases during DNA synthesis past the oxidation-damaged base 8-oxodG. *Nature (London)* **349**, 431-434.

Shigenaga, M.K., Aboujaoude, E.N. Chen, Qin and Ames, B.N. (1994) Assays of oxidative DNA damage biomarkers 8-oxo-2'-deoxyguanosine and 8-oxoguanine in nuclear DNA and biological fluids by high-performance liquid chromatography with electrochemical detection methods. *Meth. Enzymol.* **234**, 16-33.

Shima, T., Sarna, T, Swartz, H. M., Stroppolo, A., Gerbasi, R., and Zecca, L. (1997) Binding of iron to neuromelanin of human substantia nigra and synthetic melanin: an EPR spectroscopy study. *Free Rad. Biol. Med.* **23**, 110-119.

Singh, R. J., Karoui, H., Gunther, M. R., Beckman, J. S., Mason, R. P., Kalyanaraman, B. (1998) Reexamination of the mechanism of hydroxyl radical adducts formed from the

reaction between familial amyotrophic lateral sclerosis-associated Cu,Zn superoxide dismutase mutants and H2O2. *Proc. Natl. Acad. Sci. U S A.* **95,** 6675-6680.

Slupska, M.M., Baikalov, C., Luther W.M., Chiang, J.H., Wei, Y.F. and Miller, J. H. (1996) Cloning and sequencing a humal homolog (hMYH) of the Escherichia coli MutY gene whose function is required for the repair of oxidative DNA damage. *J. Bacteriol.* **13,** 3885-3892.

Sofic, E., Lange, K. W., Jellinger, K., and Riederer, P. (1992) Reduced and oxidized glutathione in the substantia nigra of patients with Parkinson's disease. *Neurosci. Lett.* **142**, 128-130.

Soule, H.D., Maloney, T.M., Wolman, S.R., Peterson, W.D., Brenz, R., McGrath, C.M., Russo, J., Pauley, R.J., Jones, R.F., and Brooks, S.C. (1990) Isolation and Characterization of a Spontaneously Immortalized Human Breast Epithelial Cell Line, MCF-10. *Cancer Res.* **50**, 6075-6086.

Stanbridge, E. J. (1990) Human tumor suppressor genes. *Annu. Rev.* Genet. **24**, 615-657.

Steenken, S. (1989) Purine bases, nucleosides, and nucleotides: aqueous solution redox chemistry and transformation reactions of their radical cations and e^- and OH adducts. *Chem. Rev.* **89**, 503-520.

Stern G. M., ed. (1990) *Parkinson's disease.* John Hopkins University Press, Baltimore, MD.

Swartz, H. M. (1979) Free radicals in cancer. CIBA Symposium No. 67, *Submolecular Biol. and Cancer,* pp. 107-124.

Swartz, H. M. (1986) Use of electron spin resonance spectroscopy to study cancer, in *Magn. Reson. in Cancer,* P. S. Allen, D. P. J. Boisvert, and B. C. Lentle, (Eds.), Pergamon Press, Oxford, U.K., pp. 169-177.

Swartz, H. M. (2003) Potential medical (clinical) applications of EPR: Overviews and perspectives in *In Vivo EPR(ESR): Theory and Applications, Biol. Magn. Reson.,* L.J. Berliner, (Ed.), Plenum Publishing Co., NY, **18**, 599-621.

Swartz, H. M., Sarna, T., and Zecca L. (1992), Modulation by neuromelanin of the availability and reactivity of metal ions. *Ann. Neurol.* **32**, S69-S75.

Szatrowski, T.P. and Nathan, C.F. (1991) Production of large amounts of hydrogen peroxide by human tumor cells. *Cancer Res.* **51**, 794-798.

Taylor W. O. (1978) Edridge-Green Lecture, 1978. Visual disabilities of oculocutaneous albinism and their alleviation. *Trans. Ophthalmol. Soc. U. K.* **98**, 423-445.

Taylor, H. R., West, S., Munoz, B., Rozenthal, F. S., Bressler, S. B., and Bressler, N. M. (1992) The long-term effects of visible light on the eye. *Arch. Ophthalmol.,* **110**, 99-104.

Timmins, G.S. Liu, K.J. Bechara, E. J.H. Kotake, Y. and Swartz, H.M. (1999). Trapping of free radicals with direct *in vivo* EPR detection: a comparison of 5,5-dimethyl-1-pyrroline-N-oxide (DMPO) and 5-diethoxyphosphoryl-5-methyl-1-pyrroline-N-oxide (DEPMPO) as spin traps for $HO\bullet$ and $SO4\bullet^-$, *Free Rad. Biol. Med.,* **27**, 329-333.

Tsai-Wu, J.-J., Radicella, P. and Lu, A.-L. (1991) Nucleotide sequence of the *Escherichia coli micA* gene required for A/G-specific mismatch repair: Identity of MicA and MutY. *J. Bacteriol.* **173**, 1902-1910.

Turk, P.W. and Weitzman, S.A. (1995) Free radical DNA adduct 8-OH-deoxyguanosine affects activity of HPA II and MSP 1 restriction endonucleases. *Free Rad. Res.* **23**, 255-258.

Upadhyay, S., Li, G., Liu, H., Chen, Y.Q., Sarkar, F.H. and Choi Kim, H-R. (1995) bcl-2 suppresses expression of $p21^{WAF1/C1P1}$ in breast epithelial cells. *Cancer Res.* **55**, 4520-4524.

Van der Kemp, P.A., Thomas, D., Barbey, R., Oliveira, R.D. and Boiteux, S. (1996) Cloning and expression of *Escherichia coli* of the OGG1 gene of saccharomyces cerevisial, which

codes for a DNA glycosidose that excises 7,8-dihidro-8-oxoguanine and 2,6-diamino-4-hydroxy-5-N-methylformamido pyrimidine. *Proc. Natl. Acad. Sci. USA* **93**, 5197-5202.

Van Woert, M. H., Prasad, K. N., and Borg D. C. (1966) Spectroscopic studies of *substantia nigra* pigment in human subjects. *J. Neurochem.* **14**, 707-716.

Vile, G.F., Basu-Modak, S., Waltner, C. and Tyrrell, R.M. (1994) Heme oxygenase 1 mediates an adaptive response to oxidative stress in human skin fibroblasts. *Proc. Natl. Acad. Sci. USA* **91**, 2607-2610.

Weiberg, R. A. (1989) Oncogenes, antioncogenes, and the molecular basis of multistep carcinogenesis. *Cancer Res.* **49**, 3713-3721.

Weiter, J. J., Delori, F. C., Wing, G. L., and Fitch, K. A. (1985) Relationship of senile macular degeneration to ocular pigmentation. *Am. J. Ophthalmol.* **99**, 185-187.

Weitzman, S.A. and Gordon, L.I. (1990) Inflamation and cancer: role of phagocyte-generated oxidants in carcinogenesis. *Blood* **76**, 655-663.

Weitzman, S.A., Turk, P.W., Milkowski, D.H. and Kozlowski, K. (1994) Free radical adducts induce alterations in DNA cytosine methylation. *Proc. Natl. Acad. Sci. USA* **91**, 1261-1264.

Wiedau-Pazos, M., Goto, J. J., Rabizadeh, S., Gralla, E. B., Roe, J. A., Lee, M. K., Valentine, J. S., Bredesen, D. E. (1996) Altered reactivity of superoxide dismutase in familial amyotrophic lateral sclerosis. *Science* **271**, 515-518.

Wilson, H. R., Mets, M. B., Nagy, S. E., and Kressel, A. B. (1988) Albino spatial vision as an instance of arrested visual development. *Vision Res.* **28**, 979-990.

Wood, J. M., Jimbow, K., Boissy, R. E., Slominski, A., Plonka, P. M., Slawinski, J., Wortsman, J., and Tosk, J. (1999) What's the use of generating melanin? *Exp. Dermatol.* **8**, 153-164.

Worrillow, L.J., Travis, L.B., Smith, A.G., Rollinson, S., Smith, A.J., Wild, C.P., Holowaty, E.J., Kohler, B.A., Wiklund, T., Pukkala, E., Roman, E., Morgan, G.J. and Allan, J.M. (2003) An intron splice acceptor polymorphism in hMSH2 and risk of leukemia after treatment with chemotherapeutic agents. *Clin. Cancer Res.* **9**, 3012-3020.

Xanthoudakis, S. and Curran, T. (1994) Analysis of c-Fos and c-Jun redox-dependent DNA binding activity. *Meth. Enzymol.* **234**, 163-174.

Xanthoudakis, S., Miao, G.G. and Curran, T. (1994) The redox and DNA-repair activities of Ref-1 are encoded by nonoverlapping domains. *Proc. Natl. Acad. Sci. USA* **91**, 23-27.

Yamaguchi, K.T., Stewart, R.J., Wang, H.M., Hudson, S.E., Vierra, M., Akhtar, A., Hoffman, C., and George, D. (1992) Measurement of free radicals from smoke inhalation and oxygen exposure by spin trapping and ESR spectroscopy. *Free Rad. Res. Commun.* **16,** 167-174.

Yao, K.-S., Xanthoudakis, S., Curran, T. and O'Dwyer, PJ. (1994) Activation of AP-1 and of a nuclear redox factor, REF-1, in the response of HT29 colon cancer cells to hypoxia. *Mol. Cell Biol.* **14**, 5997-6003.

Yeh, Y.-C., Chang, D.-Y., Masin, J. and Lu, A.-L. (1991) Two nicking enzyme systems specific for mismatch-containing DNA in nuclear extracts from human cells. *J. Biol. Chem.* **266**, 8480-6484.

Young, R. W. (1988) Solar radiation and age-related macular degeneration. *Surv. Ophthalmol.* **32**, 252-269.

Zarbin, M. A. (1998) Age-related macular degeneration: review of pathogenesis. *Eur. J. Ophthalmol.* **8**, 199-206.

Zareba, M., Bober, A., Korytowski, W., Zecca, L., and Sarna T. (1995) The effect of a synthetic neuromelanin on yield of free hydroxyl radicals generated in model systems. *Biochim. Biophys. Acta* **1271**, 343-348.

Zecca, L. and Swartz H. M. (1993) Total and paramagnetic metal ions in human substantia nigra and its neuromelanin. *J. Neural. Transm. Park. Dis. Dement. Sect.* **5**, 203–213.

Zecca, L., Tampellini, D., Gatti, A., Crippa, R., Eisner, M., Sulzer, D., Ito, S., Fariello, R., and Gallorini M. (2002) The neuromelanin of human substantia nigra and its interaction with metals. *J. Neural. Transm.* **109,** 663–672.

Zhang, H., Joseph, J., Felix, C., and Kalyanaraman, B. (2000) Bicarbonate enhances the hydroxylation, nitration, and peroxidation reactions catalyzed by copper, zinc superoxide dismutase. *J. Biol. Chem.* **275,** 14038-14045.

Zhang, H., Joseph, J., Gurney, M., Becker, D., and Kalyanaraman, B. (2002) Bicarbonate enhances peroxidase activity of Cu, Zn-superoxide dismutase-Role of carbonate anion radical and scavenging of carbonate anion radical by metalloporphyrin antioxidant enzyme mimetics. *J. Biol. Chem.* **277**, 1013-1020.

Chapter 4

Superoxide Generation from Nitric Oxide Synthase

Role of cofactors and protein-interaction

Jeannette Vásquez-Vivar[1,2], Pavel Martásek[3], and B. Kalyanaraman[1,2]

[1] Biophysics Research Institute and [2] Free Radical Research Center, Medical College of Wisconsin, Milwaukee, Wisconsin 53226. [3] Department of Biochemistry, University of Texas Health Science Center, San Antonio, Texas 78284. USA.

Abstract: Application of the loop gap resonator technology and improvement in spin trapping methodologies have enormously increased our understanding of the mechanisms of superoxide formation from nitric oxide synthases. In this chapter we discuss the key role of cofactors such as tetrahydrobiopterin and protein-protein interactions in superoxide release from endothelial NOS. The pathophysiological effects of NOS-mediated superoxide generation in cardiovascular system are discussed.

1. INTRODUCTION

There is much interest in identifying the sources and mechanisms regulating superoxide formation in the vasculature. This follows mounting evidence in the literature showing that elevation of superoxide formation is critical for the pathophysiology of hypertension, diabetes arteriosclerosis, and stroke. At present, it is recognized that the univalent reduction of oxygen to generate superoxide depends on different systems according cell type. In smooth muscle cells, inflammatory cells and adventitial fibroblasts the flavoprotein containing enzyme, NADPH oxidase has been shown to be the major locus for superoxide formation. The mitochondrial respiratory chain has been identified as an important source of superoxide in neuronal cells and cardiac myocytes. In endothelial cells, nitric oxide synthase (NOS) has been proposed as a potential source of superoxide. In this chapter, we reviewed the potential mechanisms regulating superoxide formation from NOS.

1.1 Nitric Oxide Synthases

Nitric oxide synthase is a flavo- and heme- containing enzyme that catalyses the two-step conversion of arginine to citrulline and nitric oxide ($^{\bullet}NO$) with the formation of the stable intermediate N-hydroxyarginine (Feldman et al., 1993). The three isoforms of the enzyme, neuronal (nNOS or NOS-1), inducible (iNOS or NOS-2) and endothelial (eNOS or NOS-3), differ with respect to specific enzyme activity, cellular location and regulation(Feldman et al. 1993; Nathan and Qie, 1994). All active isoforms, however, are homodimers of identical subunits consisting of reductase domain, with binding sites for FMN, FAD and NADPH, and an oxygenase domain with binding sites for heme group, tetrahydrobiopterin (BH_4) and arginine (Raman et al., 2000; Cranet et al., 1997) Electron transfer from the reductase to the oxygenase domain of NOS is stimulated by calcium-dependent calmodulin binding to a linker polypeptide sequence consisting of nearly 20 aminoacids between the domains (Fig. 1).

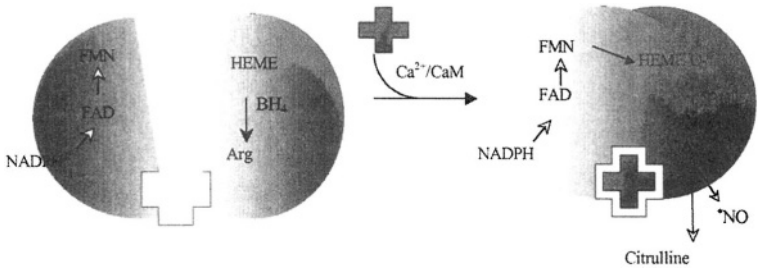

Figure 1. Scheme showing the calcium/calmodulin-mediated activation of an NOS subunit. Modified from Griffith & Stuehr (1995) *Annual Review of Physiology* 57, 707.

Calmodulin binding to NOS shows a remarkable difference between the isoforms. Inducible NOS (iNOS) binds with high affinity calmodulin so that the enzyme is produced in the active state due to fast binding even at basal intracellular calcium levels. Consequently, $^{\bullet}NO$ output from iNOS is mainly regulated at the transcriptional level. Unlike iNOS, however, neuronal and endothelial NOS are found in cells in a resting state, and calcium/calmodulin binding is required for their activation (Griffith and Stuehr, 1995). Several processes modulate the calcium requirement for calmodulin binding to eNOS (Lin et al., 2000). Generally, agonist stimulated calcium uptake into the cell precipitate calmodulin binding to eNOS and production of $^{\bullet}NO$. Activation of the enzyme, however, has been reported to occur at basal intracellular calcium levels. The apparent lack of calcium-dependence for activation of eNOS has been linked to displacement of an autoinhibitory loop located within the FMN domain at the reductase domain of the enzyme (Salerno et al., 1997). Similarly, phosphorylation of the serine residue 1179

(bovine and 1177 in the human enzyme) was shown to increase NOS activity at basal level of intracellular calcium. This phenomenon was attributed to facilitated electron transfer and diminished calmodulin dissociation from the protein (McCabe et al., 2000). This indicates that there are several pathways that can enhance eNOS activity. The exact mechanism controlling ligand-induced activation of NOS and their impact in pathophysiology remains a subject of active investigation.

1.2 Protein Interactions Regulating Endothelial And Neuronal Nitric Oxide Synthase Activity

In addition to calmodulin, several other protein interactions have been shown to be important for regulating calcium-dependent NOS activation *in vivo*. In endothelial cells, eNOS interacts with caveolin, the intracellular domain of certain G-protein coupled receptors and with heat shock protein 90 (HSP90). Most of these interactions are facilitated by the localization of the enzyme in the cell. N-Myristoylation of eNOS targets the enzyme to specialized cytoplasmic membrane domains, the caveolae (Garcia-Cardeña et al., 1997). In this structure, eNOS interacts with the integral protein, caveolin, in a resting state (Ju et al., 1997; Michel et al., 1997; Sowa et al., 2001). It has been shown that eNOS interacts with the caveolin-1 scaffolding peptide (Cav-1SP) and that dissociation of eNOS from caveolin-1 is mediated by calcium/calmodulin in a competitive manner (Ju et al., 1997; Michel et al., 1997; Sowa et al., 2001; Feron et al., 1998). Similarly, in skeletal muscle and cardiac myocytes eNOS has been shown to interact with caveolin-3 (Feron et al., 1996). In contrast to "caveolin mechanism", the inhibition of eNOS by G-protein-coupled receptors (Boulanger and Vanhoutte, 1997) such as bradykinin BR2, angiotensin-II AT_1 and the endothelin-1 ET_B receptor is not competitive with calcium/calmodulin. It has been shown that a direct interaction of the receptor inhibits NOS activity. For instance B2R blocks electron transfer reactions between the flavins and heme group (Golser et al., 2000). Whether or not this is a general mechanism controlling enzyme activation by these receptors remains unclear. Unlike these interactions, a positive regulatory effect from eNOS-protein interaction occurs with HSP90 (Garcia-Cardeña et al., 1998). This interaction has been reported to augment $^{\bullet}NO$ formation by the endothelium. Augmentation of HSP90 in cells has been reported in the cytoprotective effects of estrogens Russell et al., 2000), statins (Brouet et al., 2001) and ischemic pre-conditioning. The actions of HSP90 on eNOS activity have been attributed to a facilitated displacement of the enzyme from caveolin-1 complex (Gratton et al., 2000).

Regulation of nNOS activity *in vivo* is complex and depends on the cell type expressing the enzyme. In both skeletal muscle and the brain, nNOS is

associated with particulate fractions. In skeletal muscle, nNOS was shown to be associated with caveolin-3, a component of the dystrophin complex (Venema et al., 1997). As a consequence of this interaction, nNOS activity is inhibited. In brain cells, nNOS activity is inhibited by interaction with PIN (protein inhibitor of neuronal NOS, a dynein light chain (Jaffrey et al., 1996), CAPON (Jaffrey et al., 1998) and with dexras-1 protein (Fang et al., 2000). Evidence indicates that the mechanism of inhibition is likely to involve nNOS trafficking in the cell rather than a direct effect in electron-transfer and/or calmodulin-binding to the enzyme. Association of nNOS to PSD-95 (post-synaptic density-95) (Sattler et al., 1999) has been proposed to ensure an efficient coupling of N-methyl-D-aspartate receptor mediated calcium/influx with nNOS activation. This mechanism links elevation of nNOS activity to excitotoxic calcium signaling. Recently, interaction of HSP90 with nNOS was reported to enhance enzyme activity. The mechanisms proposed for HSP90 effects include facilitation of heme incorporation into the protein and increased calcium/calmodulin binding (Bender et al., 1999; Song et al., 2001).

1.3 Electron Transfer Reactions And Oxygen Activation by NOS

Previous studies by others have shown that calcium stimulated calmodulin-binding to NOS facilitates heme-Fe(III) reduction by NADPH-derived electrons to form heme-Fe(II) (Mansuy et al., 1995). This reaction stimulates oxygen binding to the heme group to generate a ferrous-dioxygen complex (Couture et al., 2000) (equation 1). Formation of this complex is required to initiate the reaction leading to arginine oxidation.

$$\text{NADPH} \rightarrow \text{FMN} \rightarrow \text{FAD} \xrightarrow{Ca^{2+}/CaM} \text{Heme-Fe(II)-O}_2 \qquad (1)$$

This sequence of reactions suggested that enzyme activity is controlled by either rate of electron transfer between flavins or between flavins and heme-Fe(III) (Nishida et al., 1999; Miller et al., 1999; Santolini et al., 2001). Studies with NOS chimera proteins that have swapped reductase domains indicated that the rate of heme reduction is the limiting step in eNOS catalytic mechanism. This has been confirmed by kinetic studies showing that the rates of flavin, heme reduction and heme nitrosyl species followed the order: iNOS>nNOS>eNOS (Miller et al., 1999; Abu-Soud et al., 2000).

Tetrahydrobiopterin (BH_4) is another key factor controlling NOS activity. Crystal structure of the iNOS and eNOS oxygenase domain shows that BH_4 binds in the vicinity of a heme pocket kept in place by several water-bridged H bonds and van der Waals contacts (Raman et al., 1998). The pyrimidine ring of BH_4 was shown to coordinate with the propionate group of eNOS

heme group, orienting BH_4- pyrazine nitrogen (N-5) towards the heme group (Raman et al., 2000; Raman et al., 1998). Two critical observations were evident in this model: (1) only fully reduced BH_4 tightly binds to the protein and its interaction with the protein limits oxidation of the cofactor and, (2) binding of the cofactor is not followed by conformational changes of the binding site. Previous studies also have shown that BH_4 is important to promote a shift of heme spin state, stabilize the dimeric conformation of the protein and to augment substrate affinity for the enzyme. Although all these aspects are important in the efficiency of catalysis, none of them fully explain the strict requirement of BH_4 for enzyme activity (Raman et al., 2000; Ortiz de Montellano et al., 1998). The close proximity of BH_4 to the heme group suggested that BH_4 plays a role in oxygen activation. The mechanism however, was different from aromatic hydroxylases in which BH_4 is directly involved in oxygen activation undergoing two-electron oxidation (Kaufman, 1995; Kappock and Caradonna, 1996). This was indicated by the lack of evidence for BH_4 undergoing two-electron oxidation to generate either the quinonoid 5,6-dihydrobiopterin or 7,8-dihydrobiopterin (Giovanelli et al., 1991). Also, there was no evidence for the reduction of the oxidized isoforms by an NOS dihydropteridine reductase-like activity (Witteveen et al., 1999).

Early studies indicated that nNOS catalyzes the electron transfer from NADPH to molecular oxygen to generate hydrogen peroxide by a calcium/calmodulin-dependent mechanism (Schmidt et al., 1992; Heinzel et al., 1992; List et al., 1997). This reaction was taken as an indication of increased flavin reduction at the reductase domain of the enzyme. Thus, it was anticipated that activation of oxygen occurred at the reductase domain of the enzyme through direct electron transfer between reduced flavins, FMN and/or FAD and oxygen (Schmidt et al., 1992). Parallel observations indicated that NADPH oxidase activity of nNOS was linked to a diaphorase-like activity of the enzyme in the brain (Dawson et al., 1991). This observation supported the idea that oxygen reduction by nNOS proceeded through a two-electron mechanism. Conversely, it was shown that endothelial isoform show little or no NADPH oxidase activity (List et al., 1997). Thus, there was significant controversy on whether or not superoxide was generated by NOS. Electron paramagnetic resonance spin trapping studies with DMPO presented first evidence showing that superoxide was indeed released from nNOS (Pou et al., 1992). The mechanism of superoxide formation, however, remained unclear. In this study was shown that L-arginine analogs have a dissimilar effect on superoxide release from the enzyme while the role of BH_4 was totally unknown because of the lack of BH_4-free NOS. Expression of recombinant wild type BH_4-free NOS (Martásek et al., 1996; Roman et al., 1995) enabled the examination of the cofactor on superoxide formation from NOS.

2. SUPEROXIDE DETECTION FROM NOS: LOOP GAP RESONATOR AND NOVEL SPIN TRAPS

NOS is a flavoprotein that can reduce several superoxide detectors such as cytochrome c, nitroblue tetrazolium (Vásquez-Vivar et al, 1999a), adenochrome and lucigenin (Vásquez-Vivar et al., 1997a) in a SOD-insensitive manner. Thus, none of these compounds can be used to detect superoxide from the enzyme because of the ambiguity of the results. Electron paramagnetic resonance (EPR) spin trapping methodology is the only available technique for unambiguous superoxide detection in biological systems. Despite this fact, superoxide detection using EPR spin trapping methodology has been limited because of the low sensitivity, low persistence and decomposition of the spin adduct. These limitations have been circumvented by the introduction of the loop gap resonator technology and improvement in the existing spin-trapping methodology.

The advantage of the use of the X-band loop gap resonator (Froncisz and Hyde, 1992) over the conventional cavity resonators is that a small amount of material can be used without compromising the signal-to-noise ratio. The decrease in sample volume allows a greater number of measurements often necessary to quantify superoxide production from purified enzyme that present variations in enzyme activity higher than two-fold such as that for neuronal and endothelial NOS.

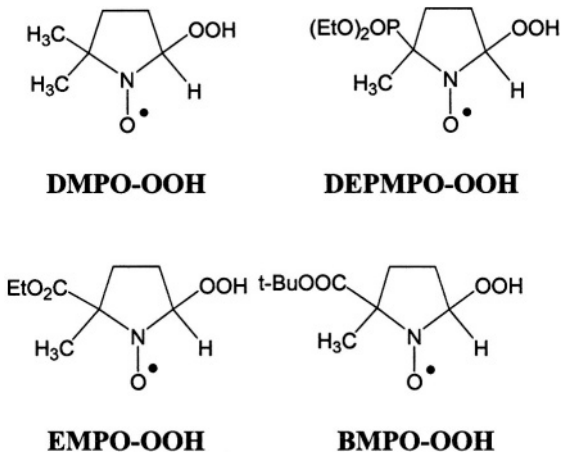

Figure 2. Chemical structure of the superoxide spin adducts described in this work.

One of the most frequently used spin traps in free radical biology has been 5,5'-dimethyl-1-pyrroline *N*-oxide (DMPO) (Fig. 2). This compound

has been successfully used for detection of carbon, sulphur and oxygen-centered free radicals. However, its application for detecting superoxide is complicated by the fact that the DMPO-superoxide adduct spontaneously decays to form the DMPO-hydroxyl adduct (Fig. 3). This makes quantification of superoxide nearly impossible. This problem prompted new chemical modeling and synthesis research towards designing improved superoxide spin traps. The first of this series introduced in our studies was the phosphorylated analog of DMPO, the 5-(diethoxyphosphoryl)-5-methyl-1-pyrroline N-oxide (DEPMPO) (Frejaville et al., 1995). The DEPMPO-superoxide adduct (DEPMPO-OOH) showed remarkable persistence compared to DMPO-OOH, which allows detection of superoxide for ≥30 min after the reaction is initiated with high sensitivity (Roubaud et al., 1995) (Fig. 3). In addition, the decay of DEPMPO-OOH is not followed by the appearance of secondary radical species, thus the only variation over time is the signal intensity of the spectrum. This improved persistence and stability are critical for superoxide quantification. Although DEPMPO met these criteria, there were other problems: (1) complexity of the ESR spectrum because of the presence of phosphorous atom (I=1/2) and formation of isomers that can undergo chemical exchange and (2) the lack of availability of pure spin trap. The first problem was ameliorated by the replacement of the phosphoryl group by a carbonyl group in the pyrrolidine ring. The resultant spin trap, 5-ethoxycarbonyl-5-methyl-1-pyrroline N-oxide (EMPO) (Olive et al., 2000) and the ^{15}N-labeled analog [^{15}N]-EMPO (Zhang et al., 2000) presented stability comparable to DEPMPO, generated a simpler EPR spectrum, which was particularly useful in systems generating superoxide at low rates. With the synthesis of the solid cyclic nitrone spin trap, 5-*tert*-butoxycarbonyl-5-methyl-1-pyrroline N-oxide (BMPO) (Zhao et al., 2001), a new breakthrough in spin trapping methodology was accomplished. This compound shows persistence and improved sensitivity by generating simpler superoxide adduct EPR spectrum. Also, BMPO is a water-soluble solid that can be easily purified by recrystallization, which is clearly an advantage as availability of pure spin traps minimizes artifacts.

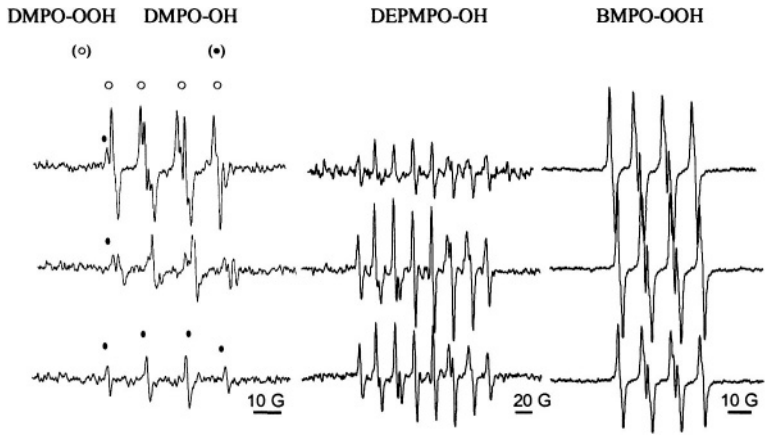

Figure 3. Comparative persistence of superoxide spin adduct from DMPO, DEPMPO and BMPO.

2.1 Superoxide Generation from NOS: Mechanisms and Regulation

Reductase domain. Superoxide formation from the reductase domain of NOS was examined in wild type neuronal and endothelial NOS. Also, eNOS and nNOS reductase domains carrying the calmodulin linker were examined. It was verified that none of these proteins generated significant amounts of superoxide in the absence of calcium/calmodulin (Fig. 4). Although the crystal structure of the reductase domain of NOS is not fully resolved, the available structural and functional evidence demonstrates that they are similar to NADPH-cytochrome P450 (Zhang et al., 2001). The reductase domain of nNOS and eNOS can directly reduce several electron acceptors such as cytochrome c, 2,6-dichlorophenolindophenol and ferricyanide. The rates of reduction are enhanced upon calmodulin binding to full length enzyme or NOS-reductase domain containing the CaM linker (Roman et al., 2000; Gachhui et al., 1996). This suggests that there exists an additional role of calmodulin in NOS catalysis i.e. to enhance the electron transfer between FAD and FMN. This effect has recently been associated with displacement of a 40 amino acids peptide neighboring eNOS-FMN module considered an autoinhibitory motif present in wild type enzyme. Upon addition of calmodulin, however, neither nNOS nor eNOS reductase domain significantly increased superoxide formation (Fig. 4) indicating that oxygen reduction by flavins is a marginal process.

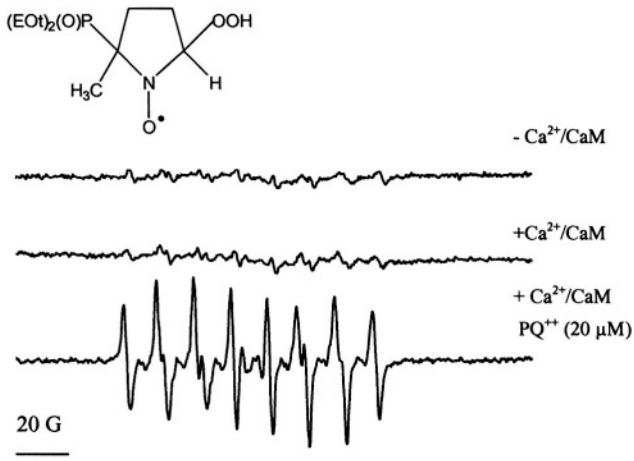

Figure 4. Superoxide generation from eNOS reductase domain stimulated by calcium/calmodulin and paraquat.

Reduction of the redox-active electron acceptors is a mechanism by which the reductase domain of NOS can enhance superoxide formation. This mechanism implies that the electron acceptor binds closely to FAD or the FMN domain, and gets reduced by NADPH-derived electrons. Upon rapid reaction with oxygen, the reduced compound regenerates and produces superoxide (Fig. 4). Since this reaction depends on the rates of flavin reduction, calmodulin can accelerate the process depending upon whether binding site of the drug is before or after the first flavin (FAD) gets reduced by NADPH. For example, superoxide formation from methyl viologen (or paraquat, PQ^{++}) redox cycling is not stimulated by calmodulin (data not shown). This suggests that FAD at the reductase domain of the enzyme reduces PQ++. Although the latter is a very likely possibility, it is also possible that this result indicates a weak interaction between PQ^{++} and the protein. The latter is indicated by the significant difference observed with another redox-cycling structural analog, lucigenin that generates superoxide several times faster than PQ^{++} by a mechanism that is calmodulin-independent.

Caveolin inhibits eNOS and nNOS enzyme activity by interrupting electron transfer from the reductase domain to the oxygenase domains. Studies of the eNOS reductase domain indicate that in addition to competing for calmodulin binding, caveolin-1 scaffolding peptide (Cav-1 SP) inhibits electron transfer at the reductase domain of the enzyme. This implicates that Cav-1 SP controls electron transfer rates between FMN/FAD and from the flavins to electron acceptors (Ghosh et al., 1998). The reductase domain of

NOS activates a series of redox-active compounds. By this mechanism is likely that NOS plays a key role in toxicology. An important example is the anthracycline antibiotic, doxorubicin (or adriamycin) that is reduced by the reductase domain of eNOS (Vásquez-Vivar et al., 1998). As a consequence of this reaction, formation of nitric oxide by the enzyme is inhibited while superoxide and hydrogen peroxide are increased several fold. Inhibition of electron transfer reactions by cav-1 SP (Zhao et al., 2001) could inhibit doxorubicin activation. Potentially, this represents a powerful therapeutic target for controlling the toxicity associated with chemotherapy. Studies with wild-type eNOS, however, showed that cav-1 SP did not affect superoxide production resulting from the eNOS-mediated doxorubicin redox cycling (Fig. 5).

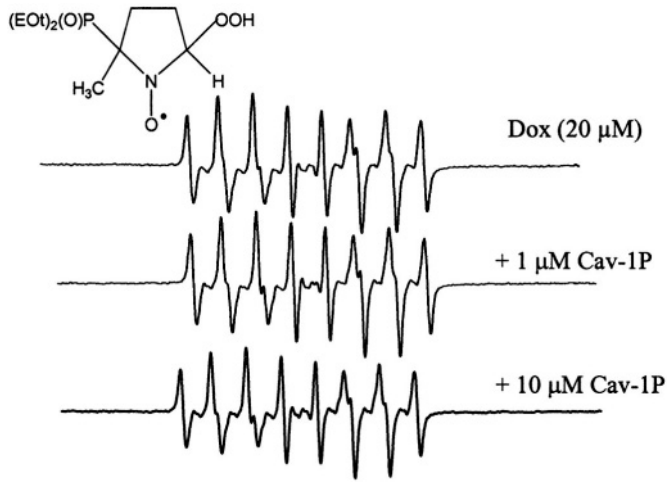

Figure 5. Superoxide generation from eNOS catalyzed doxorubicin-redox cycling.

This result indicates that either doxorubicin efficiently competes for the binding site at the reductase domain with Cav-1 SP or that the drug is reduced in the FAD pocket. These results indicate that the effects of Cav-1 SP on reductive activation of xenobiotics will depend on the locus of drug reduction. Potentially, an efficient inhibition will result from blocking FAD reduction by NADPH.

Oxygenase domain. Reduction of the heme-Fe(III) by NADPH-derived electrons facilitates oxygen binding to the reduced heme group to form a ferrous-dioxygen complex (Eq. 1). In analogy to the catalytic cycle of P450-dependent mono-oxygenation, it was envisaged that superoxide could be the decomposition product of the ferrous-dioxygen complex (Ledbetter et al., 1999). This mechanism was demonstrated by the inhibitory effect of P450-

like inhibitors such as imidazole, cyanide and phenyldiazene on superoxide formation (Vásquez-Vivar et al., 1998). As superoxide formation was dependent on calcium/calmodulin we concluded that superoxide is released from the oxygenase domain of the enzyme. This mechanism was also confirmed for nNOS (Vásquez-Vivar et al., 1999b; Yoneyama et al., 2001). This evidence suggested that modifications in the heme iron-spin state and stability of the heme-dioxygen complex determine the rates of superoxide formation by the enzyme.

Arginine binds in close proximity to the heme group, and it has been shown to facilitate the conversion of the heme group from low to high spin state (Salerno et al., 1996). Because the effects of arginine binding to NOS can be isolated from the "substrate" effects using a BH_4-free enzyme, we used a recombinant protein expressed in *E. coli* that is naturally devoid of BH_4. Saturating concentrations of arginine were shown to increase superoxide release from eNOS indicating that substrate binding controls heme-reduction (Vásquez-Vivar et al., 2002a). However, an opposite effect was observed for nNOS, which significantly diminished superoxide production upon arginine and/or N-hydroxyarginine binding (Vásquez-Vivar et al., 1999b). Collectively, these results indicated that interaction of the ferrous-dioxygen complex with the guanidino group of arginine is important for preventing superoxide release from the heme-dioxygen complex and thus, the architecture of the arginine binding site controls electron transfer rates and thereby efficiency of catalysis. The effects of NOS inhibitors on superoxide release were examined. L-NAME was shown to significantly decrease superoxide release from nNOS (Pou et al., 1992; Vásquez-Vivar et al., 1999b), but not from eNOS (Vásquez-Vivar et al., 2002a), whereas L-NMMA effects were discrete in both isoforms. These results indicate that occupation of the binding site is not the only factor involved in the control of superoxide release. The latter was verified with thiocitrulline and 7-nitroindazole that prevented superoxide release in an efficient manner. These results supported their direct and tight interaction with the heme group to prevent oxygen activation.

The different effects of arginine on superoxide release from the enzyme indicated that the heme-dioxygen complex needs to be stabilized in order to drive catalytic cycle. Thus, the efficiency of heme-dioxygen reduction by the reductase domain of NOS is critical. In the absence of BH_4, this reaction is very slow facilitating the dissociation of superoxide. Evidence in support of a redox role for BH_4 in NOS catalysis was presented by low temperature (Bec et al., 1998) and EPR spin trapping studies (Pou et al., 1992; Vásquez-Vivar et al., 1999b; Vásquez-Vivar et al., 2002a). We showed that reconstitution of the substrate-free nNOS with BH_4 inhibited superoxide release in a concentration-dependent fashion while increasing hydrogen peroxide formation (Vásquez-Vivar. et al., 1999b). This indicates that BH_4 by

reducing ferrous dioxygen complex inhibits superoxide release while increasing the heme-peroxo intermediate. This was the first functional evidence that BH_4 participates as a redox switch in NOS catalytic cycle. Following studies on the role of BH_4 in superoxide formation from eNOS indicated that the "substrate" of BH_4 maybe different from the heme-dioxygen complex. If BH_4 reduces only heme-dioxygen complex thus, hydrogen peroxide is an obligatory product of the decay heme-peroxo intermediate in the absence of substrate. For eNOS, however, formation of hydrogen peroxide was not detected, at any of the BH_4 concentrations tested (Vásquez-Vivar et al., 2002a). A remarkable effect of BH_4 on eNOS is that the cofactor diminishes NADPH oxidation indicating that the cofactor also controls electron transfer rates from reductase to oxygenase domain. Together, our results show that BH_4 plays a unique role in NOS catalysis controlling oxygen activation and formation of heme intermediates.

Comparison of the effects of BH_4 with other analogues such as 5-methyl-tetrahydrobiopterin 6-methyl-tetrahydrobiopterin, 6-(S)-5,6,7,8-tetrahydro biopterin and oxidized forms 7,8-dihydrobiopterin and sepiapterin demonstrated that BH_4 was the most efficient inhibitor of superoxide release from eNOS. The fact that 6-(S) isomer is less efficient than the 6-(R) isomer indicates that binding affinity, in part, confers inhibition efficiency (Vásquez-Vivar et al., 2002a). In addition, these results demonstrated that only fully reduced BH_4 inhibits superoxide release. This supports the idea that BH_4 acts as a redox-switch in the catalytic mechanism. To further examine this role, we anticipated that displacement of BH_4 from its binding site would increase superoxide formation from eNOS. Competition experiments showed that supplementation of eNOS incubation mixtures with oxidized BH_4, under turnover conditions, uncouples NADPH from arginine oxidation inhibiting $^{\bullet}NO$ formation and enhancing superoxide release (Vásquez-Vivar et al., 2002a) (Fig. 6). This result demonstrates that BH_4 acts as a redox switch that critically controls superoxide release from eNOS.

From a pathological point of view, this result indicated that under in vivo conditions the ratio between fully reduced and oxidized BH_4 may control superoxide formation from NOS. It has been shown that eNOS activity in endothelial cells can be augmented by supplementation with BH_4 (Katusic et al., 2001). Thus, a deficient BH_4 concentration has been linked to endothelial dysfunction in cigarette smoking, diabetes, hypercholesterolemia, hypertension, and arteriosclerosis (Katusic et al., 2001; Vásquez-Vivar et al., 2002b). The mechanism by which BH_4 supplementation ameliorates vascular function, however, is unclear. EPR kinetic studies on the reaction between BH_4 and superoxide indicated that direct scavenging of superoxide by BH_4 is an unlikely possibility (Vásquez-Vivar et al., 2001). Thus, it is plausible that BH_4 supplementation diminishes superoxide release from eNOS. This intriguing mechanism may shed light on the role of BH_4 in the control of

$^{\bullet}NO$ production in the vasculature. Certainly, the mechanisms regulating BH_4 in the endothelium warrant further investigation to fully appraise the role of BH_4 in disease and health.

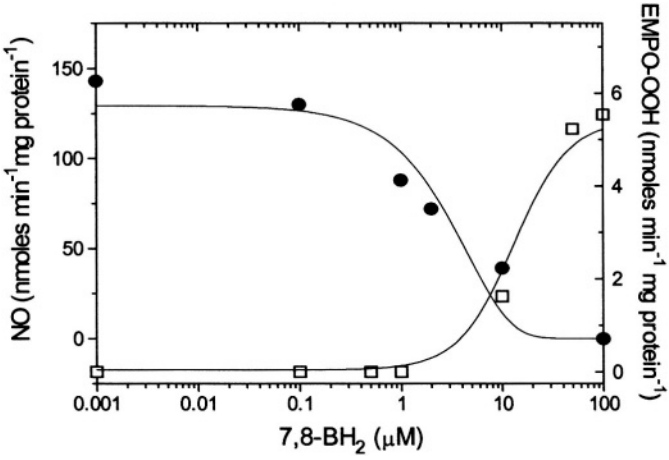

Figure 6. 7,8-dihydrobiopterin enhances superoxide and inhibits $^{\bullet}NO$ formation from eNOS. *(Printed with permission Biochemical Journal)*

3. SUMMARY

Superoxide formation from nNOS and eNOS occurs at the oxygenase domain of the enzyme by a calcium/calmodulin-dependent process. The EPR spin trapping studies using the loop gap resonator have shown that BH_4 modulates the formation of superoxide and $^{\bullet}NO$ from NOS. BH_4 inhibits superoxide release by mechanisms that are not fully understood. Oxidized BH_4 analogs efficiently compete for BH_4 binding site in NOS, thereby uncoupling NADPH from arginine oxidation and enhancing superoxide release from the enzyme. It is likely that the control of superoxide release from NOS in vivo depends on the intracellular balance between fully reduced and oxidized BH_4 metabolites. This may represent a physiological relevant mechanism by which $^{\bullet}NO$ and superoxide can be altered in disease states such as hypertension, hypercholesterolemia and diabetes.

4. REFERENCES

Abu-Soud, H.M., Ichimori, K., Presta, A. and Stuehr, D.J., 2000, Electron transfer, oxygen binding and nitric oxide feedback inhibition in endothelial nitric oxide synthase. *J. Biol. Chem.* **275**: 17349-17357.

Bec, N., Gorren, A.C.F., Voelker, C., Mayer, B. and Lange, R., 1998, Reaction of neuronal nitric-oxide with oxygen at low temperature. Evidence for reductive activation of the oxy-ferrous complex by tetrahydrobiopterin. J. Biol. Chem. 273: 13502-13508.

Bender, A.T., Silverstein, A.M., Demady, D.R., Kanelakis, K.C., Noguchi, S., Pratt, W.B., and Osawa, Y., 1999, Neuronal nitric oxide synthase is regulated by the hsp90-based chaperone system in vivo. *J. Biol. Chem.* **274**: 1472-1478.

Boulanger, C.M. and Vanhoutte, P.M., 1997, G-proteins and endothelium-dependent relaxations, *J.Vasc. Res.* **34**: 175-185.

Brouet, A., Sonveaux, P., Dessy, C., Moniotte, S., Balligand, J-L., and Feron, O., 2001, HSP90 and caveolin are key targets for the proangiogenic nitric oxide-mediated effects of statins. *Circ. Res.* **89**: 866-873.

Couture, M., Stuehr, D.J., and Rousseau, D.L., 2000, The ferrous dioxygen complex of the oxygenase domain of neuronal nitric oxide synthase. *J. Biol. Chem.* **275**: 3201-3205.

Crane, B.R., Arvai, A.S., Gachhui, R., Wu, C., Ghosh, D.K., Getzoff, E.D., Stuehr, D.J., and Tainer, J.A., 1997, The structure of nitric oxide synthase oxygenase domain and inhibitor complexes. *Science* **278**: 425-431.

Dawson, T.M., Bredt, D.S., Fotuhi, M., Hwang, P.M., Snyder, S.H., 1991,Nitric oxide synthase and neuronal NADPH diaphorase are identical in brain and peripheral tissues. *Proc. Natl. Acad. Sci. USA* **88**:7797-7801.

Fang, M., Jaffrey, S.R., Sawa, A., Ye, K., Luo, X., and Snyder, S.H., 2000, Dexras: A G-protein specifically coupled to neuronal nitric oxide synthase via CAPON. *Neuron* **28**: 183-193.

Feldman, P.L., Griffith, O.W., and Stuehr, D.J., 1993, The surprising life of nitric oxide. Chem. & Eng. News (Dec. 20) 26-38.

Feron, O., Belhassen, L., Kobzik, L., Smith, T.W., Kelly, R.A. and Michel, T., 1996, Endothelial nitric oxide synthase targeting to caveolae. Specific interactions with caveolin isoforms in cardiac myocytes and endothelial cells. *J. Biol. Chem.* **271**: 22810-22814.

Feron, O., Sladana, F., Michel, J.B., and Michel, T., 1998, The endothelial nitric-oxide synthase-caveolin regulatory cycle. *J. Biol. Chem.* **273**: 3125-3128.

Frejaville, C., Karoui, H., Tuccio, B., LeMoigne, F., Culcasi, M., Pietri, S., Lauricella, R. and Tordo, P., 1995, 5-(Diethoxyphosphoryl)-5-methyl-1-pyrroline N-oxide: a new efficient phosphorylated nitrone for the in vitro and in vivo spin trapping of superoxide. *J. Med. Chem.* **38**: 258-265.

Froncisz, W., and Hyde, J.S., 1992, The loop gap resonator: a new microwave lumped circuit ESR sample structure. *J. Magn. Res.* **47**: 515-521.

Garcia-Cardeña, G., Martásek, P., Masters, B.S.S., Skidd, P.M., Couet, J,, Li, S., Lisanti, M.P., and Sessa, W.C., 1997, Dissecting the interaction between nitric oxide synthase (NOS) and caveolin. Functional significance of the NOS caveolin binding domain in vivo. J. Biol. Chem. 272: 25437-25440.

Garcia-Cardeña, G., Fan, R., Shah, V., Sorrentino, R., Cirino, G., Papapetropoulos, A., and Sessa, W.C., 1998, Dynamic activation of endothelial nitric oxide synthase by HSP90. *Nature* **392**: 821-824.

Gachhui, R., Presta, A., Bentley, D.F., Abu-Soud, H.M., McArthur, R., Brudvig, G., Ghosh, D.K., and Stuehr, D.J., 1996, Characterization of the reductase domain of rat neuronal

nitric oxide synthase generated in the methylotrophic yeast pichia pastoris. Calmodulin response is complete within the reductase domain itself. *J. Biol. Chem.* **271**: 20594-20602.

Ghosh, S., Gachhui, R., Crooks, C., Wu, C., Lisanti, M.P., and Stuehr, D.J., 1998, Interaction between caveolin-1 and the reductase domain of endothelial nitric oxide synthase. *J. Biol. Chem.* **273**: 22267-22271.

Giovanelli, J., Campos, K.L., and Kaufman, S., 1991, Tetrahydrobiopterin, a cofactor for rat cerebellar nitric oxide synthase, does not function as a reactant in the oxygenation of arginine. *Proc. Natl. Acad. Sci. USA* **88**: 7091-7095.

Golser, R., Gorren, A.C.F., Leber, A., Andrew, P., Habish, H-J., Werner, E.R., Schmidt, K., Venema, R.C. and Mayer, B., 2000, Interaction of endothelial and neuronal nitric-oxide synthases with the bradykinin B2 receptor. Binding of an autoinhibitory peptide to the oxygenase domain blocks uncoupled NADPH oxidation. *J. Biol. Chem.* **275**:5291-5296.

Gratton, J.P., Fontana, J., O'Connor, D.S., Garcia-Cardena, G., McCabe, T.J., and Sessa, W.C., 2000, Reconstitution of an endothelial nitric-oxide synthase (eNOS), hsp90, and caveolin-1 complex in vitro. Evidence that hsp90 facilitates calmodulin stimulated displacement of eNOS from caveolin-1. *J. Biol. Chem.* **275**: 22268-22272.

Griffith, O.W., and Stuehr, D.J., 1995, Nitric oxide synthases: properties and catalytic mechanism. Ann. Rev. Physiol. 57: 707-736.

Heinzel, B., John, M., Klatt, P., Bohme, E. and Mayer, B., 1992, Ca^{2+}/calmodulin-dependent formation of hydrogen peroxide brain nitric oxide. *Biochem. J.* **281**: 627-630.

Jaffrey, S.R., and Snyder, S.H., 1996, PIN: an associated protein inhibitor of neuronal nitric oxide synthase. *Science* **274**: 774-777.

Jaffrey, S.R., Snowman, A.M., Eliasson, M.J.L., Cohen, N.A., and Snyder, S.H., 1998, CAPON: a protein associated with neuronal nitric oxide synthase that regulates its interactions with PSD95. *Neuron* **20**: 115-124.

Ju, H,, Zou, R., Venema, V.J., and Venema, R.C., 1997, Direct interaction of endothelial nitric oxide synthase and caveolin-1 inhibits synthase activity. *J. Biol. Chem.* **272**: 18522-18525.

Kappock, T.J., and Caradonna, J.P., 1996, Pterin-dependent amino acid hydroxylases. *Chem. Rev.* **96**: 2659-2756.

Katusic, Z., 2001, Vascular endothelial dysfunction: does tetrahydrobiopterin play a role? *Am. J. Physiol. Heart Circ. Physiol.* **281**: H981-H986.

Kaufman, S., 1995, Tyrosine hydroxylase. In: *Advances in Enzymology & Related Areas of Molecular Biology* **70**: 103-220.

Ledbetter, A.P., McMillan, K., Roman, L.J., Masters, B.S.S., Dawson, J.H., and Sono, M., 1999, Low-temperature stabilization and spectroscopic characterization of the dioxygen complex of the ferrous neuronal nitric oxide synthase oxygenase domain. *Biochemistry* **38**: 8014-8021.

Lin, S., Fagan, K.A., Li, K-X., Shaul, P.W., Cooper, D.M.F., and Rodman, D.M., 2000, Sustained endothelial nitric oxide synthase activation requires capacitative Ca^{2+} entry. *J. Biol. Chem.* **275**: 17979-17985.

List, B.M., Klosch, B., Volker, C., Gorren, A.C.F., Sessa, W.C., Werner, E.R., Kukovetz, W.R., Schmidt, K., and Mayer, B., 1997, Characterization of bovine endothelial nitric oxide synthase as a homodimer with down-regulated uncoupled NADPH oxidase activity: tetrahydrobiopterin binding kinetics and role of haem in dimerization. *Biochem J.* **323**: 159-165.

Mansuy, D., and Renaud, J-P., 1995, Heme-thiolate proteins different from cytochromes P450 catalyzing monooxygenations. In: *Cytochrome P450: Structure, Mechanism and Biochemistry* (Ortiz de Montellano P, Ed.). Pp 537-574. Plenum Press, New York.

Martásek, P., Liu, Q., Liu, J., Roman, L.J., Gross, S.S., Sessa, W.C., Masters, B.S., 1996, Characterization of bovine endothelial nitric oxide synthase expressed in E. coli. *Biochem. Biophys. Res. Commun.* **219**:359-365.

McCabe, T.J., Fulton, D., Roman, L.J., and Sessa, W.C., 2000, Enhanced electron flux and reduced calmodulin dissociation may explain "calcium-independent" eNOS activation by phosphorylation. *J. Biol. Chem.* **275**: 6123-6128.

Michel, J.B., Feron, O., Sacks, D. and Michel, T., 1997, Reciprocal regulation of endothelial nitric-oxide synthase by Ca2+-calmodulin and caveolin. *J. Biol, Chem.* **272**: 15583-15586.

Miller, T.R., Martásek, P., Omura, T., and Masters, B.S.S., 1999, Rapid kinetic studies of electron transfer in the three isoforms of nitric oxide synthase. *Biochem. Biophys. Res. Commun.* **265**: 184-188.

Nathan, C., and Xie, Q-W., 1994, Regulation of biosynthesis of nitric oxide. J. Biol. Chem. 269: 13725-13728.

Nishida, C.R., and Ortiz de Montellano, P.R., 1999, Autoinhibition of endothelial nitric-oxide synthase. Identification of an electron transfer control element. *J. Biol. Chem.* **274**: 14692-14698.

Olive, G., Mercier, A., LeMoigne, F., Rockenbauer, A., and Tordo, P., 2000, 2-ethoxycarbonyl-2-methyl-3,4-dihydro-2H-pyrrole-1-oxide: evaluation of the spin trapping properties. *Free Radical Biol. Med.* **28**: 403-408.

Ortiz de Montellano, P.R., Nishida, C., Rodriguez-Crespo, I., and Gerber, N., 1998, Nitric oxide synthase structure and electron transfer. *Drug Metab. Disp.* **26**: 1185-1189.

Pou, S., Pou, W.S., Bredt, D.S., Snyder, S.H., and Rosen, G.M., 1992, Generation of superoxide by purified brain nitric oxide synthase. *J. Biol. Chem.* **267**: 24173-24176.

Raman, C.S., Li, H., Martásek, P., Kral, V., Masters, B.S. and Poulos, T.L., 1998, Crystal structure of constitutive endothelial nitric oxide synthase: a paradigm for pterin function involving a novel metal center. *Cell.* **95**: 939-950.

Raman, C.S., Martásek, P., and Masters, B.S.S., 2000, Structural themes determining function in nitric oxide synthases. In: The porphyrin handbook. (Kadish KM, Smith KM, Guilard R, Eds) Vol. 4/Biochemistry and binding: activation of small molecules, Pp. 293-339, Academic Press, London.

Roman, L.J., Sheta, E.A., Martasek, P., Gross, S.S., Liu, Q., Masters, B.S., 1995, High-level expression of functional rat neuronal nitric oxide synthase in Escherichia coli. *Proc. Natl. Acad. Sci. USA* **92**:8428-8432.

Roman, L.J., Martásek, P., Miller, R.T., Harris, D.E., de la Garza, M.A., Shea, T.M., Kim, J-JP, and Masters, B.S.S., 2000, The C termini of constitutive nitric oxide synthase control electron flow through the flavin and heme domains and affect modulation by calmodulin. *J. Biol. Chem.* **275**: 29255-29232.

Roubaud, V., Sankarapandi, S., Kuppusamy, P., Tordo, P., and Zweier, J.L., 1997, Quantitative measurement of superoxide generation using spin trap 5-(diethoxyphosphoryl)-5-methyl-1-pyrroline-N-oxide. *Anal. Biochem.* **247**: 404-411.

Russell, K.S., Haynes, M.P., Caulin-Glaser, T., Rosneck, J., Sessa, W.C., and Bender, J.R., 2000, Estrogen stimulates heat shock protein 90 binding to endothelial nitric oxide synthase in human vascular endothelial cells. Effects on calcium and NO release. *J. Biol. Chem.* **275**, 5026-5030.

Salerno, J.C., Martásek, P., Roman, L.J., and Masters, B.S.S., 1996, Electron paramagnetic resonance spectroscopy of the heme domain of inducible nitric oxide synthase: binding of ligands at the arginine site induces changes in the heme ligand geometry. *Biochemistry* **35**: 7616-7630.

Salerno, J.C., Harris, D.E., Irizarry, K., Patel, B., Morales, A.J., Smith, S.M., Martásek, P., Roman, L.J., Masters, B.S.S., Jones, C.L., Weissman, B.A., Liu, Q. and Gross, S.S., 1997,

An autoinhibitory control element defines calcium-regulated isoforms of nitric oxide synthase. *J. Biol. Chem.* **272**: 29769-29777.

Santolini, J., Adak, S., Curran, C.M.L., and Stuehr, D.J., 2001, A kinetic stimulation model that describes catalysis and regulation in nitric oxide synthase. *J. Biol. Chem.* **276**: 1233-1243.

Sattler, R., Xiong, Z., Lu, W-Y., Hafner, M., McDonald, J.F., and Tymianski, M., 1999, Specific coupling of NMDA receptor activation to nitric oxide neurotoxicity by PSD-95 protein. Science **284**: 1845-1848.

Schmidt, H.H.H.W., Smith, R.M., Nakane, M., and Murad, F., 1992, Ca^{2+}/calmodulin-dependent NO synthase Type I: a biopteroflavoprotein with Ca^{2+}/calmodulin-independent diaphorase and reductase activities. *Biochemistry* **31**: 3243-3249.

Song, Y., Zweier, J.L., and Xia, Y., 2001, Heat-shock protein 90 augments neuronal nitric oxide synthase activity by enhancing Ca^{2+}/calmodulin binding. *Biochem J.* **355**: 357-360.

Sowa, G., Pypaert, M. and Sessa, W.C., 2001, Distinction between signaling mechanism in lipid rafts vs. caveolae. *Proc. Natl. Acad. Sci. USA* **98**: 14072-14077.

Vásquez-Vivar, J., Hogg, N., Pritchard, K.A. Jr., Martásek, P., and Kalyanaraman, B., 1997a, Superoxide anion formation from lucigenin: an electron paramagnetic resonance spin trapping study. *FEBS Lett.*. **403**: 127-130.

Vásquez-Vivar, J., Martásek, P., Hogg, N., Masters, B.S.S., Pritchard, K.A. Jr, and Kalyanaraman, B., 1997b, Endothelial nitric oxide synthase-dependent superoxide generation from adriamycin. *Biochemistry* **36**: 11293-11297.

Vásquez-Vivar, J., Kalyanarman, B., Mártasek, P., Hogg, N., Masters, B.S.S., Karoui, H., Pritchard, K.A. Jr., 1998, Superoxide generation by endothelial nitric oxide synthase: the influence of cofactors. *Proc. Natl. Acad. Sci USA* **95**: 9220-9225.

Vásquez-Vivar, J., Martásek, P., Hogg, N., Karoui, H., Masters, B.S.S., Pritchard, K.A. Jr and Kalyanaraman, B., 1999a, Electron spin resonance spin-trapping detection of superoxide generated by neuronal nitric oxide synthase. *Methods Enzymol.* **301**: 169-177.

Vásquez-Vivar, J., Hogg, N., Martásek, P., Karoui, H., Pritchard, K.A. Jr., and Kalyanaraman, B., 1999b, Tetrahydrobiopterin-dependent inhibition of superoxide generation from neuronal nitric oxide synthase. *J. Biol. Chem.* **274**: 26736-26742.

Vásquez-Vivar, J., Whitsett, J., Martásek, P., Hogg, N., and Kalyanaraman, B., 2001, Reaction of tetrahydrobiopterin with superoxide: EPR kinetic analysis and characterization of the pteridine radical. *Free Radical Biol. Med.* **31**: 975-985.

Vásquez-Vivar, J., Martásek, P., Whitsett, J., Joseph, J., and Kalyanaraman, B., 2002a, The ratio between tetrahydrobiopterin and oxidized tetrahydrobiopterin analogues controls superoxide release from endothelial nitric oxide synthase: an EPR spin trapping study. *Biochem J.* **362**:723-739.

Vásquez-Vivar, J., Duquaine, D., Whitsett, J., Kalyanaraman, B., and Rajagopalan S., 2002b, Altered tetrahydrobiopterin metabolism in Atherosclerosis. Implications for use of oxidized tetrahydrobiopterin analogues and thiol antioxidants. *Arterioscler. Thromb. Vasc. Biol.* **22**: (in press).

Chapter 5

In Vivo Spin Trapping of Free Radical Metabolites of Drugs and Toxic Chemicals Utilizing Ex Vivo Detection

Ronald P. Mason and Maria B. Kadiiska
Free Radical Metabolite Section, Laboratory of Pharmacology and Chemistry, National Institute of Environmental Health Sciences, National Institutes of Health, Research Triangle Park, North Carolina 27709

Abstract: This chapter represents a comprehensive compilation of all the various spin-trapping studies on free radical metabolites of toxic chemicals and drugs using *ex vivo* detection. A review is presented of the recent literature, including *ex vivo* detection techniques and advances in spectrometer sensitivity.

In vivo spin trapping with ex vivo detection of free radical metabolites has been comprehensively reviewed through 1992 (Knecht and Mason, 1993). Other recent review articles have concentrated on techniques (Mason and Knecht, 1994; Mason, 1996), approaches (Mason, 2000), chemistry (Towner, 2000), and ex vivo detection (Tomasi et al., 2000); this review will concentrate on ex vivo detection of free radical metabolites of toxic chemicals and drugs trapped in vivo.

1. SPIN TRAPS

A fifth spin trap, 5-diethoxyphosphoryl-5-methyl-1-pyrroline *N*-oxide (DEPMPO) has been added to the four spin traps commonly used in biological systems, 2-methyl-2 nitrosopropane (MNP), phenyl-*N*-*tert*-butylnitrone (PBN), α-(4-pyridyl 1-oxide)-*N*-*tert*-butylnitrone (POBN), and 5,5-dimethyl-1-pyrroline *N*-oxide (DMPO). DEPMPO is superior to DMPO for the detection of oxygen-centered radicals because the DEPMPO-superoxide radical adduct is 15-fold more persistent than its DMPO analogue, DEPMPO is clearly superior to DMPO in the detection of

superoxide during the reperfusion of ischemic isolated rat hearts (Frejaville *et al.,* 1994; Frejaville *et al.,* 1995). It should be noted that the superoxide is presumably trapped in the perfusate, not intracellularly, because the rate constant for trapping superoxide with DEPMPO is, like DMPO, very small. This low rate of trapping should preclude the intracellular trapping of superoxide in the presence of superoxide dismutase, which reacts with superoxide at a nearly diffusion-limited rate.

Although DEPMPO has been used to detect hydroxyl radical in mice treated with 5-aminolevulinic acid and Fe^{3+} using *in vivo* detection (Timmins *et al.,* 1999), it has not been widely used, the expense and impurity of commercial DEPMPO being major obstacles. MNP is relatively insoluble and the most toxic of the common spin traps. The aromatic nitrobenzene spin trap is extremely toxic. Although DMPO, PBN, and POBN are not particularly toxic compounds, the high doses used in spin trapping do cause toxic effects (Janzen *et al.,* 1995; Schaefer *et al.,* 1996; Khan *et al.,* 2003).

2. EX VIVO DETECTION TECHNIQUES

2.1 FOLCH EXTRACTION

Results of the first *in vivo* spin-trapping study were reported in 1979. In these experiments, the spin trap PBN and carbon tetrachloride were given to a rat through a stomach tube (Lai *et al.,* 1979). After one hour, the liver was homogenized in chloroform/mehthanol/buffer mixture, and the chloroform layer separated.

The chloroform layer contains sufficient water, which has a high dielectric constant, that a conventional 3mm quartz tube cannot be tuned in the microwave cavity unless the chloroform is first dried with anhydrous sodium sulphate. Alternatively the sample can be cooled to -70°C which freezes the water and consequently lowers the dielectric constant of the sample (Albano *et al.,* 1982). In any case, the sample must be bubbled with nitrogen to deoxygenate the solution because the concentration of oxygen present in air-saturated chloroform is high enough to broaden the lines of the ESR spectrum significantly. The greatest advantage of the extraction method is that the radical adduct is transferred from a sample with a high dielectric constant, the biological tissue, to a solvent with a lower dielectric constant, the chloroform solution. This enables the use of larger sample volumes, which increases sensitivity. In addition, the sample can be easily concentrated by evaporation of the chloroform layer. In favorable cases, the sample volume can be concentrated to a few microlitres where the loop-gap resonator can give greatly increased sensitivity (Kalyanaraman *et al.,* 1991).

The greatest limitation of chloroform extraction is that only nonpolar radical adducts such as the PBN adducts of the trichloromethyl and lipid-derived radicals can be detected. In addition, the radical adduct must be stable enough to survive not only the biological environment in which it was made, but the time required for the solvent extraction and evaporation. Of additional concern are at least two hypothetical problems. First, since the extraction technique requires homogenization of the tissue, this physical destruction may itself lead to free radical formation in some manner (*i.e.,* the release of iron and subsequent hydroxyl radical generation). Second, nucleophilic attack by the radical precursor on a nitrone spin trap forms the corresponding hydroxylamine of the radical adduct. The oxidation of such hydroxylamines to radical adduct impostors is facile. Nucleophilic attack on the nitrone is greatly facilitated by non-aqueous solvents because water, with its high dielectric constant, stabilizes the charged and/or polar reactants in the nucleophilic reaction and, in general, greatly inhibits this type of chemistry. For example, fluoride is a strong nucleophile in non-polar solvents, but not in water where it is protonated.

2.2 DETECTION OF RADICAL ADDUCTS IN BIOLOGICAL FLUIDS

A more recent approach to *in vivo* spin trapping has been to examine biological fluids such as urine, bile, and blood (or plasma) directly for spin adducts (Knecht *et al.,* 1993). Deoxygenation of samples is not usually necessary due to the low solubility of oxygen in water (approximately 250 μM), although deoxygenation will occasionally narrow the sharpest lines and is certainly necessary if deuterated PBN is being used to increase resolution (Janzen *et al.,* 1987). In practice, both the extraction of tissues and the examination of biological fluids should be used. If the Folch extraction method is used, the aqueous/methanol layer should also be examined utilizing a flat cell. Regardless of how the samples are obtained for ESR analysis, the relatively short lifetime of many radical adducts, *e.g.,* DMPO-superoxide radical adduct, will preclude their *ex vivo* detection. Even the relatively stable DMPO-hydroxyl radical adduct, which appears commonly in *in vitro* investigations (as an impurity in the DMPO if nothing else), has never been detected *ex vivo.*

In summary, radical formed *in vivo* can be spin-trapped and detected by ESR in Folch extracts of tissue or in biological fluids such as bile, blood, and urine. Only nonpolar radical adducts such as those of trichloromethyl and lipid-derived radicals can be detected with organic extraction, whereas ionic free radical metabolites or macromolecules will be detected in predominantly aqueous biological fluids such as urine. In principle, ionic,

polar, and non-polar radical adducts can be detected in bile, which contains biliary micelles.

2.3 ARTEFACTUAL EX VIVO RADICAL ADDUCT FORMATION

Since the detection of radical adducts occurs *ex vivo,* the question of the possible *ex vivo* formation of these radical adducts needs to be addressed. Even in the original spin-trapping investigation of the *in vivo* formation of the trichloromethyl radical, Lai *et al.* checked for *ex vivo* radical formation by mixing Folch extract from fresh liver tissue, CCl_4, and PBN and then extracting this mixture with chloroform/methanol (Lai *et al.,* 1979). After the extraction procedure was carried out, no radical adducts were detected.

Although it may not be logically possible to prove that *ex vivo* free radical formation has not occurred, it is possible to demonstrate that it is occurring and to design measures to prevent its occurrence. Trace transition metals catalyze many free radical reactions. Their presence either in the biological sample or in the collection vessel needs to be guarded against. In a study of α-hydroxyethyl radical formation by ethanol-treated alcohol dehydrogenase-deficient deermice, Desferal (a very strong Fe^{3+} chelator) was used to suppress the Fenton chemistry during the collection and breaking of gall bladders (Knecht *et al.,* 1990).

In an investigation of *in vivo* hydroxyl radical generation in iron overload, biliary iron caused *ex vivo* hydroxyl radical formation. This could be totally prevented when bile samples were collected into 2,2′-dipyridyl, which stabilizes Fe^{2+} (Burkitt *et al.,* 1991). *Ex vivo* radical adduct formation was undetectable even when Fe^{2+} was added to the 2,2′-dipyridyl in the collection tube. This chelator also suppressed a very weak radical adduct signal obtained when animals were administered PBN alone. In a related study of acute copper toxiciry (Kadiiska *et al.,* 1992), the addition of both bathocuproinedisulphonic acid (a Cu(I)-stabilizing chelator) and 2,2′-dipyridyl to the bile collection tube was found to be necessary to inhibit *ex vivo* hydroxyl radical formation.

Ex vivo lipid peroxidation is clearly a concern in all *in vivo* experiments where sample handling and treatment occur and needs to be addressed no matter what technique is used to assess free radical formation. In an investigation of ozone-initiated free radical formation, a-tocopherol was added to the chloroform/methanol solution prior to extraction in an attempt to suppress *ex vivo* lipid peroxidation (Kennedy *et al.,* 1992). The α-tocopherol phenoxyl radical is sometimes detected in such extractions, because this free radical is very stable in the absence of reductants. Good success with high concentrations of very pure phenol, which does not form a

stable radical, has been obtained in a study of POBN/$^{\bullet}$L formation in an Acute Respiratory Distress Syndrome (ARDS) model (Sato *et al.,* 2002).

3. SENSITIVITY ADVANCE

The major obstacle to the *in vivo* detection of free radical metabolites is that the rate of radical formation is limited by the animal. The *in vivo* rate of free radical formation is typically much lower than chemical or photochemical systems. For this reason, sensitivity is of paramount importance in biological ESR. Until recently, the use of the TM_{110} cavity with a 17-mm wide flat cell gave state-of-the-art sensitivity. The recent introduction by Bruker of a super-high Q cavity has led to an increase in aqueous sensitivity, allowing the detection of 2 nanomolar aqueous nitroxide in less than 20 min with a signal-to-noise ratio of three-to-one (http://epr.niehs.nih.gov/). This remarkable signal-to-noise is accomplished while actually making the instrument easier to tune.

4. APPLICATIONS OF SPIN TRAPPING

4.1 Carbon Tetrachloride

The first spin-trapping studies *in vivo* were performed with carbon tetrachloride (Lai *et al.,* 1979), and free radicals from this compound have been extensively studied (Knecht and Mason, 1993). More recent investigations have shown that the $^{\bullet}CCl_3$ radical is not significantly scavenged by metallothionein *in vivo* (Hanna *et al.,* 1993). Although carbon tetrachloride-induced hepatotoxicity was less severe with increasing age in the rat, PBN/ $^{\bullet}CCl_3$ radical adduct formation was similar at all ages (Rikans *et al.,* 1994). Apparently, other factors are involved in these age-associated changes in CCl_4-induced hepatotoxicity. Dietary zinc deficiency had no effect on *in vivo* PBN/$^{\bullet}CCl_3$ radical adduct formation (Xu and Bray., 1994).

4.2 Ethanol

The POBN/α-hydroxyethyl radical adduct was first detected *in vivo* in the bile of deer mice administered ethanol and POBN by gavage (Knecht *et al.,* 1990). Pretreatment with a high-fat, ethanol-containing diet was required for detection of the radical adduct. Detection of an apparently lipid-derived radical adduct of POBN was similarly dependent upon ethanol and high-fat pretreatment (Knecht *et al.,* 1990). Similar results have been

reported in rats with intravenous administration of POBN (Reinke *et al.,* 1997). With intravenous administration of high concentrations of POBN (700 mg/kg), POBN/α-hydroxyethyl could be detected in normal rats with moderate concentrations of blood alcohol (Moore *et al.,* 1995).

POBN/α-hydroxyethyl radical adduct as well as its ESR-silent hydroxylamine form can be detected by HPLC with electrochemical detection (Stoyanovsky and Cederbaum, 1998) or analyzed by GC/MS after trimethylsylilation (Castro *et al.,* 1997).

POBN/α-hydroxyethyl radical adduct has also been detected in a rat model resembling clinical alcoholic liver injury (Knecht *et al.,* 1995). Destruction of Kupffer cells by chronic treatment with $GdCl_3$ decreased the radical adduct concentration 50% and eliminated hepatic damage. Endotoxin, which activates Kupffer cells, increased the POBN/α-hydroxyethyl radical adduct concentration threefold (Chamulitrat *et al.,* 1998). Chronic pancreatitis is also caused by alcohol abuse, and POBN/α-hydroxyethyl is detected in pancreatic secretions (Iimuro *et al.,* 1996) where it is diminished by saturated fat (Kono, 2001b).

The α-hydroxyethyl radical oxidizes ascorbate, GSH, and α-tocopherol (Stoyanovsky *et al.,* 1998), which regenerates ethanol. In fact, vitamins C and E largely prevent POBN/$^{\bullet}CH(OH)CH_3$ formation *in vivo* (Navasumrit *et al.,* 2000). *In vivo* formation of POBN/$^{\bullet}CH(OH)CH_3$ in mice is unaffected by the cytochrome $P\text{-}450_{2E1}$ knockout. POBN/$^{\bullet}CH(OH)CH_3$ in bile is diminished by NADPH oxidase knockout (Kono *et al.,* 2000) and by an NADPH oxidase inhibitor (Kono *et al.,* 2001). POBN/$^{\bullet}CH(OH)CH_3$ in bile is also decreased by medium-chain triglycerides (Kono *et al.,* 2000) and over-expression of Cu/Zn- (Wheeler *et al.,* 2001a) and Mn- (Wheeler *et al.,* 2001a) superoxide dismutase. Related alcohols such as ethylene glycol (Kadiiska and Mason, 2000a) and methanol (Kadiiska *et al.,* 2000b) are also oxidized to carbon-centered free radicals.

The two-electron oxidation product of ethanol is acetaldehyde, which itself is oxidized to a free radical (Nakao *et al.,* 2000). Similarly, the two-electron oxidation product of methanol, formate, like acetaldehyde, is oxidized to a free radical (Dikalova *et al.,* 2001).

4.3 Iron

Hydroxyl radical formation results from the reaction of ferrous iron with hydrogen peroxide, the Fenton reaction.

$$Fe^{2+} + H_2O_2 \rightarrow Fe^{2+} + {}^{-}OH + {}^{\bullet}OH$$

To circumvent the many artifacts associated with DMPO/$^{\bullet}$OH formation, a well-known reaction has been used in which the hydroxyl radical is converted to the methyl radical via its reaction with dimethyl sulfoxide. Alone, DMSO is relatively nontoxic and is, therefore, an ideal reagent for the *in vivo* detection of hydroxyl radical.

$$(CH_3)_2SO + {}^{\bullet}OH \rightarrow CH_3SOOH + {}^{\bullet}CH_3$$

The DMSO-dependent methyl radical can then be detected as its long-lived PBN adduct in the bile of rats fed a diet containing 0.12% ferric citrate (Kadiiska *et al*., 1995).

$$PBN + {}^{\bullet}CH_3 \rightarrow PBN/{}^{\bullet}CH_3$$

The use of [^{13}C]DMSO demonstrated that the dominant spectrum detected in rat bile was the PBN/$^{\bullet}{}^{13}CH_3$ radical adduct. Since the Fenton reaction requires hydrogen peroxide, a substance which catalyzes hydrogen peroxide formation should increase PBN/$^{\bullet}CH_3$ formation. The activity of the herbicide paraquat (PQ^{2+}) is attributed to its ability to catalyze the formation of superoxide and, subsequently, hydrogen peroxide. Paraquat undergoes an enzymatic single-electron reduction to form the paraquat radical cation $PQ^{\bullet+}$, which is then oxidized by molecular oxygen to form the superoxide radical, $O_2^{\bullet-}$. Through its participation in repeated cycles of reduction and oxidation, PQ^{2+} catalyzes superoxide radical formation. The formation of superoxide radical and the resulting hydrogen peroxide during the "futile cycling" of PQ^{2+} is thought responsible for its pulmonary toxicity to man. Although paraquat catalyzes superoxide and hydrogen peroxide formation, when we administered paraquat to our iron-poisoned rat model, only a modest increase of radical adduct formation occurred (Burkitt *et al.,* 1993).

4.4 Copper

In contrast to iron, the PBN/$^{\bullet}CH_3$ radical adduct was detected in the bile of copper-poisoned rats only after they had been given paraquat (Kadiiska *et al.,* 1993b). Apparently, hydrogen peroxide was limiting *in vivo* in the copper analog of the Fenton reaction.

$$Cu^{1+} + H_2O_2 \rightarrow Cu^{2+} + {}^{-}OH + {}^{\bullet}OH$$

When the experiment was repeated in the absence of copper or PQ^{2+}, no radical adducts were detected, thereby confirming the dependence of radical formation on the co-administration of both copper and PQ^{2+}. The fact that copper or PQ^{2+} alone causes no detectable radical adduct formation may be attributed to their inability to form hydroxyl radicals at detectable concentrations due to strong defense systems against oxidative stress in

living organisms. For instance, GSH binds Cu^{1+} as a stable complex which reacts slowly, if at all, with hydrogen peroxide to form the hydroxyl radical (Hanna and Mason, 1992).

Ascorbate, which reduces both Cu^{2+} and Fe^{3+}, increases PBN/$^{\bullet}CH_3$ formation from undetectable levels in the case of copper poisoning (Kadiiska *et al.,* 1992). Interestingly, iron-dependent formation of PBN/$^{\bullet}CH_3$ is dependent on co-administration of ascorbate in young rats, but not in old rats (Kadiiska *et al.,* 1997a).

4.5 Xenobiotic-Initiated Lipid-Derived Radicals

The measurement of lipid peroxidation by spin-trapping techniques is of special interest. Lipid peroxidation is a widely invoked mechanism of toxicity, but the various techniques used for assaying this process may often be inaccurate. In addition, lipid radical adducts may be the only surviving evidence of xenobiotic free radical metabolites, which themselves cannot be detected by spin trapping, and thus may be useful in implicating a free radical mechanism in the metabolism and toxicity of a xenobiotic. For example, a lipid-derived radical adduct was detected in bile of copper-challenged rats deficient in both vitamin E and selenium (Kadiiska *et al.,* 1993a). Similarly, an endogenous POBN adduct detected after the administration of Cr(VI) was detected in bile (Kadiiska *et al.,* 1994). This radical adduct had hyperfine coupling constants very similar to the POBN/pentyl radical adduct (Kadiiska *et al.,* 1998), which is the dominant adduct formed from unsaturated fatty acids by lipoxygenase (Iwahashi *et al.,* 1996). Unfortunately, these hyperfine coupling constants are not unique, and the exact origin of this radical adduct is still unknown. However, the fact that the formation of this radical adduct is associated with lipid peroxidation as quantified by increases in F_2-isoprostane levels in bile is again highly suggestive that this radical adduct is lipid-derived (Kadiiska *et al.,* 1998). This same type of radical adduct is detected in organic extracts of lungs from rats intratracheally instilled with asbestos (Ghio *et al.,* 1998). Similarly, lung exposure to oil fly ash (an emission source air pollution particle) forms a POBN adduct thought to be lipid-derived such as the POBN/pentyl radical adduct (Kadiiska *et al.,* 1997b). The same signal was observed after lung instillation of either a mixture of vanadium, nickel, and iron sulfates or $VOSO_4$ alone, which are all found in oil fly ash. We concluded that after instillation of an air pollution particle in the rat, ESR analysis of lung tissue demonstrates *in vivo* free radical production and that this generation of free radicals appears to be catalyzed by soluble metals in the oil fly ash.

5. COMPLETE TABLE OF ALL FREE RADICAL METABOLITES DETECTED BY EX VIVO ESR

Table 1 lists all publications of *in vivo* free radical formation with *ex* vivo detection. An examination of this table reveals how productive this approach has been in a variety of systems and in multiple laboratories. Taken as a whole, these ESR studies are the strongest data supporting the causal role of free radical metabolites in the toxicity of many chemicals.

Table 1. In Vivo Formation of Free Radical Metabolites Detected by Ex Vivo ESR

Year	Radical Adduct	Authors
1979	PBN/$^{\bullet}CCl_3$ from CCl_4 detected in organic extract of liver	Lai *et al.*
1980	PBN/$^{\bullet}{}^{13}CCl_3$ from $^{13}CCl_4$ detected in organic extract of liver	Poyer *et al.*
1981	PBN/$^{\bullet}CHClCF_3$ from halothane detected in organic extract of liver	Poyer *et al.*
1982	PBN/$^{\bullet}CCl_3$ from CCl_4 detected in organic extract of liver	Albano *et al.*
1982	PBN/$^{\bullet}CHClCF_3$ from halothane detected in organic extract of liver	Plummer *et al.*
1984	PBN/$^{\bullet}$L from 3-methylindole detected in organic extract of lungs	Kubow *et al.*
1984	$HO(CH_3O)_2PBN/^{\bullet}L$ and $HO(CH_3O)_2PBN/^{\bullet}CCl_3$ from CCl_4 detected in organic extract of liver administered $(CH_3O)_3PBN$	McCay *et al.*
1984	PBN/$^{\bullet}CHClCF_3$ from halothane detected in organic extract of liver	Fujii *et al.*
1985	PBN/$^{\bullet}$L from 3-methylindole detected in organic extract of lungs as affected by cysteine and diethylmaleate	Kubow *et al.*
1985	PBN/$^{\bullet}CHCl_2$ from chloroform detected in organic extract of liver with related radical adducts from bromoform, bromodichloromethane, and iodoform	Tomasi *et al.*
1986	PBN/$\bullet CO_2^-$ from CCl_4 detected in urine	Connor et. al.
1987	$HO(CH_3O)_2PBN/\bullet L$ from ethanol detected in organic extract of liver and heart as affected by high fat	Reinke et al.
1988	PBN/$\bullet CCl_3$ from CCl_4 detected in organic extract of liver affected by ethanol and high fat	Reinke et al.
1988a	DMPO/thiyl Hb from phenylhydrazine detected in whole blood	Maples et al.
1988b	DMPO/thiyl Hb and PBN/thiyl Hb from phenylhydrazine and DMPO/thiyl Hb from hydrazine-based drugs in whole blood	Maples et al.
1988	PBN/$\bullet CO_2^-$ from $CBrCl_3$ in urine	LaCagnin et al.
1988	PBN/$\bullet CCl_3$ and PBN/$\bullet CO_2^-$ from CCl_4 detected in bile	Knecht and Mason
1990	PBN-d_{14}/$\bullet CHClCF_3$ from halothane detected in liver extract	Janzen et al.
1990a	DMPO/thiyl Hb from hydroperoxides in whole blood	Maples et al.
1990b	DMPO/thiyl Hb from phenylhydroxylamine or nitrosobenzene in whole blood	Maples et al.
1990	POBN/$\bullet CH(OH)CH_3$ and POBN/$\bullet$L from ethanol and high fat detected in bile	Knecht et al.
1991	POBN/$\bullet$? from cigarette smoke/ endotoxin detected in organic extract of plasma	Murphy et al.

Year	Radical Adduct	Authors
1991	PBN-d_{14}/•$CH(OH)CH_3$, PBN-d_{14}/•CH2R and PBN-d_{14}/•OL from ethanol in organic extract of liver	Reinke et al.
1991	PBN/•CO_2^- from CCl_4 detected in plasma. PBN/•CCl_3 from CCl_4 detected in organic extract of plasma	Reinke and Janzen
1991	PBN/•$CHClCF_3$ from halothane and PBN/•CCl_3 from CCl_4 detected in bile	Hughes et al.
1991	PBN/•$CHBr_2$ from bromoform and PBN/•CCl_3 from $CBrCl_3$ in bile	Knecht and Mason
1991	PBN/•CH_3 from attack of hydroxyl radical from Fe^{2+} on DMSO detected in bile	Burkitt and Mason
1992	PBN/•CH_3 from procarbazine detected in organic extract of several organs especially blood	Goria-Gatti et al.
1992	PBN/•CCl_2CH_3 from 1,1,1-trichloroethane detected in organic extract of liver	Dürk et al.
1992	PBN/•$CHClCHCl_2$ from 1,1,2,2-tetrachloroethane detected in organic extract of liver	Paolini et al.
1992	POBN/•? From cotton smoke detected in organic extract of plasma	Yamaguchi et al.
1992	PBN/•CO_2^- from CCl_4 detected in plasma affected by ethanol	Reinke et al.
1992	POBN/•? from ozone detected in organic extract of lungs	Kennedy et al.
1992	PBN-d_{14}/•$^{13}CHClCF_3$ from halothane detected in bile	Knecht et al.
1992	PBN/•CCl_3, PBN/•CO_2^-, and PBN/[GSH-•CCl_3] from CCl_4 detected in bile	Sentjurc et. al.
1992	POBN/•L from oxidized fatty acids detected in bile	Chamulitrat et. al.
1992	PBN/•CH_3 from attack of hydroxyl radical from Cu^{2+} and ascorbate on DMSO detected in bile	Kadiiska et al.
1993	DMPO/•OR and DMPO/•C from E. coli/TNF detected in extract of liver	Lloyd et al.
1993	PBN/•CH_3 from attack of hydroxyl radical from Fe^{2+} and ascorbate on DMSO detected in bile as affected by paraquat and desferrioxamine	Burkitt et al.
1993a	POBN/•L from Cu^{2+}- treated vitamin E- and selenium-deficient rats detected in bile	Kadiiska et al.
1993b	PBN/•CH_3 from attack of hydroxyl radical from Cu^{2+} and paraquat on DMSO detected in bile	Kadiiska et al.
1993	PBN/•CCl_3 from CCl_4 detected in organic extract of liver unaffected by Zn^{2+}, Cr^{3+}, and metallothionein	Hanna et al.
1994	PBN/•CCl_3 from carbon tetrachloride detected in liver extract unaffected by age	Rikans et al.
1994	PBN/•CCl_3 unaffected by dietary Zn deficiency	Xu and Bray
1994	POBN/•L from Cr(VI) detected in bile	Kadiiska et al.
1995	POBN/•$CH(OH)CH_3$ from acute ethanol detected in bile	Moore et al.
1995	POBN/•$CH(OH)CH_3$ from ethanol detected in bile affected by chronic ethanol and high fat diet as mediated by Kuppfer cells	Knecht et al.
1995	PBN/•CH_3 from attack of hydroxyl radical from dietary iron or DMSO detected in bile	Kadiiska et al.

Year	Radical Adduct	Authors
1996	PBN/•OR, PBN/•C, and POBN/•C from ozone detected in organic extract of lung and liver	Vincent et al.
1996	PBN/•$CH(OH)CH_3$ from ethanol detected in pancreatic secretion	Iimuro et al.
1997	POBN/•$CH(OH)CH_3$ and POBN/•L from ethanol detected in bile as affected by dietary fats	Reinke and McCay
1997	POBN/•$CH(OH)CH_3$ and POBN/•L from ethanol detected in bile as affected by chronic ethanol	Reinke et al.
1997a	PBN/•CH_3 from attack of hydroxyl radical from Fe^{2+} on DMSO detected in bile as affected by ascorbate and age	Kadiiska et al.
1997b	POBN/•L from air pollution particle detected in organic extract of lung	Kadiiska et al.
1997	POBN/•L from hippocampal extracellular space during kainic acid-induced seizures	Ueda et al.
1998	POBN/•L from asbestos detected in organic extract of lung	Ghio et al.
1998	POBN/•$CH(OH)CH_3$ from ethanol enhancement by endotoxin as mediated by Kupffer cells	Chamulitrat et al.
1998	POBN/•L from haloperidal detected in microdialysate of right striatum	Yokoyama et al.
1998	POBN/•L from Cr(VI) detected in bile is probably POBN/pentyl	Kadiiska et al.
1999	POBN/•$CH(OH)CH_3$ is unaffected by cytochrome $P\text{-}450_{2E1}$ knockout	Kono et al.
2000	POBN/•$CH(OH)CH_3$ formation is prevented by vitamins C and E	Navasumrit et al.
2000	POBN/•C_6H_5 in bile and extracted from cecal contents from 1,3-diphenyl-1-triazene	Kadiiska et al.
2000a	POBN/•$CH(OH)CH_2OH$ in bile from ethylene glycol	Kadiiska and Mason
2000	POBN/•CH_3 in bile from tert-butylhydroperoxide	Hix et al.
2000	POBN/•CH_3 in bile from acetaldehyde	Nakao et al.
2000	POBN/•$CH(OH)CH_3$ in bile is diminished in NADPH oxidase knockout mice	Kono et al.
2000b	POBN/•CH_2OH in bile from methanol	Kadiiska and Mason
2000	POBN/•$CH(OH)CH_3$ is diminished by medium-chain triglycerides	Kono et al.
2001a	POBN/•$CH(OH)CH_3$ is decreased by Cu/Zn-SOD overexpression	Wheeler et al.
2001	POBN/•$CH(OH)CH_3$ is decreased by an NADPH oxidase inhibitor	Kono et al.
2001	POBN radical adducts in pancreatic secretions are diminished by saturated fat	Kono et al.
2001	POBN/•CO_2^- in urine and bile from formate	Dikalova et al.
2001b	POBN/•$CH(OH)CH_3$ is decreased by Mn-SOD expression	Wheeler et al.
2002	Unknown PBN radical adduct from liver extract of Cd-intoxicated mice	Liu et al.
2002	POBN/ •L from lipopolysaccharide in organic extract of lung.	Sato et al.

6. REFERENCES

Albano, E., Lott, K.A.K., Slater, T.F., Stier, A., Symons, M.C.R., and Tomasi, A., 1982, Spin-trapping studies on the free-radical products formed by metabolic activation of carbon tetrachloride in rat liver microsomal fractions isolated hepatocytes and *in vivo* in the rat, *Biochem. J.* **204**: 593-603.

Burkitt, M.J. and Mason, R.P., 1991, Direct evidence for *in vivo* hydroxyl-radical generation in experimental iron overload: An ESR spin-trapping investigation, *Proc. Natl. Acad. Sci. USA* **88**: 8440-8444.

Burkitt, M.J., Kadiiska, M.B., Hanna, P.M., Jordan, S.J., and Mason, R.P., 1993, Electron spin resonance spin-trapping investigation into the effects of paraquat and desferrioxamine on hydroxyl radical generation during acute iron poisoning, *Mol. Pharmacol.* **43**: 257-263.

Castro, G.D., Delgado de Layño, A.M.A., and Castro, J.A., 1997, Hydroxyl and 1-hydroxyethyl free radical detection using spin traps followed by derivatization and gas chromatography-mass spectrometry, *Redox Report.* **3**:343-347.

Chamulitrat, W., Jordan, S.J., and Mason, R.P., 1992, Fatty acid radical formation in rats administered oxidized fatty acids: *In vivo* spin trapping investigation, *Arch. Biochem. Biophys.* **299**: 361-367.

Chamulitrat, W., Carnal, J., Reed, N.M., and Spitzer, J.J., 1998, In vivo endotoxin enhances biliary ethanol-dependent free radical generation, *Am. J. Physiol. Gastrointest. Liver Physiol.* **37**: *274,* G653-G661.

Connor, H.D., Thurman, R.G., Galizi, M.D., and Mason, R.P., 1986, The formation of a novel free radical metabolite from CCl_4 in the perfused rat liver and *in vivo, J. Biol. Chem.* **261**: 4542-4548.

Dikalova, A.E., Kadiiska, M.B., and Mason, R.P., 2001, An *in vivo* ESR spin-trapping study: free radical generation in rats from formate intoxication- role of the Fenton reaction, *Proc. Natl. Acad. Sci. USA* **98**: 13549-13553.

Dürk, H., Poyer, J.L., Klessen, C., and Frank, H., 1992, Acetylene, a mammalian metabolite of 1,1,1 -trichloroethane, *Biochem. J.* **286**: 353-356.

Frejaville, C., Karoui, H., Tuccio, B., le Moigne, F., Culcasi, M., Pietri, S., Lauricella, R., and Tordo, P., 1994, 5-diethoxyphosphoryl-5-methyl-1-pyrroline *N*-oxide (DEPMPO): a new phosphorylated nitrone for the efficient *in vitro* and *in vivo* spin trapping of oxygen-centered radicals, *J. Chem. Soc., Chem. Commun.* **No. 15:** 1793-1794.

Frejaville, C., Karoui, H., Tuccio, B., le Moigne, F., Culcasi, M., Pietri, S., Lauricella, R., and Tordo, P., 1995, 5-(diethoxyphosphoryl)-5-methyl-1-pyrroline *N*-oxide: A new efficient phosphorylated nitrone for the *in vitro* and *in vivo* spin trapping of oxygen-centered radicals, *J. Med. Chem.* **38**: 258-265.

Fujii, K., Morio, M., Kikuchi, H., Ishihara, S., Okida, M., and Ficor, F., 1984, *In vivo* spin-trap study on anaerobic dehalogenation of halothane, *Life Sci.* **35**: 463-468.

Ghio, A.J., Kadiiska, M.B., Xiang, Q.-H., and Mason, R.P., 1998, In vivo evidence of free radical formation after asbestos instillation: an ESR spin trapping investigation, *Free Radical Biol. Med.* **24**: 11-17.

Goria-Gatti, L., Iannone, A., Tomasi, A., Poli, G., and Albano, E., 1992, *In vitro* and *in vivo* evidence for the formation of methyl radical from procarbazine: a spin-trapping study, *Carcinogenesis* **13**: 799-805.

Hanna, P.M. and Mason, R.P., 1992, Direct evidence for inhibition of free radical formation from Cu(I) and hydrogen peroxide by glutathione and other potential ligands using the EPR spin-trapping technique, *Arch. Biochem. Biophys.* **295**: 205-213.

Hanna, P.M., Kadiiska, M.B., Jordan, S.J., and Mason, R.P., 1993, Role of metallothionein in zinc(II) and chromium(III) mediated tolerance to carbon tetrachloride hepatoxicity: evidence against a trichloromethyl radical-scavenging mechanism, *Chem. Res. Toxicol.* **6**: 711-717.

Hix, S., Kadiiska, M.B., Mason, R.P., and Augusto, O., 2000, In vivo metabolism of *tert*-butyl hydroperoxide to methyl radicals. EPR spin-trapping and DNA methylation studies, *Chem. Res. Toxicol.* **13**: 1056-1064.

Hughes, H.M., George, I.M., Evans, J.C., Rowlands, C.C., Powell, G.M., and Curtis, C.G., 1991, The role of the liver in the production of free radicals during halothane anaesthesia in the rat. Quantification of *N-tert*-butyl-α-(4-nitrophenyl)nitrone (PBN)-trapped adducts in bile from halothane as compared with carbon tetrachloride, *Biochem. J.* **277**: 795-800.

Iimuro, Y., Bradford, B.U., Gao, W., Kadiiska, M., Mason, R.P., Stefanovic, B., Brenner, D.A., and Thurman, R.G., 1996, Detection of α-hydroxyethyl free radical adducts in the pancreas after chronic exposure to alcohol in the rat, *Mol. Pharmacol.* **50**: 656-661.

Iwahashi, H., Deterding, L.J., Parker, C.E., Mason, R.P., and Tomer, K.B., 1996, Identification of radical adducts formed in the reactions of unsaturated fatty acids with soybean lipoxygenase using continuous flow fast atom bombardment with tandem mass spectroscopy, *Free Radical Res.* **25**: 255-274.

Janzen, E.G., Towner, R.A., and Haire, D.L., 1987, Detection of free radicals generated from the *in vitro* metabolism of carbon tetrachloride using improved ESR spin trapping techniques, *Free Radical Res. Comms.* **3:** 357-364.

Janzen, E.G., Towner, R.A., Krygsman, P.H., Haire, D.L., and Poyer, J.L., 1990, Structure identification of free radicals by ESR and GC/MS of PBN spin adducts from the *in vitro* and *in vivo* rat liver metabolism of halothane, *Free Radical Res. Comms.* **9**: 343-351.

Janzen, E.G., Poyer, J.L., Schaefer, C.F., Downs, P.E., and Dubose, C.M., 1995, Biological spin-trapping II. Toxicity of nitrone spin traps: dose-ranging in the rat, *J. Biochem. Biophys. Meth.* **30**: 239-247.

Kadiiska, M.B., Hanna, P.M., Hernandez, L., and Mason, R.P., 1992, *In vivo* evidence of hydroxyl radical formation after acute copper and ascorbic acid intake: Electron spin resonance spin-trapping investigation, *Mol. Pharmacol.* **42**: 723-729.

Kadiiska, M.B., Hanna, P.M., Jordan, S.J., and Mason, R.P., 1993a, Electron spin resonance evidence for free radical generation in copper-treated vitamin E- and selenium-deficient rats: *in vivo* spin-trapping investigation, *Mol. Pharmacol.* **44**: 222-227.

Kadiiska, M.B., Hanna, P.M., and Mason, R.P., 1993b, *In vivo* ESR spin trapping evidence for hydroxyl radical-mediated toxicity of paraquat and copper in rats, *Toxicol. Appl. Pharmacol.* **123**: 187-192.

Kadiiska, M.B., Xiang, Q.-H., and Mason, R.P., 1994, In vivo free radical generation by chromium (VI): an electron spin resonance spin-trapping investigation, *Chem. Res. Toxicol.* **7:** 800-805.

Kadiiska, M.B., Burkitt, M.J., Xiang, Q.-H., and Mason, R.P., 1995, Iron supplementation generates hydroxyl radical in vivo: an ESR spin-trapping investigation, *J. Clin. Invest.* **96**: 1653-1657.

Kadiiska, M.B., Burkitt, M.J., Xiang, Q.-H., and Mason, R.P., 1997a, Effect of acute iron and ascorbic acid administration on free-radical generation in young and older rats: an ESR spin-trapping investigation, *Environ. Nutr. Interact.* **1**: 143-159.

Kadiiska, M.B., Mason, R.P., Dreher, K.L., Costa, D.L., and Ghio, A.J., 1997b, *In vivo* evidence of free radical formation in the rat lung after exposure to an emission source air pollution particle, *Chem. Res. Toxicol.* **10**: 1104-1108.

Kadiiska, M.B., Morrow, J.D., Awad, J.A., Roberts, II, L.J., and Mason, R.P., 1998, Identification of free radical formation and F_2-isoprostanes in vivo by acute Cr(VI) poisoning, *Chem. Res. Toxicol.* **11**: 1516-1520.

Kadiiska, M.B., De Costa, K.S., Mason, R.P., and Mathews, J.M., 2000, Reduction of 1,3-diphenyl-1-triazene by rat hepatic microsomes, by cecal microflora, and in rats generates the phenyl radical metabolite: an ESR spin-trapping investigation, *Chem. Res. Toxicol.* **13**: 1082-1086.

Kadiiska, M.B. and Mason, R.P., 2000a, Acute methanol intoxication generates free radicals in rats: an ESR spin trapping investigation, *Free Radical Biol. Med.* **28**: 1106-1114.

Kadiiska, M.B. and Mason, R.P., 2000b, Ethylene glycol generates free radical metabolites in rats: an ESR in vivo spin trapping investigation, *Chem. Res. Toxicol.* **13:** 1187-1191.

Kalyanaraman, B., Parthasarathy, S., Joseph, J., and Froncisz, W., 1991, EPR spectra in a loop-gap resonator for a spin-trapped radical from a low-density lipoprotein lipid, *J. Mag. Res.* **92**: 342-347.

Kennedy, C.H., Hatch, G.E., Slade, R., and Mason, R.P., 1992, Application of the EPR spin-trapping technique to the detection of radicals produced *in vivo* during inhalation exposure of rats to ozone, *Toxicol. Appl. Pharmacol.* **114**: 41-46.

Khan, N., Wilmot, C.M., Rosen, G.M., Demidenko, E., Sun, J., Joseph, J., O'Hara, J., Kalyanaraman, B., and Swartz, H.M., 2003, Spin traps: In vitro toxicity and stability of radical adducts, *Free Radical Biol. Med.* **34**: 1473-1481.

Knecht, K.T. and Mason, R.P., 1988 *In vivo* radical trapping and biliary secretion of radical adducts of carbon tetrachloride-derived free radical metabolites, *Drug Metab. Dispos.* **16**: 813-817.

Knecht, K.T., Bradford, B.U., Mason, R.P., and Thurman, R.G., 1990 *In vivo* formation of a free radical metabolite of ethanol, *Mol. Pharmacol.* **38**: 26-30.

Knecht, K.T. and Mason, R.P., 1991, The detection of halocarbon-derived radical adducts in bile and liver of rats, *Drug Metab. Dispos.* **19** 325-331.

Knecht, K.T., DeGray, J.A., and Mason, R.P., 1992, Free radical metabolism of halothane *in vivo:* radical adducts detected in bile, *Mol. Pharmacol.* **41**: 943-949.

Knecht, K.T. and Mason, R.P., 1993, *In vivo* spin trapping of xenobiotic free radical metabolites, *Arch. Biochem. Biophys.* **303**: 185-194.

Knecht, K.T., Adachi, Y., Bradford, B.U., Iimuro, Y., Kadiiska, M.B., Xiang, Q.-H., and Thurman, R.G., 1995, Free radical adducts in the bile of rats treated chronically with intragastric alcohol: inhibition by destruction of Kupffer cells, *Mol. Pharamcol.* **47**: 1028-1034.

Kono, H., Bradford, B.U., Yin, M., Sulik, K.K., Koop, D.R., Peters, J.M., Gonzalez, F.J., McDonald, T., Dikalova, A., Kadiiska, M.B., Mason, R.P., and Thurman, R.G., 1999, CYP2E1 is not involved in early alcohol-induced liver injury, *Am. J. Physiol. Gastrointest. Liver Physiol.* **277**: G1259-G1267.

Kono, H., Enomoto, N., Connor, H.D., Wheeler, M.D., Bradford, B.U., Rivera, C.A., Kadiiska, M.B., Mason, R.P., and Thurman, R.G., 2000, Medium-chain triglycerides inhibit free radical formation and TNF-α production in rats given enteral ethanol, *Am. J. Physiol. Gastrointest. Liver Physiol.* **278:** G467-G476.

Kono, H., Rusyn, I., Uesugi, T., Yamashina, S., Connor, H.D., Dikalova, A., Mason, R.P., and Thurman, R.G., 2001a, Diphenyleneiodonium sulfate, an NADPH oxidase inhibitor, prevents early alcohol-induced liver injury in the rat, *Am. J. Physiol. Gastrointest. Liver Physiol.* **280**: G1005-G1012.

Kono, H., Nakagami, M., Rusyn, I., Connor, H.D., Stefanovic, B., Brenner, D.A., Mason, R.P., Arteel, G.E., and Thurman, R.G., 2001b, Development of an animal model of

chronic alcohol-induced pancreatitis in the rat, *Am. J. Physiol. Gastrointest. Liver Physiol.* **280**: G1178-G1186.

Kubow, S., Janzen, E.G., and Bray, T.M., 1984, Spin-trapping of free radicals formed during *in vitro* and *in vivo* metabolism of 3-methylindole, *J. Biol. Chem.* **259:** 4447-4451.

Kubow, S., Bray, T.M., and Janzen, E.G., 1985, Spin-trapping studies on the effects of vitamin E and glutathione on free radical production induced by 3-methylindole, *Biochem. Pharamcol.* **34**: 1117-1119.

LaCagnin, L.B., Connor, H.D., Mason, R.P., and Thurman, R.G., 1988, The carbon dioxide anion radical adduct in the perfused rat liver: relationship to halocarbon-induced toxicity, *Mol. Pharmacol.* **33**: 351-357.

Lai, E.K., McCay, P.B., Noguchi, T., and Fong, K.-L., 1979, *In vivo* spin-trapping of trichloromethyl radicals formed from CCl_4, *Biochem. Pharmacol.* **28**: 2231-2235.

Lloyd, S.S., Chang, A.K., Taylor, Jr., F.B., Janzen, E.G., and McCay, P.B., 1993, Free radicals and septic shock in primates: the role of tumor necrosis factor, *Free Radical Biol. Med.* **14**: 233-242.

Lui, J., Kadiiska, M.B., Corton, J.C., Qu, W., Waalkes, M.P., Mason, R.P., Liu, Y., and Klaassen, C.D., 2002, Acute cadmium exposure induces stress-related gene expression in wild-type and metallothionein-I/II-null mice, *Free Radical Biol. Med.* **32**: 525-535.

Maples, K.R., Jordan, S.J., and Mason, R.P., 1988a, *In vivo* rat hemoglobin thiyl free radical formation following phenylhydrazine administration, *Mol. Pharmacol.* **33**: 344-350.

Maples, K.R., Jordan, S.J., and Mason, R.P., 1988b, *In vivo* rat hemoglobin thiyl free radical formation following administration of phenylhydrazine and hydrazine-based drugs, *Drug Metab. Dispos.* **16**: 799-803.

Maples, K.R., Eyer, P., and Mason, R.P., 1990a, Aniline-, phenylhydroxylamine-, nitrosobenzene-, and nitrobenzene-induced hemoglobin thiyl free radical formation *in vivo* and *in vitro, Mol. Pharmacol.* **37**: 311-318.

Maples, K.R., Kennedy, C.H., Jordan, S.J., and Mason, R.P., 1990b, *In vivo* thiyl free radical formation from hemoglobin following administration of hydroperoxides, *Arch. Biochem. Biophys.* **277**: 402-409.

Mason, R.P. and Knecht, K.T., 1994, *In vivo* detection of radical adducts by electron spin resonance, *Methods Enzymol.* **233**: 112-117.

Mason, R.P., 1996, *In vitro* and *in vivo* detection of free radical metabolites with electron spin resonance, In *Free Radicals: A Practical Approach,* Punchard, N.A. and Kelly, F.J., eds, pp. 11-24, Oxford University Press, New York.

Mason, R.P., 2000, *In vivo* spin trapping – from chemistry to toxicology. In *Toxicology of the Human Environment: The critical role of free radicals,* Rhodes, C., ed., Taylor and Francis, London, pp.49-70.

McCay, P.B., Lai, E.K., Poyer, J.L., Dubose, C.M., and Janzen, E.G., 1984, Oxygen- and carbon-centered free radical formation during carbon tetrachloride metabolism. Observation of lipid radicals *in vivo* and *in vitro, J. Biol. Chem.* **259**: 2135-2143.

Moore, D.R., Reinke, L.A., and McCay, P.B., 1995, Metabolism of ethanol to 1-hydroxyethyl radicals *in vivo:* detection with intravenous administration of α-(4-pyridyl-1-oxide-*N*-*t*-butylnitrone), *Mol. Pharmacol.* **47**: 1224-1230.

Murphy, P.G., Myers, D.S., Webster, N.R., Jones, J.G., and Davies, M.J., 1991, Direct detection of free radical generation in an *in vivo* model of acute lung injury, *Free Radical Res. Comms.* **15**: 167-176.

Nakao, L.S., Kadiiska, M.B., Mason, R.P., Grijalba, M.T., and Augusto, O., 2000, Metabolism of acetaldehyde to methyl and acetyl radicals: in vitro and in vivo electron paramagnetic resonance spin-trapping studies, *Free Radical Biol. Med.* **29**: 721-729.

Navasumrit, P., Ward, T.H., Dodd, N.J.F., and O'Connor, P.J., 2000, Ethanol-induced free radicals and hepatic DNA strand breaks are prevented *in vivo* by antioxidants: effects of acute and chronic ethanol exposure, *Carcinogenesis* **21**: 93-99.

Paolini, M., Sapigni, E., Mesirca, R., Pedulli, G.F., Corongiu, F.P., Dessi, M.A., and Cantelli-Forti, G., 1992, On the hepatoxicity of 1,1,2,2-tetrachloroethane, *Toxicology* **73**: 101-115.

Plummer, J.L., Beckwith, A.L.J., Phil, D., Bastin, F.N., Adams, J.F., Cousins, M.J., and Hall, P., 1982, Free radical formation *in vivo* and hepatoxicity due to anesthesia with halothane, *Anesthesiology* **57**:160-166.

Poyer, J.L., McCay, P.B., Lai, E.K., Janzen, E.G., and Davis, E.R., 1980, Confirmation of assignment of the trichloromethyl radical spin adduct detected by spin trapping during ^{13}C-carbon tetrachloride metabolism *in vitro* and *in vivo, Biochem. Biophys. Res. Comms.* **94**: 1154-1160.

Poyer, J.L., McCay, P.B., Weddle, C.C., and Downs, P.E., 1981, *In vivo* spin-trapping of radicals formed during halothane metabolism, *Biochem. Pharmacol.* **30**: 1517-1519.

Reinke, L.A., Lai, E.K., DuBose, C.M., and McCay, P.B., 1987, Reactive free radical generation *in vivo* in heart and liver of ethanol-fed rats: correlation with radical formation *in vitro, Proc. Natl. Acad. Sci. USA* **84**: 9223-9227.

Reinke, L.A., Lai, E.K., and McCay, P.B., 1988, Ethanol feeding stimulates trichloromethyl radical formation from carbon tetrachloride in liver, *Xenobiotica* **18**: 1311-1318.

Reinke, L.A. and Janzen, E.G., 1991, Detection of spin adducts in blood after administration of carbon tetrachloride to rats, *Chem.-Biol. Interact.* **78**: 155-165.

Reinke, L.A., Kotake, Y., McCay, P.B., and Janzen, E.G., 1991, Spin-trapping studies of hepatic free radicals formed following the acute administration of ethanol to rats: in vivo detection of 1-hydroxyethyl radicals with PBN, *Free Radical Biol. Med.* **11**: 31-39.

Reinke, L.A., Towner, R.A., and Janzen, E.G., 1992, Spin trapping of free radical metabolites of carbon tetrachloride *in vitro* and *in vivo:* effect of acute ethanol administration, *Toxicol. Appl. Pharmacol.* **112**: 17-23.

Reinke, L.A., Moore, D.R., and McCay, P.B., 1997, Free radical formation in livers of rats treated acutely and chronically with alcohol, *Alcoholism: Clin. Exp. Res.* **21**: 642-646.

Reinke, L.A. and McCay, P.B., 1997, Spin trapping studies of alcohol-initiated radicals in rat liver: influence of dietary fat, *J. Nutr.* **127**: 899S-902S.

Rikans, L.E., Hornbrook, K.R., and Cai,Y., 1994, Carbon tetrachloride hepatoxicity as a function of age in female Fischer 344 rats, *Mech. Aging Dev.* **76**: 89-99.

Sato, K., Kadiiska, M.B., Ghio, A.J., Corbett, J., Fann, Y.C., Holland, S.M., Thurman, R.G., and Mason, R.P., 2002, In vivo lipid-derived free radical formation by NADPH oxidase in acute lung injury induced by lipopolysaccharide: a model for ARDS, *FASEB J.* **16**: 1713-1720.

Schaefer, C.F., Janzen, E.G., West, M.S., Poyer, J.L., and Kosanke, S.D., 1996, Blood chemistry changes in the rat induced by high doses of nitronyl free radical spin traps, *Free Radical Biol. Med.* **21**: 427-436.

Sentjurc, M. and Mason, R.P., 1992, Inhibition of radical adduct reduction and reoxidation of the corresponding hydroxylamines in in vivo spin trapping of carbon tetrachloride-derived radicals, *Free Radical Biol. Med* **13**: 151-160.

Stoyanovsky, D.A. and Cederbaum, A.I., 1998, ESR and HPLC-EC analysis of ethanol oxidation to 1-hydroxyethyl radical: rapid reduction and quantification of POBN and PBN nitroxides, *Free Radical Biol. Med.* **25**: 536-545.

Stoyanovsky, D.A., Wu, D., and Cederbaum, A.I., 1998, Interaction of 1-hydroxyethyl radical with glutathione, ascorbic acid, and α-tocopherol, *Free Radical Biol. Med.* **24**: 132-138.

Timmins, G.S., Liu, K.J., Bechara, E.J.H., Kotake, Y., and Swartz, H.M., 1999, Trapping of free radicals with direct in vivo EPR detection: a comparison of 5,5-dimethyl-1-pyrroline-

N-oxide and 5-diethoxyphosphoryl-5-methyl-1-pyrroline-*N*-oxide as spin traps for $HO^{\bullet}$ and $SO^{4\bullet-}$, *Free Radical Biol. Med.* **27**: 329-333.

Tomasi, A., Albano, E., Biasi, F., Slater, T.F., Vannini, V., and Dianzani, M.U., 1985, Activation of chloroform and related trihalomethanes to free radical intermediates in isolated hepatocytes and in the rat in vivo as detected by the ESR-spin trapping technique, *Chem.-Biol. Interact.* **55**: 303-316.

Tomasi, A., Iannone, A., Ferrari, M., and Quaresima, V., 2000, *Ex vivo* detection of free radicals. In *Toxicology of the Human Environment: The critical role of free radicals,* Rhodes, C., ed., Taylor and Francis, London, pp.71-87.

Ueda, Y., Yokoyama, H., Niwa, R., Konaka, R., Ohya-Nishiguchi, H., and Kamada, H., 1997, Generation of lipid radicals in the hippocampal extracellular space during kainic acid-induced seizures in rats, *Epilepsy Res.* **26**: 329-333.

Vincent, R., Janzen, E.G., Chen, G., Kumarathasan, P., Haire, D.L., Guenette, J., Chen, J.Z., and Bray, T.M., 1996, Spin trapping study in the lungs and liver of F344 rats after exposure to ozone, *Free Radical Res.* **25**: 475-488.

Wheeler, M.D., Kono, H., Yin, M., Rusyn, I., Froh, M., Connor, H.D., Mason, R.P., Samulski, R.J., and Thurman, R.G., 2001a, Delivery of the Cu/Zn-superoxide dismutase gene with adenovirus reduces early alcohol induced liver injury in rats, *Gastroenterology* **120**: 1241-1250.

Wheeler, M.D., Nakagami, M., Bradford, B.U., Uesugi, T., Mason, R.P., Connor, H.D., Dikalova, A., Kadiiska, M., and Thurman, R.G., 2001b, Overexpression of manganese superoxide dismutase prevents alcohol-induced liver injury in the rat, *J. Biol. Chem.* **276**: 36664-36672.

Xu, Z. and Bray, T.M., 1994, Electron spin resonance spin trapping studies of the effects of dietary zinc deficiency on free radical production in vitro and in vivo under acute oxidative stress, *J. Nutr. Biochem.* **5:** 490-494.

Yamaguchi, K.T., Stewart, R.J., Wang, H.M., Hudson, S.E., Vierra, M., Akhtar, A., Hoffman, C., and George, D, 1992, Measurement of free radicals from smoke inhalation and oxygen exposure by spin trapping and ESR spectroscopy, *Free Radical Res. Commun.* **16**: 167-174.

Yokoyama, H., Kasai, N., Ueda, Y., Niwa, R., Konaka, R., Mori, N., Tsuchihashi, N., Matsue, T., Ohya-Nishiguchi, H., and Kamada, H., 1998, In vivo analysis of hydrogen peroxide and lipid radicals in the striatum of rats under long-term administration of a neuroleptic, *Free Radical Biol. Med.* **24**: 1056-1060.

Chapter 6

Post Processing Strategies in EPR Spin-Trapping Studies

Agnes Keszler and Neil Hogg
National Biomedical EPR Center, Department of Biophysics, Medical College of Wisconsin, Milwaukee, Wisconsin 53226

Abstract: Collection of EPR spectra in digital format permits post processing that can be more meaningful than multiple-scan averaging, especially for spectra that are overlapping and changing with time, as is characteristic of spectra acquired in spin-trapping studies. It is demonstrated that multiple linear regression analysis of multiple spectra acquired in time-sequence can provide kinetic information even when the signal-to-noise of a single scan is poor.

1. INTRODUCTION

Recording devices for EPR spectrometers have come a long way since the days of the humble chart recorder. Digitization and storage of the signal has allowed a range of post-processing strategies to be employed to improve the quality of the data. These include accumulation (or averaging) strategies and the use of noise filters. Signal averaging has been used extensively in EPR spin trapping studies to improve the signal-to-noise ratio; however this approach is only appropriate for signals that do not change as a function of time. Most spin adduct species are, however, not stable (the word often used is 'persistent'). Signal averaging discards all temporal information as a trade-off for good signal-to-noise. This emphasizes signals that decay slowly over signals that decay rapidly, and quantification of the signals will give an average concentration across the time of collection. However, this trade-off need not be made, as statistical methods exist that allow effective signal averaging without loss of temporal information. This chapter explores the use of these and other techniques, and introduces more sophisticated post-processing methodology into the spin-trapping arena. The basic philosophy is not to discard information until it is confirmed that the information is not

useful. The basic mechanism to achieve this end is to save all raw data and process it later.

2. METHODS

The tools used in this study were coded into Windows-based C++ program using Microsoft Visual C++. The program directly accesses data files from the Bruker EMX platform and can perform singular value decomposition (SVD), data matrix reconstruction and multiple linear regression. The SVD algorithm was taken from Numerical Recipes in C (Press et al., 2002). This algorithm will compute the SVD of a 100 x 1024 matrix in one or two seconds on a 500 MHz processor. All EPR data were collected on a Bruker EMX spectrometer incorporating an Aqua-X sample cell.

3. SIGNAL AVERAGING

Signal averaging in spin-trapping has been regarded as a necessary evil. In order to achieve a sufficient signal-to-noise ratio to allow identification, simulation and/or integration of the collected spectra, extensive signal accumulation is often necessary. As mentioned, in a situation where spin adducts are not stable, signal averaging distorts the relative intensities of component spectra. The spectroscopist has to make a decision either to scan slowly with a large time constant, or to scan rapidly using a small time constant. In the former case, the operator may experience significant signal decay within a single scan. In principal, the kinetic information about the rate of change of component spectra could be extracted from a single scan that was take over the reaction time course. However, the kinetic information is not sampled continuously (i.e. only where the component of interest has signal intensity). In addition, this method would not work well when there is a large difference between the rates of decay/formation of the component species. The alternative (to accumulate rapidly and often) discards all temporal information, but minimizes signal drop-off within each scan. However, if each scan is stored separately and not summed, the temporal information is retained. Using the Bruker EMX platform, this is achieved by setting the experiment type to 'incremental sweep,' setting number of x scans to 1, and setting the y resolution parameter to the number of scans desired (n). This will generate a file containing n spectra appended head to tail. The trick is then to extract the temporal and spectral data from this data set. The simplest form of post-processing would be to sum all n spectra and get the average spectrum, losing all kinetic information. It is also

possible to average smaller blocks of data to trade off between time resolution and spectral signal-to-noise. However, signal averaging is a bad technique because it makes no use of the fact that one scan is related to the other n–1 scans. The fact that only a small subset of spectral shapes appears in all scans (albeit at differing intensities) can be used as addition information to improve signal post-processing.

4. MULTIPLE LINEAR REGRESSION OF EPR DATA

A kinetic spin-trapping experiment, collected as described above, can be described as a collection of n spectra, each containing noise in addition to the spectral shapes of the radical adducts. Each spectrum will therefore be the sum of the noise and the pure spectrum of each species multiplied by a coefficient. If we can obtain pure spectra of each component species and use them as basis spectra for multiple linear regression, it is possible to extract the kinetic profile of each species. In addition, if we arrange so that every pure spectrum represents an equal number of spins, then the coefficients directly map to spin-adduct concentrations and the concentration time course of each component can be obtained. This process is illustrated in Fig. 1 for an experiment in which peroxynitrite (1 mM) was rapidly mixed with a solution containing DMPO (50 mM) and glutathione (1 mM). The solution was immediately transferred via syringe to a Bruker Aqua-X cell and spectra obtained with an individual scan time of 10.24 s, up to a total of 100 scans. Unfortunately, the software that controls data collection in the Bruker EMX spectrometer is not designed to accurately time repeated collections, and it is not possible to know precisely at what time each of the 100 spectra is collected. The delay between scans appears to depend mainly on the total number of scans requested. Preliminary data collected using the Bruker Elexsys platform shows that these limitations are absent, and accurate repetitive-scan kinetics can be performed. For the studies presented here, we always collected 100 scans and measured the average time for each scan as 11.4 s, and this number has been used throughout this study.

It has been previously demonstrated that the reaction between peroxynitrite and glutathione gives a mixture of both DMPO-OH adducts and DMPO-SG adducts (Augusto et al., 1994). Figure 1A shows an overlay of the raw data and illustrates that these two spin-adducts have very similar spectra that overlap significantly. Averaging these 100 spectra (Fig. 1B) clearly improves signal-to-noise, but dramatically underemphasizes the importance of the DMPO-SG adduct. Multiple linear regression analysis of this data set using the pure (simulated) spectra from Fig. 1C is shown in Fig. 1D, and extracts the time courses of both spin adducts. The data here is

presented in units of area and can easily be converted to concentration with reference to an appropriate standard. Multiple linear regression tools are widely available components of most spreadsheet programs.

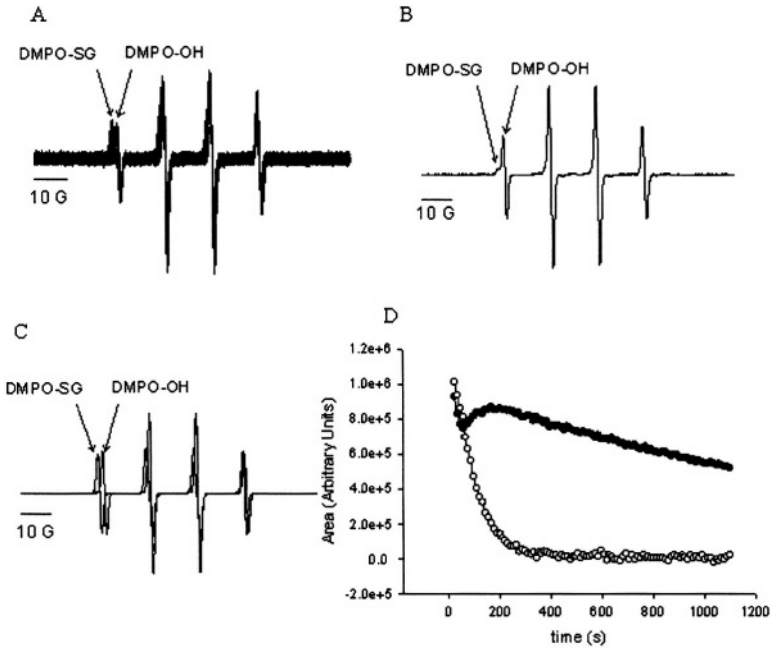

Figure 1. Multiple linear regression of spin trapping data. Peroxynitrite (1 mM) was incubated with DMPO (50 mM) and glutathione (1 mM) in phosphate buffer (1 M pH 7.4 containing 1 mM DTPA. The mixture was immediately transferred to an Aqua-X cell in the cavity of a Bruker EMX spectrometer, and 100 total spectra were taken every 11s with a scan time of 10.24s. Approximately 20s elapsed before the first scan was obtained. A) Overlay of 100 spectra, B) Sum of 100 spectra, C) Simulated spectra of DMPO-OH and DMPO-SG normalized so that the area under the absorption spectrum equals unity, D) Multiple linear regression of each of the data spectra against the spectra in C giving the contribution of DMPO-OH (•) and DMPO-SG (O) as a function of time. Spectrometer Conditions: Scan width, 100G; microwave power, 10 mW, modulation amplitude, 1G; conversion time, 10.24 ms: time constant. 10.24 ms.

This approach requires that the number of participating species is known, and that accurate simulations of each spectrum can be obtained. Although in principal, simulations of the species can be obtained from knowledge of the hyperfine splitting constants, in practice the simulations need to be obtained by least-squares fitting of line shape/width parameters as well as hyperfine splitting constants to give the best possible representation of the shape of the individual species. We find that the WinSim program developed by David Duling at NIEHS is ideal for this purpose (Duling, 1994). The problem still

arises, however, of what data to use in the least-squares fit. Attempting to fit to the sum of all spectra (Fig. 1B) will not give a good representation of DMPO-SG, and attempting to fit to an individual spectrum from the raw data will be hampered by poor signal-to-noise. In this example, it would be possible to get a better representation of DMPO-SG by averaging only the first 10 or so spectra where DMPO-SG is extant; however, in other situations it may not be possible to isolate each species, particularly if some species are present in relatively small amounts. Both the problems of *a priori* knowledge of the number of species and accurate simulations of the component spectra can be addressed by using singular value decomposition.

5. SINGULAR VALUE DECOMPOSITION

Singular value decomposition (SVD) is a statistical algorithm that will isolate the principal components from a data matrix. This algorithm has previously found application in many branches of spectroscopy (Saltiel et al., 1994, 1999; Zimanyi et al., 1999; El-Kemary et al., 2003; Mainardi et al., 2002; Tomczak and Djermoune, 1992; Patrick et al., 2003; Xu et al., 2003; Roussis and Proulx, 2003; Birkinshaw, 2003; Kassem and Bartha, 2003; Schmidt et al., 2003), including EPR (Meier et al., 1995). In the latter case, it was used for deconvoluting metalloprotein spectra from temperature-dependence studies. In this section, we will discuss in detail the use of SVD with time-dependent spin-trapping data. This method is most useful when the amplitude, but not the shape of the spectrum, of the constituent species changes as a function of a dependent parameter e.g. time or temperature. Thus, it is less suited to situations where incremental broadening of an EPR spectrum is used. Here, we will discuss a practical application of SVD rather than present a rigorous mathematical treatment. An in-depth discussion of the use of SVD to analyze experimental data can be found in (Henry and Hofrichter, 1992).

If the matrix A is a data set consisting of m data points and n sequentially recorded spectra (i.e. m rows and n columns), SVD will factorize the matrix according to the equation $\mathbf{A} = \mathbf{USV}^T$. Figure 2 illustrates a SVD factorization of the data shown in Fig. 1. As the analytical value of SVD depends strongly on consistency of spectral shapes, it is important that the data are baseline corrected and properly aligned with respect to field.

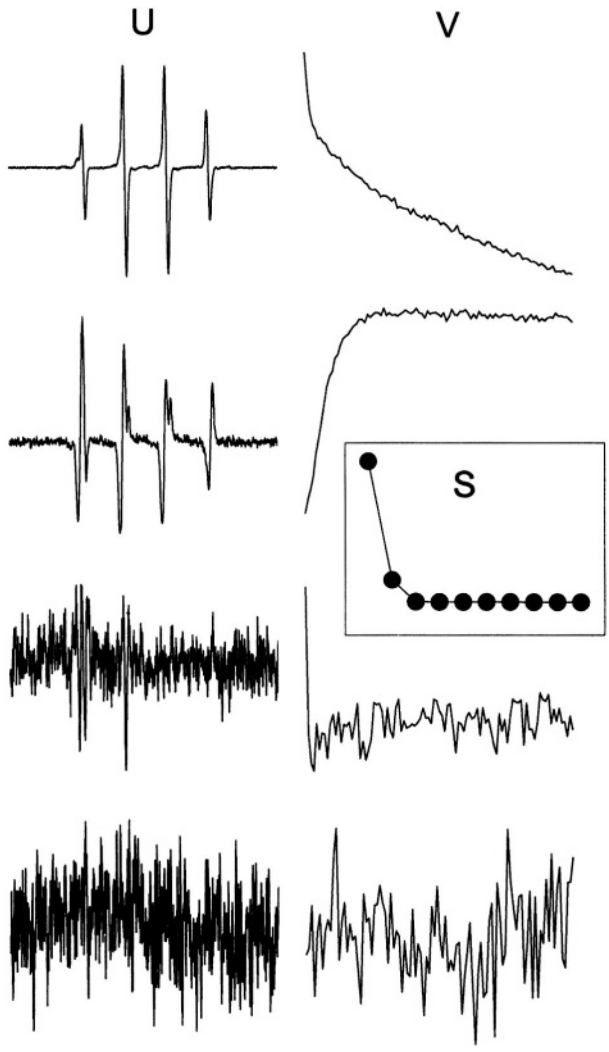

Figure 2. Singular value decomposition of the data set from Fig. 1A. The data from Fig. 1A was subject to SVD. The first four columns of the U matrix and the first four columns of the V matrix were then plotted in descending order. Inset: The diagonal values of the S matrix plotted against spectrum number.

The first important piece of information that can be obtained from the SVD is the number of linearly independent components (rank) in the matrix. This is not the same as the number of species but relates more to the number of transformations. For example, if species Q spontaneously decays to species R and both have EPR spectra, then the changes in Q and R will be linearly dependent, as both the decay of Q and the formation of R will occur

with identical kinetic constants. Examination of the S matrix indicates that it is a diagonal matrix (i.e. a matrix with non-zero values only on the diagonal) of dimensions m × n whose values are ordered in decreasing magnitude (i.e. $s_{11}>s_{22}>s_{33}\ldots$). The number of non-zero values in the S matrix (referred to as the singular values) gives you the number of independently changing processes. In real data containing noise, all of the singular values will be non-zero, but it is likely that only the larger values will represent signal and the rest will be present due to noise. As the values are calculated in decreasing magnitude, simply plotting the diagonal values of the S matrix (Fig. 2 inset) will give an indication of how many non-noise components are present. In this case, the first two points are clearly larger than the rest, indicating that only two kinetic processes are occurring. The immediate implication is that the signal changes in Fig. 1 can be represented by two kinetic processes. In this case a 'process' means a spectrum multiplied by a time course. In other words, we should be able to recreate the salient features of Fig. 1 with two spectra of *m* points each and two time courses of *n* points each. In our example (100 spectra of 1024 points), the storage requirement for the data could thus be reduced from 102400 numbers to 2248 numbers.

So far, we have identified that only two processes are necessary to describe the data, but what are these processes? The answer can be found in the U and V matrices. Simply put, the U matrix columns contain the spectral information for each kinetic process and the columns of the V matrix (or the rows of V^T) contain the time course information. Figure 2 shows the first four columns of the U matrix and the first four columns of the V matrix. What is immediately obvious is that the majority of the spectral data is found in the first two columns of the U matrix and that other 98 columns contain mainly noise (only two are shown). This pattern is paralleled in the V matrix columns. Examination of the third component of the U matrix indicates that it contains a small but significant part of the data, perhaps suggesting that we should increase the number of contributing processes to three. However, the corresponding time course (third column of the V matrix) shows that this component is only present in the first spectrum collected. We have often noticed using the Bruker EMX system that the first spectrum, when performing rapid-repeat scans, is often stretched (not just shifted), and SVD nicely illustrates this problem. As the distortion is difficult to correct, we usually resort to dropping the first scan from the data set before analysis.

The fact that SVD has isolated the signal from the noise illustrates the utility of SVD as a noise filter. Having identified that only two components are present in the data, we can reconstruct the data set using only these components. Reconstruction is achieved by multiplying USV^T using only the first two columns of each matrix. This is shown in Fig. 3A. The residual difference between Fig. 3A and Fig. 1A shown in Fig. 3B shows that we have effectively isolated the entire signal and significantly reduced the noise.

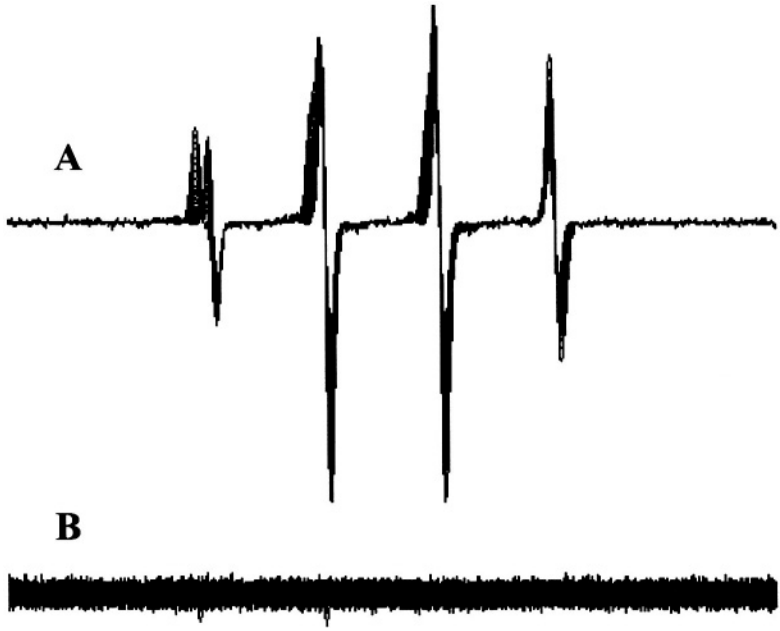

Figure 3. Reconstruction of data from Fig. 1A using only the first two components of Fig. 2. A) The data set obtained by multiplying the first two U, S and V components from Fig. 2. B) The residual obtained upon subtraction of Fig. 3 A from Fig. 1 A.

6. Simulating the columns of the U matrix:

The significant components in the column of the U matrix (Fig. 2) are linear combinations of the underlying EPR spectra (Henry and Hofrichter, 1992). It should be emphasized that although the U matrix columns (particularly the first column) have the appearance of EPR spectra, the column vectors of the U matrix are not spectra of 'real' species, but linear combination of such spectra. Each U column could thus be regarded as a sum of each 'real' spectrum (normalized for spin) multiplied by a coefficient (which could be a negative number). If we can determine these coefficients for each U column, then we can transform the matrices to represent real spectra and real time courses.

It follows that it should be possible to simulate every significant U matrix column with the same set of EPR parameters, changing only the relative contribution of the species. This facilitates a more accurate and robust simulation of the participating species, which can be used as basis spectra for the multiple linear regression process described above (in fact the simulations shown in Fig. 1C were obtained in this way). Simulations of the first two columns of the U matrix from Fig. 2 are shown in Fig. 4. This

figure shows the data, simulation and residual for the first two columns of the U matrix. The parameters used for the simulation of each species are given in the figure legend. It is of interest to note that the first U column contains 82.7% DMPO-OH and 17.3% DMPO-SG, and the second U column contains 16% DMPO-OH and 84% DMPO-SG. In the latter case, the DMPO-SG contribution is inverted (i.e. a negative coefficient). Fortunately, this can be easily simulated using WinSim by setting the contribution to a negative number before fitting. The fact that the contributions of the two species are weighted to different extents in the two U columns allows the WinSim-based fitting procedure to achieve good simulations of the two columns (Fig. 4). Ideally, both columns should be fitted simultaneously to obtain the optimum set of parameters; however, this is currently not possible with WinSim and fitting has to be performed sequentially and iteratively. We have successfully used this approach to examine a three-component system, by including ammonium formate in the glutathione/peroxynitrite system. SVD analysis of the data set resulted in three principal components, and with the aid of those we could successfully simulate the spectra of all the EPR active species (adducts of thiyl, hydroxyl and formyl radicals) and derive their kinetic profiles (data not shown). It is likely, however, that systems containing four or more species may test the limitations of the available tools.

Once good simulations of the U matrix components are obtained, simulations of the pure spectra can be easily obtained. Normalizing the area of these pure spectra to unity is a useful trick that allows the results of linear regression to be obtained in terms of double-integrated area, and therefore proportional to concentration. Identical processing of data collected from stable standards of known concentration allows simple conversion of area to spin-adduct concentration.

An alternative and perhaps more efficient way to derive the time courses of the individual species (i.e. Fig. 1D) is to use the information contained within the V matrix. As with the U matrix, each column of this matrix is a linear sum of the time courses of the underlying species. As we know (through simulation) the contribution of each species in the columns of the U matrix, it is then a simple process to combine the columns of the V matrix, with the appropriate weighting, to give the time courses for the individual species. The two methods give essentially identical results.

Figure 4. Simulation of the first two U matrix components from Fig. 2. The simulation, data and residual for the first and second component (in descending order) of the U matrix from Fig. 2. Simulations were performed using WinSim from NIEHS. Both data sets are simulated with an identical set of parameters for DMPO-OH (calculation type = nitroxide, a^N = 14.90 G, a^H=14.66 G, lw1=.50, lw2=.45, lw3=.50, Lorentzian 17%) and DMPO-SG (calculation type = nitroxide, a^N = 14.98 G, a^H=16.05 G, lw1=.59, lw2=.54, lw3=.65, Lorentzian 56%). The first U column contained 82.7% DMPO-OH and 17.3% DMPO-SG, whereas the second U matrix column contained 16% DMPO-OH and 84% DMPO-SG (inverted).

Figure 5A shows a reconstruction of the data using the simulations from Fig. 4 and their associated time courses from Fig. 1D. The residual of this reconstruction from the original data shows that this process accounts for most of the signal present in the original data. The signal in the residual is primarily due to imperfections in the simulations as shown in Fig. 4. It is not yet clear whether it is the imperfections in the simulation that give rise to the complex kinetic behavior of the DMPO-OH adduct observed in Fig. 1D, or whether the observed time course is indicative of more complex chemistry than had previously been thought. This aspect is currently under investigation.

In our recent study (Keszler et al., 2003), we analyzed superoxide spin-trapping using xanthine/xanthine oxidase by three different traps, using the methods described here in order to assess the presence and kinetics of hydroxyl radical and superoxide adduct formation.

Figure 5. Reconstruction of data from the simulations of DMPO-OH and DMPO-SG and their time courses from Fig. 1D. A) The data set obtained by multiplying the time courses from Fig. 1D with the simulated spectral components. B) The residual obtained upon subtraction of Figure 5A from Figure 1 A.

6. CONCLUSIONS

The power of data post-processing has been underappreciated in EPR spin-trapping studies. This chapter has shown, by example, a method for the deconvolution of multi-component spin-trapping data. The method uses simple technology available to most spectroscopists, and allows the study of kinetic processes even in situations where the signal-to-noise ratio of a single scan is poor. Importantly, it can replace the inefficient process of signal averaging in spin-trapping experiments, achieving a comparable improvement in signal-to-noise without loss of temporal information. The general collection policy could be stated as 'scan as fast as possible as many times as possible throughout the time course of the reaction and store all the data.' In order to avoid unnecessarily large data files, this policy can be amended for practicality. In the example described here, we used a scan time of about 10 seconds. If we had chosen 2 s, we would have to have collected five times as many scans (500 in total) for the same coverage. The disadvantage of larger data files is not so much increased storage (as on modern computers disk space is cheap and plentiful), but increased processing time. However, the major overhead in terms of data processing time using these techniques is taken up converting files into different formats rather than in the computations per se. As these tools have tremendous utility in kinetic EPR experiments, it would save much time if they were built into collection/ analysis packages. Another issue of using this collection policy is that of delayed gratification. With signal averaging, one can observe the appearance of signals in real time as the sample is scanned, however, using the above approach, the signal-to-noise ratio of each scan never improves, and it may be that underlying spectral changes are only seen after post-processing. This could easily be remedied if the collection software stored each spectrum individually, yet still displayed the accumulated sum.

The techniques described here may allow rapid-scan, rapid-mix EPR to be performed at biologically relevant concentrations of radical, and we are currently examining their usefulness in stopped-flow and continuous-flow situations.

Modern computing power makes the techniques describe here a practical and viable alternative to current practice and should make pre-prescribed signal averaging an obsolete technique in spin-trapping experiments.

7. REFERENCES

Augusto, O., Gatti, R. M., and Radi, R. (1994) Spin-trapping studies of peroxynitrite decomposition and of 3-morpholinosydnonimine *N*-ethylcarbamide autooxidation: Direct

evidence for metal-independent formation of free-radical intermediates *Arch. Biochem. Biophys* **310,** 118-125.

Birkinshaw, K. (2003) Deconvolution of mass spectra measured with a non-uniform detector array to give accurate ion abundances. *J. Mass Spectr.* **38,** 206-210.

Duling, D. R. (1994) Simulation of multiple isotropic spin-trap EPR spectra *J. Magn. Res. B.* **104,** 105-110.

El-Kemary, M. A., Etaiw, Sel-D., El-Baradie, H. Y. (2003) New approach for evaluation optical absorption measurements of charge transfer complexes between dimethoxynaphtalenes and tetracyanoethylene: singular value decomposition method. *Spectrochim. Acta. Part A, Mol. Biomol. Spectr* **59,** 1621-1630.

Henry, E. R. and Hofrichter, J. (1992) Singular value decomposition: Application to analysis of experimental data. *Methods Enzymol.* **210,** 129-195. Mainardi, L. T., Origgi, D., Scotti, G., Cerutti, S. (2002) A wavelength packets decomposition algorithm for quantification of in vivo (l)H-MRS parameters. *Med. Eng. Phys.* **24,** 201-208.

Kassem, M. N., Bartha, R. (2003) Quantitative proton short-echo-time LASER spectroscopy of normal human white matter and hippocampus at 4 Tesla incorporating macromolecule subtraction. *Magn. Res. Med.* **49,** 918-927.

Keszler A., Kalyanaraman, B., Hogg, N. (2003) Comparative investigation of superoxide trapping by cyclic nitrone spin-traps: The use of singular value decomposition and multiple linear regression analysis. *Free Rad. Biol. Med.* (in press).

Meier A. E., Whittaker M. M., Whittaker W. W. (1995) EPR polarization studies on Mn catalase from *Lactobacillus plantarum. Biochemistry* **35,** 348-360.

Patrick, E. L., Ray, C. J., Meyer, G. D., Ortiz, T. P., Marshall, J. A., Brozik, J. A., Summers, M. A., Kenny, J. W. 3rd (2003) Non-localized ligand-to-metal charge transfer excited states in (Cp)2Ti(IV)(NCS)2. *J. Am. Chem. Soc.* **125,** 5461-5470.

Press, W. H., Teukolsky, S. A., Vetterling, W. T., and Flannery, B. P. (2002) *Numerical Recipes in C: The art of Scientific computing* Cambridge University Press, Cambridge.

Roussis, S. G., Proulx, R. (2003) Reduction of chemical formulas from the isotopic peak distributions of high-resolution mass spectra. *Anal. Chem.* **75,** 1470-1482.

Saltiel, J., Choi, J. O., Sears, Jr., D. F., Eaker, D. W., Mallory, F. B., Mallory, C. W. (1994) Effect of spectral shift on the resolution of trans-1-(2-naphthyl)-2-phenylethene conformer UV spectra based on principal component analysis with self-modeling. *J. Phys Chem.* **98,** 13162-13170.

Saltiel, J., Zimányi, L., Kulcsár, Á., Lanyi, J. K., Sears, Jr., D. F. Singular value decomposition with self-modeling applied to determine bacteriorhodopsin intermediate spectra. Analysis of simulated data. *Proc. Nat. Acad. Sci.* **96,** 4408-4413.

Schmidt, M., Rajagopal, S., Ren, Z., Moffat, K. (2003) Application of singular value decomposition to the analysis of time-resolved macromolecular x-ray data. *Biophys. J. 84,* 2112-211-29.

Tomczak, M., Djermoune el H. (2002) A subband ARMA modeling approach to high-resolution NMR spectroscopy. *J. Magn. Res.* **158,** 86-89.

Xu, H., Dehghani, H., Pogue, B. W., Springett, R., Paulsen, K. D., Dunn, J. F. (2003) Near-infrared imaging in the small animal brain: optimization of fiber positions. *J. Biomed. Optics* **8**,102-110.

Zimányi, L., Kulcsár, Á., Lanyi, J. K., Sears, Jr., D. F., Saltiel, J. (1999) Intermediate spectra and photocycle kinetics of the Asp96=>Asn mutant bacteriorhodopsin determined by singular value decomposition with self-modeling. *Proc. Nat. Acad. Sci.* **96,** 4414-4419.

Chapter 7

Biophysical Studies of Melanin:

Paramagnetic, Ion-Exchange and Redox Properties of Melanin Pigments and Their Photoreactivity

Tadeusz Sarna and Przemyslaw M. Plonka
Department of Biophysics, Faculty of Biotechnology, Jagiellonian University, Krakow, Poland

Abstract: Melanin is a ubiquitous biological pigment with unusual physicochemical properties. This paper emphasizes selected aspects of melanin research in which significant contributions have been made thanks to the application of EPR spectroscopy. A historical overview of the last 25 years of EPR studies of melanin is given. These studies have led to development of the concept of melanin being a.natural antioxidant that can protect pigment cells from oxidative stress by sequestration of redox-active metal ions, quenching of electronically excited states of photosensitizing dye molecules and singlet oxygen, and by scavenging of reactive free radicals. The paper also briefly reviews results of recent melanin studies that employed alternative techniques such as transient optical spectroscopy with femtosecond time resolution, photoacoustic calorimetry and scanning electron and atomic force microscopies. It is concluded that time-domain EPR and very high frequency EPR spectroscopy are expected to be powerful tools for studying the photodynamics and structure of melanin free radicals and their interactions with the environment and physicochemical agents.

1. INTRODUCTION

Melanin is a key component of the human pigmentary system. Pigmentation of the human skin, hair and eyes is, to a large extent, determined by the ability of specialized cells – the melanocytes – to synthesize the brown-black eumelanin, the yellow-reddish pheomelanin, or a mixture of both polymers (Hearing, 1998). A contemporary view of melanin biosynthesis is shown in Fig. 1. Of course, skin, hair and eye melanocytes of individuals with the most severe types of albinism that lack the active machinery necessary for melanin synthesis are devoid of any

melanin (King, 1998). Although the biological function of melanin is not fully understood, it is widely believed that melanin pigmentation plays an important role in photoprotection of the skin and eyes (Kollias *et al.,* 1991; Sarna, 1992).

The complexities of melanins due to their physicochemical properties and inherent heterogeneities make it difficult to reach specific conclusions as to their properties and structure. Attempts to characterize melanins have involved a large number of different experimental techniques and methodological approaches. Although these have led to large amounts of data, the conclusions on composition and structure of melanins are incomplete and some times contradictory. In spite of these limitations, much of what is known about melanin is due to the use of sophisticated physical and chemical approaches. This is particularly true in the case of EPR spectroscopy, whose application to melanin research was of crucial importance for understanding basic redox and ion-exchange properties of this unusual class of biopolymers and the nature of their photoreactivity (Sarna and Swartz, 1993).

Because of the extent of the subject and the purpose of this book, our coverage is illustrative rather than comprehensive. We will particularly emphasize those aspects of melanin research in which significant contributions have been made through direct or indirect application of EPR spectroscopy. For a number of years, such studies were carried out in a close collaboration between the National Biomedical EPR Center, Medical College of Wisconsin, and the Department of Biophysics, Jagiellonian University, Poland. It is fair to say that melanin research gained new momentum when a long-standing problem in the biophysics of melanin was brought by one of us to the attention of Jim Hyde, who saw a solution and proposed specific experiments to test it (Sarna *et al.,* 1976).

2. MELANIN AS A FREE RADICAL AND ANTIOXIDANT

One of the most unusual features of melanin as a biopolymer is its persistent EPR signal (Blois *et al.,* 1964). Indeed, melanin was among the first biological materials examined by EPR spectroscopy (Commoner *et al.,* 1954). Contrary to one view shared by many melanin researchers, that melanin free radicals are stable, the content of melanin free radicals and their corresponding EPR signal intensity can easily be modified by a number of physicochemical agents (Sealy *et al.,* 1980).

An intriguing observation related to melanin radicals was reported by Blois *et al.* (1964). Their early EPR study indicated that paramagnetic metal

ions such as iron(III) or copper(II) were able to quench the melanin EPR signal. Although the exact mechanism of this phenomenon was not known, it was suggested that the quenching could represent chemical interaction between the unpaired electrons of the melanin free radical centers and of paramagnetic metal ions. Eight years later, another unusual interaction between melanin and transition metal ions was reported (Sarna and Lukiewicz, 1972). The Polish researchers showed that binding of diamagnetic multivalent metal ions such as zinc(II) and cadmium(II) by melanin led to a marked increase in the intensity of its EPR signal.

These and other seemingly confusing EPR observations of melanin were explained in a series of papers published during over a decade-long scientific collaboration between the center in Milwaukee and Jagiellonian University. Thus it has been shown that loss of melanin EPR signal amplitude (without apparent changes in the signal linewidth) due to the interaction of melanin radicals with copper ions was purely magnetic in nature and did not involve any chemical reaction of melanin free radical centers (Sarna *et al,* 1976). Using lanthanide ions such as La(3+), Gd(3+) and Dy(3+), which have similar chemical properties but quite different magnetic properties (La(3+) is diamagnetic and both Gd(3+) and Dy(3+) are paramagnetic; Gd(3+) has a relatively long spin-lattice relaxation time at 77 K and Dy(3+) has a much shorter spin-lattice relaxation time), it was possible to observe consistent changes in the amplitude and microwave power saturation of the melanin EPR signal as a function of the type and concentration of the added metal ions. The changes served as experimental observables in competition experiments between diamagnetic and paramagnetic metal ions for melanin binding sites, and between melanin and EDTA for paramagnetic metal ions. These EPR observations were among the first clear evidence for the existence of several specific types of metal binding sites in melanin.

A similar experimental approach was used in a follow-up study to determine the spatial distribution of melanin binding sites in respect to the intrinsic melanin radical centers (Sarna *et al.,* 1981). Assuming a uniform distribution of the binding sites within the melanin polymer, a reasonably good fit of the experimental data (EPR signal amplitude of melanin free radicals as a function of concentration of bound-to-melanin Mn(II)) with the calculated dependence was found. The average distance between the interacting metal ions and melanin free radicals was estimated to be 0.7 nm for the closest proximity of both paramagnetic species.

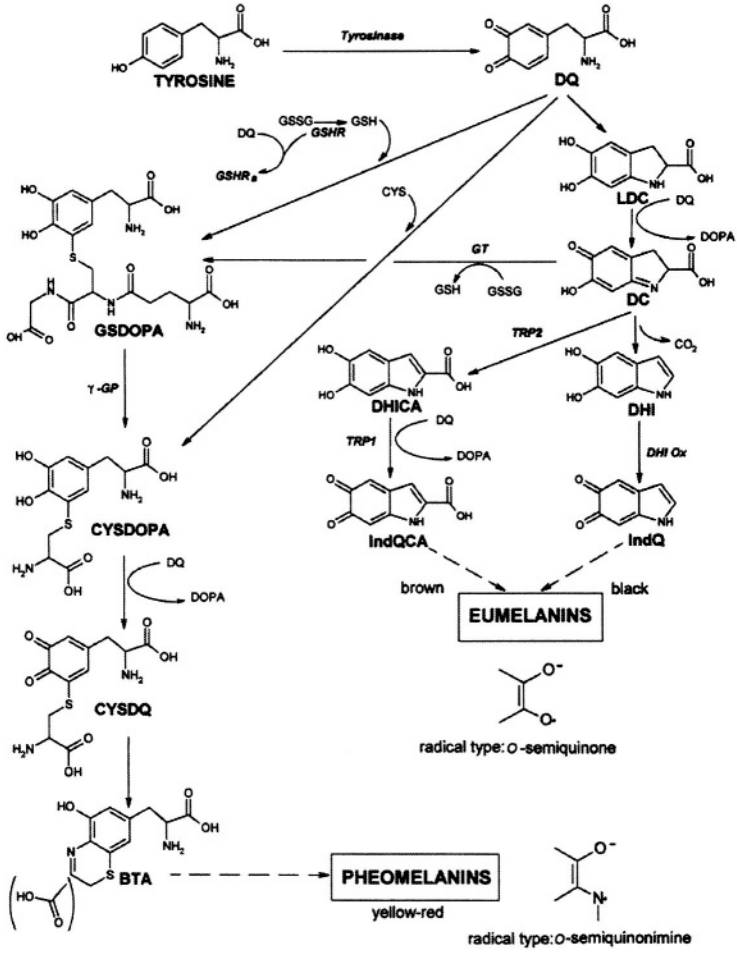

Figure 1. A contemporary view of melanin biosynthesis; the schematic indicates key enzymes and intermediates involved in the synthesis of eu- and pheomelanins (Sealy *et al.* 1982b; Riley 1998; Nappi and Ottaviani 2000; Ortonne and Balotti 2000; Oyehaug *et al.,* 2002). **Enzymes:** DHI OX – DHIoxidase (tyrosinase and/or peroxidase); γ-GP - γ-glutamyl transpeptidase; GSHR – glutathione reductase; $GSHR_B$ – glutathione reductase inactivated by covalently bound DQ; GT – glutathione transpeptidase; TRP1 –tyrosinase-related protein-1 (DHICA oxidase); TRP2 tyrosinase-related protein -2 (DC tautomerase). **Intermediates:** BTA - benzothiazinylalanines; CYS – L-cysteine; CYSDOPA – cysteinylDOPA; CYSDQ – cysteinylDOPAquinone; DC – DOPAchrome; DHI – 5,6-dihydroxyindole; DHICA – 5,6-dihydroxyindole-2-carboxylic acid; DOPA – 3,4-dihydroxyphenylalanine; DQ – DOPAquinone; GSDOPA – glutathionylDOPA; GSH – glutathione (reduced); GSSG – glutathione (oxidized); IndQ – Indole-5,6-quinone, IndQCA – Indole-5,6-quinone-2-carboxylic acid; LDC – leucoDC.

Using X-band EPR spectroscopy and the isotope $^{63}Cu(II)$ as a molecular probe, the molecular nature of the main binding sites in two synthetic melanins and natural melanin from bovine choroid was studied. (The use of single copper isotope ^{63}Cu with nuclear spin $^3/_2$ results in better spectral resolution than is possible using copper ions containing both ^{63}Cu and ^{65}Cu.) It clearly showed that, depending on the pH of the system, copper(II) can form a number of complexes with melanin that involve different functional groups of the polymer and exhibit different stabilities. At pH < 7, monodendate complexes with melanin carboxyl groups are predominantly formed, even though in eumelanins bidendate nitrogen-carboxyl complexes are also formed. The corresponding magnetic parameters are within the range: $g_{\|} = 2.26 - 2.34$, $A_{\|} = 460 - 560$ MHz and $g_{\perp} = 2.066 - 2.076$. At pH 7 and above, copper(II) binds to bidendate phenolic hydroxyl groups, but the number of such sites is much less in natural melanins than in synthetic dopa-melanin. The corresponding magnetic parameters are: $g_{\|} = 2.24 - 2.26$, $A_{\|} =$ 560 – 579 MHz and $g_{\perp} = 2.050$. The assignment of complexes with Cu(II) to functional groups of melanin has been further supported by EPR and elemental analysis of chemically modified synthetic dopa-melanin (Sarna *et al.,* 1981).

Although natural melanin granules always exist as complex supermolecular structures consisting of the melanin polymer, proteins, lipids and possibly carbohydrates, it has been demonstrated that the melanin component of the pigment granules is chiefly responsible for binding of metal ions. Thus metal-ion binding sites are the same both with and without protein, although with some differences in relative populations.

In a seminal study, Felix *et al.* explained another aspect of the metal-ion interaction with melanin (1978a). It concerns the so-called "zinc effect" or "magnetic reaction" of melanins that manifests as a substantial increase in the amplitude and integrated intensity of the melanin EPR signal after complexing of diamagnetic multivalent metal ions such as zinc(II) (Sarna and Lukiewicz, 1972). It has been demonstrated that these changes are due to the generation of melanin radicals. The molecular nature of inducible melanin radicals (extrinsic free radical centers) is determined by the chemical structure of the monomer units of the melanin polymer that are engaged in redox equilibria:

$$Q + QH_2 \underset{k_d}{\overset{k_c}{\rightleftharpoons}} 2SQ^- + 2H^+$$

where Q denotes *o*-quinone, QH_2 is *o*-hydroquinone and SQ^- stands for *o*-semiquinones in the case of eumelanins.

The ratio between the comproportionation rate constant k_c and disproportionation rate constant k_d determines the observable concentration of extrinsic melanin radicals. Thus, any agent that can modify either k_c or k_d

will affect the content of melanin radicals and the corresponding EPR signal intensity. The "zinc effect" can be explained by stabilization of the melanin radicals that results from chelation of metal ions by the *o*-semiquinone groups. As a result, a new equilibrium is established pulling the relationship to the right, which manifests as an increase in the observable EPR intensity.

The reversible complexation of metal ions with melanin free radicals is a general phenomenon. Indeed zinc, as well as cadmium, was found to interact strongly with other free radical species that possess the structural and electronic requirements for chelation. This EPR approach for the study of short-lived free radicals of *o*-semiquinone or flavonoid semiquinone character, first introduced by the Milwaukee group, was coined "spin stabilization" (Felix and Sealy, 1982; Kalyanaraman *et al.,* 1984a; 1984b).

The effect of complexing of diamagnetic multivalent metal ions on the melanin EPR signal is an important diagnostic test that can be used to determine the molecular nature of the melanin subunits. It has been shown that the structure of the chelating radicals can be inferred from line width changes that reflect hyperfine splittings associated with the metal ions (Felix and Sealy, 1981). Thus radicals complexed with the ^{113}Cd(II) isotope (nuclear spin ½) in synthetic melanins derived from dopa, catechol and cysteinyldopa have splittings of about 0.35 mT, 0.7 mT and 1.5 mT, respectively (Sealy, 1984). This approach has been successfully used for identification of the dominant type of extrinsic free radical centers present in natural eumelanins, pheomelanins and mixed type melanins (Sealy *et al.,* 1982b).

EPR has proven to be useful not only for non-destructive detection of melanin in various biological systems (Sarna and Swartz, 1978; Swartz *et al.,* 1979; Pilas and Sarna, 1985; Enochs *et al.,* 1993; Sarna *et al.,* 2002; Plonka *et al.,* 2003), but also for unambiguous differentiation of natural melanins (Sealy *et al.,* 1982a; Jimbow *et al.,* 1984; Vsevolodov *et al.,* 1991). An example of eu- and pheomelanin EPR signals at X-band are shown in Fig. 2.

The concept of the comproportionation equilibrium between the fully oxidized, fully reduced and semioxidized (reduced) subunits of melanin played a critical role in the development of current understanding of electron-exchange properties of melanin. It has become clear that seemingly unrelated effects, such as changes in melanin EPR signal intensity induced by diamagnetic metal ions, pH, oxidizing or reducing agents, and irradiation with visible light, are based on a similar phenomenon – a shift in the comproportionation equilibrium. Melanin is now viewed as a dynamic system, whose properties are determined by intramolecular equilibria of melanin functional groups, including the free radical centers (Sarna and Swartz, 1998).

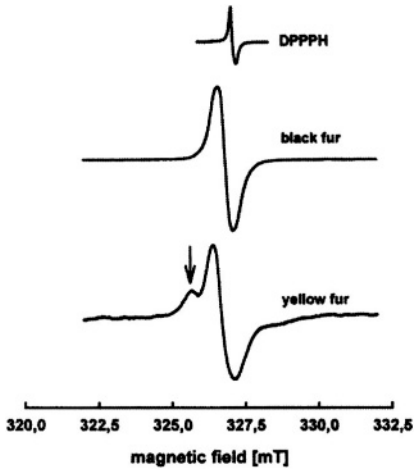

Figure 2. Representative EPR spectra of natural eu- and pheomelanins detected in hair of Mongolian gerbils. Upper spectrum shows typical eumelanin signal at X-band, while lower spectrum is indicative of significant contribution of pheomelanin. Arrow indicates low-field ^{14}N hyperfine compound of the pheomelanin signal typical of *o*-semiquinonimine radicals (Sealy *et al.* 1982a, 1982b; Plonka *et al.* 2003; see also Fig. 1). The spectra were recorded for the dry hair shaft samples at room temperature using Varian X-band spectrometer. Parameters of the assay: microwave power – 6,3 mW. modulation amplitude – 0,5 mT. DPPH – signal of the free-radical marker (a powder sample of diphenylpicrylhydrazyl, g=2,0036).

Reversible generation of melanin free radicals by visible light has been observed in early EPR studies of melanin (Cope *et al.,* 1963; Ostrovsky and Kayushin, 1963). Although it cannot be ruled out that this phenomenon has no biological significance and represents only a marginal route of utilization of the energy of absorbed photons, such a photoreactivity of melanin has always been intriguing and helped stimulated interest in melanin research.

An analysis of the decay of the photoinduced ESR signal of melanin after termination of the irradiation revealed second-order kinetics, suggesting that recombination was the primary process responsible for termination of the photoinduced radicals (Felix *et al.,* 1979). Since second-order kinetics are typically observed for free radicals in solutions, the data seem to indicate that the free radicals in melanin at ambient temperatures have a substantial degree of molecular mobility.

Quantum yields for the steady state formation of melanin radicals were found to be generally low; for dopa-melanin, the quantum yield reached 0.01 only at the shortest wavelengths of the UVC region, and it was well below 0.001 in the visible region (Sarna and Sealy, 1984a). A significant enhancement in the rate of free radical production was observed for several different melanins when the radicals were induced by a photosensitized reaction (Sarna *et al.,* 1985b). Thus, excitation of Rose Bengal, used as a

photosensitizer, in the absence of oxygen, resulted in almost a 500-fold increase in the rate of radical formation when cysteinyldopa-melanin was examined. Even for dopa-melanin, the rate of photosensitized formation of melanin radicals was 30 times greater than the intrinsic photogeneration of melanin radicals.

Two mechanisms of the photosensitized formation of melanin free radicals have been considered (Sealy *et al.,* 1984). The first consists of an energy transfer between the excited Rose Bengal molecules and appropriate melanin moieties. In a simplistic way, this mechanism can be viewed as an enhancement in the efficiency of melanin to absorb photons and generate electronically excited melanin. The second mechanism involves an electron transfer between melanin and the excited Rose Bengal molecules. Unfortunately, no data exist that would unambiguously support one or the other mechanism. Laser flash photolysis experiments carried out to detect melanin-induced quenching of the triplet excited state of Rose Bengal or melanin-induced formation of Rose Bengal free radicals failed to provide convincing evidence of either mechanism (Sarna and Truscott, unpublished). On the other hand, the photosensitized formation of melanin radicals, observed in the presence of an exogenous electron donor, may indirectly support the electron transfer mechanism (Reszka and Chignell, 1993; Dunford *et al.,*1995).

Photoionization and photohomolysis of melanin in the wavelength range of 240–300 nm was demonstrated by EPR spin trapping using 5,5-dimethyl-1-pyrroline-1-oxide (Kalyanaraman *et al.,* 1984c). At longer wavelengths, irradiation of melanin leads to production of both reducing and oxidizing equivalents of the polymer and, hence, enhances melanin's reducing and oxidizing power (Sarna *et al.,* 1985a).

In the presence of oxygen, the photochemistry of melanins becomes quite complex; there is a formation of reactive oxygen species and melanin can be irreversibly bleached (Felix *et al.,* 1978b; Chedekel *et al.,* 1978; Korytowski *et al.,* 1987; Korytowski and Sarna, 1990). It was demonstrated that aerobic photoreactivity of melanin could be conveniently studied by EPR oximetry (Sarna *et al.,* 1980). This method, originally introduced by Backer *et al.* (1977), has been refined and mastered in numerous studies carried out in Milwaukee and Krakow by the collaborating teams (Hyde and Subczynski, 1989). EPR oximetry measurements of oxygen consumption induced by photoexcited melanins revealed that the quantum yield of the photoprocess was low, similar to the quantum yield of photogeneration of melanin free radicals (Sarna and Sealy, 1984b; Sarna *et al.,* 1984). In addition, both processes exhibited similar wavelength dependence, which differed from melanin absorption spectrum. It appears that the chromophores most active in free radical production and oxygen reduction are not the major

chromophores that absorb visible and near UV light. From the observed effect of catalase (Sarna *et al.,* 1980; Sarna and Sealy, 1984b) and from direct measurements (Korytowski and Sarna, 1990), it has been inferred that hydrogen peroxide is the major product of melanin-induced photoreduction of oxygen. It is now believed that hydrogen peroxide is actually a secondary product of the photoreaction of melanin with oxygen, with the primary product being superoxide anion (Korytowski and Sarna, 1990; Rozanowska *et al.,* 2002).

The discovery of the free radical properties of melanin led to the hypothesis that melanin might act as a free radical trap, thereby protecting cells from the effects of free radicals formed in biologic oxidation-reduction reactions (Mason *et al.,* 1960). There is a fairly extensive but amorphous literature on potential antioxidant properties of melanin (Goodchild *et al.,* 1984; Korytowski *et al.,* 1986; Ostrovsky *et al.,* 1987; Scalia *et al.,* 1990; Porebska-Budny, 1992; Bustamante *et al.,* 1993; Reszka *et al.,* 1998; Stepien *et al.,* 2000). The most direct data on scavenging of various free radicals by synthetic melanins have been obtained by the pulse radiolysis technique (Sarna *et al.,* 1986; Dunford *et al.,* 1995; Rozanowska *et al.,* 1999). Thus hydroxyl radicals exhibited the strongest reactivity with both dopa- and cysteinyl-dopa melanin, with the apparent bi-molecular rate constant being $\sim 10^9 M^{-1} s^{-1}$ (assuming that an average melanin subunit has a molecular weight of 200) (Sarna *et al.,* 1986). Both synthetic melanins were good scavengers of hydrated electron and carbon-centered radicals derived from methanol or ethanol (Rozanowska *et al.,* 1999). Although both melanins intercepted the peroxyl radical $CCl_3O_2^{\cdot}$ $(\sim 10^8 M^{-1}s^{-1})$ very efficiently, the reactivity of the melanins with milder oxidizing radicals such as $^{\cdot}OOCH_2OH$ or $^{\cdot}OOCH_3CHOH$ was significantly slower $(2.7 \times 10^4 - 2 \times 10^6 M^{-1}s^{-1})$. The predominant mode of interaction of radicals with melanin appears to be an electron transfer; however at least a part of the reaction of $CCl_3O_2^{\cdot}$ with the two types of synthetic melanin results in radical addition (Rozanowska *et al.,* 1999).

The results of the studies reviewed on melanin-free radical interaction are consistent with melanin being an efficient scavenger of strongly oxidizing and reducing radicals. However, it seems unlikely that this property of melanin plays a key role in the protection of pigment cells against oxidative damage. This is because free radicals with very high or very low one-electron potential are likely to interact indiscriminately with many components of the cell where the radicals are randomly generated. Unless "site-specific" formation of reactive free radicals is considered, natural melanin present in cells as pigment granules is a very inefficient scavenger of short-lived reactive species. A special case in which the free radical-scavenging abilities of melanin might be of importance is if the

generation of reactive species is within the melanin granule or in close proximity. This has been demonstrated for copper(II) ions bound to melanin (Korytowski and Sarna, 1990). After reduction of Cu(II) ions bound to melanin by a photosensitized reaction, the Cu(I) ions were able to catalyze free radical decomposition of exogenous hydrogen peroxide; however, hydroxyl radicals formed in such a reaction were very efficiently intercepted by the melanin polymer and only a very small number of these strongly oxidizing species escaped the melanin milieu (Korytowski and Sarna, 1990). Another example of a system in which melanin could act as a very powerful antioxidant is a photo-oxidation reaction sensitized by positively charged dye molecules (Bielec *et al.,* 1986; Losi *et al.,* 1993; Wrobel *et al,* 1997; Sarna *et al.,* 1998). It was found that complexing such photosensitizing dye cations by melanin leads to remarkably efficient deactivation of their electronically excited states and complete loss of the dye photosensitizing activity. Using time-resolved femtosecond absorption and picosecond emission spectroscopies, it has recently been demonstrated that binding of tetra (4-N,N,N,N-trimethylanilinium) porphyrin to melanin facilitates ultrafast energy transfer from the excited porphyrin to melanin (Ye *et al.,* 2002). The excited energy is then rapidly converted into heat. The entire process could be viewed as an important photoprotective mechanism.

It appears that in cells, melanin principally exerts its antioxidant activity by binding of redox-active metal ions (Swartz *et al.,* 1992). Such an antioxidant action of melanin has clearly been demonstrated in model studies with dopa-melanin (Pilas *et al.,* 1988), dopamine-melanin (Zareba *et al.,* 1995) and RPE melanosomes (Sarna *et al.,* 1998). The data show that iron ions that are bound to melanin are an inefficient catalyst for free radical decomposition of hydrogen peroxide. Ferric ions, after binding to melanin, become significantly more difficult to reduce by mild reductants that are present in biological systems. Sequestration of iron ions has been identified as a major mechanism for the inhibitory effects of melanin on lipid peroxidation (Korytowski *et al.,* 1995). An important role of the degree of iron binding to melanin on the antioxidant/pro-oxidant actions of melanins in photoprotection has been considered in an independent study (Krol and Liebler, 1998).

Since red-skinned individuals, particularly of Celtic origin, whose skin contains pheomelanin, are quite sensitive to solar radiation and highly susceptible to skin cancer (Urbach *et al.,* 1974), and pheomelanin is commonly considered to be much more photoreactive and photolabile than eumelanin, the possible role of pheomelanin in triggering critical changes in sun-exposed skin should be considered. Although early work seemed to support the postulate that pheomelanin was particularly photolabile (Chedekel, 1977), later study of photobleaching of eumelanin and

pheomelanin suggested that eumelanin was actually more susceptible to aerobic degradation (Wolfram and Albrecht, 1987). On the other hand, the most comprehensive comparative measurements of the yields of photoformation of melanin radicals and photoconsumption of oxygen in synthetic and natural eumelanins and pheomelanins did not reveal any significant differences between the two types of melanin pigments (Sarna *et al.,* 1984; Sarna and Sealy, 1984b).

Interestingly, a striking difference in the photochemistry of eumelanin and pheomelanin precursors (see Fig. 1) has been observed by EPR spin trapping (Pilas *et al.,* 1986) and, independently, by laser flash photolysis (Land *et al.,* 1986). Thus, even though irradiation with UVB (or UVC) of dopa, 2,5-cysteinyldopa, 2,5-S,S-dicysteinyldopa and 4-hydrooxy-benzothiazole leads both to photoionization and photohomolysis of these compounds, unlike dopa, the cysteinyldopas also form carbon-centered alanyl radicals via photodecomposition of the cysteinyl group. Therefore, it cannot be ruled out that the observed mutagenicity of pheomelanin precursors (Koch and Chedekel, 1986) during UV irradiation could be linked to the photoproduction of carbon-centered alanyl radicals. Regrettably, this interesting study has not reached a stage that would allow for drawing of any definite conclusion about the proposed phototoxic role of pheomelanin precursors.

Although the antioxidant abilities of melanin demonstrated in various model systems its optical properties and the higher resistance to UV radiation of highly pigmented cells compared to non-pigmented or lightly pigmented cells supports the notion that melanin is an efficient photoprotective pigment, there are intriguing observations that seem to contradict this view. Thus, it was reported that irradiation of bovine RPE cells *in vitro* with blue light from an argon laser resulted in relatively fast oxidation of exogenous ascorbate (Glickman and Lam, 1992). To elucidate the mechanism of melanin-dependent photo-oxidation of ascorbate, EPR spectroscopy, EPR oximetry and oxidase electrodes were employed (Rozanowska *et al.,* 1997). This study showed that ascorbate is oxidized by photoinduced melanin radicals via a one-electron transfer reaction. The reduced melanin is then reoxidized by molecular oxygen with the formation of superoxide anion and hydrogen peroxide. Even though the biological implication of the melanin-mediated photo-oxidation of an important cellular antioxidant such as ascorbate remains unknown, the formation of reactive oxygen species that accompanies this process may represent a potential risk to RPE cells.

An interesting and as yet unresolved issue is the origin of the intrinsic radical centers that are detected by EPR in different melanins. It has been postulated that these centers are residual radicals formed during

melanogenesis that have been trapped within the growing polymers and become inaccessible to chemical agents (Blois *et al.,* 1964). Using spin stabilization procedures, free radical intermediates that accompany tyrosinase-catalyzed oxidation of selected melanin and non-melanin substrate molecules have been detected (Korytowski *et al.,* 1987). The data can be summarized as: i) *o*-semiquinones were formed via a comproportionation reaction between the reduced and oxidized forms of the substrate, ii) for quinones that are cyclizable, such as dopaquinone, only one type of free radicals was detected, iii) non-cyclizable quinones, such as N-acetyldopamine, gave rise to secondary radicals, which were identified as 5-hydroxy-substituted *o*-semiquinones.

These results indicate that in the presence of spin-stabilizing metal ions, the semiquinone becomes an important intermediate in the enzymatic oxidation of dopa and other materials that form a quinone that rapidly cyclizes. Unfortunately, it is not known whether results from experiments with spin stabilization can be extrapolated to *in situ* conditions where melanin synthesis actually occurs in melanocytes. The observed difference in the decay kinetics of semiquinones from cyclizable and the non-cyclizable quinones is rather interesting.

The hydroxy-substituted semiquinones formed from the latter may have similar cytotoxic potential as semiquinones from hydroxy-substituted catechol(amine) that have been shown to interact efficiently with molecular oxygen (Kalyanaraman *et al.,* 1988).

The ESR study of early stages of *in vitro* melanogenesis has not revealed the exact molecular nature of the melanin intrinsic radicals. Taking advantage of higher spectral resolution offered by higher microwave frequency, computer simulations of Q-band dopa-melanin spectra showed the presence of four species, each with axial anisotropy (Pasenkiewicz-Gierula and Sealy, 1986). EPR spectra of dopa-melanin at an even higher microwave frequency (W-band) are consistent with the model that there are at least two quite different types of melanin radicals (Nilges *et al.,* 1992). The first type is pH-dependent, and is seen only above pH 5. It has a spectrum that is nearly identical to that of an *o*-benzosemiquinone anion radical ($g_{\|} = 2.00233$ and $g_{\perp} = 2.00552$). The second type of radical is pH-independent and has $g_{\|} = 2.00232$ and $g_{\perp} = 2.00383$. It is not a protonated radical such as a semiquinone cation, but is probably a radical associated with defects in the polymer backbone since it was found to be dependent upon aggregation (Nilges, 1998). It seems that this radical species may best characterize the intrinsic paramagnetism of melanin.

3. OTHER EXPERIMENTAL APPROACHES AND FUTURE PROSPECTS

Perhaps the most important aspect of applying EPR to the study of pigmented systems is its potential ability to quantify melanin and determine its molecular nature in a non-destructive way. The amount and type of melanin present in pigmented cells is considered one of the factors that determines the photosensitivity of the cells (Kollias *et al.,* 1991; Schmitz *et al.,* 1995; Hill *et al.,* 1997; Hill and Hill, 2000; Kobayashi *et al.*, 2001). Thus, the amount of melanin and its type in the human skin could be viewed as an indicator of the skin susceptibility to solar radiation. Also, it appears that the incidence of age-related macular degeneration correlates inversely with the pigmentation of the ocular iris (Weiter *et al.,* 1985; Young, 1988; Pauleikhoff and Holz, 1996). Although eumelanin and pheomelanin were detected in epidermal tissue of Caucasians of skin phototype I and II (Thody *et al.,* 1991) and the presence of both melanin pigments in the human iris has been reported (Prota *et al.,* 1998), these assays were based on HPLC detection of characteristic degradation products of eumelanin and pheomelanin. However, the yield of some of the degradation products is very low (Ito and Fujita, 1985), which significantly complicates the analysis and makes the determination of melanin in biological samples less reliable. The EPR assay, on the other hand, has proven to be highly specific and reliable in determination of melanin in model and several biological systems (Pilas and Sarna, 1985; Katsuda *et al.,* 1990; Enochs *et al.,* 1993). Very recently, the method has been used to detect a loss of melanin from human retinal pigment epithelium with aging (Sarna *et al.,* 2002). Although the mechanism of this phenomenon is not fully understood, it may have important biological implications.

Unfortunately, EPR methods have their own limitations, with the most severe being relatively low sensitivity. Thus, the minimum amount of melanin that can be unambiguously detected in frozen samples by EPR at X-band is currently about 1 microgram. Hopefully, with the improved sensitivity of modern EPR spectrometers and development of new loop-gap resonators, this limitation to melanin detection will soon be improved.

The other aspect of EPR applications to study of melanins that has not, as yet, been exploited, is spectral and temporal resolution of very high frequency EPR and Fourier Transform EPR, respectively. In a preliminary W-band EPR study of melanin from human RPE donors of different ages, a striking pattern in the changes of magnetic parameters of melanin radicals with age was observed (Rozanowska *et al.,* 1993). At pH 7, the most prominent changes were a reduction in signal intensity at g ~2.005, with a concomitant increase at lower magnetic field, corresponding to g ~2.006.

Although the molecular nature of these changes has not been determined, the measurements indicate the potential of EPR spectroscopy at very high frequency to resolve minute differences in the structure of melanin free radicals and/or their microenvironments that may occur with age or as a result oxidative insult (Sarna *et al.,* 2002).

Time-domain EPR, such as FT-EPR or saturation recovery, are expected to be powerful tools for studying the photodynamics of melanin free radicals and the nature of their precursors. The only time-resolved measurement of melanin free radicals induced by white light (with millisecond time resolution) that the authors are aware of revealed a new transient species formed in photoirradiated melanin samples that decayed rapidly (in milliseconds) at both ambient and cryogenic temperature (Felix *et al.,* 1979). The time profile of the photoinduced spectrum indicated the occurrence of chemically-induced dynamic electron polarization. The data were interpreted in terms of the involvement of a triplet-state intermediate.

Such an interpretation, however, seems inconsistent with most recent studies of melanin photodynamics using time-resolved femtosecond and picosecond absorption spectroscopy (Nofsinger *et al.,* 2001). In this study, no long-lived melanin transients with typical triplet state properties have been observed. On the other hand, a very fast repopulation of the melanin ground state detected was a clear indication of an efficient internal conversion. Thorough analysis of time-resolved changes in the melanin EPR signal induced by nanosecond laser pulses using FT-EPR could shed new light on the formation mechanism of photoinduced melanin radicals.

Similarly, applications of saturation recovery and electron spin echo are likely to play an important role in developing a better understanding of the molecular structure of melanin radicals, their spatial distribution and their local environment. The use of saturation transfer and electron spin echo techniques to study melanin has been described in two early papers (Sarna and Hyde, 1978; Okazaki *et al.,* 1985). These preliminary studies indicated that while the spin-lattice relaxation time of natural melanin from the choroid of bovine eyes at 193 K was on the order of 15 microseconds and relatively unchanged, spin-spin relaxation times exhibited substantial variation among various melanins (Sarna and Hyde, 1978).

One of the most exciting recent developments in biophysical studies of melanin has been the application of advanced imaging techniques such as scanning electron, atomic force and tunneling microscopies. This led to development of the concept of melanin being an aggregate of relatively small oligomers (Clancy and Simon, 2001; Clancy *et al.,* 2000; Zajac *et al.,* 1994). It has been postulated that the degree of aggregation of these building blocks determines melanin's ability to act as a protective agent, by efficient scavenging of free radicals and conversion of the energy of the

absorbed photons into heat, or as a sensitizer by contributing to the generation of reactive oxygen species (Nofsinger *et al.,* 2002). Using photoacoustic calorimetry, in which the melanin samples were excited by 0.8 – 0.8 μJ, 10 ps pulses of 351 nm, the Simon group was able to observe remarkable differences in the percentage of energy of the absorbed photons that was released as heat for different molecular sizes of sepia melanin (Nofsinger *et al.,* 1999). Thus, while high (Mw > 10,000) and medium (10,000 < Mw < 3000) molecular weight factions of this eumelanin released about 90% of the absorbed energy as heat, a low molecular (Mw > 1000) weight faction retained almost 55% of the absorbed energy. The results were interpreted as an indication of the photoformation of a long-lived energetic intermediate by the Mw < 1000 fraction. The photoacoustic data establish that the reaction with O_2 occurs after the formation of the long-lived reactive species. Interestingly, the absorption spectrum of the small eumelanin fraction (Mw <1000) was found to have the same shape as the action spectrum for photogeneration of melanin radicals (Sama and Sealy, 1984a). Transient absorption experiments revealed that large eumelanin aggregates released the absorbed energy of UVA photons within 20 ps (Nofsinger *et al.,* 2001).

Although melanins are known to be very poor fluorophores (Kozikowski *et al.,* 1984; Gallas and Eisner, 1987), recent steady-state and time-resolved measurements revealed interesting properties of different melanins (Docchio *et al.,* 1991; Teuchner *et al.,* 2000; Forest *et al.,* 2000; Nofsinger and Simon, 2001). Perhaps the most significant was the observation that the emission decay for sepia eumelanin is strongly nonexponential, exhibiting decay components on the tens-of-picoseconds to several nanoseconds time scale (Forest *et al.,* 2000). The nonexponential decay was concluded to be a reflection of the structural disorder of eumelanin. Time-resolved population decays revealed that small eumelanin aggregates were responsible for long-lived emission dynamics (lifetimes greater than 1 ns), while large eumelanin aggregates are the source of short emission decay (lifetimes less than 1 ns) (Nofsinger and Simon, 2001). The rapid and nonexponential depolarization dynamics were attributed to energy transfer. Polarized emission decays for the large and small aggregates indicated that energy transfer occurred both within the same and different fundamental building blacks of eumelanin.

An intriguing and perhaps confusing issue of the concept of fundamental building blocks of eumelanin is their actual size. While the Simon group, using a simple ultrafiltration procedure, was able to obtain various sized fractions of Sepia melanin, it is surprising that the smallest fraction had a molecular weight below 1000. Assuming that the molecular weight of probable monomeric units of eumelanin – dihydroxyindoles and dihydroxyindoles carboxylic acids (Prota, 1992)) – is about 150, the

fundamental building block of melanin would consist of six or fewer monomers.

It is an open question whether such a small entity can still be considered "melanin." Based on wide-angle X-ray diffraction analysis of dried synthetic tyrosine-melanin and scanning tunneling microscopy measurements, it was proposed that the melanin fundamental units – protomolecules – consist of three stacked sheets of five to eight 5,6-indolquinone residues (or their reduced forms) in each sheet (Cheng *et al.,* 1994; Zajac *et al.,* 1994). The molecular weight of such a melanin protomolecule would be at least 2–3 times larger than that isolated by the Simon group. There is little doubt that advanced microscopy and imaging techniques will play increasingly important roles in future melanin study.

4. REFERENCES

Backer, J. M., Budker, V. G., Eremenko, S. I., and Molin, Y. N. (1977). Detection of the kinetics of biochemical reactions with oxygen using exchange broadening in the ESR spectra of nitroxide radicals. *Biochim. Biophys. Acta* **460**, 152-156.

Bielec, J., Pilas, B., Sarna, T., and Truscott, T. G. (1986) Photochemical studies of porphyrin-melanin interaction. *J. Chem. Soc. Faraday Trans.* **82**, 1469-1474.

Blois, M. S., Zahlan, A. B., and Maling, J. E. (1964) Electron spin resonance studies on melanins. *Biophys. J.* **4**, 471-490.

Bustamante, J., Bredeston, L., Malanga, G., and Mordoh, J. (1993) Role of melanin as a scavenger of active oxygen species. *Pigment Cell Res.* **6**, 348-353.

Chedekel, M. R., Post, P. W., Deibel, R. M., and Kalus, M. (1977) Photodestruction of phaeomelanin. *Photochem. Photobiol.* **26**, 651-653.

Chedekel, M. R., Smith, S. K., Post, P. W., Pokora, A., and Vessell, D. L. (1978) Photodestruction of pheomelanin: role of oxygen. *Proc. Natl. Acad. Sci. U. S. A.* **75**, 5395-5399.

Cheng, J., Moss, S. C., and Eisner, M. (1994) X-ray characterization of melanins--II. *Pigment Cell Res.* **7**, 263-73.

Clancy C. M. R., Nofsinger, J. B., and Simon, J. D. (2000) A hierarchical self-assembly of eumelanin. *J. Phys. Chem. B* **104**, 7871-7873.

Clancy, C. M. and Simon, J. D. (2001) Ultrastructural organization of eumelanin from Sepia officinalis measured by atomic force microscopy. *Biochemistry* **40**, 13353-13360.

Commoner, B., Townsend, J., and Pake, G. W. (1954) Free radicals in biological materials. *Nature* **174**, 689-691.

Cope, F. W., Sever, R. J., and Polis, B. D. (1963) Reversible free radical generation in the melanin granules of the eye by visible light. *Arch. Biochem. Biophys.* **100**, 171-177.

Docchio F, Boulton M, Cubeddu R, Ramponi R, Barker PD. (1991) Age-related changes in the fluorescence of melanin and lipofuscin granules of the retinal pigment epithelium: a time-resolved fluorescence spectroscopy study. *Photochem. Photobiol.* **54**, 247-253.

Dunford, R., Land, E. J., Rozanowska, M., Sarna, T., and Truscott, T.G. (1995) Interaction of melanin with carbon- and oxygen-centered radicals from methanol and ethanol. *Free Radical Biol. Med.* **19**, 735-740.

Enochs, W. S., Nilges, M. J., and Swartz, H. M. (1993) A standardized test for the identification and characterization of melanins using electron paramagnetic resonance (EPR) spectroscopy. *Pigment Cell Res.* **6,** 91-99.

Felix, C, C., Hyde, J. S., Sarna, T., and Sealy, R. C. (1978a) Interactions of melanin with metal ions. Electron spin resonance eviodence for chelate complexes of metal ions with free radicals. *J. Amer. Chem. Soc.* **100,** 3922-3926.

Felix, C. C., Hyde, J. S., Sarna, T., and Sealy, R. C. (1978b) Melanin photoreactions in aerated media. Electron spin resonance evidences for production of superoxide and hydrogen peroxide. *Biochem. Biophys. Res. Commun.* **84,** 335-341.

Felix, C. C., Hyde, J. S., and Sealy, R. C. (1979) Photoreactions of melanin: a new transient species and evidence for triplet state involvement. *Biochem. Biophys. Res. Commun.* **88,** 456-461.

Felix, C. C. and Sealy, R. C. (1981) Electron spin resonance characterization of radicals from 3,6-dihydroxyphenylalanine: semiquinone anions and their metal chelates. *J. Amer. Chem. Soc.* **103,** 2831-2836.

Felix, C. C. and Sealy, R. C. (1982) *o*-Benzosemiquinone and its metal chelates. Electron spin resonance investigation of radicals from photolysis of catechol in the presence of complexing metal ions. *J. Amer. Chem. Soc.* **104,** 1555-1560.

Forest, S. E., Lam, W. C., Millar, D. P., Nofsinger, J. B., and Simon, J. D. (2000) A model for the activated energy transfer within eumelanin aggregates. *J. Phys. Chem. B* **104,** 811-814.

Gallas, J. M. and Eisner M. (1987) Fluorescence of melanin-dependence upon excitation wavelength and concentration. *Photochem. Photobiol.* **45,** 595-600.

Glickman, R. D. and Lam, K. W. (1992) Oxidation of ascorbic acid as an indicator of photooxidative stress in the eye. *Photochem. Photobiol.* **55,** 191-196.

Goodchild, N. T., Kwock, L., and Lin, P.-S. (1984) Melanin: a possible cellular superoxide scavenger. In Rodgers, M. A. J. and Powers E. L., eds., *Oxygen and Oxy-Radicals in Chemistry and Biology.* Academic Press, New York, 645-648.

Hearing, V. J. (1998) Chapter 30. Regulation of Melanin Formation. In Nordlund, J. J., Boissy, R. E., Hearing, V. J., King, R. A., and Ortonne, J.-P., eds., *The Pigmentary System. Physiology and Patophysiology.* Oxford University Press, New York-Oxford, 423-438.

Hill, H. Z. and Hill, G, J. (2000) UVA, pheomelanin and the carcinogenesis of melanoma. *Pigment Cell Res.* **13,** 140-144.

Hill, H. Z., Hill, G. J., Cieszka, K., Plonka, P. M., Mitchell, D. L., Meyenhofer, M. F., Xin, P., and Boissy, R. E. (1997) Comparative action spectrum for ultraviolet light killing of mouse melanocytes from different genetic coat color backgrounds. *Photochem. Photobiol.* **65,** 983-989.

Hyde, J. S. and Subczynski, W. K. (1989) Spin-label oximetry. In Berliner L. J. and Reuben, J., eds. *Biological Magnetic Resonance. Vol. 8. Spin Labeling. Theory and Applications.* Plenum Press, New York, 399-425.

Ito, S. and Fujita, K. (1985) Microanalysis of eumelanin and phaeomelanin in hair and melanomas by chemical degradation and liquid chromatography. *Anal. Biochem.* **144,** 527-535.

Jimbow, K., Miyake, Y., Homma, K., Yasuda, K., Izumi, Y., Tsutsumi, A., and Ito, S. (1984) Characterization of melanogenesis and morphogenesis of melanosomes by physicochemical properties of melanin and melanosomes in malignant melanoma. *Cancer Res.* **44,** 1128-1134.

Kalyanaraman, B., Felix, C. C., and Sealy, R. C. (1984a). Electron spin resonance-spin stabilization of semiquinones produced during oxidation of epinephrine and its analogues. *J. Biol. Chem.* **259,** 354-358.

Kalyanaraman, B., Felix, C. C., and Sealy, R. C. (1984b) Peroxidatic oxidation of catecholamines. A kinetic electron spin resonance investigation using the spin stabilization approach. *J. Biol. Chem.* **259,** 7584-7589.

Kalyanaraman, B., Felix, C. C., and Sealy, R. C. (1984c) Photoionisation and photohomolysis of melanins: an electron spin resonance – spin trapping study. *J. Amer. Chem. Soc.* **106,** 7327-7330.

Kalyanaraman, B., Korytowski, W., Pilas, B., Sarna, T., Land, E. J., and Truscott, T. G. (1988) Reaction between ortho-semiquinones and oxygen: pulse radiolysis, electron spin resonance, and oxygen uptake studies. *Arch. Biochem. Biophys.* **266,** 277-284.

Katsuda, H., Kobayashi, T., Saito, H., Matsunaga, T., and Ikeya, M. (1990) Electron spin resonance imaging of mouse B16 melanoma. *Chem. Pharm. Bull. Tokyo* **38,** 2838-2840.

King, R. A. (1998) Chapter 38. Genetic Hypomelanoses: Disorders Characterized by Generalized Hypomelanoses, pp. 553-592. Albinism. In Nordlund, J. J., Boissy, R. E., Hearing, V. J., King, R. A., and Ortonne, J.-P., eds., *The Pigmentary System. Physiology and Patophysiology.* Oxford University Press, New York-Oxford, 553-575.

Kobayashi, N., Katsumi, S., Imoto, K., Nakagawa, A., Miyagawa, S., Furumura, M., and Mori, T. (2001) Quantitation and visualization of ultraviolet-induced DNA damage using specific antibodies: application to pigment cell biology. *Pigment Cell Res.* **14,** 94-102.

Koch, W. H. and Chedekel, M. R. (1986) Photoinitiated DNA damage by melanogenic intermediates in vitro. *Photochem. Photobiol.* **44,** 703-710.

Kollias, N., Sayre, R. M., Zeise, L., and Chedekel, M. R. (1991) Photoprotection by melanin. *J. Photochem. Photobiol. B* **9,** 135-160.

Korytowski, W., Kalyanaraman, B., Menon, I. A., Sarna, T., and Sealy, R. C. (1986) Reaction of superoxide anions with melanins: electron spin resonance and spin trapping studies. *Biochim. Biophys. Acta* **882,** 145-153.

Korytowski, W., Pilas, B., Sarna, T., and Kalyanaraman, B. (1987) Photoinduced generation of hydrogen peroxide and hydroxyl radicals in melanins. *Photochem. Photobiol.* **45,** 185-190.

Korytowski, W. and Sarna, T. (1990) Bleaching of melanin pigments. Role of copper ions and hydrogen peroxide in autooxidation and photooxidation of synthetic dopa-melanin. *J. Biol. Chem.* **265,** 12410-12416.

Korytowski, W., Sarna, T., Kalyanaraman, B., and Sealy, R. C. (1987) Tyrosinase-catalyzed oxidation of dopa and related catechol(amine)s: a kinetic electron spin resonance investigation using spin-stabilization and spin label oximetry. *Biochim. Biophys. Acta* **924,** 383-392.

Korytowski, W., Sarna, T., and Zareba, M. (1995) Antioxidant action of neuromelanin: the mechanism of inhibitory effect on lipid peroxidation. *Arch. Biochem. Biophys.* **319,** 142-148.

Kozikowski, S. D., Wolfram, L. J., and Alfano, R. R. (1984) Fluorescence spectroscopy of melanins. *IEEE J. Quantum Electron.* **QE-20,** 1379-1382.

Krol, E. S. and Liebler, D. C. (1998) Photoprotective actions of natural and synthetic melanins. *Chem. Res. Toxicol.* **11,** 1434-1440.

Land, E. J., Thompson, A., Truscott, T. G., Subbarao, K. V., and Chedekel, M. R. (1986) Photochemistry of melanin precursors: dopa, 5-S-cysteinyldopa and 2,5-S,S'-dicysteinyldopa. *Photochem. Photobiol.* **44,** 697-702.

Losi, A., Bedotti, R., Brancaleon, L., and Viappiani, C. (1993) Porphyrin-melanin interaction: effect on fluorescence and non-radiative relaxations. *J. Photochem. Photobiol. B* **21,** 69-76.

Mason, H. S., Ingram, D. J. E., and Allen, B. (1960) The free radical property of melanins. *Arch. Biochem. Biophys.* **85,** 225-230.

Nappi, A. J., and Ottaviani, E. (2000) Cytotoxicity and cytotoxic molecules in invertebrates. *BioEssays* **22,** 469-480.

Nilges, M. J. (1998) Chapter 32. Advances in Physical Analysis of Melanins. In Nordlund, J. J., Boissy, R. E., Hearing, V. J., King, R. A., and Ortonne, J.-P., eds., *The Pigmentary System. Physiology and Patophysiology.* Oxford University Press, New York-Oxford, 451-459.

Nilges, M. J. B., Pilas, B., Enochs, W. S., and Swartz, H. M. (1992) Identification and Differentiation of free radicals in melanins: VHF-EPR spectroscopy. Abstract presented at the 4th Annual Meeting of the European Society for Pigment Cell Research, Berlin 1992.

Nofsinger, J. B., Forest, S. E., and Simon, J. D. (1999) Explanation for the disparity among absorption and action spectra for eumelanin. *J. Phys. Chem. B* **103,** 11428-11432.

Nofsinger, J. B. and Simon, J.D. (2001) Radiative relaxation of Sepia eumelanin is affected by aggregation. *Photochem. Photobiol.* 74, 31-37.

Nofsinger J. B., Liu, Y., and Simon, J. D. (2002) Aggregation of eumelanin mitigates photogeneration of reactive oxygen species. *Free Radical Biol. Med.* **32**, 720-730.

Nofsinger J. B.,Ye, T., and Simon, J. D. (2001) Ultrafast non-radiative relaxation dynamics of eumelanin. *J. Phys. Chem. B* **105,** 2864-2866.

Okazaki, M., Kuwata, K., Miki, Y., Shiga, S., and Shiga, T. (1985) Electron spin relaxation of synthetic melanin and melanin-containing human tissues as studied by electron spin echo and electron spin resonance. *Arch. Biochem. Biophys.* **242,** 197-205.

Ortonne, J.- P. and Ballotti, R. (2000) Melanocyte biology and melanogenesis: what's new? *J. Dermatol. Treatment* **11,** S15-S26.

Ostrovsky M. A. and Kayushin, L. P. (1963) ESR study of retina under lighting. *Dokl. Akad. Nauk SSSR* **151,** 986-988.

Ostrovsky, M. A., Sakina, N. L., and Dontsov, A. E. (1987) An antioxidative role of ocular screening pigments. *Vision Res.* **27,** 893-899.

Oyehaug, L., Plathe, E., Vage, D. I., and Omholt, S. W. (2002) The Regulatory Basis of Melanogenic Switching. *J. Theor. Biol.* **215,** 449-468.

Pasenkiewicz-Gierula, M. and Sealy, R. C. (1986) Analysis of the ESR spectrum of synthetic DOPA-melanin. *Biochim. Biophys. Acta* **884,** 510-516.

Pauleikhoff, D. and Holz, F. G. (1996) Age-related macular degeneration. 1. Epidemiology, pathogenesis and differential diagnosis. *Ophthalmologie* **93,** 299-315.

Pilas, B., Felix, C. C., Sarna, T., and Kalyanaraman, B. (1986) Photolysis of pheomelanin precursors: an ESR-spin trapping study. *Photochem. Photobiol.* **44,** 689-696.

Pilas, B. and Sarna, T. (1985) Quantitative determination of melanin in pigmented cells by electron spin resonance spectroscopy. In Bagnara, J., Klaus S. N., Paul, E., and Schartl M., eds., *Pigment Cells 1985. Biological, Molecular and Clinical Aspects of Pigmentation. Proceedings of the XIIth International Pigment Cell Conference Giessen, Federal Republic of Germany,* University of Tokyo Press, Tokyo, 97-103.

Pilas, B., Sarna, T., Kalyanaraman, B., and Swartz, H. M. (1988) The effect of melanin on iron associated decomposition of hydrogen peroxide. *Free Radical Biol. Med.* **4**, 285-293.

Plonka, P. M., Slominski, A. T, Pajak, S., and Urbanska, K. (2003) Transplantable melanomas in gerbils (Meriones unguiculatus). II – melanogenesis. *Exp. Dermatol.* **12,** in press.

Porebska-Budny, M., Sakina, N. L., Stepien, K. B., Dontsov, A. E., and Wilczok, T. (1992) Antioxidative activity of synthetic melanins. Cardiolipin liposome model. *Biochim. Biophys. Acta* **1116,** 11-16.

Prota G. (1992) *Melanins and Melanogenesis.* Academic Press, San Diego-California.

Prota, G., Hu, D. N., Vincensi, M. R., McCormick, S. A., and Napolitano, A. (1998) Characterization of melanins in human irides and cultured uveal melanocytes from eyes of different colors. *Exp. Eye Res.* **67,** 293-299.

Reszka, K. J. and Chignell, C. F. (1993) EPR and spin-trapping investigation of free radicals from the reaction of 4-metoxybenzendiazonium tetrafluoroborate with melanin and melanin precursors. *J. Amer. Chem. Soc.* **115,** 7752-7760.

Reszka, K. J., Matuszak, Z., and Chignell, C. F. (1998) Lactoperoxidase-catalyzed oxidation of melanin by reactive nitrogen species derived from nitrite (NO2-): an EPR study. *Free Radical Biol. Med.* **25,** 208-216.

Riley, P. A. (1998) Mechanisms of inhibition of melanin pigmentation. In In Nordlund, J. J., Boissy, R. E., Hearing, V. J., King, R. A., and Ortonne, J.-P., eds., *The Pigmentary System. Physiology and Patophysiology.* Oxford University Press, New York-Oxford, 401-422.

Rozanowska, M., Bober, A., Burke, J. M., and Sarna, T. (1997) The role of retinal pigment epithelium melanin in photoinduced oxidation of ascorbate. *Photochem. Photobiol.* **65,** 472-479.

Rozanowska, M., Korytowski, W., Rozanowski, B., Skumatz, C., Boulton, M. E., Burke, J. M., and Sarna, T. (2002) Photoreactivity of aged human RPE melanosomes: a comparison with lipofuscin. *Invest. Ophthalmol. Vis. Sci.* **43,** 2088-2096.

Rozanowska, M., Kukulski, T., Burke, J., Nilges, M., Pilas, B., Korytowski, W., and Sarna, T. (1993) OR7 - Photooxidation of retinal pigment melanin – a model for melanin aging. *Pigment Cell Res.* **6,** 272-273.

Rozanowska, M., Sarna, T., Land, E. J., and Truscott, T. G. (1999) Free radical scavenging properties of melanin interaction of eu- and pheo-melanin models with reducing and oxidising radicals. *Free Radical Biol. Med.* **26,** 518-525.

Sarna, T. (1992) Properties and function of the ocular melanin--a photobiophysical view. *J Photochem. Photobiol. B* **12,** 215-258.

Sarna, T., Burke, J. M., Korytowski, W., Rozanowska, M., Skumatz, C. M. B., Zareba, A., and Zareba, M. (2002) Loss of melanin in human RPE with aging. *Exp. Eye Res.,* in press.

Sarna, T., Duleba, A., Korytowski, W., and Swartz, H. (1980) Interaction of melanin with oxygen. *Arch. Biochem. Biophys.* **200,** 140-148.

Sarna, T. and Hyde, J. S. (1978) Electron spin-lattice relaxation times of melanin. *J. Chem. Phys.* **69,** 1945-1948.

Sarna, T., Hyde, J. S., and Swartz, H. M. (1976) Ion-exchange in melanin: an electron spin resonance study with lanthanide probes. *Science* **192,** 1132-1134.

Sarna, T., Korytowski, W., Pasenkiewicz-Gierula, M., and Gudowska, E. (1981) Ion-exchange studies in melanins. In Seiji, M., ed., *Pigment Cell 1981. Phenotypic Expression in Pigment Cells. Proceedings of the XIth International Pigment Cell Conference Sendai, Japan,* University of Tokyo Press, Tokyo, 23-29.

Sarna, T., Korytowski, W., and Sealy R. C. (1985a) Nitroxides as redox probes of melanins: dark-induced and photoinduced changes in redox equilibria. *Arch. Biochem. Biophys.* **239,** 226-233.

Sarna, T. and Lukiewicz, S. (1972) Electron spin resonance on living cells. IV. Pathological changes in amphibian eggs and embryos. *Folia Histochem. Cytochem.* **10,** 265-278.

Sarna, T., Menon I. A., and Sealy, R. C. (1984) Photoinduced oxygen consumption in melanin systems--II. Action spectra and quantum yields for pheomelanins. *Photochem. Photobiol.* **39,** 805-809.

Sarna, T., Menon I. A., and Sealy, R. C. (1985b) Photosensitization of melanins: a comparative study. *Photochem. Photobiol.* **42,** 529-532.

Sarna, T., Pilas, B., Land, E. J., and Truscott, T. G. (1986) Interaction of radicals from water radiolysis with melanin. *Biochim. Biophys. Acta* **883,** 162-167.

Sarna, T., Rozanowska, M., Zareba, M., Korytowski, W., and Boulton, M. (1998). Retinal melanin and lipofuscin: possible role in photoprotection and phototoxicity of human RPE. In Hoenigsmann, H., Knobler R. M., Trautinger, F., and Jori, G., eds., *Landmarks in Photobiology. Proceedings of the 12th International Congress of Photobiology,* OEMF spa, Milano, 418-421.

Sarna, T. and Sealy, R. C. (1984a) Free radicals from eumelanins: quantum yields and wavelength dependence. *Arch. Biochem. Biophys.* **232,** 574-578.

Sarna, T. and Sealy, R. C. (1984b) Photoinduced oxygen consumption in melanin systems. Action spectra and quantum yields for eumelanin and synthetic melanin. *Photochem. Photobiol.* **39,** 69-74.

Sarna, T. and Swartz, H. M. (1978) Identification and characterization of melanins in tissues and body fluids. *Folia Histochem. Cytochem.* **16,** 275-286.

Sarna, T. and Swartz, H. M. (1993) Interactions of melanin with oxygen (and related species). In Scott, G., ed., *Atmospheric Oxidation and Antioxidants. Volume III,* Elsevier, Amsterdam-London-New York-Tokyo, 129-169.

Sarna, T. and Swartz, H. M. (1998) Chapter 25. The physical properties of melanins. In Nordlund, J. J., Boissy, R. E., Hearing, V. J., King, R. A., and Ortonne, J.-P., eds., *Pigmentary System Physiology and Pathophysiology,* Oxford University Press, New York-Oxford, , 333-357.

Scalia, M., Geremia, E., Corsaro, C., Santoro, C., Baratta, D., and Sichel, G. (1990) Lipid peroxidation in pigmented and unpigmented liver tissues: protective role of melanin. *Pigment Cell Res.* **3,** 115-119.

Schmitz, S., Thomas, P. D., Allen, T. M., Poznansky, M. J., and Jimbow, K. (1995) Dual role of melanins and melanin precursors as photoprotective and phototoxic agents: inhibition of ultraviolet radiation-induced lipid peroxidation. *Photochem. Photobiol.* **61,** 650-655.

Sealy RC. (1984) Radicals in melanin biochemistry. *Methods Enzymol.* **105,** 479-483.

Sealy, R. C., Felix, C. C., Hyde, J. S., Swartz, H. M., (1980) Structure and reactivity of melanins: influence of free radicals and metal ions. In Pryor, W. A., ed., *Free Radicals in Biology,* Academic Press, New York, pp. 209-259.

Sealy, R., Hyde, J., Felix, C., Menon, I., and Prota, G. (1982a) Eumelanins and phaeomelanins: characterization by electron spin resonance spectroscopy. *Science* **217,** 545-547.

Sealy, R., Hyde, J., Felix, C., Menon, I., Prota, G., Swartz, H. M., Persad, S., and Haberman, H. F. (1982b) Novel free radicals in synthetic and natural pheomelanins: distinction between dopa melanins and cysteinyldopa melanins by ESR spectroscopy. *Proc. Natl. Acad. Sci. U. S. A.* **79,** 2885-2889.

Sealy, R. C., Sarna, T., Wanner, E. J., and Reszka, K. (1984) Photosensitization of melanin: an electron spin resonance study of sensitized radical production and oxygen consumption. *Photochem. Photobiol.* **40,** 453-459.

Stepien, K., Zajdel, A., Wilczok, A., Wilczok, T., Grzelak, A., Mateja, A., Soszynski, M., and Bartosz, G. (2000) Dopamine-melanin protects against tyrosine nitration, tryptophan oxidation and Ca(2+)-ATPase inactivation induced by peroxynitrite. *Biochim. Biophys. Acta* **1523,** 189-195.

Swartz, H. M., Sarna, T., and Varma, R. R. (1979) On the natural and excretion of the hepatic pigment in the Dubin-Johnson syndrome. *Gastroenterology* **76,** 958-964.

Swartz, H. M., Sarna, T., and Zecca, L. (1992) Modulation by neuromelanin of the availability and reactivity of metal ions. *Ann. Neural.* **32,** S69-S75.

Teuchner K., Ehlert, J., Freyer, W., Leupold, D., Altmeyer, P., Stuecker M., and Hoffman, K. (2000) Fluorescence studies on melanin by stepwise two-photon femtosecond laser excitation. *J. Fluoresc.* **10,** 275-281.

Thody, A. J., Higgins, E. M., Wakamatsu, K., Ito, S., Burchill, S. A., and Marks, J. M. (1991) Pheomelanin as well as eumelanin is present in human epidermis. *J. Invest. Dermatol.* **97,** 340-344.

Urbach, F., Epstein, J. H., and Forbes, P. D. (1974) Ultraviolet carcinogenesis: experimental, global and genetic aspects. In Fitzpatrick, T. B., Pathak, M. A., Harber, L. C., Seiji, M., and Kukita A., eds., *Sunlight and Man.* University of Tokyo Press, Tokyo, 259-283.

Vsevolodov, E., Ito, S., Wakamatsu, K., Kuchina, I., and Latypov, I. (1991) Comparative analysis of hair melanins by chemical and electron spin resonance methods. *Pigment Cell Res.* **3,** 30-34.

Weiter, J. J., Delori, F. C., Wing, G. L., and Fitch, K. A. (1985) Relationship of senile macular degeneration to ocular pigmentation. *Am. J. Ophthalmol.* **99,** 185-187.

Wolfram , L. J. and Albrecht, L. (1987) Chemical and photo-bleaching of brown and red hair. *J. Soc. Cosmet. Chem.* **82**, 179-191.

Wrobel, D., Planner, A., Hanyz, I., Wielgus, A., and Sarna, T. (1997) Melanin-porphyrin interaction monitored by delayed luminescence and photoacoustics. *J. Photochem. Photobiol. B* **41,** 45-52.

Ye, T., Simon, J. D., and Sarna, T. (2002) Ultrafast energy transfer from bound tetra(4-N,N,N,N-trimethylanilinium) porphyrin to synthetic dopa and cysteinyldopa melanins. *Photochem. Photobiol.,* in press.

Young R. W. (1988) Solar radiation and age-related macular degeneration. *Surv. Ophthalmol.* **32,** 252-269.

Zajac, G. W., Gallas, J. M., Cheng, J., Eisner, M., Moss, S. C., and Alvarado-Swaisgood, A. E. (1994) The fundamental unit of synthetic melanin: a verification by tunneling microscopy of X-ray scattering results. *Biochim. Biophys. Acta* **1199,** 271-278.

Zareba, M., Bober, A., Korytowski, W., Zecca, L., and Sarna, T. (1995) The effect of a synthetic neuromelanin on yield of free hydroxyl radicals generated in model systems. *Biochim. Biophys. Acta.* **1271,** 343-348.

Chapter 8

Application of Spin Labels To Membrane Bioenergetics

(Photosynthetic Systems of Higher Plants)

Alexander N. Tikhonov[1] and Witold K. Subczynski[2]

[1] Department of Biophysics, Faculty of Physics, M. V. Lomonosov Moscow State University, Moscow, 119899, Russia, [2]National Biomedical EPR Center, Department of Biophysics, Medical College of Wisconsin, Milwaukee, Wisconsin 53226

Abstract: Following a brief overview of photosynthesis and the macro structure of chloroplasts, examples are presented of the use of nitroxyl spin labels and spin probes to investigate the processes of electron transport, proton transport, and oxygen transfer in chloroplasts. pH-sensitive nitroxyl radicals can be observed inside and outside thylakoids under various conditions, such as different levels of light. Oxygen consumption can be measured via the effect of oxygen on line width of the free radical. Lipid-soluble spin probes monitor changes in the biological membranes.

1. INTRODUCTION

Photosynthesis is one of the most important biological processes. The great mass of experimental data obtained in numerous laboratories all over the world has given detailed information on the composition and molecular structure of the light-harvest complexes, electron transport chain (ETC) and ATP synthases in energy-transducing organelles of photosynthetic organisms — higher plants, cyanobacteria and photosynthetic bacteria (Lehninger *et al.,* 1993; Blankenship, 2002). In this chapter, we will consider several aspects of the use of nitroxide radicals to investigate the processes of electron and proton transport, as well as the related processes of oxygen transfer, in chloroplasts — the energy-transducing organelles of the plant cell.

Figures 1 and 2 depict a cross section of a chloroplast and a schematic of a chloroplast's ETC. In higher plants and cyanobacteria, photosynthetic ETC converts the energy of light absorbed by the light-harvesting complexes into the energy of macroergic chemical compounds (NADPH and ATP) by

means of three large pigment-protein complexes located in the thylakoid membranes: photosystem 1 (PS1), photosystem 2 (PS2) and cytochrome b_6f–complex (bf-complex). PS 1 and PS2 contain reaction centers (P_{700} and P_{680}, respectively) activated by light, and a number of incorporated electron carriers (Jordan *et al.,* 2001; Zouni *et al.,* 2001). Light-induced electron transport from the water splitting complex of PS2 to the terminal electron acceptor of PSl ($NADP^+$) is mediated by the bf-complex and three mobile electron carriers, plastoquinone (Q), plastocyanine (Pc) and ferredoxin (Fd), that provide the electron transfer between PS2, the bf-complex, PS 1 and the ferredoxin-NADP-reductase (FNR) complex. Plastoquinone is an essential component of photosynthetic ETC that couples electron transfer to proton translocation across the thylakoid membrane. The oxidized plastoquinone molecule, Q, binds to PS2 at the acceptor side (bound Q is called a secondary plastoquinone, Q_B) and then accepts two electrons in tandem from the anion radical of tightly bound primary plastoquinone Q_A and two protons from the chloroplast stroma. The reduced plastoquinone molecule (plastoquinol, QH_2) dissociates from PS2 and migrates inside the thylakoid membrane to the bf-complex. According to Mitchell's Q-cycle mechanism, QH_2 is oxidized at the Q_o site of the bf-complex close to the thylakoid lumen (internal volume of the thylakoid), Plastocyanine is a mobile electron carrier localized in the lumen that couples the bf-complex to the PS1 reaction center P_{700}.

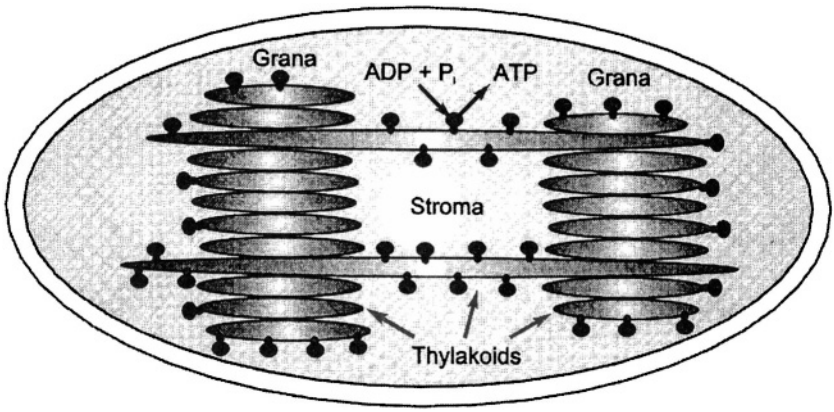

Figure 1. Schematic representation of a chloroplast cutaway. Flattened vesicles symbolize the thylakoids that contain the electron transport chain and ATP synthase complexes.

Due to the asymmetrical arrangement of ETC complexes in the thylakoid membrane, the functioning of chloroplast ETC causes translocation of protons into the thylakoid lumen, leading to generation of a transmembrane electrochemical gradient of protons, $\Delta\bar{\mu}_{H^+}$. The transmembrane difference in electrochemical potentials $\Delta\bar{\mu}_{H^+}$ (the so-called "proton potential") is the driving force for proton translocation through ATP synthase (Mitchell, 1961;

1966; Skulachev, 1988; Haraux and de Kouchkovsky, 1998; McCarty *et al.,* 2000). The two components of the proton potential, $\Delta\varphi$ (transmembrane electric potential difference) and ΔpH (transmembrane pH difference), actuate the operation of the ATP synthase machinery. However, the question of how much of the free energy is stored in the form of a pH gradient or electric potential difference $\Delta\varphi$ still remains (Kaim and Dimroth, 1999; Kramer *et al.,* 1999).

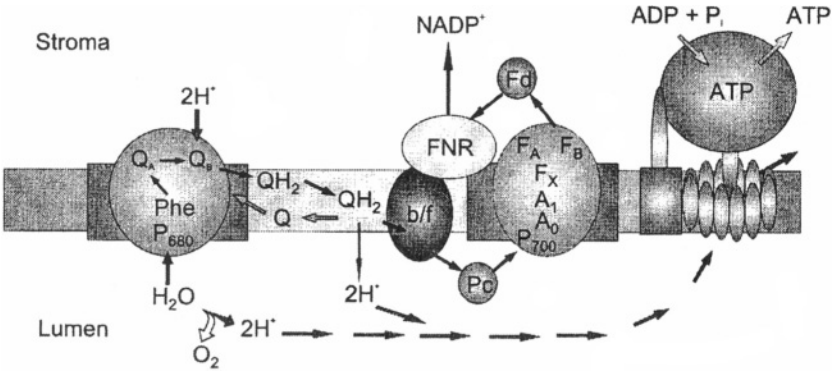

Figure 2. Arrangement of chloroplast's ETC and ATP synthase complexes in a thylakoid membrane. Photosystem 2 (PS2) contains the photoreaction center P_{680}. The photoexcited reaction center P_{680} donates an electron to the primary acceptor pheophitine (Phe). From the reduced Phe molecule, the electron is transferred to the primary plastoquinone Q_A and then to the secondary plastoquinone Q_B. The doubly-reduced secondary quinon $Q_B^{=}$ accepts two protons from the stroma, $Q_B^{=} + 2H^+ \rightarrow (QH_2)_B$. The protonated molecule of the secondary plastoquinol $(QH_2)_B$ dissociates from PS2, $(QH_2)_B \rightarrow QH_2$, then diffuses to the bf-complex. The cytochrome bf-complex and plastcyanine (Pc) mediate the electron transfer from QH_2 to photosystem 1 (PS1). Photosystem 1 contains the photoreaction center P_{700}, which donates an electron through the system of electron carriers firmly bound to PS1 (A_0, A_1, F_x, F_A, F_B) to soluble ferredoxin (Fd). The electron is then delivered through the ferredoxin-NADP-reductase complex (FNR) to the terminal electrion acceptor $NAPH^+$. For details of the three-dimensional structures of PS1 and PS2 complexes see Jordan *et al.,* 2001, and Zouni *et al.,* 2001. Translocation of hydrogen ions H^+ from the thylakoid lumen (internal part of the thylakoid) to the stroma occurs through the membrane sector CF_0 of ATP synthase (CF_1-CF_0 complex). For details of the molecular architecture of the ATP synthase see Abrahams *et al.,* 1994 and Stock *et al.,* 1999.

The light-induced acidification of the thylakoid lumen also plays an important role in the feedback control of electron flow in chloroplasts. It has long been known that the rate of plastoquinol oxidation by the bf-complex (the rate-limiting step in the electron flow between two photosystems) strongly depends on the intrathylakoid pH (Rumberg and Siggel, 1969; Tikhonov *et al.,* 1981; Blumenfeld and Tikhonov, 1994; Kramer *et al.,* 1999; Jahns *et al.,* 2002). The rate of plastoquinol oxidation decreases with the

light-induced acidification of the thylakoid lumen. Therefore, the light-induced decrease in the intrathylakoid pH should cause a slowing of the electron flow from PS2 to PS1. The extent of light-induced acidification of the thylakoid lumen depends on the metabolic state of the chloroplasts. During basal electron transport, i.e., when a supply of substrates for ATP formation is limited (metabolic State 4), the efflux of protons through ATP synmase is small. Therefore, rather strong acidification of the thylakoid lumen (pH_{in} < 5-5.5 at an external pH = 7.5-8.0) occurs in State 4, which leads to the essential retardation of electron flow between two photosystems (Fig. 3, bottom drawing). When ADP and inorganic phosphate are present in excess (Fig. 3, upper drawing, metabolic State 3), the intrathylakoid pH also decreases in the course of chloroplast illumination, but less than in State 4 (due to the efflux of protons from the lumen through ATP synthase in State 3). Since more significant slowing of electron flow occurs at the lower in trathylakoid pH, the rate of electron transport coupled to ATP synthesis (State 3) is supported at a higher level than during the basal electron transport (State 4).

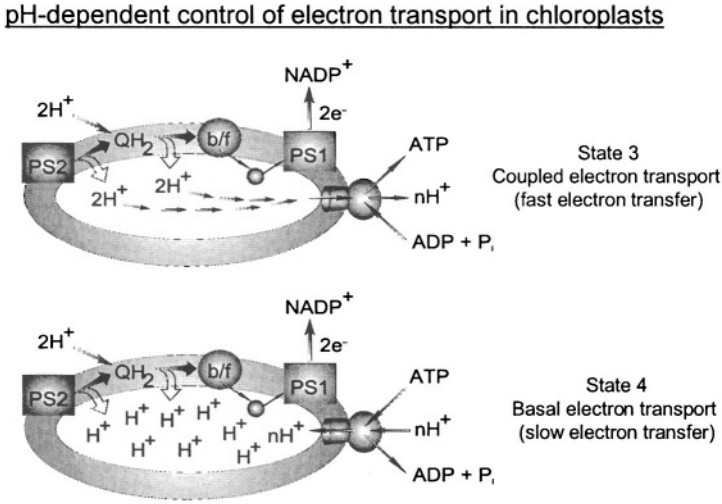

Figure 3. Photosynthetic control of electron transport in chloroplasts. Upper drawing depicts a thylakoid functioning under conditions of intensive ATP synthesis (electron transport is coupled to ATP formation, metabolic State 3). Bottom drawing depicts a thylakoid in a state of photosynthetic control (basal electron transport, metabolic State 4). ATP synthase is the reversible molecular machine that can provide ATP from ADP and orthophosphate P_i (State 3) or hydrolyze ATP to ADP and P_i (State 4).

In this chapter, we will consider how different kinds of spin labels can be used to investigate the structural and functional characteristics of chloroplasts. Of course, we do not pretend to completely review the great body of literature regarding the numerous aspects of using spin labels in

bioenergetics (see, for instance, Kocherginsky and Swartz, 1999). We will focus our attention on three topics: (1) new applications of pH-sensitive spin labels to measure the proton potential in chloroplasts (Section 2), (2) oximetry of photosynthetic systems (Section 3), and (3) elucidation of the role of the physical state of thylakoid membranes in the regulation of photosynthetic activity of chloroplasts (Section 4). These topics have been at the center of the authors' interests for the two last decades, and therefore, most of the illustrations presented in this chapter have been redrawn from our previously published papers.

2. THE USE OF PH-SENSITIVE SPIN LABELS TO MEASURE THE PROTON POTENTIAL IN CHLOROPLASTS

The question 'How acidic is the lumen?' (Kramer *et al.,* 1999) is still debated in bioenergetics literature because the transmembrane pH difference is one of the most important parameters of membrane bioenergetics. In contrast to mitochondria and bacteria that use mostly the electric component, $\Delta\varphi$, of the proton potential for ATP synthesis, it is commonly believed that in thylakoids of higher plant chloroplasts, the transmembrane pH gradient provides the main contribution to the proton potential. If the ΔpH value were the only component of the proton motive force, then the drop in lumen pH during illumination of chloroplasts should not exceed about 5.0. However, as was demonstrated by Tikhonov *et al.* (Tikhonov *et al.,* 1981; Tikhonov and Timoshin, 1985; Ryzhikov and Tikhonov, 1988; 1991), and later by Kramer *et al.,* (1999), the pH of the thylakoid lumen does not decline below 5.8 during normal *in vivo* photosynthesis. It was proposed (Kramer *et al.,* 1999; Kaim and Dimroth, 1999) that ATP synthesis by F-type ATP synthase is dependent on the transmembrane voltage, i.e., the electric component $\Delta\varphi$ could contribute significantly to the steady-state value of the proton potential in chloroplasts. This conclusion was confirmed by measurements of $\Delta\varphi$ from the electrochromic carotenoid band shift in isolated spinach thylakoids. Thus, the question 'How acidic is the lumen?' is still valid for bioenergetics.

The two most frequently used methods for ΔpH measurements in energy-transducing organelles are based on pH-indicating probes. They are (1) calculation of ΔpH from the partitioning of permeable amines between the inner volume of the vesicles and the suspending medium (Rottenberg and Grunwald, 1972; Bamberger *et al.,* 1973), and (2) measurement of the spectral response of pH-sensitive indicators loaded into the vesicles (Junge, 1982). EPR spin probes have already demonstrated their potential for monitoring pH under physiological conditions in plant chloroplasts (Cafiso

1989; Cafiso and Hubbell, 1978a; 1978b; 1981; Quintinilha and Mehlhorn, 1978; Mehlhorn *et al.,* 1982; Tikhonov and Timoshin, 1985; Wille, 1988; Magnitski *et al.,* 1996; Magnitski and Tikhonov, 1995; 1998). An advantage of using pH-sensitive spin probes is that their EPR spectra usually are not masked by the EPR signals from the electron transport components.

In this section, we will consider two approaches to quantitative determination of ΔpH in chloroplasts with spin labels. One is based on the threshold effect of concentration-dependent broadening of the EPR spectrum of TEMPAMINE (4-amino-2,2,6,6-tetramethylpiperidine-1-oxyl) (developed by Magnitski *et al.,* 1996; and Magnitski and Tikhonov, 1995; 1998). It is important to note that tempamine (TA) provides an adequate tool for measuring the bulk-to-bulk ΔpH, because TA does not bind to the thylakoid membranes. Another method is based on the use of pH-sensitive imidazoline nitroxide radicals (Khramtsov *et al.,* 1982; 1985; Khramtsov and Weiner, 1988; Khramtsov and Volodarsky, 1998). Contrary to conventional methods based on the use of the fluorescent amines (Rottenberg and Grunwald, 1972; Bamberger *et al.,* 1973), neither of these methods must evaluate the internal volume of thylakoids.

2.1 TEMPAMINE as a probe for measuring the transmembrane pH difference

An amine distribution technique for ΔpH measurements is based on the assumption that the partition of probing molecules between the vesicles' interior and the surrounding medium is determined by the ratio of hydrogen ion activities inside to outside the vesicles (Fig. 4). Unfortunately, many of the widely used molecular indicators ΔpH of (e.g., 9-aminoacridine or neutral red) are not adequate probes for measuring the bulk-to-bulk phase ΔpH in chloroplasts because they bind to thylakoid membranes. Binding of pH indicator molecules to the membrane could lead to essential overestimation of ΔpH (Lolkema *et al.,* 1982). The water-soluble spin label TEMPAMINE (TA) is one of the amine-type molecular probes used for quantitative measurements of the intrathylakoid pH (pH_{in}). There is indirect evidence that TA molecules which accumulate inside the thylakoids in response to acidification of the thylakoid lumen do not bind to the membrane, although the mobility of TA molecules inside the thylakoids is slowed by a factor of about 10 compared to TA in the external bulk phase (Berg *et al.* 1979; Tikhonov and Timoshin, 1985; Magnitski *et al.,* 1996; Magnitski and Tikhonov, 1995; 1998). The illumination of chloroplasts causes additional hindrance of TA rotation inside the thylakoids (Nesbitt and Berg, 1980; 1982). These results might indicate that interaction of TA with thylakoid membranes is a challenge to TA as a probe for quantitative measurements of bulk-to-bulk ΔpH. In order to justify the applicability of

TA to quantitative measurements of ΔpH, Trubitsin *et al.* (2001) recently investigated the interaction of TA molecules with bean chloroplasts suspended in media of different osmolarity. Their results demonstrated that inside the thylakoid, the majority of TA molecules were localized in the osmotic volume of the thylakoids, i.e., in the bulk of the thylakoid lumen. They concluded that TA could be used as an adequate probe for bulk-to-bulk ΔpH.

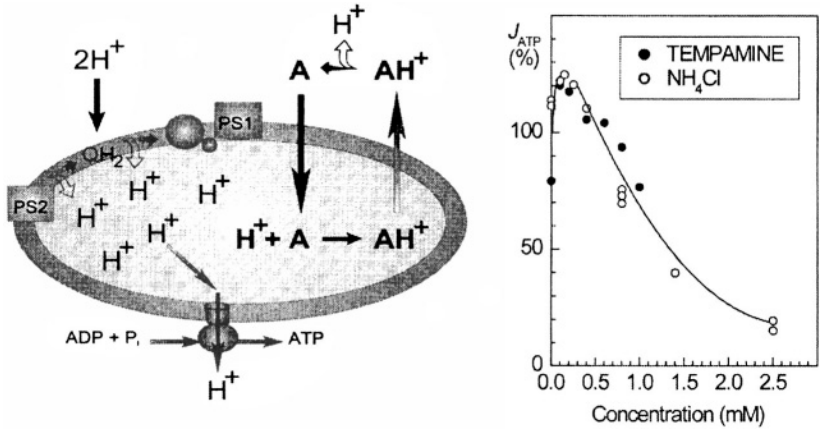

Figure 4. Illustration of the light-induced accumulation of amines inside thylakoid. The neutral form of pH-indicating amine molecule, A, easily penetrates the thylakoid lumen. Inside the thylakoid, the pH value is lower than outside ($pH_{in} < pH_{out}$). Therefore, in the bulk of the lumen, the reaction of the protonation of the A molecules is further shifted toward the protonated form of amine, AH^+. Membrane permeability for the protonated molecule AH^+ is low compared to the neutral form A. Therefore, acidification of the lumen leads to accumulation of amine molecules inside the vesicle. The extent of the amine accumulation in the lumen depends on the transmembrane pH difference (see details in text). Amines are potential uncouplers of photophosphorylation, because the leak of AH^+ from the thylakoid to the stroma will provide efflux of protons from the lumen to the stroma, thus inhibiting the ΔpH-driven ATP synthesis. The box at right shows the effects of TEMPAMINE and NH_4Cl on the rate of photophosphorylation in the chloroplasts (Wasniowska *et al.,* 2002).

2.1.1 Visualization of TEMPAMINE molecules inside the thylakoid

TEMPAMINE molecules easily penetrate the thylakoid, forming a partition between the thylakoid lumen and the external volume. Visualization of TA molecules localized inside the thylakoid can be realized by addition of a membrane-impermeable paramagnetic compound, chromium oxalate (CrOx), which broadens the EPR signal from TA in the external medium (Berg and Nesbitt, 1979). This method is based on the different permeability of thylakoid membranes to spin label molecules and

the broadening agent. Paramagnetic molecules of CrOx dissolved in the suspending medium cause a broadening of the EPR spectrum of TA molecules localized outside the thylakoid ('external' EPR signal). In the meantime, closed thylakoid membranes maintain their barrier functions for CrOx, precluding a broadening of the EPR signal of TA molecules localized inside the thylakoid ('internal' EPR signal). Figure 5 (spectrum a) shows that the first-derivative EPR spectrum of TA in a chloroplast-suspending medium represents a triplet produced by the nitroxide radicals rapidly tumbling ($\tau_c \cong 4 \cdot 10^{-11}$ s) in polar surroundings. Addition of the paramagnetic compound (15 mM CrOx) causes an essential broadening of this signal (Fig. 5, spectrum b). When CrOx is added to a chloroplast suspension, the EPR signal (Fig. 5, spectrum c) represents the superposition of two signals – one the broadened triplet from TA localized outside the thylakoid and the other the triplet of narrow lines given by TA molecules localized inside the thylakoids ('internal' signal). The difference EPR signal (Fig. 5, spectrum d) is attributed to TA molecules localized in the aqueous phase of chloroplast osmotic volume (thylakoid lumen). This conclusion follows from two observations: (1) the difference spectrum is characterized by the isotropic hyperfine splitting constant a_{iso} = 16.9 G, which is typical of nitroxide radicals in a polar surroundings; and (2) the intensity of the difference signal depends on the thylakoid volume which was changed by variations in the osmolarity of the suspending medium (Trubitsin *et al.*, 2001). It should be noted that earlier authors generally used fairly high concentrations of CrOx ($\geq$ 40-80 mM) to provide an essential broadening of the 'external' EPR signal. However, Magnitsky *et al.* (1996) reported that when the concentration of CrOx exceeded 15-20 mM, penetration of CrOx molecules into the thylakoid lumen caused some broadening of the 'internal' signal. To minimize the influence of CrOx on the 'internal' EPR signal, it is necessary to add CrOx at concentrations no higher than 15 mM. In this case, the 'external' EPR signal is markedly broadened, while the 'internal' EPR signal given by TA molecules localized in the lumen is practically unaffected by CrOx.

The shape of the 'internal' EPR signal (Fig. 5, spectrum d) differs slightly from the shape of the TA signal in the external medium, indicating a hindrance to TA rotation in the lumen. The mobility of TA molecules inside the thylakoid, described in terms of the apparent correlation time τ_c, was retarded by a factor of 10, as compared to TA rotation outside the thylakoid. There might be two reasons for the slowing of the rotation of TA inside the thylakoids: (1) high viscosity of the aqueous medium inside the thylakoid, and/or, (2) interaction of TA with the internal surface of the thylakoid membrane (e.g., TA binding or anchoring to the membrane).

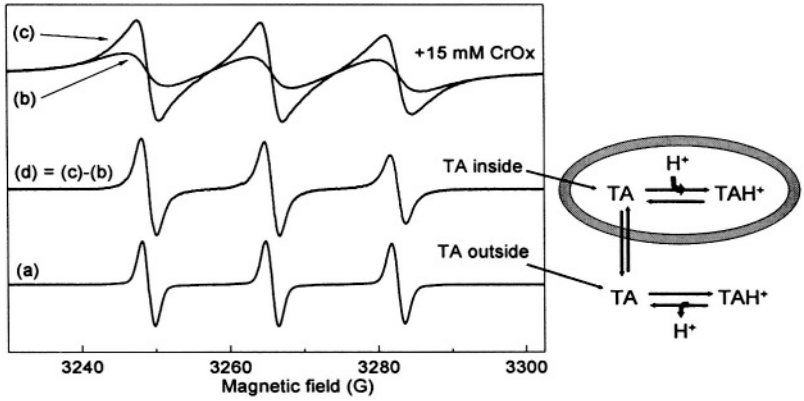

Figure 5. EPR signals of TEMPAMINE: (a) spin label in buffer solution (without chloroplasts and CrOx); (b) spin label in buffer solution in the presence of 15 mM CrOx; (c) spin label in bean chloroplast suspension in the presence of 15 mM CrOx; (d) the difference signal in bean chloroplast suspension (see detail in text and in Magnitsky *et al.,* 1996).

Certain peculiarities of the 'internal' EPR signal (higher amplitude of the low field line compared to the amplitude of the central line) might indicate that TA molecules perform slightly anisotropic rotations inside the thylakoids that are caused by TA interaction with the membrane (Tikhonov and Timoshin, 1985). To discriminate between these factors, Trubitsin *et al.* (2001) investigated how the mobility of TA depended on the internal volume of chloroplasts. They concluded that TA binding to the membrane could not be considered a dominant factor in slowing the rotation of TA inside the thylakoid. After sufficient incubation (12 hours at 4°C) of chloroplasts in a high-osmotic medium (500-800 mM sucrose), the intensity of the 'internal' EPR signal decreased by a factor of 2.5 due to a shrinkage of thylakoids. If TA binding to the membrane were the main reason for slowing down TA rotation inside the thylakoid, one would expect that the shrinkage of thylakoids should lead to an increase in the apparent correlation time τ_c. However, a decrease in the internal volume was not accompanied by changes in the value of τ_c. The lack of correlation between the variable internal volume and TA mobility inside the thylakoids can be considered evidence that most TA molecules localized inside the thylakoids are dissolved in the bulk of the intrathylakoid osmotic volume. The relatively high viscosity of TA surroundings inside the thylakoid can be explained by the presence of biopolymers (proteins, chloroplast DNA, carbohydrates) in a rather small volume of the thylakoid lumen.

2.1.2 Determination of ΔpH from TEMPAMINE partitioning in chloroplasts

Similar to other penetrating amines (Rottenberg and Grunwald, 1972; Bamberger *et al.,* 1973), the steady state ratio of TA concentrations inside, C_{in}, and outside, C_{out}, the thylakoid should be determined by the ratio of the activities of hydrogen ions inside, $[H^+]_{in}$, and outside, $[H^+]_{out}$, the thylakoid:

$$C_{in}/C_{out} = ([H^+]_{in} + K_a)/([H^+]_{out} + K_a), \quad (1)$$

where K_a is the equilibrium constant of the reaction of TA protonation ($TA + H^+ \leftrightarrow TH^+$). In experiments with chloroplasts, the external pH is usually lower than 8.0-8.5. The pK_a for TA molecules is about 8.9 (Wan *et al.,* 1995), i.e., $K_a << [H^+]_{out} \leq [H^+]_{in}$. Therefore the transmembrane pH difference, ΔpH, can be calculated as

$$\Delta pH = \lg([H^+]_{in}/[H^+]_{out}) = \lg(C_{in}/C_{out}) \quad (2)$$

Having measured the ratio C_{in}/C_{out}, one can determine the ΔpH. The quantification of TA concentrations, however, is not a trivial task. In order to determine concentrations of C_{in} and C_{out} it is necessary to (1) discriminate between the 'internal' and 'external' TA molecules, (2) measure the number of TA molecules accumulated inside the thylakoid, and (3) find the volume of the thylakoid lumen.

As mentioned above, visualization of TA molecules inside the thylakoid can be realized by broadening the 'external' EPR signal with membrane-impermeable paramagnetic compounds (e.g., potassium ferrycyanide or chromium oxalate). The light-induced uptake of TA by thylakoids can be detected as an enhancement of the 'internal' EPR signal from TA molecules accumulating inside the thylakoids (Quintinilha and Mehlhorn, 1978; Tikhonov and Timoshin, 1985; Cafiso, 1989). The light-induced increase in amplitude of this signal is inhibited by ionophores (e.g., gramicidin D or NH_4Cl), which dissipate the proton gradient in thylakoids. It is noteworthy, however, that there are certain limitations for quantitative measurement of TA uptake by this method. First, the sensitivity of the method is restricted by the very low concentrations of TA in the chloroplast suspension (<< 2.5-5 μM of TA), which must be used to avoid distortion of the 'internal' EPR signal from the concentration-dependent broadening of the signal given by the TA molecules accumulating inside the thylakoid. Second, the influence of CrOx on the electron transport chain or ATP synthase cannot be excluded.

Magnitsky and Tikhonov (Magnitsky and Tikhonov, 1995; 1998; Magnitsky *et al.,* 1996) described another approach to quantifying the concentration of TA molecules accumulating inside the thylakoids in

response to light-induced generation of ΔpH. It is based on the effect of spin-exchange broadening of the EPR signal from TA molecules concentrated in the thylakoid lumen. Fig. 6 shows that the peak-to-peak amplitude (A_{pp}) of the EPR signal from TA in aqueous solution increases proportionally to TA concentration up to $[T]_\vartheta = 2.5$ mM, while it declines from the linear law as the concentration of TA becomes higher than 2.5 mM. The deviation from the linear law and further drop in the A_{pp} value are caused by the broadened EPR line due to more frequent collisions of TA molecules at high concentrations (Fig. 6). For TA molecules localized inside the thylakoid, the threshold concentration of TA was determined as $[T]_\vartheta = 2.5\text{-}3.5$ mM (Magnitsky *et al.*, 1996).

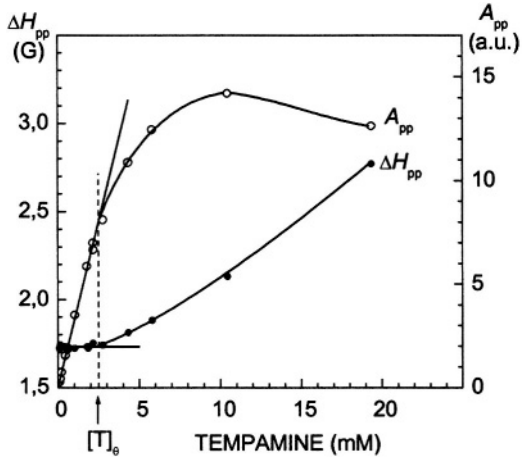

Figure 6. Dependencies of the spectral parameters of the EPR signal on concentration of TEMPAMINE in water solution. Parameters A_{pp} and ΔH_{pp} are the peak-to-peak height and width, respectively, of the low field component of the EPR signal (for details, see Tikhonov and Timoshin, 1985; Magnitski and Tikhonov, 1994, 1998).

The threshold nature of this effect provides the basis for the quantitative determination of $[T]_{in}$ and determination of the ΔpH generated in the course of chloroplast illumination. Figure 7 is a typical pattern of light-induced amplitude changes in the low field component of the EPR spectrum from TA molecules in a chloroplast suspension that contains 0.3 mM TA (in the absence of CrOx). Illumination of chloroplasts decreases the amplitude of this signal. After the illumination ceases, leakage of TA molecules from the thylakoids is accompanied by a rise in signal amplitude. A reversible, light-induced decrease in signal amplitude (parameter ΔA) is caused by the EPR line broadening because of TA concentrating inside the thylakoid. The irreversible decrease in the EPR signal (parameter ΔI) is explained by the loss of TA paramagnetism from its interaction with the chloroplast electron

transport chain (more details in Section 4.1.2). Reversible changes characterized by parameter ΔA are inhibited by protonophores that prevent generation of ΔpH, while an irreversible decrease in signal height signal due to TA reduction (parameter ΔI) was observed in the presence of protonophores.

The threshold nature of the concentration-dependent broadening effect also provides the basis for quantitative determination of $[T]_{in}$ from the dependence of parameter ΔA on the concentration C_o of TA in chloroplast suspension. Actually, the concentration-dependent broadening of the EPR signal should manifest itself only if the light-induced concentration of TA in the thylakoid lumen crosses the threshold level, i.e., if $[T]_{in} \geq [T]_{\vartheta}$. Therefore, measuring the dependence of the light-induced broadening effect (parameter ΔA) on concentration of TA in the suspension of chloroplasts, can reveal a concentration $C_o^* = [T]_o^*$, below which the light-induced broadening effect is not observed ($\Delta A \approx 0$, Fig. 8). The transmembrane pH difference can be calculated using the relationship $\Delta pH = \lg([T]_{in}^*/[T]_o^*)$.

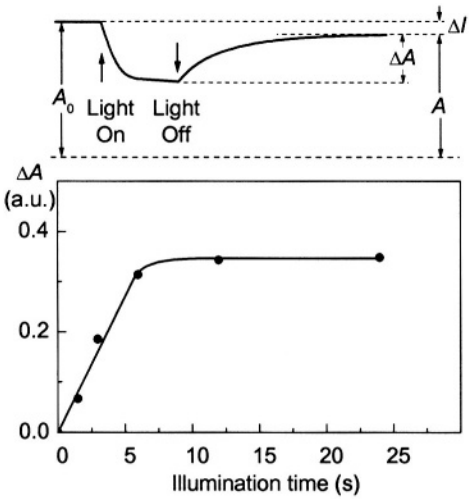

Figure 7. Kinetics of TEMPAMINE uptake by bean chloroplasts determined from the concentration dependent effect of the EPR line broadening. Top: light-induced height changes of the low field component of the EPR signal. Bottom: kinetics of the reversible light-induced changes in signal amplitude corrected for TA reduction by chloroplasts (parameter $\Delta A/A$).

A more sophisticated algorithm for calculating ΔpH from the dependence of parameter ΔA on the concentration of TA in chloroplast suspension takes into account another factor of the spectrum broadening – the hindrance to TA rotation inside the thylakoids and variability of the internal volume (Magnitski *et al.,* 1996). The advantages of this method for measuring ΔpH

are: (1) it is possible to determine the internal concentration of TA without using a broadening agent, (2) It is not necessary to determine the intrathylakoid volume, and (3) the concentration range of probing molecules is below the level when TA molecules could cause an essential influence on photophosphorylation in chloroplasts. Indeed, similar to other amino-type uncouplers, at rather high concentrations, TA can inhibit ATP synthesis in chloroplasts. It is important to note, however, that the 50% drop in the rate of ATP synthesis was observed (Wasniowska *et al.,* 2002) at a TA concentration of about 1.1 mM (Fig. 4), i.e., TA revealed its uncoupling activity only at concentrations higher than those used to measure the ΔpH value ($\leq$ 0.2-0.4 mM).

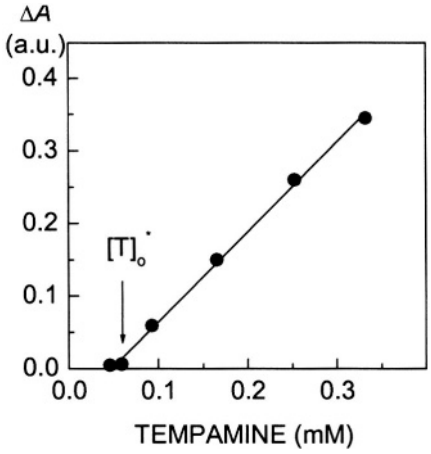

Figure 8. Light-induced broadening of the TEMPAMINE EPR signal (parameter ΔA) versus concentration of the spin label in chloroplast suspension. The lack of a broadening effect at TA concentrations below $[T]_o^*$ indicates that the concentration of TA inside the thylakoids does not reach the threshold level $[T]_0 \cong$ 2.5-3.5 mM (see explanation in text).

Using TA as an indicator of proton potential, ΔpH was measured in chloroplasts functioning with PS 1 -driven cyclic and noncyclic electron flow in states of photosynthetic control and intensive photophosphorylation (Tikhonov and Timoshin, 1985; Tikhonov and Shevyakova, 1985; Masarova and Tikhonov, 1988; Blumenfeld and Tikhonov, 1994; Magnitsky and Tikhonov, 1995; 1998). It was shown that ATP synthesis in chloroplasts could efficiently proceed under relatively small ΔpH in stroma-exposed thylakoids (ΔpH = 1.4-2.2, depending on experimental conditions). The data obtained are consistent with the possibility of alternative (localized or delocalized) mechanisms of coupling proton transport to ATP synthesis in chloroplasts (Williams, 1978; Haraux and de Kouchkovsky, 1998; Westerhoff *et al.,* 1984; Gilmyarova *et al.,* 1985; Dilley *et al.,* 1987; 1991;

Tikhonov and Blumenfeld, 1985; Theg *et al.,* 1988; Blumenfeld and Tikhonov, 1994).

2.2 Determination of intrathylakoid pH in chloroplasts with imidazoline nitroxides

Different derivatives of imidazoline nitroxides represent a rather wide class of pH-sensitive spin probes that already found applications in chemistry and biology (Khramtsov *et al.,* 1982; 1985; Khramtsov and Weiner, 1988; Khramtsov and Volodarsky, 1998). Recently, Trubitsin *et al.* (2001) were first to measure the light-induced changes in the pH of the thylakoid lumen of bean chloroplasts, using pH-sensitive derivatives of imidazoline nitroxides, 4-amino-2,2,5,5-tetramethyl-3-imidazoline-1-oxyl (ATI) characterized by pK = 6.2 (Fig. 9).

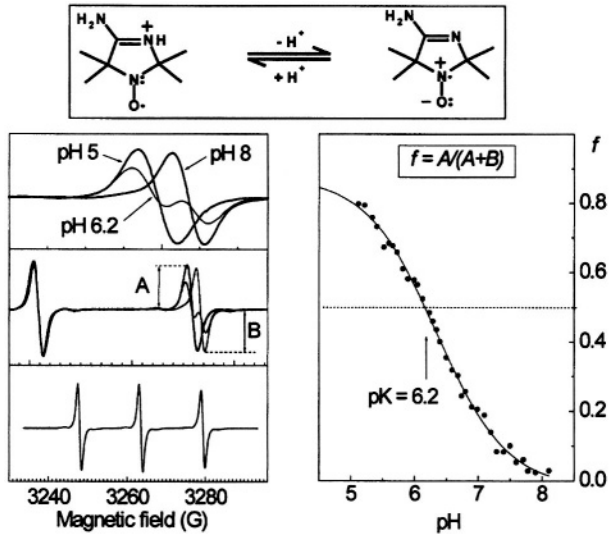

Figure 9. Upper box: structural formulas of two forms of the spin label ATI. Left-side box: EPR spectra of ATI at different pH levels; right-side box: dependence the spectral parameter f on the pH of ATI water solution.

This nitroxide was produced by Grigoriev with collaborators. Similar to the above-described experiments with TA, chromium oxalate was used to broaden the EPR signal from the ATI radicals localized outside the thylakoids. The EPR signal from the 'internal' ATI molecules represented a triplet of slightly broadened lines. The integral intensity of this signal decreased with the osmotically induced shrinkage of thylakoids. It was shown that the EPR spectrum from the 'internal' ATI molecules was sensitive to variations of the lumen pH. The illumination of chloroplasts

induced changes in the line shape of the 'internal' EPR signal caused by acidification of the thylakoid lumen (Fig. 10). The light-induced changes were inhibited by the addition of uncouplers (gramicidin D, nigericin, NH_4Cl) that precluded the formation of ΔpH. To quantify the light-induced acidification of the thylakoid lumen, Trubitsin *et al.* (2001) obtained the relevant calibration curves by measuring spectral parameters of the 'internal' EPR signals at different pH_{out} in the dark ($pH_{in} \approx pH_{out}$). Using this method, they determined the transmembrane pH difference in bean chloroplasts functioning in different metabolic states. In the state of photosynthetic control (without added Mg-ADP), the values of ΔpH measured with spin labels coincided with that values determined earlier by the kinetic method (Rumberg and Siggel, 1969; Tikhonov *et al.,* 1981). Under the conditions of intensive ATP synthesis, the efflux of protons from the thylakoid through the operating ATP synthase caused some decrease in the ΔpH values. The data demonstrated the validity of using imidazoline nitroxides as adequate indicators of ΔpH in chloroplasts.

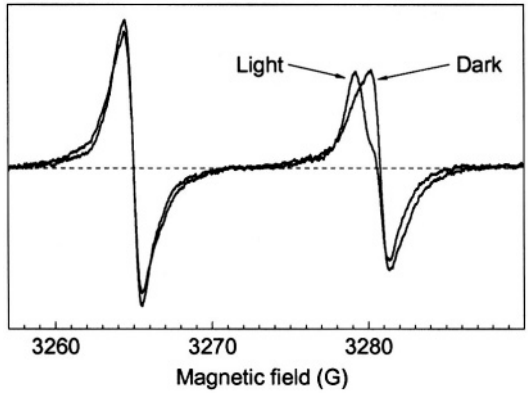

Figure 10. Light-induced changes in the EPR spectrum of ATI inside the thylakoids of bean chloroplasts (spectra were obtained in collaboration with B.V.Trubitsin, spin label ATI was produced by I.A. Grigor'ev).

2.3 Amphiphilic spin labels as indicators of membrane potential

The distribution of charged amphiphilic spin labels between the membrane and aqueous environments was used to measure the electric potential of thylakoid membranes (Cafiso and Hubbell, 1978a; 1981; Quintinilha and Mehlhorn, 1978; Mehlhorn and Packer, 1979; Tikhonov *et al.,* 1981; 1982; 1983; Cafiso, 1989; Gilmyarova *et al.,* 1986; Khomutov *et al.,* 1989a; 1989b; 1996). To illustrate how changes in surface potential of

the thylakoid membrane can be detected with amphiphilic spin labels, consider the behavior of spin labels that have electric charges of opposite signs. In the positively charged molecule 4-dodecyldimethylammonium-1-oxyl-2,2,6,6-tetramethyl-piperidine (CAT_{12}) and negatively charged molecule 16-doxylstearic acid spin label (16-SASL), the carboxyl group of 16-SASL is negatively charged because it is deprotonated in a physiological range of pH. It has been demonstrated that illumination of chloroplasts induces the appearance of extra negative charges on the external surface of the thylakoid membrane, initiating redistribution of spin labels between the membrane and aqueous environments (Tikhonov *et al.,* 1981). The height of the narrow high field component of the EPR spectrum given by CAT_{12} molecules localized in an aqueous medium decreases in response to switching on the actinic light. Negatively charged molecules 16-SASL demonstrate the effect of an opposite sign: the height of the 'polar' component increases in response to chloroplast illumination. Thus, positively charged molecules of CAT_{12} are pulled into the membrane, while the negatively charged molecules of 16-SASL are pushed out from the hydrophobic domain of the thylakoid membrane. After ceasing the illumination, positively charged CAT_{12} molecules are displaced from the membrane, while negatively charged 16-SASL molecules are pulled into the membrane. Reversible changes in the EPR spectra of amphiphilic spin labels, which are sensitive to changes in the surface potential of the membrane, can be inhibited by uncouplers (gramicidin, NH_4Cl) that dissipate the proton potential difference across the thylakoid membrane. Tikhonov *et al.* (1981) found that during the steady-state illumination of coupled chloroplasts, the electric potential Ψ of the outer surface of the thylakoid membrane became more negative ($\Delta\Psi = \Psi_{Light} - \Psi_{Dark} = -15$ mV), which is in agreement with earlier studies (Cafiso and Hubbell, 1978b; 1981; Quintinilha and Mehlhorn, 1978; Mehlhorn and Packer, 1979; Barber, 1980; 1982).

Amphiphilic spin labels were also applied to assay the buffer capacity of thylakoid membranes. Using a method based on selective modification of the membrane surface electric potential by charged amphiphilic detergents, Khomutov and collaborators (Gilmiyarova et al, 1986; Khomutov *et al.,* 1989a; 1996) quantified the contribution of different membrane domains into the buffering capacity of bean thylakoids. They demonstrated that a significant number of protons consumed by thylakoids during the illumination of chloroplasts bind to the proton-accepting groups located on the outer surface of the thylakoid membrane. This is because the illumination of chloroplasts leads to a decrease in surface potential on the outer side of the thylakoid membrane. About 50% of the protons consumed by illuminated thylakoids bind to the sequestered proton-accepting groups that are out of equilibrium with the protons accumulating in the bulk phase

of the thylakoid lumen. This supports the idea that local intramembrane and/or membrane-bound proton pools could play an important role in accumulating energy for ATP formation by ATP synthases of energy-transducing organelles (Westerhoff *et al.,* 1984; Gilmyarova *et al.,* 1985; Dilley *et al.,* 1987; Blumenfeld and Tikhonov, 1994).

3. SPIN-LABEL OXIMETRY IN PHOTOSYNTHETIC SYSTEMS

Spin-label oximetry methods have been widely used to study oxygen concentration, oxygen transport and oxygen consumption in model and biological systems (for review see Hyde and Subczynski, 1989; Swartz and Glockner, 1989; Hyde *et al.,* 1990; Grucker, 2000). Surprisingly, the number of works that apply the spin-label oximetry approach to study oxygen production by photosynthetic organisms (photosynthetic bacteria, algae, and higher plants) is very small. In this part of the chapter, we will review these papers and stress the significance of oximetry measurements for photosynthetic systems.

The earliest works used molecular probes, in which nitroxide spin labels were directly dissolved in the investigated systems (Strzalka *et al.,* 1986; 1990; Belkin *et al.,* 1987; Subczynski *et al.,* 1990). In these studies, EPR spectra of spin labels were affected not only by interaction of nitroxide moieties with molecular oxygen but also by photoinduced reduction and oxidation processes in which the free radical fragment of spin labels was involved. Nitroxides can easily interact with the functioning ETC of photosynthetic apparatus, being reduced to diamagnetic hydroxylamines. Additionally, hydroxylamines can be oxidized back to paramagnetic nitroxide molecules by interacting with different electron carriers in ETC (see details in Section 4.1.1.). The method proposed by Subczynski *et al.* (1990), which is based on superhyperfine structure of 3-carbamoyl-2,2,5,5-tetramethyl-3-pyrroline-1-yloxy (CTPO), diminished, but did not eliminate, errors arising from spin label reduction. Strzalka *et al.* (1986; 1990) tried to separate photoinduced changes in EPR signal amplitude coming from the interaction of the spin label with molecular oxygen from those coming from the spin label reduction, by monitoring the photoinduced changes of the signal amplitude at low and high (saturating) microwave powers. This gave a good qualitative separation but not quantitative evaluations. It seems that only the introduction of the microscopic spin label probe approach helped overcome these difficulties and permitted quantitative evaluation of oxygen concentration *in vitro* and *in situ* in photosynthetic systems (Ligeza *et al.,* 1992; 1994). The microscopic spin label probe approach was successfully applied earlier to study oxygen concentration in animal cell suspensions,

animal tissue, and intact animals (Chan *et al.,* 1989; Glockner *et al.,* 1991; Swartz *et al.,* 1991; see also the chapter by Swartz and Subczynski in this book). In a microscopic spin label probe, the free radical nitroxide moiety is isolated from water-soluble reductants and paramagnetic ions that might interfere with spin-label oximetry measurements. Other microscopic solid-state paramagnetic probes were also used to monitor oxygen production and oxygen consumption in photosynthetic systems such as spinach PS2 membranes and bean leaves. They include microcrystals of lithium phtalocyanine (Tang *et al.,* 1991) and a derivative of coal called fusinite (Ligeza *et al*., 1997).

3.1 Oxygen permeability of thylakoid membranes

Experimental evidence shows that oxygen plays a critical role in the regulation of electron transport in native chloroplasts (Halliwell, 1981; Edwards and Walker, 1983; Badger, 1985; Asada and Takahashi, 1987; Robinson, 1988; Schreiber and Neubauer, 1990; Kobayashi and Heber, 1994; Schreiber *et al.,* 1995; Hoefnagel *et al.,* 1998; Backhausen *et al.,* 2000). (1) Oxygen acts as a mediator of pseudocyclic electron transport, (2) oxygen is involved in chloroplast photorespiration, (3) the concentration of oxygen in chloroplasts controls ATP formation (Malkin and Chain, 1980; Chapman *et al.,* 1980), and (4) the presence of oxygen seems to be a necessary condition for normal functioning of chloroplast ETC *in situ.* Therefore, one of the questions concerning the regulatory role of oxygen is whether local concentrations of oxygen in different compartments of a chloroplast are modulated to such a high level that they affect the redox states of ETC components, and thus influence electron flow in the chloroplast. The asymmetrical arrangement of ETC components in the thylakoid membrane makes this highly probable. A water-splitting complex of PS2 (side of the release of oxygen) is exposed to the thylakoid interior, while the components of ETC that can consume oxygen are located at the outer side of the thylakoid membrane or in the bulk phase of the chloroplast stroma (Mehler, 1951). High local concentrations of oxygen inside a chloroplast can also stimulate formation of active forms of oxygen (superoxide anion radicals, hydrogen peroxide), which should lead to the photodestruction of pigments and degradation of proteins (Riistama *et al.,* 1996; Belkin *et al.,* 1987). However, due to the subcompartmentalization of chloroplasts, it is practically impossible to directly measure an oxygen concentration difference across the thylakoid membrane or determine a local concentration of oxygen in a certain chloroplast compartment. Application of microscopic paramagnetic oxygen-sensitive probes (see, e.g., Ligeza *et al.,* 1992; 1994; 1997) appears to be promising for monitoring changes in oxygen level inside a leaf or in the chloroplast suspension, but this approach

would provide only a general picture without specific details, i.e., the results of oxygen production or its consumption.

The potential existence of oxygen gradients in chloroplasts is closely associated with the value of the oxygen permeability coefficient through the thylakoid membrane. The coefficient of the thylakoid membrane of spinach chloroplasts *(Spinacia oleracea)* has been estimated by Ligeza *et al.* (1998) from the profile of the oxygen diffusion-concentration product across the membrane using a procedure developed earlier (Subczynski *et al.,* 1989; Subczynski and Markowska, 1992). The profile was obtained by observing collisions of molecular oxygen with the nitroxide moiety of lipid-soluble spin labels: 5-, 9-. 12-, and 16-doxylstearic acid (5-, 9-, 12-, and 16-SASL) located at various distances from the membrane surface, as shown in Fig. 11. The peak-to-peak linewidth of the central component of the EPR spectrum of nitroxide spin labels was used as an oxygen sensitive parameter. Oxygen-induced line broadening measured as a difference of linewidths for samples equilibrated with pure oxygen (at 1 atm pressure) and nitrogen is proportional to the product of the local oxygen diffusion coefficient and the local oxygen concentration in the membrane (Windrem and Plachy, 1980).

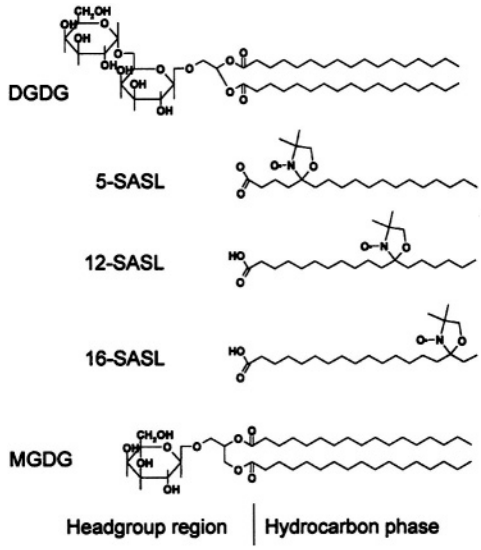

Figure 11. Chemical structures of spin labels used in oximetry measurements and monogalactosyldiacylglycerol (MGDG) and digalactosyldiacylglycerol (DGDG). Spin labels are intercalated in the membrane with the hydrophylic part (left side) in the polar head-group region of the membrane. Locations of the nitroxide moiety in the stearic acid molecule are shown. The main components of thylakoid membrane polar lipids are uncharged galactolipids, MGDG and DGDG, which together account for about 70 mol% of total polar lipids in spinach thylakoids (Nishihara *et al.,* 1980).

3.1.1 Spin labeling of thylakoid membranes

Successful measurement of oxygen-induced line broadening depends on the manner of spin labelling of the thylakoid membranes. Lipid soluble spin labels are usually added to biological samples from ethanol solution (Lai *et al.,* 1980). This leads to the presence of narrow lines in the EPR spectrum from the spin label dissolved in water. Ligeza *et al.* (1998) first prepared a spin label film on the bottom of a beaker. The suspension of thylakoid membranes isolated from spinach chloroplasts was then added to the beaker and shaken. After sufficient shaking, the sample was transferred to an Eppendorf tube and centrifuged to obtain a thick membrane suspension which was transferred to a thin-walled gas-permeable capillary made of the methylpentane polymer (TPX, Hyde and Subczynski, 1989), for EPR measurement. This allowed for recording the spectra with a good signal-to-noise ratio for samples equilibrated with nitrogen and pure oxygen at 1 atm pressure.

Being dissolved in the thylakoid membrane, stearic acid spin labels (SASLs) give EPR spectra that are typical of nitroxide radicals located in hydrophobic membranes (Fig. 12). The spectra presented in Fig. 12 show no evidence of signals that might come from nitroxide radicals located in aqueous surroundings. This example excludes the superposition of "hydrophobic" and "polar" signals, and thus allows use of the line-width of the central component (H_{pp}) as the most sensitive parameter for evaluating the broadening effect of oxygen dissolved in the lipid bilayer.

3.1.2 Profile of oxygen diffusion-concentration product across the thylakoid membrane

Figure 13 shows the oxygen-induced line broadening profile of the central line of the EPR spectra of SASLs in a thylakoid membrane obtained at 20°C. The oxygen-induced line broadening increases with the penetration of the nitroxide radical in the hydrophobic core of the membrane, resulting in maximal value in the central region of the membrane. This profile is also expressed as a ratio of the oxygen diffusion-concentration product in the thylakoid membrane to that in water. The value of the oxygen diffusion-concentration product in all membrane locations is higher than that measured in water – about two times higher in the membrane center. The membrane oxygen permeability coefficient was estimated from this profile using the procedure developed by Subczynski *et al.* (1989). At 20°C, the oxygen permeability coefficient for the lipid portion of the thylakoid membrane was found to be 39 cm/s. This value is 20% higher than the oxygen permeability coefficient of a water layer of the same thickness as the thylakoid membrane.

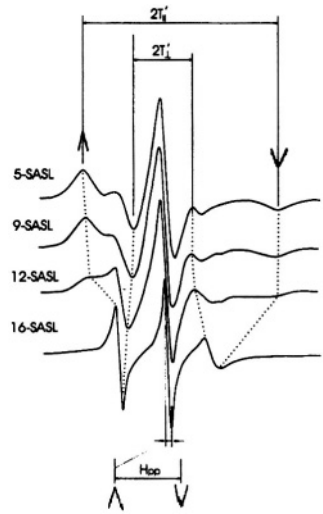

Figure 12. EPR spectra of doxylstearic acid spin labels (5-, 9-, 12- and 16-SASL) in thylakoid membranes recorded at 20°C for samples equilibrated with nitrogen. Peak-to-peak central linewidths were recorded with expanded abscissa (magnetic field scan range by a factor of 10).

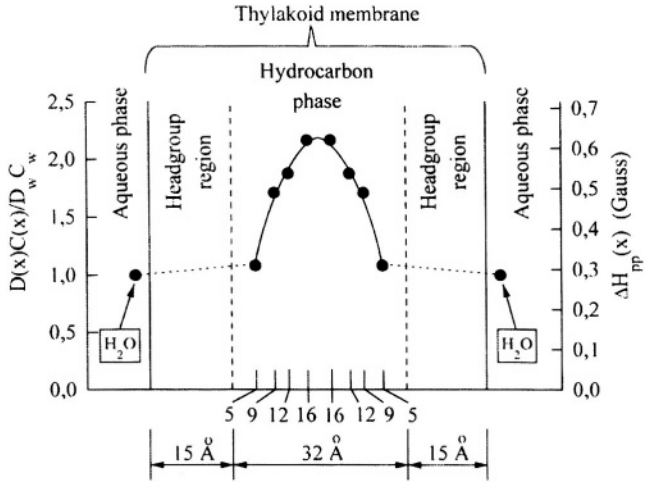

Figure 13. Profile of the relative oxygen diffusion-concentration product (or oxygen-induced EPR line broadening) across a thylakoid membrane at 20°C. Approximate locations of nitroxide fragments of spin labels are indicated by arrows. Data for the aqueous environment (indicated by H_2O), were obtained with 16-SASL, which at pH 9.5 is fairly soluble in water. Data points represent mean +/- S.D. (n = 4) (from Ligeza *et al.,* 1998).

3.1.3 Oxygen concentration difference across the thylakoid membrane

Knowledge of the oxygen permeability coefficient and the rate of oxygen production by functioning leaf chloroplasts illuminated with saturating actinic light allowed Ligeza *et al.* (1998) to calculate the possible light-induced oxygen concentration gradients across the thylakoid membrane. If a thylakoid was considered an oxygen-transparent sphere (Fig. 14A), the concentration difference was ~5 nM. However, under normal physiological conditions, thylakoids of grana, which contain water-splitting complexes, represent compressed disk-like vesicles. In this case, oxygen diffusion should proceed predominantly through the narrow side surface of the disk exposed to the stroma (Fig. 14B). The oxygen concentration difference was calculated as ~0.1 μM in this situation. Thus, the oxygen gradient across the thylakoid appears to be negligible.

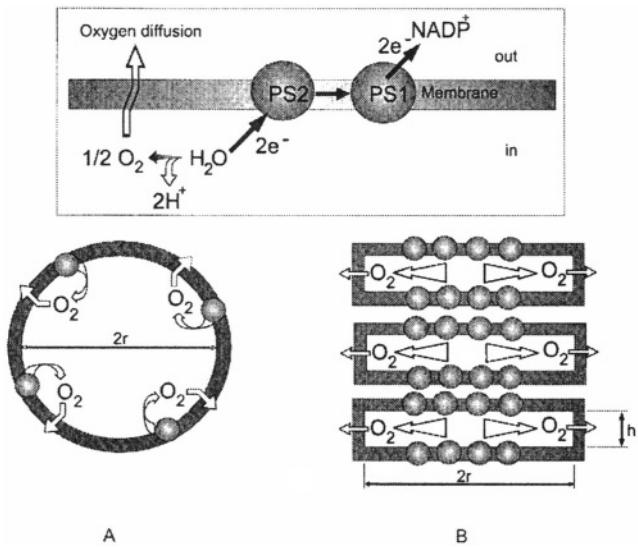

Figure 14. Top: Schematic representation of non-cyclic electron transport in the thylakoid membrane and transmembrane diffusion of oxygen produced by the PS2 water-splitting complex. Bottom: Schematic of the thylakoid assuming a spherical shape (A) or as a disc-like vesicle (B). Dimensions used for calculation of the oxygen concentration difference across the thylakoid membrane are indicated.

Thylakoid membranes belong to a group of protein-rich membranes with a typical protein-to-lipid ratio (w/w) of 1.5 (Quinn and Williams, 1983). Because integral membrane proteins (Altenbach *et al.,* 1990; Subczynski *et al.,* 1992b) are rather impermeable to oxygen, the photoinduced oxygen concentration difference across the thylakoid membrane can be increased

several times by a factor proportional to the ratio of the surface area of thylakoid to the surface area of its lipid bilayer portion. With this correction, Ligeza *et al.* (1998) concluded that the oxygen concentration difference generated by illumination of the leaf should be negligible (less than 1 μM). Similarly, evaluations presented by Subczynski *et al.* (1991; 1992a), based on the measured oxygen membrane permeability coefficient show that oxygen concentration differences across mammalian cell plasma membranes and mitochondrial membranes are also in the nanomolar region.

3.2 Oxygen concentration in the suspension of isolated chloroplasts using microscopic spin-label probe

Ligeza *et al.* (1992; 1994) used a newly developed spin-label oximetry approach with BSA-coated paraffin oil particles containing a cholestane spin label (CSL) as a microscopic probe. The amplitude of the EPR signal from CSL measured at a saturating microwave power was used as an oxygen sensitive parameter. This microscopic probe brought new advantages, facilitating its application to studying photochemically active photosynthetic systems. Because it is water insoluble, CSL has an extremely low rate of exchange (through the water bulk phase) between paraffin oil particles and other hydrophobic regions of biological systems (Schreier *et al.,* 1978), as compared to SASL spin labels used for preparation of other microscopic spin-label probes (Liu *et al.,* 1994). The method's sensitivity is increased due to: (1) a high T_1 value of CSL (Kusumi *et al.,* 1982), (2) a favorable partition coefficient of oxygen in paraffin oil (Linke, 1965), and (3) the use of a hydrocarbon solvent of comparable (or larger) molecular weight than that of spin label. The latter results in a favorable relationship between the rate of the translational and rotational diffusions of the spin label and oxygen. Oxygen diffuses in this medium as readily as in water (Subczynski and Hyde, 1984). On the other hand, the rate of CSL translational diffusion is expected to significantly decrease, while rotational diffusion of CSL in the paraffin oil medium is relatively fast. With decreased CSL-CSL collision, a high concentration of spin label (e.g., 2×10^{-2} M) can be used without significant line broadening effects. At low microwave power, oxygen does not affect the EPR signal amplitude of CSL in paraffin oil particles. However, at saturating microwave power (200 mW), the EPR signal amplitude increases when oxygen concentration rises.

Using this method, Ligeza *et al.* (1994) demonstrated the ability to monitor the kinetics of light induced changes in oxygen concentration in the dense suspension of chloroplasts isolated from bean leaves (*Vicia faba*) in the presence of the electron mediator methylviologen. Switching on the white light induced fast oxygen consumption, using up all the oxygen within a few seconds. This was indicated by an immediate decrease in the

amplitude of the EPR signal from CSL (curve 2 in Fig. 15). The drop in oxygen concentration at the initial stages of chloroplast illumination is a reversible process: after turning off the illumination, the amplitude of the EPR signal increased, indicating a restoration of oxygen in the chloroplast suspension. The process of oxygen recovery in the dark may be accounted for by superoxide dismutase and catalase reactions. The rise in oxygen concentration in the dark indicates the presence of significant amounts of superoxide radicals and hydrogen peroxide, which can be a source for oxygen production because of superoxide dismutase and catalase reactions. The lack of corresponding light-induced changes in the CSL signal at low microwave power demonstrates that there are no light-induced changes in CSL concentration (curve 1 in Fig. 15). Reversible changes in amplitude of the EPR signal corresponding to fast light-induced oxygen consumption and its production in the dark can be repeated several times (curve 2 in Fig. 15). After lengthy illumination, however, the ability of chloroplasts to regenerate oxygen in the dark disappears. At this stage, essential exhaustion of oxygen takes place, which is accompanied by the loss of CSL paramagnetism. This can be seen by a decrease in the amplitude of the EPR signal recorded at both low and high microwave power (curves 1 and 2 in Fig. 15). Kinetic behavior of the light-induced EPR signal from P_{700}^{+} correlates with the behavior of the EPR signal from CSL. Concomitant with the essential disappearance of oxygen (curve 2 in Fig. 15) is a decrease in the concentration of oxidized centers P_{700}^{+} (curve 3 in Fig. 15).

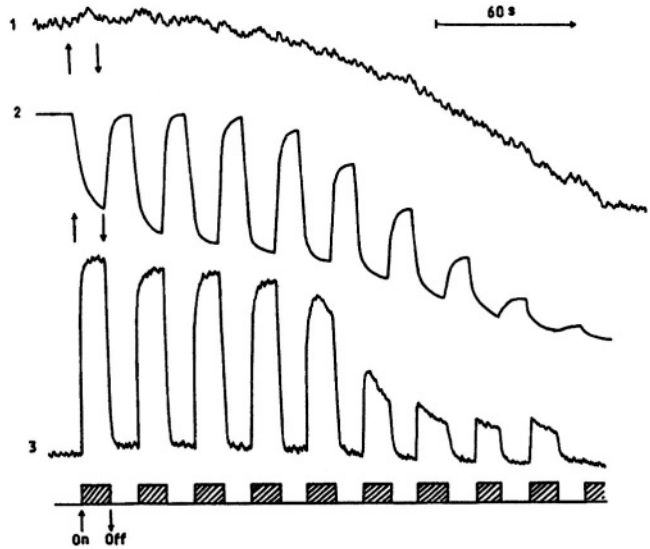

Figure 15. Kinetics of the light-induced changes in amplitude of the low-field peak of the EPR spectrum of CSL in paraffin oil particles in a suspension of bean chloroplasts. (1) Microwave power 1 mW; (2) microwave power 200 mW. (3) Kinetics of the light-induced changes in the amplitude of the EPR signal from oxidized reaction center P_{700}^{+} (from Ligeza *et al.,* 1994).

This new approach to spin-label oximetry appears to be fruitful for studying light-induced modulation of oxygen concentration in photosynthetic systems. In a concentrated suspension of chloroplasts, application of the molecular spin-label probe method based on measurements of EPR signal amplitude (Strzalka *et al.,* 1986; 1990; Belkin *et al.,* 1987) or using the superhyperfine structure parameter of the EPR spectra of spin probe CTPO (Subczynski *et al.,* 1990), is limited due to the fast chemical reduction of nitroxide radicals. The main advantage of the microscopic spin-label probe approach is the relatively high protection of spin probe molecules from the action of chemically active metabolites. However, it should be noted here that the time-resolved EPR oximetry approach developed by Strzalka *et al.* (1986; 1990) has been successfully used to determine the oxygen release kinetics in spinach thylakoids and PS2 membranes (Razeghifard and Pace, 1997; 1999). They observed the oxygen release kinetics with a half-life of ~0.85 ms and ~1.45 ms for thylakoids and PS2 membranes, respectively. These results clearly show that oxygen release is retarded in detergent-solubilized PS2 membranes in comparison to thylakoids as native physiological samples.

3.3 Light-induced production and consumption of oxygen by chloroplasts *in situ*

Incomplete reduction of oxygen by the chloroplast and mitochondria electron transport chains leads to formation of superoxide radicals and hydrogen peroxide (Harbour and Bolton, 1975; Asada and Takahashi, 1987). Additionally, in chloroplasts, the interaction of molecular oxygen with triplet state photoreaction centers results in the production of highly reactive singlet oxygen (Macpherson *et al.,* 1993), which is responsible for the photodestruction of pigments and degradation of chloroplast proteins (Vass *et al.,* 1992; Aro *et al.,* 1993). An increase in the concentration of oxygen as a result of chloroplast functioning should stimulate the formation of these active forms of oxygen, and thus could provoke substantial injuries in the energy transducing apparatus of these organelles. This has been well documented in the case of chloroplasts and mitochondria functioning *in vitro* (Vass *et al.,* 1992; Aro *et al.,* 1993). It was also shown that under certain conditions, a light-induced, supersaturated oxygen concentration can be created in the aqueous solution surrounding cyanobacteria, which leads to photo-induced damage to both photosynthesis and respiration (Belkin *et al.,* 1987). The question remains, however, whether oxygen produced by chloroplasts in a plant cell can be accumulated inside the leaf to a concentration so high it could be considered dangerous.

3.3.1 The use of paraffin oil particles

The application of paraffin oil particles described in the previous section for monitoring oxygen production in the interior of a bean leaf has had limited success (Ligeza *et al.,* 1994). Figure 16 demonstrates a typical pattern of light-induced response in an EPR signal from CSL in a bean leaf, recorded at room temperature. For a signal recorded at high microwave power, switching on a white light induces an increase in signal amplitude caused by oxygen production in the leaf (stage A-B-C). The drop in signal amplitude observed after stopping the illumination can be explained by oxygen consumption from certain metabolic processes, as well as by diffusion of oxygen from the leaf tissue into the atmosphere (stage C-D). The subsequent rise in signal amplitude (stage D-E) may be accounted for by oxygen production from the reaction of catalase with H_2O_2. Hydrogen peroxide that accumulates in the leaf because of light-induced oxygen reduction by chloroplasts could partly compensate for oxygen consumption in the dark. There is unambiguous evidence that the changes in oxygen concentration, and not changes in nitroxide radical concentration, cause the variation in EPR signal amplitude from CSL. This stems from the fact that the fast light-induced response of the EPR signal is detected only at high microwave power (curve 1, Fig. 16), and is absent at low power (curve 2, Fig. 16). The light-induced oxygen release exhibits an overshoot (stage A-B-C of curve 1, Fig. 16) that correlates with the well-known nonmonotonous behavior of the PS1 reaction center, P_{700} (Tikhonov and Ruuge, 1975; Tikhonov *et al.,* 1981; Andreeva and Tikhonov, 1983; Ryzhikov and Tikhonov, 1988).

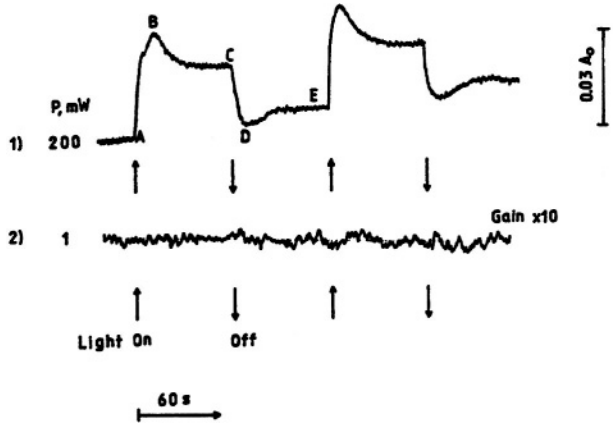

Figure 16. Kinetics of the light-induced changes in the amplitude of the low-field peak the EPR spectrum of CSL in paraffin oil particle emulsion injected into a bean leaf of (1) microwave power 200 mW, (2) microwave power 1 mW. A_0, the amplitude of the low-field peak of the EPR spectrum in the dark for a sample equilibrated with a gas mixture of 30% air and 70% nitrogen (from Ligeza *et al.,* 1994).

The light-induced amplitude increase of the CSL EPR signal was transformed into changes in the oxygen partial pressure by using the calibration curve presented by Ligeza *et al.* (1994). It follows that light induces only a very small increase in average oxygen partial pressure inside the leaf – about 7 mmHg – which corresponds to the increase in oxygen concentration in water of about 10 μM. It should be noted that to monitor oxygen evolution inside a leaf, an emulsion of BSA-coated paraffin particles containing CSL was injected into the leaf through the midrib with the help of a micro-syringe. EPR measurements were performed just after injection, and water filling the intercellular compartments of the leaf had no time to evaporate.

3.3.2 The use of fusinite

In 1997, Ligeza *et al.* used a new microscopic probe method that has also been used for monitoring oxygen in animal tissues (Swartz *et al.,* 1991; Liu *et al.,* 1993). The method is based on the use of small solid-state paramagnetic particles (a coal derivative called fusinite, Swartz *et al.,* 1991) with EPR spectra that depend on oxygen concentration. Ligeza *et al.* (1997) used small fusinite particles injected into bean leaves to monitor oxygen production and consumption by chloroplasts and mitochondria *in situ.* The main advantages of this approach are: (1) high sensitivity of the EPR spectrum (narrow singlet line) given by a coal particle to changes in oxygen partial pressure; (2) chemical and structural stability of this oxygen probe (paramagnetic fragments in the bulk of a coal particle are well-protected from redox transformations and other side effects, such as the influence of paramagnetic metal ions, pH, etc.); (3) independence of the EPR signal response to changes in oxygen partial pressure on the solvent surrounding the fusinite particles; and (4) the lack of toxic effects of coal particles on biological tissues.

Ligeza *et al.* (1997) monitored the photosynthetic oxygen production and respiratory oxygen consumption in the interior of a bean leaf by following the amplitude of the EPR spectra of fusinite particles injected into a leaf (Fig. 17, curves A and C) or placed on the surface of the control sample of a bean leaf (without fusinite, Fig. 17, curve B). All EPR measurements were made for a low microwave power at which the increase of oxygen partial pressure leads to line broadening of the EPR spectrum of fusinite particles and a corresponding decrease in its amplitude. The explicit decrease in oxygen concentration due to respiration in the dark, and light-induced oxygen production were observed only in the case of the closed, water-filled chamber that prevented oxygen exchange with the surrounding atmosphere (Figs. 17A and B). Using the calibration curves of Ligeza *et al.* (1997), it was calculated that the decrease in EPR signal magnitude corresponds to a

two-fold increase in the concentration of oxygen after 5 min of illumination. For dark-adapted leaves, production of oxygen after the first illumination (curve 1) becomes visible only after a lag-phase (about 2 min), while the second illumination (curve 2) results in immediate production of oxygen. This difference reflects the well-known regulatory phenomenon of the light-induced transition of photosynthetic apparatus in intact leaves from State 1 (dark-adapted leaf) to State 2 (a leaf after illumination) (Allen, 1992; McCormac *et al.,* 1994). The similarity in time-courses of the light-induced changes in the EPR signal amplitude presented in Fig. 17A (fusinite inside the leaf) and in Fig. 17B (fusinite outside the leaf) demonstrates that injection of a fusinite suspension does not inhibit metabolic activity of plant cell mitochondria and chloroplasts.

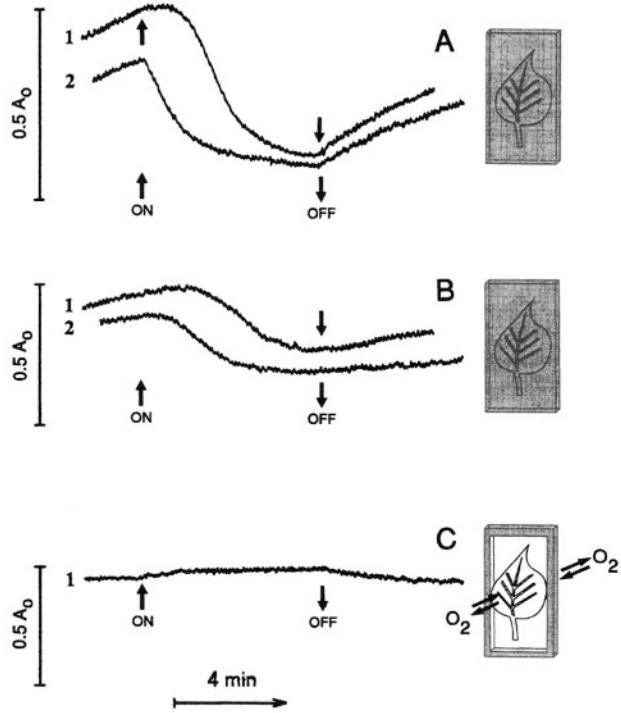

Figure 17. Typical patterns of the time-courses of light-induced changes in EPR signal amplitude from fusinite particles injected into a leaf (A,C) or placed on the leaf surface (B). Curves 1 and 2 correspond to the first and second illumination cycles, respectively. Before the first illumination, the sample was adapted to the dark for about 30 minutes. Each curve 2 is a continuation of the corresponding curve 1. A_0 is the amplitude of the EPR spectrum of fusinite injected into the leaf and equilibrated with air. The drawing at right shows whether the leaf (4 mm × 5 mm piece) is in a closed or open chamber (from Ligeza *et al.,* 1997).

Under normal physiological conditions, however, when the sample is exposed to air (the leaf in the open holder), no significant changes in the level of oxygen partial pressure inside the leaf, either in the dark or during illumination, were observed (Fig. 17C). The EPR measurements in Fig. 17C were performed 24 hours after fusinite injection, so that the excess water injected into the intercellular compartments of the leaf had enough time to evaporate. Had EPR measurements been performed immediately after injection of the fusinite suspension, as was the case with the measurements using the microscopic water-soluble probe (CSL containing BSA coated paraffin oil particles, Ligeza *et al.,* 1994), a small, light-induced accumulation of oxygen inside the leaf would have been recorded. This indicates that the water filling the intracellular compartments imposes a substantial barrier to oxygen diffusion. The diffusion coefficient for oxygen in water is substantially smaller (about 10,000 times) than in air. Under normal physiological conditions, intensive production of oxygen by chloroplasts is compensated by the fast efflux of oxygen from the leaf to the surrounding atmosphere and very fast long distance diffusion of oxygen from chloroplasts to the leaf stomata that occur through the water-free intercellular compartments of the leaf interior. As has been described above, the thylakoid membranes of chloroplasts as well as other lipid bilayer membranes are not barriers to oxygen transport (see Subczynski and Hyde, 1998, for review). This observation has led to the conclusion that the ventilation of the leaf interior appears to be sufficient for maintaining oxygen partial pressure at practically the same level, both in the dark and in the course of intensive light-induced production of oxygen by chloroplasts. Such good ventilation should protect leaf tissues from dangerous increases in the level of oxygen evolved by chloroplasts.

This does not mean that the functioning of the photosynthetic apparatus of chloroplasts will not produce the toxic forms of oxygen (superoxide radicals, hydrogen peroxide) that can arise due to oxygen interaction with reduced electron transport carriers. An increased steady-state yield of toxic forms of oxygen could be expected because of the light-induced increase in oxygen concentration. However, the high permeability of thylakoid membranes to oxygen and the good ventilation of the leaf interior will mediate the increase in oxygen concentration and diminish the production of dangerous active forms of oxygen.

4. USE OF SPIN LABELS TO STUDY STRUCTURE-FUNCTION RELATIONSHIPS IN CHLOROPLASTS.

Lipid soluble spin labels have been widely used to study relationships between the structural properties of thylakoid membranes and their functional characteristics (Torres-Pereira *et al.,* 1974; Murata and Fork, 1976; Murata and Ono, 1979; Subczynski *et al.,* 1975, 1976; Ruuge *et al.,* 1977a, 1977b; Tikhonov and Ruuge, 1978; Tikhonov *et al.,* 1980a, 1980b, 1982, 1983, 1984; Fork *et al.,* 1979; Lutova and Tikhonov, 1983b; Timoshin *et al.,* 1984; Li *et al.,* 1989; Golovina *et al.,* 1997; Vogg *et al.,* 1998; Kota, 1999; Navair-Izzo, 2000; Calucci *et al.,* 2001; Quartacci *et al.,* 2000; Yruela *et al.,* 2001; Kota *et al.,* 2002a; for reviews, see Berliner, 1976; Marsh, 1981; Kocherginski and Swartz, 1995). Along with fluorescent dyes (Osváth *et al.,* 2001; Teuber *et al.,* 2001), lipid-soluble spin labels can be used as molecular probes for testing the physical properties and structural changes in the lipid domains of chloroplast membranes. One of most important advantages of using nitroxide radicals as molecular probes for photosynthetic membranes is that the EPR spectra of spin labels are usually not masked by the EPR spectra of the electron transport components. Site-specific spin labeling has been used to get inside the membrane proteins of energy-transducing membranes (Altenbach *et al.,* 1990; Vogel, 2000; for a review, see Feix and Klug, 1998; Cafiso, 2002). In this section, we will consider the application of lipid-soluble spin labels to the study of structural changes in the lipid domains of thylakoid membranes that control rates of electron transport and ATP synthesis in chloroplasts of higher plants. Among different types of lipid-soluble nitroxide radicals, the derivatives of stearic acid (SASLs) are the most convenient probes for testing structural changes in thylakoid membranes.

4.1 Interaction of nitroxide radicals with the chloroplast electron transport chain.

The use of nitroxide radicals as membrane probes is often complicated by their relatively high chemical reactivity (see for review Kocherginski and Swartz, 1995). It is well known that spin labels can interact with the chloroplast ETC and lose their paramagnetic properties (Maruyama and Ohnishi, 1974; Subczynski *et al.,* 1975; Ruuge *et al.,* 1977a; 1977b). This 'negative' property of spin labels, however, turns out to be a useful instrument for studying the electron transport processes in chloroplasts. It is not surprising, therefore, that both properties of spin labels, the sensitivity of their EPR spectra to environment changes and the chemical reactivity of

nitroxide radicals, are used to investigate structure-function relationships in chloroplast membranes (Ruuge *et al.,* 1977a; 1977b; Tikhonov *et al.,* 1978; 1980a; 1980b; for a review of earlier works see Kukushkin and Tikhonov, 1988). Below we will consider some biochemical aspects of the nitroxide radical interactions with thylakoid membranes.

4.1.1 Light-induced redox changes of nitroxide radicals

A general scheme of the interaction of nitroxide radicals with the chloroplast ETC is presented in Fig. 18. This model is based on an inhibitory analysis of the light-induced redox changes of spin labels with paramagnetic groups localized in different regions of the thylakoid membrane or in an aqueous phase outside the thylakoids (Ruuge *et al.,* 1977a). There are good reasons to believe that the loss of spin label paramagnetism is determined mainly by the reduction in the nitroxide radicals rather than their oxidation. For water-soluble spin labels localized outside the thylakoids, nitroxide radical reduction is caused by their interaction with the electron donors on the acceptor side of PS2. Inhibitor analysis shows that the plastosemiquinone $Q_A^{\bullet}$ can donate an electron to nitroxide radicals (Ruuge *et al.,* 1977b, Khomutov *et al.,* 1981). Figure 18 shows that DCMU, an inhibitor of electron flow from the primary quinone $Q_A^{\bullet}$ to the secondary quinone Q_B, essentially increases the rate of 2,2,6,6-tetramethylpiperidine-1-oxyl (TEMPO) reduction when it is added at concentrations sufficient to inhibit electron flow from PS2 to P_{700}^{+}. Stimulation of TEMPO reduction by DCMU (Khomutov *et al.,* 1981) can be explained by accumulation of $Q_A^{\bullet}$ radicals due to the inhibition of $Q_A^{\bullet}$ oxidation by the secondary quinone Q_B. Only at fairly high concentrations of DCMU, which completely inhibit the operation of PS2 due to its action on the donor side of the water-splitting complex (Vermaas and Govindjee, 1981), is the light-induced reduction of TEMPO suppressed (Fig. 18). The electron flow inhibitor DBMIB, which prevents oxidation of the plastoquinol pool by the b/f-complex, insignificantly effects the light-induced reduction of TEMPO (Khomutov *et al.,* 1981). These results show that electron carriers reduced on the acceptor side of PS2 serve the role of electron donors to nitroxide radicals. The acceptor side of PS1 may be another site of the nitroxide reduction by chloroplast's ETC.

Light-induced re-oxidation of previously reduced nitroxide radicals, i.e., diamagnetic hydroxylamines, was observed in experiments with the lipid-soluble spin labels (SASLs) with free-radical fragments that are buried in the depth of the thylakoid membrane. According to (Ruuge *et al.,* 1977a; 1977b; for a review see Kocherginsky and Swartz, 1995), the reoxidation of lipid-soluble spin labels is determined by electron transfer from hydroxyl-amines to oxidized high-potential electron carriers of bf-complexes (Fe-S

Rieske center and cytochrome f) and/or plastocyanine. Illumination of chloroplasts with a far-red light ($\lambda > 700$ nm), which predominantly excites PS1, causes oxidation of electron carriers between two photosystems. This process is accompanied by a reoxidation of the hydroxylamine groups of SASLs (Subczynski *et al.,* 1975; Ruuge *et al.,* 1977a). The rates of both reactions, reduction and reoxidation of the lipid-soluble spin labels, are determined by the accessibility of the nitroxide radicals to the electron carriers and mobility of the oxazolidine free-radical fragments within the membrane. It has also been shown that the rate of light-induced reduction of water soluble spin labels correlates with the physical state (fluidity) of the thylakoid membrane that could determine the accessibility of the membrane donors to spin label molecules (Khomutov *et al.,* 1981).

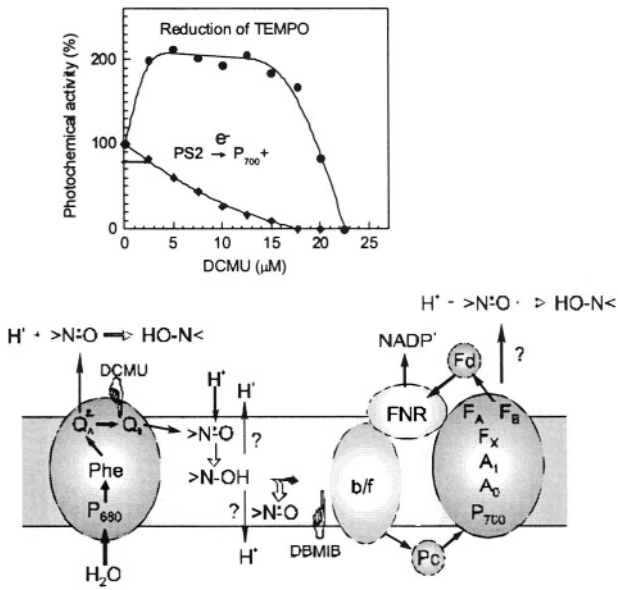

Figure 18. Spin label redox changes due to nitroxide interactions with the chloroplast electron transport chain. Top box shows the influence of DCMU on the partial photochemical reactions in chloroplasts: the photochemical activity of PS2 (determined as a number of electrons transferred to P_{700}^{+} in response to a short light pulse), and the rate of TEMPO reduction by chloroplasts (adopted from Khomutov *et al.,* 1981).

4.1.2 Influence of spin labels on photochemical activity of chloroplasts

It is noteworthy that the use of SASLs for testing the photochemical activity of chloroplasts or probing membrane conformation and dynamics

requires caution in the interpretation of experimental data. It has been demonstrated that lipid soluble spin labels can act as an efficient uncoupler of photophosphorylation in chloroplasts and other energy-transducing organelles (see Kocherginsky and Swartz, 1995, for a review). However, systematic study of their perturbing effect in chloroplast membranes is very limited (Tsapin *et al.,* 1974; Vozvishaeva *et al.* 1974). Recently, the effects of nitroxide radicals on electron transport, proton uptake and photophosphorylation in bean chloroplasts and their dependence on the radical position in the lipid bilayer of the thylakoid membrane were studied (Wasniowska *et al.,* 2002). Figure 19 shows the dependence of light-induced uptake of protons (ΔH^+), the rate of ferricyanide reduction (J_e), and the rate of ATP synthesis (J_{ATP}) on concentrations of SASL, stearic acid and the water-soluble spin label TEMPOL (4-hydroxy-2,2,6,6-tetramethylpiperidine-1-oxyl). Addition of SASLs decreases the uptake of protons (Fig. 19A) and stimulates electron flow (Fig. 19B). The effect depends on the concentration of SASLs and the position of the nitroxide moiety along the acyl chain.

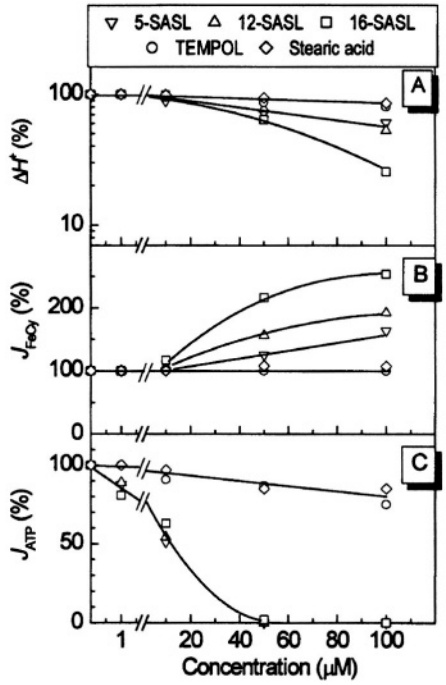

Figure 19. Effects of SASLs on light-induced uptake of protons, ΔH^+, by chloroplasts (A), the rate of electron transport from water to artificial electron acceptor ferrycynide ions, J_{FeCy} (B), and the rate of ATP synthesis in bean chloroplasts (C) (from Wasniowska *et al.,* 2002).

The difference in efficiencies of 5-, 12-, and 16-SASL can be explained by the differing mobilities of their nitroxide radical fragments within the thylakoid membrane. It is well known that 16-SASL exhibits the highest rotational motion, wobbling and rate of vertical displacement in the lipid domain of membranes compared to 5-SASL and 12-SASL (Yin and Subczynski, 1996). SASLs cause much stronger inhibitory effects on the rate of ATP formation than on proton uptake and the rate of electron transport. ATP synthesis is completely inhibited at low concentrations of SASL in chloroplast suspension (≈ 0.05 mM), while light-induced uptake of protons is reduced only by 20-30%. Neither stearic acid nor the water-

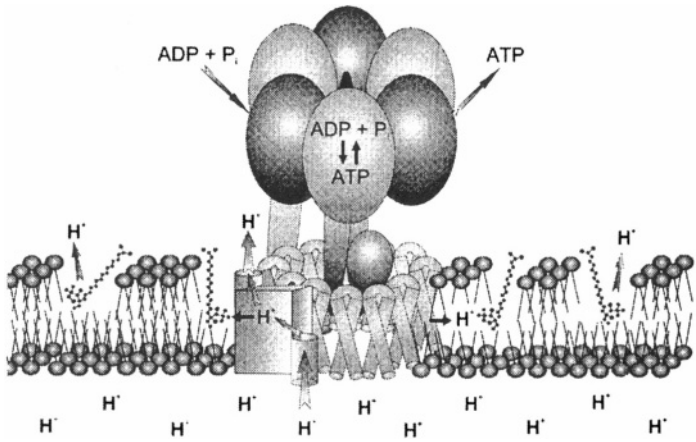

Figure 20. Tentative uncoupling action of SASLs due to direct interaction of the nitroxide radical with the membrane sector of the ATP synthase (from Wasniowska *et al.,* 2002).

soluble spin label TEMPOL cause inhibition of photophosphorylation at this concentration. Water soluble spin labels (TEMPOL and TEMPAMINE), have lower effects on ATP synthesis than SASLs have. This indicates that SASLs can interact directly with the ATP synthase. It is suggested that the uncoupling effects of SASLs are realized by the interaction of nitroxide radicals with the membrane sector (CF_0) of the ATP synthase by providing a direct escape route for protons from the core of the coupling membrane (Fig. 20).

4.2 Thermoinduced regulation of photosynthetic processes in chloroplasts

There are a great number of publications exploring the relationships between the physical state of biological membranes and the activity of membrane enzymes in biochemical and physiological processes. The

relationship between the structural characteristics of the lipid domains of thylakoid membranes and photosynthetic activity of chloroplasts has been a subject of intensive experimental study (see Berry and Björkman, 1980, and Albertsson, 1995, for reviews). A large body of information regarding the role of the physical state of membrane lipids in regulating photosynthetic processes has come from comparative studies of the temperature dependencies of thylakoid membrane fluidity and partial reactions of photosynthetic electron transport (see Fork *et al.,* 1979; Gounaris *et al.,* 1984; Kukushkin and Tikhonov, 1988; Kocherginski and Swartz, 1995; Vogg *et al.,* 1998; Kota, 1999; Calucci *et al.,* 2001; Quartacci *et al.,* 2000; Yruela *et al.,* 2001; Kota et al, 2002b, for references). One way to show a tight relationship between the physical state of membrane lipids and the functional characteristics of chloroplasts is by comparison of the temperature dependencies of SASL behavior and the rates of electron transport in chloroplasts measured by EPR. EPR techniques provide efficient tools for investigating electron transport in chloroplasts by measuring the kinetics of the light-induced redox transients of the reaction center P_{700} (Tikhonov *et al.,* 1981; Blumenfeld and Tikhonov, 1994).

The plastoquinone molecule is a mobile electron and proton carrier that provides linkage between PS2 and the bf-complex, and performs translocation of protons into the thylakoid (Fig. 2). Oxidation of plastoquinol by a bf-complex is the rate-limiting step in the chain of electron transport between two photosystems (Stiehl and Witt, 1969; Witt, 1979). It is not surprising that thermoinduced changes in the physical state of thylakoid membranes can influence the mobility of plastoquinone and its interaction with PS2 and bf-complexes. In order to illustrate the role of thermoinduced structural changes in thylakoid membranes in regulating chloroplast photochemical activity, one may compare the temperature dependencies of the electron flow rate between two photosystems and the lipid domain fluidity in thylakoid membranes. Figure 21 demonstrates the temperature dependence of the characteristic time of electron flow between two photosystems, $\tau_{1/2}$, determined by the EPR method from the kinetics of P_{700}^{+} reduction, and the order parameter *S* for 5-SASL (Tikhonov and Ruuge, 1978; Tikhonov *et al.,* 1980a; 1980b; 1981; 1982; 1983; Timoshin *et al.,* 1984). Parameter $\tau_{1/2}$ was determined as a half time of P_{700}^{+} reduction in response to short pulses of white light. A plot of the temperature dependence of the kinetic parameter $\tau_{1/2}$ reveals clearly expressed inflection, demonstrating that the rate of electron transport sharply increases with a rise in temperature up to the inflection point temperature, T_0, but remains almost the same at higher temperatures. It is important to note that the characteristic temperatures T_0 determined from the plot for the 'kinetic' parameter $\tau_{1/2}$ always fall in a relatively narrow temperature interval where the temperature dependence of the 'structural' parameter *S* also shows

characteristic breaks. This result has been interpreted in terms of membrane fluidization with the rise of temperature. According to Tikhonov *et al.* (1983), the size of 'fluid' domains in the thylakoid membrane increases with the temperature rise, accelerating the plastoquinone turnover between PS2 and the bf-complex. At high enough temperatures ($T \geq T_0$), when the main body of the lipid domain in the thylakoid membrane is already in the 'fluid' state, the temperature increase does not cause further acceleration of electron transport from PS2 to P_{700}^+. Thermoinduced structural changes in thylakoid membranes determined with 5-SASL are also detected by other SASL

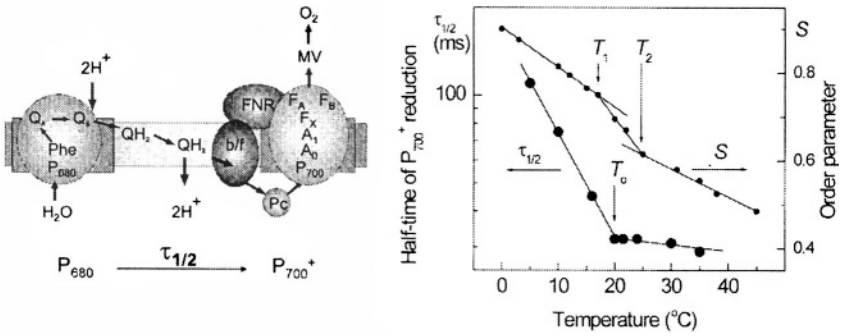

Figure 21. Temperature dependencies of the characteristic time $\tau_{1/2}$ of electron transport between two photosystems and the order parameter *S* of 5-SASL in the thylakoid membranes of bean chloroplasts (adopted from Tikhonov and Ruuge, 1978). Kinetic parameter $\tau_{1/2}$ was determined as a half-time of the reduction of oxidized reaction centers P_{700}^+ in response to the actuation of PS 1 reaction centers P_{680} by the short light pulse (7 μs).

molecules characterized by different positions of the nitroxide radical along the hydrocarbon chain (see Kukushkin and Tikhonov, 1988). Comparison of the behavior of SASLs in thylakoid membranes to their mobility in other biological membranes and model lipid systems permits the conclusion that the characteristic breaks in the temperature dependencies of the 'structural' parameters (order parameter *S* or the rotational correlation time τ_c) indicate the thermoinduced transitions in the lipid domains of thylakoid membranes have a cooperative character.

Similar results regarding the structure-function relationships in thylakoid membranes were obtained when the ordering and mobility of SASLs in thylakoid membranes were compared to the rates of ATP synthesis in chloroplasts and proton efflux from the thylakoids (Tikhonov *et al.,* 1983; Timoshin *et al.,* 1984). It was shown that the temperature dependence of the rate of ATP formation in bean chloroplasts had a bell-like shape, with its maximum at the temperature that always coincided with the characteristic temperature T_0 of the structural transitions determined from the temperature dependence of the order parameter *S* for 5-SASL. A similar correlation was observed when thermoinduced structural changes in thylakoid membranes

were compared to the rate of proton leak from the thylakoid lumen. The characteristic temperature T_0 determined from the Arrhenius plots of 'structural' (order parameter S and rotation correlation time τ_c) and 'kinetic' (rates of electron and proton transport) parameters significantly changed with variations of plant growth conditions (e.g., a temperature in the greenhouse) or plant species. Chloroplasts isolated from plants grown at low temperatures demonstrated a shift in characteristic breaks in the Arrhenius plots for structural and kinetic parameters to lower temperatures compared to plants grown at higher temperatures (Fork *et al.,* 1979; Tikhonov *et al.,* 1978; 1980a; 1980b; 1982; 1983; Lutova and Tikhonov, 1983a). Such a correlation between the structural and kinetic parameters was observed for preparations of chloroplasts from different plant species. For instance, chloroplasts from melon leaves showed a higher break temperature (T_0 = 35°C) compared to chloroplasts from cucumber leaves (T_0 = 25°C), demonstrating a genetically-determined difference between heat-loving (melon) and cold-resistant (cucumber) plants (Lutova and Tikhonov, 1983b). In other words, with the help of lipid soluble spin labels, one can easily discriminate between chloroplasts isolated from the leaves of melon or cucumber.

Thus, the results of spin label studies of thermoinduced structural transitions in thylakoid membranes indicate that an adaptation in the photosynthetic apparatus of higher plants to changes in environmental temperature and light (Boardman, 1977; Berry and Björkman, 1980; Buchanan, 1981; Gounaris *et al.,* 1984; Leegood and Edwards, 1996, Allen and Ort, 2001) could be realized by fitting the fluidity of the lipid domains to an optimal level. Alterations in the membrane fluidity can be controlled by temperature-induced changes in the composition of unsaturated and saturated lipids in thylakoid membranes (Moon *et al.,* 1995; Nie and Baker, 1991; for references related to the mechanisms of cell adaptation to temperature variations, see Alexandrov, 1977, 1994). The influence of the physical state of lipids on the activity of membrane enzymes was demonstrated not only in chloroplasts, but also in other energy-transducing systems (see, for instance, Luzikov *et al.,* 1983, 1984; Mansurova *et al.,* 1984; Kocherginski and Swartz, 1995).

5. CONCLUDING REMARKS

In this chapter, we have considered three potential applications of spin labels to investigate the function of energy-transducing organelles of plant cells *in vitro* (isolated chloroplasts) and *in situ* (chloroplasts inside a leaf). The use of pH-sensitive spin labels (Section 2) clearly demonstrates the ability of spin labelling techniques to measure proton potential in

chloroplasts. Of course, there are certain difficulties when the spin labels are applied to investigate actively metabolizing biochemical systems that come mainly from the reactivity of nitroxide radicals. Nevertheless, in many cases pH-sensitive spin labels give some obvious advantages over conventional molecular pH-indicators, such as when the EPR spectra of spin labels are not masked by the EPR spectra of electron transport carriers. We hope that further achievements in the chemistry of nitroxide radicals will lead to production of a new collection of pH-sensitive spin labels that would be more protected from reducing agents. The review of spin-label oximetry methods in Section 3 shows that different kinds of paramagnetic probes can be used to monitor production and consumption of oxygen in the suspension of isolated chloroplasts and in intact photosynthetic systems such as inside a leaf. To our knowledge, paramagnetic probes are the only indicators that can be used to measure light-induced changes in the concentration of oxygen in a leaf interior. A brief review of applications of lipid soluble spin labels to investigate structure-function relationships in energy-transducing membranes (Section 4) demonstrates that the physical state of membrane lipids may be considered an important factor in regulating photosynthetic processes in chloroplasts. Additional progress could help determine the molecular mechanisms of photosynthetic adaptations to varying environment conditions. This will come from modern EPR techniques such as electron-electron double resonance, multifrequency EPR, saturation recovery EPR, and multiquantum EPR, all of which grew out of the work of Jim Hyde.

ACKNOWLEDGMENTS

This work was supported by grants RR01008, GM27665 and GM61236 from the National Institutes of Health of the USA (WKS), and grants 03-04-48981 from the Russian Foundation for Basic Research and grants 99-1086 and 01-0483 from the INTAS (ANT). The authors thank Dr. Christopher C. Felix, Medical College of Wisconsin, for critical reading of the manuscript and Beverly Ventura for her editorial assistance.

6. REFERENCES

Abrahams, J. P., Leslie, A. G. W, Lutter, R., and Walker, J. E., 1994, Structure at 2.8 Å resolution of F_1-ATPase from bovine heart mitochondria, *Nature* **370**:621-628.

Albertsson, P.-A., 1995, The structure and function of the chloroplast photosynthetic membrane – a model for the domain organization, *Photosynth. Res,* **46**:141–149.

Alexandrov, V.Ya., 1977, *Cells, molecules and temperature.* Springer-Verlag, New York.

Alexandrov, V.Ya., 1994, Functional aspects of cell response to heat shock, *Int. Rev. Cytol.,* **148**:171-227.

Allen, J. F., 1992, Protein phosphorylation in regulation of photosynthesis, *Biochim. Biophys, Acta* **1098**:275-335.

Allen, D. J., and Ort, D. R., 2001, Impact of chilling temperatures on photosynthesis in warm-climate plants, *TRENDS in Plant Science* **6**:36-42.

Altenbach, C., Marti, T., Khorana,H. G., and Hubbell, W. L., 1990, Transmembrane protein structure: Spin labeling of bacteriorhodopsin mutants, *Science* **248**:1088-1092.

Andreeva, A. S., and Tikhonov, A. N., 1983, Comparative study on the kinetics of electron transport and the slow chlorophyll fluorescence changes in bean leaves, *Photobiochem. Photobiophys.* **6**:261-266.

Aro, E.-M., Virgin, I., and Andersson, B., 1993, Photoinhibition of photosystem II. Inactivation, protein damage and turnover, *Biochim. Biophys. Acta* **1143**:113-134.

Asada, K., Takahashi, 1987, Production and scavenging of active oxygen in photosynthesis, in *Photoinhibition.* D. J. Kyle, C. B. Osmond, and C. J. Arntzen Eds., Elsevier, Amsterdam, 227-287.

Backhausen, J. E., Camillo Kitzmann, C., Horton, P., and Scheibe, R., 2000, Electron acceptors in isolated intact spinach chloroplasts act hierarchically to prevent over-reduction and competition for electrons, *Photosynth. Res.* **64**: 1–13.

Badger, M. R., 1985, Photosynthetic oxygen exchange, *Annu. Rev. Plant Physiol.* **36:**27–53.

Bamberger, E. S., Rottenberg, H., and Avron, M., 1973, Internal pH, **ΔpH,** and the kinetics of electron transport in chloroplasts, *Eur. J. Biochem.* **34**:557-563.

Barber, J., 1980, Membrane surface charges and potentials in relation to photosynthesis, *Biochim. Biophys. Acta* **594**:253-308.

Barber, J., 1982, Influence of surface charges on thylakoid structure and function, *Ann. Rev. Plant. Physiol.* **33**:261-395.

Belkin, S., Mehlhorn, R. J., and Packer, L., 1987, Determination of dissolved oxygen in photosynthetic systems by nitroxide spin-probe broadening, *Arch. Biochem. Biophys.* **252**:487-495.

Berg, S. P., and Nesbitt, D. M., 1979, Chromium oxalate: a new spin label broadening agent for use with thylakoids, *Biochim. Biophys. Acta* **548**:608-615.

Berg, S. P., Lusczakoski, D. M., and Morse II P.D., 1979, Spin label motion in the internal aqueous compartment of spinach thylakoids, *Arch. Biochem. Biophys.* **194**:138-148.

Berliner, L. J., *1976,* Spin Labeling: Theory and Applications. *Academic Press, New York.*

Berry, J. and Björkman, O., 1980, Photosynthetic response and adaptation to temperature in higher plants. *Annu. Rev. Plant. Physiol. 31:491–543.*

Blankenship, R.E., 2002, *Molecular Mechanisms of Photosynthesis.* Blackwell Science Inc., Malden, MA.

Blumenfeld, L. A., and Tikhonov, A. N., 1994, *Biophysical Thermodynamics of Intracellular Processes. Molecular Machines of the Living Cell.* Springer-Verlag, New York.

Boardman, N. K., 1977, Comparative photosynthesis of sun and shade plants, *Ann. Rev. Plant Physiol.* **28**:335 - 377.

Buchanan, B. B., 1981, Role of light in the regulation of chloroplast enzymes, *Ann. Rev. Plant Physiol.* **31**:341-374.

Cafiso, D. S., 1989, Electron paramagnetic resonance methods for measuring pH gradients, transmembrane potentials, and membrane dynamics, *Methods Enzymol.* **172**:331-345.

Cafiso, D. S., 2002, Peptide-membrane interactions determined using site-directed spin labeling, in *Current Topics in Membranes, V.52, Peptide-Lipid Interactions,* Simon, S.A., and Mclntosh, T.J., Eds., Academic Press, San Diego, San Francisco, New York, Boston, London, Sydney, Tokyo, 3-29.

Cafiso, D. S., and Hubbell, W. L., 1978a, Estimation of transmembrane pH gradients from phase equilibria of spin-labeled amines, *Biochemistry* **17**:3871-3877.

Cafiso, D. S., and Hubbell, W. L., 1978b, Estimation of transmembrane potentials from phase equilibria of hydrophobic paramagnetic ions, *Biochemistry* **17**:187-195.

Cafiso, D. S., and Hubbell, W. L., 1981, EPR determination of membrane potentials, *Annu. Rev. Biophys. Bioeng.* **10**:217-244.

Calucci, L. Navari-Izzo, F., Pinzino, C., Sgherri, C. L. M., 2001, Fluidity changes in thylakoid membranes of durum wheat induced by oxidative stress: A spin probe EPR study, *J. Phys. Chem.* **105**: 3127-3134.

Chan, H.-C., Glockner, J. F., and Swartz, H. M., 1989, Oximetry in cells and tissue using a nitroxide-liposome system, *Biochim. Biophys. Acta* **1014**:141-144.

Chapman, K. S. R., Berry, J. A., and Hatch, M. D., 1980, Photosynthetic metabolism in bundle sheath cells of the C_4 species *Zea mays:* source of ATP and NADPH and the contribution of photosystem II, *Arch. Biochem. Biophys.* **202**:330-341.

Dilley, R. A., 1991, Energy coupling in chloroplasts: a calcium gated switch controls proton fluxes between localized and delocalized proton gradients, *Curr. Top. Bioenerg.* **16**:265-318.

Dilley, R. A., Theg, S. M., and Beard, W. A., 1987, Membrane-proton interactions in chloroplasts bioenergetics: Localized proton domains *Ann. Rev. Plant Physiol.* **38**:347-368.

Edwards, G., and Walker, D. A., 1983, *C3, C4: Mechanisms, and Cellular and Environmental Regulation of Photosynthesis.* Blackwell, Oxford.

Feix, J. B., and Klug, C. S., 1998, Site-directed spin labeling of membrane proteins and peptide-membrane interaction, *in Biological Magnetic Resonance, Spin Labeling, The Next Millenium.* L. J. Berliner Ed., Plenum Press, New York, 251-279.

Fork, D., Murata, N., and Sato, N., 1979, Effect of growth tempertaure on the lipid and fatty composition, and the dependence on the temperature of light-induced redox reactions of cytochtome f and of light energy redistribution in the thermophylic blue-green alga *Sinechococcus lividus, Plant Physiol.* **63**:524-530.

Gilmiyarova, S. G., Khomutov, G. B., and Tikhonov, A. N., 1986, Surface potential of thylakoid membrane and the processes of energy transduction in chloroplasts. 1. Effects of surface potential modifiers, *Biological Membranes (USSR)* **3**:173-184.

Gilmiyarova, S. G., Masarova, M., and Tikhonov, A. N., 1985, Electron and proton transport coupling to photophosphorylation, and intramembrane localization of protons, *Biophysics (USSR)* **30**:709-710.

Glockner, J. F., Chan, H.-C., and Swartz, H. M., 1991, *In vivo* oximetry using a nitroxide-liposome system, *Magn. Reson. Med.* **20**:123-133.

Golovina, E. A., Tikhonov, A. N., and Hoekstra, F. A., 1997, An electron paramagnetic resonance spin probe study of membrane permeability changes with seed ageing, *Plant Physiol.* **114**:383-389.

Gounaris, K., Brain, A. P. R., Quinn, P. J., and Williams, W. P., 1984, Structural reorganization of chloroplast thylakoid membranes in response to heat-stress, *Biochim. Biophys. Acta* **766**:198–208.

Grucker, D., 2000, Oxymetry by magnetic resonance: applications to animal biology and medicine, *Progress Nucl. Magnet. Reson. Spectr.* **36**:241-270.

Halliwell, B., 1982, *Chloroplast Metabolism: The Structure and Function of Chloroplast in Green leaf Cell.* Clarendon Press, Oxford.

Haraux, F., and de Kouchkovsky, Y., 1998, Energy coupling and ATP synthase. *Photosynth. Res.* **57**:231-251.

Harbour, J. R., and Bolton, J. R., 1975, Superoxide formation in spinnage chloroplasts: electron spin resonance detection by spin trapping, *Biochem. Biophys. Res. Com.* **64**:803-807.

Hoefnagel, M. H. N., Atkin, O. K., and Wikich, J. T., 1998, Interdependence between chloroplasts and mitochondria in the light and dark, *Biochim. Biophys. Acta* **1366**:235-255.

Hyde, J. S., and Subczynski, W. K., 1989, Spin-label oximetry, in *Biological Magnetic Resonance. Vol. 8. Spin Labeling. Theory and Applications,* L. J. Berliner and J. Reuben, Eds., Plenum, New York, 399-425.

Jahns, P., Graf, M., Munekage, Y., and Shikanai, T., 2002, Single point mutation in the Rieske iron-sulfer subunit of cytochrome b_6/f leads to an altered pH dependence of plastoquinol oxidation in *Arabidopsis, FEBS Letters* **519**:99-102.

Jordan, P., Fromme, P., Witt, H.-T., Klukas, O., Saenger, W., and Krauß N., 2001, Three-dimentional structure of cyanobacterial photosystem I at 2.5 Å resolution, *Nature* **411**:909-917.

Junge, W., 1982, Electrogenic reactions and proton pumping in green plant photosynthesis, *Curr. Top. Membr. Transp.* **16**:431-463.

Kaim, G., and Dimroth, P., 1999, ATP synthesis by F-type ATP synthase is obligatorily dependent of the transmembrane voltage, *EMBO J.* **18**:4118-4127.

Khomutov, G. B., Barguth, S. A., Ryzhikov, S. B., and Tikhonov, A. N., 1989a, The interaction of manganese ions with the thylakoid membranes, *Plant Physiol. (USSR)* **36**:669-674.

Khomutov, G. B., Gilmiyarova, S. G., and Tikhonov, A. N., 1989b, Surface potential of thylakoid membrane and the processes of energy transduction in chloroplasts. 3. The light-induced pH changes in chloroplast suspension, *Biological Membranes (USSR)* **6:**995-1008.

Khomutov, G. B., Gilmiyarova, S. G., and Tikhonov, A. N., 1996, EPR study of surface potential and buffer capacity of thylakoid membranes, *Curr. Top. Biophys.* **20**:31-35.

Khomutov, G. B., Tikhonov, A. N., and Ruuge, E. K., 1981, Electron paramagnetic resonance study of electron transport in photosynthetic systems. 11. Effects of photosynthetic control: dependence of the rate of electron transport on the energization of bean chloroplast thylakoid membrane, *Mol. Biol. (USSR)* **15**:182-198.

Khramtsov, V. V., and Volodarsky, L. B., 1998, Use of imidazoline nitroxides in studies of chemical reactions: ESR measurement of concentration and reactivity of protons, thiols, and nitric oxide, in: *Biological Magnetic Resonance. Vol.14. Spin Labeling: The Next Millenium.* L. J. Berliner Ed., Plenum Press, New York, 1998,109-180.

Khramtsov, V. V., and Weiner, L. M., 1988, Proton transfer reactions in free radicals. Spin pH probes, *Russian Chemicals Reviews* **57**:824-839.

Khramtsov, V. V., Weiner, L. M., Eremenko, S. I., Belchenko, O. L, Schastnev, P. V., Grigor'ev, I. A., and Reznikov, V. A., 1985, Proton exchange in stable nitroxyl radicals of imidazoline and imidazolidine series, *J.Magn.Reson.* **61**:397-408.

Khramtsov, V. V., Weiner, L. M., Grigor'ev, I. A., and Volodarsky, L. B., 1982, Proton exchange in stable nitroxyl radicals. EPR study of the pH of aqueous solutions, *Chem. Phys. Lett.* **91**:69-75.

Kobayashi, Y., and Heber, U., 1994, Rates of vectorial proton transport supported by cyclic electron flow during oxygen reduction by illuminated intact chloroplasts, *Photosynth. Res.* **41**:419–428.

Kocherginski, N., and Swartz, H. M., 1995, *Nitroxide spin labels: reactions in biology and chemistry.* CRC Press, Boca Raton.

Kota, Z., Horvath, L. I., Droppa, M., Horvath, G., Farkas, T., and Pali, T., 2002a, Protein assembly and heat stability in developing thylakoid membranes during greening, *Proc. Nat. Acad. Sci. USA* **99**:12149-12154.

Kota, Z., Szalontai, B., Droppa, M., Horvath, G., and Pali, T., 2002b, The formation of the inverted hexagonal phase from thylakoid membranes upon heating, *Cel. Mol. Biol. Letts.* **7**:126-128.

Kota, Z., Szalontai, B., Droppa, M., Horvath, G., and Pali, T., 1999, Fourier transform infrared and electron paramagnetic resonance spectroscopic studies of thylakoid membranes, *J. Mol. Struct.* **481**:395-400.

Kramer, D. M., Sacksteder, C. A., and Cruz, J. A., 1999, How acidic is the lumen? *Photosynth. Res.* **60**:151-163.

Kukushkin, A. K., and Tikhonov, A. N., 1988, *Lectures on Biophysics of Plant Photosynthesis (in Russian).* Moscow State University Press, Moscow.

Kusumi, A., Subczynski, W. K., and Hyde, J. S., 1982, Oxygen transport parameter in membranes as deduced by saturation recovery measurements of spin-lattice relaxation times of spin labels, *Proc. Natl. Acad. Sci. USA* **79**:1854-1858.

Lai, C.-S., Hopwood, L. E., and Swartz, H. M., 1980, Electron spin resonance studies of changes in membrane fluidity of Chinese hamster ovary cells during the cell cycle, *Biochim. Biophys. Acta* **602**:117-126.

Leegood, R. C. and Edwards, G. E., 1996, Carbon metabolism and photorespiration: temperature dependence in relation to other environmental factors, in *Photosynthesis and the Environment,* Baker, N. R., Ed., Kluwer Academic Publishers, Dordrecht, 191–221.

Lehninger, A. L., Nelson, D. L., and Cox, M. M., 1993, *Principles of biochemistry.* Worth, New York.

Li, G., Knowles, P. F., Murphy, D. J., Nishida, I., and Marsh, D., 1989, Spin-label ESR studies of lipid-protein interactions in thylakoid membranes, *Biochemistry* **28**:7446-7452.

Ligeza, A., Tikhonov, A. N., and Subczynski, W. K., 1997, In situ measurements of oxygen production using paramagnetic fusinate particles injected into a bean leaf, *Biochim. Biophys. Acta* **1319**:133-137.

Ligeza, A., Tikhonov, A. N., Hyde, J. S., and Subczynski, W. K., 1998, Oxygen permeability of thylakoid membranes: Electron paramagnetic resonance spin labeling study, *Biochim. Biophys, Acta* **1365**:453-463.

Ligeza, A., Wisniewska, A., and Subczynski, W. K., 1992, Paraffin oil particles as microscopic probes for oxygen measurement in biological systems: ESR spin-label oximetry, *Curr. Top. Biophys.* **16**:92-98.

Ligeza, A., Wisniewska, A., Subczynski, W. K., and Tikhonov, A. N., 1994, Oxygen production and consumption by chloroplasts in situ and in vitro as studied with microscopic spin label probes, *Biochim. Biophys Acta* **1186**:201-208.

Linke, W. F., 1965, *Solubilities: Inorganic and metal organic compounds* II.4th ed. American Chemical Society, Washington, DC, 1233-1236.

Liu, K. J., Gast, P., Moussavi, M., Norby, S. W., Vahidi, N., Walczak, T., Wu, M., and Swartz, H. S., 1993, Lithium phthalocyanine: a probe for electron paramagnetic resonance oximetry in viable biological systems, *Proc. Natl. Acad. Sci. USA* **90**:5438-5442.

Liu, K. J., Greenstaff, M. W., Jiang, J. J., Suslick, K. S., Swartz, H. M., and Wang, W., 1994, In vivo measurement of oxygen concentration using sonochemically synthesized microspheres, *Biophys. J.* **67**:895-901.

Lolkema, J. S., Hellingwert, K. J., and Konigs, W. N., 1982, The effect of "probe binding" on the quantitative determination of the proton-motive force in bacteria. *Biochim. Biophys. Acta* **681**:85-94.

Lutova, M. I., and Tikhonov, A. N., 1983a, The comparison of two higher plant species regarding the resistance of Hill reaction to high temperature and to hydrolytic enzymes. *Plant Physiol. (USSR)* **30**:1194-1200.

Lutova, M. I., and Tikhonov, A. N., 1983b, High temperature after-effect on photosynthesis and electron transport in wheat leaves, *Biophysics (USSR)* **28**:284-287.

Luzikov, V. N., Novikova, L. A., Tikhonov, A. N., and Zubatov, A. S., 1983, Correlation between the rate of proteolysis of mitochondrial translation products and fluidity of the mitochondrial inner membrane of *Saccharomices cervisiae, Biochem. J.* **214**:785-794.

Luzikov, V. N., Novikova, L. A., Zubatov, A .S., and Tikhonov, A. N., 1984, Physical state of the mitochondrial inner membrane as a factor controlling the proteolysis of mitochondrial translational products in yeasts, *Biochim. Biophys. Acta* 775:22-30.

Macpherson, A. N., Telfer, A., Barber, J., and Truscot, G. T., 1993, Direct detection of singlet oxygen from isolated Photosystem II reaction centers, *Biochim. Biophys. Acta* **1143**:301-309.

Magnitsky, S. G., and Tikhonov, A. N., 1995, Generation of ΔpH in chloroplasts suspended in the media with different ion composition and osmolarity, *Biophysics (Russia)* **40**:347-358.

Magnitsky, S. G., and Tikhonov, A. N., 1998, Determination of the intrathylakoid pH in chloroplasts from the exchange broadening of the EPR spectrum of spin label Tempoamine, *Biophysics (Russia)* **43**:69-76.

Magnitsky, S. G., Masarova, M., and Tikhonov, A. N., 1996, Determination of transmembrane pH difference in chloroplasts using the effect of concentrational broadening of tempoamine EPR spectrum. *Curr. Top. Biophys.* **20**:25-30.

Malkin, R., and Chain, R. K., 1980, The relationship of the cyclic and non-cyclic electron transport pathways in chloroplasts, *Biochim. Biophys. Acta* **591**:381-390.

Mansurova, S. E., Dukhovich, V. F., Spiridonova, V. A., Shakhov,Yu. A., Velandia, A. E., Khrapova, N. V., and Tikhonov, A. N., 1984, The effect of phospholipids on the activity of mitochondrial pyrophosphatases. Lipidized soluble mitochondrial pyrophosphatases: the coupling factor for oxidation and phosphorylation, *Biochem. Intern.* **8**:749-755.

Marsh, D., 1981, Electron spin resonance: spin labels, *in* Membrane Spectroscopy. E. Grell, Ed., Springer-Verlag, Berlin, 51-142.

Maruyama, K., and Ohnishi, S., 1974, A spin-label study of the photosynthetic bacterium Rhodospirillum ruvrum. Reduction and regeneration of nitroxide spin-labels, *J. Biochem.* **75**:1153-1164.

Masarova, M., and Tikhonov, A. N., 1988, The light-induced uptake of protons and photophosphorylation in chloroplasts under the conditions of simultaneous and separate functioning of two photosystems, *Biophysics (USSR)* **33**:889-891.

McCarty, R. E., Evron, Y., and Johnson, E .A., 2000, The chloroplast ATP synthase: a rotary enzyme? *Ann. Rev. Plant Physiol. Plant Mol. Biol.* **51**:83-109.

McCormac, D. J., Bruce, D., and Greenberg, B. M., 1994, State transitions, light-harvesting antenna phosphorilation and light-harvesting antenna migration *in vivo* in the higher plant *Spirodela oligorrhiza, Biochim. Biophys. Acta* **1187**:301-312.

Mehler, A. N., 1951, Studies on reactions of illuminated chloroplasts. I. Mechanism of the reduction of oxygen and other Hill reagents. *Arch. Biochem. Biophys.* **33**:65-77.

Mehlhom, R. J., Candau, P. and Packer, L., 1982, Measurement of volumes and electrochemical gradients with spin probes in membrane vesicles, *Methods Enzymol.* **88**:751-762.

Mehlhorn, R. J., and Packer, L., 1979, Membrane surface potential measurements with amphiphilic spin labels, *Methods Enzymol.* **56**:515-526.

Mitchell, P., 1961, Coupling of phosphoruylation to electron and hydrogen transport by chemiosmotic type of mrchanism, *Nature* **191**:144-148.

Mitchell, P., 1966, Chemiosmotic coupling in oxidative and photosynthetic phosphorylation. *Biol. Rev.* **41**:445-502.

Moon, B. Y., Higashi, S., Gombos, Z., and Murata, N., 1995, Unsaturation of the membrane lipids of chloroplasts stabilizes the photosynthetic machinery against low-temperature photoinhibition in transgenic tobacco plants, *Proc. Natl. Acad. Sci. U.S.A.* **92**:6219-6223.

Murata, N., and Fork, D., 1976, Temperature dependence of the light-induced spectral shift of caritenoids in *Cyanidim caldarum* and higher plant leaves, *Biochim. Biophys. Acta* **461**:365-378.

Murata, N., and Ono, T.-A., 1979, Temperature dependence of the photosynthetic activities in the thylakoid membranes from the blue-green alga *Anacystic nidulance, Biochim. Biophys. Acta* **545:**69-76.

Navari-Izzo, F., Quartacci, M. F., Pinzino, C., Rascio, N., Vazzana, C., and Sgherri, C. L. M., 2000, Protein dynamics in thylakoids of the desiccation-tolerant plant *Boea hygroscopia* during dehydration and rehydration, *Plant Physiol.* **124**:1427-1436.

Nesbitt, D. M., and Berg, S. P., 1980, Proton involvement with the light-induced hindrance of spin label motion in the lumen of spinach thylakoids, *Biochim. Biophys. Acta* **593**:353-361.

Nesbitt, D. M., and Berg, S. P., 1982, The influence of spinach thylakoid lumen volume and membrane proximity on the rotational motion of spin label tempamine, *Biochim. Biophys. Acta* **679**:169-174.

Nie, G. Y., and Baker, N. R., 1991, Modifications to thylakoid composition during development of maize leaves at low growth temperatures, *Plant Physiol.* **95:**184-191.

Nishihara, M., Yokota, K., and Kito, M., 1980, Lipid molecular species composition of thylakoid membranes, *Biochim. Biophys. Acta* **617**:12-19.

Osváth, S., Larson, J. W., and Wraight, C. A., 2001, Site specific labeling of *Rhodobacter sphaeroides* reaction centers with dye probes for surface pH measurements, *Biochim. Biophys. Acta* **1505**:238-247.

Quartacci, M. F., Pinzino, C., Sgherri, C. L. M., Dalla Vecchia, F., and Navari-Izzo. F., 2000, Growth in excess copper induces changes in the lipid composition and fluidity of PSI1-enriched membranes in wheat, *Physiol. Plantarum* **108**:87-93.

Quinn, P. J., and Williams, W. P., 1983, The structural role of lipids in photosynthetic membranes, *Biochim. Biophys. Acta* **737**:223-266.

Quintinilha, A. T., and Mehlhorn, R. J., 1978, pH gradient across thylakoid membranes measured with a spin-labeled amine, *FEBS Lett.* **91**:104-108.

Razeghifard, M. R., and Pace, R. J., 1997, Electron paramagnetic resonance kinetic studies of the S states in spinach PSII membranes, *Biochim. Biophys. Acta* **1322**:141-150.

Razeghifard, M. R., and Pace, R. J., 1999, EPR kinetic studies of oxygen release in thylakoids and PSII membranes: A kinetic intermediate in the S-3 to S-0 transition, *Biochemistry* **38**: 1252-1257.

Riistama, S., Puustinen, A., Garcia-Horsoman, A., Iwata, S., Michel, H., and Wikström, M., 1996, Channelling of dioxygen into the respiratory enzyme, *Biochim. Biophys. Acta* **1275**:1-4.

Robinson, J.M., 1988, Does O_2-photoreduction occur within chloroplasts *in vivo*? *Physiol. Plant.* **72**:666-680.

Rottenberg, H., and Grunwald, T., 1972, Determination of ΔpH in chloroplasts. 3. Ammonium uptake as a measure of ΔpH in chloroplasts and sub-chloroplast particles, *Eur. J. Biochem.* **25:**71-74.

Rumberg, B., and Siggel, U., 1969, pH changes in the inner phase of the thylakoids during photosynthesis, *Naturwissenschaften* **56**:130-132.

Ruuge, E. K., Subczynski, W. K., and Tikhonov, A. N., 1977a, The structure of higher plants chloroplasts membranes as studied with paramagnetic probes, *Mol. Biol. (USSR)* **11**:646-655.

Ruuge, E. K., Subczynski, W. K., and Tikhonov, A. H, 1977b, EPR study of electron transport in photosynthetic systems of higher plants. 5. The interaction of paramagnetic probe I(12.3) with bean chloroplasts membranes, *Biophysics (USSR)* **22**:840-845.

Ryzhikov, S. B., and Tikhonov, A. N., 1988, The regulation of the rate of electron transport in photosynthetic membranes of higher plants, *Biophysics (USSR)* **33**:642-646.

Ryzhikov, S. B., and Tikhonov, A. N., 1991, Transmembrane pH difference in leaves of higher plants as measured with water soluble spin labels, *Biophysics (USSR)* **36**:70-73.

Schreiber, U., and Neubauer, C, 1990, O_2-dependent electron flow, membrane energization and the mechanism of nonphotochemical quenching of chlorophyll fluorescence, *Photosynth. Res.* **25:**279–293.

Schreiber, U., Hermann, H., Asada, K., and Neubauer, C., 1995, O_2-dependent electron flow in intact spinach chloroplasts: Properties and possible regulation of the Mehler-ascorbate peroxidase cycle, in *Photosynthesis: From Light to Biosphere,* Vol II, Mathis, P, Ed., Kluwer Academic Publishers, Dordrecht, 813–818.

Schreier, S., Polnaszek, C. F., and Smith, J. C. P., 1978, Spin labels in membranes. Problem in practice, *Biochim. Biophys. Acta* **515**:375-436.

Skulachev V.P., 1988, *Membrane bioenergetics.* Springer-Verlag, New York.

Stiehl, H. H., and Witt, H. L., 1969, Quantative treatment of the function of plastoquinone in photosynthesis, Z *Naturforsh* **24b**: 1588-1598.

Stock, D., Leslie, A. G. W., and Walker, J. E., 1999, Molecular architecture of the rotary motor in ATP synthase, *Science* **286**:1700-1705.

Strzalka, K., Sarna, T., and Hyde, J. S., 1986, ESR oximetry measurement of photosynthetic oxygen evolution by spin-probe technique, *Photobiochem. Photobiophys.* **12**:67-71.

Strzalka, K., Walczak, T., Sarna, T., and Swartz, H. M., 1990, Measurement of time-resolved oxygen concentration changes in photosynthetic systems by nitroxide based ESR oximetry, *Arch. Biochem. Biophys.* **281**:312-318.

Subczynski, W. K., and Hyde, J. S., 1984, Diffusion of oxygen in water and hydrocarbons using an electron spin resonance spin label technique, *Biophys. J.* **45**:743-748.

Subczynski, W. K., and Hyde, J. S., 1998, Membranes: barriers or pathways for oxygen transport, in *Oxygen Transport to Tissue XX, Advances in Experimental Medicine and Biology,* A. G. Hudetz, Ed., Plenum, New York, 399-408.

Subczynski, W. K., and Markowska, E., 1992, Effect of carotenoids on oxygen transport within and across model membranes, *Curr. Top. Biophys.* **16**:62-68.

Subczynski, W. K., Cieslikowska, D., and Tikhonov, A. N., 1990, Light-induced oxygen uptake in chloroplasts: ESR spin-label oximetry, *Photosynthetica* **24**:75-84.

Subczynski, W. K., Hopwood, L. E., and Hyde, J. S., 1992a, Is the mammalian cell plasma membrane a barrier to oxygen transport? *J. Gen. Physiol.* **100**:69-87.

Subczynski, W. K., Hyde, J. S., and Kusumi, A., 1989, Oxygen permeability of phosphatidylcholine-cholesterol membranes, *Proc. Natl. Acad. Sci. USA* **86**:4474-4478.

Subczynski, W. K., Hyde, J. S., and Kusumi, A., 1991, Effect of alkyl chain unsaturation and cholesterol intercalation on oxygen transport in membranes: A pulse ESR spin labeling study, *Biochemistry* **30**:8578-8590.

Subczynski, W. K., Renk, G. E., Crouch, R. K., Hyde, J. S., and Kusumi, A., 1992b, Oxygen diffusion-concentration product in rhodopsin as observed by a pulse ESR spin labeling method, *Biophys. J.* **63**:573-577.

Subczynski, W. K., Ruuge, E. K., and Tikhonov, A. N., 1975, Paramagnetic probes interaction with the chloroplast membranes of higher plants, *Plant Physiol. (USSR)* **22**:882-890.

Subczynski, W. K., Ruuge, E. K., and Tikhonov, A. N., 1976, Structural reorganization of chloroplast membranes studied by the technique of paramagnetic probes, *Plant Physiol. (USSR)* **23**:660-665.

Swartz, H. M., and Glockner, J. F., 1989, Measurements of concentration of oxygen in biological systems in EPR techniques, in *Advance EPR in Biology and Biochemistry.* A. J. Hoff, Ed., Elsevier, Amsterdam, 753-782.

Swartz, H. M., Boyer, S., Gast, P., Glockner, J. F., Hu, H., Liu, K. J., Moussavi, M., Norby, S. W., Vahidi, N., Walczak, T., Wu, M., and Clarkson, R. B., 1991, Measurements of pertinent concentration of oxygen *in* vivo, *Magn. Reson. Med.* **20**:333-339.

Tang, X.-S., Moussavi, M., and Dismukes, G. C. 1991, Monitoring oxygen concentration in solution by ESR oximetry using lithium phtalocyanine: Application to photosynthesis, *J. Am. Chem. Soc.* **113**:5914-5915.

Teuber, M., Rögner, M., and Berry, S., 2001, Fluorescent probes for non-invasive bioenergetic studies of whole cyanobacterial cells, *Biochim. Biophys. Acta* **1506**:31-46.

Theg, S. M., Chiang, G., and Dilley, R .A., 1988, Protons in the thylakoid membrane-sequestered domains can directly pass through the coupling factor during ATP synthesis in flashing light. *J. Biol. Chem.* **263**:673-681.

Tikhonov, A. N., and Blumenfeld, L. A., 1985, Hydrogen ions concentration in subcellular systems: physical meaning and the methods for determination, *Biophysics (USSR)* **30**:527-537.

Tikhonov, A. N., and Ruuge, E. K., 1978, EPR study of electron transport in photosynthetic systems of higher plants. 7. Effect of temperature on the electron transport between two photosystems and structural state of chloroplast membrane, *Mol. Biol. (USSR)* **12**:1024-1046.

Tikhonov, A. N., and Shevyakova, A. V., 1985, Electron transport, uptake of protons, and their coupling to photophosphorylation in chloroplasts. 3. Protons uptake by chloroplasts functioning under various metabolic states, *Biological Membranes (USSR)* **2**:349-362.

Tikhonov, A. N., and Timoshin, A. A., 1985, Electron transport, uptake of protons, and their coupling to photophosphorylation in chloroplasts. 2. Spin label Tempoamine as a probe for monitoring the light--induced uptake of protons by chloroplasts, *Biological Membranes (USSR)* **2**:349-362.

Tikhonov, A. N., Khomutov, G. B., and Ruuge, E. K., 1980a, Electron spin resonance study of electron transport in photosynthetic systems. 9. The temperature dependence of the kinetics of P700 redox transients in bean chloroplasts induced by flashes with different duration, *Mol. Biol. (USSR)* **14**:157-172.

Tikhonov, A. N., Khomutov, G. B., and Ruuge, E. K., 1980b, Electron spin resonance study of electron transport in photosynthetic systems. 10. Effects of magnesium ions on the structural state of thylakoid membrane and kinetics of electron transport between two photosystems in bean chloroplasts, *Mol. Biol. (USSR)* **14**:1065-1079.

Tikhonov, A. N., Khomutov, G. B., and Ruuge, E. K., 1984, Electron transport control in chloroplasts. Effects of magnesium ions on the electron flow between two photosystems, *Photobiochem. Photobiophys.* **8:**261-269.

Tikhonov, A. N., Khomutov, G. B., Ruuge, E. K., and Blumenfeld, L. A., 1981, Electron transport control in chloroplasts. Effects of photosynthetic control monitored by the intrathylakoid pH, *Biochim. Biophys. Acta* **637**:321-333.

Tikhonov, A. N., Timoshin, A. A., and Blumenfeld, L. A., 1983, Electron transport kinetics, proton transfer, photophosphorylation in chloroplasts, and their relation to thermoinduced structural changes in the thylakoid membrane, *Mol Biol. (USSR)* **17**:1236-1248.

Tikhonov, A. N., Timoshin, A. A., Ruuge, E .K., and Blumenfeld, L. A., 1982, Surface potential of thylakoid membrane, the light-induced uptake of protons and photophosphorylation in chloroplasts, *Proc. Acad. Sci. USSR* **266**:730-733.

Timoshin, A. A, Tikhonov, A. N., and Blumenfeld, L. A., 1984, Thermoinduced structural changes in ATP synthase as a factor controlling energy transduction in chloroplasts, *Biophysics (USSR)* **29**:338-340.

Torres-Pereira, J., Mehlhorn, R., Keith, A. D., and Packer, L., 1974, Changes in membrane lipid structure of illuminated chloroplasts: studies with spin-labeled and freeze-fractured membranes, *Arch. Biochem. Biophys.* **160**:90-99.

Trubitsin, B. V., Grigoriev, I. A., and Tikhonov, A. N., 2001, The use of imidazoline nitroxide for measuring intrathylakoid pH in chloroplasts, Abstracts of 3rd International Conference on nitroxide radicals, Kaiserslautern, Germany, p. 17.

Tsapin, A. I., Timofeev, K. N., Gol'dfel'd, M. G., Filiushina, A. V., and Krendeleva, T. E., 1974, Effect of iminoxyl radicals and their reduction products on photochemical reactions of chloroplasts, *Biophysics (USSR)* **19**:122-126.

Vass, I., Styring, S., Hundal, T., Koivuniemi, A., Aro, E.-M., and Andersson, B., 1992, Reversible and irreversible intermediates during photoinhibition of photosystem II: stable reduced Q_A species promote chlorophyll triplet formation, *Proc. Natl. Acad. Sci. USA* **89**:1408-1412.

Vermaas, W. G. G., and Govindjee, 1981, The acceptor side of photosystem II in photosynthesis. *Photochem. Photobiol.* **34**:775-793.

Vogel, P. D., 2000, Insight into ATP synthase structure and function usung affinity and site-specific spin labelling, *J. Bioenerg. Biomembr.* **32**:413-421.

Vogg, G. Heim, R. Gotshy, B., Beck, E, and Hansen, J. 1998, Frost hardening and photosynthetic performance of Scots pine (Pinus sylvestris L.). II. Seasonal changes in the fluidity of thylakoid membranes, *Planta* **204**:201-206.

Vozvishaeva, L. D., Goldfield, M. G., Hangulov, S. V., and Tzapin, A. I., 1974, Uncoupling of photophosphorylation in chloroplasts by hydrophobic nitroxide radicals, *Biophysics (USSR)* **19**:1030-1033.

Wan, X., Fu, T.-C., Funk, A., and London, R. E., 1995, Differential clearance of nitroxide MRI contrast agents from rat cerebral ventricles, *Brain Research Bull.* **36**:91-96.

Wasniowska, A., Subczynski, W. K., and Tikhonov, A. N., 2002, Inhibition of ATP synthesis in chloroplasts by lipid soluble nitroxide radical spin labels, *Curr. Top. Biophys.* **26**:83-91.

Westerhoff, H. V., Melaudri, B. A., Venturoli, G., Azzone, G. F., and Kelt, D. B., 1984, Mosaic protonic coupling hypothesis for free energy transduction, *FEBS Lett,* **165**: 1-5.

Wille, B., 1988, Thylakoid volume, proton translocation and buffering capacity as measured with spin-label techniques, *Biochim. Biophys. Acta* **936**:513-530.

Williams, R. J. P., 1978, The multifarious coupling of energy transduction, *Biochim. Biophys. Acta* **505**:1-44.

Windrem, D. A. and Plachy, W. Z., 1980, The diffusion-solubility of oxygen in lipid bilayers, *Biochim. Biophys. Acta* **600**:655-665.

Witt, H.-T., 1979, Energy conservation in the functional membrane of photosynthesis. Analysis by light pulse and electric pulse methods. The general role of the electric field, *Biochim. Biophys. Acta* **505**:355-427.

Yin, J.-J., and Subczynski, W. K., 1996, Effects of lutein and cholesterol on alkyl chain bending in lipid bilayers: a pulse electron paramagnetic resonance spin labeling study, *Biophys. J.* **71**:832-839.

Yruela, I., Alfonso, M., Garcia-Rubio, I., Martinez, J. I., Picorel, R., and Alonso, P. J., 2001, Spin label electron paramagnetic resonance study in thylakoid membranes from a new

herbicide-resistant D1 mutant from soybean cell cultures deficient in fatty acid desaturation, *Biochim. Biophys. Acta* **1515**:55-63.

Zouni, A., Witt, H.-T., Kern, J., Fromme, P., Krauß, N., Saenger, W., and Orth, P., 2001, Crystal structure of Photosystem II from *Synechococcus elongatus* at 3.8 Å resolution, *Nature* **409**:739-743.

III

In Vivo EPR and Physiology

Chapter 9

EPR Spectroscopy of Function *In Vivo*

Origins, Achievements, And Future Possibilities

Harold M. Swartz and Nadeem Khan
Department of Diagnostic Radiology, Dartmouth Medical School, Hanover, New Hampshire 03755 USA

Abstract: EPR can be used to study free radicals *in vivo,* environmental and biophysical parameters in cells and tissues, and to report metabolism, physiology, and biochemistry. The authors have attempted to judge which of these types of measurements will be productive for studies in animals and in humans. It is envisioned that a large number of *in vivo* applications of EPR will grow in importance as well as in technical capability in the near future. The most likely clinical applications will be oximetry and radiation dosimetry.

1. INTRODUCTION

In vivo EPR clearly is an important new capability, but because it still is in a rapid growth stage, it is not yet fully clear how it will be utilized. Some of the potential applications for *in vivo* EPR appear to have strong or even unique capabilities. Some of these already are being used fairly extensively. There also are many potential areas of application that have not yet been explored very thoroughly. The aim of this chapter is to survey the uses that already have been identified, provide an indication of what kinds of information might be obtained, and to provide an assessment of the potential utility of each use. We consider potential applications both in experimental animals and in human subjects.

The basic rationale for carrying out *in vivo* EPR comes from two types of considerations. There are some measurements that one would like to be able to make in living subjects, especially for clinical purposes. In addition, when studying mechanisms and modifications of physiological and pathophysiological processes, there often is added value in making measurements in intact animals, where all of the factors that can affect

processes are fully active (in comparison with studies in model systems or even isolated organs, where systemic factors, effects from other organ systems, etc. do not occur). However, because of the complexity and difficulty of carrying out *in vivo* EPR and the availability of other methods for some of the measurements, the measurements that are made with *in vivo* EPR should provide some specific advantages.

The types of measurements that have been or could be made with *in vivo* EPR are summarized in Table 1. We have attempted to make judgments as to which of these are likely to be productive, and then discuss them in this review. This turns out to be a large number of types of measurements, indicating that *in vivo* EPR is likely to continue to grow in applications as well as capabilities.

Many of the potentially most valuable applications fall in the category that we term as *in vivo* measurements of function. This is an area that has been of particular interest to Jim Hyde in both *in vivo* EPR and NMR. He has facilitated many of the developments in *in vivo* EPR through his role as an advisor to the *in vivo* EPR programs at centers at Illinois and Dartmouth, as well as development of many techniques (such as loop gap resonators) that have been adapted for *in vivo* EPR.

Many of the technical aspects, including the ways in which *in vivo* EPR can be carried out and the technical challenges that are involved have been considered in previous reviews and will not be covered here, but the reader is encouraged to consult these for more details (Swartz, 2002a; Swartz and Berliner, 1998, 2002; Swartz and Halpern, 1998).

We consider here the various potential capabilities of *in vivo* EPR, with a somewhat arbitrary set of descriptors, based principally on the type of parameter that is measured rather than on the physiological or pathophysiological process that is studied. Some of these have partial overlap.

Most of the applications require the administration of a paramagnetic reporter molecule, but a few use paramagnetic species that already are present in the subject. When adding the paramagnetic molecule (or in the case of spin trapping and some protonitroxides, the precursor molecules), the potential effect of these “drugs” also needs to be considered.

Table 1*

Meaurement	Method	Reference
Free Radicals		
Oxygen, Carbon, and Sulfur centered radicals	Spin trapping	Buettner and Mason, 1990
Radical intermediates of drugs, enzymes	Spin trapping, direct observation	Knecht and Mason, 1993; Fujii et al., 1994
Nitric oxide	Spin trapping	Vainin, 1999
Long-lived radiation-induced radicals in hard tissues	Direct observation	Stachowicz et al., 1993
Environmental and Biophysical Parameters in Cells and Tissues		
Oxygen – repeated measurements	Oxygen-sensitive particulate paramagnetic materials	Swartz, 2002a
Oxygen – imaging	Soluble stable free radicals	He et al., 2002
Charge and potential of cells/membranes	Appropriate nitroxides	Cafiso, 1989
Viscosity	Appropriate nitroxides	Halpern et al., 1999
pH	Specific nitroxides	Gallez et al., 1998b
Temperature	Appropriate nitroxides	Eckburg et al., 1996
Macromolecular motion	Effect on attached nitroxides	Cafiso, 1989
Polarity, hydrophilicity	Effect on spectra of nitroxides	Cafiso, 1989
Membrane fluidity	Lipophilic nitroxides	Borbat et al., 2001
Metabolism, Physiology, and Biochemistry, in vivo		
Redox state	Nitroxides	Suzuki-Nishimura and Swartz, 1998
Thiol groups	Special nitroxides	Khramtsov et al., 1997
Cell viability	Paramagnetic materials	Dobrucki et al., 1991
Perfusion	Paramagnetic tracers	Gallez et al., 1996a
Redox active metal ions	Direct observation	Liu and Shi, 2001
Oxygen consumption	Appropriate nitroxides	James et al., 1995
Site-specific interactions in membranes	Nitroxides introduced by site-specific mutagenesis	Glasgow et al., 1999
Pharmacokinetics	Paramagnetic labels	Mader et al., 1996b
Metabolism of drugs	Nitroxides attached near site of metabolic change	Mader, 1998
Penetration of water (mobilization of drugs) into implanted drugs	Nitroxides with spectra that reflect motion	Mader et al., 1997

* References are provided as good starting points for more thorough information.

Applications in human subjects provide both a tremendous opportunity and many challenges. These have been reviewed recently, and the reader is referred to these for more details (Swartz, 2002b; Swartz and Walczak 1996, 1998). We believe that the critical step for the successful introduction of *in vivo* EPR into clinical medicine is to demonstrate at least one or two significant applications for which *in vivo* EPR provides clinically useful information that is significantly better than can be provided by other

approaches. If this occurs, then the technique may become widely used and other clinical applications are very likely to be developed and used widely, analogous to the situation with clinical NMR. And, also similar to NMR, the whole field of *in vivo* EPR then would very likely be greatly stimulated. The key steps for the initial clinical application(s) include:

1. Establishing application(s) where *in vivo* EPR has clear advantages.
2. Developing techniques for *in vivo* EPR where safety issues can be successfully overcome. While the technique itself is unlikely to cause problems due to the magnetic or electromagnetic fields that are used, the paramagnetic compounds that are administered must be shown to be safe and efficacious.
3. Surmounting potential limitations of sensitivity and depths at which the measurements can be made for each potential application.

Considering these potential problems and opportunities, it is our judgment that clinical applications will become established, starting with two types of applications:

1. Utilizing the ability of *in vivo* EPR to make repeated measurements of oxygen in tissues, especially for guiding treatment of cancer and for evaluating effectiveness of treatments for peripheral vascular disease.
2. For after-the-fact dosimetry of unexpected exposures to radiation where conventional dosimeters are not in place. This is most likely to occur under battlefield conditions or as the result of the deliberate dissemination of radiation by a terrorist attack.

In order to provide an overview of the current and future potential uses of the various types of measurements, each section concludes with our judgment as to both experimental and clinical uses. In view of the low reliability of such predictions, these should be viewed only as potentially interesting speculations.

2. OXYGEN

This has been the most extensive use of *in vivo* EPR, and seems quite likely to remain a leading application. Overall oximetry, including *in vivo* EPR, is covered in detail in Ch. 10 “EPR oximetry in biological and model samples.” *In vivo* EPR has been reviewed thoroughly recently, and the reader is refered to these reviews for more extensive considerations of this very important application (Swartz, 2002a; Swartz and Clarkson, 1998).

The prominent role of oximetry for *in vivo* EPR is due both to the importance of oxygen in many physiological and pathophysiological processes and also some unique capabilities of *in vivo* EPR to measure

oxygen *in vivo*. Both EPR imaging and spectroscopy have very strong capabilities for measuring oxygen *in vivo*. These capabilities are often complementary.

The basis of EPR oximetry is the paramagnetic nature of molecular oxygen, which therefore affects the EPR spectra of other paramagnetic species by altering their relaxation rates, and perhaps via other mechanisms as well. These effects then can be calibrated to the amount of oxygen that is present in the environment of the paramagnetic materials (Fig. 1). Two important classes of oxygen sensitive paramagnetic materials are used in EPR oximetry: particulates and soluble. The particulates are carbonaceous materials with unpaired electrons distributed over complex arrays of atoms and crystalline materials (especially lithium phthalocyanine, often abbreviated as LiPc) with pools of unpaired electrons. The properties of the particulates that have been especially useful for EPR oximetry are their stability and strong response of their spectra to the presence of oxygen. Their stability makes it feasible to carry out repeated measurements from the same site, sometimes for periods of more than a year.

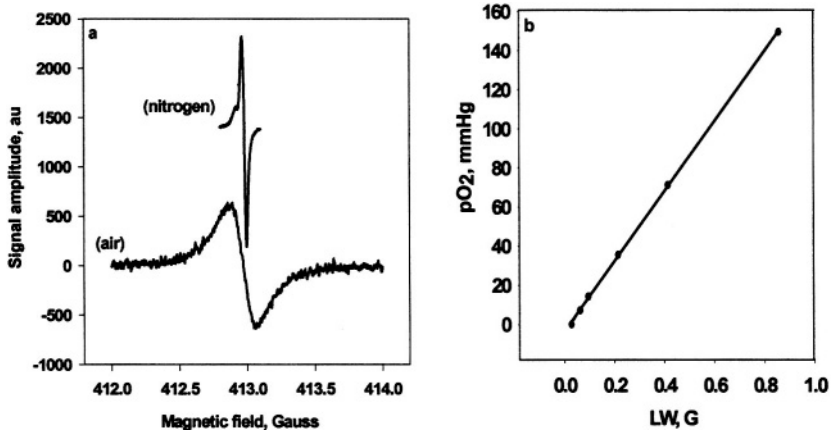

Figure 1. Use of oxygen sensitive materials for pO_2 measurements: (a) EPR spectra of lithium phthalocyanine (LiPc) in air, and nitrogen (b) Calibration of the line width of EPR spectra of LiPc with pO_2.

Soluble free radicals are the other type of oximetry materials. Their response to oxygen is not as large as the particulates, but because they become widely distributed *in vivo,* they are especially suitable for making images that reflect the distribution of oxygen. The nitroxides are usually employed for this type of oximetry, but in principle, any soluble stable free radical could be used. The lines broaden by a predictable amount based on Heisenberg spin exchange, and the resulting change in spin relaxation time. The nitroxides tend to be eliminated fairly rapidly through bioreduction and excretion, and therefore need to be administered before each series of

measurements. The discovery that the reduction of nitroxides is dependent on the oxygen concentrations has raised additional possibilities for measuring oxygen concentrations by using the rate of their disappearance (Swartz, 1989). Recently a new class of materials, the "trityls", has been developed and appear to have excellent properties for EPR oximetry, especially for imaging (Ardenkjaer-Larsen et al., 1998; Reddy et al., 2002). The key properties of the new class of materials are the narrowness of the line and the stability of the paramagnetism.

The principal *spectroscopic* approaches for oximetry use oxygen sensitive paramagnetic particulates, although there also are some important spectroscopic applications based on oxygen sensitive soluble paramagnetic materials. This approach has been used experimentally, especially for following oxygenation in tumors, including the effects of treatment on the levels of oxygen. It also has been used extensively to study ischemia-reperfusion damage and other processes in the brain. The method has also been used very productively to measure oxygen in skin, subcutaneous tissue, muscle, heart, liver, and kidney. The ability to make repeated measurements with high accuracy and minimal invasion are especially important aspects of this approach. With the development of the multisite measurements (Grinberg et al., 2001; Smirnov et al., 1993) the most significant limitation of the method (for applications where the oxygen concentration may be heterogeneous) has been significantly diminished.

2.1 Expected Applications in Experimental and Clinical Studies

In vivo oximetry in experimental animals already is a very important application and is likely to continue to grow. The particular strength of this approach is the capability of making repeated measurements of oxygen from the same sites with little or no invasion. This may be the most important experimental use of *in vivo* EPR, even though other applications also are likely to be very valuable.

The use of *in vivo* oximetry in the clinic is clearly the most likely initial extensive clinical application of *in vivo* EPR. The first clinical applications will be in two areas:

1. Measuring oxygen in tumors with the aim of enhancing therapy by providing information that can be used to schedule treatments more optimally in regard to the concentration of oxygen. This is important because the response of tumors to therapy, especially radiation therapy but also chemotherapy, is very sensitive to the concentration of oxygen in the tumor.

2. Measuring oxygen in tissues at risk in peripheral vascular disease. This information will be very useful for evaluating the status of the disease and the response to therapy.

3. NITRIC OXIDE

Nitric oxide ($NO^{\bullet}$) has many important potential physiological roles, such as a regulator of vasomotor tone in the cardiovascular system, a cytotoxic factor, and a neurotransmitter in the central nervous system (Collier and Valance, 1989; Palmer et al., 1987; Zweier et al., 2001). In order to understand the mechanism by which $NO^{\bullet}$ mediates various biological processes, accurate methods for its measurement are required. These are challenging because it is a diffusible free radical with a short lifetime. Free, or non-complexed, $NO^{\bullet}$ cannot be detected *in vivo* by EPR, but some of the species produced by reactions of $NO^{\bullet}$ give EPR spectra characteristic of trapping $NO^{\bullet}$. The use of these traps forms the basis for EPR measurements of $NO^{\bullet}$. Background information and references to early studies can be found in Khramtsov and Volodarsky (1998); Venkataraman et al. (2002), and Nagano and Yoshimura (2002).

In vivo EPR spin trapping and imaging of $NO^{\bullet}$ has been used extensively, especially for continuous monitoring (Fujii and Yoshimura, 2000; Jackson et al., 2001; James et al., 1999; Komarov et al., 1993; Lai and Komarov, 1994). The method uses the characteristic EPR spectra that are observed when nitric oxide is complexed with iron dithiocarbamates. Another possibility is to use nitronyl nitroxides, have a characteristic 5-line pattern due to interaction of the unpaired electron with two equivalent nitrogens. Upon reaction with $NO^{\bullet}$, nitronyl nitroxides are converted to iminonitroxides, in which the two nitrogens are no longer equivalent because the oxygen has been removed from one of them. The EPR spectrum after reacting with $NO^{\bullet}$ is a nine-line pattern, which is easily distinguished from the starting nitronyl nitroxide spectrum (Joseph et al., 1993).

Because these methods have somewhat limited sensitivity, they are most useful with high levels of nitric oxide. Because of the large amounts of traps that are required, it is necessary to determine whether the trapping is altering the process that is being investigated, either by removal of substantial amounts of $NO^{\bullet}$ or from effects of the substances that are administered.

There are some approaches that can increase sensitivity, and these are being actively pursued. The most generally applicable approach is to develop more specific and stable traps for nitric oxide and to improve the sensitivity of the low frequency *in vivo* EPR spectrometers.

In the meantime, there have been some approaches that combine *in vivo* EPR with the more sensitive higher frequencies that ordinarily cannot be used for direct measurements *in vivo*. Komarov et al. (1993) and Lai and Komarov (1994) directly detected $NO^{\bullet}$ in endotoxin-shocked mice using MGD (N-methyl-D-glucamine dithiocarbamate) and Fe (II), using a S-band EPR spectrometer operating at 3.5 GHz, and with a 4-mm loop-gap resonator. While this is a very important advance, this approach is restricted to the tail due to the non-resonant absorption of the microwave in the hydrated parts of the body. Another approach was demonstrated by Kotake et al. (1999), who continuously monitored *in vivo* $NO^{\bullet}$ formation using a continuous flow of externally diverted bile through an EPR sample cell set into an X-band EPR cavity. This method is suitable for monitoring real-time modulation of $NO^{\bullet}$ levels by drugs or pathophysiological processes, and perhaps the sensitivity will be sufficient to monitor some physiological processes. The applicability of this technique, however, is limited to situations where fluids from the potential site of $NO^{\bullet}$ can be diverted into the X-band resonator.

One of the potential advantages of using *in vivo* EPR for the measurement of $NO^{\bullet}$ is the possibility of combining this with measurements of pO_2. This is illustrated in Fig. 2; pO_2 was measured at two different locations in the liver along with the simultaneous measurement of nitric oxide, after the mice were subjected to LPS (lipopolysaccharide)-induced septic shock (James et al., 1999).

3.1 Expected Applications in Experimental and Clinical Studies

The measurement of nitric oxide in experimental animals *in vivo* is a very attractive application, because of the paucity of techniques to make such measurements *in vivo* and the ability to combine these measurements with EPR oximetry. The EPR technique, however, has limited sensitivity, and therefore has been used principally for the study of endotoxic shock, which produces large amounts of nitric oxide and with drugs that release large amounts of $NO^{\bullet}$. More extensive use will require the development of better trapping agents.

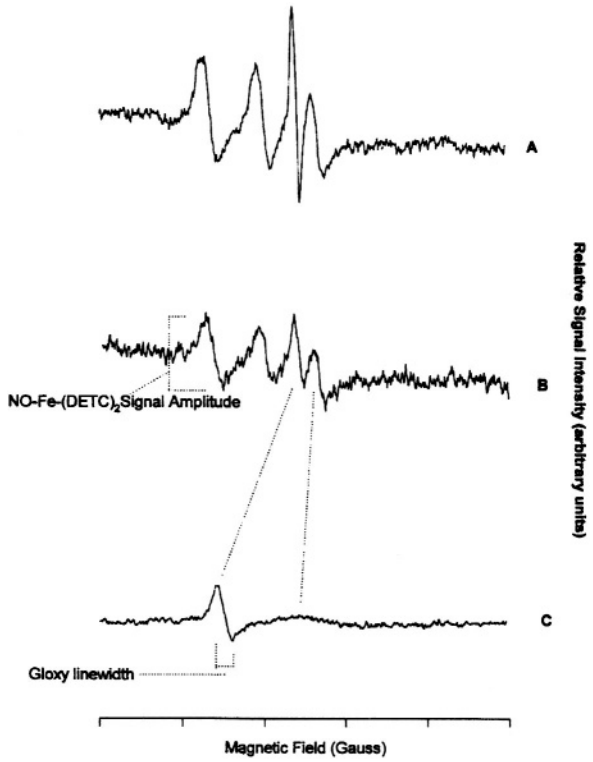

Figure 2. (A) A typical spectrum observed on addition of an aliquot of a saturated $NO^{\bullet}$ solution to saline containing DETC (diethyldithiocarbamate), iron sulfate, sodium citrate, and particles of oxygen sensitive coal (gloxy) *in vitro* using a L-band (1.1 GHz) EPR spectrometer. The EPR spectrum is composed of two species; a three line with characteristics typical of $NO\text{-}Fe\text{-}(DETC)_2$ complex (g_{iso}= 2.04 Gauss; a_N = 13.04 Gauss), and a single line (g = 2.0028) arising from gloxy (used to report pO_2). For more details, please refer to James et al. (1997). (B) Spectrum recorded *in vivo* from the liver region of a mouse injected with SNP (sodium nitroprusside). Gloxy was implanted 7 days earlier, and DETC, iron sulfate, and sodium citrate was injected 30 minutes prior to SNP injection. (C) Spectrum recorded from the liver same as above in (B), but with spectrometer conditions optimized for recording the EPR signal from gloxy. The signals from gloxy and $NO\text{-}Fe\text{-}(DETC)_2$ are clearly distinguishable, and thus allows the measurement of both pO_2 and nitric oxide simultaneously. For more details please refer to James et al. (1999).

The measurement of nitric oxide in the clinic would be very attractive. This type of measurement has the special advantage in that the trapping agents, the dithiocarbamates, already are cleared for use in human subjects. The limiting aspects are, as in experimental animals, sensitivity. We are actively looking at another approach that could be used clinically: to place immobilized nitric oxide trapping agents in high concentration in catheters,

and then to measure nitric oxide in the blood stream in conjunction with clinical procedures that already utilize catheters to measure heart function.

4. pH

The pH is a critical parameter in a number of physiological and pathophysiological processes. The commonly used experimental approaches for the measurement of pH are based on electrochemical methods employing a glass electrode or related sensors with a carbon fiber or optical fiber microelectrodes (Galster, 1991; Mignano and Baldini, 1996). These approaches are simple and reliable but are invasive. Non-invasive methods have been developed using NMR, absorption spectroscopy, or fluorescence spectroscopy (Bhujwalla et al., 1998; Marechal et al., 1999; Ojugo et al., 1999; Russell et al., 1994), but have their own limitations, such as low sensitivity or a requirement of optical transparency of the samples.

The development of paramagnetic pH-sensitive nitroxides has made possible the accurate determination of pH by EPR spectroscopy (Khramtsov et al., 1982; Khramtsov and Weiner, 1988). Spectroscopic features of the probes, in particular the hyperfine coupling constant and the g value, are sensitive to the protonation of the ring nitrogen (non-nitroxide), which affects the spin density on the nitrogen of the nitroxide group. Spin probes have been developed with different pK_a values so that by proper choice of the spin probe, one can investigate virtually any pH range. The capability of using this approach *in vivo* was shown using 1.1 GHz EPR to measure the pH in the stomach of mice Fig. 3, (Gallez et al., 1996b). The advantage of the method includes noninvasiveness, continuous measurement, and instant response.

4.1 Expected Applications in Experimental and Clinical Studies

In vivo measurements of pH in experimental animals are likely to be a limited but potentially productive application. Under some circumstances the use of EPR to measure pH non-invasively will have advantages over other potential methods. The emphasis is likely to be on its non-invasive nature and the ability to make repeated measurements.

The use of *in vivo* EPR to measure pH in the clinic is not likely to be a significant application in the near future. The types of applications that could be made with *in vivo* EPR in the near future seem to be well covered by existing technologies.

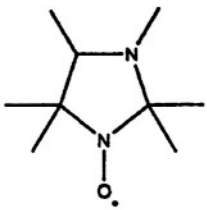

HM

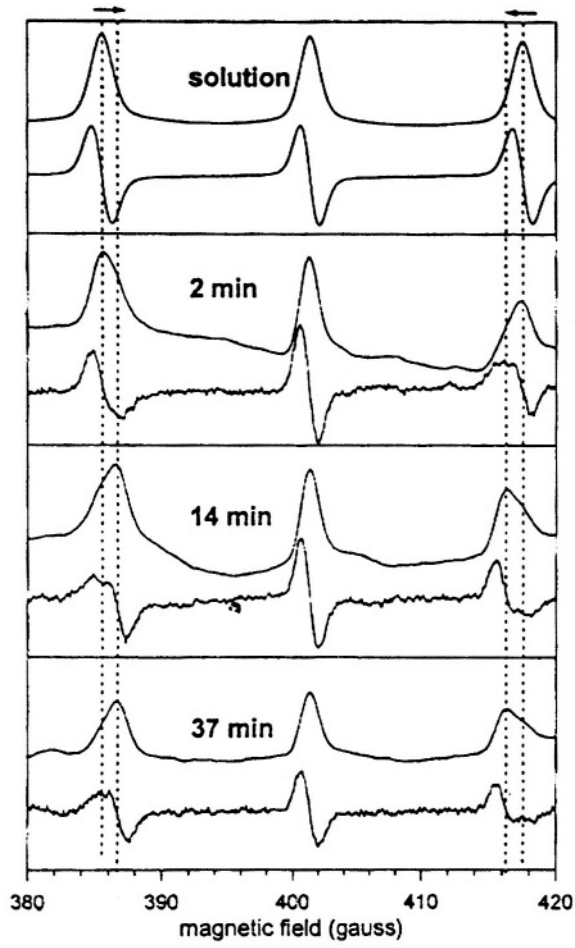

Figure 3. EPR spectra (first derivative) and integrated spectra (absorption) recorded from solution, and *in vivo* from the stomach of a mouse after administration of 250µl of a 2mM solution of the nitroxide (HM) in 1:2 diluted Madrox, a commercial antacid containing 40 mg of magnesium hydroxide and 45 mg of aluminum hydroxide per ml. The dotted lines show the two hyperfine splitting values for the protonated/non-protonated forms of the nitroxide. Note the change with the time of the hyperfine splitting (increase of the protonated part) of the nitroxide under these conditions, which is a measure of the pH in the system. For more details please refer to Gallez et al. (1996b).

5. BIOPHYSICAL PARAMETERS INCLUDING CHARGE, MACROMOLECULAR MOTION, MEMBRANE FLUIDITY, VISCOSITY, AND MEMBRANE POTENTIAL

For many years the ability of EPR, using nitroxides, to follow such parameters has been a very fruitful application in model systems and, to a lesser extent, in intact cells. These applications are based on the sensitivity of the EPR spectra of the nitroxides to various environmental parameters, including the motion of the nitroxide itself (Cafiso, 1989). These types of applications usually are based on the effect of motion on anisotropic components of the hyperfine spectra of the nitroxides, the effects of charge and solubility of the splittings between lines, and/or the selective localization of the nitroxides based on their physical and chemical properties (solubility, charge, and specific reactions with groups such as SH).

In model systems and cells it is fairly straightforward to obtain the concentration, localization, and stability of the nitroxides that is needed for the studies. This is more of a challenge when attempting to use this approach *in vivo,* because of the number of different microenvironments that occur *in vivo* and the effects of metabolism on nitroxides. Nevertheless, there have already been some useful applications *in vivo* and there is a potential for much more widespread use. These potential uses are attractive because the parameters that are measured are often very difficult to measure with other techniques.

The potential for carrying out biophysical measurements *in vivo* has been demonstrated by Halpern et al. (1999). Using low frequency *in vivo* EPR (260 MHz), they compared the average microviscosity of the total aqueous compartment of murine fibrosarcomas and that of normal leg tissue in mice, Fig. 4. The viscosity is obtained by using the Stokes-Einstein model, which relates solute rotational diffusion constants to solvent viscosity. The rotational diffusion constant is obtained from the spectra, using the fact that this constant is proportional to the spectral line-width differences: $\Delta B_2 - \Delta B_1$.

5.1 Expected Applications in Experimental and Clinical Studies

Measurements of biophysical parameters in experimental animals *in vivo* are a potentially rich source of types of information that cannot readily be made by other techniques. It is perhaps surprising that so far there have been few reports of these types of measurements. This is likely to change in the future, especially if appropriate problems that would benefit from such measurements are identified.

The use of these capabilities in the clinic will depend on the identification of problems where such data will be of immediate clinical use. This approach also will require the development and testing for safety of the probes that will be used.

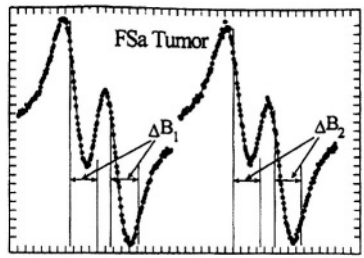

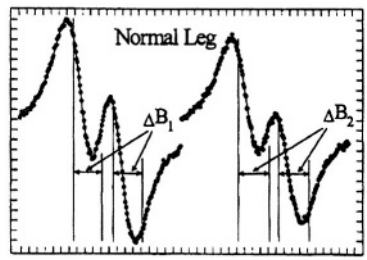

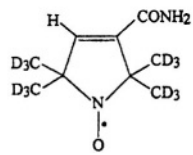

Figure 4. The spectra of the spin probe obtained from a normal leg of a C3H mouse, and a tumor-bearing leg of a C3H mouse, after intraperitoneal injection of 0.7 ml of 30 mM of the spin probe shown in the figure. ΔB_1 and ΔB_2 are the separate nitrogen manifold line widths. The normal tissue spectra emphasize the difference between the two manifolds; the difference between manifolds was reduced in tumors. The spectral data were fit to a sum function approximation to the Voigt spectral shape using a Levinberg-Marquardt nonlinear least-squares fitting algorithm. The parameter extracted from the spectral fit function $\Delta\Delta B = \Delta B_2 - \Delta B_1$, is proportional to the aqueous compartment microviscosity (Stokes-Einstein model). For more details please refer to Halpern et al. (1999).

6. THIOLS

Thiols have a key role in the cell in a wide array of biochemical and biological responses. Optical and chromatographic methods also have been used for quantitative determination of sulfhydryl groups (Packer, 1995) but cannot be used *in vivo*. An EPR method (Weiner, 1995) has been developed

that uses imidazoline biradical disulfide nitroxides $^{\bullet}R_1S\text{-}SR_1{}^{\bullet}$. These nitroxides have dramatic changes in EPR spectra when involved in thiol-disulfide exchange, Fig. 5. With *in vitro* samples this method can measure 0.1-1 μM thiols and their reactivity, even in colored and highly absorbing samples. One of the potential disadvantages of using this method under physiological conditions is the consumption of the thiols, which can cause irreversible damage to the system under study (Nohl et al., 1995). Khramtsov et al. (1997) have developed an imidazoline biradical disulfide reagent that retains the advantages of the previous method but has slower rates of the reactions with thiols. The slow kinetics make it possible to apply a kinetic approach for thiol determination at physiological pH, which allows non-invasive thiol measurement in functioning biological systems. This approach may be suitable for *in vivo* applications.

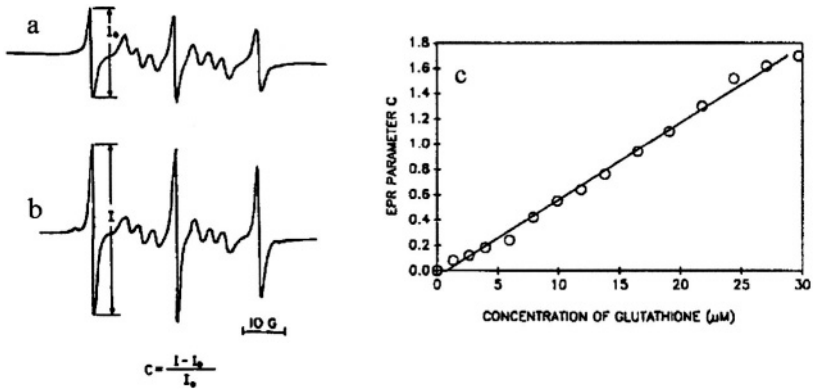

Figure 5. Change of the EPR spectrum of a biradical $RS^{\bullet}\text{-}SR^{\bullet}$ after its reaction with GSH (glutathione). Spectrum (a) was obtained from 8×10^{-5} M $RS^{\bullet}\text{-}SR^{\bullet}$ alone in the phosphate buffer solution (pH 7.3), and spectrum (b) was obtained from the same solution after 1.6×10^{-5} M GSH was added. (c) Effect of GSH on the empirical EPR parameter C of biradical $RS^{\bullet}\text{-}SR^{\bullet}$. GSH was added gradually to the phosphate buffer (pH 7.3) with 8×10^{-5} M $RS^{\bullet}\text{-}SR^{\bullet}$ and then an EPR spectrum was taken after each addition of a known concentration of GSH. For more details please refer to Weiner
et al. (1991).

6.1 Expected Applications in Experimental and Clinical Studies

In vivo measurements of thiols in experimental animals is potentially a very important application because of the paucity of methods to make such measurements and the importance of thiols in many pathologies, especially those related to abnormalities of the redox balance, such as ischemia-

reperfusion and oxidative damage. The key to these applications is the development of the kinetic approach, because that seems to be a requirement for effective use *in vivo*.

The use of *in vivo* measurements of thiols in the clinic will depend on the success of developments in animals. Once that is established and the paramagnetic probes to make the measurements have been demonstrated to be safe for use in human subjects, there are some very attractive clinical applications. These would focus on quantitative measurements of thiols to determine the potential for deleterious oxidations due to changes in disease or diet.

7. REACTIVE FREE RADICALS (DETECTED BY SPIN TRAPPING)

EPR in many situations is the technique of choice to study reactive free radicals, because of its specificity and sensitivity. In intact biological systems, however, the concentrations of the radicals of interest often are too low for direct detection. Fortunately, the technique of spin trapping (Buettner and Mason, 1990) provides a means to measure many of the reactive free radicals of interest. Spin trapping initially was applied successfully to pure and model systems. Applications to cellular systems are more complex because of the instability of many spin adducts in such systems, and the potential for many different free radicals to be present (Sentjurc et al., 1995; Swartz, 1990). These problems have not been solved entirely yet but considerable progress has been made, so that spin trapping studies of viable cells, tissues, and even *in vivo* now have been carried out, yielding important and useful results. The spin traps themselves generally are stable *in vivo* and not toxic, so with the development of traps that lead to stable spin adducts it is likely that this will be an area with widespread utilization.

Until recently, with a few exceptions, the stability of the spin adducts has been the limiting factor for *in vivo* spin trapping. While a few reactive radicals of interest could be trapped, e.g. the sulfite radical, the spin adducts of most oxygen centered and carbon centered radicals could not be studied *in vivo* except under very strenuous conditions (Halpern et al., 1995). The development of the phosphorylated spin traps have changed the situation dramatically, permitting the trapping of even the hydroxyl radical *in vivo* under conditions that are likely to be applicable to a number of problems of high interest.

Direct *in vivo* EPR was applied successfully to the study of sulfite radicals using spin trapping (Jiang et al., 1995; Liu et al., 1999). The DMPO-

thiyl spin adduct detected earlier with X-band EPR from rat blood or with L-band EPR from the rat tail has been confirmed by direct evidence of the formation of DMPO-hemoglobin thiyl spin adduct using spin trapping *in vivo,* Fig. 6 (Jiang et al., 1996). Timmins et al. (1999) successfully demonstrated the direct *in vivo* spin trapping of hydroxyl radicals in mice treated with 5-aminolevulinic acid (ALA) and with iron overload, using low frequency (L-band) *in vivo* EPR, Fig. 7, spectrum b. Further evidence for the presence of hydroxyl radicals is shown in spectrum c. In the presence of DMSO, methyl radicals were generated by the reaction of hydroxyl radicals with DMSO resulting in a characteristic spectrum of both methyl and hydroxyl radical adducts.

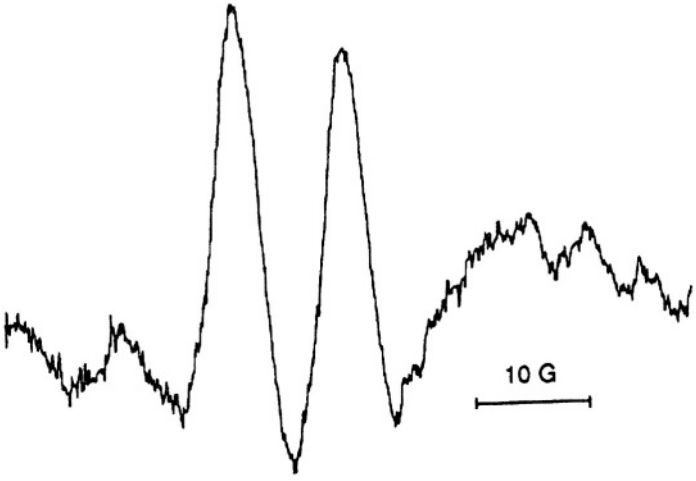

Figure 6. A typical 1.1 GHz EPR spectrum of the DMPO/Hb thiyl free radical detected from an intact rat. After anesthesia the rat was treated with DMPO, 13 mmol/Kg, intragastric and an LD_{50} dose of phenylhydrazine hydrochloride, 188mg/Kg, i.g. The spectra were collected 0.5 hour after the treatment. The EPR spectrum of the radical adducts had two major lines and the magnetic parameters used to simulate this spectrum were the g tensor (g_{xx} = 2.0105, g_{yy} = 2.0057, and g_{zz} = 2.0024), the nitrogen hyperfine coupling tensor (A_{xx} = 5.7, A_{yy} = 2.6., and A_{zz} = 34.5G) and the hydrogen hyperfine coupling tensor (A_{xx} = 11.9, A_{yy} = 10.4 and A_{zz} = 11.9G). The EPR signal at liquid nitrogen temperature did not show much difference as compared to the spectrum at room temperature, indicating that the radical adduct was a macromolecular immobilized on the EPR time scale. For more details please refer to Jiang et al. (1996).

7.1 Expected Applications in Experimental and Clinical Studies

Measurements of reactive free radicals in experimental animals are at an early but promising stage. The ability to test hypotheses and experimental findings *in vivo* would greatly benefit studies of oxidative damage, and other processes that are thought to involve reactive free radicals. Further progress depends on at least two factors. The first is the delineation of specific pathophysiological conditions with testable hypotheses that require measurements *in vivo* of the free radicals that are produced. The second is the development of improved spin traps that are nontoxic, and whose adducts are sufficiently stable in cells, and provide characteristic spectra of sufficient intensity.

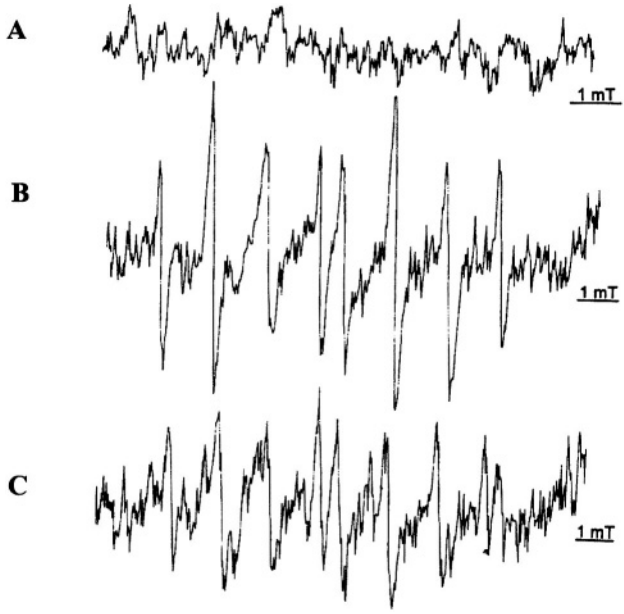

Figure 7. EPR spectra of hydroxyl radical adducts recorded *in vivo* in mice treated with 5-aminolevulinic acid/$FeNH_4(SO_4)_2.12H_2O$ (each 200mg/kg). Spectrum A was recorded using DMPO as a spin trap (10 mmol/Kg), spectrum B was recorded using DEPMPO (10mmol/Kg), and spectrum C was recorded using the same conditions as B but with prior administration of DMSO (10g/Kg). This resulted in the radical adduct from the generation of methyl radicals by the reaction of DMSO with hydroxyl radicals. For more details please refer to Timmins et al. (1999).

The use of measurements of reactive free radicals in the clinic will depend on the success of developments in animals. Once that is established and the paramagnetic probes to make the measurements have been

demonstrated to be safe for use in human subjects, there are some very attractive potential clinical applications.

8. FREE RADICAL FORMS OF DRUGS AND TOXINS

While EPR is specific for detecting and characterizing free radicals, there are few radical intermediates of interest of drugs or physiological reactions that occur in sufficient concentrations to be detectable by *in vivo* EPR. There are some exceptions, however, and several of these have been studied already, and more are likely to be found in the future.

Using low-frequency EPR, Mader et al. (1995) detected free radicals from the skin of hairless mice after topical application of anthralin. Detection of free radicals arising from food after oral administration is another field where *in vivo* EPR could have a useful role. Recently, free radicals arising from licorice-flavored sweets were directly, and non-invasively, detected after oral administration to mice (Gallez et al., 2000). Fujii et al. (1994) first demonstrated the use of EPR to study free radical reactions in live mice and excised muscle tissues resulting from the metabolism of nitrosobenzene. Fujii et al.(1999) also provided *in vivo* evidence for the generation of a nitroxyl-like free radical from illuminated nifedipine in mice.

8.1 Expected Applications in Experimental and Clinical Studies

Direct measurements of free radicals in experimental animals have been made with several compounds. To date, the number of such molecules has been limited, and therefore this type of application has been limited. It is not clear that there will ever be a large number of molecules that can be followed usefully by this approach, and thus this type of application is likely to remain relatively minor.

Direct measurement of free radicals in the clinic is an attractive possibility because it would not require the administration of a paramagnetic or other drug to make the observation possible. But, as noted for experimental animals, it is not clear that there will be a significant number of suitable radicals that are both observable and have a clinical rationale for studying them.

9. OXIDATION, REDUCTION, AND REDOX METABOLISM

In functioning biological systems nitroxides can undergo reduction to the hydroxylamines (Swartz et al., 1995; Swartz and Timmins, 2001). Although in principle nitroxides can be electron donors, producing oxoammonium cations, the more common oxidation is the conversion of the hydroxylamine back to the nitroxide. Within cells, the usual metabolism of nitroxides is the reduction to the hydroxylamine by the electron transport system at the level of ubiquinone. The predominant site for oxidation of the hydroxylamine is in the membrane. An extensive review of the metabolism of nitroxides was published in 1995 (Kocherginsky and Swartz, 1995).

The reversible oxidation-reduction cycle between nitroxides and hydroxylamines can be exploited to follow redox metabolism *in vivo.* This is potentially valuable, because there are few other ways to follow the kinetics of redox reactions *in vivo.* The reactions of nitroxides and hydroxylamines in the presence of cells tend to be dominated by enzymatic mechanisms, although these reactions also can occur non-enzymatically. At very low concentrations of oxygen, oxygen dependent changes in the rate of reduction of nitroxides occur.

While the reduction of nitroxides can be a useful indicator of redox metabolism, there are very significant potential problems in carrying out such experiments *in vivo.* Typically a nitroxide is administered, and the rate of disappearance from the whole organism or some specific area is followed over time. The complexities arise because there are several different mechanisms that can affect the rate of change of the amount of paramagnetic nitroxide that is observed. Certainly one is the reduction to the hydroxylamine. This may be opposed, in part, by reoxidation of the hydroxylamines, and therefore the observed rate will be affected by factors that affect the rate of reoxidation as well as the rate of reduction of the nitroxide. The amount of nitroxide that is observed also can be affected by changes in the rate of perfusion into and out of the volume that is being followed. The amount of nitroxide that is present also can be affected by the rate of excretion. In principle there also can be apparent changes that are due to alterations in the diffusion of nitroxides across potential barriers such as blood vessel walls, and cell membranes. There also can be apparent changes in the intensity of the nitroxide signal that reflects altered motion or other mechanisms that lead to line broadening. There also can be irreversible reactions of nitroxides through other mechanisms, such as direct reactions with strongly oxidizing species such as reactive free radicals. This formidable list of possible alternative mechanisms for the decrease in the intensity of the EPR spectra from nitroxides *in vivo* puts a very difficult

burden on the researcher who tries to interpret the change in terms of a particular mechanism.

The determination of low oxygen concentrations using nitroxides has considerable potential because a range of important pathologies is associated with low concentrations of oxygen, such as in tissues undergoing an ischemic episode and in tumors. It is well established in tumors that there can be considerable heterogeneity in pO_2, and very hypoxic regions may be the determining factor for the response to therapy (Hockel et al., 1996). The effect of oxygen on the rate of reduction of 5-doxyl stearate has been used to obtain oxygen dependent EPR spectroscopy *in vitro* using the differential rate of metabolism of 5-doxylstearate (Chen and Swartz, 1989). The resulting changes in the concentration of nitroxides reflected the amount of reduction that had occurred. The oxygen dependent metabolism of nitroxides can be used with NMR to provide images that reflect this process (Swartz et al., 1986).

9.1 Expected Applications in Experimental and Clinical Studies

The measurement of oxidation, reduction, and redox metabolism *in vivo* in experimental animals already is a widely used application and is likely to continue to grow. Nitroxides are usually used for these measurements, and they appear to have few undesirable side effects that would limit their use. As noted above, the interpretation of the results of such studies is complex but with careful attention to the potential sources of change in the signal can be very useful, and definitive data may be obtained in many circumstances.

The measurement of oxidation, reduction, and redox metabolism *in vivo* in the clinic is a potentially valuable capability because of the paucity of alternative methods to make such measurements. In order for this to be established as a clinical tool, however, several obstacles need to be overcome. The safety of the use in human subjects of systemically administered nitroxides needs to be established. While the results in animals suggest that they are unlikely to be very toxic, the procedures for obtaining clearance for use in humans are costly and complex and so far, it is not clear that there is a source of funding for such studies. If that barrier can be overcome, this may become a major use, although the clinical conditions for which it would be used are not yet delineated. There may be some clinical potential for making redox measurements in skin, including going to higher frequencies to increase sensitivity. Using S-band (3 GHz) EPR, Herrling et al. (1996) measured the kinetics of clearance of millimolar concentration of nitroxide labels applied to the human skin; however, they could not achieve sufficient sensitivity for *in vivo* imaging of free radicals in skin. Recent

results by He et al. (2001) are more encouraging, indicating that adequate signal to noise can be achieved under some circumstances.

10. PARAMAGNETIC STATES OF METAL IONS

While there are many paramagnetic metal ions *in vivo,* only a few have EPR spectra that can be resolved under the conditions needed for measurements *in vivo.* Most metal ions have such broad lines at 37° C that they cannot be observed, but chromium and manganese are interesting and potentially important exceptions. When these elements have paramagnetic states that can be followed by *in vivo* EPR, it may be possible to obtain data that cannot readily be obtained by other techniques because the EPR method responds to specific oxidation states of the elements.

Using 1.2 GHz EPR with a cylindrical shaped loop gap resonator, direct *in vivo* detection of Cr(V) in a living mouse was demonstrated by Liu et al. (1996), Fig. 8. Intravenous injection of Cr(VI) in mice generated Cr(V), which was found predominantly in the liver with a small amount in the blood. In addition to inhalation as the main route for occupational exposure, skin can be a route for chromium to enter into humans and to exert its carcinogenicity. Liu et al. (1997) investigated the reduction of chromate on the skin of living rats using 1.1 GHz EPR with a surface coil resonator. A topical application of Cr(VI) on the skin of rats generated the transient species, Cr(V).

10.1 Expected Applications in Experimental and Clinical Studies

In vivo measurements of metal ions in experimental animals have been carried out and some useful data have been obtained. The number of problems for which such measurements are important seems to be limited, however, and therefore this is not likely to become a major use of *in vivo* EPR.

In vivo measurement of metal ions in the clinic is attractive because it does not require the administration of another drug to make the measurements. So far, however, there have not been circumstances defined where such measurements would be useful clinically.

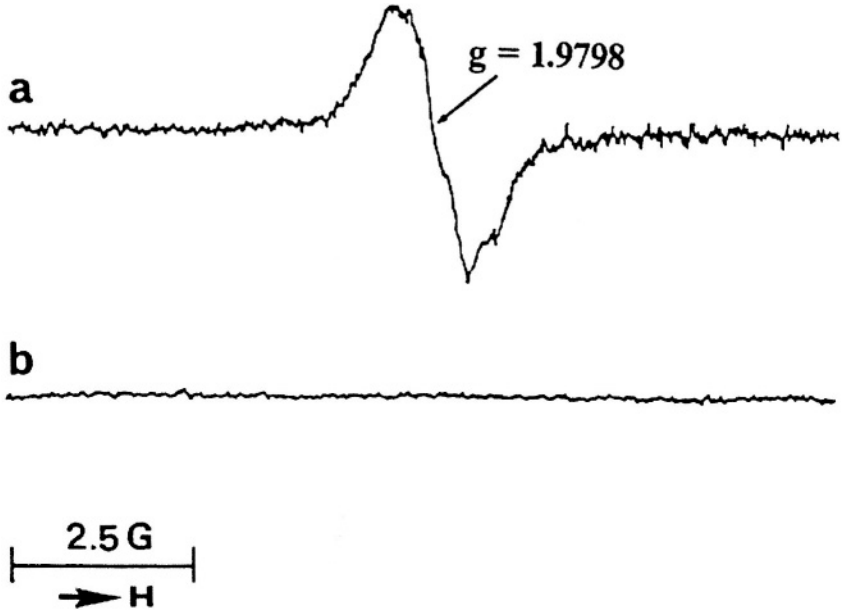

Figure 8. 1.2 GHz EPR spectrum of Cr(V) from a whole mouse. Spectrum "a" was recorded 5 minutes after intravenous injection of 100 μl of 100mM sodium dichromate into the mouse through the tail vein. Spectrum "b" was recorded after the animal was injected with saline instead of dichromate. For more details please refer to Liu et al. (1996).

11. TEMPERATURE

The temperature *in vivo* at specific locations can be an important parameter, but the methods to measure this non-invasively are limited. There are several types of temperature dependent phenomena that potentially can be used with EPR to determine temperature *in vivo.* Some of the oxygen-sensitive particulates, such as LiPc, have temperature dependent linewidths, so if the oxygen is kept constant, the spectral changes can be used to measure temperature. There also have been some published positive results from using more complex systems that can be administered to animals, such as albumin microspheres, that have oxygen-dependent changes that reflect temperature, Fig. 9 (Eckburg et al., 1996). This approach has potential clinical applications, in particular in optimizing the treatment of cancer with hyperthermia. This technology can be applied to measure different temperature ranges by varying the composition of the medium of the nitroxides.

11.1 Expected Applications in Experimental and Clinical Studies

The measurement of temperature *in vivo* in experimental animals has been shown to be feasible. In view of the limited number of alternatives to make such measurements non-invasively, it seems possible that this approach will grow in the future.

The most likely use of such measurements in the clinic would be in conjunction with the use of therapeutic hyperthermia. Because of the limited scope for such measurements and since it would require the clearance of the paramagnetic material to make the measurements, this seems unlikely to become a major clinical application.

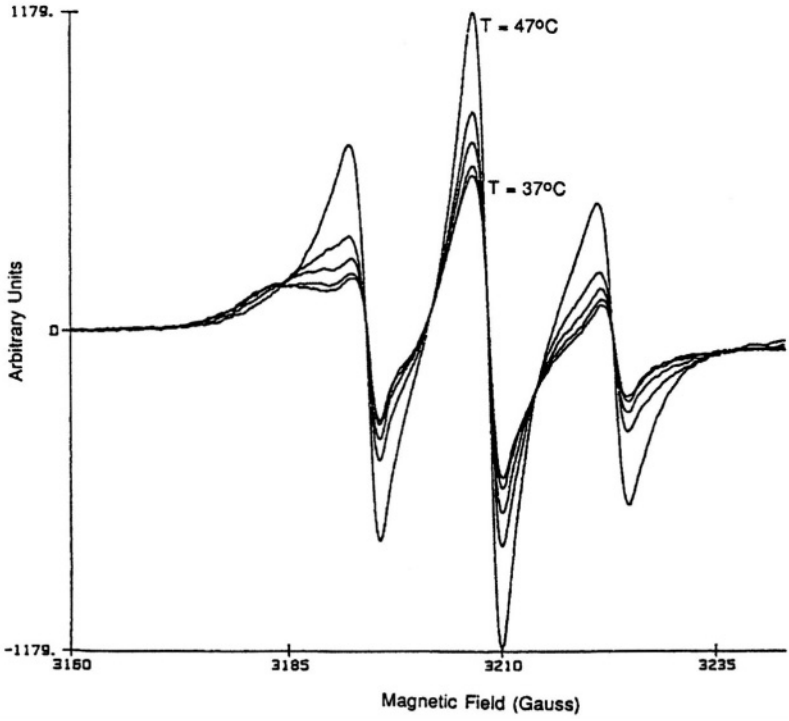

Figure 9. An example of the temperature dependence of the EPR spectrum between 37 °C and 47°C for 3-doxyl-5Δ-cholestane in 1 mole % cholesterol and 99 mole % methyl docosanoate encapsulated in microspheres. For more details please refer to Eckburg et al. (1996).

12. VIABILITY

An EPR-based assay for the viability of cells has been developed and applied to spheroids (Dobruicki et al., 1991). The method is based on the ability of viable cells to exclude a charged paramagnetic ion, a capability that is lost when the cells become non-viable. The effect of the paramagnetic ions are visualized by their effects on intracellular nitroxides, whose spectra become very broad (and hence difficult to see) when the cell permits the metal ion to enter the cell. This approach was very useful in delineating areas of viability in the spheroid tumor model.

12.1 Expected Applications in Experimental and Clinical Studies

The application of this technique to *in vivo* studies in animals would be very useful but difficult. The approach using the exclusion of paramagnetic metal ions by viable cells does not seem feasible. It might be possible, however to use a cellular function such as the ability to hydrolyze an ester bond of a nitroxide as an assay of cell functionality.

The use of this technique in the clinic is unlikely to occur unless progress is made in applications in experimental animals.

13. PHARMACOKINETICS

The use of *in vivo* EPR for pharmacological studies is a wide and promising field, as has been pointed out in recent reviews (Mader et al., 1996b; Mader, 1998). These can effectively use the measurements of most of the parameters discussed elsewhere in this article. Paramagnetic tags have been used to follow the time course and distribution of the drug (usually the paramagnetic tag is obtained by the attachment of a nitroxide group to the drug, but in some cases the drug itself is a sufficiently stable free radical so it can be studied directly). This approach has been exploited to follow the behavior of implanted drugs, including following parameters in the implant such as the release of the drug, the penetration of water, the pH, and the mobility of the drug. *In vivo* EPR also has been used to follow the generation and decay of free radical intermediates of drugs and toxins.

13.1 Expected Applications in Experimental and Clinical Studies

The application of this approach in experimental animals already is an important application and is likely to grow considerably because of the unique data that can be obtained with this approach.

The use of this approach *in vivo* in the clinic is very attractive. The most likely early applications would be in studying drug delivery systems in situ. This will, however, require the clearance of the paramagnetic labels for use in human subjects. If the measurements seem sufficiently valuable to someone in a pharmaceutical company, this could occur. There is a variant that potentially would be applicable immediately in some circumstances: when the delivery system is sterilized by radiation and the radiation-induced signals have properties that are appropriate for the desired measurements (Mader et al., 1996a).

14. PERFUSION USING WASHOUT OF PARAMAGNETIC TRACERS

The perfusion of tissues usually is investigated using water-soluble or blood-pool contrast agents in nuclear medicine, computed tomography, or MRI. It has been shown that the washout of paramagnetic nitroxides can be used effectively for this purpose, and it potentially can be combined with the sensitivity to oxygen of their bioreduction to also obtain information on the oxygenation of the tissue. The simplicity of this approach, combined with the additional information that can be gained from the effects on the EPR spectra of oxygen or other parameters (such as pH), make this a potentially productive application.

Studies illustrating the potential of this technique were done by Gallez et al. (1996a), who investigated perfusion and hypoxia simultaneously in mice by following the change in intensity and the shape of the EPR spectra, using 1.1 GHz EPR, after injection directly into normal tissue or tumors (MTG-B and RIF-1 tumors).

14.1 Expected Applications in Experimental and Clinical Studies

The application of this technique in experimental animals has considerable potential, although to date it has been used only sparingly.

The use *in vivo* in the clinic is likely to occur if appropriate substances receive clearance for use in human subjects. This use is not likely to provide the impetus for such clearance.

15. RADIATION DOSIMETRY

Ionizing radiation induces large numbers of unpaired electrons. In solutions the unpaired electrons react and recombine very quickly so that potential EPR signals are gone within microseconds or nanoseconds. In solid materials, however, the unpaired electrons may be stabilized and observed. In mammalian teeth and bones, this stabilization can persist for very long times and even has been utilized for dating ancient skeletal remains. This stability of unpaired electrons in tissues irradiated *in vivo* has been known for many years (Brady et al., 1968), and has been applied to measure radiation dose retrospectively, especially utilizing isolated teeth, (Gualtieri et al., 2001; Skvortsov et al., 2000). With the development of *in vivo* EPR techniques, it has become possible to make measurements *in vivo* without having to remove the teeth. Because the *in vivo* EPR technique uses a lower frequency (1200 MHz), the sensitivity is much lower than that obtained with isolated teeth where 9,000 MHz is used, and the samples can be cooled and/or concentrated to achieve higher sensitivity (the EPR signal is in the enamel of the teeth, which can be isolated and concentrated). As shown in Fig. 10, there is sufficient sensitivity to make it feasible to make these measurements *in vivo* at the doses of interest. The *in vivo* method is likely to be able to provide data as low as 50-150 cGy; this dose range extends down to radiation doses that are unlikely to cause severe symptoms in periods of days or months. Thus, this technique has the potential for use to screen large numbers of people after potential exposure to clinically significant radiation; such exposures can occur potentially under battlefield conditions or dispersal of radiation from the action of terrorists.

15.1 Expected Applications in Experimental and Clinical Studies

There does not appear to be any significant use of this technique in experimental animals, except as needed for development of the clinical applications.

The use of this technique in human subjects seems very promising. It would provide a capability that does not exist with any method—the capability to determine after the fact whether an individual has received a clinically significant amount of radiation and if so, to determine the dose

with sufficient precision to allow for effective decision-making. Individuals could be classified into appropriate groups such as no treatment is needed, maximum therapeutic attention is warranted, or only symptomatic therapy is appropriate. It is quite possible that *in vivo* EPR dosimetry using teeth in situ will become a standard part of the plans for dealing with exposures to potentially life threatening levels of ionizing radiation.

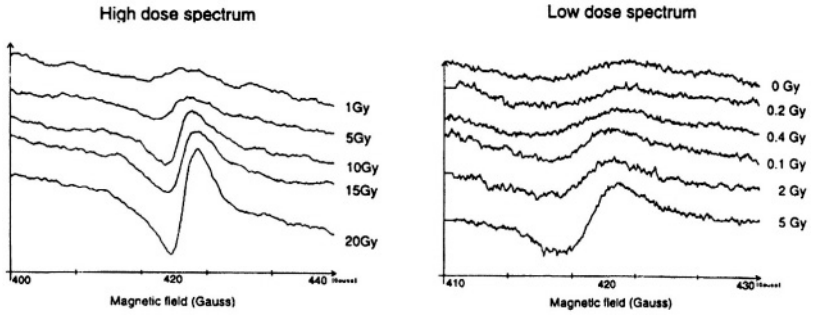

Figure 10. EPR signals from human teeth at 1.1 GHz. In the lower dose range (0 to 5 Gy) a higher receiver gain was used, and therefore the noise is higher. For details please refer to Miyake et al. (2000).

We are in the process of building a prototype instrument for use in human subjects. We will be able to calibrate it by studies in patients undergoing radiation therapy, where the doses to the teeth are known with great accuracy.

16. CONCLUSIONS

In vivo EPR spectroscopy already has provided very useful measurements of a number of important parameters in experimental animals. Oximetry is the most prominent application, especially for repeated measurements in tissues. Other prominent uses that already have been implemented include measurements of free radicals (including nitric oxide), several aspects of pharmacology, and measurements of redox metabolism. It seems quite likely that similar types of measurements also will be made useful in human subjects, especially oximetry. The use of *in vivo* EPR for "after-the-fact" dosimetry for exposures due to terrorist actions or war also seems likely to be an important application in human subjects. There also are a number of other types of measurements, especially of biophysical parameters that may be effectively applied in the near future. It seems very likely that *in vivo* EPR will be a major experimental tool for many

applications, and routine clinical applications have a reasonably probability as well.

ACKNOWLEDGMENTS

This work was supported by PO1 EB002180, "Measurement of pO_2 in Tissues *In Vivo* and *In Vitro"* and used the facilities of P41 EB002032, "EPR Center for the Study of Viable Systems." We also would like to thank the many colleagues who have made very significant contributions to the progress and results described here; many of their names are included in the cited references. Finally, we would like to acknowledge the important role that Jim Hyde has had in these developments as an instrumental innovator and advisor for our research endeavors.

17. REFERENCES

Ardenkjaer-Larsen, J. H., Laursen, I., Leunbach, I., Ehnholm, G., Wistrand, L. G., Petersson, J. S., and Golman, K. (1998) EPR and DNP properties of certain novel single electron contrast agents intended for oximetric imaging, *J. Magn. Reson.* **133**, 1-12.

Bhujwalla, Z. M., McCoy, C. L., Glickson, J. D., Gillies, R. J., and Stubbs, M. (1998) Estimations of intra- and extracellular volume and pH by ^{31}P magnetic resonance spectroscopy: effect of therapy on RIF-1 tumours, *Br. J. Cancer* **78**, 606-611.

Borbat, P. P., Costa-Filho, A. J., Earle, K. A., Moscicki, J. K., and Freed, J. H. (2001) Electron spin resonance in studies of membranes and proteins, *Science* **291**, 266-269.

Brady, J. M., Aarestad, N. O., and Swartz, H. M. (1968) *In vivo* dosimetry by electron spin resonance spectroscopy, *Health Physics* **15**, 43-47.

Buettner, G. R., and Mason, R. P. (1990) Spin-trapping methods for detecting superoxide and hydroxyl free radicals *in vitro* and *in vivo, Methods Enzymol,* **186**, 127-133.

Cafiso, D. S. (1989) Electron paramagnetic resonance methods for measuring pH gradients, transmembrane potentials, and membrane dynamics, *Methods Enzymol.* **172**, 331-345.

Chen, K., and Swartz, H. M. (1989) The products of the reduction of doxyl stearates in cells are hydroxylamines as shown by oxidation by ^{15}N-perdeuterated tempone, *Biochim. Biophys. Acta,* **992**, 131-133.

Collier, J., and Vallance, P. (1989) Second messenger role for NO widens to nervous and immune systems, *Trends Pharmacol. Sci.* **10**, 427-431.

Dobruicki, J. W., Sutherland, R. M., and Swartz, H. M. (1991) Non-perturbing test for cytotoxicity in isolated cells and spheroids, using electron paramagnetic resonance, *Magn. Reson. Med.* **19**, 42-55.

Eckburg, J. J., Chato, J. C., Liu, K. J., Grinstaff, M. W., Swartz, H. M., Suslick, K. S., and Auteri, F. P. (1996) The measurement of temperature with electron paramagnetic resonance spectroscopy, *J. Biomech. Eng.* **118**, 193-200.

Fujii, H., and Berliner, L. J. (1999) *In vivo* EPR evidence for free radical adducts of nifedipine, *Magn. Reson. Med.* **42**, 691-694.

Fujii, H., Zhao, B., Koscielniak, J., and Berliner, L. J. (1994) *In vivo* EPR studies of the metabolic fate of nitrosobenzene in the mouse, *Magn. Reson. Med.* **31,** 77-80.

Fujii, S., and Yoshimura, T. (2000) Detection and imaging of endogenously produced nitric oxide with electron paramagnetic resonance spectroscopy *Antioxid. Redox Signal,* **2,** 879-901.

Gallez, B., Bacic, G., Goda, F., Jiang, J., O'Hara, J. A., Dunn, J. F., and Swartz, H. M. (1996a) Use of nitroxides for assessing perfusion, oxygenation, and viability of tissues: *in vivo* EPR and MRI studies, *Magn. Reson. Med.* **35,** 97-106.

Gallez, B., Baudelet, C., and Debuyst, R. (2000) Free radicals in licorice-flavored sweets can be detected noninvasively using low frequency electron paramagnetic resonance after oral administration to mice, *J. Nutr.* **130,** 1831-1833.

Gallez, B., Mader, K., and Swartz, H. M. (1996b) Noninvasive measurement of the pH inside the gut by using pH-sensitive nitroxides. An *in vivo* EPR study, *Magn. Reson. Med.* **36,** 694-697.

Galster, H. (1991) *pH Measurements: Fundamentals, Methods, Applications, Instrumentation,* VCH, Weinhein.

Glasgow, B. J., Gasymov, O. K., Abduragimov, A. R., Yusifov, T. N., Altenbach, C., and Hubbell, W. L. (1999) Side chain mobility and ligand interactions of the G strand of tear lipocalins by site-directed spin labeling, *Biochemistry* **38,** 13707-13716.

Grinberg, O. Y., Smirnov, A. I., and Swartz, H. M. (2001) High spatial resolution multi-site EPR oximetry. The use of convolution-based fitting method, *J. Magn. Reson.* **152,** 247-258.

Gualtieri, G., Colacicchi, S., Sgattoni, R., and Giannoni, M. (2001) The Chernobyl accident: EPR dosimetry on dental enamel of children, *Appl. Radiat. Isot.* **55,** 71-79.

Halpern, H. J., Chandramouli, G. V., Barth, E. D., Yu, C., Peric, M., Grdina, D. J., and Teicher, B. A. (1999) Diminished aqueous microviscosity of tumors in murine models measured with *in vivo* radio frequency electron paramagnetic resonance, *Cancer Res.* **59,** 5836-5841.

Halpern, H. J., Yu, C., Barth, E., Peric, M., and Rosen, G. M. (1995) In situ detection, by spin trapping, of hydroxyl radical markers produced from ionizing radiation in the tumor of a living mouse, *Proc. Natl. Acad. Sci. USA,* **92,** 796-800.

He, G., Samouilov, A., Kuppusamy, P., and Zweier, J. L. (2001) *In vivo* EPR imaging of the distribution and metabolism of nitroxide radicals in human skin, *J. Magn. Reson.* **148,** 155-164.

He, G., Samouilov, A., Kuppusamy, P., and Zweier, J. L. (2002) *In vivo* imaging of free radicals: applications from mouse to man, *Mol Cell Biochem.* **234-235,** 359-367.

Herrling, T. E., Groth, N. K., and Fuchs, J. (1996) Biochemical EPR imaging of skin, *Appl. Magn. Reson.* **11,** 471-486.

Hockel, M., Schlenger, K., Mitze, M., Schaffer, U., and Vaupel, P. (1996) Hypoxia and radiation response in human tumors, *Semin. Radiat. Oncol.* **6,** 3-9.

Jackson, S. K., Madhani, M., Thomas, M., Timmins, G. S., and James, P. E. (2001) Applications of *in vivo* electron paramagnetic resonance (EPR) spectroscopy: measurements of pO_2 and NO in endotoxin shock, *Toxicol. Lett.* **120,** 253-257.

James, P.E., Grinberg, O.Y., Goda, F., O'Hara, J.A. and Swartz, H.M. (1997) Gloxy: An oxygen-sensitive coal for accurate measurement of low oxygen tensions in biological systems, *Magn. Reson. Med.* **38,** 48-58.

James, P. E., Jackson, S. K., Grinberg, O., and Swartz, H. M. (1995) The effects of endotoxin on oxygen consumption of various cell types *in vitro:* An EPR oximetry study, *Free Rad. Biol. Med.* **18,** 641-647.

James, P. E., Miyake, M., and Swartz, H. M. (1999) Simultaneous measurement of NO and PO_2 from tissue by *in vivo* EPR, *Nitric Oxide,* **3,** 292-301.

Jiang, J. J., Liu, K. J., Jordan, S. J., Swartz, H. M., and Mason, R. P. (1996) Detection of free radical metabolite formation using *in vivo* EPR spectroscopy: evidence of rat hemoglobin thiyl radical formation following administration of phenylhydrazine, *Arch. Biochem. Biophys.* **330,** 266-270.

Jiang, J., Liu, K. J., Shi, X., and Swartz, H. M. (1995) Detection of short-lived free radicals by low frequency ESR spin trapping in whole living animals: Evidence of sulfur trioxide anion free radical generation *in vivo, Arch. Biochem. Biophys.* **319,** 570-573.

Joseph, J., Kalyanaraman, B., and Hyde, J.S. (1993) Trapping of nitric oxide by nitronyl nitroxides, an electron spin resonance investigation. *Biochem. Biophys. Res. Commun.* **192,** 926-934.

Khramtsov, V. V., Marsh, D., Weiner, L., Grigoriev, I. A., and Volodarsky, L. B. (1982) Proton exchange in stable nitroxyl radicals. EPR study of the pH of aqueous solutions, *Chem. Phys. Lett.* **91,** 69-72.

Khramtsov, V. V. and Volodarsky, L. B. (1998) Use of Imidazoline Nitroxides in Studies of Chemical Reactions. ESR Measurements of the Concentration and Reactivity of Protons, Thiols, and Nitric Oxide. *Biol. Magn. Reson.* **14,** 109-180.

Khramtsov, V. V., and Weiner, L. M. (1988) Proton exchange in stable nitroxyl radicals: pH-sensitive spin probes, *Imidazoline Nitroxides,* Vol. II, CRC Press, Boca Raton, FL, 37-80.

Khramtsov, V. V., Yelinova, V. I., Glazachev, Yu. I., Reznikov, V. A., and Zimmer, G. (1997) Quantitative determination and reversible modification of thiols using imidazolidine biradical disulfide label, *J. Biochem. Biophys. Methods* **35,** 115-128.

Knecht, K. T., and Mason, R. P. (1993) *In vivo* spin trapping of xenobiotic free radical metabolites, *Arch. Biochem. Biophys.* **303,** 185-194.

Kocherginsky, N., and Swartz, H. M. (1995) *Nitroxide Spin Labels, Reactions in Biology and Chemistry,* CRC Press, Boca Raton, FL.

Komarov, A., Mattson, D., Jones, M. M., Singh, P. K., and Lai, C.S. (1993) *In vivo* spin trapping of nitric oxide in mice, *Biochem. Biophys. Res. Commun.* **195,** 1191-1198.

Kotake, Y., Moore, D. R., Sang, H., and Reinke, L. A. (1999) Continuous monitoring of *in vivo* nitric oxide formation using EPR analysis in biliary flow, *Nitric Oxide* **3,** 114-122.

Lai, C. S., and Komarov, A. M. (1994) Spin trapping of nitric oxide produced *in vivo* in septic-shock mice, *FEBS Lett.* **345,** 120-124.

Liu, K. J., Mader, K., Shi, X., and Swartz, H. M. (1997) Reduction of carcinogenic chromium (VI) on the skin of living rats, *Magn. Reson. Med.* **38,** 524-526.

Liu, K. J., Miyake, M., Panz, T., and Swartz, H. M. (1999) Evaluation of DEPMPO as a spin trapping agent in biological systems, *Free Rad. Biol. Med.* **26,** 714-721.

Liu, K. J., and Shi, X. (2001) *In vivo* reduction of chromium (VI) and its related free radical generation, *Mol. Cell Biochem.* **222,** 41-47.

Liu, K. J., Shi, X., Jiang, J., Goda, F., Dalai, N., and Swartz, H. M. (1996) Low frequency electron paramagnetic resonance investigation on metabolism of chromium (VI) by whole live mice, *Ann. Clin. Lab. Science* **26,** 176-184.

Mader, K. (1998) Pharmaceutical applications of in *vivo* EPR, *Phys. Med. Biol.* **43,** 1931-1935.

Mader, K., Bacic, G., Domb, A., Elmalak, O., Langer, R., and Swartz, H. M. (1997) Noninvasive *in vivo* monitoring of drug release and polymer erosion from biodegradable polymers by EPR spectroscopy and NMR imaging, *J. Pharm. Sci.* **86,** 126-134.

Mader, K., Bacic, G., and Swartz, H. M. (1995) *In vivo* detection of anthralin-derived free radicals in the skin of hairless mice by low-frequency electron paramagnetic resonance spectroscopy, *J. Invest. Dermatol.* **104,** 514-517.

Mader, K., Gallez, B., Liu, K. J., and Swartz, H. M. (1996a) Non-invasive *in vivo* characterization of release processes in biodegradable polymers by low-frequency electron paramagnetic resonance spectroscopy, *Biomaterials* **17,** 457-461.

Mader, K., Gallez, B., and Swartz, H. M. (1996b) *In vivo* EPR: An effective new tool for studying pathophysiology, physiology, and pharmacology, *App. Rad. Isot.* **47,** 1663-1667.

Marechal, X., Mordon, S., Devoisselle, J. M., Begu, S., Query, B., Neviere, R., Buys, B., Dhelin, G., Lesage, J. C, Mathieu, D., and Chopin, C. (1999) *In vivo* application of intestinal pH measurement using 2',7'-bis(carboxyethyl)-5,6-carboxyfluorescein (BCECF) fluorescence imaging, *Photochem. Photobiol.* **70,** 813-819.

Mignano, A. G., and Baldini, F. (1996) Biomedical sensors using optical fibres, *Rep. Prog. Phys.* **59,** 1-28.

Miyake, M., Liu, K. J., Walczak, T. M., and Swartz, H. M. (2000) *In vivo* EPR dosimetry of accidental exposures to radiation: experimental results indicating the feasibility of practical use in human subjects, *Appl. Radiat. Isot.* **52,** 1031-1038.

Nagano, T. and Yoshimura, T. (2002) Bioimaging of Nitric Oxide. *Chem. Rev.* **102,** 1235-1269

Nohl, H., Stolze, K., and Weiner, L. M. (1995) Noninvasive measurement of thiol levels in cells and isolated organs, *Methods Enzymol.* **251,** 191-203.

Ojugo, A. S., McSheehy, P. M., McIntyre, D. J., McCoy, C., Stubbs, M., Leach, M. O., Judson, I. R., and Griffiths, J. R. (1999) Measurement of the extracellular pH of solid tumors in mice by magnetic resonance spectroscopy: a comparison of exogenous ^{19}F and ^{31}P probes, *NMR Biomed.* **12,** 495-504.

Packer, L. (1995) *Biothiols Methods Enzymol.* (ed.) **251,** 529.

Palmer, R. M., Ferrige, A. G., and Moncada, S. (1987) Nitric oxide release accounts for the biological activity of endothelium-derived relaxing factor, *Nature* **327,** 524-526.

Reddy, T. J., Iwama, T., Halpern, H. J., and Rawal, V. H. (2002) General synthesis of persistent trityl radicals for EPR imaging of biological systems, *J. Org. Chem.* **67,** 4635-4639.

Russell, D. A., Pottier, R. H., and Valenzeno, D. P. (1994) Continuous noninvasive measurement of *in vivo* pH in conscious mice, *Photochem. Photobiol.* **59,** 309-313.

Sentjurc, M., Swartz, H. M., and Kocherginsky, N. (1995) Metabolism, toxicity, and distribution of spin traps, in *Nitroxide Spin Labels, Reactions in Biology and Chemistry,* CRC Press, Boca Raton, FL 199-206.

Skvortsov, V. G., Ivannikov, A. I., Stepanenko, V. F., Tsyb, A. F., Khamidova, L. G., Kondrashov, A. E., and Tikunov, D. D. (2000) Application of EPR retrospective dosimetry for large-scale accidental situation, *Appl. Radiat. Isot.* **52,** 1275-1282.

Smirnov, A. I., Norby, S. W., Clarkson, R. B., Walczak, T., and Swartz, H. M. (1993) Simultaneous multi-site EPR spectroscopy *in vivo, Magn. Reson. Med.* **30,** 213-220.

Stachowicz, W., Burlinska, G., Michalik, J., Dziedzic-Goclawska, A., and Ostrowski, K. (1993) Applications of EPR spectroscopy to radiation treated materials in medicine, dosimetry, and agriculture, *Appl. Radiat. Isot.* **44,** 423-427.

Suzuki-Nishimura, T., and Swartz, H. M. (1998) Characterization of redox activity in resting and activated mast cells by reduction and reoxidation of lipophilic nitroxides, *Gen. Pharmacol.* **31,** 617-623.

Swartz, H. M. (1989) Metabolically responsive contrast agents, in *Advances in Magnetic Resonance Imaging,* Feig, E., (Ed.), Ablex Publishing Company, Norwood, N.J., 49-71.

Swartz, H. M. (1990) Principles of the metabolism of nitroxides and their implications for spin trapping, *Free Rad. Res. Comms.* **9,** 399-405.

Swartz, H.M. (2002a) The measurement of oxygen *in vivo* using EPR techniques, in *Bialogical Magnetic Resonance - Volume 20: In vivo EPR (ESR): Theory and Applications.* Berliner, L. J. (Ed.), Plenum Publishing Co., NY.

Swartz, H. M. (2002b) Potential medical (clinical!!!) applications of EPR: overview and perspectives, in *Biological Magnetic Resonance - Volume 20: In vivo EPR (ESR): Theory and Applications.* Berliner, L.J. (Ed.), Plenum Publishing Co. NY.

Swartz, H.M., and Berliner L. J. (1998) *In vivo* EPR, in *Foundations of Modern EPR,* World Scientific Publishing, Singapore/New Jersey/London. Eaton, S., Eaton, G., and Salikhov, K. (Eds), 361-378.

Swartz, H.M., and Berliner, L. (2002) Introduction and *in vivo* EPR, in *Biological Magnetic Resonance - Volume 20: In vivo EPR (ESR): Theory and Applications.* Berliner, L.J. (Ed.), Plenum Publishing Co., NY.

Swartz, H. M., Chen, K., Pals, M., Sentjurc, M., and Morse, P. D. 2nd. (1986) Hypoxia-sensitive NMR contrast agents, *Magn. Reson. Med.* **3,** 169-174.

Swartz, H. M., and Clarkson, R. B. (1998) The measurement of oxygen *in vivo* using EPR techniques, *Phys. Med. Biol.* **43,** 1957-1975.

Swartz, H. M., and Halpern, H. (1998) EPR studies of living animals and related model systems *(In vivo* EPR), in *Spin Labeling: The Next Millenium,* L.J. Berliner (Ed.), Plenum Publishing, New York, NY, 367-404.

Swartz, H. M., Sentjurc, M., and Kocherginsky, N. (1995) Metabolism and distribution of nitroxides in tissues and organs, in *Nitroxide Spin Labels, Reactions in Biology and Chemistry,* CRC Press, Boca Raton, FL 149-152.

Swartz, H. M., and Timmins, G. S., (2001) The metabolism of nitroxides in cells and tissues used to study functional biological systems *in vitro* and *in vivo,* in *Free Radicals in Toxicology,* Rhodes, C.J., Ed.

Swartz, H.M., and Walczak, T. (1996) An overview of considerations and approaches for developing *in vivo* EPR for clinical applications, *Res. Chem. Intermed.* **22,** 511-523.

Swartz, H. M., and Walczak, T. (1998) Developing *in vivo* EPR oximetry for clinical use, *Adv. Exp. Med. Biol* **45,** 243-252.

Timmins, G. S., Liu, K. J., Bechara, E. J., Kotake, Y., and Swartz, H. M. (1999) Trapping of free radicals with direct *in vivo* EPR detection: a comparison of 5,5-dimethyl-1-pyrroline-N-oxide and 5-diethoxyphosphoryl-5-methyl-1-pyrroline-N-oxide as spin traps for HO and $SO4^-$, *Free Rad. Biol. Med.* 27, 329-333.

Vanin, A. F. (1999) Iron diethyldithiocarbamate as spin trap for nitric oxide detection. *Methods Enzymol.* **301,** 269-279.

Venkataraman, S., Martin, S. M., and Buettner, G. R. (2002) Electron Paramagnetic Resonance for Quantitation of Nitric Oxide in Aqueous Solutions. Nitric Oxide, Part D, *Methods in Enzymology* **359,** 3-18.

Weiner, L. M. (1995) Quantitative determination of thiol groups in low and high molecular weight compounds by electron paramagnetic resonance, *Methods Enzymol.* **251,** 87-105.

Weiner, L. M., Hu, H., and Swartz, H. M. (1991) Development of EPR method for measurement of cellular sulfhydryl groups, *FEBS* **290,** 243-246.

Zweier, J. L., Fertmann, J., and Wei, G. (2001) Nitric oxide and peroxynitrite in post-ischemic myocardium, *Antioxid. Redox Signal* **3,** 11-22.

Chapter 10

EPR Oximetry in Biological and Model Samples

Witold K. Subczynski[1] and Harold M. Swartz[2]
[1]National Biomedical EPR Center,Department of Biophysics, Medical College of Wisconsin, Milwaukee, Wisconsin 53226; [2]Department of Radiology, Dartmouth Medical School, Hanover, New Hampshire 03755

Abstract: The well-known broadening of CW EPR spectra due to collision of the free radical with molecular oxygen in solution has been made into a tool for measuring oxygen concentration in numerous biological systems. The principles of the measurement of oxygen by this method are described, both for spin labels and for oxygen-sensitive particulate probes, such as coals, India ink, and lithium phthalocyanine. Applications are described for cell respiration, membrane permeability, and *in vivo* measurements on animal organs.

1. INTRODUCTION

The application of spin-label oximetry to biological and model systems dates back about 35 years. Backer et al. (1977) first emphasized that the resolution of the proton superhyperfine structure in the EPR spectrum of spin label I (Fig. 1) is very sensitive to the concentration of oxygen, and can be used as a parameter in measurements of oxygen consumption in mitochondria and cell suspensions. However, other scientists did not commonly use that spin label. Instead, spin label II (Fig. 1), obtained from Rozantzev's laboratory in Moscow, began being used more extensively, starting in early 1978 in the Department of Biophysics, Jagiellonian University, Krakow, Poland where it was employed to measure oxygen concentrations in tumor cell suspensions (Pajak et al., 1978). This spin label was later named CTPO (Popp and Hyde, 1981), which is the name commonly accepted and used in the literature. The changes of the superhyperfine structure in its EPR signal were parameterized as a function

of oxygen concentration. A useful parameter, called the "*K* parameter," was introduced by Sarna et al. (1980) (Fig. 2), and numerous calibration curves showing *K* as a function of oxygen concentration, temperature, spin label concentration, and microwave power have been published (e.g. Lai et al., 1982). Because of its high polarity, CTPO samples oxygen in the aqueous phase. A number of other spin labels that use superhyperfine structure for oximetry measurements also have been utilized (Morse et al., 1985; Chan et al. 1989), but CTPO (with the *K* parameter and Lai's calibration curves) has remained a widely used probe for oximetry measurements. It also should be that Povich (1975a; 1975b) seems to be the first who stated explicitly the important principle that the effects of oxygen on the EPR spectra measurements depend on both oxygen concentration and diffusion when using soluble free radicals for oximetry.

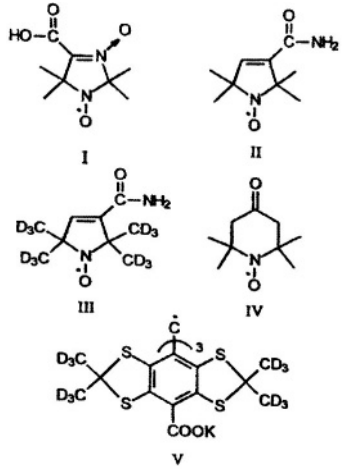

Figure 1. Chemical structures of spin-label molecular probes.

In 1980, the focus for development of EPR oximetry moved to the National Biomedical ESR Center at the Medical College of Wisconsin in Milwaukee. Here, EPR spectra of CTPO were carefully calibrated for measurement of oxygen consumption in cell suspensions during the cell cycle and during significant biochemical reactions (Sarna et al., 1980; Lai et al., 1982; Sarna and Sealy, 1984; Subczynski and Kusumi, 1985; Ankel et al., 1986; Kalyanaraman et al., 1987). It was also here that T_1 sensitive methods for evaluation of the product of oxygen diffusion-concentration in membranes were introduced and developed (Subczynski and Hyde, 1981; Kusumi et al., 1982; Yin and Hyde, 1987; Subczynski et al., 1989). It was shown that spin-label oximetry can be used as a quantitative method,

because every collision of oxygen with a spin label contributes to changes in an EPR spectrum in both T_1 and T_2 sensitive methods (Hyde and Subczynski, 1984, 1989; Subczynski and Hyde, 1981, 1984). The tremendous progress in development of spin-label oximetry was aided by the use of an oxygen permeable plastic, based on methyl pentene polymers, called TPX, for construction of sample containers, including capillaries (Popp and Hyde, 1981; Subczynski and Hyde, 1981). This facilitated equilibration of EPR samples with the desired partial pressure of oxygen. In all these developments, Professor James S. Hyde was a key individual. (Presently TPX rods can be purchased from Midland Plastic, Inc. (Madison, WI) and TPX capillaries together with the holder can be obtained from Molecular Specialties, Inc., Milwaukee, WI).

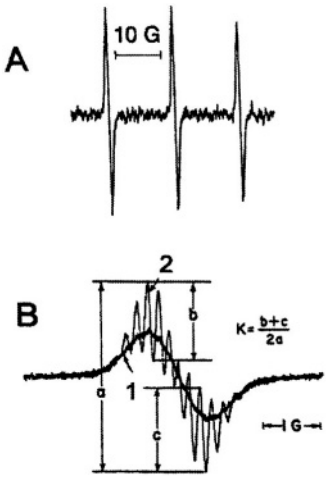

Figure 2. The EPR spectrum of an aerated solution of the 1.1×10^{-4} M CTPO in water (A). The central field component of the EPR spectrum of CTPO in air-saturated (1) and nitrogen-saturated (2) water (B). Spectra were recorded at 37°C. Definition of the *K* parameter is indicated.

The most significant contribution made by Jim Hyde, however, was in the development of T_1-sensitive oximetry methods including saturation recovery (the absolute T_1 method (Kusumi et al., 1982; Yin and Hyde, 1987; Subczynski et al., 1989)), CW saturation (Subczynski and Hyde, 1981), passage display (Froncisz et al., 1985), and the multiquantum approach (Mchaourab and Hyde, 1993; Mchaourab et al., 1994).

The contribution of Jim Hyde to *in vivo* oximetry also should be noted. His development, together with Wojciech Froncisz, of loop-gap resonators (Froncisz and Hyde, 1982) permitted measurements to be made at low

frequencies for larger water containing samples, including small laboratory animals (Lukiewicz and Lukiewicz, 1984; Lukiewicz, 1985). The first *in vivo* oximetry measurement, which is co-authored by Hyde, was done on mice (Subczynski et al., 1986). It gave significant data about changes in oxygen concentration in the peritoneal cavity when the gas the animal breathed was changed from air to pure oxygen.

Subsequently as additional *in vivo* oximetry methods based on EPR have been developed elsewhere, the National Biomedical ESR Center has continued to be involved in these developments in many important ways, including extensive interactions with the centers that are focused on this technique. In this chapter we consider both the initial method in which spin labels (nitroxides) are used as the oxygen sensitive paramagnetic probes, which is termed spin label oximetry, and the other methods that have been developed subsequently (but which have not displaced spin label oximetry). Because the *in vivo* methods of EPR oximetry have been thoroughly reviewed recently (Swartz and Clarkson, 1998; Swartz. 2003) and have not been as central to the ESR Center in Milwaukee, we have focused especially on applications to model and cellular systems in this chapter.

2. MEASUREMENT OF OXYGEN USING SPIN-LABEL PROBES

Even though molecular oxygen is paramagnetic, having a triplet ground state, no EPR spectrum has been recorded for oxygen dissolved in liquids near physiological temperatures. Fortunately, methods exist in which bimolecular collisions of molecular oxygen (paramagnetic, fast-relaxing, unobservable through EPR) with different spin-label probes (slow-relaxing, observable through EPR) are used to monitor the product of oxygen diffusion-concentration. Under appropriate conditions this product can be separated, giving the ability to measure the oxygen concentration or oxygen diffusion coefficient (Hyde et al., 1983; Hyde and Subczynski, 1989).

2.1 The Smoluchowski Equation

Because the collision between molecular oxygen and the free radical moiety of a spin label is at the heart of spin label oximetry, analyses of the EPR data are based on the Smoluchowski equation,

$$\omega = 4\,\pi r_0 (D_{SL} + D_O) C \qquad (1)$$

where r_o is the interaction distance between oxygen and nitroxide radical spin labels (4.5 Å; Windrem and Plachy, 1980) and C is the oxygen concentration expressed in molecules per unit volume. To measure the collision rate, an experimental observable, ω_{exp}, is related to the actual collision frequency, ω:

$$\omega_{exp} = 4\pi p\, r_o (D_{SL} + D_O) C \qquad (2)$$

where p is the probability that a spectroscopically observable event occurs when a collision takes place. This equation predicts how frequently a given spin-label molecule encounters surrounding oxygen molecules. It does not take into account the concentration of spin labels.

Usually the diffusion coefficient of oxygen, D_O, is much greater than the diffusion coefficient of the spin label, D_{SL}. The macroscopic diffusion coefficients of molecular oxygen in water (low viscosity environment) at 37, 20, and 10°C are 3.0×10^{-5}, 2.0×10^{-5}, and 1.5×10^{-5} $cm^2\ s^{-1}$, respectively (St. Denis and Fell, 1971). At these temperatures, values for the diffusion coefficients obtained for the smallest spin label d-Tempone in water are 0.9×10^{-5}, 0.6×10^{-5}, and 0.45×10^{-5} $cm^2\ s^{-1}$, respectively. These values were obtained from EPR line broadening data presented by Molin et al. (1980). The value of 0.72×10^{-5} $cm^2\ s^{-1}$ for translational diffusion of di-t-butyl nitroxide in water at 26°C was obtained by Ahn (1976) using a capillary diffusion method. In more viscous environment such as lipid bilayer membranes the difference between diffusion coefficient of oxygen and diffusion coefficient of lipid spin labels is much greater reaching two – three orders of magnitude (see Subczynski et al., 1984; 1986; 1992a for more data and discussion).Therefore, a useful simplification can be made by neglecting the diffusion coefficient of the spin label, relative to that of oxygen:

$$\omega_{exp} = 4\pi p\, r_o D_O C \qquad (3)$$

If this is possible, the experimental observation yields the oxygen diffusion-concentration product, $D_O C$. The interaction distance, r_o, can be adjusted to force the equality of the oxygen diffusion coefficient obtained from measuring the diffusion against a concentration gradient (macroscopic diffusion) and that from the Smoluchowski equation (self diffusion). It was shown that for spin labels, this agreement is obtained for $pr_o = 4.5$ Å (Hyde and Subczynski, 1984, 1989; Subczynski and Hyde, 1984). This is what makes the EPR spin label oximetry method quantitative.

2.2 Basic Methodological Approaches

Initially, the term *spin-label oximetry* was used to describe the application of nitroxide radical spin labels to oximetry measurements. It is now often broadened to include the use of any soluble paramagnetic substance that possesses an EPR spectrum sensitive to collisions with molecular oxygen, and occasionally even to the particulate paramagnetic probes that have been introduced, especially for *in vivo* oximetry. In this paper we reserve the use of the term to oximetry with soluble free radicals, and use the more general term "EPR oximetry" to apply to all types of oxygen-sensitive paramagnetic materials.

The three major methodological approaches used for spin-label oximetry can be classified as molecular, microscopic, and macroscopic. In the first approach, spin label molecules are directly dissolved in the examined systems. In the second and third approaches the paramagnetic material is confined. For soluble materials, the solution is confined within liposomes, proteinaceous microspheres, oil droplets, or plastic capillaries that prevent its mixing with the investigated system, while molecular oxygen can freely diffuse in and out of microscopic and macroscopic probes. Differentiating between the microscopic and macroscopic methods is somewhat arbitrary. The size of the microscopic probe should be smaller than the size of the cell (a few microns in diameter). The size of the macroscopic probe can be as large as 1 - 2 cm.

Oximetry with particulates, while having some similarities with spin label oximetry, is sufficiently different that it is useful to consider them separately. The particulates always provide localized information at the sites where the particles are located. When studies are done with a slurry of small particles, then the similarities with microscopic spin label oximetry are considerable. Most studies with particles, however, are done with macroscopic particles that are placed at one or more sites of interest. The most important role of oximetry based on the particulates is for *in vivo* oximetry in which repeated measurements from the same sites are needed.

2.2.1 Molecular Spin-Label Probes

The use of spin-label molecular probes I and II (CTPO) for oximetry has already been mentioned. Professor Howard Halpern at the 29th Rocky Mountain Conference in Denver, Colorado, described a partially deuterated CTPO analog (spin label III, Fig. 1) in August 1987. This spin label has only two resolved superhyperfine lines in its EPR spectrum, which arise from the interaction of an unpaired electron with the ring proton. This spectral feature is used to distinguish the broadening associated with self-

interaction from that due to environmental oxygen (Halpern et al., 1990). The authors also report a 20-fold increase in the sensitivity of the EPR spectrum to oxygen exchange broadening.

The spin label Tempone (spin label IV, Fig. 1) is one of the few nitroxide spin labels that shows no resolved proton coupling, and possesses a very narrow EPR line (0.25) G when dissolved at low concentration in a deoxygenated water solution. Narrower lines of 0.15 G can be obtained with deuteration of this spin label. Tempone has been used to measure oxygen consumption in biochemical reactions (Reszka and Sealy, 1984; Bielec et al., 1986), to record fast changes of oxygen concentration during photosynthesis (Strzalka et al., 1986; 1990), and to monitor the intracellular oxygen concentration (Wood et al., 1989).

Recently, a new type of oxygen-sensitive EPR molecular probe, triaryl methyl radical (trityl) (structure V in Fig. 1), was introduced (Ardenkjaer-Larsen et al., 1998). Trityls offer the possibility of an order-of-magnitude improvement in the signal-to-noise ratio, spatial resolution, and physiological sensitivity for *in vivo* spectral-spatial EPR imaging because of their very narrow linewidth (in the absence of oxygen it is approximately 25 mG). Images (with two spatial dimensions) of a mouse tumor were presented using this new type of stable free radical (Halpern et al., 1998).

2.2.2 Microscopic Spin-Label Probes

As can be seen from the Smoluchowski equation, the effect of molecular oxygen on EPR spectral characteristics of soluble oxygen-sensitive molecules depends on the diffusion-concentration product of oxygen in the solvent surrounding them. If they are dissolved in solvents with high oxygen solubility and high oxygen diffusion coefficients, they will be more sensitive to changes in oxygen tension. Hydrocarbons like paraffin oil or hexane are solvents which dissolve oxygen 4 - 10 times more than water (Linke, 1965), while the diffusion of oxygen is about as fast as in water (Subczynski and Hyde, 1984). The idea of having spin labels always surrounded by such solvents has been exploited in the oxygen-sensitive microscopic spin-label approach. Typical examples of microscopic spin-label probes are BSA-coated paraffin oil particles containing cholestane spin labels (Ligeza et al., 1992, 1994), or BSA-coated hexane particles containing stearic acid spin labels (Liu et al., 1994). Using such probes, it is possible to isolate nitroxides from water-soluble reductants and paramagnetic ions that might interfere with spin-label oximetry measurements. In these particles, the same hydrocarbon solvent that dissolves oxygen very well always surrounds spin label molecules. Therefore, the partial pressure of oxygen is the only factor that can influence the EPR spectrum of spin labels in the

microscopic probe. Such microscopic probes (a few micrometers in diameter) are readily and uniformly distributed within the sample, thus giving a rapid response to changes in oxygen partial pressure. For the purpose of protection against diffusion out of the liposome, liposomes containing the charged water soluble spin label 4-trimethylamonium-2,2,6,6,-tetramethylpiperidine-1-oxyl (Cat 1) were also used as a microscopic probe (Chan et al., 1989; Glockner et al., 1991).

2.2.3 Macroscopic Spin-Label Probes

The idea described above of enhancing the spin-label response to changes in oxygen partial pressure and isolating the spin-label solution from chemical and paramagnetic interference was used even earlier by Lukiewicz et al., who introduced macroscopic spin-label probes for *in vivo* oximetry measurements in 1984. The first experiments involved perdeutero ^{15}N Tempone solution in light paraffin oil, injected into the peritoneal cavity of a mouse (Fig. 3A). However, the spin label leaked out of the oil drop into the aqueous environment of the mouse body. To protect the spin label from leaking, the paraffin oil solution was enclosed in a gas-permeable TPX capsule before being placed in the peritoneal cavity of a mouse (Fig. 3B). *In vivo* oximetry measurements were performed at L-band using an EPR spectrometer with a loop-gap resonator (Subczynski et al., 1986). This method was further developed, and then used to measure the steady-state concentration of oxygen in solid tumors, which is critical for radiation therapy and experimental oncology (Lukiewicz, 1985).

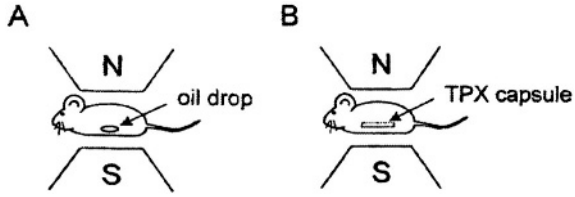

Figure 3. Diagram illustration of *in vivo* oximetry measurements. Mice (2-3 weeks old, weight approx. 20 g) were inserted into a cylinder of an L-band loop-gap resonator 25 mm in diameter and 30 mm long. An oil drop containing ^{15}N Tempone was injected into the peritoneal cavity of the animal (A). The TPX capsule containing a paraffin-oil solution of ^{15}N Tempone positioned in the peritoneal cavity of the animal (B).

2.2.4 Oximetry Based on Particulates

This approach uses insoluble, particulate materials based on carbonaceous materials (coals, charcoals, or India ink) or certain crystalline forms of lithium phthalocyanine (LiPc). These materials have EPR lines that are very sensitive to the presence of oxygen, often broadening several fold more in magnitude than the soluble materials used for EPR spin label oximetry. The mechanisms for the broadening can be quite complex and have been considered recently in detail in a review (Swartz and Clarkson, 1998). While used principally for measurements *in vivo* (Swartz, 2003), these probes also have been used for measurement of oxygen partial pressure in intact leaves (Ligeza et al., 1997) and in cellular systems (James et al, 1997; Vahidi et al., 1994).

2.3 Averaged and Local Oximetry Measurements

In the molecular probe method, spin label molecules are distributed more or less uniformly throughout the sample. Since the probe samples the fluid uniformly, the experimental parameter is proportional to the integral of the concentration over the sample volume - an important point if there is any reason to believe that oxygen gradients are present. If the sample being investigated is a homogenous fluid, the average oxygen concentration is easily determined using, for example, CTPO as a spin probe (Lai et al., 1982). If a molecular probe is applied to measure oxygen concentration in complex systems such as cells, the interpretation of the EPR data may be only qualitative. In such a system, the spin probes may not be uniformly distributed, and oxygen concentration can differ from place to place, and the oxygen diffusion coefficient can be different in different parts of the sample. Some of these difficulties can be avoided if the microscopic probe method is used. In this method the same solvent always surrounds label molecules, so the changes in the EPR spectrum are only related to the changes in oxygen partial pressure around the microscopic probe. This is schematically illustrated in Fig. 4 for a cell that is in equilibrium with a set percentage of air in the air/nitrogen mixture. Microscopic probes can easily be taken into the cell by phagocytosis, as was shown for BSA-coated paraffin droplets by Ito et al. (1981), who used them to study the phagocytic process of mouse peritoneal macrophages.

The approaches described above measure oxygen concentration and/or oxygen partial pressure averaged throughout the sample. However, if the spin-label molecule can be attached to a specific site of a protein or placed at a certain depth in the membrane, local oximetry measurement is possible. Measurement of oxygen accessibility to a certain spin-labelled amino acid is

necessary for depth-determination in site-directed spin labeling (SDSL) (Feix and Klug, 1998). Local oximetry measurements in the membrane are necessary for obtaining profiles of the oxygen diffusion-concentration product across the membrane, evaluation of the membrane permeability coefficient for oxygen, and discrimination of membrane domains. This subject will be discussed later in this chapter.

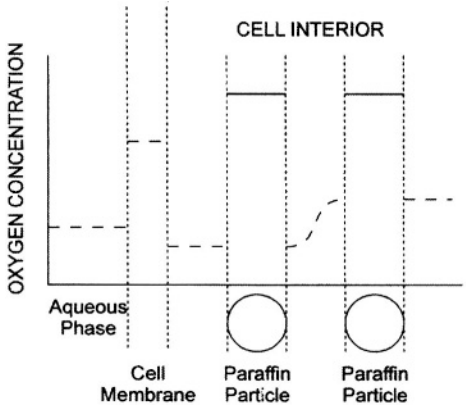

Figure 4. Schematic illustration of the local oxygen concentration sensed in the cell by molecular probes (- - - - -) and microscopic probes (---------) for the system in equilibrium with the set oxygen partial pressure (partial pressure of oxygen across the system is the same). The molecular probes measure the local (real) oxygen concentration which can significantly vary throughout the system (broken line). The concentration of oxygen inside the microscopic probes (paraffin particles containing a spin label) is the same, reflecting the partial pressure of oxygen with which the system was equilibrated. In this illustration oxygen consumption within the cell is neglected.

2.4 Oxygen Concentration, Partial Pressure, and Tension

Oxygen concentration, partial pressure of oxygen, and oxygen tension are mutually related values that, in principle, can be derived from one another. Oxygen concentration is expressed in moles per liter and is used for oxygen (solute) dissolved in bulk solvents. We can also talk about the local oxygen concentration in a certain region of the model and biological sample. Partial pressure of oxygen (torr or mm Hg) reflects the amount of oxygen in gas mixture and equals the pressure that oxygen would exert if it occupied the space by itself. For systems in equilibrium, the oxygen concentration in solution is determined exactly by the partial pressure of oxygen and the

solubility coefficient. For example, the concentration of oxygen in water saturated with air at 37°C (air contains 20.95% oxygen, which corresponds to a partial pressure of 159 mmHg, if the total pressure of air is one atmosphere) equals 220 μM. Oxygen tension is used mainly to describe oxygen concentration in systems that are not in equilibrium with gas phase (and usually not in equilibrium at all), like the human or animal body. It describes the very local oxygen concentration and is equal to the partial pressure of oxygen (the same units, torr or mm Hg) which, for system in local equilibrium, will give that certain local oxygen concentration.

In all EPR approaches described above the immediately measured value is the partial pressure of oxygen because for all oxygen sensitive paramagnetic materials, calibration curves can be produced that relate the observed EPR spectral parameter with the partial pressure of oxygen with which the probe is equilibrated (independently of the location of the probe: in gaseous phase, in a given solution, or in more complex environment). These calibration curves were produced for the molecular spin-label probe CTPO by saturating the CTPO water solution with a given oxygen/nitrogen mixture (with a given partial pressure of oxygen) and measuring the K parameter (Lai et al., 1982). They were produced for microscopic spin-label probes, BSA-coated paraffin oil particles, (Ligeza et al., 1992; 1994), as well as for particulate materials, coal derivative particles – fusinite (Ligeza et al., 1997). Also, EPR spectral parameter of a macroscopic spin probe, a TPX capsule containing ^{15}N Tempone solution in paraffin oil, was calibrated as a function of the partial pressure of oxygen (Subczynski et al., 1986).

Most often the molecular spin-label probe is dissolved in water for use in cell suspensions or for chemical reactions. In those cases the partial pressure of oxygen describes exactly the oxygen concentration in water phase (at a given temperature) and the calibration curves can be expressed as a function of oxygen concentration. These types of measurements (changing of oxygen concentration) were performed for measurements of oxygen consumption in CHO cell suspensions using CTPO (Lai et al., 1982; Ligeza et al., 1992) and in liposome suspension for measurement of lipid peroxidation (Subczynski and Kusumi, 1985; Kalyanaraman et al., 1987). The spin probe Tempone also was used for measurements of oxygen consumption (changing of oxygen concentration) in photo induced chemical reactions (Reszka and Sealy, 1984). Often, it is assumed that the environment surrounding the EPR probe is very similar to pure water and final data are expressed in concentration units. This was done for the microscopic spin-label probe (Ligeza et al., 1994), and for particulate materials (fusinite) (Ligeza et al., 1997) injected into the intact leaf as well as for a macroscopic spin-label probe implanted in the peritoneal cavity of a mouse (Subczynski et al., 1986). These assumptions, however, should be carefully justified.

Oxygen tension in tumors and different parts of animal body have been measured with the particulate oxygen sensitive paramagnetic materials such as coals, charcoals, India ink, or certain crystalline forms of lithium phthalocyanine. After placing one or more deposits of oxygen sensitive paramagnetic materials at sites of interest in rodents and then making repeated measurements only oxygen tension can be evaluated because surrounding tissue has no uniform structure and uniform solubility of oxygen (see section 7. OXIMETRY *IN VIVO* for more details). It is the local oxygen tension (local partial pressure of oxygen) in the very close vicinity of the particulate materials that is measured. These data cannot be transformed to concentration because at the same oxygen tension (oxygen partial pressure) oxygen solubility in different parts of tissue (cytoplasm, membranes) is different. It should be pointed here that the driving force for oxygen flow is not the difference in oxygen concentration but difference in partial pressure of oxygen (oxygen tension). Fig. 4 illustrates this situation in which for the system in equilibrium (oxygen consumption inside the cell is inhibited or neglected) the partial pressure of oxygen is the same in all points in the system but the local oxygen concentrations differ significantly. In this system net oxygen transport between different regions does not occur.

3. MEASUREMENTS IN CELL SUSPENSIONS

In early papers, the spin-label oximetry method was applied to measure the oxygen consumption rate in cell suspensions (Backer et al., 1977; Pajak et al., 1980; Sarna et al., 1980; Lai et al., 1982; see also reviews Swartz and Glockner, 1989; and Hyde and Subczynski, 1989). The closed-chamber approach was used in all of these measurements. In the closed-chamber method, cells are sealed into a gas-tight sample tube, enabling measurement of the rate of oxygen consumption by following the total concentration of oxygen in the sample. However, for studies seeking to determine oxygen concentrations in biological systems, an open-chamber approach usually is used. The open-chamber method offers the advantage of avoiding changes in oxygen concentration during an experiment. In this method, oxygen diffuses from the gas phase to the liquid phase in which it is used by the cells during respiration. Under steady-state conditions, the total respiration rate equals the rate at which oxygen diffuses into the sample. Typically, thin-walled capillaries made of gas permeable plastics such as Teflon (Plachy and Windrem, 1977) or the methyl pentene polymer TPX (Popp and Hyde, 1981; Subczynski and Hyde, 1981) have been used in EPR open-chamber measurements. This was the approach used by Swartz and collaborators in a series of studies that indicated that substantial gradients of oxygen

concentrations can occur across cell plasma membranes (Glockner et al., 1989; Hu et al., 1992).

Measurement of oxygen concentration in cell suspensions using EPR spin-label oximetry methods requires a relatively small sample volume, usually about 200 microliters (Lai et al., 1982). In some EPR approaches, the volume can be as small as 1 microliter (Froncisz et al., 1985). However, the concentration of cells has to be high, about 10^6-10^7 cells/ml for the closed-chamber approach (Lai et al., 1982) and 10^7 - 10^8 cells/ml for the open-chamber approach (Chan et al., 1989; Glockner et al., 1989, 1993; Hu et al., 1992). In the closed-chamber approach, the molecular spin-label probe is usually charged so that it is selectively located in the aqueous phase and does not penetrate into the cells. To measure the intracellular oxygen concentration directly, the EPR signal coming from molecular probes outside the cells has to be selectively suppressed. This is usually accomplished by using line-broadening agents such as $K_3Fe(CN)_6$ or potassium tris(oxalato) chromate III (CrOX), which do not penetrate the cell plasma membrane. These need to be used at fairly high concentrations (20 - 100 mM) so that the only visible EPR signal is from spin labels inside the cells.

3.1 Closed-Chamber Measurements

The measurements described below (Ligeza et al., 1994) basically repeat those made by Lai et al. (1982), using a much higher cell suspension density and paying attention not only to the oxygen concentration but also to the amplitude of the EPR spectrum of CTPO. The results are presented in Fig. 5. Fig. 5C shows that even at a cell suspension of 3×10^6 cells/ml, oxygen consumption is so rapid that it is difficult to measure its consumption rate. The integrated intensity of the EPR signal, which reflects the concentration of spin label remains essentially constant during these measurements. However, most often the EPR signal amplitude is recorded during this type of experiment. The increase in the signal amplitude at the beginning of the measurements is the result of the EPR line narrowing when oxygen is removed from the sample. This can be seen in Fig. 2 for the EPR signal of CTPO in a water solution equilibrated with air and nitrogen. For higher cell densities, a rapid decrease in the signal amplitude is also observed under these conditions, and the oxygen concentration drops to zero almost immediately after enclosing the sample in the Pasteur pipette. For a cell density of 50×10^6 cells/ml, the signal drops to 20% of its initial intensity during the first hour (Fig. 5A). The signal can be almost completely restored with $K_3Fe(CN)_6$, which indicates that the spin label has been reduced to its hydroxylamine. Swartz et al. (1986) reported that the rate of reduction of

some nitroxides in cell suspensions dramatically increased in anaerobic conditions. This suggests that nitroxides can be used as electron acceptors in cells.

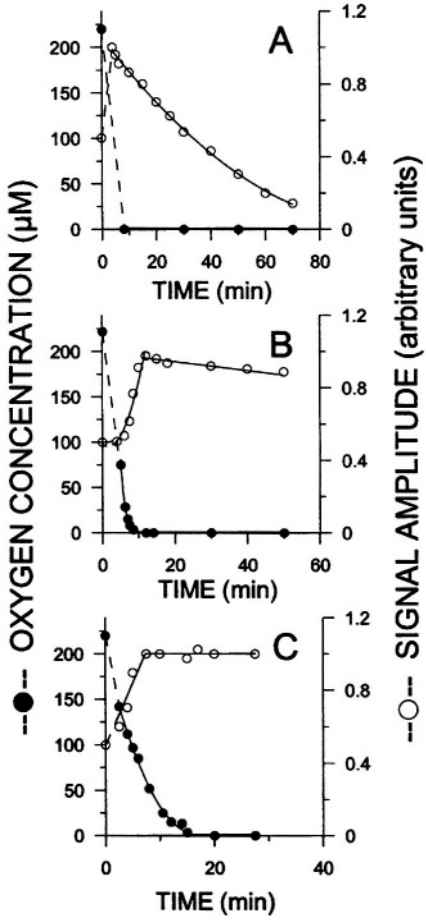

Figure 5. Kinetics of oxygen consumption by CHO cells in Earle medium at 37°C in a closed-chamber system for different cell densities (--●--): (A) 50×10^6 cells/ml, (B) 6×10^6 cells/ml, (C) 3×10^6 cells/ml. Kinetics of the changes of the EPR signal amplitude of CTPO during time course of oxygen consumption (--○--). Broken lines indicate kinetics between the sample preparation (air saturated samples) and beginning of the EPR measurements (adapted from Ligeza et al., 1994, with permission from Current Topics in Biophysics).

3.2 Open-Chamber Measurements

In the measurements described below (Ligeza et al., 1994) high density CHO cell suspensions enclosed in a TPX capillary and containing CTPO as an oxygen-sensitive molecular probe were used. Conditions were similar to those used for oxygen gradient measurements (Chan et al., 1989; Glockner et al., 1989, 1993; Hu et al., 1992). The oxygen flow through the plastic capillary wall from the gas around it to the cell suspension depends on the oxygen permeability coefficient of the plastic wall, and is proportional to the difference of oxygen partial pressure outside and inside the capillary (in the sample, just close to the capillary wall). Inside the capillary, in the liquid sample, diffusion is the only mechanism of oxygen transport (no stirring is applied). Oxygen is consumed constantly by cells distributed uniformly inside the capillary. To prevent or reduce cell sedimentation, the final medium contained 0.2 % methyl cellulose E4M (Dow), which is preferable to agar (0.1 %), which exhibits a tendency to aggregate in the sample tube. Oxygen consumption was not affected by this addition (Lai et al., 1982).

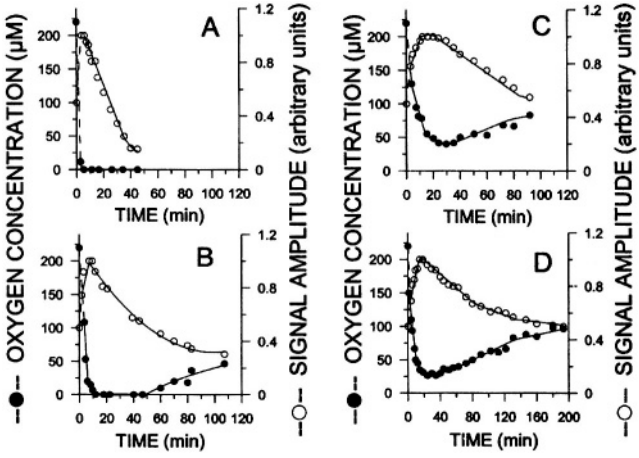

Figure 6. Changes in oxygen concentration in a CHO cell suspension in Earle medium (A, B, C) and Hanks medium (D) at 37°C in an open-chamber system for different cell densities (--●--): (A) 60×10^6 cells/ml, (B) 20×10^6 cells/ml, (C) 10×10^6 cells/ml, (D) 10×10^6 cells/ml. Kinetics of the changes in the EPR signal amplitude of CTPO during the time course of oxygen consumption (--○--). Inside the EPR cavity, the system was continuously equilibrated with a gas mixture of 47.5% air, 47.5% nitrogen and 5% carbon dioxide. Before positioning inside the cavity, the sample was equilibrated with air. Broken lines indicate kinetics between the sample preparation and beginning of the EPR measurements (adapted from Ligeza et al., 1994, with permission from Current Topics in Biophysics).

The results for different densities of cell suspensions are presented in Fig. 6. Several features are especially notable: (1) For higher cell densities (60×10^6 cells/ml), oxygen concentration dropped to zero in about five minutes and stayed at that level during further measurements (about 40 minutes) (Fig. 6A), while at lower cell densities (20×10^6 cells/ml), oxygen concentration dropped to zero after about 10 minutes. After about 50 minutes, it started to increase again to a fairly high level (~50 μM after 100 minutes) (Fig. 6B). (2) At a cell density of $10x\times10^6$ cells/ml, the oxygen concentration dropped to its minimum value of ~30 μM after about 25 minutes, but started to increase again, reaching 100 μM (practically the concentration in equilibrium with the gas outside the capillary, which contains 47.5% air) after 3 hours (Fig. 6C and 6D). (3) Significant spin label reduction was observed after the concentration of oxygen dropped to zero or reached a minimum. (4) The rate of spin label reduction was roughly proportional to the density of cell suspension.

These results raised at least two questions: (1) Why, after reaching the minimum (or zero) level, did the oxygen concentration increase again? (2) Why was the spin label reduced in the aerated sample? The answer may be found, at least in part, in a quantitative evaluation of some of the variables.

3.2.1 Pool of Substrates for Cell Respiration

D-glucose is the major source of energy for CHO cells suspended in an Earle or Hanks media. In the cell, oxygen is consumed mainly during respiration and this process can be summarized as follows:

$$C_6H_{12}O_6 + 6O_2 \rightarrow 6CO_2 + 6H_2O + \text{Energy} \qquad (4)$$

How long can the medium provide substrates for cell respiration? Both Earle and Hanks media contain 1 g of glucose/l. A simple calculation shows that for a cell density of 10^8 cells/ml, glucose will be exhausted after 90 minutes, assuming that all cells are working with the maximum respiration rate ($V = 6\times10^{-17}$ moles O_2/(s×cell); Lai et al., 1982). This calculation shows that respiratory substrates are in substantial excess in the medium; therefore, the increase in oxygen concentration observed in open-chamber measurements cannot be explained by the lack of substrates. Another potential factor is the accumulation of products of cell metabolism that are not removed using the open-chamber system. This may be a cause of the apparent change in cell metabolism, which is indicated by an increase in spin-label reduction and decrease in the rate of oxygen consumption by the cells (Fig. 6).

3.2.2 Profile of Oxygen Concentration Inside the Open Chamber

Inside the oxygen-permeable capillary, oxygen diffuses from the wall to the capillary center through the suspension of respiring cells. After the system reaches equilibrium, a steady oxygen concentration profile is created inside the capillary. Boag (1969) gives the expressions for the spatial profile of oxygen concentration for the penetration of oxygen into a cylinder of metabolizing tissue (capillary with metabolizing cell suspension in the case described here), assuming that the rate of oxygen consumption is uniform inside the cylinder and independent of oxygen concentration. These conditions were fulfilled in the described experiment: the cells were uniformly distributed and the rate of oxygen consumption remained constant to a very low oxygen concentration (Lai et al., 1982; Froncisz et al., 1985). There are two distinct cases: (1) if the radius R of the capillary is large enough, the oxygen concentration reaches zero at $r = a$ ($C_{r=a} = 0$) and remains zero for $r < a$, and (2) the oxygen concentration on the axis $r = 0$ is $C_{r=0} \geq 0$ (see Fig. 7). In the first case, the radius a is determined by the equation:

$$\frac{4C_R D_O}{\rho V R^2} = 1 - \frac{a^2}{R^2} - \frac{a^2}{R^2} \ln \frac{R^2}{a^2} \tag{5}$$

and the profile of oxygen concentration for $r > a$ is described by the equation:

$$C = \frac{(r^2/a^2) - 1 - 2\ln(r/a)}{(R^2/a^2) - a - 2\ln(R/a)} C_R. \tag{6}$$

In the second case, the profile of oxygen concentration is described by the equation:

$$C = C_R - \frac{\rho V}{4D_O}(R^2 - r^2). \tag{7}$$

The concentration in the capillary center at $r = 0$ is given by:

$$C_{r=0} = C_R - \frac{\rho V R^2}{4D_O}. \tag{8}$$

The radius of the capillary, R_o, for which the oxygen concentration just falls to zero in the capillary center equals:

$$R_O = \sqrt{4D_O C_R / \rho V}. \tag{9}$$

In these equations, C_R is the oxygen concentration just at the inner wall of the capillary (at radius R). V is the oxygen consumption rate per cell, ρ is the cell density and D_O is the oxygen diffusion coefficient in the medium.

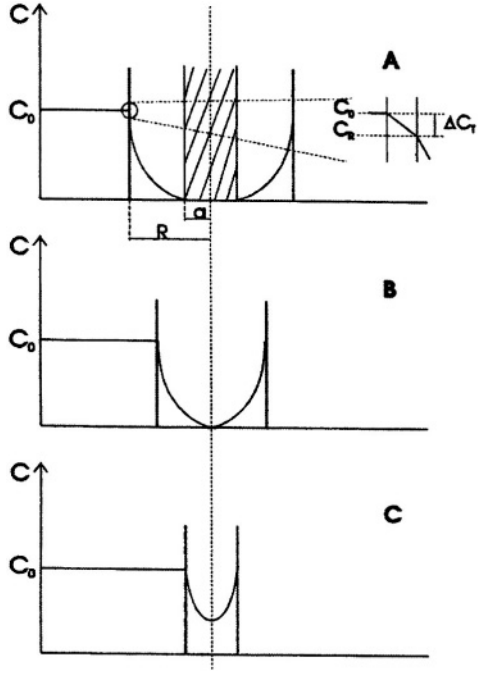

Figure 7. Profiles of the oxygen concentration (C) inside open-chamber capillaries with different capillary diameters and containing cell suspensions with the same cell densities. (A) For the large diameter (2R), the oxygen concentration drops to zero at the radius *a.* Cross-hatched area indicates cells in anoxic conditions. (B) For this dimension, the oxygen concentration drops to zero at the capillary center. (C) At all sites, the oxygen concentration is greater than zero. Insert in Fig 7A indicates the drop in oxygen concentration across the capillary wall (ΔC_T) from C_O (the concentration of oxygen in water equilibrated with the gas outside the capillary) to C_R (the concentration of oxygen in cell suspension just at the inner capillary surface) (from Ligeza et al., 1994, with permission from Current Topics in Biophysics).

Let us assume that outside the capillary there is pure air and that the oxygen partial pressure difference across the capillary wall equals zero. In that case, the radius R_o obtained from Eq. 9 is $R_o = 0.6$ mm for the capillary filled with the CHO cell suspension of density $\rho = 10^8$ cells/ml (consuming oxygen at 37°C with a rate $V = 6\times10^{-17}$ moles O_2/(s×cell) (Lai et al., 1982)). At this temperature, the oxygen diffusion coefficient in water is $D_O = 3\times10^{-5}$ cm^2/s (St. Denis and Fell, 1971) and the oxygen concentration for water equilibrated with air $C_R = 220$ μM (Hitchman, 1978]). This cell density is

often used in open-chamber measurements (Chan et al., 1989; Glockner et al., 1989, 1993; Hu et al., 1992).

The experiments described above used a TPX capillary of R = 0.35 mm, a gas mixture outside the capillary containing 47.5% air (C_R = 105 μM), and maximal and minimal cell densities of 6×10^7 and 10^7 cells/ml respectively. According to Eq. (8), the oxygen concentration in the capillary center for these samples drops to the value $C_{r=0}$ = 63 μM and 98 μM, respectively. In these evaluations, it was assumed that the drop of oxygen partial pressure across the capillary wall is zero. It was shown experimentally that after the change of the gas outside this TPX capillary at 37°C from air to nitrogen, the oxygen concentration in the water sample inside the capillary drops by a factor of e during 1.5 min. Knowledge of this characteristic time allowed for evaluation of the permeability coefficient of the TPX wall as 21 (μM O_2/atm)×(cm/s). Assuming that all CHO cells were respiring at the maximum rate, the oxygen partial pressure difference across the TPX capillary wall for cell densities of 10^7, 3×10^7 and 6×10^7 cells/ml equals 0.05, 0.1 and 0.3 atm, respectively. These can be related to the difference of oxygen concentration in water of 55, 110, and 330 μM, respectively.

These calculations correlate well with the results presented in Fig. 6. The drop in oxygen concentration across the TPX wall (65 - 75 μM) for a cell density of 10^7 cells/ml is comparable to the evaluated value of 55 μM (Fig. 6C and 6D). For higher cell densities, oxygen concentration drops to zero (Figs. 6A and 6B). As can be seen from these evaluations, there are four parameters which characterize the cell suspension and the open-chamber capillary which are critical – cell density, cell respiration rate, radius of the capillary and permeability of the capillary wall to oxygen. The following conclusions can be made: (1) Spin-label reduction is not significant during the timespan of the experiments in the closed-chamber system, presumably because the experiment is concluded before the oxygen is exhausted. (2) Substrates for cell respiration are not exhausted in closed-chamber experiments. (3) The oxygen consumption rate of the cells is not constant during the timespan of the experiment in the open-chamber system, and that is manifested by the later increase in oxygen concentration in the sample. (4) The decrease in the oxygen consumption rate occurs much earlier than exhaustion of the substrates for cell respiration. (5) The decrease in the oxygen consumption rate is accompanied by significant spin-label reduction. (6) For dense cell suspensions, a significant oxygen partial pressure difference across the capillary wall can be created. (7) For dense cell suspensions, the decrease in oxygen concentration from the capillary wall to its center can be as great as 100 - 200 μM. (8) Therefore, it is possible that for cells with a high respiration rate, the cells located near the center of the

capillary will be anoxic. These consideration should be taken into account during measurements with an open-chamber system.

4. OXYGEN SOLUBILITY AND DIFFUSION IN LIPID BILAYER MEMBRANES

The most important parameter in understanding chemical reactions involving oxygen is the product of its local diffusion coefficient and local concentration. This product is of fundamental interest in itself, and separation into its component factors (the diffusion coefficient and concentration) is not necessary. Spin-label oximetry allows measurement of this product in restricted domains such as membranes, or more accurately, at a certain depth in membranes. For oxygen, the important chemical reactions that occur within the membrane include lipid peroxidation and the formation of reactive oxygen species. Recently, the reaction of NO with oxygen within the lipid bilayer membrane attracted the attention of researchers (Singh et al., 1994; Stamler, 1995). It was shown that in the hydrophobic environment of a model or biological membrane, this reaction is approximately 300 times faster than in water (Liu et al., 1998). Hydrophobic compartments of the cell should therefore be considered to be important sites of NO disappearance. For these types of reactions spin-label oximetry and spin-label NO-metry (Subczynski et al., 1996; Lomnicka and Subczynski, 1996; Subczynski and Hyde, 1998b) can give the basic data on oxygen and NO local diffusion-concentration product. We will refrain from discussing chemical reactions involving molecular oxygen any further.

Spin-label oximetry makes it possible to measure the transport of oxygen both within and across the lipid bilayer model membrane and in the lipid portion of biological membranes (Kusumi et al., 1982; Subczynski et al., 1989). This approach was used to obtain profiles of the oxygen diffusion-concentration product across the membrane. Knowledge of these profiles makes it possible to evaluate the membrane oxygen permeability coefficient (Subczynski et al., 1989). In these types of experiments, samples (spin-labeled liposomes or biological membrane suspensions) should be precisely equilibrated with the given partial pressure of oxygen at a defined temperature. This is possible with the use of TPX gas permeable capillaries (Popp and Hyde, 1981; Subczynski and Hyde, 1981; Hyde and Subczynski, 1989). The importance of the TPX gas-exchanging sample cell to the development of spin-label oximetry and its application in membranous systems has been very great.

4.1 Oxygen Transport Parameter

If it is possible to put a spin label in restricted domains such as a membrane, its bimolecular collision frequency with oxygen in this specific environment can be recorded. In the T_1-sensitive methodology applied to lipid bilayer membranes, the bimolecular collision rate is evaluated in terms of an oxygen transport parameter using a saturation recovery EPR technique (Kusumi et al., 1982; Subczynski et al., 1989, 1991a). Previously, the notation used for the oxygen transport parameter was $W(x)$ (Kusumi et al., 1982: Subczynski et al., 1989, 1991a, 1992a, 1998; Ashikawa et al., 1994). However, in the paper by Kawasaki et al. (2001), this was changed to $2P(x)$ because different W values were used to indicate electron spin transition rates. In this review, $2P(x)$ will be used for the oxygen transport parameter as well. $2P(x)$ at location x in the membrane is defined as

$$2P(x) = T_1^{-1}(x, \text{air}) - T_1^{-1}(x, N_2) \tag{10}$$

where the T_1s are the spin-lattice relaxation times of the nitroxide in samples equilibrated with atmospheric air and nitrogen, respectively. According to the Smoluchowski equation (Eq. 3), the collision rate is thus proportional to the product of the local translational diffusion coefficient of oxygen $D_O(x)$ and the local oxygen concentration $C_O(x)$ in a membrane equilibrated with atmospheric air

$$2P(x) = AD_O(x)C_O(x), \qquad A = 8\pi p r_o \tag{11}$$

As noted, p is close to one (Hyde and Subczynski, 1989). In this equation, x indicates the different depths in the membrane at which EPR measurements were performed. These measurements can be easily done by attaching the nitroxide moiety to different carbon atoms of the hydrocarbon chain in stearic acid or phosphatidylcholine molecules, or to their polar head groups (see scheme in Fig. 8). Note that $2P(x)$ is a value extrapolated to a sample equilibrated with 100% air and that $C(x)$ is proportional to the oxygen partial pressure in the equilibrating gas mixture.

Profiles of the oxygen transport parameter across the membrane allow one to understand the movement of oxygen molecules within the lipid bilayer membranes and calculate the oxygen permeability coefficient across model and biological membranes (Subczynski et al., 1989, 1991a, 1992a; Subczynski and Markowska, 1992; Ashikawa et al., 1994; Ligeza et al., 1998; Marsh, 2001). The fluid-phase model and biological membranes show similar bell-shaped profiles of $2P(x)$, with the oxygen diffusion-concentration product in the membrane center being a few times greater than that in or near the head group region. The typical profile of the oxygen transport parameter $2P(x)$ across the 1-palmitoyl-2-oleoylphosphatidylcholine (POPC) bilayer obtained with the use of

phospholipid spin labels is shown in Fig. 9. Profiles of the product of oxygen diffusion-concentration across the lipid bilayer membranes can be also obtained using the linewidth (T_2) method as was shown by Smirnov et al. (1996)

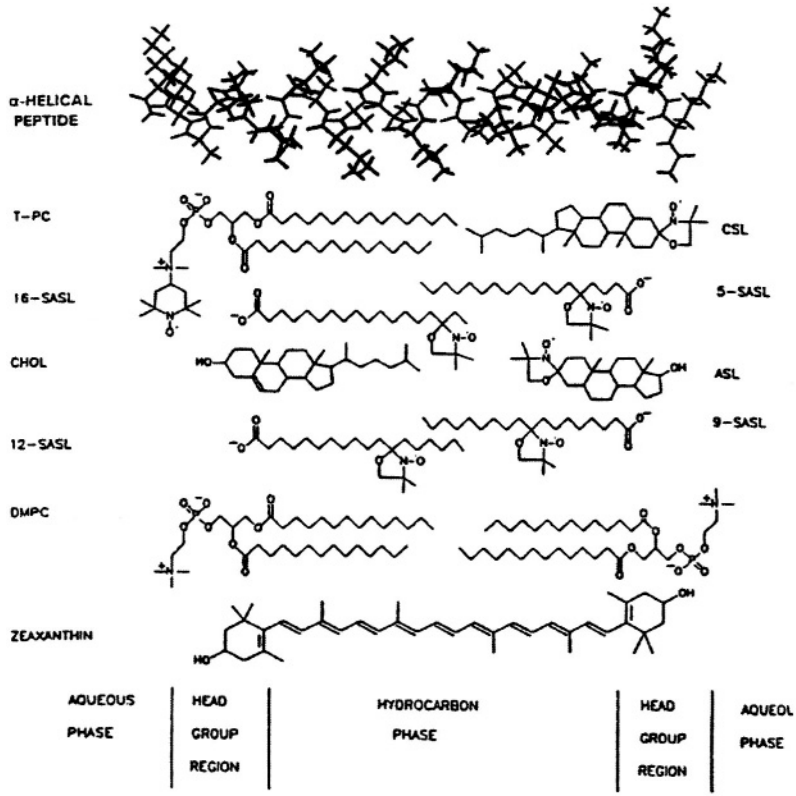

Figure 8. Cross-section of the DMPC membrane including membrane modifiers (cholesterol, CHOL), polar carotenoid - zeaxanthin, and transmembrane α-helical peptide – Ac-$K_2(LA)_{12}K_2$-amide) and lipid spin labels. Locations across the membrane are illustrated.

4.2 Oxygen Membrane Permeability Coefficient

One of the most fundamental properties of biological membranes is that they are barriers to the permeation of polar molecules. This is largely due to the hydrophobicity of the membrane interior. However, it cannot be automatically applied to the permeation of small solutes such as oxygen and nitric oxide, even though some experimental data suggest this to be true (Nicholson and Roughton, 1951; Holland, 1967; Chan et al., 1989; Glockner et al., 1989, 1993; Hu et al., 1992; Vaughn et al., 2001). It is practically

impossible to measure the membrane permeability of oxygen directly by the creation of fast decaying gradients. There is, however, another approach in which oxygen transport parameter profiles across the membrane, obtained for samples in equilibrium with oxygen and nitrogen (without creating any fast decaying oxygen gradients), are used to calculate the permeability coefficient (Subczynski et al., 1989). The membrane permeability coefficient, P_M, is a useful physical characteristic of a membrane as a whole which connects the oxygen flux across the membrane, J, with the difference in oxygen concentration in the aqueous phase on either side of the membrane (C''- C'):

$$J = -P_M(C'' - C') \tag{12}$$

P_M can be calculated from the $2P(x)$ profiles on the basis of Diamond and Katz's theory (1974) developed for permeability of nonelectrolytes, according to the procedure developed by Subczynski et al. (1989). In this approach, it is necessary to make an integration of $(D_O(x)C_O(x))^{-1}$, which is a measure of the resistance of the membrane to oxygen transport over its entire thickness, h. The product $(D_O(x)C_O(x))^{-1}$ can be related to the oxygen transport parameter through Eqs. 10 and 11. The final equation for the membrane permeability coefficient, which is based on the oxygen transport parameter profiles, as that shown in Fig. 9, has the form (Subczynski et al., 1989):

$$P_M = \frac{1}{AC_o(\text{water})}\left[\int_0^h \frac{dx}{2P(x)}\right]^{-1} \tag{13}$$

Here, $C_O(\text{water})$ is the oxygen concentration in the aqueous phase equilibrated with air. However, the uncertainty of A $(=8\pi pr_o)$ in Eq. (11) could lead to a possible error. Fortunately, since A is remarkably independent of solvent viscosity, temperature, hydrophobicity and spin-label species (Hyde and Subczynski, 1984, 1989; Subczynski and Hyde, 1984), the ratio of the permeability coefficient across the membrane, P_M, to the permeability of the water layer of the same thickness, h, as the membrane, P_W, obtained using the same EPR method, can cancel this error. The oxygen permeability of a water layer of thickness h equals:

$$P_W = \frac{1}{AC_o(\text{water})}\left[\frac{h}{2P(\text{water})}\right]^{-1}. \tag{14}$$

The oxygen transport parameter in water, $2P$(water), can be measured using water soluble spin label d-Tempone (Subczynski et al., 1989, 1991a, 1992a). Using T_1 measurements in membranes and in water, the ratio of P_M(pulse EPR)/P_W(pulse EPR) can be determined. The permeability coefficient of oxygen in a water layer of thickness h, can also be determined from the macroscopic oxygen diffusion coefficient in bulk water, D_O(water) (St. Denis and Fell, 1971), according to the equation:

$$P_w = D_O(water)/h. \tag{15}$$

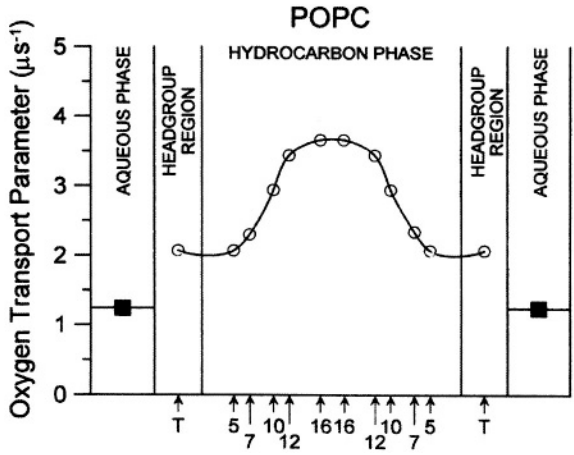

Figure 9. Profile of the oxygen transport parameter, $2P$(x), across the POPC bilayer obtained at 35°C with the n-PC spin labels (○). The oxygen transport parameter in the aqueous phase was obtained with d-Tempone, and is shown for comparison (■). Approximate locations of nitroxide moieties of spin labels are indicated by arrows.

The P_M (pulse EPR) value is evaluated using Eq. (13) with the integration performed based on figures such as Fig. 10 (top), where $(2P(x))^{-1}$ is plotted as a function of distance from the center of the membrane. The manner of integration of the oxygen permeability coefficient across a water layer of the same thickness as a membrane (Eq. 14) is shown in Fig. 10 (bottom). The ratio of P_M(pulse EPR)/P_W(pulse EPR) is simply the ratio of these two integrals. Using T_1 measurements in membranes and in water, the ratio of P_M(pulse EPR)/P_W(pulse EPR) can be determined, and using the value of P_W obtained from Eq. (15), we arrive at a value of the oxygen permeability coefficient across the membrane. Data for different membranes and conditions are collected in Table 1. The membrane oxygen permeability

coefficient can also be obtained using oxygen-induced EPR line-broadening measurements. For details see Subczynski and Markowska (1992) and Subczynski and Hyde (1998a, 1998b).

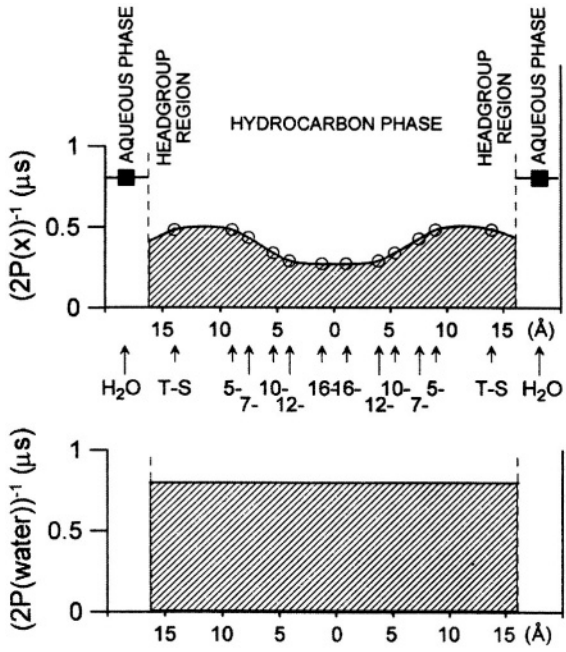

Figure 10. (Top) $(2P(x))^{-1}$ is plotted as a function of the distance from the center of the POPC (1-palmitoyl-2-oleoylphosphatidylcholine) membrane equilibrated with air at 35°C to show the oxygen permeability barriers and method of integration based on Eq. 13 (i. e., measuring the hatched area under the solid curve). The thickness of the membrane and positions of the nitroxide moieties are assumed to be the same as evaluated earlier for EYPC (egg yolk phosphatidylcholine) bilayer (Subczynski et al., 1989, 1991a). (Bottom) $(2P(water))^{-1}$ at 35°C plotted for the water layer of the same thickness as the membrane to illustrate the method of integration based on Eq. 14 (i. e., measuring the hatched area under the solid line).

Table 1. Oxygen permeability coefficients for different membranes.

Membrane	Temperature (°C)	P_M(cm s^{-1})	Reference
DMPC[a]	8	5.3	Subczynski et al., 1989
DMPC	25	105.0	Subczynski et al., 1992a
DMPC	38	185.0	Subczynski et al., 1989
DMPC–10% zeaxanthin	25	59.0	Subczynski et al., 1992[a]
DMPC–50% cholesterol	38	38.0	Subczynski et al., 1989
EYPC[b]	25	119.0	Subczynski et al., 1992a
EYPC	40	201.5	Subczynski et al., 1991
EYPC–10% zeaxanthin	25	88.0	Subczynski et al., 1992a
EYPC–50% cholesterol	40	73.4	Subczynski et al., 1991
CHO plasma membrane	37	42.0	Subczynski et al., 1992[b]
Thylakoid membrane	20	39.5	Ligeza et al., 1998
SLOT[c]	35	34.7	Ashikawa et al., 1994
Purple membrane	35	21.3	Ashikawa et al., 1994

[a]Gel-phase membrane
[b]Egg yolk phosphatidylcholine (EYPC) membrane
[c]Measurements for slow oxygen-transport domain in reconstituted membranes of BR and DMPC (BR/DMPC=1/40).

4.3 Effect of Membrane Modifiers in Model Membranes

4.3.1 Cholesterol

Membrane modifiers affect oxygen transport parameter profiles differently in different membrane regions. Cholesterol significantly decreases oxygen transport in the polar head group region and in the hydrocarbon region near the polar head groups, and increases it in the membrane center (Subczynski et al., 1989, 1991). Cholesterol affects the hydrophobicity profile across the phospholipid bilayer in a similar manner, increasing hydrophobicity in the membrane center and decreasing it in and near the polar head group region (Marsh and Watts, 1981; Subczynski et al., 1994; Marsh, 2001). It therefore can be assumed that the solubility (distribution of oxygen molecules within the lipid bilayer) makes a significant contribution to the cholesterol-induced changes in the oxygen transport parameter profile. Some resistance to oxygen permeability across the membrane is located in and near the head group region. In the center, oxygen transport parallel to the membrane surface seems to be more effective than the transport across the cytosol. As can be seen from Table 1, cholesterol at high concentration decreases the membrane permeability to oxygen in fluid-phase model membranes by a factor of 3 - 5.

4.3.2 Carotenoids

Polar carotenoids like lutein and zeaxanthin decrease the oxygen diffusion-concentration product in saturated and unsaturated membranes (Subczynski et al., 1991b). The effect is strongest in the membrane center and negligible in the head group region. At 10 mol%, polar carotenoids decrease the value of P_M of model membranes by a factor of 2 (Subczynski and Markowska, 1992). Polar carotenoids significantly increase the hydrophobicity of the membrane interior (Wisniewska and Subczynski, 1998), which suggests their strong effect on the oxygen translational diffusion coefficient rather than oxygen concentration within the lipid bilayer. The different effects of cholesterol and polar carotenoids on oxygen transport can result from different structures and different localization of these molecules in the membrane. The cholesterol molecule is located in one half of the bilayer, and its rigid plate-like portion extends to the depth of the 7^{th} to 10^{th} carbon atoms in lipid hydrocarbon chains (McIntosh, 1978). In contrast, one carotenoid molecule influences both halves of the lipid bilayer and, with two polar groups interacting with opposite hydrophilic surfaces of the membrane; it can brace together the two halves of the bilayer like a tie-bar (Rohmer et al., 1979). Therefore, the oxygen diffusion-concentration product is reduced in those regions of the bilayer to which the rigid portion of the molecule of the modifier extends (see scheme in Fig. 8).

4.3.3 Transmembrane α-Helical Peptides

Surprisingly, the transmembrane α-helical peptides of similar structures, L_{24} and $(LA)_{12}$ (Ac-$K_2L_{24}K_2$-amide and Ac-$K_2(LA)_{12}K_2$-amide, respectively), affect oxygen transport in the POPC bilayer in a strikingly different way (Subczynski et al., 1998, 2003). The effect of L_{24} is minimal in the membrane center and increases towards the head group region. $(LA)_{12}$ decreases oxygen transport very strongly across the entire lipid bilayer. The effect is strongest in the membrane center, where 10 mol% of $(LA)_{12}$ decreases this parameter by about 50% (as compared to no effect from L_{24}). Close to the polar head group, the 10 mole% of $(LA)_{12}$ decreases the oxygen transport parameter by 40%, compared to the 20% decrease caused by L_{24}. The much stronger effect of $(LA)_{12}$ is ascribed not only to the increased roughness of its hydrophobic surface but also to the increased motional freedom of its leucine side chains. In L_{24} the leucine side chains are packed tightly, giving a smooth hydrophobic surface. In $(LA)_{12}$ they are separated by the small methyl groups of the alanine side chains, giving them additional motional freedom and the ability to protrude between the phospholipid hydrocarbon chains. These differences are not detected by conventional

EPR spectra, showing once again that oxygen is more sensitive in detecting differences in the dynamic organization of the membrane. It can be speculated that the major effect of these peptides, $(LA)_{12}$ in particular, on the oxygen transport parameter is through the decrease of oxygen translational diffusion because both peptides increase the hydrophobicity across the POPC bilayer (Subczynski et al., 1998, 2002). Thus, a comparison of the effects of membrane modifiers on the oxygen transport parameter profile and the hydrophobicity profile across the lipid bilayer can help analyze which component of the oxygen diffusion-concentration product – diffusion coefficient or concentration – is primarily affected.

4.4 Biological Membranes

The spin-label oximetry approach allows for evaluation of the oxygen permeability coefficient only in the lipid-bilayer portion of biological membranes. Because of this, the overall (average) membrane permeability should be further corrected for the presence of integral membrane proteins. P_M values for biological membranes are listed also in Table 1. It was shown that the oxygen permeability coefficient measured in the lipid bilayer portion of the Chinese hamster ovary plasma membrane is about two times lower than that of an appropriate water layer (Subczynski et al., 1992a), while that of the thylakoid membrane is about the same as that of the water layer (Ligeza et al., 1998). The smallest P_M is observed for lipid domains crowded with integral membrane proteins. The lipid domain of the purple membrane isolated from *Halobacterium halobium* shows a P_M about 6 to 10 times smaller than that of the fluid-phase lipid bilayer (Ashikawa et al., 1994). To obtain a depth measurement using SDSL, calibration of the accessibility of different relaxation agents including oxygen (accessibility profiles) into the lipid bilayer of the given membrane is performed using n-PC (1-palmitoyl-2-(n-doxylstearoyl)phosphatidylcholine) spin labels and CW saturation measurements (Altenbach et al., 1994; Feix and Klug, 1998). The accessibility profiles cannot be directly related to the membrane oxygen permeability coefficient, but can show the ability of oxygen to penetrate into the lipid bilayer. These calibrations were also performed for biological membranes, e.g. rod outer segment disk membranes by Farahbakhsh et al. (1992), showing that this membrane is also easily penetrated by oxygen.

As has already been shown, oxygen transport across the membrane depends significantly on membrane constitution. Cholesterol at high concentrations significantly decreases oxygen transport across the lipid bilayer (Subczynski et al., 1989, 1991a). Here it must be noted that cholesterol is especially abundant in the plasma membrane of mammalian cells. Also, protein content in the membrane can affect oxygen permeability

in two ways. First, integral membrane proteins are practically impermeable to oxygen (Altenbach et al., 1990; Subczynski et al., 1992b). Because of that, the oxygen concentration difference across the membrane, evaluated on the basis of knowledge of the oxygen permeability coefficient of the lipid bilayer portion of the membrane, should be increased by a factor proportional to the surface area of the membrane divided by the surface area of its lipid bilayer portion. Second, integral membrane proteins affect the oxygen permeability of the lipid bilayer itself mainly by creating protein-rich domains with trapped lipids (Ashikawa et al., 1994) and/or cholesterol-rich raft domains stabilized by the presence of clustered proteins (Kawasaki et al., 2001). In the cholesterol-rich raft domain of the influenza viral (IFV) membrane, oxygen transport was decreased by a factor of 16 compared to bulk lipids (Kawasaki et al., 2001). These studies, however, introduce another level of complication that will be discussed in the next section.

The overall conclusion from this type of investigation is that biological membranes are not barriers to oxygen transport, and oxygen concentration differences across cell plasma membranes, even during intensive respiration, are negligible. Evaluations presented by Subczynski et al. (1991a) show that this difference is in the nanomolar range for cell and mitochondrial membranes. A membrane overloaded with cholesterol and integral proteins can be a barrier only if the cell or mitochondrion radius is very small, becoming comparable to the membrane thickness itself (Subczynski et al., 1992a).

5. DOT METHOD (METHOD OF DISCRIMINATION BY OXYGEN TRANSPORT)

Molecular oxygen as a membrane probe has certain unique characteristics: its small size and appropriate level of hydrophobicity allow it to enter the small vacant pockets transiently formed in lipid bilayer membranes. Because of this, the molecular collision rates between oxygen and nitroxide radical spin labels placed at specific locations in the membrane are sensitive to the dynamics of *gauche-trans* isomerization of lipid alkyl chains and to the structural nonconformability of neighboring lipids (Subczynski et al., 1991a). Thus, the three-dimensional dynamic structure of the lipid bilayer membrane can be investigated using the spin-label oximetry approach. The oxygen transport parameter was successfully used as a sensitive monitor of the membrane structure and dynamics because the effect of oxygen on the spin-lattice relaxation time of spin labels is generally much greater than the motional effects (Kusumi et al., 1982).

The DOT method (the method of discrimination by oxygen transport) developed by Ashikawa et al. (1994) was successfully used to indicate the existence of lipid domains in model and biological membranes with different oxygen transport parameters. In this type of measurement, the lipid spin label is located in the membrane domains with fast and slow oxygen transport. Because the DOT method is based on the measurements of T_1 of lipid spin labels in the absence and presence of oxygen, which ranges from 0.1 to 10 μs, the exchange rate of spin labels between these domains must be slower than or comparable to these times. If the exchange rate is faster, the oxygen collision rate cannot distinguish the existing domains. This was the case in the reconstituted membranes of bacteriorhodopsin (BR) and dimyristoylphosphatidylcholine (DMPC) for a low BR/lipid ratio (1/80) (Ashikawa et al., 1994). In the absence and presence of molecular oxygen (up to 50% of atmospheric air), only single exponential saturation-recovery curves were observed for lipid spin labels with the oxygen transport parameter about 1.5 times smaller than in a pure lipid bilayer. Because it is evident that the lipid bulk and lipid boundary regions around BR molecules coexist in this sample (East et al., 1985; Ryba et al., 1987; Horvath et al., 1988; Marsh, 1997), the exchange rate of lipids between the bulk and the boundary regions must be much faster than the time range of the method. Therefore, in the following sections, the bulk plus boundary regions will be indicated as the BULK domain for simplicity.

5.1 SLOT (Slow Oxygen Transport) Domains

In membranes consisting of two lipid environments with different oxygen transport rates (slow oxygen transport (SLOT) domain and fast oxygen transport (BULK) domain) and exchange rates of the spin-labeled lipids between these domains slower than 10^4 s^{-1}, the EPR saturation-recovery signal will be a simple double-exponential curve with time constants of $T_1^{-1}(f_{air}, \text{SLOT})$ and $T_1^{-1}(f_{air}, \text{BULK})$.

$$T_1^{-1}(f_{air}, \text{SLOT}) = 2P_1 f_{air} + T_1^{-1}(N_2, \text{SLOT}) \tag{16}$$

$$T_1^{-1}(f_{air}, \text{BULK}) = 2P_2 f_{air} + T_1^{-1}(N_2, \text{BULK}) \tag{17}$$

Here "x" in Eqs. (10) and (11) is changed to the two-membrane domain, BULK and SLOT, and the depth is fixed. The same lipid spin label is distributed between the BULK and SLOT domains. Because $C(x)$ is proportional to the partial pressure of oxygen in the equilibrating gas mixture, the fraction of air in the gas mixture, f_{air}, used in actual experiments is introduced. $2P_1$ and $2P_2$ are oxygen transport parameters in each domain.

Because these $2P$ values are the rates of collision between the spin label and molecular oxygen extrapolated to a sample equilibrated with 100% air, $2Pf_{air}$ represents the collision rate in a sample equilibrated with a gas containing f_{air} air. In general, $T_1^{-1}(N_2, SLOT)$ and $T_1^{-1}(N_2, BULK)$ are close in the membrane and the presence of two types of lipid domains often can be clearly manifested only after the introduction of molecular oxygen to the sample. The collision rate of molecular oxygen with the nitroxide group of the spin label can differ substantially between the two domains.

This approach allows for detecting the presence of a specific lipid domain that exhibits a slow oxygen transport rate. The SLOT domain was detected in BR reconstituted membranes at a BR/lipid ratio of 1/40, in which the oxygen transport rate was smaller by a factor of 5 than in the BULK region (Ashikawa et al., 1994). This domain is thought to be protein rich, in which every lipid molecule is in contact with two proteins or with protein and boundary lipids (thus the lipids are sandwiched either between two proteins or between a protein and boundary lipids) and its hydrocarbon chain motion is suppressed to the level of the gel-phase membrane. The exchange rate of lipids between this domain and the BULK domain has not been observed.

Recently, two different oxygen transport rates were detected in DMPC membranes containing 20 mol% cholesterol (Subczynski, preliminary results). As can be seen from Figs. 11A and 11B, a double (but not a single) exponential can be fitted to the saturation-recovery signal of lipid spin labels in this membrane in the presence of oxygen. In the absence of oxygen, a single exponential fit is satisfactory. This fluid-fluid membrane microheterogeneity exists only up to 45°C and can be related to coexisting phases, the so-called liquid-ordered (l_o) and liquid-disordered (l_d) phases (Almeida et al., 1992). Two-component saturation-recovery signals of a fatty acid spin label were observed in the IFV membrane, indicating the presence of the SLOT domain (Kawasaki et al., 2001). However, saturation recovery signals exhibit more complex behaviour, and this case will be analyzed in detail below.

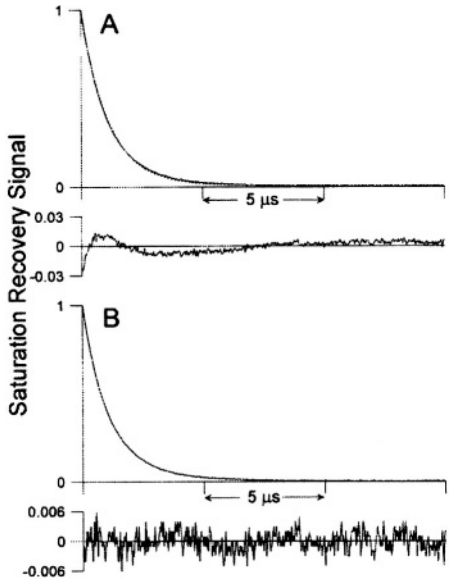

Figure 11. Saturation-recovery signal and curve fitting for 5-SASL in DMPC bilayer containing 20 mol% cholesterol. The recovery curve was obtained at 30°C for a sample equilibrated with 50% air in air/nitrogen mixture. Simulations and experimental saturation-recovery signals are superimposed for single-exponential fitting (A) and for double-exponential fitting (B). The difference between the experimental data and the fitted curve is shown in the lower part of each recovery curve. The time constants are 1.73 μs and 0.84 μs from the double-exponential fitting.

5.2 Exchange of Lipids Between the SLOT Domain and the BULK Domain (Outline of Theory)

In the following section, all equations will be expressed using electron spin transition rates; i.e.,

$$W_{10} = (1/2)T_1^{-1}(\mathrm{N_2}, \mathrm{SLOT}) \tag{18}$$

$$W_{20} = (1/2)T_1^{-1}(\mathrm{N_2}, \mathrm{BULK}) \tag{19}$$

$$W_1 = (1/2)T_1^{-1}(f_{\mathrm{air}}, \mathrm{SLOT}) \tag{20}$$

$$W_2 = (1/2)T_1^{-1}(f_{\mathrm{air}}, \mathrm{BULK}). \tag{21}$$

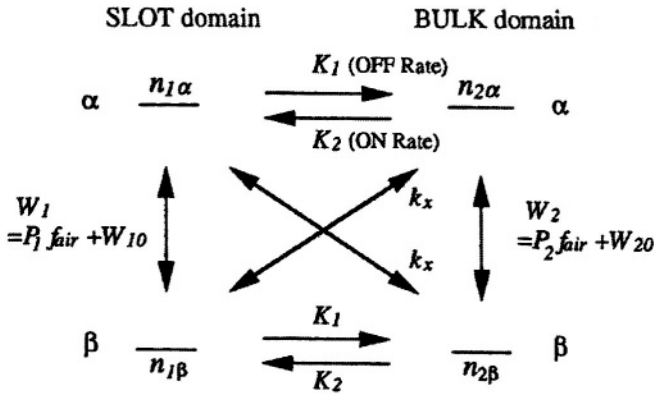

Figure 12. A scheme for analyzing saturation-recovery signals of spin labels in the presence of two domains that possess different oxygen transport rates: the SLOT domain and the BULK (bulk plus boundary) domain. An important point in this scheme is that it includes exchanges of lipid-type spin labels between the two domains (K_1 and K_2, outbound and inbound rates of the SLOT domain, respectively). The assumption is that all spin-label molecules are available for the exchange processes. In addition, this scheme includes the following two relaxation processes: (1) Electron spin transition of the spin label in each domain. The transition rates W_1 and W_2, are linear functions of the partial pressure of air, f_{air}, in the equilibrating gas mixture, W_{10} and W_{20} are the electron spin transition rates at $f_{air} = 0$, and $2P_1$ and $2P_2$ are the rates of oxygen collision with the spin label in a sample equilibrated with air. (2) Heisenberg exchange between the spins in different domains (k_X is the Heisenberg exchange rate). The three states of the doxyl nitrogen nuclear spin are assumed to mix into a single state because of fast nuclear spin relaxation (Popp and Hyde, 1982; see also Yin et al., 1987). The *n* values represent the instantaneous spin populations per unit volume of the four levels (from Kawasaki et al., 2001, © 2001, with permission from the Biophysical Society).

A theory has been developed to include the exchange of lipid-type spin labels between two domains that possess different oxygen transport rates (Kawasaki et al., 2001). The saturation-recovery signal of spin labels distributed between the two coexisting lipid domains in the membrane was analyzed based on the scheme shown in Fig. 12. Three relaxation processes are involved in saturation recoveries of spin labels exchanging between the two domains. The first is electron spin-lattice relaxation at each domain; the electron spin-lattice relaxation rates, W_1 and W_2, are linear functions of f_{air} ($W_1 = P_1 f_{air} + W_{10}$ and $W_2 = P_2 f_{air} + W_{20}$), and W_{10} and W_{20} are the electron spin-lattice relaxation rates at $f_{air} = 0$. The second process is the physical exchange of lipids (spin labels) between the two domains (K_1 and K_2 are the exchange rates). It is assumed that all spin label molecules are available for the exchange reaction, that is, the domains must be small for this formalism to be valid. The third is the Heisenberg exchange between the spins in different domains (k_x is the Heisenberg exchange rate).

Following Yin, Pasenkiewicz-Gierula and Hyde (1987), a set of rate equations was set up by Kawasaki et al. (2001) with the following solution:

$$I(t, f_{air}, N) = I_1[1 - \exp\{-(A - B)t\}] + I_2[1 - \exp\{-(A + B)t\}] \quad (22)$$

$$A(f_{air}, N) = W_1 + W_2 + (1/2)(K_1 + K_2 + k_X N) \quad (23)$$

$$B(f_{air}, N) = [(W_1 - W_2)^2 + (W_1 - W_2)\{K_1 - K_2 + (K_1 - K_2)k_X N/(K_1 + K_2)\} + (1/4)(K_1 + K_2 + k_X N)^2]^{1/2} \quad (24)$$

where $I(t, f_{air}, N)$ is the observed saturation-recovery signal, I_1 and I_2 are constants to be defined by initial conditions. The N represents the total number of spins per unit volume and is proportional to the number of spin probes incorporated in the membrane and the n values represent the instantaneous spin populations per unit volume of the four levels (see Fig. 12).

$$N = n_{1\alpha} + n_{1\beta} + n_{2\alpha} + n_{2\beta}. \quad (25)$$

As discussed below, all the rate constants (W_{10}, P_1, W_{20}, P_2, K_1, K_2, and k_X) are determined by obtaining saturation-recovery signals at various partial pressures of oxygen (at low spin-label concentrations), and at various concentrations of the spin label without oxygen. Dependencies of A and B^2 on oxygen concentration can be determined by the following equations obtained from Eqs. (20), (21), (23), and (24) (assuming $N = 0$, i.e., for a low concentration of the spin label):

$$\mathrm{A(fair) = (P_1 + P_2)fair + W_{10} + W_{20} + (1/2)(K_1 + K_2)} \quad (26)$$

$$B(f_{air})^2 = (P_1 - P_2)^2 f_{air}^2 + (P_1 - P_2)[2(W_{10} - W_{20}) + (K_1 - K_2)]f_{air} + (W_{10} - W_{20})^2 + (W_{10} - W_{20})(K_1 - K_2) + (1/4)(K_1 + K_2)^2 \quad (27)$$

Dependencies of A and $(A - B)(A + B)$ on the spin label concentration, N, in the absence of oxygen ($f_{air} = 0$) can be obtained from

$$A(N) = (1/2)k_X N + W_{10} + W_{20} + (1/2)(K_1 + K_2) \quad (28)$$

$$(A(N) - B(N))(A(N) + B(N)) = [W_{10} + W_{20}(W_{10} - W_{20})(K_1 - K_2)/(K_1 + K_2)]k_X N + 4W_{10}W_{20} + 2W_{10}K_2 + 2W_{20}K_1. \quad (29)$$

All coefficients on the right side of Eqs. (26-29) are determined by fitting the curves of A versus f_{air}, B^2 versus f_{air}, A versus N, and $(A - B)(A + B)$ versus N. Because there are only seven rate constants, all of them can be determined by solving these equations for coefficients.

5.3 Protein-Rich Rafts in Influenza Viral Membranes

The theory described above was applied to the analysis two-component saturation-recovery signals of a fatty acid spin label observed in the influenza viral (IFV) membrane (Kawasaki et al., 2001). The rate constants that were evaluated are listed in Table 2. The oxygen transport rate in the SLOT domain is smaller than in the BULK domain by a factor of 16. This suggests the possibility that the SLOT domain in the IFV membrane may not simply be a protein-rich region, but cholesterol rich and protein rich as well, because cholesterol can further reduce the oxygen collision rate (Subczynski et al., 1989, 1991a).

It has been proposed that the SLOT domain in the IFV membrane is the cholesterol-rich raft domain stabilized by the trimers of hemagglutinin and/or the tetramers of neuraminidase, the major protein components in the IFV membranes (Webster et al., 1982; Wilson et al., 1981; Varghese et al., 1983). The exchange rates from and to the SLOT domain were estimated to be 7.7 and 4.6×10^4 s^{-1}, respectively (Table 2). This indicates that the residency time of lipids in the SLOT domain is substantially longer than in the boundary region (East et al., 1985; Ryba et al., 1987; Horvath et al., 1988; Marsh, 1997), and suggests that the SLOT domain may play an important role in the function of the plasma membrane. Each individual SLOT domain may be small, but the entire SLOT domain occupies a substantial area within the IFV membrane. From the ratio of the inbound (K_2) to the outbound (K_1) rates of the lipid in the SLOT domain, the SLOT domains as a whole may occupy about one-third of the membrane.

5.4 Comments for Application of the DOT (Discrimination by Oxygen Transport) Method

It should be re-emphasized that the SLOT (slow oxygen transport) domain, which is a protein-rich raft domain in the IFV (influenza viral) membrane, is a dynamic structure. Either the constituent lipid molecules stay in the SLOT and BULK (bulk lipids plus boundary lipids) domains for less than 20 μs (the inverse of K_2, the slower exchange rate) or these domains are constantly formed and dispersed at an average of every 20 μs. The DOT method developed for analysis of pulse EPR spin label data using molecular oxygen as a probe is useful in studying SLOT domains,

particularly protein-stabilized cholesterol-rich raft domains, and the exchange of lipids between the SLOT domain and BULK domain. For more information see the recent review in this subject by Subczynski and Kusumi (2003).

Table 2: Evaluation of rate constants ($\times 10^6$ s^{-1}) described in Fig. 12 observed at 30°C in IFV membrane (from Kawasaki et al., 2001).

	SLOT domain	BULK domain
Oxygen transport parameter	$2P_1 = 0.14$	$2P_2 = 2.2$
Lipid exchange rate	$K_1 = 0.077$	$K_2 = 0.046$

6. OXIMETRY MEASUREMENTS CONFIRM QUALITY OF MOLECULAR DYNAMICS SIMULATION OF MEMBRANES

In the previous sections, we emphasized that molecular oxygen is a sensitive probe for studying membrane organization and dynamics, and noted that the oxygen transport parameter (Kusumi et al., 1982) is a sensitive and useful parameter to describe the three-dimensional dynamic structure of lipid bilayer membranes. Support for this statement also comes from molecular dynamics (MD) simulations. The idea of vacant pockets, which was introduced by Subczynski et al. (199la), is similar to the kink model presented by Trauble (1971) and Pace and Chan (1982). But the concept of vacant pockets covers a wider range of packing defects in the membrane and vacant pockets formed by a variety of mechanisms contribute to oxygen transport in the membrane. Oxygen molecules jump from one pocket to the adjacent one or move with the movement of the pocket itself due to rapid *gauche-trans* isomerization of phospholipid hydrocarbon chains. This hypothesis is supported by MD simulation, which shows that free voids exist in the hydrocarbon interior of the bilayer that are commonly large enough to accommodate small molecules such as oxygen or NO. These free voids are most common in the bilayer center (Stouch and Bassolino, 1996) which is reflected in profiles of the oxygen diffusion-concentration product (Kusumi et al., 1982; Subczynski et al., 1989, 1991a, 1998; Ashikawa et al., 1994).

MD simulations also indicate that small molecules (smaller than benzene) experience enhanced diffusion in the lipid bilayer membranes, with a diffusion rate a few times greater in the bilayer center (Stouch and Bassolino, 1996). This also agrees with oximetry measurements, which show that oxygen diffusion in membranes is as fast as in water, even though there may be a difference of one or two orders of magnitude in macroscopic viscosity (Subczynski and Hyde, 1981, 1984). Additionally, Kusumi et al. (1982) showed that oxygen diffusion in the fluid-phase PC bilayer is

isotropic, based on measurements of collision rates between oxygen and lipid-soluble spin labels with a different orientation of the π-orbital of the nitroxide radical relative to the membrane normal. This experimental result, which was criticized because the membrane is conventionally described as an anisotropic environment for the diffusion of small molecules, was confirmed by MD simulations of movement of other low molecular weight non-electrolytes in lipid bilayer membranes. For example, the calculated average coefficients of NO translational diffusion in both lateral and transversal directions in the phosphatidylcholine (PC) bilayer appear to be the same (Pasenkiewicz-Gierula and Subczynski, 1996). Similarly, the lateral diffusion coefficient profile of water molecules in a PC bilayer obtained from MD simulations was very similar to the transverse profile (Marrink and Berendsen, 1994).

The model based on MD simulations splits the lipid bilayer membrane into four regions, each of which has its own spatial characteristics. The exact location of the boundary regions are somewhat arbitrary; however, the qualitative idea of the four-region model is considered applicable to different bilayer membranes (Marrink and Berendsen, 1994). The first two regions belong to the head group region of the membrane (low and high density head group regions) while the other two regions describe the interior of the membrane (high and low tail density regions). On the basis of oxygen transport parameter measurements, three regions of the lipid bilayer membranes could be distinguished: the head group region with low oxygen transport and low activation energy of oxygen diffusion; the near head group region (the alkyl chain region up to the depth of about the ninth carbon) with a low oxygen transport parameter and higher activation energy of oxygen diffusion; and the central region where the oxygen transport parameter is a few times higher and activation energy is the lowest (Subczynski et al., 1989, 1991a, 1998). This discussion demonstrates that the spin-label oximetry approach is not only excellent for the study of membrane structure and dynamics, but also provides experimental information by which the quality of a membrane simulation can be assessed.

7. OXIMETRY *IN VIVO*

This topic has been reviewed comprehensively recently (Swartz and Clarkson (1998); Swartz (2003), and is discussed briefly in Ch. 9 by Swartz and Khan. Therefore we will cover only the general principles here and briefly describe some of the applications for both experimental and potential clinical uses. The measurement of pO_2 *in vivo* using EPR has some features that provide potential advantages for many applications. It already has led to

many very useful applications in animals and this clearly will expand significantly. There is a strong possibility that EPR oximetry also will have significant applications in clinical medicine.

The approaches and the applications differ depending on whether one uses soluble spin probes or particulates. The two approaches often are complimentary and sometimes can be used effectively in combination. The characteristics of EPR oximetry that appear to be especially useful often are complementary to existing techniques for measuring oxygen in tissues. These characteristics include capabilities of making repeated measurements from the same site (using particulates), imaging (using soluble probes), high sensitivity for low levels of oxygen, and non-invasive options. The existing EPR techniques are especially useful for studies in small animals, where the depth of measurements is not an over-riding issue. In larger animals and potentially in human subjects, the non-invasive techniques seem to be immediately applicable to study phenomena very near the surface (within 10 mm), while invasive techniques have some very promising uses for other sites. There also is a possibility of extending the non-invasive approach to greater depths by using lower frequency EPR. Measurements of pO_2 by EPR may take on added value when combined logically with other measurements that can be made especially well with *in vivo* EPR; for example it is possible to measure both nitric oxide and oxygen simultaneously (James et al., 1999a).

The clinical uses of EPR oximetry that seem especially promising and likely to be undertaken in the near future are based on the particulates. These include long term monitoring of the status and response to treatment of peripheral vascular disease and optimizing cancer therapy by enabling it to be modified on the basis of the pO_2 measured in the tumor. The *in vivo* applications of this technique have occurred because of the development of oxygen sensitive paramagnetic materials that are very sensitive to changes in the pO_2 and, in some cases, quite stable in tissues for long periods of time. These advances have been able to be used effectively because of instrumental developments that have made it feasible to make EPR measurements in intact animals.

Depending on the nature of the experiment and the techniques that are used, EPR oximetry can report on the $[O_2]$ or the pO_2 and can be used to study a wide range of oxygen levels from very low to well above physiological levels. Because of the versatility of EPR oximetry, usually a particular EPR oximetry technique will be optimal for a particular range of values or the types of measurements that are needed: e.g. whether single or repetitive, if repetitive for what length of time; the level of pO_2 that is likely to be encountered; whether data are needed as detailed maps (i.e. images), or

from paired sites, or from a single site; and the location of the site at which the measurement is to be made.

The volume that is resolved can vary from having a single volume which is defined by the size of the sample or the sensitive volume of the detector to having a full image composed of very small well-defined voxels. There are two extremes that often are termed spectroscopy and imaging respectively. There also are some alternatives between these two extremes, as noted below. The approach of choice usually will depend on the biological information that is being sought and the signal/noise that is available in the system.

The use of spectroscopy potentially has the advantage of maximum sensitivity. With spectroscopy all of the information is used for a single spectrum, potentially providing the best signal/noise achievable from the system. There also is the potential to obtain the maximum information content, with the full richness of the EPR spectrum being available. The disadvantage of spectroscopy is the limitation on spatial resolution of the information. With particulate paramagnetic materials (which can be as small as 100 microns), it is possible to obtain spectra from several sites simultaneously, when the particles are located in discrete positions and an appropriate magnetic field gradient is applied (Smirnov et al., 1993). In many situations this type of spatial resolution will be entirely sufficient for the purpose of the study.

Imaging techniques have the advantage of providing spatial resolution of the pO_2. Under some circumstances, especially when heterogeneity may be a large and important variable, this can be the biologically most important information. It is achieved, however, at the cost of the loss of signal/noise that is intrinsic with dividing the information into separate volumes and, potentially, the limitations on the information content in each resolved volume (usually this is limited to a single parameter such as intensity). Under conditions in which there is very good signal/noise, imaging can be combined with spectroscopy, providing spectral-spatial images in which much or all of the information content of the EPR spectrum is available in each voxel. In order to obtain a usable distribution of the oxygen-sensitive paramagnetic materials imaging, usually uses soluble paramagnetic materials; this leads to the need to readminister the compound for repeated measurements.

A potentially important approach for expanding the use of the oxygen sensitive paramagnetic materials is to encapsulate them in inert gas permeable materials such as plastics (Swartz and Walczak, 1996; Gallez et al., 1996; Gallez et al., 1998). This could have several advantages including extending the range and effectiveness of types of materials that can be used in experiments with animals and in accelerating the use of the oxygen

sensitive paramagnetic materials in human subjects. The use of appropriate materials would decrease or eliminate entirely the potential for undesired interactions between the paramagnetic materials and the tissues. This would facilitate the use of materials with excellent spectroscopic properties but whose responsiveness to oxygen is not sufficiently stable in some tissues (e.g. LiPc in skeletal muscle). It also is possible that some of the new materials will be found to have potentially toxic interactions with tissues and the coating would eliminate such interactions (e.g. some of the chars may cause effects by binding biologically important materials to their surfaces, potentially depleting them locally). The feasibility of the use of encapsulation has been demonstrated *in vitro* and in limited experiments in animals, and there do not appear to be any substantial obstacles to this approach. The use of encapsulation could be combined with some of the more invasive approaches that have been suggested to extend the depth at which measurements can be made at the higher range of frequencies, such as the catheter-needle probe and the implantable resonator. For the latter the paramagnetic material could be positioned at a site within the resonator where there would be maximum sensitivity. Encapsulation also would make it feasible immediately to use other materials in addition to India ink in human subjects. These could be in the form of macroscopic structures which then could be removed when the observation period was completed and thereby avoid the potential problems involved with the evaluation of the effects of materials which are permanently present in tissues. If the encapsulating materials are substances that are approved for permanent placement in tissues, then it would not be necessary to remove them even at the end of the observation period.

A number of studies have demonstrated that when inserted properly and allowed to reach equilibration, the paramagnetic materials do not perturb the local pO_2 as measured by other techniques and physiological parameters. It is necessary, of course, to ensure in each experimental setup that the presence of the paramagnetic material has not unduly disturbed the physiology. The physiological/pathophysiological meaning of these measurements depends on the particular study but when appropriate considerations are used, the data can provide very useful information.

The soluble paramagnetic materials can have lifetimes for oximetry that range from seconds to hours. The principal factors affecting these lifetimes are the extent of metabolism to non-paramagnetic forms and excretion. The particulate materials usually have much longer biological lifetimes, but their responsiveness to oxygen may not persist even though they remain in situ without obvious reactions of the tissues to their presence. The long term stability of the responsiveness to oxygen that can be achieved with the particulate paramagnetic materials under certain conditions varies from

relatively short term for LiPc in muscle (about a week) to very long term (probably years or more) for most of the carbon-based materials and LiPc in some environments (e.g. the spinal cord).

Both imaging and spectroscopy of pO_2 have been achieved with the soluble paramagnetic materials. While most of the results to date with the particulate materials have used spectroscopy with localization defined by the position of the particles, with the use of a magnetic field gradient the method has been able to resolve spectra at multiple sites simultaneously. Useful results with multisite spectroscopy have been obtained in the heart (Smirnov et al., 1993), kidneys (James et al., 1996), brain (Liu et al., 1995), and tumors (Grinberg et al., 2001).

The study of fast processes has been accomplished principally with spectroscopy with particulate materials, although very impressive time-resolved studies in the heart have been obtained by gated acquisition of images of soluble nitroxides in the isolated heart (see chapter 16). With spectroscopy of particles, time resolution of the order of seconds to minutes has been achieved. In the heart, for example, the first point at 15 seconds showed the full response (Swartz et al., 1994) and less than a minute was resolved in kidney, skeletal muscle, and brain (Liu et al., 1993).

7.1 Measurements in Tumors

The most extensive applications of EPR oximetry are likely to be in tumors because of the close relationship between the pO_2 and tumor therapy. The response of tumors to ionizing radiation and, in some cases, to chemotherapy, is greatly affected by the local amount of oxygen, with the sensitivity decreasing by up to a factor of three when the partial pressure is below 5-10 torr. EPR oximetry has the potential to make such measurements accurately and, perhaps most importantly, on a repeated basis.

So far, most of the studies have been done at 1200 MHz but, using a very low frequency *in vivo* EPR spectrometer (250 ± 20 MHz) Halpern et al (1994; 1996) measured the concentration of oxygen in a fibrosarcoma in mice and the effect of perfluorocarbon/carbogen on the oxygen concentration, using a specially designed nitroxide which also has the potential for providing information on viscosity.

The potential value of *in vivo* EPR for following the pO_2 in tumors has been shown with the particulate oxygen sensitive paramagnetic materials (Swartz et al., 1994; Goda et al., 1995a, 1995b; O'Hara et al., 1995, 1997b, 1998; James et al., 199b; Pogue et al., 1999). After placing one or more deposits of oxygen sensitive paramagnetic materials at sites of interest in rodents and then making repeated measurements over several days or weeks using restrained but awake animals and a surface detector it has been shown

to be feasible to: measure the pO_2 in several different types of tumors; follow changes in pO_2 during growth; measure the effects of therapy on the pO_2 in tumors; use radiation-induced changes in pO_2 to enhance the effectiveness of subsequent doses of radiation by delivering these doses at the time when the pO_2 was relatively high; and combine EPR oximetry with NMR techniques (Dunn et al., 1995). These approaches have the potential of providing clinical physicians with a method to individualize therapy for each patient by selecting the appropriate type and timing of treatment on the basis of the pO_2 measured in the patient's tumor both initially and then during the course of therapy (O'Hara et al., 1997a, 1998).

While technically more challenging, EPR imaging of tumors has considerable potential for both basic and applied studies in which the distribution of oxygen can be defined and followed. It has been an important motivation for the development of imaging (Sotgiu, 1985; Nishikawa et al., 1985; Halpern et al., 1986, 1989). There have been several studies in model systems that have demonstrated the potential of EPR imaging to measure and image oxygen concentrations in living systems. Halpern et al. (1994) have published an oxygen sensitive 2-D (one spatial dimension) full spectral-spatial image of a mouse tumor. In this proof of principle study, the oxygen tension resolution was approximately 5 torr and the spatial resolution was 5 mm. This initial tumor image shows lower oxygen tension in the center of the tumor mass than in the periphery, consistent with the expectation of an hypoxic tumor core. See ch. 11 by Williams and Halpern for more recent results showing improved resolution.

7.2 Brain and Spinal Cord

EPR oximetry provides a potentially very useful method directly to follow changes in the pO_2 under various physiological and pathophysiological conditions in this organ whose metabolism usually involves a high rate of oxidative phosphorylation, and therefore the brain potentially is quite vulnerable to changes in the pO_2. This seems especially useful for situations in which repeated measurements of brain pO_2 are needed over a period of time. LiPc has been especially useful for *in vivo* studies of the pO_2 in the central nervous system because of its sensitivity to the relatively high concentrations of oxygen that occur normally in these tissues. Some results already have been obtained with *in vivo* EPR on the pO_2 in brain as a function of the breathing gas, with the use of various anesthetics, on adaptations to chronic hypoxia of the type likely to occur at high altitudes, and to monitor the extent of ischemia and reperfusion (Liu et al., 1993, 1995, 1997; Taie et al., 1999; Grinberg et al., 2000). These studies included the use of more than one site at which the pO_2 was measured

simultaneously, providing a very effective comparison between the experimentally manipulated side and the control side in the brain. EPR oximetry also has been used effectively to follow the effects of ionizing radiation on the pO_2 in the spinal cord, demonstrating an unexpected increase of pO_2 in animals followed for up to 9 months.

7.3 Heart

Oxygen has a critically important role in this organ because of the high rate of aerobic metabolism but direct studies have been difficult because of the motion. EPR oximetry provides a means to make such measurements in a non-destructive manner with the accuracy and sensitivity needed for these measurements. While a few oximetry studies have been carried out in the heart in situ in the rat, most of the EPR oximetry studies of the heart have used the isolated beating heart. These studies have provided some excellent insights into various physiological parameters that affect the level of oxygen in the wall of the heart, the effects of some drugs on the pO_2 in the heart, and the effects of treatments such as "ischemic preconditioning" (Friedman et al., 1995, 1996; Grinberg et al., 1997a, 1997b). As EPR oximetry has developed it has been increasingly used in combination with other measures of cardiac function. This enables the information provided by EPR oximetry to be used most effectively to unravel pathophysiology. Using this approach it has been possible to investigate the hypothesis that cardiomyopathy can be a result of an autoimmune process in which the distribution of oxygen becomes quite heterogeneous (Friedman et al., 1998). In this case the crucial experimental result was an increase in the scatter of the values for myocardial pO_2 rather than a change in absolute pO_2. The relationship of the amount of oxygen in the heart to oxidative damage associated with ischemia-reperfusion injury is another critical issue which has been able to be investigated using EPR oximetry in combination with the unique capabilities of EPR also to measure directly free radicals (Kuppusamy et al., 1994; Zweier et al., 1991).

7.4 Skeletal Muscle

The measurement of pO_2 in skeletal muscle is of great interest for understanding the energetics of muscle function. It would be especially valuable to be able to relate the pO_2 to measurements of key metabolites such as those that can be measured by NMR (e.g. ATP, inorganic phosphate, and lactic acid). EPR oximetry appears to have the capability for making the desired measurement of pO_2 in skeletal muscle and some results have been reported using both carbon-based materials and LiPc (Chan et al., 1989;

Glockner et al., 1991; Glockner and Swartz 1992) and also nitroxides in cyclohexane filled albumin microspheres (Liu et al., 1994).

7.5 Liver

The liver has a very complex blood supply, receiving blood via both the hepatic artery and the portal vein. It also has a complex microscopic anatomy in regard to the circulation of blood, with input from the portal triad, distribution via the sinusoids, and then collection via the central veins. As a consequence the liver has a number of pathophysiological conditions which seem to be very much affected by the local pO_2, but conventional methods are difficult to use in this organ. Consequently, EPR oximetry has been used to study pO_2 in the liver and some useful and interesting data already have emerged (Glockner et al., 1991; Goda et al., 1995a; Nakashima et al., 1995a, 1995b; Jiang et al., 1996). It is possible to use the different physical properties of the paramagnetic materials and/or the way that they are administered to affect their localization within the liver and thereby obtain measurements at functionally different sites within the liver. The use of either liposomes of the appropriate size or particles of India ink results in the selective accumulation of the paramagnetic material in the Kupffer cells and therefore provides measurements of the pO_2 at this site. Average global pO_2 can be obtained with the use of macroscopic materials such as crystals of lithium phthalocyanine. Using both types of measurements in the same animal, some preliminary evidence was obtained which indicates that the pO_2 in the Kupffer cells may be lower than in hepatocytes. The effects of acute ligation on the pO_2 also were studied. The effects on the pO_2 in the Kupffer cells from the hepatotoxin, carbon tetrachloride, were able to be followed over a two-week period, using India ink particles that had localized in the Kupffer cells (Nakashima et al., 1995a).

7.6 Kidney

The number of measurements of levels of oxygen in the kidney are limited because of the technical difficulties of making such measurements. The difficulties arise because of the deep location of the kidneys, the complex pattern of blood supply within the kidney, and the motion of the kidneys due to respiration. Therefore, the capabilities of EPR oximetry may be very important and useful for this organ. Some results already have been reported for EPR measurements of the pO_2 in both isolated perfused kidneys and *in vivo* (Liu et al., 1993; James et al., 1996, 1997, 1999b). The techniques used for these measurements included simultaneous measurements in the cortex and medulla of the kidney; these are useful

because of their different blood supplies and different responses to changes in the circulatory system. As expected from results with other techniques, the baseline pO_2 of the cortex was higher than that of the medulla. In response to the injection of endotoxin the pO_2 of the medulla increased while that of the cortex decreased, and the two became approximately equal. This effect could be eliminated by the administration of an inhibitor of nitric oxide synthase, suggesting that the effect was mediated by nitric oxide. It also is possible to use *in vivo* EPR to measure the nitric oxide directly (James et al., 1999b).

7.7 Skin and Underlying Tissues

Within the skin there are a number of processes that should be greatly affected by the amount of oxygen, including burns and wounds, especially in regard to factors that may affect the rate of healing. If one extends the definition of skin to include the immediately underlying tissues including some muscles, then this encompasses a region of great potential clinical utility: the status of the tissues at risk in peripheral vascular disease (Swartz and Walczak 1996, 1998). Because of its location, the skin is fully accessible to the relatively higher frequency *in vivo* EPR (e.g. 1200 MHz), in contrast to many other sites where depth of sensitivity can be limiting. To date there are only a few reported studies of EPR oximetry in skin (Hatcher et al., 1993; Swartz et al., 1994; Goda et al., 1995a), but it seems likely that this will change in the near future. The areas that are likely to have particular emphasis include wound healing and peripheral vascular disease. There is a considerable potential for early clinical studies using EPR oximetry in skin, including the potential of taking advantage of the properties of India ink for EPR oximetry.

8. FINAL REMARKS

Spin-label oximetry permits measurement of the collision rate of molecular oxygen with the nitroxide moiety of spin labels, and calculation of the product of the local oxygen diffusion coefficient and the local oxygen concentration. Separation of this product into component factors, diffusion and concentration, is, however, inherently difficult. Bimolecular collision occurs at the molecular level, while the concentration and diffusion are bulk properties of the surrounding medium. In homogenous fluids, such as the aqueous phase, separation is possible and has been verified. In a heterogeneous system, separation seems intrinsically impossible. Good examples of heterogeneous systems for which spin-label oximetry is

intensively applied are macromolecules with specifically attached spin labels, or anisotropic lipid bilayer membranes with spin labels placed at a certain depth. For the latter system, an average oxygen concentration in the lipid bilayer was obtained in conceptually different experiments (Subczynski and Hyde, 1983; Smotkin et al., 1991).

ACKNOWLEDGMENTS

This work was supported by grants RR01008, GM27665 and GM61236 from the National Institute of Health of the U.S.A. (WKS) and the NCRR supported EPR Center for Viable Systems, NIH grant P41RR11602 and NCI grant P01CA91597.

9. REFERENCES

Ahn, M.-K. (1976) Diffusion coefficients of paramagnetic species in solution, *J. Magn. Reson.* **22**, 289-293.

Almeida, P. F. F., Vaz, W. L. C., and Thompson, T. E. (1992) Lateral diffusion in the liquid phase of dimyristoylphosphatidylcholine/cholesterol bilayers: A free volume analysis, *Biochemistry* **31**, 6739-8747.

Altenbach, C., Greenhalgh, D. A., Khorana, H. G., and Hubbell, W. L. (1994) A collision gradient method to determine the immersion depth of nitroxides in lipid bilayers: Application to spin-labeled mutants of bacteriorhodopsin, *Proc. Natl. Acad. Sci. USA* **91**, 1667- 1671.

Altenbach, C., Marti, T., Khorana, H. G., and Hubbell, W. L. (1990) Transmembrane protein structure: Spin labeling of bacteriorhodopsin mutants, *Science* **248**, 1088-1092.

Ardenkjaer-Larsen, J. H., Laursen, I., Leunbach, I., Ehnholm, G., Wistrand, L.-G., Petersson, J. S., and Golman, K. (1998) EPR and DNP properties of certain novel single electron contrast agents intended for oximetric imaging, *J. Magn. Reson.* **133**, 1-12.

Ankel, E., Felix, C. C., and Kalyanaraman, B. (1986) The use of spin label oximetry in the study of photodynamic inactivation of Chinese hamster ovary cells, *Photochem. Photobiol.* **44**, 741-746.

Ashikawa, L, Yin, J.-J., Subczynski, W. K., Kouyama, T., Hyde, J. S., and Kusumi, A. (1994) Molecular organization and dynamics in bacteriorhodopsin-rich reconstituted membranes: discrimination of lipid environments by the oxygen transport parameter using a pulse ESR spin-labeling technique, *Biochemistry* **33**, 4947-4952.

Backer, J. M., Budker, V. G., Eremenko, S. I., and Molin, Yu. N. (1977) Determination of the kinetics of biochemical reactions with oxygen using exchange broadening in the ESR spectra of nitroxide radicals, *Biochim. Biophys. Acta* **460**, 152-156.

Bielec, J., Pilas, B., Sarna, T., and Truscott, T. G. (1986) Photochemical studies of phorphyrin-melanin interactions, *J. Chem. Soc. Faraday Trans.* **282**, 1469-1474.

Boag, J. W. (1969) Oxygen diffusion and oxygen depletion problems in radiobiology, *Curr. Top. Radiobiol. Res.* **5**, 141-195.

Chan, H.-C., Glockner, J. F., and Swartz, H. M. (1989) Oximetry in cells and tissue using a nitroxide-liposome system, *Biochim. Biophys. Acta* **1014**, 141-144.

Diamond, J., and Katz, Y. (1970) Interpretation of nonelectrolyte partition coefficients between dimyristoyl lecithin and water, *J. Membr. Biol.* **17**, 121-154.

Dunn, J. F., Ding, S., O'Hara, J. A., Liu, K. J., Rhodes, E., Weaver, J. B., and Swartz, H. M. (1995) The apparent diffusion constant measured by MRI correlates with pO_2 in a RIF-1 tumor, *Magn. Reson. Med.* **34**, 515-519.

East, J. M., Melville D., and Lee, A. G. (1985) Exchange rates and numbers of annular lipids for the calcium and magnesium ion dependent adenosine triphosphate, *Biochemistry* **24**, 2615-2623.

Farahbakhsh, Z. T., Altenbach, C., and Hubbell, W. L. (1992) Spin labeled cysteins as sensors for protein-lipid interaction and conformation in rhodopsin, *Photochem. Photobiol.* **56**, 1019-1033.

Feix, J. B., and Klug, C. S. (1998) Site-directed spin labeling of membrane proteins and peptide-membrane interaction, in *Biological Magnetic Resonance, Vol. 14. Spin Labeling: The Next Millennium,* L. J. Berliner, Ed., Plenum Press, New York, 251-281.

Friedman, B. J., Grinberg, O. Y., Isaacs, K.., Walczak, T. M., and Swartz, H. M. (1995) Myocardial oxygen tension and relative capillary density in isolated perfused rat hearts. *J. Mol. Cell Cardiol.* **27**, 2551-2558.

Friedman, B. J., Grinberg, O. Y., Isaacs, K., Ruuge, E. K., and Swartz, H. M. (1996) Effect of repetitive ischemia on local myocardial oxygen tension in isolated perfused and hypoperfused rat hearts, *Magn. Reson. Med.* **35**, 214-220.

Friedman, B. J., Grinberg, O. Y., Ratcliffe, N. R., Swartz, H. M., and Hickey, W. F. (1998) Acute hemodynamic and coronary circulatory of experimental autoimmune myocarditis, *Heart Vessels* **13**, 58-62.

Froncisz, W., and Hyde, J. S. (1982) The loop-gap resonator: A new microwave lumped circuit ESR sample structure, J. *Magn. Reson.* **47**, 515-521.

Froncisz, W., Lai, C.-S., and Hyde, J. S. (1985) Spin-label oximetry: Kinetic study of cell respiration using a rapid-passage T_1-sensitive electron spin resonance display, *Proc. Natl. Acad. Sci. USA* **82**, 411-415.

Gaidarov, I., Santini, F., Warren, R. A., and Keen, J. H. (1998) Spatial control of coated-pit dynamics in living cells, *Nat. Cell Biol.* **1**, 1-7.

Gallez, B., Debuyst, R., Liu, K. J., Demeure, R., Dejehet, F., and Swartz, H. M. (1996) Development of biocompatible implants of fusinite for *In Vivo* oximetry, *MAGMA* **4**, 71-75.

Gallez, B., Debuyst, R., Dejehet, F., Liu, K. J., Walczak, T., Swartz, H. M., Goda, F., Demeure, R., and Taper, H. (1998) Small particles of fusinite and carbohydrate chars coated with aqueous soluble polymers: preparation and applications for *In Vivo* EPR oximetry. *Magn. Reson. Med.* **40**, 152-159.

Glockner, J. F., Chan, H.-C., and Swartz, H. M. (1991) *In Vivo* oximetry using a nitroxide-liposome system, *Magn. Reson. Med.* **20**, 123-133.

Glockner, J. F., Norby, S.-W., and Swartz, H. M. (1993) Simultaneous measurement of intracellular and extracellular oxygen concentration using a nitroxide-liposome system, *Magn. Reson. Med.* **29**, 12-18.

Glockner, J. F., and Swartz, H. M. (1992) *In Vivo* EPR oximetry using two novel probes: fusinite and lithium phthalocyanine, in *Adv. Exp. Biol. Med.,* **317**, W. Erdmann and D. F. Bruley, Eds., Plenum Press, New York, 229-234.

Glockner, J. F., Swartz, H. M., and Pals, M. A. (1989) Oxygen gradients in CHO cells: Measurement and characterization by electron spin resonance, *J. Cell Physiol.* **140**, 505-511.

Goda, F., Liu, K. J., Walczak, T., O'Hara, J. A., Jiang, J., and Swartz, H. M. (1995a) *In vivo* oximetry using EPR and Indian ink, *Magn. Reson. Med.* **33**, 237-245.

Goda, F., O'Hara, J. A., Rhodes, E. S., Liu, K. J., Dunn, J. F., Bacic, G., and Swartz, H. M. (1995b) The changes of oxygen tension in experimental tumors after a single dose of X-ray irradiation, *Canc. Res.* **55**. 2249-2252.

Grinberg, O. Y., Friedman, B. J., and Swartz, H. M. (1997a) Intramyocardial pO_2 measured by EPR, *Adv. Exp. Med. Biol.* **428**, 261-268.

Grinberg, O. Y., Grinberg, S. A., Friedman, B. J., and Swartz, H. M. (1997b) Myocardial oxygen tension and capillary density in the isolated perfused rat heart during pharmacological intervention, *Adv. Exp. Med. Biol.* **411**, 171-181.

Grinberg, O. Y., Hou, H., and Swartz, H. M. (2000) Direct repeated measurements of pO_2 in the brain during ischemia and reperfusion, *Ischemic Blood Flow in the Brain* (Y. Fukuuchi, M. Tomita and A. Koto, eds.), **6**:381-389. Springer-Verlag Tokyo. Keio University Symposia for Life Science and Medicine.

Grinberg, O. Y., Smirnov, A.I., and Swartz, H.M. (2001) High spatial resolution multi-site EPR oximetry: the use of a convolution-based fitting method, *J. Magn. Reson.* **152**, 247-258.

Halpern, H. J., Bowman, M. K., Spencer, D. P., van Polen, J., Dowey, E. M., Massoth, R. J., Nelson, A. C., and Teicher, B. A. (1989) An imaging radiofrequency electron spin resonance spectrometer with high resolution and sensitivity for in vivo measurements, *Rev. Sci. Instr.* **60**, 1040-1050.

Halpern, H. J., Chandramouli, G. V. R., Williams, B. B., Barth, E. D., and Galtsev, V. (1998) Challenge of 3- and 4-dimensional *in vivo* spectral spatial EPR imaging at radiofrequency with narrow line spin resonance, *Twenty first International EPR Symposium,* Denver, Abstract No. 124.

Halpern, H. J., Perik, M., Nguyen, T-D., Spencer, D. P., Teicher, B. A., and Lin, Y. J. (1990) Selective isotopic labeling of a nitroxide spin label to enhance sensitivity for T2 oximetry, *J. Magn. Reson.* **90**, 40-51.

Halpern, H. J., Spencer, D. P., van Polen, J., Bowman, M. K., Massoth, R. J., Teicher, B. A., Downy, E. M., and Nelson, A. C. (1986) A low frequency imaging electron spin resonance spectrometer for non-invasive measurement of tumor oxygenation and other parameters characterizing tumor radiosensitivity, *Radiation Oncology/Biology/Physics* **12**, 217-218.

Halpern, H. J., Yu, C., Peric, M., Barth, E., Grdina, D. J., and Teicher, B. A. (1994) Oxymetry deep in tissues with low-frequency electron paramagnetic resonance, *Proc. Natl. Acad. Sci. USA* **91**, 13047-13051.

Hatcher, M. E., and Plachy, W. Z. (1993) Dioxygen diffusion in the stratum corneum: An EPR spin label study. *Biochim. Biophys. Acta.*. **1149**, 73-78.

Hitchman, M. L., 1978, *Measurement of Dissolved Oxygen.* Wiley, NY.

Holland, R. A. (1967) Kinetics of combination of O_2 and CO with human hemoglobin F in cells and in solution, *Respir. Physiol.* **3**, 307-317.

Horváth L. I., Brophy, P. J., and Marsh, D. (1988) Exchange rates at the lipid-peptide interface of myelin proteolipid protein studied by spin-label electron spin resonance, *Biochemistry* 27, 46-52.

Hu, H., Sosnovsky, G., and Swartz, H. M. (1992) Simultanous measurements of the intra- and extra-cellular oxygen concentration in viable cells, *Biochim. Biophys. Acta* **1112**, 161-166.

Hyde, J. S., and Subczynski, W. K. (1984) Simulation of ESR spectra of the oxygen-sensitive spin-label probe CTPO, *J. Magn. Reson.* **56**, 125-130.

Hyde, J. S., and Subczynski, W. K. (1989) Spin-label oximetry, in *Biological Magnetic Resonance. Vol. 8. Spin Labeling. Theory and Applications,* L. J. Berliner and J. Reuben, Eds. Plenum, New York, 399-425.

Hyde, J. S., Subczynski, W. K., Froncisz, W., and Lai, C.-S. (1983) Spin label oximetry: Measurement of oxygen concentration in biological samples, *Bull. Magn. Reson.* **5,** 180-182.

Ito, J. S., Uede, M. J., Okuda, T. S., and Ohnishi, S. I. (1981) Phagocytosis by macrophages II. The dissociation of the attachment and ingestion steps, *J. Cell Sci.* **51,** 189-201.

James, P. E., Bacic, G., Grinberg, O. Y., Goda, F., Dunn, J., Jackson, S. K., and Swartz, H. M. (1996) Endotoxin induced changes in intrarenal pO_2 measured by *in vivo* electron paramagnetic resonance oximetry and magnetic resonance imaging, *Free Rad. Biol. Med.* **21,** 25-34.

James, P.E., Grinberg, O. Y., Goda, F., Panz, T., O'Hara, J. A., and Swartz, H. M. (1997) Gloxy: an oxygen-sensitive coal for accurate measurement of low oxygen tensions in biological systems, *Magn. Reson. Med.* **37,** 48-58.

James, P. E., Miyake, M., and Swartz, H. M. (1999a) Simultaneous measurement of NO and pO_2 from tissue by *in vivo* EPR, *Nitric Oxide: Biology and Chemistry* **3,** 92-301.

James, P. E., O'Hara, J. A., Grinberg, S. A., Panz, T., and Swartz, H. M. (1999b) Impact of the antimetastatic drug batimastat on tumor growth and pO_2 measured by EPR oximetry in a murine mammary adenocarcinoma, *Adv. Exp. Med. Biol.* **471,** 487-496.

Jiang, J., Nakashima, T., Shima, T., Liu, K. J., Goda, F., and Swartz, H. M. (1996) Measurement of pO_2 in liver using EPR oximetry, *J. of Appl. Physiol.* **80,** 552-558.

Kalyanaraman, B., Feix, J. B., Sieber, F., Thomas, J. P., and Girotti, A. W. (1987) Photodynamic action of merocyanine 540 on artificial and natural cell membranes: Involvement of singlet molecular oxygen, *Proc. Natl. Acad. Sci. USA* **84,** 2999-3003.

Kawasaki, K., Yin, J.-J., Subczynski, W. K., Hyde, J. S., and Kusumi, A. (2001) Pulse EPR detection of Hpid exchange between protein-rich raft and bulk domains in the membrane: Methodology development and its application to studies of influenza viral membrane, *Biophys. J.* **80,** 738-748.

Kuppusamy, P., Chzhan, M., Vij, K., Shteynbuk, M., Lefer, D. J., Giannella, E., and Zweier, J. L. (1994) Three-dimensional spectral-spatial EPR imaging of free radicals in the heart: a technique for in vivo imaging of tissue metabolism and oxygenation, *Proc. Natl. Acad. Sci.* USA **91,** 3388-3392.

Kusumi, A., Subczynski, W. K., and Hyde, J. S. (1982) Oxygen transport parameter in membranes as deduced by saturation recovery measurements of spin-lattice relaxation times of spin labels, *Proc. Natl. Acad. Sci. USA* **79,** 1854-1858.

Lai, C.-S., Hopwood, L. E., Hyde, J. S., and Lukiewicz, S. J. (1982) ESR studies of O_2 uptake by Chinese hamster ovary cells during the cell cycle, *Proc. Natl. Acad. Sci. USA* **79,** 1854-1858.

Ligeza, A., Swartz, H. M., and Subczynski, W. K. (1994) Spin-label oximetry in dense cell suspensions: Problems in closed- and open-chamber methods, *Curr. Top. Biophys.* **18,** 29-38.

Ligeza, A., Tikhonov, A. N., and Subczynski, W. K. (1997) *In situ* measurements of oxygen production and consumption using paramagnetic fusinite particles injected into a bean leaf, *Biochim. Biophys. Acta* **1319,** 133-137.

Ligeza, A., Tikhonov, A., Hyde, J. S., and Subczynski, W. K. (1998) Oxygen permeability of thylakoid membranes: Electron paramagnetic resonance spin labeling study, *Biochim. Biophys. Acta* **1365,** 453-463.

Ligeza, A., Wisniewska, A., and Subczynski, W. K. (1992) Paraffin oil particles as microscopic probes for oxygen measurement in biological systems: ESR spin-label oximetry, *Curr. Top. Biophys.* **16,** 92-98.

Linke, W. F. (1965) *Solubilities: Inorganic and metal organic compounds* II. 4th ed. American Chemical Society, Washington, DC, 1233-1236.

Liu, K. J., Bacic, G., Hoopes, P. J., Jiang, J., Dunn, J. F., and Swartz, H. M. (1995) Assessment of cerebral pO_2 by EPR oximetry in rodents: effects of anesthesia, ischemia, and breathing gas, *Brain Res.* **685,** 91-98.

Liu, K. J., Gast, P., Moussavi, M., Norby, S. W., Vahidi, N., Walczak, T., Wu, M., and Swartz, H. M. (1993) Lithium phtalocyanine: A probe for electron paramagnetic resonance oximetry in viable biological systems, *Proc. Natl. Acad. Sci. USA* **90,** 5438-5442.

Liu, K. J., Grinstaff, M. W., Jiang, J. J., Suslick, K. S., Swartz, H. M., and Wang, W. (1994) *In vivo* measurement of oxygen concentration using sonochemically synthesized microspheres, *Biophys. J.* **67,** 896-901.

Liu, K. J., Hoopes, P. J., Rolett, E. L., Beerle, B., Azzawi, A., Goda, F., Dunn, J. J., and Swartz, H. M. (1997) Effect of anesthesia on cerebral tissue oxygen and cardiopulmonary parameters in rats, *Adv. Exp. Med. Biol.* **428,** 33-39.

Liu, X., Miller, M. J. S., Joshi, M. S., Thomas, D. D., and Lancaster, J. R. (1998) Accelerated reaction of nitric oxide with O_2 within the hydrophobic interior of biological membranes, *Proc. Natl. Acad. Sci. USA* **95,** 2175-2179.

Lomnicka, M., and Subczynski, W. K. (1996) Spin-label NO-metry, *Curr. Top. Biophys.* **20,** 76-80.

Lukiewicz, S. J. (1985) *In vivo* electron spin resonance spectroscopy, *Radio and Microwave Spectr.* **54,** 37-54.

Lukiewicz, S. J., and Lukiewicz, S. G. (1984) *In vivo* ESR spectroscopy of large biological objects, *Magn. Reson. Med.* **1,** 297-298.

Marrink, S.-J., and Berendsen, H. J. C. (1994) Simulation of water transport through a lipid membrane, *J. Phys. Chem.* **98,** 4155-4168.

Marsh, D. (1997) Stoichiometry of lipid-protein interaction and integral membrane protein structure, *Eur. Biophys. J.* **26,** 203-208.

Marsh, D. (2001) Polarity and permeation profiles in lipid membranes, *Proc. Natl. Acad. Sci. USA* **98,** 7777-7782.

Marsh, D., and Watts, A. (1981) ESR spin label studies of liposomes, in *Liposomes: from Physical Structure to Therapeutic Applications,* C. G. Knight, Ed., Elsevier/North-Holland Biomedical Press, Amsterdam, 139-188.

Mchaourab, H. S., and Hyde, J. S. (1993) Dependence of the multi-quantum EPR signal on the spin lattice relaxation time. Effect of oxygen in spin-labeled membranes, *J. Magn. Reson. B* **101,** 178-184.

Mchaourab, H. S., Hyde, J. S., and Feix, J. B. (1994) Binding and state of aggregation of spin-labeled ceocropin AD in phospholipid bilayer: Effects of surface charge and fatty acyl chain length, *Biochemistry* **33,** 6691-6699.

McIntosh, T. J. (1978) The effect of cholesterol on the structure of phosphatidylcholine bilayers, *Biochim. Biophys. Acta* **513,** 43-58.

Miettinen, H. M., Matter, K., Hunziker, W., Rose., J. K., and Mellman, I. (1992) Fc receptor endocytosis is controlled by cytoplasmic domain determinant that actively prevents coated pit localization, *J. Cell Biol.* **116,** 875-888.

Molin, Y. N., Salikhov, K. M., and Zamaraev, K. I. (1980) *Spin Exchange,* Springer-Verlag, New York, 111-115.

Morrow, M. R., Huschilt, J. C., and Davis, J. H. (1985) Simultaneous modeling of phase and calorimetric behavior in an amphiphilic peptide/phospholipid model membrane, *Biochemistry* **24,** 5396-5406.

Morse II, P. D., and Swartz, H. M. (1985) Measurement of intracellular oxygen concentration using the spin label TEMPOL, *Magn. Reson. Med.* **2,** 114-127.

Nakashima, T., Jiang, J,, Goda, F., Shima, T., and Swartz, H. M. (1995a) The measurement of pO_2 in mouse liver *in vivo* by EPR oximetry using India ink, *Magn. Reson. Med. (Japan)* **6,** 158-160.

Nakashima, T., Goda, F., Jiang, J., Shima, T., and Swartz, H. M. (1995b) Use of EPR oximetry with India ink to measure the pO_2 in the liver *in vivo* in mice, *Magn. Reson. Med.* **34,** 888-892.

Nicholson, P., and Roughton, F. J. W. (1951) A theoretical study of the influence of diffusion and chemical reaction velocity on the rate of exchange of carbon monoxide and oxygen between the red blood corpuscle and surrounding fluid, *Proc. Roy. Soc. B* **138,** 241-264.

Nishikawa, H., Fujii, H., and Berliner, L. J. (1985) Helices and surface coils for low-field *in vivo* ESR and EPR imaging applications, *J. Magn. Reson.* **62,** 79-86.

O'Hara, J. A., Goda, F., Demidenko, E., and Swartz, H. M. (1998) Effect on regrowth delay in a murine tumor of scheduling split dose irradiation based on direct pO_2 measurements by electron paramagnetic resonance oximetry, *Radiat. Res.* **150,** 549-556.

O'Hara, J. A., Goda, F., Dunn, J. F., and Swartz, H. M. (1997a) Potential for EPR oximetry to guide treatment planning for tumors, *Adv. Exp. Med. Biol.* **428,** 233-242.

O'Hara, J. A., James, P. E., Panz, T., Grinberg, O. Y., Jain, N., Dunn, J., and Swartz, H. M. (1997b) Determining the anatomic position and histological effects in tumors of gloxy, an oxygen sensitive paramagnetic material, *Adv. Exp. Med. Biol.* **428,** 107-113.

Pace, R. J., and Chan, S. I. (1982) Molecular motions in lipid bilayers. III. Lateral and transversal diffusion in bilayers, *J. Chem. Phys.* **76,** 4241-4247.

Pajak, S., Cieszka, K., Gurbiel, R., Subczynski, W. K., and Lukiewicz, S. J. (1978) EPR measurements of the oxygen consumption by tumor cells, *Third meeting of the Polish Biophysical Society,* Wroclaw-Olesnica, Book of Abstracts, p. 70.

Pajak, S., Subczynski, W. K., Panz, T., and Lukiewicz, S. J. (1980) Rate of oxygen consumption of hamster melanoma cells as a factor influencing their radioresistance, *Folia Histochem. Cytochem.* **18,** 33-39.

Pasenkiewicz-Gierula, M., and Subczynski, W. K. (1996) Structure and dynamics of lipid bilayer membranes - comparison of EPR and molecular dynamics simulation results, *Curr. Top. Biophys.* **20,** 93-98.

Plachy, W. Z., and Windrem, D. A. (1977) A gas-permeable EPR sample tube, *J. Magn. Reson.* **21,** 237-239.

Pogue, B. W., O'Hara, J. A., Liu, K. J., Hasan, T., and Swartz, H. M. (1999) Photodynamic treatment of the RIF-1 tumor with verteporfin with online monitoring of tissue oxygen using electronic paramagnetic resonance oximetry, *SPEI* **3691,** 108-114.

Popp, C. A., and Hyde, J. S. (1981) Effects of oxygen on EPR spectra of nitroxide spin-label probes of model membranes, *J. Magn. Reson.* **43,** 249-258.

Povich, M. J. (1975 a) Measurements of dissolved oxygen concentrations and diffusion coefficients by electron spin resonance, *Anal. Chem.* **47,** 346-347.

Povich, M. J. (1975b) Electron spin resonance oxygen broadening, *J. Phys. Chem.* **79,** 1106-1109.

Reszka, K., and Sealy, R. C. (1984) Photooxidation of 3,4-dihydroxyphenylalanine by hematoporphyrin in aqueous solution: An electron spin resonance study using 2,2,6,6-tetramethyl-4-piperidone 1-oxyl (Tempone), *Photochem. Photobiol.* **39,** 293-299.

Rohmer, M., Bouvier, P, and Ourisson, G. (1979) Molecular evolution of biomembranes: structural equivalents and phytogenic precursor of sterols, *Proc. Natl. Acad. Sci. USA* **76,** 847-851.

Ryba, N. J. P., Horváth, L. I., Watts, A., and Marsh, D. (1987) Molecular exchange at the lipid-rhodopsin interface: spin-label electron spin resonance studies of rhodopsin-dimyristoylphosphatidylcholine recombinants, *Biochemistry* **26,** 3234-3240.

Sarna, T., and Sealy, R. C. (1984) Photoinduced oxygen consumption in melanin systems. Action spectra and quantum yields for eumelanin and synthetic melanin, *Photochem. Photobiol.* **39,** 69-74.

Sarna, T., Duleba, A., Korytowski, W., and Swartz, H. M. (1980) Interaction of melanin with oxygen, *Arch. Biochem. Biophys.* **200,** 140-148.

Singh, R. J., Hogg, N., Mchaourab, H. S., and Kalyanaraman, B. (1994) Physical and chemical interactions between nitric oxide and nitroxides, *Biochim. Biophys Acta* **1201,** 473-441.

Smirnov, A. I., Clarkson, R. B., and Belford, R. L. (1996) EPR linewidth (T_2) method to measure oxygen permeability of phospholipid bilayers and its use to study the effect of low ethanol concentrations, *J. Magn. Reson. B* **111**:149-157.

Smirnov, A. I., Norby, S. W., Clarkson, R. B., Walczak, T., and Swartz, H. M. (1993) Simultaneous multi-site EPR spectroscopy *in vivo, Magn. Reson. Med.* **30,** 213-220.

Smotkin, E. S., Moy, F. T., and Plachy, W. Z. (1991) Dioxygen solubility in aqueous phosphatidylcholin dispersion, *Biochim. Biophys. Acta* **1061,** 33-38.

Sotgiu, A. (1985) Resonator design for *in vivo* ESR spectroscopy, *J. Magn. Reson.* **65,** 206-214.

Stamler, J. S. (1995) in *Biochemical Pharmacological and Clinical Aspects of Nitric Oxide,* B. A. Weissman, N. Allon and S. Shapira, Eds., Plenum, New York, 67-78.

St. Denis, C. E., and Fell, C. J. (1971) Diffusivity of oxygen in water, *Can. J. Chem. Eng.* **49,** 885.

Stouch, T. R., and Bassolino, D. (1996) Movement of small molecules in lipid bilayers: Molecular dynamics simulation studies, in *Biological membranes,* K. Merz Jr. and B. Roux, Eds., Birkhauser, Boston, 255-280.

Strzalka, K., Sarna, T., and Hyde, J. S. (1986) ESR oximetry measurement of photosynthetic oxygen evolution by spin-probe technique, *Photobiochem. Photobiophys.* **12,** 67-71.

Strzalka, K., Walczak, T., Sarna, T., and Swartz, H. M. (1990) Measurement of time-resolved oxygen concentration changes in photosynthetic systems by nitroxide based ESR oximetry, *Arch. Biochem. Biophys.* **281,** 312-318.

Subczynski, W. K., and Hyde, J. S. (1981) The diffusion-concentration product of oxygen in lipid bilayers using the spin-label T_1 method, *Biochim. Biophys. Acta* **643,** 283-291.

Subczynski, W. K., and Hyde, J. S. (1983) Concentration of oxygen in lipid bilayer using a spin-label method, *Biophys. J.* **41,** 283-286.

Subczynski, W. K., and Hyde, J. S. (1984) Diffusion of oxygen in water and hydrocarbons using an electron spin resonance spin label technique, *Biophys. J.* **45,** 743-748.

Subczynski, W. K., and Hyde, J. S. (1998a) Membranes: barriers or pathways for oxygen transport, in *Oxygen Transport to Tissue XX, Advances in Experimental Medicine and Biology,* A. G. Hudetz, Ed., Plenum, New York, 399-408.

Subczynski, W. K., and Hyde, J. S. (1998b) Spin-label NO-metry in lipid bilayer membranes, in *Nitric Oxide in Transplant Rejection and Anti-Tumor Defense,* S. J. Lukiewicz and J. L. Zweier, Eds., Kluwer, Boston,, 95-107.

Subczynski, W. K., and Kusumi, A. (1985) Detection of oxygen consumption during very early stages of lipid peroxidation by ESR nitroxide spin probe method, *Biochim. Biophys. Acta* **821,** 259-263.

Subczynski, W. K., and Markowska, E. (1992) Effect of carotenoids on oxygen transport within and across model membranes, *Curr. Top. Biophys.* **16,** 62-68.

Subczynski, W. K., Hopwood, L. E., and Hyde, J. S. (1992a) Is the mammalian cell plasma membrane a barrier to oxygen transport?, *J. Gen. Physiol.* **100,** 69-87.

Subczynski, W. K., Hyde, J. S., and Kusumi, A. (1989) Oxygen permeability of phosphatidylcholine-cholesterol membranes, *Proc. Natl. Acad. Sci. USA* **86,** 4474-4478.

Subczynski, W. K., Hyde, J. S., and Kusumi, A. (1991a) Effect of alkyl chain unsaturation and cholesterol intercalation on oxygen transport in membranes: A pulse ESR spin labeling study, *Biochemistry* **30**, 8578-8590.

Subczynski, W. K. and Kusumi, A. (1985) Detection of oxygen consumption during very early stages of lipid peroxidation by ESR nitroxide spin probe method, *Biochim. Biophys. Acta* **821**, 259-263.

Subczynski, W. K. and Kusumi, A. (2003) Dynamics of raft molecules in the cell and artificial membranes: approaches by the pulse EPR spin labelling and single molecule optical microscopy, *Biochim. Biophys. Acta* **1610**, 231-243.

Subczynski, W. K., Lewis, R. N. A. H., McElhaney, R. N., Hodges, R. S., Hyde, J. S., and Kusumi, A. (1998) Molecular organization and dynamics of 1-palmitoyl-2-oleoylphosphatidylcholine bilayers containing a transmembrane helical peptide, *Biochemistry* **37**, 3156-3164.

Subczynski, W. K., Lomnicka, M., and Hyde, J. S. (1996) Permeability of nitric oxide through lipid bilayer membranes, *Free Rad. Res.* **24**, 343-349.

Subczynski, W. K., Lukiewicz, S., and Hyde, J. S. (1986) Murine *in-vivo* L-band ESR spin-label oximetry with a loop-gap resonator, *Magn. Reson. Med.* **3**, 747-754.

Subczynski, W. K., Markowska, E., and Sielewiesiuk, J. (1991b) Effect of polar carotenoids on the oxygen diffusion-concentration product in lipid bilayers. An ESR spin label study, *Biochim. Biophys. Acta* **1068**, 68-72.

Subczynski, W. K., Pasenkiewicz-Gierula, M., McElhaney, R. N., Hyde, J. S., and Kusumi, A. (2003) Molecular organization and dynamics of 1-palmitoyl-2-oleoylphosphatidylcholine membranes containing a transmembrane α-helical peptide with dynamic surface roughness, *Biochemistr.***42**, 3939-3948.

Subczynski, W. K., Renk, G. E., Crouch, R. K., Hyde, J. S., and Kusumi, A. (1992b) Oxygen diffusion-concentration product in rhodopsin as observed by a pulse ESR spin labeling method, *Biophys. J.* **63**, 573-577.

Subczynski, W. K., Wisniewska, A., Yin, J.-J., Hyde, J. S., and Kusumi, A. (1994) Hydrophobic barriers of lipid bilayer membranes formed by reduction of water penetration by alkyl chain unsaturation and cholesterol, *Biochemistry* **33**, 7670-7681.

Swartz, H. M. (2003) The measurement of oxygen *in vivo* using EPR techniques, in *Biological Magnetic Resonance* **18***: In Vivo EPR (ESR): Theory and Applications.* L.J. Berliner, Ed., Plenum Publishing Co., New York. 404-440.

Swartz, H. M., and Clarkson, R. B. (1998) The measurement of oxygen *in vivo* using EPR techniques, *Phys. Med. Biol.***43**, 1957-1975.

Swartz, H. M., and Glockner, J. F. (1989) Measurements of concentration of oxygen in biological systems in EPR techniques, in *Advance EPR in Biology and Biochemistry,* A. J. Hoff, Ed., Elsevier, Amsterdam, 753-782.

Swartz, H. M., and Glockner, J. F. (1991) Measurement of oxygen by ESRI and ESRS, in *Imaging and In Vivo EPR,* G. R. Eaton, S. S. Eaton and K. Ohno, Eds., CRC Press, Boca Roton, 261-290.

Swartz, H. M., Boyer, S., Gast, P., Glockner, J. F., Hu, H., Liu, K. J., Moussavi, M., Norby, S. W., Vahidi, N., Walczak, T., Wu, M., and Clarkson, R. B. (1991) *Magn. Reson. Med.* **20**, 333-339.

Swartz, H. M., Chen, K., Pals, M., Sentjurc, M., and Morse II, P. D. (1986) Hypoxia sensitive NMR contrast agents, *Magn. Reson. Med.* **3**, 169-174.

Swartz, H. M., Liu, K. J., Goda, F., and Walczak, T. (1994) India ink: a potential clinically applicable EPR oximetry probe, *Magn. Reson. Med.* **30**, 229-232.

Swartz, H. M., and Walczak, T. (1996) An overview of considerations and approaches for developing *in vivo* EPR for clinical applications, *Chem. Intermed.* **22**, 511-23.

Swartz, H. M., and Walczak, T. (1998) Developing *in vivo* EPR oximetry for clinical use, *Adv. Exp. Med. Biol.* **454,** 243-252.

Taie, S., Leichtweis, S., Liu, K. J., Miyake, M., Grinberg, O. Y., Demidenko, E., and Swartz, H. M. (1999) The effects of ketamine/xylazine and pentobarbital anesthesia on cerebral tissue oxygen tension, blood pressure, and arterial blood gas in rats, *Adv. Exp. Med. Biol.* **471,** 189-198.

Träuble, H. (1971) The movement of molecules across lipid membranes: A molecular theory, *J. Membr. Biol.* **4:**193-208.

Vahidi, N., Clarkson, R. B., Liu, K. J., Norby, S. W., Wu, M., and Swartz, H. M., 1994, *In Vivo* and *In Vitro* EPR oximetry with fusinite: A new coal-derived, particulate EPR probe, *Magn. Reson. Med.* **31,** 139-146.

Varghese, J. N., Laver, W. G., and Colman, P. M. (1983) Structure of the influenza glycoprotein antigen neuraminidase at 2.9 Å resolution, *Nature* **303**, 35-40.

Vaughn, M. W., Huang, K. T., Kuo, L., and Liao, J. C. (2001) Erythrocyte consumption of nitric oxide: Competition experiment and model analysis, *Nitric Oxide: Biology and Chemistry* **5**, 18-31.

Webster, R. G., Laver, W. G., Air, G. M., and Schild, G. C. (1982) Molecular mechanisms of variation in influenza viruses, *Nature* **296,** 115-121.

Wilson, I. A., Skehel, J. J., and Wiley, D. C. (1981) Structure of the hemagglutinin membrane glycoprotein of influenza virus at 3 Å resolution, *Nature* **289**, 366-378.

Windrem, D. A., and Plachy, W. Z. (1980) The diffusion-solubility of oxygen in lipid bilayers, *Biochim. Biophys. Acta,* **600,** 655-665.

Wisniewska, A., and Subczynski, W. K. (1998) Effects of polar carotenoids on the shape of the hydrophobic barrier of phospholipid bilayers, *Biochim. Biophys. Acta* **1368,** 235-246.

Wood, R. K., Dobrucki, J. W., Glockner, J. F., Morse II, P. D., and Swartz, H. M. (1989) Spectral-spatial ESR imaging as a method of noninvasive biological oximetry, *J. Magn. Reson.* **85,** 50-59.

Yin, J.-J., Pasenkiewicz-Gierula, M., and Hyde, J. S. (1987) Lateral diffusion of lipids in membranes by pulse saturation recovery electron spin resonance, *Proc. Natl. Acad. Sci. USA* **84**, 964-968.

Yin, J.-J., and Hyde, J. S. (1987) Spin-label saturation-recovery electron spin resonance measurements of oxygen transport in membranes, *Z. Phys. Chem. (Munich)* **153,** 57-65.

Zweier, J. L., Thompson-Gorman, S., and Kuppusamy, P. (1991) Measurement of oxygen concentration in the intact beating heart using electron paramagnetic resonance spectroscopy: a technique for measuring oxygen concentration in situ, *J. Bioenerg. Biomembr.* **23,** 855-871.

Chapter 11

In vivo EPR Imaging

Benjamin B. Williams and Howard J. Halpern
Department of Radiation and Cellular Oncology, University of Chicago, Chicago, Illinois 60637

Abstract: Aspects of *in vivo* EPR imaging are discussed, including low frequency spectrometer design, spin probe development, data acquisition and image reconstruction for spatial and spectral-spatial imaging, and the types of biological measurements that can be made using these techniques.

1. A BRIEF HISTORY OF *IN VIVO* EPR IMAGING

The frequencies at which the first electron paramagnetic resonance experiments were performed were those applicable to living systems many centimeters in diameter (Zavoisky, 1945). The resonance frequency used, 133 MHz, now appears to be an excellent choice for penetration deep into the tissues of human-sized animal samples. It is near that used for late generation high-field MRI at magnetic fields of 3 or more Tesla (Chen et al., 1999; Robitaille et al., 1999). Early, and perhaps the earliest, measurements with EPR in a living animal were carried out by Piette and co-workers (Feldmen et al., 1975). These X-band measurements avoided the problem of tissue penetration by burying a helical resonator inside the liver of a living rat. These measurements demonstrated the feasibility of *in vivo* EPR.

Berliner and Fujii (1985), realizing that *in vivo* measurements that were less invasive required lower frequencies than X-band, developed an L-band system. Operating at 1.8 GHz, they showed 1-dimensional images of the cross section of a piece of celery. A solution of the nitroxide TEMPOL was allowed to wick up through the capillaries of the celery, producing two spatially distinct signals. The sample was placed within and perpendicular to the loop of a single-loop resonator. Subsequently they showed 2-D spatial images of the distribution of the nitroxide carboxyproxyl in a melanoma

grown in the tail of a mouse at similar frequencies after injecting the mouse with nitroxide (Berliner et al, 1987). This work demonstrated the first *in vivo* EPR images.

Measurements were made of the diminution of signal from various nitroxides in selected organs in mice, using surface coils for localization, by Bacic et al. (1989). Utsumi et al. (1990) have used both localized spectroscopy and imaging to assess redox states and the effects of toxins on various animal tissues. Surface coil measurements were shown by Kuppusamy et al. at L-band that documented heterogeneous reduction of CTPO and TEMPOL by tumors as well as differential tumor and normal tissue bioreduction of TEMPOL in mice (Kuppusamy et al., 2002). Sotgiu has imaged bioreduction of nitroxides in rat organs as well (Alecci, 1994).

Until recently, the only medically reliable oxygen measurement was the arterial blood gas, essentially a whole body oxygenation measurement. The difficulty of obtaining information about the concentrations of molecular oxygen in tissues cannot be overestimated. Oxygen levels in tissues and tumors can be measured using the widths of spectral lines of embedded or injected EPR substrate. Bacic et al. (1993) showed localized tumor oxygenation by measuring the CW EPR line widths of particles of fusinite, a coal derivative, placed in various portions of a mouse tumor. Halpern et al. (1994) first demonstrated an image of oxygen concentration in a living animal. They showed a 2-D spectral-spatial image of deuterated CTPO having ^{1}H on ring position 4 in a tumor grown in the leg of a mouse. The sample was placed in a resonator with diameter sized to increase filling factor. The operating frequency was 250 MHz. By using a mathematical spectral fitting algorithm to accurately estimate the oxygen-broadened line widths, this image could be used to obtain oxygenation from different 1-dimensional portions of a tumor with approximately 5 mm resolution. Velan et al. (2000) presented images obtained at L-band of carbamoyl-proxyl in the tail of a rat. The large vessels of the tail are clearly defined. Different oxygenation of arteries and veins are also seen at submillimeter resolution. Elas et al. (2003) have shown images of oxygen concentration in a tumor in the leg of a mouse with 1 mm resolution and 3 torr oxygen resolution. These images of oxygen concentration were quantitative and correlated well with a more qualitative image obtained from MRI T_2* images obtained in the same tumor. These quantitative images provide the first relatively high resolution full-imaging glimpses into the oxygenation status of tissue deep in a living animal. Because they are quantitative, images obtained at different times can be compared. Comparisons will require sophistication because the tissue, even the general tissue contour, does change with time.

Novel approaches to EPR imaging include pulsed RF with time-domain signal acquisition, as discussed in the Chapter by Murali Krishna. Bourg et al. (1993) investigated pulsed EPR signal acquisition to derive an EPR image of solvated electrons and LiPc at 300 MHz. A related form of imaging relying on resonant preparation of the electron spins of a substrate injected into living animals but using MRI as the read-out, an Overhauser enhanced MRI or OMRI, was shown by Grucker and Lurie with nitroxyls (Grucker 1990; Lurie et al., 1998). OMRI was significantly advanced with the remarkable syntheses at Nycomed Innovations Inc. (Malmo, SW) of the triarylmethyl (TAM) species, allowing high spatial resolution images of oxygen concentration. Their OMRI images (Golman et al., 2000) and those by the NIH (Krishna et al., 2002) show quantitative oxygenation and have been considered for application to humans. Longitudinally detected ESR (LODESR) images of oxygen concentration have been demonstrated by Panagiotelis et al. (2001). Advantages of LODESR include the insensitivity of the resonator Q to motion because of the low frequency. (Yokoyama et al., 1997). Foster et al. (2001) have shown that images of oxygen concentration could be obtained in rats with LODESR.

In vivo spin trapping has been pursued with both imaging and localized spectroscopy. Komarov et al. (1993) first showed spectra from the tail of a mouse into which the nitric oxide (NO) spin trap N-methyl-D-glucamine dithiocarbamate was injected simultaneously with the NO donor sodium nitroprusside. Halpern et al. (1995) first demonstrated the feasibility of obtaining spectra of hydroxyl radical, induced by radiation production, in a tumor into which the spin trap 4-POBN and ethanol had been injected. Yoshimura et al. (1995) have shown images of NO in rats after the rat was physiologically challenged with a septic shock model.

2. IMAGES OF LIVING ANIMALS NEED:

2.1 Low Frequency

Loss Mechanism: For images of an animal of the size often studied in cancer research (mice and larger), it is difficult to use conventional X-Band EPR for all but the most superficial structures (e.g., skin) due to non-resonant loss of the exciting electromagnetic radiation. Bacic et al. (1989) show the amplitude of L-Band microwave radiation as a function of depth in a mouse. Such absorption and the dispersion that must accompany it (Abragam, 1961) will significantly affect spectral shapes, although it is likely that this can be modeled, at least crudely, and corrected with spectral fitting (Halpern et al., 1993; Robinson et al., 1999). The mechanism for the

tissue loss of RF microwave power appears, at frequencies well above 1 GHz, to be dominated by dielectric loss (frictional loss due to driven water dipole oscillation) while at frequencies significantly lower than 1 GHz the loss appears to be dominated by conductive (Ohmic) losses in the conductive tissue fluids. (Schwan and Foster, 1980). The extremely heterogeneous tissue dielectric and conductive environment make modeling this difficult. This would seem to make the theoretical studies of RF absorption (Bottomley and Andrew, 1978) less useful and the direct human measurements by Roschmann (1987) both very useful. Despite the heterogeneity of tissue characteristics, the application of the theoretical treatment by Bottomley to various tissue models appears to give results roughly similar to the measurements by Roschmann. This is shown in Fig. 1.

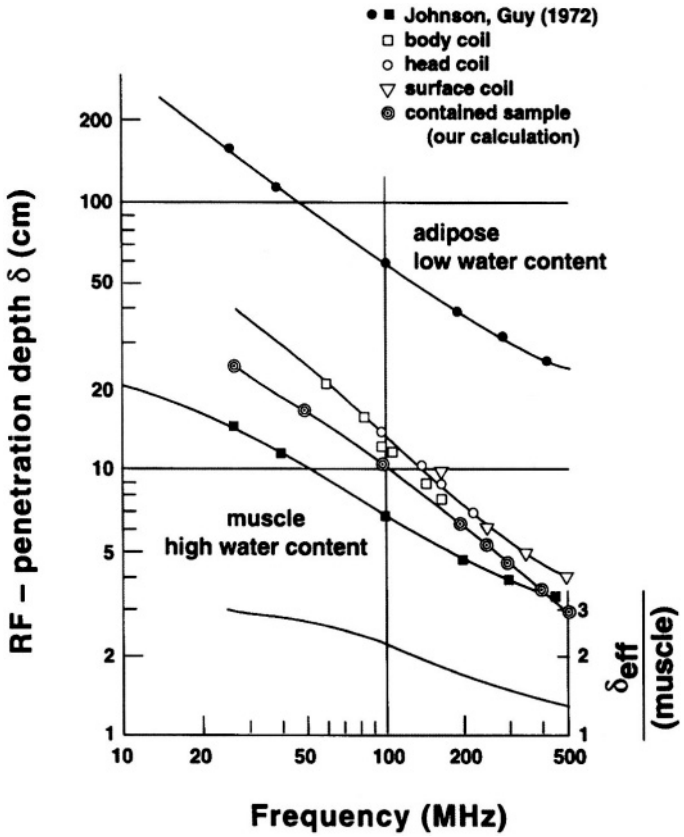

Figure 1. Plot, modified from Roschmann (1987), of the skin depth vs. frequency of the RF field. The double circles represent the depth at which the power reaches 1/e of its surface

value in a cylindrical phantom with approximate physiologic mixture of adipose and muscle. These were calculated by solution of Maxwell's equations in a cylindrical geometry.

Sensitivity as a function of frequency: The CW EPR signal voltage, V_s, at the end of the transmission line connected to the resonator can be expressed as

$$V_s = \chi'' \eta Q \sqrt{P_A Z_0} \tag{1}$$

where Q is the loaded Q of the resonator, P_A is the microwave power to the resonator produced by the external microwave source, Z_0 is the characteristic impedance of the transmission line (in Ω), χ'' is the imaginary component of the effective RF susceptibility, and η is the filling factor (Rinard et al., 1999a; Bloembergen et al., 1948; Feher, 1957). The general expression for the sample susceptibility gives, through the Boltzmann factor, a frequency dependence as a single power of frequency. $Q = \nu/\Delta\nu$. Thus, one derives the squared frequency dependence of the signal, *S,* as derived, for example, in Abragam's book using an inductive coupling assumption (Abragam, 1961). However, the sensitivity of the measurement is proportional to the signal-to-noise *(S/N)* figure. For large, *in vivo* samples, the noise will be dominated by the sample noise and not the voltage fluctuations in the wall of the resonator down to very low frequencies (~2 MHz) for tissue samples and diameters on the order of 10 cm (Hoult and Lauterbur, 1979). Note that, as derived by Rinard et al. (2003), the MRI concept of "sample noise," which arises from the additional resistive loss in the resonator due to the lossy sample, and not just to animal motion, is equivalent to the EPR point of view that the loss changed the resonator Q and required changing the coupling to the resonator, resulting in both the signal and noise voltages being transformed by the new coupling ratio $\sqrt{Z_0/R}$. The sample voltage fluctuations will dominate and, in simple conductor models, give a noise that is directly proportional to the frequency (Hoult and Lauterbur, 1979). Treatments based on tissue losses or human measurements imply a tissue noise dependence on frequency of $N \sim \nu^{1.2}$ (Foster, 1992). Thus,

$$S/N \alpha \nu^{0.8} \tag{2}$$

and the frequency dependence of tissue loss is much smaller than conventionally thought (Rinard et al., 1999).

2.2 Resonators

Surface Coils: The original *in vivo* measurements of EPR signals in animals were made with surface coils. For large animal samples which are too large to fit in a resonator, the only means by which measurements can be made will be with surface coils. For *in vivo* applications, these resonators were described by Nishikawa et al. (1985). Distribution of RF power at L-band in the fringe field from a split-ring resonator used as a surface coil resonator was shown by Bacic et al. (1989). At L-Band, 1 cm of tissue reduces the RF field amplitude to approximately 1/e of its value at the surface. Surface coil resonators suffer from problems with poor filling factor and energy loss through radiative mechanisms. Matching these very low impedance resonators to the bridge can be troublesome. A very clever solution to this problem involves coupling to a surface coil resonator with the return flux from a loop-gap resonator {T. Walczak, private communication}. The coupling and adaptive matching of the surface coil can be accomplished with the use of electronically tunable capacitors (varactors) as this group has also demonstrated (Hirata et al., 2000). Kuppusamy et al. (2002) used two surface coils on either side of the mouse tumor sample. The coils were placed in a Helmholtz configuration, improving filling factor relative to a single coil.

Loop Gap and other lumped component resonators: The development of loop gap resonators (LGRs) and lumped component resonators for EPR, as described in the chapter by Rinard and Eaton, is crucial for high filling factors at frequencies of 1 GHz or less. A one-loop one-gap LGR is shown in Fig. 2. One advantage of LGRs is their efficiency of conversion of input power (P) to RF magnetic field (B_1). The ratio

$$\Lambda = B_1 / \sqrt{P} \tag{3}$$

is a determinant of the "sensitivity" of a resonator (Froncisz and Hyde, 1982). It can be measured using saturation curves for samples with well known relaxation properties, or by comparison with another resonator with a well defined Λ. Eq. (1) contains parameters that determine the EPR sensitivity. These include Q and filling factor, η. The Q will likely be dominated by the sample loss, over which, as discussed above, we have little control. The other factor that can be controlled is the filling factor. We discuss manipulation of filling factor in the context of a cylindrical LGR (see, for example, Froncisz and Hyde, 1982; Hyde and Froncisz, 1989). More complicated situations arise as the B_1 distribution varies in different LGR configurations (Wood et al., 1984).

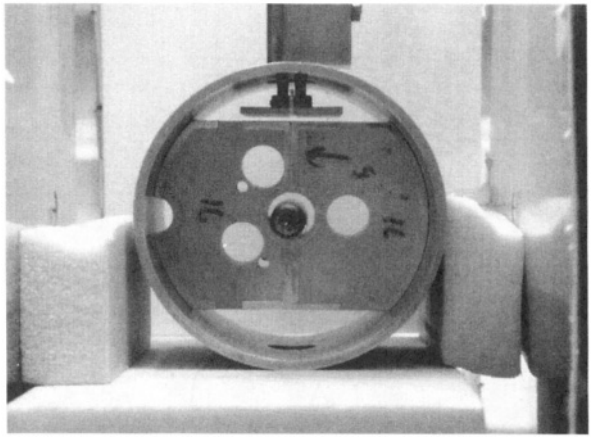

Figure 2. 16 mm inner-diameter loop-gap resonator, shown installed in the RF shield with a small sample vial. Also shown, are the capacitive coupling elements. The length of the resonator is 15mm. The resonator was machined from ABS plastic. The conductive surfaces were plated to the plastic. This consists of 12.5 μm of copper and a flash of approximately 2 μm of gold. The holes in the body of the resonator are for use with a immobilization jig designed to hold the mice and keep them mechanically isolated from the resonator.

For a simple 1 loop, 1 or 2 gap resonator, we can approximate the resonator as an infinite cylinder surrounded by the infinitely long RF shield. Thus, the length of the resonator, L_{Res}, and the length of the RF shield, $L_{\text{RF Shield}}$, are assumed to be equal and to go to infinity. This approximation is shown in Fig. 3. The RF magnetic field in the resonator, $B_{1,\text{Res}}$, is assumed to be constant across its cross-section, A_{Res}, while the RF magnetic field in the flux return, $B_{1,\text{ RF Shield}}$, is also constant across its cross-section, $A_{\text{RF Shield}}$. Assuming that the resonator is fully filled with sample, the filling factor, η, is a maximum. Defining $\eta_{\max}$ to be the filling factor of the idealized resonator when filled with sample

$$\eta_{\max} = \frac{\int_{V_{Sample}} B_1^2 dV}{\int_{V_{Total}} B_1^2 dV} \approx \frac{B_{1,\text{Res}}^2 A_{\text{Res}} L_{\text{Res}} (\to \infty)}{B_{1,\text{Res}}^2 A_{\text{Res}} L_{\text{Res}} (\to \infty) + B_{1,\text{RF Shield}}^2 A_{\text{RF Shield}} L_{\text{RF Shield}} (\to \infty)} \quad (4)$$

$$\approx \frac{B_{1,\text{Res}}^2 A_{\text{Res}}}{B_{1,\text{Res}}^2 A_{\text{Res}} + B_{1,\text{RF Shield}}^2 A_{\text{RF Shield}}} = \frac{1}{1 + \dfrac{B_{1,\text{RF Shield}}^2 A_{\text{RF Shield}}}{B_{1,\text{Res}}^2 A_{\text{Res}}}} \quad (5)$$

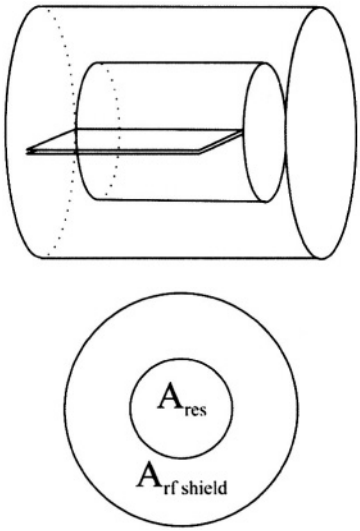

Figure 3. Top: Schematic diagram of a 1 loop-1 gap resonator, positioned inside an RF shield. Bottom: Definition of the areas used in calculation of filling factors.

where V_{Sample} is the volume of the sample and V_{Total} is the volume of all space. Here, $B_{1,\,\mathrm{RF\ Shield}}$ is the B_1 between the resonator and the surrounding RF shield as in Fig. 3 and $A_{\mathrm{RF\ Shield}}$ is the area of the annulus between the resonator and the RF shield. We also have, from the absence of divergence of magnetic flux,

$$B_{1,\mathrm{Res}} A_{\mathrm{Res}} = B_{1,\mathrm{RF\ Shield}} A_{\mathrm{RF\ Shield}} \,. \tag{6}$$

Thus,

$$\eta_{\max} \approx \frac{1}{1+\dfrac{A_{\mathrm{Res}}}{A_{\mathrm{RF\ Shield}}}} = \frac{A_{\mathrm{RF\ Shield}}}{A_{\mathrm{Res}} + A_{\mathrm{RF\ Shield}}} = \frac{A_{\mathrm{Tot}} - A_{\mathrm{Res}}}{A_{\mathrm{Tot}}} \,. \tag{7}$$

As long as the area of the resonator is small with respect to the area of the RF shield flux return, $\eta_{\max}$ will be unaffected by the area of the flux return annulus. However, when it approaches that of the flux return annulus, $\eta_{\max}$ will be affected. Practically, if the radius of the resonator r_{Res} is less than half that of the RF shield, $r_{\mathrm{RF\ Shield}}$, a deterioration of $\eta_{\max}$ of less than 25% results. This effect is also evident in the calculations by Smith et al. for NMR birdcage resonators (Hayes et al., 1985; Collins et al., 1997). A practical consideration that needs to be confronted for biological

measurements is that the sensitivity Λ (in equation [3]) will also diminish as the volume of the resonator increases. Larger samples require larger enclosing resonators and make measurements more difficult. For some conditions of spectrometer power and sample size, it may be preferable to use a surface coil resonator to perform localized spectroscopy or imaging, rather than include the entire sample in a resonator such as a LGR or birdcage coil.

Resonators other than loop-gap or cavity resonators have been developed for EPR use at frequencies from 10 to 1000 MHz. Variants of saddle coil resonators have been used at high frequencies; the optimized Alderman-Grant resonators have been used for EPR even at 7.5 GHz (Alderman and Grant, 1979; Koptioug et al., 1997). Birdcage resonators are a general form of resonator with capacitive and inductive elements distributed evenly about the azimuthal aspect of a cylindrical resonant structure (Hayes et al., 1985; Collins et al., 1997). The Alderman-Grant resonator can be regarded as a four element birdcage resonator. Birdcage resonators are particularly well suited for magnet systems whose main magnet coils and gradient coils are cylindrical and coaxial with the axis of the birdcage resonator. The B_1 magnetic fields of the birdcage resonator are oriented perpendicular to the cylinder axis. These have been developed for MRI, but could be used for EPR at frequencies similar to those used for MRI. A general limit on their construction is the approximation that the phase of the RF is constant across the elements of the resonator. Practically, this means that the general size of the resonator should be less than 1/8 the free space wavelength of the RF.

Sotgiu (1985) developed designs of re-entrant loop gap resonators that are extremely insensitive to environmental perturbation and easily inductively coupled. These were designed to operate both at L-band and at MHz RF frequencies. At L-Band frequencies, He et al. (2001) have shown that transverse electric field resonators have provided high sensitivity and integrated ability to fix the RF frequency and automatically couple the resonators. Crossed loop resonators at 250 MHz, L-band, and S-band isolate the detected EPR signal from source noise and from pulse power in pulsed EPR (Rinard et al., 1996a, 1996b, 2000, 2002a).

2.3 EPR Bridge at Radiofrequency

Since absorption of electromagnetic energy by the sample is seen as a change in the sample resistance, the elements isolating this input power from the detected signal, when using a reflection resonator setup, are called a bridge in analogy to the Wheatstone bridge which allows detection of small changes in a resistance. This is discussed at length in Poole's book (Poole, 1983).

Crucial in the design of an EPR bridge is the use of either a circulator or a magic T as a directional element. Circulators are three port electrical elements where port 1 transmits power to port 2 but isolates the power from port 3. Sometimes two circulators are combined in one housing to yield 4-port circulators, which have higher isolation. At radio-frequencies, it is difficult to obtain even a narrow band circulator with port 1-3 isolations of better than 25 dB. A magic T is a four port device that splits the power from port 1 between ports 2 and 4 but isolates the power from port 3. By terminating the power into port 4 with a matching load, nothing is reflected from this port. It then behaves like a circulator with two major exceptions. Half the power (dB), or $1/\sqrt{2}$ of the EPR signal, is lost in the matching load. However, isolations of up to 45 dB are available at radio-frequencies. This latter advantage can be more important than the disadvantage of power loss.

2.4 Automatic coupling control

Animal motions, including breathing and heart-beating, as well as idiosyncratic animal twitches, will alter cavity characteristics including its Q and both its tune frequency and the phase imparted to the radiofrequency as it is reflected from or transmitted by the resonator. These changes in Q are seen as a change in the impedance at the end of the waveguide or cable feeding the resonator. To avoid the impedance change, which has considerable effect on the signal, the coupling should be stabilized. For measurements in animals, a feedback stabilized coupling is necessary. A basic capacitively-coupled LRG (one-loop one-gap) or strip line resonator was shown by Halpern et al. (1989) to be useful at 250 MHz. The coupling involved a capacitive transformation network that could be adjusted by shunt varactors having little effect on the resonator Q. Arguing that the bulk of the signal reflected from the resonator is noise, this coupling control used that signal, obtained through a directional coupler, as an element in a feedback loop, locking the coupling. This substantially reduced animal-induced variation in the resonator coupling.

Pfenninger et al. (1995) argued that transient coupling changes derive principally from changes in the resonator Q. This group stabilized the coupling by reducing the Q variably using PIN diodes. This allowed a controllable maintenance of a constant Q. Systems described by (Hirata et al., 2000; Ono et al., 1994) showed coupling stabilization for an inductive coupling scheme for a surface coil resonator. He et al. (2001) describe automatic coupling control for a capacitive coupling system.

2.5 Automatic Cavity Tuning Control

For resonators with very high Q, it is crucial to match the frequency of the RF to the resonator tune frequency. Traditionally, this had been done by automatically shifting the frequency of the source to match the frequency of the resonator, referred to as automatic frequency control or AFC (Poole, 1983). With animal samples, the motions referred to above will also change the cavity tuning frequency. One may see considerable changes the resonator frequency. These changes have been used to monitor depth and frequency of animal breathing (Halpern et al., 1989). Automatic frequency control becomes somewhat less important as the Q of the resonator diminishes. On the other hand, as the need to maintain spectral shape fidelity increases it becomes necessary to maintain the frequency at the center of the cavity resonance.

When operating at powers of 100 mW or greater, baseline shifts become quite large with shifts in the operating frequency. Animal motion perturbs the cavity capacitance and inductance, shifting the resonator tune frequency. A major effect of animal motion is changing the interaction of the lossy animal with the RF B_1, which effectively changes the resistance in the resonator, and thus the Q. This in turn requires that the operating frequency be changed to match the shifted cavity tune. Generally, bridge balance is dependent on both the RF phase and frequency. Circulator isolation limitations result in the leakage of source RF (usually the isolation is only about 20-40 dB), which mixes with the signal returning from the cavity exiting the bridge. Optimal bridge balance involves beating the reflected signal from the cavity against this transmitted leakage RF. Changes in the RF frequency perturb this balance. This, in turn produces noise. To avoid this, stabilizing the cavity frequency and coupling in the face of animal motion becomes particularly important.

Means by which to stabilize the cavity tune have been described in the context of general bridge stabilization. Hirata et al. (2000) changed the frequency of the surface coil resonators by adjusting the capacitance of the primary resonant circuit, which directly includes the surface coil. Another general strategy is to couple the resonator to a second resonant system whose resonance frequency is near that of the primary resonator. The second system shifts or pulls the frequency of the primary resonator toward that of the secondary system. By adjusting the resonant frequency of the secondary system with an electronically controlled varactor, the frequency of the resonator can be varied to compensate for changes induced by the animal sample (He et al., 2001). This approach involves some losses due to the losses in the secondary resonant system, decreasing the signal-to-noise ratio by a factor of two.

The group at the Center for EPR Imaging *In Vivo* Physiology at the University of Chicago has obtained preliminary results from an extremely simple frequency control that does not involve a second resonant system (Subramanian et al., 2002). A loop is introduced very close to the resonator, inductively coupling to the resonator and altering the inductance of the primary resonator. By attaching a varactor to the loop through a $\lambda/4$ length of coaxial line (with suitable, non resonant blocking capacitors), the varactor appears as a variable inductor and simply changes the resonant frequency of the system. This is shown in Fig. 4. This very simple system reduces the losses in the secondary resonant system and can involve very small losses in a very high Q varactor. Varactor Q's of 10^4 or greater at 250 MHz are not uncommon.

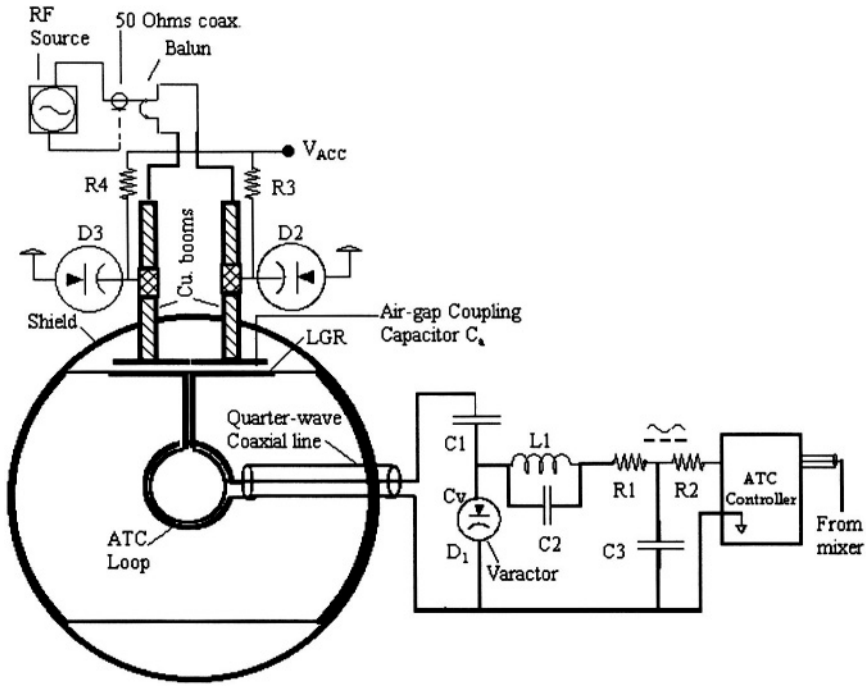

Figure 4. Schematic diagram of the automatic frequency control system in development at the Center for EPR Imaging *In vivo* Physiology at the University of Chicago.

3. LOW FIELD MAGNETS

3.1 Main Magnet

Magnet design depends on the types of resonators to be used. Surface coils, of course can be used in any magnet system in which the B_1 field can be oriented perpendicular to the main magnetic field. Resonators such as birdcage (Hayes et al., 1985; Liefer, 1997) and Alderman-Grant (Alderman and Grant, 1979) resonators which produce B_1 magnetic fields perpendicular to their cylindrical axis are convenient for use in solenoid magnets and other magnets that provide access parallel to the main magnetic field. Thus, solenoidal magnets can be used to produce the main magnetic field.

Loop gap resonators produce RF magnetic fields parallel to their cylindrical axis. Thus, access is necessary perpendicular to the axis of symmetry of the magnet. Helmholtz coils provide a simple open magnet. A loop-gap resonator can easily be oriented perpendicular to the magnetic field produced by this magnet (Halpern et al., 1989). Rinard et al. (2002b) described a four coil system that is an implementation of the general arrangement of coil loops presented by Garrett (1967). This design uses a single large pair of coils with a second, smaller pair coaxial with and outside the large pair. With minimal adjustment of the positions of the small coils, and with the diameter of the large coils of approximately 85 cm, a 30 ppm homogeneity was achieved over a sphere 15 cm in diameter (Rinard, 2002b). Six and eight coil systems (respectively 12^{th} and 16^{th} order corrected systems) offer the possibility of even more homogeneous magnetic fields over the same volume or fields with the same homogeneity tolerance over a larger volume for coils of similar size. However, as the number of coils increases, ease of access can be compromised. Odd numbers of coils can be used, although again, these can interfere with access.

Typically, the fields necessary are low enough for an air core magnet to be used. Iron core magnets are stabilized by measuring the magnetic field using Hall probes and adjusting the magnet current to achieve the proper field (Poole, 1983). This is necessary because of hysteresis, which eliminates a simple relationship between the current and the magnetic field. Air core magnets eliminate the need for such complicated measurement conditions. A 0.1 μT field uncertainty requires one part in 10^5 stability and setability at a main field of 10 mT instead of 3 parts in 10^7 at 330 mT (X-band). Care is necessary to warm the air core magnet before an experiment. When operated without magnetic field feedback, temperature expansion of the magnet can shift the field beyond the quoted part in 10^5.

3.2 Gradient Coils

Gradients for virtually all *in vivo* EPR imaging experiments (Eaton et al, 1991) differ from those used in most MRI imagers. Given the 5 to 7 order of magnitude decrease in relaxation times of electron spins relative to those of water protons, the technology of pulsed gradients is too difficult to generate gradients of sufficient magnitude in the time required to be useful. Thus, fixed stepped gradients are applied while projections (vide infra) are obtained using either CW field sweeping or broad band pulsed acquisition.

There is a considerable literature describing means to generate gradients using currents distributed over a cylinder. These are important in MRI systems using resonators that generate B_1 perpendicular to the cylinder axis. They are collectively referred to as Golay coils (Golay, 1958). Design of the current paths is described by Romeo and Hoult (1984) Unlike in MRI, from the discussion above, the gradients do not have to be shielded, given the absence of pulsed gradients and the much lower time rate of change.

Gradient coils have been designed as correction coils to be applied to the pole faces of conventional electromagnet. The formalism for their design and for optimizing the relationship between power and gradient magnitude and homogeneity is described by Anderson (1961). These techniques have been applied by Zweier et al. (1996) to L band EPR imaging to generate gradient fields as high as 150 G/cm with coils that require water cooling. Others have produced higher gradients for other imaging problems (e.g., Ohno, Eaton et al., see Eaton et al., 1991). Rinard described the design of coils to generate gradients of 10 g/cm over an 15 cm diameter sphere (Rinard et al., 2002).

4. SPIN PROBES

4.1 Spin probes used depend on the information desired

It is axiomatic that there is no single spin probe that is universally optimal for imaging. The information provided by the spin probe is often unique for the particular spin probe envisioned. For example, pH measurements would appear to require imidazolinyl or imidazolidinyl nitroxides, or biradical nitroxides. Nitroxides have been demonstrated to respond to solvent polarity.

Some chars (Boyer and Clarkson, 1994), coal variants (Vahidi et al., 1994) and lithium phthalocyanine (Liu et al., 1993; Ilangovan et al., 2002a; Ilangovan et al., 2002b) have unusually high sensitivity to oxygen. These are particulate materials that can be implanted to give one or several position

measurements of oxygen (Smirnov et al., 1993). Slurries of these solids can be infused to measure intravascular oxygenation. At present, spectral modeling has not been used to analyze data from these measurements, but the spectra appear to reveal sample heterogeneity.

Trityls have extremely narrow EPR line widths that appear to be more sensitive to oxygen than to viscosity or trityl concentration (Ardenkjaer-Larson, et al., 1998). Although the linewidth change, in gauss per torr of oxygen, is low compared to that of nitroxides, it is the fractional change in line width that determines sensitivity. This makes the trityl quite sensitive. Trityls are highly soluble molecules with molecular weights of between 1 kilodalton and 2 kilodaltons. They can be infused into animals, and they are resistant to bioreduction. In principle, by changing sidegroups on the molecule, they potentially could target the extracellular water compartment, or the intracellular water compartment.

Nitroxides: The original *in vivo* images shown by Berliner and co-workers used nitroxides as their spin probe (Berliner and Fujii, 1985). The basic nitroxide structure is shown in Fig 5a. The most common nitroxides are either five- or six- membered cyclic rings of varied saturation. A typical nitroxide, 3-carbamoyl-2,2,5,5-tetramethyl-1-pyrroline-N-oxide is shown in Fig 5b. Methyl groups flanking the N-O provide stability by preventing attack on the N-O through steric hindrance and by preventing internal H-transfer to reduce the N-O moiety. Nitroxides may be and have been used to measure oxygen concentration, self concentration, pH and microviscosity of the solvent environment. There is an enormous literature concerning nitroxides. The references given in a following section describing the various kinds of information that can be obtained from EPR images largely deal with nitroxides.

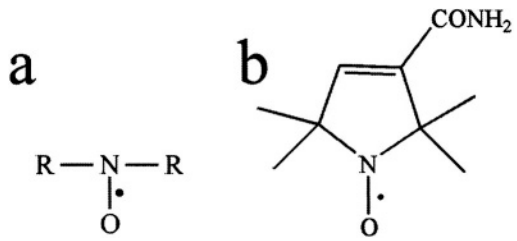

Figure 5. a) Basic chemical formula for nitroxide spin probes. b) Chemical formula for the nitroxide 3-carbamoyl-2,2,5,5-tetramethyl-1-pyrroline-N-oxide.

Trityls: Trityls are variants of the carbon centered radical triphenylmethyl radical. Until recently, trityl radicals useful for imaging were only available from Nycomed Innovations, Malmo, SW (Ardenkjaer-Larson, et al., 1998). However, recently a simplified method of synthesis

makes at least one of these compounds accessible to groups with organic synthetic ability (Reddy et al., 2002). Available trityls have 3 carboxylic acid groups, one on each of the three aryl groups surrounding the radical carbon. Each of these aryl groups has nuclear spin-zero species replacing hydrogen. The first side-chain protons are six bonds from the radical carbon, reducing splittings due to proton hyperfine interactions. This gives very weak unresolved hyperfine splittings. Much of the spin packet linewidth is due to local vibrational mode effects. The effective lifetime broadening is small giving very narrow spin packet linewidths. The spin packet linewidth of a typical trityl, OX031 (Fig. 6), is approximately 1.3 μT with an overall peak-to-peak linewidth of approximately 9 μT at 250 MHz and a spin packet linewidth of about half that at X-Band. Deuteration reduces both numbers (unpublished results from the Center for EPR Imaging *In vivo* Physiology). The narrow line gives high oxygen sensitivity, and high spatial resolution for a given gradient strength. Trityls have far less sensitivity to viscosity and temperature than nitroxides (Yong et al., 2001). This improves their characteristics as an oxygen sensor by reducing their sensitivity to confounding broadening effects.

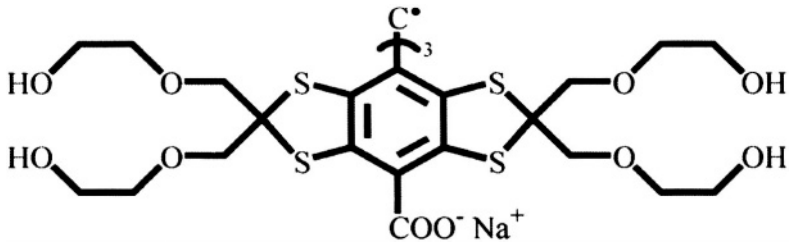

Figure 6. Chemical formula for the OX031 trityl spin probe developed by Nycomed Innovations.

Chars, coals and high spin density particulates: Discussion of the properties of chars, coals and high spin density particulates is covered by Clarkson et al. (1998). Lithium phthalocyanine, LiPc, (Lui et al., 1993) will be taken as an example of these high spin density particulates. They are extremely complicated and interesting sensors. The radicals are generated electrochemically during the synthesis of the crystals. The crystals may consist of either single or multiple domains each with a particular linewidth and each with specific responses to oxygen. Crystals of LiPc appear to consist of stacks of LiPc monomers. The unpaired electrons can hop rapidly between monomers, effectively averaging the magnetic environment encountered. This produces an exchange narrowed EPR line. In the case of LiPc, the linewidth is often comparable to the spin packet linewidth of the

trityls. The broadening of the LiPc by oxygen is at least five times that of the nitroxides and the trityls at the same oxygen concentration. Moreover, because of the high electron density in these compounds, the EPR signals are quite large for crystals a few tenths of a millimeter in dimension. Some chars and coals have sensitivity to oxygen yet another order of magnitude higher than LiPc. The deoxygenated linewidth is much larger. However, the response to oxygen is so great that an experiment with a particular power setting and modulation amplitude is typically sensitive to only a limited range of oxygen values (Boyer and Clarkson, 1994; Zweier et al., 1994). These materials have shown high oxygen sensitivity for localized spectroscopy and may be of value as a substrate for EPR imaging. There is, however, substantial variability in the EPR signals and oxygen sensitivity of seemingly similarly prepared materials.

5. INFORMATION THAT CAN BE IMAGED

5.1 Information from spatial images

Anatomy: Superb anatomic resolution has been obtained with MRI and the use of contrast agents. Using very high spin density probes, EPRI can generate high resolution images of anatomy, approaching the resolution available from water proton MRI (Zweier et al., 1998). Using slurries of ground chars, these authors were able to define the coronary vessels from a rat heart. The resolution obtained in these images approached 100 microns.

Nitroxide biodistribution and bioreduction: Nitroxides and other small molecule stable paramagnetic compounds have been monitored with localized spectroscopy or with EPR imaging to determine their biodistribution. The local decrease or increase in the EPR signal is due to local bioreduction and biodistribution. Kocherginsky and Swartz (1995) provide an excellent up to date review of this topic. A number of cellular functions determine the rate of bioreduction of nitroxides: mitochondrial cytochrome complex (P450) activity (particularly that involving the ubiquinone turnover), cellular oxygenation, and the availability of reducing equivalents, principally through glutathione and NADPH. In this sense, it provides a general measure of the redox status of tissues. However, biodistribution changes can confound simple whole animal measurements of EPR spectral amplitude or intensity.

Functionalizing drugs with spin probes to monitor pharmacokinetics: Halpern et al. (1996) reported different patterns of distribution of pyrolinyl and pyrrolidinyl nitroxides injected IP into the abdomen of living mice, depending on the 3-group attached to the nitroxide. Both positively and

negatively charged species appeared to be retained in the liver longer than uncharged species. Charged nitroxides are usually highly soluble in water, not in lipid (vide infra). Correspondingly, neutral, non-polar nitroxides are highly soluble in lipid, not water. By inference, these results would indicate that water soluble nitroxides appeared to be retained preferentially in the liver. One recent publication has discussed the distribution of a trityl (triaryl methyl) molecule (Li et al., 2002). Its three carboxylic acid residues and triply-charged state would favor similar liver retention. These results indicate that where drug molecules can be covalently functionalized to a spin label, EPR imaging can provide images of the *in vivo* distribution of the drug.

5.2 Information from spectral-spatial images

Crucial information is available from the spectrum of a spin probe. This information describes aspects of the environment, tissue fluid, or solvent in which the spin probe distributes. This is contained in both the splittings and the widths of the spectral lines. These aspects include:

Dissolved Oxygen: The widths of all lines in a multiline spectrum increase equally and linearly with the concentration of paramagnetic molecules in the environment of the spin probe. The most common endogenous paramagnetic molecule *in vivo* is O_2. Paramagnetic molecules interact with the spin probe principally through Heisenberg spin exchange (Eastman et al., 1969; Hyde and Subczynski, 1989). This is the collisional exchange of electron spin of the oxygen with that of the spin probe. The exchanged electron will be exposed to the strong, random magnetic field of the second unpaired electron in the oxygen molecule. The spin probe resonance line position will be shifted randomly, smearing or broadening the line. Heisenberg spin exchange with oxygen will broaden the spectral lines of the spin probe, not noticeably shift its spectral center, and broaden all spectral lines of the spin probe equally.

The inference of oxygen concentration from CW spectral linewidths is a T_2 sensitive method for oxygen concentration measurement. This is only one of several techniques with which to infer oxygen concentrations, T_1 sensitive methods including direct saturation measurements, passage techniques, saturation transfer, and electron double resonance (ELDOR) provide alternative methods of measuring oxygen concentrations (Hyde and Subczynski, 1989, and references therein). These may provide useful means by which to obtain images of oxygen concentration.

Spin Probe Concentration: Care must be exercised in interpreting broadening measurements since another paramagnetic species, often highly concentrated for measurements, is the spin probe itself. For narrow line spin

probes with more than one spectral line, there are two possibilities that result from Heisenberg exchange. Both possibilities will broaden the spectral line. In the first, the exchange takes place between spins in different manifolds. The effect of this form of exchange is to move the manifolds closer to their average value, since the different environments are being averaged (Currin, 1962; Freed, 1967; Gutowsky et al., 1953; McConnell, 1958). Oxygen, as well as most transition metal paramagnets, have spectra that are much broader than the spectra of typical spin probes in fluid solution. Thus, to a first approximation, the environment into which the spin probe electron is exchanged is as likely to be a higher magnetic field as a lower magnetic field than that of the native environment of the spin probe. There will then be no noticeable net shift of the spectrum by exchange with these species. The differential broadening effects described above allowed Halpern et al. (1993) to use the vinylic splitting in 3-carbamoyl-2,2,5,5-tetramethyl-1-pyrroline-N-oxide to distinguish between oxygen broadening and self broadening of nitroxide spin probes. Animal measurements involve relatively low concentrations of the spin probe. Self interaction of the spin probe for these conditions will broaden spectral lines and reduce spectral splittings, linearly with the concentration (Halpern et al., 1990; 1993)

Viscosity of fluids of living tissues: The reorientation autocorrelation time, τ_c, is the time in which the spin probe molecule rotates a certain angular distance, defined as 1 radian. Such a rotation destroys the correlation of its orientation with that at an earlier time. Small spin probe molecules rotate rapidly in a low viscosity environment. Motion averages the spectrum over any orientation dependence and narrows it. Increases in the viscosity of the fluid will interrupt the rotational motion of the spin probe, slowing its rotational motion and increasing its reorientation autocorrelation time. This creates an incomplete averaging of the line over the different orientation dependent magnetic splittings generated by the nitrogen nucleus. Incomplete averaging broadens the line. From the Debye theory (Debye, 1945; Nordio, 1976) the effect of this on a spin packet is equivalent to a lifetime reduction based broadening. In nitroxides, each of the three nitrogen hyperfine lines, corresponding to a particular nitrogen manifold, M, will have a distinct linewidth dependence on the environmental viscosity. This arises from incomplete averaging of coupling g-tensor and A-tensor anisotropies. The linewidths $\Delta B(M)$ are dependent on the nitrogen nuclear spin quantum number M = (-1, 0, 1) associated with each line (Nordio, 1976). Thus, environmental fluid viscosity will affect the spectral lines by broadening each spectral line differently in a prescribed fashion. From this, the effect of the broadening on each line can be understood and distinguished from the broadening due to oxygen. Finally, it can be used to measure the environmental viscosity. (Morse, 1977; Halpern et al., 1999)

Temperature: Nitroxide spectral lines will have a further dependence on temperature, although this is difficult to disentangle from the effect of temperature on viscosity. Typically, changes in the spectrum are plotted as a function of the ratio of viscosity to temperature. Independent of the viscosity effect, an increase in temperature will decrease the rotational correlation time and decrease the linewidth. Changes in temperature will confound measurements of other biological parameters, including oxygenation. This problem has been discussed in the context of animal oxymetry by Halpern et al. (Halpern et al., 1994). Eckberg et al. (Eckberg et al., 1996) have encapsulated nitroxides dissolved in a mixture of fatty ester and cholesterol that undergoes a phase transition at temperatures of 38 to 48 degrees C. These might be introduced into portions of animal anatomy and used for local temperature measurements.

Solvent Polarity: In general, the more polar the solvent, the higher its dielectric constant. The solvent dielectric constant has been shown to affect spectral splittings. Bales et al. (1992) present data indicating that all splittings in various nitroxides increase as the polarity of the solvent increases. They also show that for CTPO, the fractional increase in the splittings of both nitrogen hyperfine and hydrogen superhyperfine splittings is the same. This differs from the collapse of the splittings from self exchange with increasing spin probe concentration where the hydrogen splittings diminish at lower concentrations than does the nitrogen splitting. Thus, solvent polarity can be measured using nitrogen hyperfine splittings. Alternatively, the nature of the solvent, polar versus non-polar can be determined from these splittings.

Solvent pH: The groups led by Keana and Volodarsky showed that soluble spin probes can be used to measure the pH of the fluid in which they distribute (Keana et al., 1982; Khramtsov et al., 1982). For example, imidazoline nitroxides undergo protonation at acidic pH to the corresponding imidazolidine nitroxides. This produces a substantial increase on both the isotropic hyperfine splitting and the isotropic g factor. Over pH ranges of approximately 1.5 to 2 units, the spectra enable an accurate estimate of the relative amount of imidazoline and imidazolidine species. This, in turn, gives a pH measure of better than 0.1 pH units over the region of highest sensitivity (pH ~ pKa) for the particular probe.

Targeting tissue fluid compartments. A major advantage of the two forms of spin probe discussed here, nitroxides and trityls, is the possibility of synthesizing these species with specific side groups. These groups can have charge, either positive as, for example, in the case of a quaternary ammonium or negative in the case of a carboxylic acid (Kocherginsky and Swartz, 1995). They can be made less polar in the case of the synthesis of moiety with no side groups or less polar side groups, e.g., a methyl ester.

The methyl ester compounds would be expected to pass easily into cells where a much higher concentration of esterases would convert them to charged carboxylate species. They would be trapped inside cells. Bioreduction is enhanced in the cytoplasm but the more bioreduction-resistant soluble probes may be able to resist cytoplasmic reduction. Thus, the soluble spin probes can be. designed to specifically target tissue fluid compartments where they selectively accumulate (Halpern et al., 1996).

Imaging with paramagnetic compounds: relationship between linewidth and spatial resolution for a given maximum gradient The spatial resolution of an imaging experiment with soluble spin probes depends on the width of the probe spectral line and the magnitude of the applied gradient. Roughly speaking, for a given gradient *G,* the spatial resolution Δx for a probe with linewidth ΔB is (Eaton et al, 1991)

$$\Delta x = \frac{\Delta B}{G} \tag{8}$$

Thus, for a given gradient, the spatial resolution increases as the EPR linewidth is reduced. For example, a trityl with a hypoxic linewidth of 25 mG yields an order of magnitude greater resolution than that achievable with deuterated nitroxides that typically have hypoxic linewidths of 200 mG.

The oxygen sensitivity is dependent on the fractional change in the linewidth for a given change in oxygen tension. If the change in linewidth for an oxygen tension change is comparable, the sensitivity will be inversely proportional to the hypoxic linewidth. Thus, both spatial resolution and oxygen sensitivity are improved with reduced linewidth. The symmetric trityl potentially will increase both of these biologically crucial parameters by an order of magnitude.

6. EPR IMAGING

Detailed and thorough reviews of the EPR imaging literature have been written by Eaton and Eaton (1993, 1995, 1996, 1999, 2000, 2002). The techniques used in EPR imaging differ from those used in MRI because of the four to six order of magnitude difference in relaxation times. While transverse relaxation times for water hydrogen nuclei are on the order of tens to hundreds of milliseconds, those for nitroxides are, depending on measurement conditions, hundreds of nanoseconds to microseconds and those for trityls are as large as ten microseconds, depending on oxygen concentration and viscosity. MRI data is acquired with pulsed or time domain techniques. The Fourier imaging techniques used in MRI involve

the application of gradients with rise and fall times that are rapid relative to the nuclear relaxation times and spin echo detection. Gradients applied prior to readout encode position in the phase of the magnetization. Gradients applied during the readout encode position in the frequency of the magnetization. Shielded pulsed gradient coils used in MRI have rise times as small as tens of microseconds. This, however is too long a time for relaxation times of EPR probes at room temperature. During the rise time of these gradients the EPR signal could have disappeared. Thus, EPRI is commonly done with fixed and stepped gradients. These gradients are applied during either time domain acquisition or during a continuous wave magnetic field sweep. The Fourier transform of the free induction decay of the time domain signal gives a frequency spectrum that is analogous to the magnetic field spectrum acquired using CW EPR.

6.1 Spatial Imaging

Anatomic images from MRI of tissue water hydrogen nuclei derive their superb anatomic resolution from the ca. 90 molar concentration of the nuclei. Even infused spin probe concentrations will not approach within several orders of magnitude this huge water proton concentration. Thus, the spatial resolution obtained in MRI images is not likely to be obtained with EPR, although under certain circumstances EPR resolution has been quite high (Kuppusamy et al., 1995; Kuppusamy et al., 1997).

Spatial imaging typically involves filtered back projection (FBP) reconstruction using the highest gradients available consistent with signal-to-noise limits (Kuppusamy et al., 1995b), Fixed magnitude gradients with different directions are imposed on the sample and the magnetic field is swept to produce a projection. Because of this gradient, spectral components at different positions within the sample are observed at different magnetic field positions in a measured spectrum. As the gradient strength increases, the separation between the observed signals increases. Accordingly, the measured spectrum becomes broader. Thus, for diffuse samples, as the gradient magnitude increases, the signal amplitude diminishes.

From the relationship between gradient, spectral linewidth, and resolution expressed in Eq. (8), it is clear that the resolution of the images is deteriorated by the finite line width of the EPR substrate. Resolution is improved if a large G_{max} is achievable. The combination of a narrow line width and high G_{max} yields high spatial resolution. For objects where the spectral shape is uniform, spatial resolution lost due to the finite spectral linewidth can be recovered using a spectral deconvolution technique

(Kuppusamy et al., 1995b), but care must be taken to avoid the amplification of noise.

6.2 Spectral-spatial imaging

We believe that the real promise of EPR imaging lies in the capacity to create spectral-spatial images. The magnetic moment of the electron is 658 times that of the hydrogen nucleus used in MRI. This results in an increase in coupling that increases the sensitivity and specificity of the unpaired electron to environmental magnetic conditions. It is this sensitivity that enables the measurement of physiologic information discussed in Section 5.2.

Spectral-spatial imaging uses gradients of different magnitudes as well as directions. A spectrum, obtained in the presence of a magnetic field gradient with a given magnitude and direction, is a projection of a spectral-spatial object (Maltempo, 1986; Lauterbur et al., 1984; Maltempo et al., 1987). A spectral-spatial object has both spectral and spatial extent and is the representation of the spectrum at each point in an object. A set of spectra, acquired with a range of gradient magnitudes and directions, may be used to reconstruct an image of the spectral-spatial object through conventional image reconstruction techniques.

As an example of spectral-spatial imaging, we consider an object with spatial extent in one dimension. Eaton and Eaton (1995) provides an extended tutorial on the concepts of spectral-spatial imaging. Effectively, this object is an extremely thin, straight sample with, potentially, different spin probes, different spin probe concentrations, and different physical environments at each point along its length. Fig. 7 shows the effects of gradients of different magnitudes on measured spectra. Fig. 7a shows a one-dimensional spectral-spatial object as a function of spatial position, x, and swept magnetic field, B. There are three 'samples at different positions along the spatial axis, each with a common spectral center, B_0, but different linewidths. Without an applied gradient, the measured spectrum is simply the line integral of the magnetization over the spatial extent of the sample for each field point. The amplitude of the measured spectrum is the sum of the amplitudes of the individual samples and the width of the spectrum is limited by the broadest spectrum in the object. With proper normalization, such a display of line integrals over the perpendicular coordinate is what is referred to as a projection. This is analogous to projections used in computed axial tomography (CAT scans). With the imposition of a small positive magnetic field gradient along the spatial axis, as shown in Fig. 7b, the object is effectively sheared along the swept magnetic field axis. Each component is shifted along the field axis an amount proportional to its spatial position.

The measured spectrum is, again, the integration of the object over the spatial dimension. Notice that the amplitude of the measured spectrum has decreased, relative to the zero-gradient spectrum, and that the spectrum is broader. If, instead of regarding the spectral-spatial object as being sheared by a given angle, one looks at the effect of the gradient as a rotation of the spatial object by the same angle as the shearing, the effect of the gradient is to rotate the angle at which the spectral-spatial object is observed. This is shown in Fig 7c. The applied gradient changes the angle of the line of integration. After normalizing the spectral intensities and widths, the effect of the different gradients is to change the angle at which projections are acquired. This is shown in Fig 8. The angle at which projections are acquired, α, in the spectral-spatial space may be defined as

$$\tan\alpha = \frac{\Delta L}{\Delta B} G \qquad (9)$$

where ΔL is the spatial field of view for the image and ΔB is the spectral field of view for the image (Maltempo, 1986; Eaton et al., 1991). As noted above, normalized projections of the magnetization obtained in this fashion can be shown to be similar to those obtained using a CAT scan. The mathematical description of such projections of the information in an image is the Radon transform (Barrett, 1984) of the spectral-spatial object. Thus, the back projection reconstruction techniques commonly used in other forms of imaging can be applied to the calculation of the image from these projections (Lewitt, 1983). By changing the direction of the gradient, as well as its magnitude, this can be done for a three-dimensional spatial object, giving a 4-dimensional spectral-spatial image.

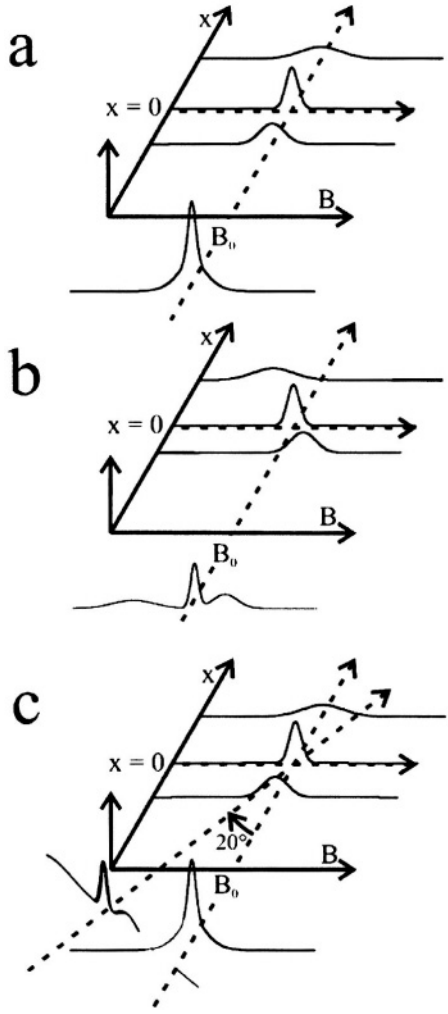

Figure 7. Spectral-spatial images are acquired by collecting spectra with various magnetic field gradients applied across the sample. The B axis represents the swept field value, not the total field. The non-horizontal dotted lines represent a line integral of spectral intensity observed with the various gradients. a) Schematic of a 2DSS object, with three components with different spatial positions and linewidths, and the spectrum acquired with no applied gradient. b) The same 2DSS object in the presence of a small positive field gradient. The line at positive x-position is shifted downfield and the line at negative x-position is shifted up field. The centered line remains unshifted. The spectrum acquired in the presence of this gradient is shown. c) Schematic of the 2DSS object, without an applied gradient, and two projections of the object. The projection at 0-degrees is the spectrum acquired with no gradient and the projection at 20-degrees is analogous to the spectrum with the positive gradient.

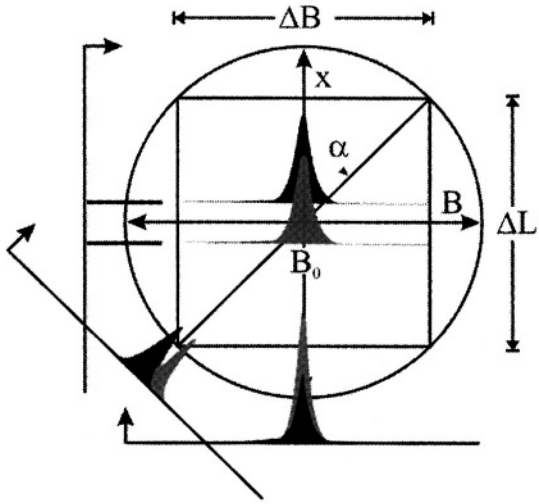

Figure 8. Two-dimensional spectral-spatial imaging geometry, showing spectra acquired with gradients of magnitudes 0, $\Delta B/\Delta L$, and ∞. The equivalence of these spectra to the Radon-transform of the 2DSS object at different values of α is demonstrated.

6.3 Image Acquisition and Reconstruction

At the Center for EPR Imaging *In vivo* Physiology, data for oxymetric images of *in vivo* mouse tumors are acquired in the following fashion. Data acquisition is performed using a 250 MHz EPR imaging spectrometer that has been described elsewhere (Halpern et al., 1989). Images are acquired using loop-gap resonators with inner diameters of either 16 mm or 19 mm, depending on the size of the tumor, and lengths of 15 mm. Heat lamps are used to maintain a temperature of approximately 37 C° at the resonator to support the temperature of the anesthetized mouse. The quality factors (Q) of the loaded resonators, measured prior to imaging, generally fall between 150 and 300. On average, -13 dBm, or 50 μW, is delivered to the cavity, resulting in an RF B_1 magnetic field strength of approximately 10 mG. Slight broadening of the Lorentzian linewidth occurs at this power for each of the trityls. This broadening is accounted for in the conversion from linewidth to pO_2.

Information is obtained from spectra by fitting them to an accurate spectral model (Halpern, et al., 1993; Peric and Halpern, 1994; Smirnov, et al., 1995, Robinson et al., 1999). The use of large Zeeman modulation amplitudes during image acquisition can be used to increase spectral signal heights and decrease the data acquisition time (Mailer et al., 2003). Through accurate modeling of the effects of this modulation on the spectra, estimates of the intrinsic spectral parameters, such as linewidth, can be made from the

overmodulated spectra (Robinson et al., 1999). Overmodulation is particularly useful in EPRI, where the magnetic field gradients broaden the observed spectra and reduce their amplitudes. By setting the modulation amplitude according to the broad features of the highest gradient spectra, the signal-to-noise ratios of these spectra can be maximized. This causes the narrower low-gradient spectra to be overmodulated. The amplitudes of the low-gradient spectra may be smaller than that observed with lower modulation amplitudes, but the decrease in SNR in these projections is more than offset by the increase observed in the high-gradient spectra. The spectral fitting algorithm described by Robinson et al. enables the intrinsic, unbroadened spectral parameters to be estimated from the reconstructed images. Typically, all of the projections are collected with modulation amplitude equal to the anoxic peak-to-peak linewidth of the spin probe. With the OX031 trityl spin probe, modulation amplitudes near 90 mG are used. An accurate measurement of the modulation amplitude is made prior to each image for incorporation into the spectral fitting procedure. The modulation frequencies used varied about 5.12 kHz, by 10's of Hz, and were set prior to each image to minimize noise.

An important consideration in the design of an EPRI experiment is the number of projections to acquire. If too few projections are acquired, aliasing artifacts will corrupt the image. Conversely, if too many projections are collected, the image acquisition time will be increased without the addition of new information. In 4-dimensional EPRI, the large amount of data necessary and the modest sensitivity, especially at high gradient strengths, threaten to make image acquisition times impractically long. Therefore, it is crucial that the minimum amount of data necessary to achieve the desired image characteristics is acquired. Several theoretical estimates of this number have been presented (Natterer and Wubbling, 2001; Pan, 1998). The radial and angular sampling densities can also be estimated from experimental estimates of the bandlimits of the image datasets.

At the Center, datasets for images of mouse tumors are typically acquired in 20-40 minutes. Projections are collected on 8×8×8 or 8×8×16 grids sampling the spatial polar, spatial azimuthal, and spectral projection angles, respectively, uniformly over 180°. The field of view sampled by each of the projections is $(25^3\text{-}40^3)\ \text{mm}^3\times 550\ \text{mG}$ when the OX031 spin probe is used. For each projection, the magnetic field is swept in approximately 0.9 seconds and 256 samples over the sweep range are recorded. Because the signal to noise is so much better for the low gradient projections, less time can be spent obtaining these projections than spent on the maximum gradient projections. The ratio in time spent on the maximum gradient projections to the minimum gradient projections depends on the gradient magnitude. The number of scans is increased as $\cos^{-1}\alpha$ where α is defined

above. Typically, 5-10 scans are acquired for the highest gradient projections and single scans were acquired for most of the lower gradient projections. With this averaging, a spectral-spatial image takes approximately twice as long as a pure spatial image.

Following data collection, experimental factors that cause the measured data to deviate from the Radon transform of the spectral-spatial object must be addressed so that associated image errors do not arise. For *in vivo* experiments, the clearance of the spin probe from the tissue during data collection must be addressed (Williams et al., 2002; Elas et al., 2003). Assuming that the wash-out from the tissue is uniform, the intensities of the projections can be scaled such that they are equal. Without this correction, streak artifacts may arise in the image due to inconsistencies in the information contained in the set of projections. The intensities of the projections were fit, as a function of time, to a single exponential and then normalized to the initial intensity prior to reconstruction. The use of a single exponential to describe the clearance is based on empirical observations of the measured clearance pattern, rather than an explicit two compartment model. If the main magnetic field strength is inferred from the programming voltage applied to a current supply, as is done at the Center, a second correction must be performed to account for the inductance of the magnetic field coils and the limited compliance voltage of the power supply (Williams et al., 2001; Oikawa et al., 1995). The current will lag, in time, behind the programming voltage and result in an apparent shift of the measured projections. If these shifts are not estimated and eliminated, they will distort the spatial and spectral shape of the object in the image. These corrections reduce image artifacts and enhance the accuracy of spatial and spectral information.

Each of the projection is smoothed with a Gaussian kernel with a FWHM of 4 points and sub-sampled from 256 points to 64 points. This process was used to average data, rather than using a larger time constant on the lock-in amplifier, in order to avoid spectral distortions related to the causal nature of lock-in filtering. Because of the sparse angular sampling often used in EPRI, images reconstructed using only the collected projections will have prominent streak artifacts. These streaks appear as ripples in the baselines of spectra in individual spatial voxels of the image, potentially corrupting the estimation of linewidths and other spectral parameters. If adequate numbers of projections are collected, additional projections can be accurately estimated through interpolation (Williams et al., 2001, Weiss et al., 1982; Elas et al., 2003; Mailer et al., 2003). By increasing the number of projections, the streak artifacts can be eliminated and accurate estimates of the spectral parameters can be made from the reconstructed images. Projection interpolation, by zero-padding the discrete Fourier transform of

the sinogram, is used to increase the number of projections by a factor of 4 for each projection angle. A spline interpolation could be used as well. Based on the observed projections, in order to achieve an adequate signal-to-noise ratio, a Ram-Lak (linear ramp) filter with a cutoff at 0.5 the Nyquist frequency (post-subsampling) is used and the images are reconstructed on a 64^4 grid. This choice of this reconstruction grid size is based the computational limits of the laboratory PCs used for processing and the pixel size necessary to support the estimated image resolution

Following image reconstruction, voxels where the spectral intensity is greater than 15% of the maximum spectral intensity in the image are identified and analyzed using the spectral fitting algorithm (Robinson et al., 1999). The measured linewidths are then converted to pO_2 according to an experimental oxygen calibration (Elas et al., 2003).

6.4 Examples of EPR images

Given the increase in signal amplitude and sensitivity at higher frequencies ($S/N \sim \nu^{0.8}$ in tissue), impressive spatial images have been obtained at L-band using high spin density carbon chars, nitroxides or trityl spin probe. An example of this is in Fig. 9, which shows two series of planar projections of RIF-1 tumors in mice, approximately 10mm in diameter. Nitroxide clearance with and without a glutathione inhibitor are shown (Kuppusamy et al., 2002).

Images have also been obtained at lower frequencies, where there is less spectral distortion due to absorption by tissues (Elas et al., 2003). At 250 MHz, the RF frequency is less than that used in some whole body human MRI units (Robitaille, 1999a). An example of a spectral-spatial image from an animal tumor is shown in Fig. 10. This represents the oxygen distribution in the tumor from the leg of a mouse. The oxygen concentration has been obtained from the width of the trityl EPR line imaged in each voxel of the leg. The image qualitatively agrees with an image of the same mouse tumor obtained using BOLD MRI.

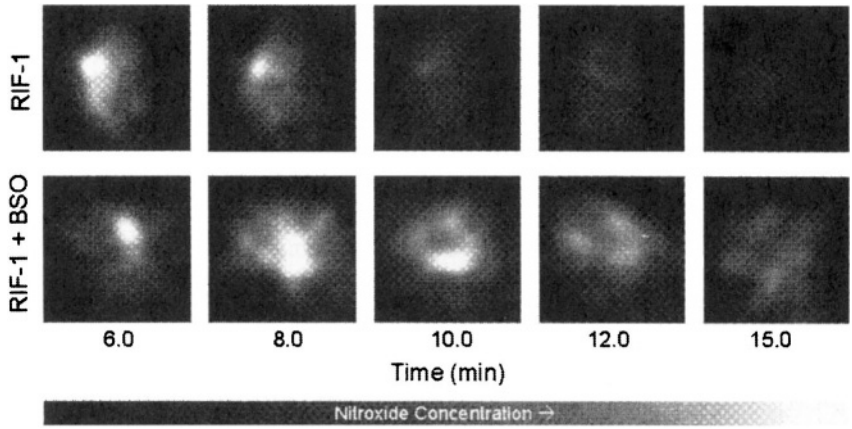

Figure 9. Two time series of planar images of nitroxide distribution in a RIF-1 mouse tumor acquired at L-band (Kuppusamy et al., 2002). Each 2D spatial image was acquired in 1.5-2.0 minutes. The tumor is approximately 10mm × 10mm × 5mm. Nitroxide clearance with and without a glutathione inhibitor is shown.

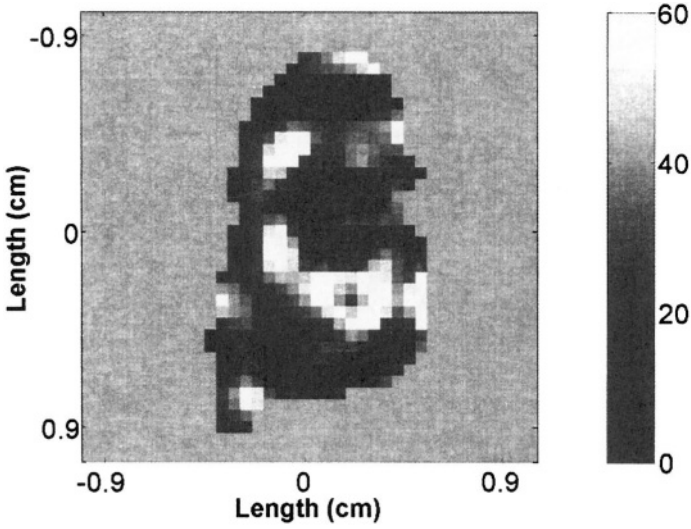

Figure 10. This image shows the oxygen concentration in a slice through an FSa tumor grown in the hind leg of a C3H mouse (Elas et al., 2003). Data acquisition was performed at 250 MHz. The oxygen concentration is derived from the linewidth measured at each spatial location and converted to partial pressure, in torr, through an experimentally determined calibration.

7. CONCLUSIONS

EPR imaging of living animal objects is a field that is evolving rapidly. Much of its capability derives from the synthesis of new spin probes with varied sensitivities to aspects of the solvents in which life processes occur, water and lipids. One may envision a variety of images that describe crucial aspects of physiology and disease. Development of the magnets and gradient coil configurations encourages novel strategies that are relatively easy to implement at the low fields used for animal imaging.

At this time, one of the most exciting capabilities lies in the ability of EPR imaging to provide quantitative oxygen tension equivalent images. James S. Hyde has been a major contributor to the understanding of EPR oxygen measurements and of the application of EPR to oxygen measurement. Indeed, the first article about EPR oxymetry read by the senior author of this chapter was by written at least in part by Jim (Lai et al., 1982). It is a pleasure to celebrate his contribution with this chapter.

Acknowledgements: We gratefully acknowledge the support of the Center for EPR Imaging In Vivo Physiology, NIH P41 EB 002034, and R01 CA 98575

8. REFERENCES

Abragam A. (1961) Principles of Nuclear Magnetism. Oxford: Oxford University; 1961.

Alderman D.W., Grant D.M. (1979) An Efficient Decoupler Coil Design which Reduces Heating in Conductive Samples in Superconducting Spectrometers. *J. Magn. Reson.* **36**, 447-451.

Alecci M., Ferrari V., Quaresima V., Sotgiu A., Ursini C.L. (1994) Simultaneous 280 MHz EPR Imaging of Rat Organs During Nitroxide Free Radical Clearance. *Biophys. J.* **67**, 1274-1279.

Anderson W. (1961) Electrical Current Shims for Correcting Magnetic Fields. *Rev. Sci. Instrum.* **32**, 241-250.

Ardenkjaer-Larsen J.H., Laursen I., Leunbach I., Ehnholm G., Wistrand L.G., Petersson J.S., Golman K. (1998) EPR and DNP Properties of Certain Novel Single Electron Contrast Agents Intended for Oximetric Imaging. *J. Magn. Reson.* 133, 1-12.

Bacic G., Liu K.J., O Hara J.A., Harris R.D., Szybinski K., Goda F., Swartz H.M. (1993) Oxygen Tension In a Murine Tumor - a Combined EPR and MRI Study. *Magn. Reson. Med.* **30,** 568-572.

Bacic G., Nilges M.J., Magin R.L., Walczak T., Swartz H.M. (1989) In Vivo Localized ESR Spectroscopy Reflecting Metabolism. *Magn. Reson. Med.* **10,** 266-272.

Bales B.L., Blum R.A., Mareno D., Peric M., Halpern H.J. (1992) Solvent and Temperature Dependence of the Hyperfine Coupling Constants in CTPO. *J. Magn. Reson.* **98**, 299-307.

Barrett H.H. (1984) The Radon Transform and its Applications. Progress in Optics. Volume XXI. North-Holland, Amsterdam.

Berliner L.J., Fuji H. (1985) Magnetic Resonance Imaging of Biological Specimens by Electron Paramagnetic Resonance of Nitroxide Spin-Labels. *Science* **227**, 517-519.

Berliner L.J., Fujii H., Wan X.M., Lukiewicz S.J. (1987) Feasibility Study of Imaging a Living Murine Tumor by Electron Paramagnetic Resonance. *Magn. Reson. Med.* **4**, 380-4.

Bloembergen, N, Purcell, E. M., and Pound, R. V. (1948), Relaxation Effects in Nuclear Magnetic Resonance Absorption. *Phys. Rev.* **73**, 679-712.

Bottomley P.A., Andrew E.R. (1978) RF Magnetic Field Penetration, Phase Shift and Power Dissipation in Biological Tissue: Implications for NMR Imaging. *Phys. Med. Biol.* **23**, 630-643.

Bourg J., Krishna M.C., Mitchell J.B., Tschudin R.G., Pohida T.J., Friauf W.S., Smith P.D., Metcalfe J., Harrington F., Subramanian S. (1993) Radiofrequency FT EPR Spectroscopy and Imaging. *J. Magn. Reson. B* **102**, 112-5.

Boyer S., Clarkson R.B. (1994) EPR Studies of an Active Carbon. *Colloids and Surfaces A* **82**, 217-224.

Chen W, Ugurbil K. (1999) High Spatial Resolution Functional Magnetic Resonance Imaging at Very-High-Magnetic Mield. *Top. Magn. Reson. Imaging* **10,** 63-78.

Clarkson R. B., Odintsov B., Ceroke P., Ardenkjaer-Larsen J. H., Fruianu M., and Belford R. L. (1998) EPR and DNP of Char Suspensions: Surface Science and Oximetry. *Phys. Med. Biol.***43**, 1907-1920.

Collins C.M., Li S., Yang Q.X., Smith M.B. (1997) A Method for Accurate Calculation of B1 Fields in Three Dimensions. Effects of Shield Geometry on Field Strength and Homogeneity in the Birdcage Coil. *J. Magn. Reson.* **125**, 233-241.

Currin J.D. (1962) Theory of Exchange Relaxation of Hyperfine Structure in Electron Spin Resonance. *Phys. Rev.* **126**, 1995-2001

Debye P. (1945) Polar Molecules. New York: Dover.

Eastman P.E., Kooser R.G., Pas M.R., Freed J.H. (1969) Studies of Heisenburg spin exchange in ESR spectra I. Linewidth and saturation effects. *J. Ghent. Phys.* **54**, 2690.

Eaton G.R., Eaton S.S., Ohno K. (1991) EPR Imaging and In Vivo EPR. Eaton G.R., Eaton S.S., Ohno K., editors. Boca Raton FL: CRC Press.

Eaton, G. R., and Eaton, S. S., (1993), Electron Paramagnetic Resonance Imaging, in "Microscopic and Spectroscopic Imaging of the Chemical State", M. Morris, ed., Marcel Dekker, Inc., ch. 11.

Eaton, G. R., and Eaton, S. S., (1995) Introduction to EPR Imaging using Magnetic Field Gradients, *Concepts in Magnetic Resonance* **7**, 49-67.

Eaton, G. R., and Eaton, S. S., (1996), EPR Imaging, *Specialist Periodical Report on Electron Spin Resonance* **15**, 169-185.

Eaton, G. R., Eaton, S. S., and Salikhov, K., eds., (1998), Foundations of Modern EPR, World Scientific Publishing, Singapore.

Eaton, G. R., and Eaton, S. S., ESR Imaging, (1999), *Handbook of Electron Spin Resonance,* C. P. Poole, Jr., and H. A. Farach, eds, vol 2, AIP Press, 327-343.

Eaton, G. R., and Eaton, S. S., (2000), EPR Imaging, *Specialist Periodical Report on Electron Spin Resonance* **17**, 109-129.

Eaton, G. R., and Eaton, S. S., (2002), EPR Imaging, in *Encyclopedia of Imaging Science and Technology,* J. P. Hornak, Editor-in-chief, Wiley, N.Y.

Eckburg J.J., Chato J.C., Liu K.J., Grinstaff M.W., Swartz H.M., Suslick K.S., Auteri F.P. (1996) The Measurement Of Temperature With Electron Paramagnetic Resonance Spectroscopy. *J. Biomech. Engineer. -Trans. ASME* **118**, 193-200.

Elas M., Williams B.B., Parasca A., Mailer C., Pelizzari C.A., Lewis M.A., Rivers J.N., Karczmar G.S., Barth E.D., Halpern H.J. (2003) Quantitative Tumor Oxymetric Images from 4D Electron Paramagnetic Resonance Imaging (EPRI), Methodology and

Comparison with Blood Oxygen Level-Dependent (BOLD) MRI. *Magn. Reson. Med.* **49**, 682-691.

Feher G. (1957) Sensitivity Considerations in Microwave Paramagnetic Resonance Absorption Techniques. *Bell Syst. Tech.* **36**, 449.

Feldman A., Wildman E., Bartolinini G., Piette L.H. (1975) In Vivo Electron Spin Resonance in Rats. *Phys. Med. Biol.* **20**, 602-12.

Foster T.H. (1992) Tissue Conductivity Modifies the Magnetic Resonance Intrinsic Signal-to- Noise Ratio at High Frequencies. *Magn. Reson. Med.* **23**, 383-385.

Foster M., Panagiotelis I., Lurie D.J. (2001) Oxygen Depletion in the Ligated Kidney- In Vivo Demonstration by RF- LODESR and FC-PEDRI. 14th Conference of the International Society of Magnetic Resonance, August 23, 2001; Rhodos, Gr.

Freed J.H. (1967) Theory of Saturation and Double Resonsnce Effects in Electron Spin Resonance Spectra. II. Exchange vs. Dipolar Mechanisms. *J. Phys. Chem.* **71**, 38-51.

Froncisz, W., and Hyde, J. S. (1982). The Loop-Gap Resonator: A New Microwave Lumped Circuit ESR Sample Structure. *J. Magn. Reson.* **47**, 515-521.

Garrett M.W. (1967) Thick Cylindrical Coil Systems for Strong Magnetic Field or Gradient Homogeneities of the 6th to 20th Order. *J. Appl. Phys.* **38**, 2563-2586.

Golay M.J.E. (1958) Field Homogenizing Coils for Nuclear Spin Resonance Instrumentation,. *Rev. Sci. Instrum.* **29**, 4.

Golman K., Petersson J.S., Ardenkjaer-Larsen J.H., Leunbach I., Wistrand L.G., Ehnholm G., Liu K. (2000) Dynamic In Vivo Oxymetry using Overhauser Enhanced MR Imaging. *J. Magn. Reson Imaging* **12**, 929-38.

Grucker D. (1990) In Vivo Detection of Injected FreeRadicals by Overhauser Effect Imaging. *Magn. Reson. Med.* **14**, 140-7.

Gutowsky H.S., Saika A. (1953) Dissociation. Chemical Exchange, and the Proton Magnetic Resonance in Some Aqueous Electrolytes. *J. Chem. Phys.* **21**, 1688-1694.

Halpern H.J., Spencer D.P., van Polen J., Bowman M.K., Massoth R.J., Nelson A.C., Dowey E.M., Teicher B.A. (1989) An Imaging Radiofrequency Electron Spin Resonance Spectrometer with High Resolution and Sensitivity for In Vivo Measurements. *Rev. Sci. Instrum.* **60**, 1040-1050.

Halpern H.J., Teicher B.A., Lin Y.J., Bowman M.K., Nguyen T.D., Spencer D.P. (1990) Selective Isotopic Labeling of a Nitroxide Spin Label to Enhance Sensitivity for T_2 Oxymetry. *J. Magn. Reson.* **90**, 40-51.

Halpern H.J., Peric M., Yu C., Bales B.L. (1993) Rapid Quantitation of Parameters from Inhomogeneously Broadened EPR Spectra. *J. Magn. Reson.* **A103**,13-22.

Halpern H.J., Yu C., Peric M., Earth E., Grdina D.J., Teicher B.A. (1994) Oxymetry Deep in Tissues with Low-Frequency Electron Paramagnetic Resonance. *Proc. Natl. Acad. Sci. USA* **91**, 13047-13051

Halpern H.J., Yu C., Barth E., Peric M., Rosen G.M. (1995) In Situ Detection, By Spin Trapping, Of Hydroxyl Radical Markers Produced From Ionizing Radiation In the Tumor Of a Living Mouse. *Proc. Natl. Acad. Sci. USA* **92**, 796-800.

Halpern H.J., Peric M., Yu C., Barth E.D., Chandramouli G.V.R., Makinen M.W., Rosen G.M. (1996) In Vivo Spin-Label Murine Pharmacodynamics Using Low-Frequency Electron Paramagnetic Resonance Imaging. *Biophys. J.* **71**,403-409.

Halpern H.J., Chandramouli G.V., Barth E.D., Yu C., Peric M., Grdina D.J., Teicher B.A. (1999) Diminished Aqueous Microviscosity of Tumors in Murine Models Measured with In Vivo Radiofrequency Electron Paramagnetic Resonance. *Cancer Res.* **59**, 5836-41.

Hayes C.E., Edelstein W.E., Schenck J.F., Mueller O.M., and Eash M. (1985) An Efficient, Highly Homogeneous Radiofrequency Coil for Whole-Body NMR Imaging at 1.5 T. *J. Magn. Reson.* **63**, 622-628.

He G., Petryakov S., Samouilov A., Chzhan M., Kuppusamy P., Zweier J.L. (2001) Development of a Resonator with Automatic Tuning and Coupling Capability to Minimize Sample Motion Noise for In Vivo EPR Spectroscopy. *J. Magn. Reson.* **149**, 218-27.

Hirata H., Walczak T., Swartz H.M. (2000) Electronically Tunable Surface-Coil-Type Resonator for L-band EPR Spectroscopy. *J. Magn. Reson.* **142**, 159-67.

Hoult D.I., Lauterbur P.C. (1979) The Sensitivity of the Zeugmatographic Experiment Involving Human Samples. *J. Magn. Reson.* **34**, 425-433.

Hyde J.S., Subczynski W.K. (1989) Spin-Label Oximetry. In: Berliner LJ, Reuben J, editors. Spin Labeling: Theory and Applications. Volume 8. New York- London: Plenum Press.

Hyde, J. S. and Froncisz, W. (1989) Loop Gap Resonators, in "Advanced EPR: Applications in Biology and Biochemistry," Hoff, A. J., ed., Elsevier, Amsterdam, pp. 277-306.

Ilangovan G., Zweier J.L., Kuppusamy P. (2000) Electrochemical preparationand EPR Studies of Lithium Phthalocyanine. Part 2: Particle Size-dependent Line Broadening by Molecular Oxygen and its Implications as an Oximetry Probe. *J. Phys. Chem. B* **104**, 9404-9410.

Ilangovan G., Zweier J.L., Kuppusamy P. (2000) Electrochemical Preparation and EPR Studies of Lithium Phthalocyanine: Evaluation of the Nucleation and Growth Mechanism and Evidence for Potential-Dependent Phase Formation. *J. Phys. Chem. B* **104**, 4047-4059.

Ilangovan G., Manivannan A., Li H., Yanagi H., Zweier J.L., Kuppusamy P. (2002) A Naphthalocyanine-based EPR Probe for Localized Measurements of Tissue Oxygenation. *Free Radio Biol Med* **32**, 139-47.

Keana J.F.W., Acarregui M.J., Boyle S.L.M. (1982) 2,2-Disubstituted-4,4-dimethyl-imidazolidinyl-3-oxy Nitroxides: Indicators of Aqueous Acidity through Variation of a_N with pH. *J. Am. Chem. Soc.* **104**, 827-830.

Khramtsov V.V., Weiner L.M., Grigoriev I.A., Volodarsky L.B. (1982) Proton Exchange in Stable Nitroxyl Radicals. EPR Study of the pH of Aqueous Solutions. *Chem. Phys. Lett.* **91**, 69-72.

Kocherginsky N., Swartz H.M. (1995) Nitroxide Spin Labels: Reactions in Biology and Chemistry. Boca Raton: CRC Press.

Komarov A., Mattson D., Jones M.M, Singh P.K., Lai C.-S. (1993) In Vivo Spin Trapping of Nitric Oxide in Mice. *Biochem. Biophys. Res. Commun.* **195**, 1191-1198.

Koptioug A.V., Edward J. Riejerse, Klaassen A.K. (1997) New Transmission-line Resonator for Pulsed EPR. *J. Magn. Reson.* **125**, 369-371.

Krishna M.C., English S., Yamada K., Yoo J., Murugesan R., Devasahayam N., Cook J.A., Golman K., Ardenkjaer-Larsen J.H., Subramanian S., Mitchell J.B. (2002) Overhauser Enhanced Magnetic Resonance Imaging for Tumor Oximetry, Coregistration of Tumor Anatomy and Tissue Oxygen Concentration. *Proc. Natl. Acad. Sci. USA* **99**, 2216-21.

Kuppusamy P., Wang P.H., Zweier J.L. (1995) Three-Dimensional Spatial EPR Imaging Of the Rat Heart. *Magn. Reson. Med.* **34**, 99-105.

Kuppusamy P., Chzhan M., Zweier J.L. (1995b) Development and optimization of three-dimensional spatial EPR imaging for biological organs and tissues. *J.Magn. Reson.* B **106**:122-30.

Kuppusamy P., Wang P.H., Chzhan M., Zweier J.L. (1997) High Resolution Electron Paramagnetic Resonanace Imaging of Biological Samples with a Single Line Paramagnetic Label. *Magn. Reson. Med.* **37**, 479-483.

Kuppusamy P., Li H., Ilangovan G., Cardounel A.J., Zweier J.L., Yamada K., Krishna M.C., Mitchell J.B. (2002) Noninvasive Imaging of Tumor Redox Status and its Modification by Tissue Glutathione Levels. *Cancer Res.* **62**, 307-312.

Lai C.S., Hopwood L.E., Hyde J.S., Lukiewicz S. (1982) ESR Studies of O2 Uptake by Chinese HamsterOvary Cells during the Cell Cycle. *Proc. Natl. Acad. Sci. USA* **79**, 1166-1170.

Lauterbur P.C., Levin D.N., Marr R.B. (1984) Theory and Simulation of NMR Spectroscopic Imaging andField Plotting by Projection Reconstruction Involving an Intrinsic Frequency Dimension. *J. Magn. Reson.* **59**, 536-41.

Leifer M.C. (1997) Resonant Modes of the Birdcage Coil. J. Magn. Reson. **124**, 51-60.

Lewitt R.M. (1983) Reconstruction Algorithms: Transform Methods. *Proc. IEEE* **71**, 390-408.

Li H., Deng Y., He G., Kuppusamy P., Lurie D.J., Zweier J.L. (2002) Proton electron double resonance imaging of the in vivo distribution and clearance of a triaryl methyl radical in mice. *Magn. Reson. Med.* **48**, 530-4.

Liu K.J., Gast P., Moussavi M., Norby S.W., Vahidi N., Walczak T., Wu M., Swartz H.M. (1993) Lithium Phthalocyanine: A Probe for Electron Paramagnetic Resonance Oximetry in Viable Biological Systems. *Proc. Natl. Acad. Sci. USA* **90**, 5438-5442.

Lurie D.J., Foster M.A., Yeung D., Hutchison J.M. (1998) Design, Construction and Use of a Large-sampleField-cycled PEDRI Imager. *Phys Med Biol* **43**, 1877-86.

Mailer C., Robinson B.H., Williams B.B., Halpern H.J. (2003) Spectral Fitting: The Extraction of Crucial Information from a Spectrum and a Spectral Image. *Magn. Reson. Med.* **49**, 1175-1180.

Maltempo M.M. (1986) Differentiation of Spectral and Spatial Components in EPR Imaging using 2-D Image Reconstruction Algorithms. *J. Magn. Reson.* **69**, 156-61.

Maltempo M.M., Eaton S.S. Eaton, G.R. (1987) Spectral-Spatial Two-Dimensional EPR Imaging, *J. Magn. Reson.* **72**, 449-455.

McConnell H.M. (1958) Reaction Rates by Nuclear Magnetic Resonance. *J. Chem. Phys.* **28**, 430-431.

Morse P.D. (1977) Use of the Spin Label Tempamine for Measuring the Internal Viscosity of Red Blood Cells. *Biochem. Biophys. Res. Commun.* **77**, 1486-1491.

Natterer F., Wübbeling F. (2001) Mathematical Methods in Image Reconstruction. Philadelphia: Society for Industrial and Applied Mathematics; p xii, 216.

Nishikawa, Fujii, Berliner. (1985) Helices and Surface Coils for Low-Field in Vivo ESR and EPR Imaging Applications. *J. Magn. Reson.* **62**, 79-86,

Nordio P.L. (1976) General Magnetic Resonance Theory. In: Berliner LJ, editor. Spin Labelling: Theory and Applications, New York: Academic Press; p 5-52.

Oikawa K., Ogata T., Lin Y., Sato T., Kudo R., Kamada H. (1995) Rapid Field Scan L-Band Electron Spin Resonance Computed Tomography System Using an Air-Core Electromagnet. *Analytical Sciences* **11**, 885-888.

Ono M., Ito K., Kawamura N., Hsieh K.C., Hirata H., Tsuchihashi N., Kamada H. (1994) A Surface-coil-type Resonator for In Vivo ESR Measurements. *J. Magn. Reson.* **104**,180-2.

Pake G., Purcell E.M. (1948) Line Shapes in Nuclear Paramagnetism. *Phys. Rev.* **74**, 1184.

Pan X. (1998) Quasi-bandlimited Properties of Radon Transforms and their Implications for Increasing Angular Sampling Densities. *IEEE Trans. Med. Imag.* **17**, 395-406.

Panagiotelis I., Nicholson I., Foster M.A., Hutchison J.M. (2001) T_{1e} and T_{2e} Maps Derived In Vivo from theRat using Longitudinally Detected Electron Spin Resonance Phase Imaging: Application to Abdominal Oxygen Mapping. *Magn. Reson. Med.* **46**, 1223-32.

Peric M., Halpern H.J. (1994) Fitting of the derivative Voigt ESR line under conditions of modulation broadening. *J. Magn. Reson.***A109**:198-202.

Pfenninger S., Froncisz W., Forrer J., Luglio J., Hyde J.S. (1995) General Method for Adjusting the Quality Factor of EPR Resonators. *Rev. Sci. Instrum.* **66**, 4857-65.

Poole C.P. (1983) Electron Spin Resonance: A Comprehensive Treatise on Experimental Techniques. 2nd edition. New York: John Wiley and Sons.

Reddy T.J., Iwama T., Halpern H.J., Rawal V.H. (2002) General Synthesis of Persistent Trityl Radicals for EPR Imaging of Biological Systems. *J. Org. Chem.* **67**, 4635-9.

Rinard, G. A., Quine, R. W., Ghim, B. T., Eaton, S. *S.* and Eaton, G. R. (1996a) Easily Tunable Crossed-Loop (Bimodal) EPR Resonator. J. *Magn. Reson.* **A122**, 50-57.

Rinard, G. A., Quine, R. W., Song, R., Eaton, G. R. and Eaton, S. S. (1999) Absolute EPR Spin Echo and Noise Intensities, *J. Magn. Reson.* **140**, 69-83

Rinard G.A., Eaton S.S., Eaton G.R., C. P. Poole J., Farach H.A. (1999a) Frequency Dependence of Electron Paramagnetic Resonance Measurements. In: Poole C, Farach H, editors. Handbook of Electron Spin Resonance. Volume 2. Springer Verlag: New York.

Rinard, G. A., Quine, R. W., and Eaton, G. R. (2000) An L-band Crossed-Loop (Bimodal) Resonator, *J. Magn. Reson.* **144**, 85-88.

Rinard G.A., Quine R.W., Eaton G.R., Eaton S.S., Barth E.D., Pelizzari C.A., Halpern H.J. (2002) Magnet and Gradient Coil System for Low-field EPR Imaging. *Magn. Reson. Engineer.* **15**, 51-58.

Rinard, G. A., Quine, R. W., Eaton, G. R. and Eaton, S. S. (2002a) 250 MHz Crossed Loop Resonator for Pulsed Electron Paramagnetic Resonance, *Magn. Reson. Engineer.* **15**, 37-46.

Rinard, G. A., Quine, R. W., Eaton, S. S., and Eaton, G. R., (2003), Frequency Dependence of EPR Sensitivity, in Biological Magnetic Resonance, L. J. Berliner, ed., in press.

Robinson B.H., Mailer C., Reese A.W. (1999) Linewidth Analysis of Spin Labels in Liquids. I. Theory and Data Analysis. *J. Magn. Reson.* **139**, 199-209.

Robitaille P.M., Kangarlu A., Abduljalil A.M. (1999) RF Penetration in Ultra High Field MRI: Challenges in Visualizing Details within the Center of the Human Brain. *J. Comput. Assist. Tomogr.* **23**, 845-9.

Robitaille P.-M.L., Warner R., Jagadeesh J., Abduljaili A.M., Kangarlu A., Burgess R.E., Yu Y., Yang L., Zhu H., Jiang Z., Bailey R.E., Chung W., Somawiharja Y., Feynan P., Rayner D.L. (1999a) Design and Assembly of an 8 Tesla Whole-Body MR Scanner. *J. Comput. Assist. Tomogr.* **23**, 808-820.

Romeo F., Hoult D.I. (1984) Magnet Field Profiling: Analysis and Correcting Coil Design. *Magn. Reson. Med.* **1**, 44.

Roschmann P. (1987) Radiofrequency Penetration and Absorption in theHuman Body: Limitations to High-field Whole-body Nuclear Magnetic Resonance Imaging. *Med. Phys.* **14**, 922-931.

Schwan H.P., Foster K.R. (1980) RF-field Interactions with Biological Systems: Electrical Properties and Biophysical Mechanisms. *Proceedings ofthe IEEE* **68**, 104-113.

Smirnov A.I., Norby S.W., Clarkson R.B., Walczak T., Swartz H.M. (1993) Simultaneous Multi-site EPR Spectroscopy In Vivo. *Magn. Reson. Med.* **30**, 213-220.

Smirnov, A.I., Belford R. L. (1995) Rapid quantitation from inhomogeneously broadened EPR spectra. *J. Magn. Reson.* **113**, 67-73.

Sotgiu A. (1985) Resonator Design for In Vivo ESR Spectroscopy. *J. Magn. Reson.* **65**, 206-214.

Subramanian V., Mailer C., Ichikawa K., Barth E., Williams B.B., Halpern H.J. (2002) Fixed-frequency Operation of a Low Frequency Continuous Wave EPR Imaging Spectrometer. N Abstracts for 44th Rocky Mountian Conference on Analytical Chemistry. Denver, CO.

Utsumi H., Muto E., Masuda S., Hamada A. (1990) In Vivo ESR Measurement of Free Radicals in Whole Mice. *Biochem, Biophys. Res. Commun.* **172**, 1342-1348.

Vahidi N., Clarkson R.B., Liu K.J., Norby S.W., Wu M., Swartz H.M. (1994) In Vivo and In Vitro EPR Oximetry with Fusinite: A New Coal-derived, Particulate EPR Probe. *Magn. Reson. Med.* **31**, 139-46.

Velan S.S., Spencer R.G., Zweier J.L., Kuppusamy P. (2000) Electron Paramagnetic Resonance Oxygen Mapping (EPROM), Direct Visualization of Oxygen Concentration in Tissue. *Magn. Reson. Med.* **43**, 804-9.

Weiss G.H., Talbert A.J., Brooks R.A. (1982) The Use of Phantom Views to Reduce CT Streaks due to Insufficient Angular Sampling. *Phys. Med. and Biol* **27**, 1151-1162.

Williams B.B., Barth E., Mailer C., Halpern H.J. (2001) Practical Considerations for Fast CW EPRI. 9th International Meeting on EPR Studies in Viable Systems, Hanover, NH.

Williams B.B., al Hallaq H., Chandramouli G.V., Barth E.D., Rivers J.N., Lewis M., Galtsev V.E., Karczmar G.S., Halpern H.J. (2002) Imaging Spin Probe Distribution in the Tumor of a Living Mouse with 250 MHz EPR: Correlation with BOLD MRI. *Magn. Reson. Med* **247**, 634-8.

Wood, R. L., Froncisz, W., and Hyde, J. S. (1984) The Loop-Gap Resonator. II. Controlled Return Flux Three-Loop, Two-Gap Microwave Resonators for ENDOR and ESR Spectroscopy. *J. Magn. Reson.* **58**, 243-253.

Yokoyama H., Sato T., Ogata T., Ohya-Nishiguchi H., Kamada H. (1997) In Vivo Longitudinally Detected ESR Measurements at Microwave Regions of 300, 700, and 900 MHz in Rats Treated with a Nitroxide Radical. *J. Magn. Reson.* **129**, 201-6.

Yong L., Harbridge J., Quine R.W., Rinard G.A., Eaton S.S., Eaton G.R., Mailer C., Barth E., Halpern H.J. (2001) Electron Spin Relaxation of Triarylmethyl Radicals in Fluid Solution. *J. Magn. Reson.* **152**, 156-61.

Yoshimura T., Fujii S., Yokoyama H., and Kamada H. (1995) In Vivo Electron Paramagnetic Resonance Imaging of NO-Bound Iron Complex in a Rat Head. *Chem. Lett.* 309-310.

Zavoisky E. (1945) Spin-Magnetic Resonance in Paramagnets. *Journal of Physics* **9**, 245.

Zweier J.L., Chzhan M., Ewert U., Schneider G., Kuppusamy P. (1994) Development Of a Highly Sensitive Probe For Measuring Oxygen In Biological Tissues. *J. Magn. Reson.* **B105**, 52-57.

Zweier J.L., Chzhan M., Wang P.H., Kuppusamy P. (1996) Spatial and Spectral-Spatial EPR Imaging Of Free Radicals and Oxygen In the Heart. *Res. Chem. Intermed.* **22**, 615-624.

Zweier J.L., Chzhan M., Samouilov A., Kuppusamy P. (1998) Electron Paramagnetic Resonance Imaging of the Rat Heart. *Phys. Med. Biol.* **43**, 1823-35.

Chapter 12

Time-Domain Radio Frequency EPR Imaging

Sankaran Subramanian and Murali C. Krishna
Radiation Biology Branch, Center for Cancer Research, National Cancer Institute, National Institutes of Health, Bethesda, MD, USA

Abstract: A brief introduction to magnetic resonance and imaging is followed by a discussion of the challenges of performing low-frequency (ca. 300 MHz) pulsed EPR. The 300 MHz parallel coil resonator and the data acquisition system used in the authors' spectrometer is described in detail, as are mathematical techniques of image reconstruction. 3D oxymetric images of mice were obtained using pulsed FID detection of T_2^* of triarylmethyl radicals injected into the mice. Single-point imaging, a technique developed for solid-state NMR, applied to pulsed EPR imaging yields artifact-free spatial images.

1. INTRODUCTION

The phenomena of nuclear magnetic resonance (NMR) and electron spin resonance (ESR), also known as electron paramagnetic resonance (EPR), were discovered more or less at the same time, the former simultaneously by two groups, Bloch and Purcell and co-workers (Bloch *et al.,* 1946; Purcell *et al.,* 1946), while the latter was discovered by Zavoisky (Zavoisky, 1945). Both phenomena are based on the intrinsic magnetic moment of the entities involved, the magnetic nucleus in NMR and the unpaired electron in EPR. The development of the two techniques took off at great speeds, NMR much more rapidly, mainly because of the Fourier transform methodology (Lowe and Norberg, 1957; Ernst and Anderson, 1966) and today it is considered most indispensable in areas of nuclear and solid sate physics, magnetic materials, analytical chemistry, structural and molecular biology and, more recently, micro imaging, diagnostic radiology and functional imaging (Field *et al.,* 1989; Gadian, 1995; Moonen *et al.,* 1999; Wuthrich, 1995).

Developments in the field of time-domain EPR, on the other hand, have been relatively slow compared to the rapid strides made in NMR mainly because of the very short spin relaxation times of the ensemble of unpaired electrons and the requirements of very special electronic components and devices that are required to parallel the advances in NMR. In this chapter we very briefly outline the development of the EPR technique from its early days where the frequency of measurement was confined to the microwave (MW) region of the electromagnetic spectrum to the present day applications in the radio frequency (RF) region (Kevan and Bowman, 1990).

In this Chapter, we review, albeit very briefly, the salient features of EPR spectroscopy with an emphasis on the time-domain applications of EPR in biological spectroscopy and imaging. This chapter is written with a view to address the following: the basic principles of EPR, historic perspectives of the development of EPR instrumentation, time-domain methods and the reason for lowering of frequency to RF regime, alternate methods of spatial encoding in EPR imaging, extraction of spectral information from *in vivo* image data for the purpose of adding a functional dimension to EPR imaging, etc. The motivation is to perform fast, quantitative, non-invasive, oxymetric imaging and to assess redox status of tissue in pathophysiological conditions. We have taken a pedagogical approach in writing this article in that we address mainly the young scientists and not so much the experts in the field. Finally we conclude the chapter with some of our recent results covering the applications of *in vivo* RF time-domain EPR to physiologic and functional imaging and possible future directions.

Functional or physiological imaging techniques in biomedical research are receiving increased attention. Such techniques, coupled with anatomical imaging methods strengthen diagnostic radiology used to detect disease states and characterize them physiologically on the basis of tissue redox status or oxygenation level, and thus guide effective therapies. Non-invasive radiological techniques such as FMRI, including BOLD-MRI (Blood Oxygen Level Dependent MRI) (Bandettini *et al.,* 1992; Kwong et al., 1992; Fowler *et al.,* 1999; Ogawa *et al.,* 1992; Moonen *et al.,* 1999) are being evaluated towards these goals. Next to X-ray, CT and ultrasound, MRI has become the most widely used radiological technique in the clinic. MRI which uses the protons in water and tissue of the animal as the spin probe for imaging is a very sensitive and expedient technique for imaging. The abundance of water in living tissue is such that one is dealing with several tens of moles in concentration and, incidentally, the nucleus of the hydrogen atom has the highest magnetic moment of all the nuclei. With the advent of time-domain NMR techniques, slice selection with shaped pulses, spatial encoding by pulsed field gradients and using gradient echo detection and Fourier transform methods, today one can generate highly resolved images of human anatomy in

almost real time. In addition to simply imaging anatomical details, additional contrast in the images using the relaxation times T_1 and T_2 leads to clearly delineated images of organs with specific pathological conditions. With BOLD-MRI, brain function has been successfully probed and has initiated the widely practiced field of fMRI (Ogawa *et al.,* 1992).

Recently there has been a novel imaging modality very similar to MRI known by two alternate names, PEDRI (Proton Electron Double Resonance Imaging) (Lurie *et al.,* 1988, 1989) or OMRI (Overhauser enhanced Magnetic Resonance Imaging) (Golman *et al.,* 1998) which utilizes the Overhauser effect by which protons are polarized in the presence of free radicals to provide sensitivity enhanced images. In the presence of a saturating EPR field the dipolar coupling between the electron and proton enhances the polarization of the latter which should theoretically be 329 times (gyromagnetic ratio of the electron (γ_e) / gyromagnetic ratio of the proton $(\gamma_p) = -658$) that of the natural polarization and of opposite sign, in a given magnetic field. A detailed treatment of this topic, however, is beyond the scope of this chapter. Suffice it to say that this technique has been shown to produce extremely interesting functional proton images (in essence, the unpaired electron distribution is indirectly imaged via the dipolar coupled protons) at fields that are two to three orders of magnitude less compared to MRI fields. Since the electronic magnetic moment is 658 times higher than of the proton one needs fields on the order of only 10 mT to produce images with good SNR (signal-to-noise ratio). At this field the electron resonance frequency is 300 MHz and that of protons is around 0.5 MHz corresponding to low field MRI. At fields used for OMRI/PEDRI the normal (unenhanced) MRI will hardly produce any image of significance, although poor outlines of anatomy may just be barely visible. However, the Overhauser enhancement in PEDRI/OMRI produces images of extremely good quality and resolution (Golman *et al.,* 2000).

It is therefore a natural to ask, "why not use EPR directly to perform *in vivo* imaging of free radicals?" Because of the very low concentrations and extremely short life times of the endogenous free radicals it is not practical to image these species directly. Therefore, to perform any EPR imaging in living systems, it is necessary to exogenously introduce a free radical probe into the animal (intraperitonially or intravenously) just as in positron emission tomography, PET (Von Schulthess, 2000). However, since EPR detects the free radicals directly and the spectral properties of the spin probe, when suitably designed, could report indirectly on physiology, it is possible to develop detection and imaging strategies in EPR where, at low levels of the spin probe, high-resolution EPR images can be obtained, which contain important physiologic information as well.

Currently several groups are developing *in vivo* EPR spectroscopy and imaging methods (Alecci *et al.,* 1992; Halpern *et al.,* 1989; Halpern *et al.,*

1994; Kuppusamy *et al.,* 1994; Liu *et al.,* 1993; Quine *et al.,* 2002; Utsumi *et al.,* 1993). Also see ch 9 and 11 in this volume. Because of the relatively large line widths of most spin probes used in EPR, continuous wave (CW) methods were preferred for data acquisition with a field sweep modality to utilize the inherent advantages low frequency modulation involving a lock-in amplifier and phase sensitive detection. Such studies have provided valuable information on the pO_2 (partial pressure of oxygen) levels in tumors (Ohara *et al.,* 1995). CW L-band imaging studies have also provided information on cardiac ischemia and tumors (Kuppusamy *et al.,* 1998; Zweier *et al.,* 1995). However, because of the relatively longer times taken for spectral data acquisition, imaging times are long (several minutes to hours depending on the dimensionality of the image), often requiring continuous infusion of the spin probe, to offset for metabolic and pharmacokinetic elimination of the probe from the system. During the imaging of live animals, the peristalsis and breathing motion disturbs the automatic frequency control (AFC) via fluctuations in the coupling between the transmitter and resonator. One needs to employ appropriate gating techniques (Kuppusamy *et al.,* 1996) as well as automatic coupling control circuits (Brivati *et al.,* 1991; Hirata *et al.,* 1997) to minimize artifacts associated with object motion during imaging experiments. A comprehensive summary of the state-of-the-art of EPR imaging and *in vivo* EPR practices up to 1990 has been published by Eaton *et al.* (1991).

With the recent availability of single line paramagnetic spin probes based on the triarylmethyl radical (Ardenkjaer-Larsen *et al.,* 1998) which are non-toxic, bio-compatible, water-soluble and are infusible (can be intravenously or intramuscularly injected into animals), time-domain EPR imaging is emerging as a potentially useful technique complementary to the other imaging modalities to obtain information such as tissue redox status (Kuppusamy *et al.,* 2002) as well as *in vivo* oxygenation level. Radio frequency (RF) EPR imaging systems operating in time-domain have been reported by us and others recently (Afeworki *et al.,* 2000; Alecci *et al.,* 1998a;1998b; Bourg *et al.,* 1993; Krishna *et al.,* 1999; Murugesan *et al.,* 1998; Subramanian *et al.,* 1999; 2002), employing narrow excitation pulses (50-100 ns) and capturing the transient responses or the free induction decay (FID) signals which last typically for 1-3 μs. In addition to minimal artifacts associated with object motion, advantages of time-domain EPR include potentially short imaging times as well. Unlike MRI, EPRI produces images, just as in PET, of only regions where the free radical spin probe is perfusing through the vasculature. We describe in the following, the basic principles of EPR imaging, CW and FT methods and their relative merits, the challenges involved in performing FT EPR at low frequencies, issues related to instrumentation and applications in small animal imaging. There is considerable promise that in the future, *in*

vivo EPRI will turn out to be an important functional imaging tool and be a very useful adjunct to PET, CT, MRI and other imaging modalities.

2. TIME-DOMAIN EPR

2.1 Fundamental Considerations

The unpaired electron, which is present in stable free radicals, transition metal and rare-earth complexes with partially filled d- and f-shells, and in radiation induced defect centers in solids, by virtue of its charge, spin and orbital angular momentum possesses a magnetic moment. For an ensemble of *free* electrons without any orbital angular momentum, the magnetic moment μ is proportional to spin angular momentum given by

$$\mu \propto (eh/4\pi mc)\,\mathbf{S} \qquad (1)$$

where, m is the mass of the electron, c the velocity of light, h the Planck's constant and **S** the spin angular momentum quantum number. The proportionality constant is called the gyromagnetic ratio of the electron or its g-factor and for a free electron it has a value of 2.002316. The factor $(eh/4\pi mc)$ is the Bohr magneton and is given the symbol β. With this, the magnetic moment μ becomes

$$\mu = g\,\beta\,S \qquad (2)$$

For free electrons S = 1/2, and in a magnetic field the electron spin vector, being a quantized entity, can take up one of two "allowed" orientations corresponding to the z-components of the angular momentum, $S_Z = \pm 1/2$. The equation of motion of the torque **T** felt by the spinning magnetic moment vector μ vector in a static magnetic field $\mathbf{B_0}$ is given by

$$\mathbf{T} = -\,\mu \times \mathbf{B_0} \qquad (3)$$

This is completely analogous to the torque experienced by a spinning top under the gravitational pull which makes the top gyrate about the gravitational axis. The torque makes the magnetic vectors precess about the magnetic field with an angular frequency ω_0 known as the Larmor frequency. The scalar potential energy corresponding to the torque is given by

$$E = -\,\mu \cdot \mathbf{B_0} \qquad (4)$$

In the magnetic field, therefore two energy levels are created with a separation given by

$$E = \pm (1/2) g\beta B_0 \qquad \Delta E = g\beta B \qquad (5)$$

Where, ΔE is known as the Zeeman splitting. The lower of the two levels is more populated as per Boltzmann statistics so that there is a net population difference between the two levels endowing the unpaired electron system with a net magnetization χB_o proportional to the strength of the field, the proportionality constant being the Curie susceptibility χ, with

$$\chi = Ng^2\beta^2 S(S+1)/3kT \qquad (6)$$

where, N is the total number of spins, k is the Boltzmann constant and T, the absolute temperature. Fig.1 is an illustrative summary of the Zeeman splitting and Larmor precession. In the absence of any external perturbation, the magnetic vectors corresponding to the net magnetization (the excess population in the lower level times the magnetic moment per electron) execute a precession with random phase (more or less uniformly distributed about the static field) so that for an ensemble of spins the vector sum of the magnetization in the transverse plane (M_{xy}) is zero, whereas there is a net total z-component of magnetization, M_z. It is this non-vanishing equilibrium z-component, known as the Zeeman polarization (or Zeeman order or Zeeman coherence) that gives us a handle to perform the resonance experiments.

In order to measure the net magnetization and its precessional frequency it is imperative to supply a circularly polarized electromagnetic radiation of the correct polarization and a circular frequency matching with the Larmor frequency which can then exchange energy with the system of spins trying to equalize the population in the two levels. What is happening phenomenologically, of course, is that when the frequency of the electromagnetic radiation matches, with the Larmor frequency (hence the name "resonance"), the net macroscopic magnetization experiences a torque that tilts it away from the Zeeman axis and can thus induce a Faraday induction current in a coil at right angles to the static field. In other words, we measure the AC susceptibility in resonance experiments corresponding to circularly polarized net magnetization, which is proportional to the total spin concentration and the strength of the field. The resonance condition is given by

$$\Delta E = (h/2\pi)\omega_0 = h\nu = g\beta B_0 \qquad (7)$$

where, ω_o is the Larmor frequency.

Once the magnetization is disturbed from its equilibrium value, there are two important relaxation processes, both of which follow first order kinetics, that restore the system back to the steady state situation. The first one is related to the magnetization in the plane transverse to the Zeeman axis. The ensemble of spins experiences a finite distribution of Larmor frequencies due to internal fluctuation and magnetic dipolar and exchange interactions, apart from any inhomogeneity in the Zeeman field. Therefore, any transverse

components of the spin magnetization vectors once created, get very soon randomized in distribution. This leads to a net zero magnetization under equilibrium condition in the plane perpendicular to the DC field. Any non-equilibrium situation created by resonance absorption, such as sudden switching on or off of the static field, etc. causes a change in the magnetization components. From a non-equilibrium situation, the transverse components always return to their equilibrium null value via the energy-conserving spin-spin relaxation process, T_2 (also known as transverse relaxation time or phase memory time) which is a measure of the spread in the Larmor frequency, either because of inherent internal isotropic interactions leading to homogeneous broadening, or due to anisotropic magnetic interactions modulated by motion as well as implicit inhomogeneity in the Zeeman field leading to inhomogeneous broadening.

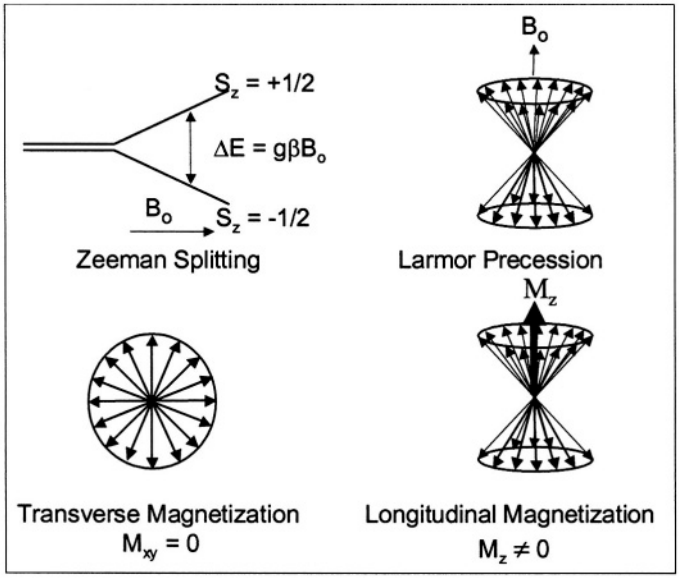

Figure 1. Schematic representation of the Zeeman splitting and Larmor precession for an ensemble of unpaired electrons placed in a DC magnetic field. To a first order approximation, the Zeeman splitting between the two levels arising out of the ensemble of 'free' electrons increases linearly with the magnitude of the DC field B_0. The spin vectors corresponding to the two 'allowed' orientations precess about the +Z and -Z axes at the Larmor frequency, but are randomly, almost uniformly, distributed over the surface of a cone with axis parallel and anti parallel to the Zeeman axis. The two figures in the bottom show that the vector sum in the transverse plane, $M_{xy} = 0$, while that along the Zeeman axis, M_z, is finite.

In other words, magnetization created in the transverse direction via energy intake, will always decay with a characteristic time constant T_2. The transverse relaxation time derived from the FID, known as T_2^*, is always

shorter than the true T_2 due to the presence of any static field inhomogeneity as well as presence of field gradients applied for the imaging *(vide infra).* The relaxation time T_2 (or T_2^*) is directly related to the measured width of the resonance absorption (Full width at half maximum height, FWHM of the spectrum), larger line width in the frequency/field domain corresponding to shorter T_2 in the time-domain. (In systems where the EPR lines are broadened by unresolved hyperfine components, there is no direct relation ship between the measured relaxation time and the observed line width). Any change from the equilibrium Zeeman magnetization will also be restored by a second relaxation process called spin lattice relaxation (or longitudinal relaxation), T_1. Here the system will have to exchange energy with the surroundings (in an energy *non*-conserving process) to reach the equilibrium Zeeman magnetization (also known as Curie susceptibility). The relaxation processes and their measurements can be best addressed by time-domain experiments and are dealt extensively in the literature (Eaton and Eaton, 2000; Farrar and Becker, 1971).

Whereas we have considered 'spin-only' systems, most organic and inorganic radicals, transition metal complexes and other metal-based paramagnetic molecules have unpaired electrons with finite orbital angular momentum and hence the magnetic moment and the g-factor become highly anisotropic and the Zeeman Hamiltonian is characterized by a g-tensor (symmetric second rank tensor). Besides the g-anisotropy, the unpaired electron, depending upon the presence of magnetic nuclei in the molecule may be further subject to hyperfine and super hyperfine splitting that can generate additional isotropic and anisotropic fine structure in the EPR spectra. An interacting magnetic nucleus with spin I will, to a first order approximation, give (2I+1) equally spaced hyperfine lines in the EPR spectrum. Such multi-line paramagnetic systems are not desirable for *in vivo* imaging applications, since any attempt to frequency encode the spatial distribution will be complicated by overlapping and redundant information which will involve additional deconvolutions to remove the hyperfine effects before the image reconstruction (Ewert and Herrling, 1986). There are excellent monographs (see for example, (Weil *et al.,* 1994)) describing the analysis of g-tensor, hyperfine tensor and quadrupolar effects, etc., and these are beyond the scope of the present article.

2.2 Optimum Frequency for In Vivo EPR Imaging

EPR spectroscopy can be performed at any frequency as long as the resonance condition of equation (7) is satisfied. As a rough approximation to understand the frequency dependence of sensitivity, without consideration of spectrometer or sample characteristics, (Abragam, 1961) we reasoned that

Boltzmann polarization (which depends on the resonance frequency) and the quantum mechanical transition probability, which would be proportional to the square of the resonance frequency at a given RF power, (Alecci *et al.,* 1991) yield a dependence of sensitivity on $\omega^2(1\text{-}\exp(\Delta E/kT)$. Taking all the parameters in frequency units, when the sensitivity was evaluated over the range of 100 MHz to 35 GHz at 300K, the result fits reasonably well to a $\omega^{5/2}$ curve. The penetration of electromagnetic radiation in biological specimens, on the other hand, decreases proportional to the inverse of the frequency. The electromagnetic skin depth δ which is the depth at which the flux density of the incident electromagnetic radiation decreases to 1/e (0.368) of its value just at the boundary is related to (a) the frequency ω, (b) the dielectric permittivity ε, (c) magnetic permittivity μ and (d) the ratio of conduction current to displacement current p. It is given by (Griffiths, 1989; Polk and Postow, 1996),

$$\delta = \omega^{-1} [\frac{\mu\varepsilon}{2}(\sqrt{1+p^2} - 1)]^{-1/2} \quad (8)$$

The actual skin depth at which the attenuation is 50% is given by $0.693\ \delta$. Most of the parameters in the above equation themselves are frequency dependent. Further, the various anatomical constituents such as tissue, nerves, fat, blood, liver, bone matter, brain etc. have widely differing dielectric and magnetic permittivities. This allows *only an approximate* quantification of the skin depth. It is, therefore, difficult to get a simple analytical expression in terms of penetration vs. frequency for a heterogeneous biomass. Table I gives the approximate skin depth, δ as a function of frequency in muscle tissue (Polk and Postow, 1996) and these values are used in the plot of Fig.2. It is therefore important to arrive at an optimum frequency for *in vivo* spectroscopy and imaging experiments (Halpern and Bowman, 1991). Frequencies above 300 MHz have skin depth below 5-6 cm radially and as such will not be practically useful in *in vivo* applications, except in the case of small animals such as mice. When the frequency is brought down to ranges below 300 MHz, we are approaching the NMR realm thereby bringing the sensitivity of EPR to such low levels as to mandate signal averaging modality, especially when resorting to the time- domain techniques. It is quite evident that sensitivity of EPR is superior at MW frequencies compared to RF range, although the penetration at such frequencies cannot handle useful dimensions of even small living systems. However, the predicted low sensitivity as we lower the frequency is, fortunately, offset for the better by the larger filling factors aided by the increased resonator volume and by the increased penetration. The reader is referred to the articles by Rinard *et al.* (2002a, 1999a; 1999b; 1999c) for a more thorough and quantitative account of the dependence of EPR sensitivity on the resonator and sample.

Table 1. Electromagnetic skin depth as a function of frequency for muscle tissue(from Eqn. (8) and the parameters for muscle tissue given in (Polk and Postow, 1996), pages 12, 88-89).

Frequency (MHz)	Approx. skin depth (δ)
1	80 cm
10	25 cm
100	8 cm
1000	0.5 cm
100000	< 0.1 cm

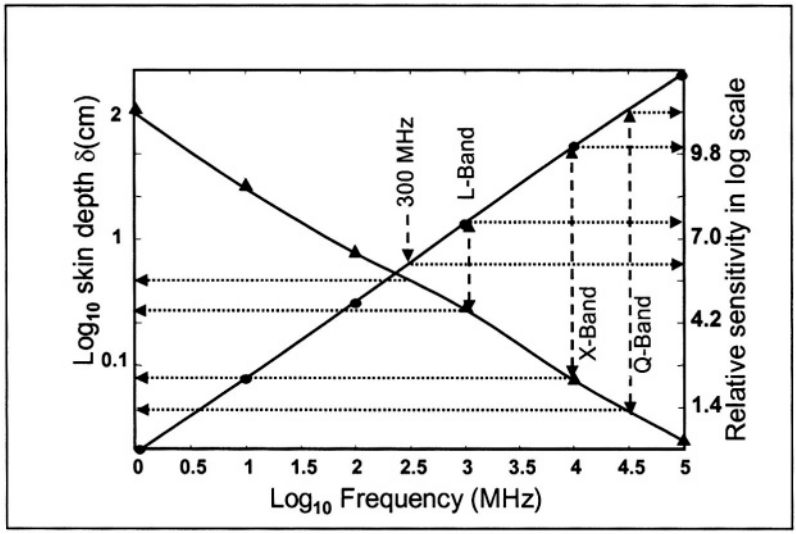

Figure 2. Semi-quantitative plot of relative sensitivity of magnetic resonance detection and penetration skin depth (δ) in muscle tissue as a function of the frequency of electromagnetic radiation. Note that the y-axes on both sides and the x-axis are in the log scale. It should be noted that the relative sensitivity is based on a $(\text{frequency})^{2.5}$ dependence. The filling factor, quality factor (Q), and spectrometer gain factors, the nature of the matched filters, etc., are assumed identical. The lossiness due to the skin depth is not taken into account in estimating the sensitivity. While X-band and Q-band frequencies are characterized by very high sensitivity, the penetration is extremely low. The figure indicates that frequencies in the range 200-300 MHz will correspond to an optimal compromise between penetration and sensitivity. It should also be noted that different anatomical constituents have very different skin depth profiles.

Eaton *et al.* (1998) and Rinard *et al.* (1999c, 2004) derived the following predictions (Table 2) of frequency dependence of EPR sensitivity. Some of the predictions were experimentally confirmed for the case of resonator resistance dominating the noise, between 250 MHz and 9.2 GHz. (Rinard *et al.,* 2002a) The general experience in MRI is that sensitivity increases approximately

linearly with increase in frequency when other variables are taken into account.

Table 2 EPR S/N at constant B_1

	Case 1 (const. Sample size, const. LGR size)	Case 2 (sample Size $\propto 1/\omega$ LGR size $\propto 1/\omega$)	Case 3 (const. sample Size, LGR size $\propto 1/\omega$)
When resonator resistance dominates	$\omega^{7/4}$	$\omega^{-1/4}$	$\omega^{11/4}$
When sample loss dominates	$\omega^{1/2}$	$\omega^{1/2}\rho^{1/2}$	$\omega\,\rho^{1/2}$
When sample Loss dominates and assuming $\rho \propto \omega^{-0.4}$	$\omega^{0.8}$	$\omega^{0.3}$	$\omega^{0.8}$

ρ is the resistivity of the tissue. Based on the data of Johnson and Guy (Johnson and Guy, 1972) the resistivity varies approximately as $\omega^{-0.4}$ from 40 to 200 MHz.

2.3 CW Versus Time-domain EPR

In the early years following the discovery, both NMR and EPR started off as continuous wave (CW) techniques and the early instruments used a field or frequency sweep modality to satisfy the resonance condition. Almost all EPR work prior to 1970 was exclusively carried out using CW X-band (9 GHz) spectrometers and extensive spectroscopic data are available in the literature on the EPR of organic free radicals, transition metal complexes, lanthanides, radiation damage in inorganic/organic solids, photochemical, electrochemical and enzymatic redox processes involving odd electron transfer, etc. In the conventional CW EPR, one uses a monochromatic radiation, usually in the MW region of the electromagnetic spectrum, and the resonance condition, which corresponds to the absorption of a precise quantum of circularly polarized radiation energy that matches with the Larmor frequency, is achieved by a slow sweep of the magnetic field. In the CW detection scheme (Poole, 1997), a microwave or RF bridge circuit which acts as a precision reflectometer, is employed with one arm connected to the incident MW source, and a second arm connected to a resonant cavity of appropriate dimensions, matched and tuned to the transmitter frequency with a high Quality factor *(vide infra).* Under critical coupling conditions, when two of the MW bridge ports, one connected to the resonant cavity via a 50Ω transmission line and the other to a reference port are exactly matched in impedance, there will be no energy transmission from the RF source to the signal detection port. Any mismatch produced by energy absorption brought about by resonance

condition will produce a signal in the receiver port, which is proportional to differences in the return losses and the input power. In order to increase the sensitivity of detection the DC field is subjected to a low frequency modulation and the modulated output signals are detected in a phase-sensitive manner and amplified using a lock-in amplifier. Because the bridge circuit uses the imbalances produced by absorption of very low quantity of energy, it is imperative that the input frequency should be very stable, and a feed back automatic frequency control (AFC) circuit and an optional automatic coupling control circuit (ACC) preserve the frequency of the incident radiation unaltered during the passage through resonance, apart from correcting for any thermal drifts in the circuitry and, when dealing with live animals, also tend to correct frequency changes in the resonator due to the animal motion. While CW methods have been in vogue for several decades mostly in the MW region (Q-band (35 GHz), L-band (1-2 GHz) especially relevant for biological studies, S-band (3-4 GHz), K-Band (18-26 GHz), W band (90-95 GHz), etc.), the application of EPR spectroscopy to live objects and biospecimens has necessitated the reduction of the measurement frequency to the radio frequency regime for reasons mentioned in the previous section. Recently several papers have appeared in the *in vivo* study of biological specimens at CW L-band. With CW EPR imaging at these low frequencies, it has been possible to probe paramagnetic species with large line widths (1-5 G) and multiple lines. In CW EPR imaging experiments using these probes, spatial as well as spectroscopic images have been obtained and physiological status could be derived non-invasively (Alecci *et al.,* 1994; Fujii and Berliner, 1985; Halpern *et al.,* 1989; Halpern *et al.,* 1996; Kuppusamy *et al.,* 1994; Liu *et al.,* 1997; Utsumi *et al.,* 1993).

In the late sixties, following Lowe and Norberg (Lowe and Norberg, 1957), Ernst and Anderson (Ernst and Anderson, 1966) introduced an epoch making development in the field of NMR when they showed that an impulse excitation of the spin system corresponds to a multichannel (broadband) excitation and the resulting response when acquired in the time-domain corresponds to a multichannel detection capturing in a 'single shot' all the information (the frequencies, amplitudes, and phases) of the spectral components. A fast Fourier transform (FT) of the impulse response (the so-called free induction decay, FID) leads to a spectrum that would be identical to the slow passage frequency swept spectrum. The advantage of the time-domain technique is that, complete spectral information can be gathered in times two to three orders of magnitude less than the corresponding frequency swept experiment. This means that several hundred spectra can be coherently added to improve the SNR, thereby making it possible to detect very low spin concentrations, and magnetic nuclei from isotopes of very low natural abundance (See for example, (Ernst, 1966)). But for the FT method, ^{13}C NMR

spectroscopy in natural abundance would not be practical. Almost all modern commercial high-resolution NMR spectrometers operate in the time-domain mode, because of the sensitivity advantage brought about by the FT method.

Whereas CW methods have proven very useful in the *in vivo* EPR study of small animals, only recently there have been attempts to perform time-domain measurements at radio frequencies (Afeworki *et al.,* 2000; Alecci *et al.,* 1998b; Devasahayam *et al.,* 2000; Murugesan *et al.,* 1998; 1997; Placidi *et al.,* 1998; Quine *et al.,* 2002; Subramanian *et al.,* 1999). The importance of time-domain methods stems from the hope that any reduction in the SNR that one encounters due to lowering the frequency may perhaps be offset by time averaging techniques well known in FT-NMR spectroscopy. Unlike in NMR or MRI where time-domain techniques have been established well over three decades, development of low frequency time-domain EPR was slower to happen. The main reason for this is that the characteristic time constants of spin dynamics of unpaired electrons that play a major role in EPR spectroscopy and imaging, namely, the spin-lattice and spin-spin relaxation times *(vide supra),* in most common stable radicals such as the nitroxides, are less than a μs, requiring electronic devices such as pulse generators, acquisition devices, RF gates, etc., that operate in the sub-microsecond regime, and these have become available commercially only recently. In the following we describe the challenges that FT EPR spectroscopy and imaging pose and how these can be overcome to some extent to produce spectra and images from live objects that may find use in our understanding of such phenomena as vascular perfusion of spin probes, effect of *in vivo* pO_2, the redox status of tissues and other metabolic effects of redox active free radicals, *in vivo,* etc. In the following we outline the requirements for a low frequency time-domain EPR spectrometer in terms of the design of optimal resonators, development of ultra short RF pulses with rise/fall times on the order of a few ns, good transmitter/receiver isolation, preamplifiers with fast recovery times, fast acquisition, rapid averaging of time-domain responses, and finally the reconstruction of 2-D and 3-D images from phantoms and mice *in vivo* using specially developed spin probes.

2.4 Imaging Principles

Around the early nineteen seventies, Lauterbur (Lauterbur, 1973) showed that it is possible to encode the spatial distribution of proton spin distribution in biological objects by measuring the spectrum in presence of linear magnetic field gradients. By collecting the projection of spin distribution in one, two or three dimensions in presence of static linear vector gradients, it is possible to reconstruct the image in as many dimensions using the filtered back-projection technique (see section IV) that is common to X-ray, ultrasound, CT, and PET.

The gradients are applied in polar coordinates, and the resulting projections are then back-projected to generate image information in a Cartesian axis system. Early nuclear magnetic resonance imaging experiments were carried out using this method. However, since the relaxation time T_2 (phase memory time) of protons in living systems can be quite long, Kumar et al. (Kumar *et al.,* 1975) came up with a method of Fourier reconstruction by which frequency encoding of the spatial distribution can be carried out *during* the transverse evolution of the spin magnetization by the application of orthogonal Cartesian set of gradients which are incremented in time steps to generate the so-called k-space information which by consecutive orthogonal Fourier transformation produces the image. This was later modified by incorporating a phase encoding step in one or two Cartesian axes by applying linear gradients for a fixed time and systematically incrementing the gradient magnitude that imparts phase differences to magnetization vectors depending on their coordinate location (Edelstein *et al.,* 1980). The resulting time-domain data can be successively Fourier transformed to produce an image of the spin density distribution. There are numerous methods of image data collection in MRI (Haacke *et al.,* 1999) all of which involve a combination of phase and frequency encoding gradients that are applied in a pulsed manner *during* the evolution of transverse spin magnetization followed by Fourier reconstruction. Using specially tailored pulse sequences it is possible to impart quantitative contrast in *in vivo* proton images based on either transverse or longitudinal relaxation times T_1 and T_2 which can then be interpreted in terms of specific pathology (for example tumor versus normal tissue). The relatively long relaxation time of the proton nucleus allows even a selection of a thin slice from the imaging object in presence of a gradient and frequency selective 'soft' pulse prior to spatial encoding, enabling very high spatial resolution.

Even with the current technology, it will not be possible to apply pulsed field gradients for spatial encoding in EPR imaging of biospecimens employing spin probes such as TAM. This is because the gradient switching times are at least on the order of milliseconds whereas the relaxation times in trityl radicals, for example, are in the microseconds range and the transverse magnetization would have decayed before the switching operation is completed. The imaging modality would therefore be based on volume excitations in presence of suitable constant vector gradients and then performing two or three-dimensional filtered back projections *(vide infra)* to synthesize the image. In the absence of imaging gradients, for a typical narrow-line EPR probe such as those derived from TAM radicals with T_2^* of approximately in the range 400 - 600 ns, the FIDs last just for 2000 to 3000 ns (approx. 5 T_2^*) before decaying to noise level. Under imaging conditions however, T_2^* becomes very short and gradients on the order of 1G/cm reduce the lifetime of the FIDs to under 1 μs. It is important that the short-lived FID

in the presence of the gradients has to be sampled as fast as possible to get the best SNR. Depending upon the overall frequency spread in the spectrum dictated by the gradient magnitude and object size, in an asymmetric object, the T_2^* becomes a function of the gradient orientation. This means that the integrated intensity of projection profiles, which should remain constant for volume excitations, will not be so, due to the fact that different fractions of the total signal in the FID will be lost in the dead time of the spectrometer and therefore, the individual projections ought to be corrected for this. A narrow long object such as a fine capillary tube containing the spin probe will have a longer T_2^* when the gradient is perpendicular to the capillary, whereas it will be much shorter when the gradient is along the axis of the capillary. For a given dead time, therefore, the SNR of the spectrum in the above two orientations of the gradient directions will be quite different and so will be the integrated intensity of the projection profiles; this will have to be corrected before the application of back-projection. Currently we limit our frequency bandwidth to about 10 MHz and with a gradient of 1G/cm we can address objects with a maximum diameter 5 cm, with a theoretical resolution of 2 mm for spin probes of line width 200 mG. The ultimate image resolution will, however, be governed by the lower of the two factors, namely pixel size and the ratio of line width to gradient magnitude. For a field of view of diameter x, with n projections the pixel resolution is given by $\pi x/n$. Thus, with a 2D field of view of 25 mm and collecting 36 projections, the pixel resolution is 2 mm. At a gradient strength of 1G/cm the limiting resolution allowed by the spin probe of line width 200 mG is also 2 mm. The overall image resolution is 2 mm. When the gradient is reduced to 0.5 G/cm with no change in the other parameters, the resolution will now be 4 mm. In order to achieve these theoretical limits of resolution one has to also satisfy sampling requirements in terms of number of samples per projection and the total number of projections (Botto *et al.,* 1996). Under larger gradients it will be necessary to remove the gradient-induced line broadening in the projections by deconvolution with the zero-gradient spectrum (Ewert and Herrling, 1986; Rollett and Higgs, 1962).

3. CHALLENGES IN TIME-DOMAIN EPR SPECTROSCOPY AND IMAGING AT RF

In the following we shall deal exclusively with time-domain RF EPR spectroscopy and imaging. In the time-domain mode, one perturbs the spin ensemble placed in a suitable resonator by a pulse by gating the continuous wave source of the electromagnetic radiation. Fig. 3 shows a schematic of time-domain signal acquisition in EPR and NMR spectroscopy. In both cases, an ensemble of spins (magnetic nuclei in NMR and unpaired electrons in

EPR) is placed in a magnetic field and perturbed by a pulse of RF radiation at or close to the resonance frequency. Since NMR spectra are spread over a very narrow range of energies (10-100 kHz), the pulse width of RF is typically in the microsecond range. The time-domain response of the nuclei, which is in the millisecond – second range can be recovered after a typical spectrometer recovery time (dead time) of several microseconds. In the case of time-domain EPR the time resolution in the experiment needs to be in the nanosecond range. Since EPR spectra are spread over a broader range (several MHz), the pulse widths should be less than 100 ns, requiring the ability to deposit narrow intense pulses to disturb the spin system. After the pulsed excitation, the weak time-domain responses (which last only for time periods comparable to the spectrometer recovery time itself) have to be acquired with a fast digitizer at rates dictated by the frequency bandwidth of the resulting spectrum. In the following sections the experimental considerations of these aspects are given in detail.

3.1 Pulsed Excitation

Pulsed excitation in time-domain magnetic resonance corresponds to simultaneously irradiating the system with a band of frequencies centered on the carrier frequency. The profile of the frequency spectrum corresponding to a square wave pulse is the sinc (sin (x)/x) function (Fig. 4). The central band of the sinc profile has a width at maximum slope of approximately inverse of the pulse width. The side lobes on either extreme are of low amplitude and have phase rolls and are of no practical use for excitation. In other words, an excitation pulse of duration 20 ns at a transmitter frequency, say, of 300 MHz, corresponds to subjecting the system simultaneously with a frequency range of 50 MHz (±25 MHz) centered on the transmitter carrier frequency, so that spectral components from 275 to 325 MHz will be more or less uniformly excited. The actual power of the pulse (pulse height) that is needed will depend upon the volume of the resonator and the conversion efficiency of the resonator in terms of the ratio of RF magnetic field to square root of RF power. For maximum transverse signal one has to employ the so-called 90° pulse that will bring the equilibrium Zeeman magnetization from the z-axis to the transverse xy plane. Once the magnetization is brought to the transverse plane, it precesses with the characteristic frequencies that are available in the system either due the internal Hamiltonians or due to the spread in the frequency brought about by the space encoding field gradients. The optimal pulse width and power that will be used for *in vivo* imaging also has to take into account one very important factor, namely, the specific absorption rate, SAR (the time derivative of the incremental energy absorbed by, or dissipated in an incremental mass contained in a volume element) which, by

convention, is the average energy in Watts dissipated per kG of body weight by the electromagnetic radiation during the imaging process. Several countries have come up with SAR standards. The Food and Drug Administration (FDA) of United States has recommended that the maximum energy that is deposited during MRI and other tissue radiation exposure protocols should not exceed a prescribed limit. The FDA SAR guidelines limit the energy dissipation to 0.4W/Kg whole body average, 8W/Kg peak at any 1 gm of tissue and 3.2 W/Kg in the head. In Canada the SAR level is 2W/Kg whole body average. These values are for specific periods of time and types of operating modes. The whole-body limit is specified as 4 W/kg for 15 min. in the FDA Guidelines issues in November, 1998. Changes may be anticipated as the field matures so the latest FDA Guidelines should be consulted.

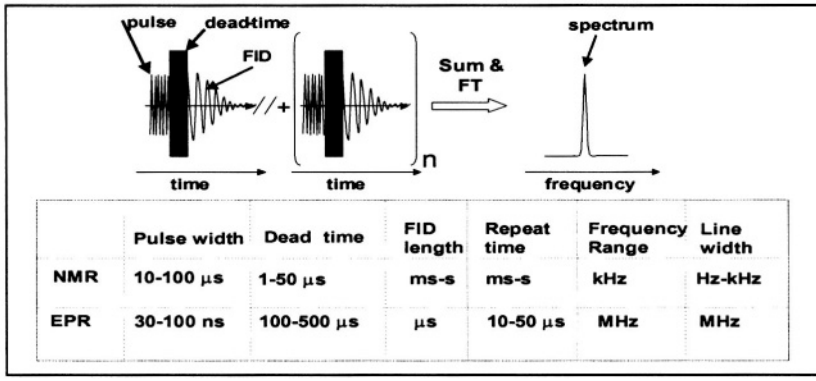

	Pulse width	Dead time	FID length	Repeat time	Frequency Range	Line width
NMR	10-100 μs	1-50 μs	ms-s	ms-s	kHz	Hz-kHz
EPR	30-100 ns	100-500 μs	μs	10-50 μs	MHz	MHz

Figure 3. Schematic representation of pulsed excitation and the response in the form of a free induction decay (FID) in time-domain NMR and EPR. The hatched area immediately following the pulse represents the dead time, which is the time gap during which the intense pulse power from the resonator dissipates to the noise level of the circuit via 'ringing' and also it includes receiver recovery time. The relative magnitudes of pulse width, FID decay time, etc., are also indicated. Large number of FIDs is to be averaged to improve SNR, and the repetition rate of excitation will be dictated by the relaxation time of the spins. The numbers indicated are approximate ranges, and will depend on the particular NMR or EPR system.

In the spectrometer system developed by us, the RF signal and the local oscillator frequencies are generated from a master phase locked RF source at 800 MHz. From this, using frequency dividers, double-balanced mixers and band pass filters, frequencies of 500, 300, 320, 50, 20 and 10 MHz were derived. The use of single master oscillator insures that all the lower frequencies derived will have a definite and constant phase relationship. The 300 MHz frequency is pulse modulated using high-speed RF gates, which consist of GaAs SPDT switches. The pulses formed by these gates have rise/fall times less than 4 ns. The phase of the pulses was alternated between 0 and 180 degrees during the data acquisition. The pulses thus formed were amplified using a 200W Class A power amplifier (Model 5066RE, Ophir RF,

Los Angeles, CA) and fed to the resonator through a diplexer (section III.4). Pulses with widths in the range 50 – 100 ns were used and were amplified up to a maximum of 280 V_{pp}.

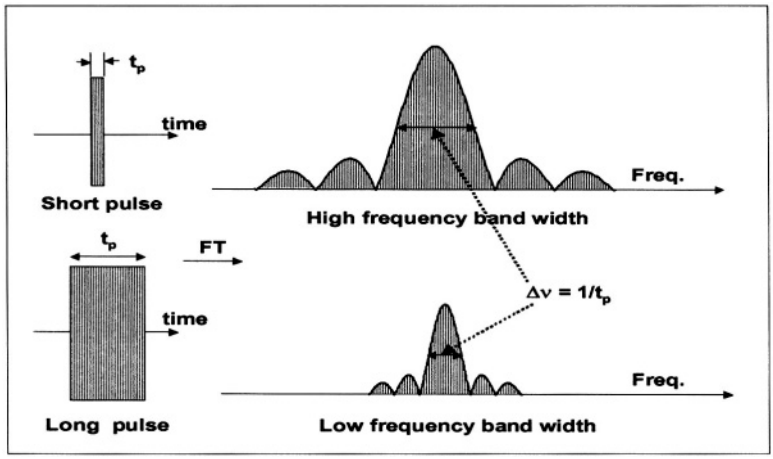

Figure 4. Schematic representation of a rectangular pulse and the corresponding profile of the power spectrum. Short duration pulses are required in time-domain EPR to produce a uniformly large bandwidth of frequencies generated by the distribution of the spins and the magnitude of the gradients. The power profile shown is the square of the sinc profile {sin(x)/x} which is the Fourier transform of a rectangular pulse. Only two side lobes are shown.

3.2 Magnet / Gradient Coils

The homogeneity of the main magnetic field is an important determinant in the optimal detection of time-domain responses in pulsed EPR spectroscopy and imaging, since appreciable inhomogeneity in the field will lead to a shortening of the transverse relaxation time (T_2*). The magnetic field inhomogeneity should be much less than the line width of the spin probes used in the experiments. For a 10-mT magnetic field corresponding to 300 MHz EPR frequency, better than 200 ppm homogeneity over the volume of interest is adequate for spin probes whose gradient-free line widths are more than 20 mG. The magnetic field gradients that are required for spatial encoding should be also of high quality with linearity better than 1% over the resonator volume. In our system the main magnetic field was generated by a Helmholz pair (30 cm i. d.) of water-cooled coils (GMW, Model 5451, Redwood city, CA), with field homogeneity better than 200 ppm in an active volume of 5 x 5 x 5 cm^3. A shielded 3-axes gradient coil system (BFG-350/10, Resonance Research Inc. Billerica, MA) with a digital power supply of 14-bit resolution was used for imaging experiments. The gradient power supply was controlled

through an IEEE interface and the gradient settling time was better than 100 ms.

3.3 Resonators

An optimal resonator in time-domain EPR should have the following characteristics: (a) adequate bandwidth to provide the spectral coverage in EPR spectroscopy and imaging experiments. For the imaging of small animals (such as mice) at 300 MHz, a bandwidth in the range of 10-20 MHz might be necessary to produce the satisfactory spatial resolution; (b) efficient conversion of the RF power to B_1 field; and (c) recovery time which is shorter than the response time of the signal.

The overall recovery time of the spectrometer depends on the resonator ring-down time and the receiver recovery time associated with preamplifier overload. The characteristic time constant of the resonator ringing depends on the operating frequency and the so-called quality factor, Q, of the resonator. Several resonator designs have been published in the literature for low frequency EPR (Alecci *et al.,* 1998b; Froncisz and Hyde, 1982; Hyde *et al.,* 1989; Ono *et al.,* 1986; Pfenninger *et al.,* 1988; Rinard *et al.,* 2002b; Sakamoto *et al.,* 1995). Well-known resonators used in MRI, such as solenoidal, saddle, surface coils, birdcage etc., were not found to be useful for pulsed RF EPR studies. The very short spin-spin relaxation times of paramagnetic systems preclude the use of these inherently high Q devices. A parallel resonant circuit with inductance L, capacitance C and resistance R (all in parallel) has a ringing transient of angular frequency ω_r and decay time constant τ_r given by

$$\omega_r = \omega_0[1 - L/(4Q^2)]^{0.5}$$
$$\tau_r = 2Q/\omega_0 \qquad (9)$$

Here, $\omega_0 = (1/2\pi)\,(LC)^{-0.5}$ and $Q = R/(\omega_0 L)$. It should be noted however, that for a conventional resonance circuit with C in parallel with a series combination of L and R, the quality factor is given by $Q = (\omega_0 L)/R$. In all our in vivo EPR imaging experiments we use a parallel coil resonator *(vide infra)* with L, C and R, all in parallel. A rule-of-thumb for 1kW incident power is that 30τ is required for the resonator energy to decay to a sufficient degree so as to allow the weak induction signals to be detected (Pfenninger *et al.,* 1995). This value will of course depend on the specific incident pulse power, resonator conversion factor, signal intensity and circuit noise power. For the fast relaxing electron spins, the receiver dead time due to the resonator ringing following the transmitter pulse can severely limit the electron induction signal available for data collection and, when the Q is high, may not even survive

beyond the dead-time. Equation (9) further indicates that the characteristic ringing time constant τ_r of a resonator is also related (inversely) to the carrier frequency ω_0. For a frequency bandwidth of 12 MHz, centered around 300 MHz, the optimal Q that would adequately cover this frequency range is 25, and τ_r is 26.5 ns. Hence immediately following the trailing edge of the RF pulse the system would be "dead" for about 500 ns. This is a much larger value than the ones encountered at pulsed X- or Q-band operations and the electron induction signals originating from most of the biologically useful EPR probes such as nitroxides would have decayed by this time. Therefore, the mandatory requirement of short recovery time and the need to cover a reasonable bandwidth of excitation (10-12 MHz), dictate the design of low Q resonators for time-domain RF EPR measurements. However, Q cannot be arbitrarily reduced. The time-domain S/N for a resonant coil with the sample fully enclosed is given by (Abragam, 1961)

$$\text{Signal/ Noise} = (\omega_0^2 N\hbar^2/4k_B T_{sample})\ \text{sqrt}\ (\mu_0 Q/4k_B T_{eff} B V_{coil}) \qquad (10)$$

V_{coil} is the coil volume, N is the total number of spins, and Q is the quality factor of the resonant circuit. ω_0 is the resonance frequency, k_B is Boltzmann's constant, and B is the receiver bandwidth. T_{sample} is the temperature of the sample, and T_{eff} is a temperature characterizing the noise of the system. S/N in Eq. [10] is defined as the time-domain signal amplitude of the free induction decay at its peak, divided by the root mean square Johnson noise. Therefore, other things being equal, the S/N depends on sqrt (Q/V). NMR probes with recovery times on the order of 10 μs have been constructed by connecting two interspersed solenoidal coils (Roeder *et al.,* 1984). For a fixed frequency, these coils can be constructed to have larger volume than a single coil probe. The reduced inductance of these coils is favorable also for reducing the recovery time of the NMR probe. We have successfully tested resonators in such configuration in time-domain EPR experiments as well (Devasahayam *et al.,* 2000).

In the design considerations, sensitivity aspects require the use of high Q resonators while bandwidth and dead time factors dictate low Q resonators. Thus key factors in the design considerations are in conflict and a compromise has to be reached. Over-coupled parallel coil resonators, having low inductance have been found to be suitable for time-domain EPR applications (Rinard *et al.,* 1994) and for *in vivo* applications (Devasahayam *et al.,* 2000).

The resonator was built by winding and supporting individual coil elements (AWG 26 Silver wire with circular cross section) on a dielectric mandrel (polymethyl-methacrylate tube). Fig. 5 provides detailed schematics of the coil positioning and winding. It can be seen that the individual coils are connected in parallel to form an array of parallel loops, which functions as the resonator. The diameter of all the coil elements in the array is equal.

Similarly, the length of the connecting leads is also kept equal so as to minimize the phase error during the application of the RF. The interior of the supporting tube houses the sample to be studied and the cylindrical axis of the resonator is kept perpendicular the DC field, B_0. The connecting leads of the resonator to the diplexer are supported by a dielectric separator which also acts as an RF shield between the input and output leads. The resulting structure, and the matching and tuning capacitors are mounted on a double-sided copper coated glass epoxy board. The resonator is energized through an SMA connector with a semi-rigid RF cable.

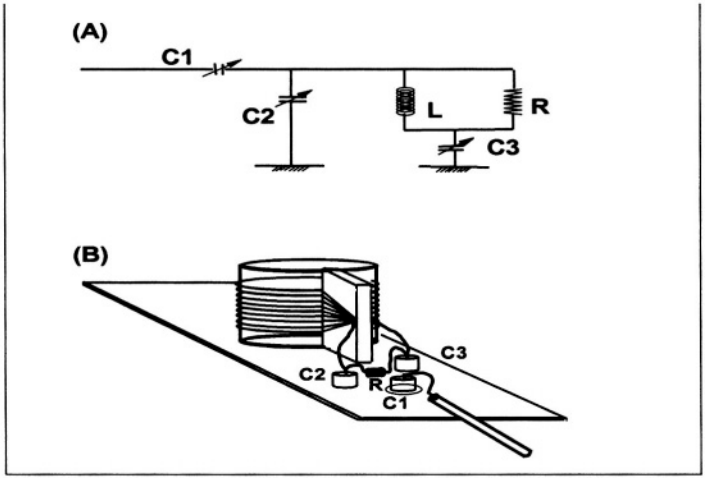

Figure 5. (A) The components of the LCR circuit that make up the resonator assembly. The values of C1 (tuning capacitor), C2 (coupling capacitor and C3 (matching capacitor) depend on the frequency and dimensions of the coil (B) Sketch of the parallel coil resonator with the RF magnetic field axis coaxial with the axis of the supporting mandrel. The resistance R is added to lower the Q. Only two capacitors are needed in principle, but the three capacitors are used for convenience. The resonator is mounted on a ground plate, which will be attached to a sliding platform for positioning inside the magnet. Resonators with dimensions of up to 80 mm diameter by 50 mm length have been successfully tested.

A cartoon of the mouse accommodated in the resonator is shown in Fig. 6A. The undamped Q of the resonator under ideal matching (to 50 Ω) conditions at 300 MHz was around 500. For imaging an object of dimension 2.5 x 2.5 x 2.5 cm cube, say under a gradient of 1.5 G/cm, the resonator bandwidth is required to be (2.5 cm x 1.5(G/cm) x 2.8 (MHz/G)) 10.5 MHz, limiting the Q of the resonator to be around ~25 at 300 MHz. Hence it is necessary to reduce the Q to the optimal level by capacitative over-coupling and/or resistive damping. Since over-coupling leads to higher B_1 field, Q reduction in these resonators was achieved by over-coupling. Additionally, a resistance (5W, 3.3 kΩ) in parallel was also used to reduce the Q, whenever it

was not possible to reduce the Q to the optimal value by over-coupling alone. Fig. 6B shows the Q-profile of this resonator when adjusted for a spectral bandwidth of ~12 MHz. The figure also depicts the effect of loading the resonator with 25 ml of aqueous phosphate buffer solution and a mouse of weight 30 g. It was noted that the placing of the electrolyte did not alter the Q profile significantly, and the presence of the animal resulted only in a small increase in the Q. The surprising, albeit small, increase in Q upon loading the animal is presumably due to the fact that the empty resonator was not coupled critically in the first place. Also when the empty resonator Q is already damped to very low values, its sensitivity to loading is much less than what would be expected in resonators that are critically coupled and have a relatively high Q. In any case, suitably adjusting the matching and tuning capacitors could further adjust Q to 20. With the Q damped to about 20, we found that the resonator ring down time for a 300 MHz, 70 ns pulse of 80 W, nominal power was about 550 ns. Reducing the Q at the expense of lowering the sensitivity could shorten this further.

In pulsed RF FT EPR the use of low Q resonators leads to very poor conversion factors. The conversion factor is defined as the oscillatory magnetic field (B_1) generated in the resonator per square root of power (Watt) applied. The conversion factor is estimated using the length (t_p) of the 90° pulse and is related to the amplitude of the oscillatory magnetic field by the equation

$$\pi/2 = \gamma_e B_1 t_p. \qquad (11)$$

With our low Q resonators used in imaging mice, we have measured that in a 25 mm dia. x 25 mm long cylindrical resonator, the 90° pulse width was 70 ns corresponding to a conversion factor of $0.014\ mT/\sqrt{W}$. The low conversion factor is due to non-critical coupling. The nominal power we apply to the resonator is around 80W and the actual power, which reaches the resonator, is much less due to several insertion losses. In fact we have measured the reflected power and the difference is only 20W. Since the filling factor of the animal is around 50-60% and accounting that 50% of flux is actually impinging inward on to the animal, the RF power seen by the animal is approx. 5 Watts. Because we are doing the experiment in the pulsed mode, we have to take into account the duty cycle that in our case consist of 70 ns pulses applied every 20 μs. T_1 of Oxo31, a compound also derived from TAM, with a narrower resonance line, is 5.9 μs and therefore, the 20 μs repetition time used here for Oxo63, which has a much broader line width, is sufficiently long to avoid saturation. This brings the average power dissipated into the animal to around [5 x (70/20000)] 17 mW. Assuming that the average body weight of the experimental mouse is around 25 gm the SAR is calculated to be 0.7W/kG

of body weight. This is an upper estimate, since all the RF power is not converted to magnetic field. A better estimate of the power dissipated in the animal might be obtained by measuring the change in Q of the high Q critically coupled resonator when the animal is introduced. If required, the actual power dissipated on to the animal can be further brought under the recommended value of SAR, by suitably reducing the duty cycle and / or pulse power.

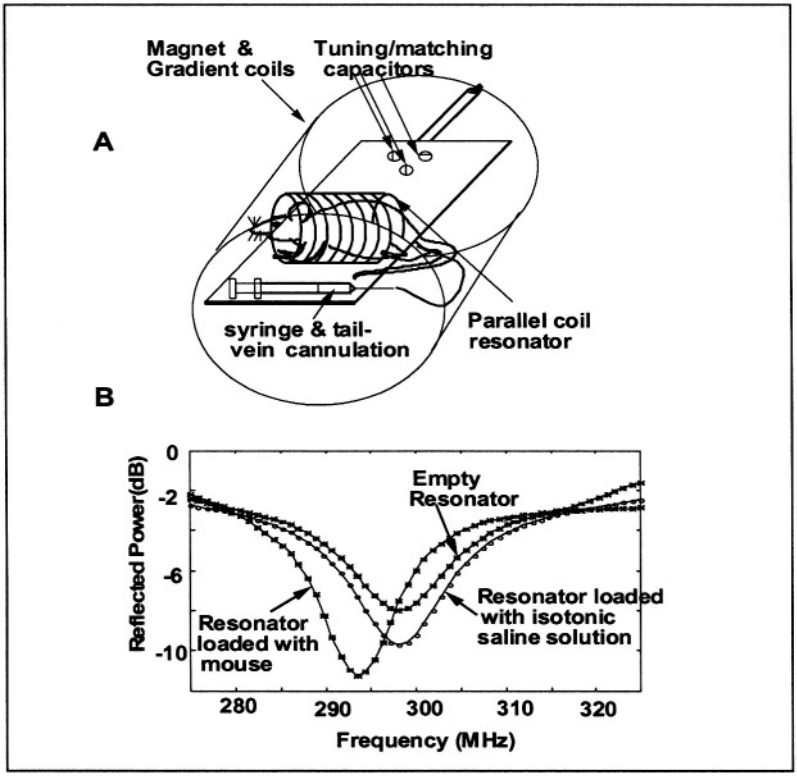

Figure 6. (A) A cartoon the resonator platform assembly showing the tuning and matching capacitors and the easy accommodation of a mouse inside the coil. The cylindrical enclosure is just a representation of the water-cooled electromagnet and a three axes gradient coil assembly. The mouse is placed in the resonator with the tail-vein cannula left in place for repeated administration of spin probe and anesthetics, as and when needed. (B) Profile of reflected power as a function of frequency for a parallel coil resonator of size 25 mm dia. x 40 mm long. The Q was kept around 20 by over coupling and resistive damping; the unloaded resonance frequency was 300 MHz. Upon loading the coil with PBS buffer solution there was only a very marginal change. The empty resonator was obviously not critically coupled and hence, when the coil was loaded by accommodating a 30g C3H mouse, there was a slight increase in the Q and a small shift to lower frequency. This was readjusted back to the desired Q by adjusting C1, C2 and C3 (see Fig. 5).

Apart from SAR considerations regarding the pulse width and pulse power, it is also important to note that an RF magnetic field of magnitude B_1 can only cover an angular frequency range $\omega = 2\pi\nu = 2\gamma B_1$ which should encompass the entire range of frequencies dispersed by the magnitude of the gradient. In fact this is the range at which the Fourier transform of a rectangular pulse crosses the axis and therefore the amplitude of the RF power droops considerably at either extreme so that one will see a drop in the intensity of spectral amplitude as one moves away from the carrier frequency. The projection profiles will not be a faithful representation of spin density profiles. This will lead to intensity anomalies in the image, especially at the outer edges of the image. Therefore, the pulse length should be shorter and B_1, concomitantly, larger to effect a reasonably uniform excitation of all the frequencies corresponding to the spatial extension of the object for a given gradient magnitude. The resonator Q-profile especially at higher Q values further compounds this. It is however possible to correct for the same using the measured Q-profile as well as the profile of the power spectrum of the pulse. It is possible, in principle, to recover signals which have de-phased during the dead time of the spectrometer by implementing the so-called echo detection scheme, which involves the application of a 90 pulse for excitation followed by a short delay on the order of T_2^* and an 180 pulse for recovering part of the transverse magnetization. However, so far, we have not been successful in detecting clean echoes.

3.4 Isolation of Transmitter and Receiver

In time-domain magnetic resonance experiments, the transmitter and the receiver are to be isolated because the transmit power may be several hundred watts, while the induction signals from the spins may just be a few tens of nanowatts. Therefore, we amplify the induction signals by at least 65 dB before digitizing the same. Because of this, when the receiver gate is opened there should be minimal leakage from the transmit power which takes a characteristic time after the transmitter pulse is switched off to decay to the thermal noise level of the circuit. The isolation between the transmit arm and receive arm can be achieved by a transmit-receive switch such as a diplexer or a circulator. It is also possible to employ the so-called crossed-loop resonator (Quine *et al.,* 2002; Rinard *et al.,* 2002b) in which the resonator consists of a transmit coil and a receiver coil with the RF field axis orthogonal which helps in isolating the transmitter and receiver and greatly reduces power leakage on to the detection arm. While this works very well for static samples, the degree of electrical isolation may be difficult to maintain during *in vivo* operations due to the animal motion. The diplexer provides the isolation by a set of crossed diodes which make the receiver arm non-conducting during the

transmit cycle and prevents any reflections returning back to the transmitter arm during the receive cycle and is the standard method adopted in pulsed NMR. The insertion loss of these devices should be very low so that the signal loss is minimal while providing an isolation of greater than 20 dB with switching times not greater than 100 ns. In our system we employ a standard $\lambda/4$ configuration diplexer (Murugesan *et al.*, 1998). The diplexer had a standard pin-diode switch assembly in the transmit path and a shunt pin-diode switch in the receive path. These diodes were maintained in a back-to-back configuration to minimize the transients in the RF paths. This arrangement provided switching times on the order of 5 ns. The receiver isolation during transmit mode was 25 dB with a transmit insertion loss of 2 dB. The insertion loss during receive mode was 0.5 dB. A circulator rather than a diplexer is normally used in CW spectrometers where it provides a good isolation. In our early spectrometers we did evaluate the use of RF circulators for pulsed operation. However, the isolation obtainable was less than the specification, due to the broadband nature of the pulsed circuit. Currently dual coaxial circulators with large bandwidth are available with isolation better than 40 dB (Renaissance Electronics Corp., Harvard, MA). However, these have not been tested.

3.5 Signal Amplification

The spectrometer can be operated either in a single channel mode at an intermediate detection frequency (IF mode) by mixing the induction signals at the carrier frequency (300 MHz) with a local oscillator frequency of 320 MHz, or in the quadrature mode (Subramanian *et al.,* 1999) with dual channel detection. In the quadrature mode, the signals were mixed with the carrier frequency down to base band using a quadrature mixer and digitized in two channels for the real and imaginary parts of the FID. In this mode, the RF power is effectively utilized and the phase and sign information of the signals is retained. In the IF mode, resonance frequency corresponds to 20 MHz, and spectral range from 280 to 320 MHz from the resonator will appear between 0 and 40 MHz. Such a configuration adequately covers the large bandwidths necessary for EPR imaging experiments, and one need not worry about the sign of the frequencies, and a single channel operation followed by magnitude mode of signal evaluation is adequate for image reconstruction.

The signals received when the spectrometer recovers after the transmit pulse are weak and last only for 1-2 μs. This signal should be amplified to a suitable level prior to digitization. The receive chain should have fast recovery and high gain. The first stage amplifier is critical in the receive chain. After suitable amplification, the resonance signals should be isolated by appropriate band pass filters and delivered to the digitization module. Thus the choice of

the front-end preamplifier is very important. The important requirements for the first stage amplifier are high gain and fast recovery.

In our earlier system a fast recovery high gain amplifier in four stages was incorporated in the first stage of the receive arm (Murugesan *et al.,* 1998). The four-stage amplifier composed of MAR series amplifiers (Mini-Circuits, Brooklyn, NY) contains BiC MOS SPDT switches (NE630/Philips Semiconductors, Sunnyvale, CA) between the stages, to prevent each amplification stage from changing its bias condition because of overload, and so assures rapid recovery. At each amplification stage, the signal is inverted in phase to minimize the transients produced by successive stages. Linear amplification with a gain of 41 dB is obtained 40 ns after the switches are on. The amplifier was centered around 300 MHz with a bandwidth of 100 MHz and a noise figure of 3 dB. In our later versions we have replaced the home-built four-stage amplifier by a low noise (<1dB), fast recovery (50 ns, as tested by us) preamplifier (Hi Level PHEMT Preamplifiers, Angle Linear, Lomita, CA).

After the first stage amplification, the signal was filtered with a 300 MHz center frequency band pass filter having a bandwidth of 42 MHz (TTE/07766-KC6-300M-14P-50-6140, TTE Inc., Los Angeles, CA) and subsequently amplified by a low-noise amplifier, A4 (Miteq 2A 150, 25 dB, Hauppauge, NY) and an RF amplifier, A5 (gain 25 dB, Model MHW590, Motorola). Adjustable attenuators were used to set the appropriate levels.

3.6 Data Acquisition System

Since the electron spin relaxation times are in the microsecond to sub-microsecond time scales, especially under the influence of the imaging gradients, the digitization-summation strategies should be fast enough to perform rapid signal averaging to enhance the signal/noise. Since each time-domain response lasts barely for 1-2 microseconds, digitization rates should be >250 MHz and the repetition rates can be faster than 10 kHz. In addition, the vertical resolution of the digitizer should have a dynamic range sufficient to read weak signals and strong signals as well.

The sampler contains four high-precision ADCs (TKAD10C) each with a sampling rate of 500 Ms/s (mega samples/s) and a vertical resolution of 8 bits. Since interleaving techniques are used to increase the sampling rate above maximum sampling rate of the individual ADCs, a very close matching of the ADCs in terms of gain, offset and sampling times over the entire operating ranges is provided by control signals. A maximum interleaved sampling rate of 1 GS/s (giga samples/s) in two-channel mode or 2GS/s in single channel mode can be realized. Signal Q and I represent the two inputs to the digitizer. The preamplifiers provide a gain and offset for the input FID signals. Internal

calibrations are also provided in the preamplifiers. Further, the preamplifiers are optimized to provide superior bandwidth (1.3 GHz), phase linearity (± 2°) and spurious free range (50 dB). However, the input range of the preamplifier is fixed at 500 mV.

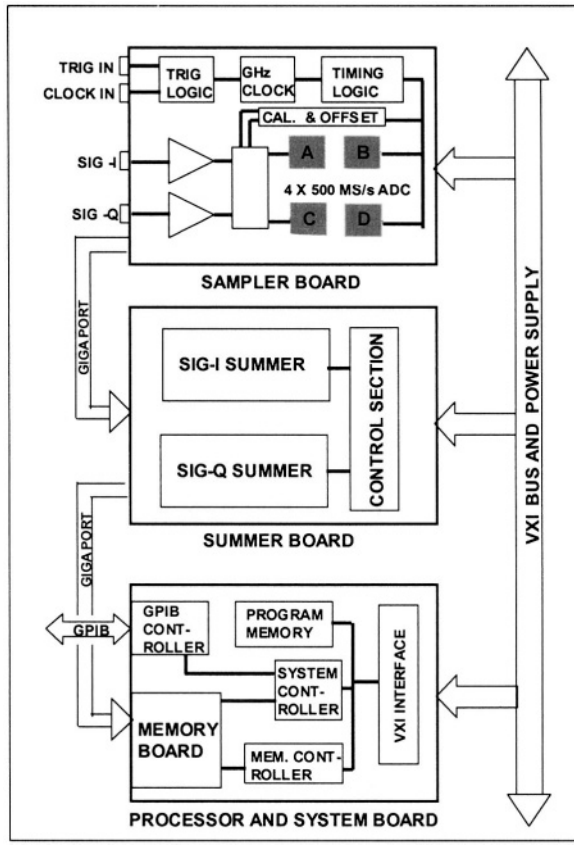

Figure 7. Block diagram of the Analytek data acquisition system showing the sub modules consisting of sampler board, the summer board and the processor board.

A block diagram of the data acquisition system used in this study, custom-built by Analytek (now part of Tektronix, Beaverton, OR), is shown in Fig. 7. The system is based on a modular design comprising of three sub-units, namely: i) a sampler, ii) a summer and iii) a processor.

All the control and timing signals are derived from the same time base. FIDs are sampled on each edge of the divided master clock for interleave mode. For the two way interleave, channels A and B sample on the positive edge whereas C and D sample on the negative edge. In the four-way mode, A and B channels sample on alternate positive edges and C and D on alternate

negative edges. A trigger controller provides triggering capability from the external source and the triggering circuitry is enabled by a control signal from the pulse generator of the EPR spectrometer.

A block diagram of the summer is given in Fig. 8A. For each FID signal, two channels are provided; totally there are four channels and these four data streams are 16 bits wide. ECL logic (Motorola 100K ECLPS series) is used to implement the data channels. The input FIFO (first-in-first-out) memories (IDT 72221) buffer the FID data from the sampler. The data from the input FIFOs are summed with a pipelined 8-bit adder and a 24-bit accumulator. Therefore, the summation FIFOs can accommodate 32-bit data for each of the FID signals. A detailed description of one of the channels is given in Fig. 8B.

The summing process begins when the processor activates a control signal to the summer, which in turn activates the sampler to send the digitized data over the four channels. After the digitized waveforms are summed, the summer reactivates the sampler to initiate the next digitizing cycle. This process repeats until a programmed number of FIDs are summed. This programmable number is a 24-bit word and hence more than 16 million repetitions with almost real-time averaging can be completed without transferring the data to the host computer. The summation process operates simultaneously with the digitization process by the sampler when it operates in a pre-trigger mode. The summing process begins when the first words have been loaded into all of the input FIFO memories. Thus, the summing process effectively overlaps the digitization process since it does not have to wait until the loading of the input FIFOs is completed. FIDs with a record length of 2 K points for both the I and Q signals can be summed at a rate of 230 kHz (re-trigger period of approximately 4.3 μs). The data output from the summer is 32-bit wide, providing a very high dynamic range for averaging. The summed 32-bit data is transferred in sequence to the processor as two 16-bit words.

The processor module contains a 32-bit microprocessor (Motorola 68340) with a memory of 64 MB. It supports a direct memory access (DMA) transfer at speeds up to 1 MB/s. The National Instruments NAT4882BPL IEEE-488.2 controller is interfaced to the microprocessor. The host computer initiates the experiment through the GPIB interface. At the start of the experiment commands are sent to calibrate the hardware. After calibration, the host computer sets the desired data acquisition parameters such as the number of repetitions of FID, the record length and the sampling frequency. After a predefined number of FIDs are summed, the data is transferred to the host computer where signal-processing routines such as digital filtering, base line correction, Fourier transformation, back projection and image rendering are carried out.

The block diagram of the 300 MHz time-domain spectrometer / imager incorporating the various components described above is given in Fig. 9. As

mentioned previously, the receiver side can be operated both in the single channel IF mode as well as a dual channel quadrature mode.

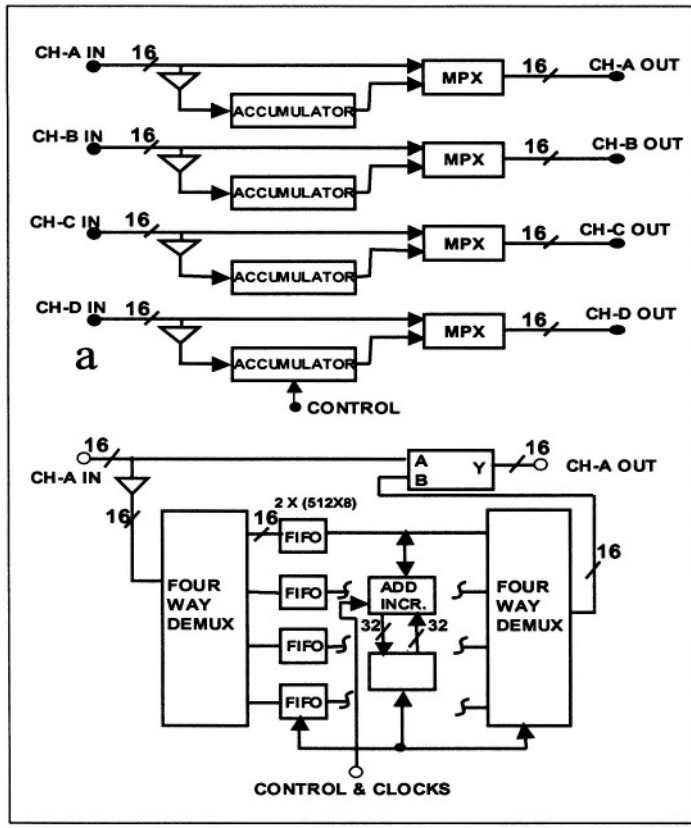

Figure 8. Block diagram of (a) the four-channel summer and (b) the detailed data routing of one of the summer channel. (Please see text for details).

3.7 Spin Probes for Time-Domain EPR Imaging

The requirements for an optimal paramagnetic spin probe useful for time-domain EPR imaging at radio frequency for *in vivo* applications are as follows:

a) The spin probe should have single line EPR spectra. Since, for imaging applications, all the spatial information can be provided by a single line, a probe with multiline EPR spectra will have information that is redundant. In addition, a decrease in sensitivity would result from a paramagnetic spin probe with multi-line spectra.

b) The EPR line width of the spin probe should be narrow such that its time-domain response at RF survives beyond the spectrometer recovery time.

c) The *in vivo* stability of the paramagnetic spin probe should be such that its half-life is longer than 10 minutes to permit 3-D image data collection.

d) The spin probe should be water-soluble such that the probe can be administered either intravenously or intraperitonially.

e) The toxicity of the spin probe should be minimal at the doses required for EPR imaging.

f) In addition, if the spectral properties of the spin probe such as the line width vary with pO_2 it will permit the estimation of tissue oxygen status from the EPR image data.

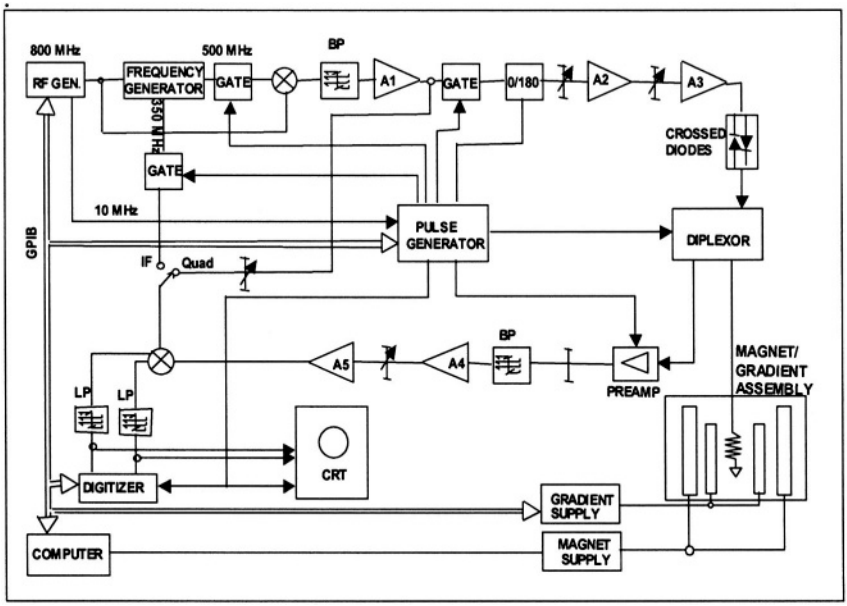

Figure 9. Block diagram of the 300 MHz time-domain EPR spectrometer / imager operating at both single channel IF and dual channel quadrature mode.

The spin probes used for time-domain imaging and oxygen mapping are stable paramagnetic species, which are non-toxic, and water-soluble, based on the triarylmethyl (TAM) skeleton. The structural details of these agents and their EPR properties are described elsewhere (Ardenkjaer-Larsen *et al.,* 1998). Recently these spin probes with a single narrow EPR resonance have been evaluated as contrast agents for dynamic *in vivo* oxymetry using Overhauser enhanced MR imaging (Golman *et al.,* 2000). Two analogs of TAM, abbreviated as Oxo31 and Oxo63 were used in our studies. The structure of these agents, their abbreviations and molecular weights are given in Fig. 10. At the present level of sensitivity of the EPR spectrometer/imager a minimum of about 10^{16} - 10^{17} spins could be detected and imaged in the parallel coil resonator (dimension 25 x 50 mm). At this level, this class of compounds is well tolerated with no observed toxicity in mice. The *in vivo* pharmacological half lives were found to be >25 minutes permitting several data sets corresponding to three-dimensional images at different times after administration could be collected. The relaxation times of some of the TAM based derivatives at RF frequency range have been reported in the literature (Ardenkjaer-Larsen *et al.,* 1998; Panagiotelis *et al.,* 2001; Yong *et al.,* 2001).

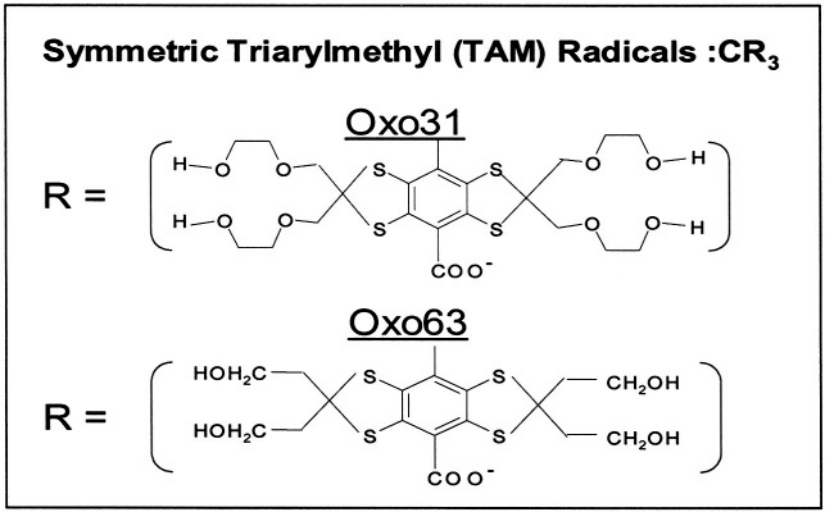

Figure 10. The molecular structure of the symmetric triarylmethyl derivatives, Oxo31 and Oxo63 used for time-domain EPR imaging.

Insoluble particulate spin probes such as fusinite (Gallez *et al.,* 1998) and lithium phthalocyanine (LiPC) (Jiang *et al.,* 1996; Liu *et al.,* 1993) have also been used to perform localized *in vivo* spectroscopy and oxymetry. A single line EPR spectrum whose line width depends linearly on the partial pressure of oxygen characterizes these solids. These agents have to be implanted surgically into the animal at specific anatomical locations for the purpose of

studying site-specific *in vivo* oxygen measurements (Swartz and Walczak, 1998). Fusinite has line widths on the order of several gauss and is not suitable for time-domain EPR. On the other hand, LiPc, which is a paramagnetic semiconductor, has line widths in the range 20-40 mG in the absence of oxygen and the line width has a linear dependence on oxygen concentration. Detailed discussion on the electrochemical synthesis of LiPc and its line width dependence on oxygen partial pressure has been reported (Ilangovan *et al.,* 1999; 2000a; 2000b). The time-domain responses from LiPc last between 1-10 μs depending on the quality of the crystals and the partial pressure of oxygen (Afeworki *et al.,* 1998). These probes ($< 0.2\ \mu m^3$) can be implanted in the muscle or other regions of interest and repeated oxygen measurements can be made *in vivo* (Liu *et al.,* 1993).

4. RECONSTRUCTION TECHNIQUES

In time-domain EPR (just as in CW EPR) we use 2D and 3D filtered back projection techniques similar to X-ray CT or PET to arrive at the images. According to Radon transform and the Central Projection theorem, it is possible to reconstruct the cross section of an object from measurements that are line integrals of the cross section function. This method has since found immense applications in astronomy, diagnostic imaging, MRI, EPR imaging, etc. Whereas in x-ray CT we reproduce the three dimensional object from projections ('shadows') based on its spatial attenuation coefficient to X-rays, in MRI and EPRI we reconstruct the image in terms of the three dimensional spatial distribution of spins. The encoding of spatial coordinates of spin density in terms of frequency is done in presence of linear magnetic field gradients that produce a "spin density shadow' analogous to differential attenuation to X-rays that occurs in CT.

4.1 Principles Behind Filtered Back-Projection

There are excellent manuals in the literature (Bracewell, 1994; Kak and Slaney, 1988; Natterer, 1986) that describe the mathematics and practice of filtered back projection in two and three dimensions and as such no elaborate description is given here. Let us first consider, for simplicity, a two dimensional density function in the xy plane f (x, y). In the case of EPR imaging f (x, y) represents a two dimensional distribution of unpaired spins. A *ray* is defined as a straight line passing through the object and is specified by its angle with respect to the x-axis and its distance from the origin. The line PQ in Fig. 11 is one such *ray* and is defined by the equation

$$x\cos\theta + y\sin\theta = q_1 \tag{12}$$

where q_1 is the distance from the origin and (x, y) are the coordinates of any point on PQ. The line integral $p\theta(q_1)$ of the spin density distribution function f(x, y) is given by

$$p\theta(q_1) = \int_{\theta q_1 line} f(x,y)ds \tag{13}$$

which is also called the ray-sum or ray projection. Using the Dirac delta function the above equation can be rewritten as

$$p\theta(q_1) = \int_{-\infty}^{\infty}\int_{-\infty}^{\infty} f(x,y)\delta(x\cos\theta + y\sin\theta - q_1)\,dxdy \tag{14}$$

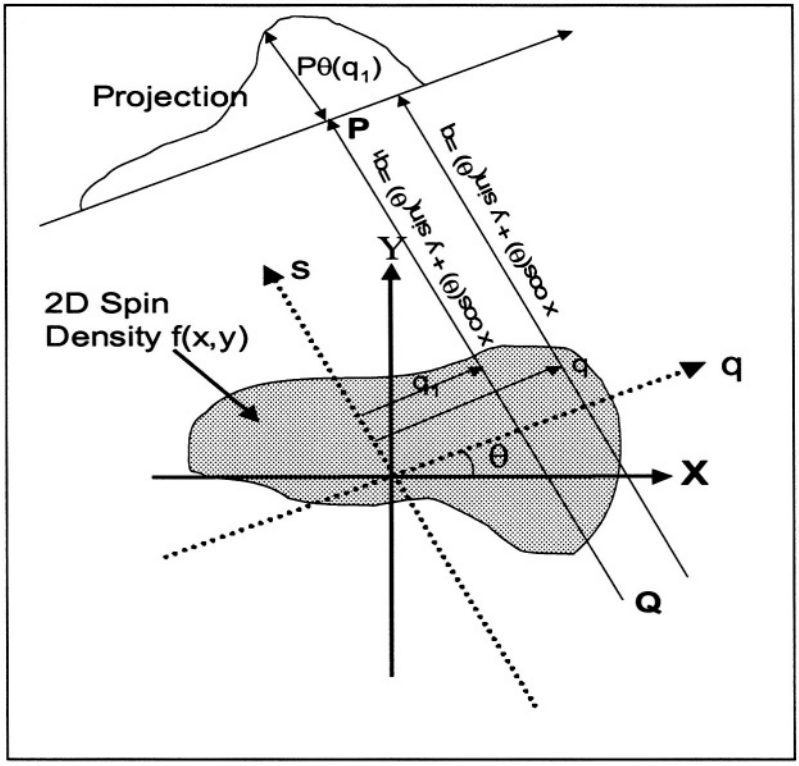

Figure 11. A two dimensional spin density function f(x,y) and its projection $P\theta(q)$ for a viewing angle θ from x-axis. (Please see eqn. 16 and the following text.)

The line integral $p\theta(q_1)$ is known as the Radon transform of f (x, y). A complete projection of a set of $p\theta(q)$ for all values of q for a given angle θ is called a *projection* or *profile.* In magnetic resonance imaging, for example, application of a linear field gradient along the x-axis will disperse the resonance frequency of f (x, y) such that all spins having the *same x-coordinate,* irrespective of their y coordinates, will have the same relative shift in frequency and will produce a ray-sum or projection which distinguishes only the x-coordinates. In simple language, such a projection will be an array of line integrals in which each *ray* represents the integrated spin density in f (x, y) along lines parallel to the y-axis. The subtle difference in the definition of ray in EPR *vis-á-vis* X-ray CT is that in the former, for a gradient along the x-axis we get projections parallel to the y-axis while in the latter, for a collimated beam direction along x-axis, we do get a projection parallel to x-axis. In other words the ray-sums in MRI and CT are rotated 90° with respect to each other when one relates these to the gradient axis and beam axis respectively. Once we have defined the projections, it is important to look into their mathematical properties. We can Fourier transform a given projection $p\theta(q)$ to $F\theta(\omega)$ as

$$F\theta(\omega) = \int_{-\infty}^{\infty} p\theta(q) \exp(-i2\pi\omega q)\, dq \qquad (15)$$

In terms of the definition of the projection in equation [15], we can rewrite $F\theta(\omega)$ as:

$$F\theta(\omega) = \int_{-\infty}^{\infty} [\int_{-\infty}^{\infty}\int_{-\infty}^{\infty} f(x,y)\,\delta(x\cos\theta + y\sin\theta - q_1)\, dxdy] \exp(-i2\pi\omega q)\, dq \qquad (16)$$

From the nature of the Dirac delta function the above equation becomes

$$F\theta(\omega) = \int_{-\infty}^{\infty}\int_{-\infty}^{\infty} f(x,y) \exp(-i2\pi(x\cos\theta + y\sin\theta))\, dxdy \qquad (17)$$

The above equation defines the Fourier slice theorem which states that the Fourier transform $F\theta(\omega)$ of the projection $p\theta(q)$ is identical to the Fourier transform of a *slice* of the density function f(x,y). The slice is a line passing through the origin of f(x,y) at an angle θ measured from the x-axis. This can be restated, according to Kak and Slaney (90) that the Fourier transform of a parallel projection of an image f(x,y) taken at an angle θ from the x-axis, gives the slice of the two dimensional Fourier transform $F(\mu,\nu)$ of the image f(x,y) at an angle θ from the μ-axis.

Since we will be acquiring the 2-D or 3-D projections of the object by rotating the gradients that are centro-symmetric with the object and EPR resonator, it is convenient to deal with manipulations in polar coordinates. For this we need the relationship between a function (say, spin density) represented in Cartesian coordinates and its Fourier transform represented in polar coordinates. This identity helps in solving for the density function in Cartesian coordinates from projection obtained in polar coordinates. It can be shown that the function f(x,y) defined by x and y rectangular coordinates, and the Fourier transform of f(x,y) in polar coordinates r and θ, namely $F(r,\theta)$ are related by

$$f(x,y) = \int_0^{\pi} [\int_{-\infty}^{\infty} F\theta(\omega) \exp(i2\pi rq) dq] d\theta \tag{18}$$

where $q = x \cos\theta + y \sin\theta$. In terms of the above equation we can reconstruct the image f(x,y) by the inverse Fourier transformation of $F\theta(\omega)$ (see Eqn. 17) given by

$$f(x,y) = \int_0^{\pi} [\int_{-\infty}^{\infty} F\theta(\omega) \exp(i2\pi\omega q) dq] d\theta \tag{19}$$

which is known as the back projection integral. The above equation can be rewritten as

$$f(x,y) = \int_0^{\pi} Q\theta(x\cos\theta + y\sin\theta) d\theta \tag{20a}$$

where

$$Q\theta(q) = \int_0^{\pi} F\theta(\omega)|\omega| \exp(i2\pi\omega q) dq \tag{20b}$$

for $q = x \cos\theta + y \sin\theta$. In other words, the projections $p\theta(q)$ are filtered using a filter function whose frequency response function is given by $|\omega|$. The filtering is implemented by multiplying the Fourier transform of $p\theta(q)$, namely, $F\theta(\omega)$ with the filter response function $|\omega|$ and then the product is inverse Fourier transformed. Therefore, $Q\theta(q)$ is called the filtered projection and the process of reconstruction of the image is known as filtered back projection. The most popular filter response functions for 2-D reconstruction are: the Shepp-Logan (Shepp and Logan, 1974), Ram-Lak (Ramachandran and Lakshminarayanan, 1971), and Hamming filters (Herman, 1980).

The above description which refers to 2-D projection and back projection, is given in terms of integral transforms involving infinitesimal increment of the projection angle and in practice it will not be possible to do so and one has

to deal with finite number of projections. Further, the frequency spectrum obtained by the Fourier transform of the projections will have finite range of frequencies outside of which the amplitude will be negligible. In other words the projections are 'band limited'. If F is the frequency beyond which the Fourier components of the spectrum corresponding to the projections are negligible, then one can define a limiting sampling interval T dictated by the Nyquist theorem given by

$$T = (2F)^{-1} \tag{21}$$

If the projection data is zero for values larger than ± q ($q=x \cos\theta + y \sin\theta$) then we can represent the projection data in discrete form as $p\theta(mT)$, with m = -n/2, - (n/2) +1, - (n/2) +2,....0....1, 2,....(n/2) –1, and the discrete FT of such a projection is given by

$$F\theta(\omega) \sim F(m.2F/n) = (2F)^{-1} \int_{k=-n/2}^{n/2-1} p\theta(k/2F) \exp[-i2\pi(mk/n)] \tag{22}$$

and similarly the filtered projection can be written as

$$Q\theta(k/2F) = (2F/n) \int_{k=-n/2}^{n/2} F\theta(m.2F/n) |m.2F/n| \exp[i2\pi(mk/n)] \tag{23}$$

with k= -n/2,...., -1,0,1,....n/2. The image is reconstructed from filtered projections obtained for k equally spaced angles from 0 to π (π to 2π projections will be identical since interchanging the sample and the gradient directions does not affect the projection profile) by the discrete approximation to the back projection integral given by

$$f(x,y) \approx \pi / k \int_{i=1}^{k} Q\theta(x\cos\theta_i + y\sin\theta_i) \tag{24}$$

Because the filtered projections are in polar coordinates whereas the image is represented in Cartesian coordinates, when there is no exact match between one of the values of q and ($x \cos\theta + y \sin\theta$), for which Q_θ (q) has been determined, the latter can always be approximated by linear interpolation.

So far we have only discussed the back projection scheme in two dimensions. For three dimensional back projection image data are to be gathered for the gradient vector positioned sequentially along equal polar and azimuthal angle intervals with both values varying from 0 to π. Thus for a 3D imaging of an object a gradient vector of constant magnitude is rotated with the polar angle varying, say in steps of 10°, from 0° to 170° and for each value

of the polar angle, varying the azimuthal angle in steps of 10° from 0° to 170°, corresponding to a total of 324 projections (18 x 18). Three dimensional projection reconstructions involve a two-stage reconstruction scheme (Marr *et al.,* 1981). In the first stage projection the azimuthal angle ϕ is fixed. From the above-mentioned mode of data collection, which involves a set of N x N projections with N having the same value of ϕ, each with N sequential values of θ, N two-dimensional filtered back-projections are first carried out. This will give N reconstructed planes each of which can be characterized by a single azimuthal angle ϕ, (see Fig. 12 A). If the number of discrete points in each projection is, say 128, this results in producing N planes each containing 128 x 128 points. These points can be represented by $P(\phi, i, j)$.

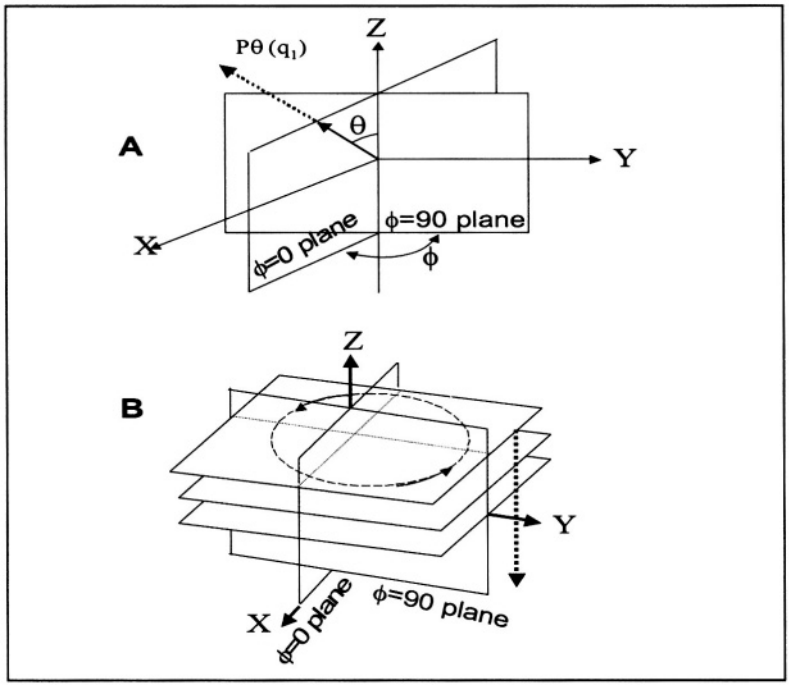

Figure 12. 3D back projection reconstruction consists of a two-stage process. The data set involving m θ steps and m ϕ steps consists of a total of m^2 projections each with, say, 128 data points. In the I stage (A) m two dimensional planar projections are carried out from the projections each of which consisted of m projections collected with a constant azimuthal angle ϕ, $P\theta_i(q)$ for a i=1, 2... m for a given ϕ. This results in m 2D projections each with 128 x128 points. Every point at the end of the 1 stage projection can be represented as $P(\phi, i,j)$, i = 1 to 128, j = 1 to 128. In the second stage (B) all points $P(\phi,i, j_1)$, i =1 to 128 are selected. These, for a given value of j, lie in planes perpendicular to the z-axis, two of which are shown. There will be a total of 128 such sets (j_1 = 1 to 128) which are to be back-projected resulting in a cubic array of dimension 128 x 128 x128 corresponding to the 3D image.

In the second stage of reconstruction, by fixing either i or j, for example $j = j_1$, all the points $P(\phi, i, j_1)$ which will lie in a plane (see Fig. 12B) is selected and once again a filtered back-projection is carried out, and this is repeated until all the j's are exhausted to yield $P(i, j, k)$ consisting of 128 image planes each containing 128 x 128 points. The resulting image data is a cubic array, which can be surface rendered or cross sections can be examined using suitable 3D visualization software. In our laboratory, we use a C^{++} program for image reconstruction and a surface rendering program, Voxelview® for image visualization.

For 2D reconstruction we find that a Ram-Lak or Shepp-Logan filter is adequate, and for 3D back projection, we either use two Shepp-Logan filters in each stage or a *single* second derivative filter, or the so-called three-point filter (Shepp, 1980) applied only during the first stage. In fact the second derivative filter also known as three-dimensional filter gives better results than two successive filters in each of the stages.

4.2 Spectral Spatial Imaging

A variant of the imaging modality can produce what is known as spectral/spatial images (Eaton *et al.,* 1991; Eaton *et al.,* 1989; Eaton and Eaton, 1986; Ewert and Herrling, 1986; Kuppusamy *et al.,* 1994; Lauterbur *et al.,* 1984; Maltempo, 1986). Consider the situation where we impose a linear gradient along the x-axis of a two dimensional spin density function f(x,y). The gradient will now provide space encoding with the spins distributed along a given line parallel to y axis resonating at one frequency, the profile itself will give spatial information along the x-axis. We can consider the x-axis as the spatial-axis. If we project this spectrum on to the y-axis we will get a single delta function line at a location which we call zero frequency. We say, that there is no spectral information. Now imagine performing the experiment, again with the gradient along the x-axis, but the magnitude doubled. The separations between any two points in frequency will now be doubled. We will however, rescale the frequency axis is such a way that it occupies the same number of points as in the first experiment. This will correspond to viewing the system in the so-called spectral/spatial domain at a *pseudo viewing angle* α to the spatial axis given by

$$\tan(\alpha) = (\text{spatial window} / \text{spectral window}) \times \text{gradient magnitude} \quad (25)$$

Increasing the gradient further and rescaling the spectrum so that it occupies the same physical width will give a more resolved view. By rescaling the various profiles proportional to the applied gradient we end up producing profiles of the object whose 2D back projection will correspond to a

spectral/spatial image with the gradient axis representing the spatial dimension and the orthogonal axis representing the spectral dimension. In practice, just as we collect 2D spatial profiles by rotating a constant gradient in the xy plane in equal intervals for 180 degrees, for a 1D-spectral-1D-spatial image we perform experiments by gradually incrementing the gradient *without* changing its direction. For a pseudo viewing angle $\alpha = 90°$ we need an infinite gradient and for α between 90° and 180° the gradient will change sign (see equation above).

Since an infinite gradient is not practical, we may have to miss some profiles close to $\alpha = 90°$, but this will not adversely affect the reconstruction. Missing angle back-projection algorithms are available in the literature (Maltempo *et al.,* 1988). Let us suppose we want to perform 2D spectral spatial (1D-spectral-1D-spatial) on an object occupying a resonator of cross section 25 mm, and we need a spectral resolution of, say 5 MHz. The value of the gradients for 18 projections for $\alpha = 0$ to 170 in 10° steps (Eq. 24) are 0, 0.1259, 0.2600 0.4124, 0.5994, 0.8513, 1.2372, 1.9625, 4.0509, ∞, -4.0509, -1.9625, -1.2372, -0.8513, -0.5994, -0.4124, -0.2600, -0.1259 G/cm. As α increases, the gradient magnitude increases rapidly, becoming infinite at $\alpha = 90°$. The missing angle range will depend on the gradient strength that can be applied limited by the capabilities of the hardware. In CW spectroscopy the sweep has to be continuously increased proportional to the gradient, and the profiles are to be sub sampled into the same number of points defined by the pixel resolution needed for the spatial axis. In time-domain data acquisition methods, since the spectra are always over sampled (in the Nyquist sense) the number of points in the spectral domain that are to be sub sampled for each gradient strength before back projection can be easily calculated. A 2-D spatial-1-D spectral imaging experiment will take the same time duration corresponding to a conventional 3-D spatial image, and a 3-D spatial and 1-D spectral image will be much more time consuming. Spectral spatial imaging has been implemented in CW EPR imaging by several researchers (Eaton *et al.,* 1987; Kuppusamy *et al.,* 1994; Maltempo *et al.,* 1987).

5. REPRESENTATIVE RESULTS FROM TIME-DOMAIN EPR IMAGING AT 300 MHZ

In the following we present a few representative examples of phantom and *in vivo* imaging carried out on mice in our laboratory at 300 MHz using the time-domain EPR spectrometer described in the previous sections.

5.1 3D Phantom Imaging

In order to test the spectrometer and resonators we have measured several phantoms containing the TAM radicals. One such phantom consisted of two holes of 4 mm diameter drilled in a Lucite cylinder of 25 mm dia. X 25 mm length. The two holes made an X-shape with the holes occupying the corners of a 25 mm square crossing each other in the center (see Fig. 13).

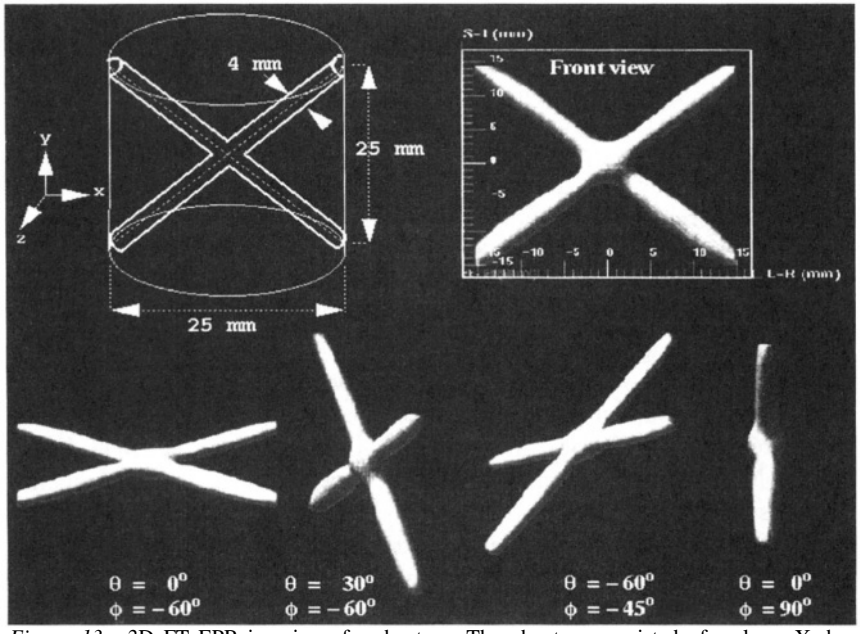

Figure 13. 3D FT EPR imaging of a phantom. The phantom consisted of a planar X-shaped drilling with the holes of the X-shape bisecting the X and Y axis of the gradient axis system (A). The holes were filled with 800 μL of TAM in saline solution and were imaged with the gradient vector spanning the polar and azimuthal dimensions in steps of 15° corresponding to a total of 144 projections. The gradient magnitude was 1.2 G/cm and the line width of the probe in the absence of the gradient was 170 mG. The three-dimensional images obtained after filtered back projection are shown at some specific orientations. In this figure, the y-axis is the polar axis. The surface rendering was done using Voxelview® in a Silicon Graphics Indigo2 workstation.

The holes were filled with 0.5 mM TAM corresponding a total volume of 600 μL corresponding to 1.9×10^{17} spins. The images were acquired at a gradient of 0.5 G/cm, which was rotated in 15° steps over the solid angles θ and ϕ over the hemisphere centered about the center of the gradient axis. For each orientation of the gradient field, 100,000 FIDs of 4K length were collected and summed (total time 2 sec.) at sampling rate of 1 Gs/s. The dwell time of the FID is thus 1 ns, corresponding to a Nyquist frequency bandwidth

of 500 MHz. Since the signals decayed to noise levels in about 2 μs, only 2000 points of the FIDs were taken for image reconstruction. These were weighted by Kaiser filter of order 3, zero filled to 8K and Fourier transformed. From the peak position of the spectrum obtained with no gradient, the center of gravity of the image in frequency terms was noted and 127 points centered around this point (for 8 K zero filling) would correspond to a frequency bandwidth of 7.75 MHz, and will cover a field of view of a sphere of diameter 55 mm well over the size of the resonator. The spectral profiles were then subjected to smoothing using Savitzky-Golay smoothing filter (Savitzky and Golay, 1964). The smoothed profiles are employed in a 2-stage projection reconstruction algorithm written in C^{++}. The resulting 3D image in terms of a 127 x 127 x 127 matrix of intensities is surface rendered using Voxelview in a Silicon Graphics Indigo2 workstation. The program can calculate distances, display slices and also provide lighting at any viewing angle. Fig. 13 also shows views of the surface rendered 3D images of the phantom and it can be seen that the images reproduce the object faithfully with little distortion.

5.2 Three-Dimensional in vivo EPR Imaging

For 3D imaging a mouse we use parallel coil resonators of 25 mm dia. X 50 mm length that snugly accommodates an anesthetized mouse from neck to the beginning of the tail. The mice were anesthetized using ketamine/xylzine (or alternatively with Isoflurane® in some experiments) and placed in a horizontal position perpendicular to the axis of the electromagnet. A cannula was attached to the tail vein and left in place (Fig. 6A) for administering further doses of the anesthetics as well as the free radical probe about 150 μL of 20 mM TAM was infused and the measurement of the EPR spectrum was started. It was found that within 2 –3 minutes the signal amplitude reached a maximum, at which point the imaging experiment started. A gradient of 0.5 G/cm was applied and 324 projections were measured for the gradient oriented in 10° steps about the polar and azimuthal angles θ and ϕ over the surface of a hemisphere centered about the resonator. Finally a zero gradient spectrum to mark the center of the resonator was also collected. For each projection 50,000 or 100,000 FIDs were summed taking either 1 or 2 seconds per projection. The image processing was carried out in an exactly similar way as what has been described above for the 3D phantom experiment. Our initial experiments produced images of internal anatomy where the unpaired spin is distributed by blood circulation. Since the images did not have the characteristic contour of the whole animal that one normally sees in an MRI image, we were not able to identify unequivocally the anatomical parts. In order to aid in the interpretation of the image we placed markers (fiducials) consisting of Teflon capillary tubes filled with 2 mM TAM surgically at

predetermined locations. Images were first gathered of the fiducials alone and then after administering the spin probe into the animal subsequent imaging was carried out. By superposing the fiducial image on the actual anatomical images we could identify the major anatomical elements such as the lung-heart, liver, kidneys, bladder, etc. Results from several mouse images carried out as a function of time after the infusion of the spin probe show that the spin probe initially accumulates in the thoracic region, very rapidly accumulates in the liver followed by the kidneys and ultimately collects in the bladder. As the spins start accumulating in the bladder, since it is now out of the circulatory domain, the image from the bladder becomes intense, so much so, that due to the dynamic range of the 8 bit digitizer, weaker signals arising from other anatomical parts become invisible. Fig. 14 shows a common feature we have seen when ketamine/xylazine anesthetic is used, in that after about 6 minutes of administering the TAM the liver and the kidneys come out brightest in the image. The clear-cut delineation of the anatomical parts and the quality of the image are quite good. In most of our mouse image experiments, 6 minutes after the infusion the thoracic region shows up, in 12 minutes the liver and kidneys are discernible, and in 16-18 minutes the bladder starts showing up. After 20 minutes only the bladder is the visible anatomical part. This trend of thoracic-to-liver-to-kidneys-to-bladder sequence of images has been seen in a reproducible manner in several independent experiments and indicates the general sequence of clearance pathway.

5.3 T_2*Weighted EPR Oxymetry

It was mentioned in the introduction that MRI uses the T_1 and T_2 (in the presence or absence of contrast agents such as Gadolinium (III) chelates) to distinguish different types of tissue. In BOLD MRI the differential oxygenation of hemoglobin is used to produce contrast. In EPR dissolved oxygen, which is a paramagnetic molecule with 2 unpaired electrons, acts as a natural *in vivo* oxymetric reporter. The width of the EPR lines are affected by spin exchange broadening due to the paramagnetic relaxation effect, and as such should provide a direct measure of pO_2 in a non-invasive manner. In simple terms, we will expect anatomical regions containing the spin probe, which are hypoxic, to give narrow lines whose time-domain response will last longer compared to signals arising out of regions which are normoxic. If this is true then one can make a qualitative distinction between regions of different pO_2 by using an approach known as convolution difference spectroscopy. We demonstrate this by applying this to the image data of mouse liver and kidneys presented in Fig. 14. It is now possible to use the same time-domain data set and reconstruct a series of back projection images by progressively deleting the first 100, 200, 300, etc. time points from the

FIDs corresponding to each gradient orientation. As we delete more points only signals from regions which have relatively longer T_2^* (narrower line width) and hence less oxygen will tend to dominate the image. One can even construct difference images by subtracting voxel by-voxel the intensities from images processed from time-domain data with sequential acquisition delays to get regions of a given pO_2.

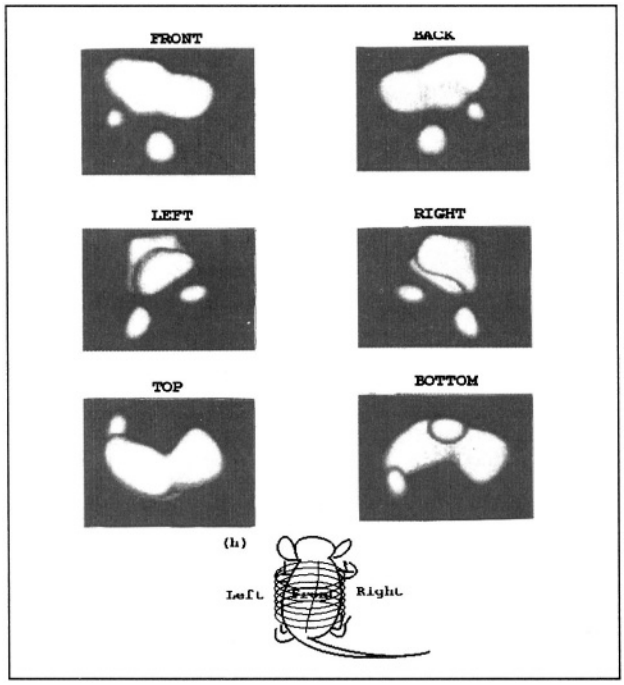

Figure 14. 3-D imaging of liver and kidneys (vide text) of a mouse with a parallel coil resonator with the positioning of the. mouse as shown in the cartoon. 150 μL of 15 mM Oxo31 were infused through tail vein cannulation. Each image consisted of 144 projections with 15°increment of angles in the polar and azimuthal angular coordinates (θ = 0 to 165 and for each θ, ϕ =1 to 165). For each projection 100,000 FIDs were averaged taking about 2 sec. per projection with a total measurement time of time of 5 minutes. Surface rendered views of the images are shown at the indicated directions. Clearly delineated picture of the liver and the two kidneys can be seen. In the right and left views the folding of the liver around the sternum can be clearly visualized.

Fig. 15 shows such a "delayed-processing" strategy applied to the liver-kidney images data, and one can clearly see that the kidneys disappear relatively faster compared to liver as the progressive delay is increased suggesting that under the condition of the ketamine/xylazine anesthetics, the liver must be more hypoxic than the kidneys. It is also possible to generate a map of spatial distribution of oxygen from the image data. To do this we first

construct an image of the object including all the time points in the FID. A series of subsequent images are then constructed by deleting progressively say the first 50, 100, 150 ns from the FIDs. The resulting images will have intensities, in each corresponding pixel of a given location, decreasing exponentially with the time delay governed by the relaxation rate of the spins in that location. In fact, the logarithm of intensities in a given pixel or voxel decreases linearly, depending on the T_2^* of the spins in that location. Since $(T_2^*)^{-1}$ is proportional to the line width, which in turn is proportional to the local pO_2, one can generate an image of $(T_2^*)^{-1}$ (by evaluating pixel wise slopes of the decay of the intensities as a function of delay) that is proportional to *in vivo* oxygen concentration.

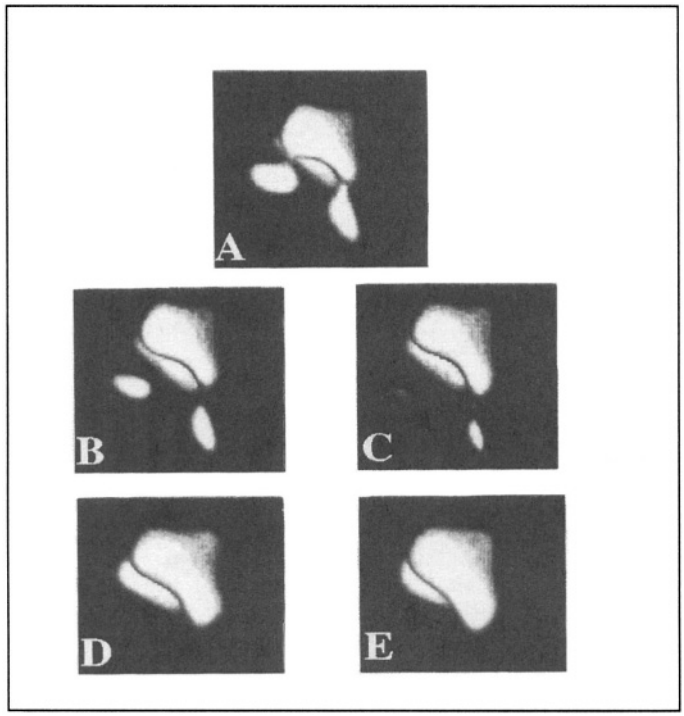

Figure 15. The effect of deleting progressively the initial data points on the image contrast. Regions, which are more oxygenated, undergo relatively rapid attenuation in intensity when the initial time points of the FID are deleted. The five images are reconstructed from the data of Fig. 15, by progressively deleting (A)10, (B)60, (C)110, (D)160 and (E)210 ns of the initial points from the FID. It can be clearly seen that the kidneys are attenuated much faster than the liver, and in (E) the kidneys are barely visible. (See text for details).

All that remains is to calibrate the relaxation rates in terms of pO_2 using spin probe phantoms of known oxygenation level. Thus one can generate an

oxymetric image of live animals from the time-domain data of a single EPR image in a non-invasive manner. The calibration of T_2^* for oxymetry is not straightforward. One has to take into account of the size of the resonator, effect of spin probe concentration and the magnitude of the gradient. Other things being equal, the incremental line width for given imaging gradient was found to be linear in oxygen concentration (for pO_2 variation from 0 to 160 mm of Hg) for the TAM radicals. Fig. 16 shows the oxymetric map of liver and kidneys of a C3H mouse anesthetized with ketamine/xylazene, showing clearly that under this anaesthetic condition liver is more hypoxic than the kidneys, and that the distribution of oxygen is quite heterogeneous.

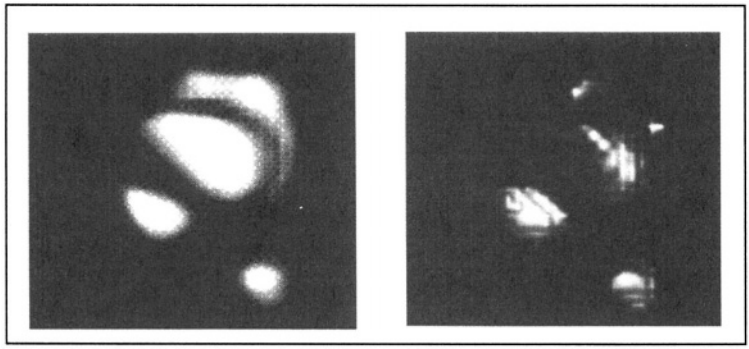

Figure 16. Surface rendered 3D spin density image (A) of liver and kidneys from a C3H mouse (side view); (B) 3D oxygen density maps from the same mouse after treating the image data using the 'delayed processing' scheme described in this chapter. It can be seen clearly that the liver is more hypoxic than the kidneys. Further, it is also evident that the oxygen distribution is quite heterogeneous. While the spin density images do not show much difference in the contrast, the relaxation rate image clearly distinguishes the liver from the kidneys in terms of oxygen distribution. The contrast due to oxygen gradients show much better in a color-coded image.

6. ALTERNATE METHOD OF SPATIAL ENCODING IN TIME- DOMAIN EPR

As we have seen, the FBP method using the free induction decays (FBP-FID) has been shown to be capable of fast RF EPR imaging of small animals such as mice. But imaging with larger gradients lead to prohibitively short T_2^* compromising the image quality. The FBP-FID has inherent drawbacks such as image artifacts and line width limited resolution. Being a pure frequency encoding method, the FBP-FID requires accurate phasing of the sampled magnetization. Besides limiting the sensitivity of the spectrometer, the dead time also leads to considerable distortion in the spectral features, if the resulting truncated FID is not properly phase corrected. The magnetization

components accumulate phase errors in proportion to their observed frequencies. The missing time interval may be too large for proper data reconstruction at high offset frequencies when the dead time is comparable to T_2^*. In addition, the T_2^* of the FID depends on the spectral range according to the equation

$$1/T_2^* = 1/T_2 + \gamma_e \Delta B/2 \quad (26)$$

where, ΔB is the variation of magnetic field over the region of interest. This leads to a differential loss in the integrated intensity of the projections, causing artifacts in the back-projected image (Yamada *et al.,* 2002). Such artifacts will be significant for oblong objects under large gradients. Attempts to increase the resolution by increasing the magnitude of the gradients will lead to further reduction of T_2^* according to equation (26). Besides, being a pure frequency encoding method, the inherent resolution is limited by the line width of the spin probe. Hence an alternative way of spatial encoding that would not be seriously affected by the relaxation time, capable of providing artifact free images, is crucial for the development of time-domain RF EPR *in vivo* imaging. Such a scheme is described below.

6.1 Single Point Imaging

Emid and Creyghton proposed a novel pure phase encoding to achieve resolution enhancement in MRI of solids (Emid and Creyghton, 1985), where very short T_2^*s preclude the application of gradient pulses during the evolution of the spin system. This method has been later reinvented for *in vivo* ^{11}B NMR imaging (Bendel *et al.,* 1990). This technique, known as single point imaging (SPI), (also referenced as constant time imaging (CTI)), has been widely applied, in different modified forms, to solid-state NMR imaging (Axelson *et al.,* 1995; Balcom *et al.,* 1996; Beyea *et al.,* 2000; Choi *et al.,* 1997). The sensitivity and resolution of SPI have been well explored in a pioneering paper by Gravina and Cory (Gravina and Cory, 1994). The method essentially consists of generating k-space information in the presence of pure phase encoding static gradients and is shown to provide artifact free images, because it does not measure the time evolution of the magnetization. The high-resolution capability of the SPI modality has also been recognized nearly 15 years ago in 1D EPR imaging (Maresch *et al.,* 1986). But, no further efforts have been made to evaluate the use of this technique in EPR imaging, perhaps due to the limitation posed by the long data acquisition time. In this section, we critically evaluate the application of SPI to RF EPR imaging by designing phantoms of different sizes and phantoms containing spin probes of different line widths.

Although the principles of SPI are well documented (Emid and Creyghton, 1985), for the sake of EPR readers a brief outline of the technique is presented in this section. A schematic representation of SPI technique is shown in Figure 17. A single, complex data point of the FID, at a fixed evolution time following the pulsed excitation, is collected in the presence of a static magnetic field gradient. As indicated, the gradient is allowed to be 'on' from the start of the pulsed excitation till the data point is accumulated after a time

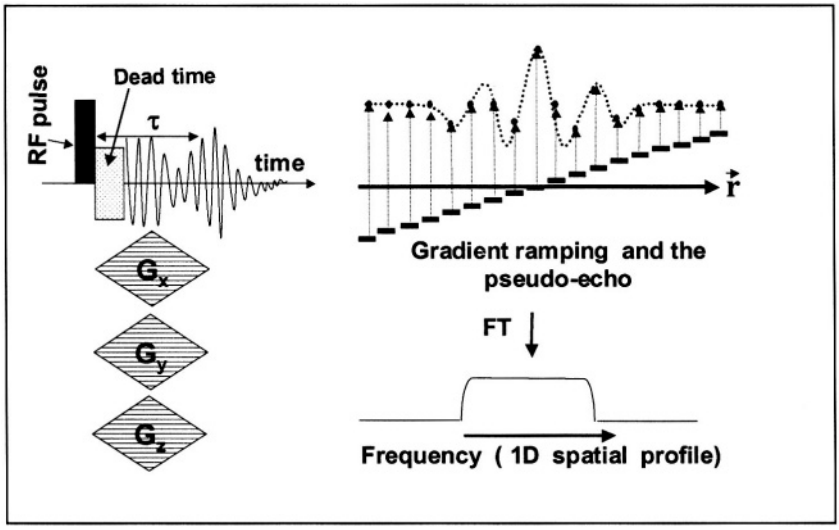

Figure 17. The schematics of SPI data collection. A single point of intensity data is collected as function of gradients at a constant delay τ from the end of the pulse. The Gradients are applied along the three Cartesian axes in a nested loop depending upon the dimensionality of the imaging. On the right, the formation of the pseudo echo as a function of the gradient ramping and the corresponding profile that results on FT is shown for one-dimensional experiment.

duration denoted as 'τ'. For one dimensional image data, the system is subjected to pulsed excitation and the signal (FID) amplitude is collected for each excitation at the same time interval 'τ'. The gradient is incrementally ramped, in equal steps, from a value of -G to +G. The amplitude variations of this single point correspond to phases accumulated as a function of the systematically increasing phase encoding gradient for the duration 'τ'. Thus in SPI, the spatial information is encoded in reciprocal space, S (k), where $k = \gamma G\tau/2\pi$, by the amplitude cycling of the applied phase gradient G. Since the phase encoding gradients are ramped in steps from a positive to negative value through zero, the resulting amplitudes simulate a "pseudo echo" which upon FT provides the one-dimensional spin profile along the phase encoding

direction. This is schematically shown at the right side of Fig. 17. The SPI signal intensity, $S(\tau)$, is related to the local electron spin density, $\rho(\mathbf{r})$ along the gradient direction $\mathbf{r}$ by,

$$S(\tau) = \iiint_{allspace} \rho(r) \exp[i\gamma G.r\tau]dr \qquad (27)$$

In the k-space formalism equation (2) may be written as

$$S(k) = \iiint_{allspace} \rho(r) \exp[i\gamma k.r\tau]dr \qquad (28)$$

Thus the signal intensity, S(k) and the spin density, $\rho(\mathbf{r})$ have a Fourier relationship and therefore direct Fourier image reconstruction algorithm can be applied. For 1D, 2D or 3D imaging, phase-encoding steps in one, two or three dimensions can be applied by a nested looping of the three orthogonal (X, Y, Z, Cartesian axes) gradients. Thus in a 2D SPI experiment, both the spatial dimensions, say X and Y, are phase encoded in contrast to the filtered back projection method using FID, which is a pure frequency encoding technique. Since the image information is collected at a *constant time interval* after the pulse, there is no information on spectral evolution. Hence the SPI images are free from distortions due to the magnetic field inhomogeneity, susceptibility variations and g- and line width anisotropy. The point spread function (PSF) and hence the resolution is unaffected by T_2^* because the magnetization is measured as a function of applied gradient and not as a function of time. The one-dimensional resolution, ΔZ along the Z-direction for a total one-dimensional field of view (FOV_z) is given by

$$\Delta Z = FOV_z / N = 2\pi / (\gamma_e G_z^{max} \tau) \qquad (29)$$

where N is the number of samples of k space measured in the Z direction and γ_e is the gyromagnetic ratio of the electron. The resolution, even for short T_2^* species, is limited mainly by the maximum gradient strength and not by the line width of the EPR spin probe. Even for a broad resonance, image resolution independent of line width can be achieved. However, the G^{max} will be determined by the field of view to be studied and the available B_1 field.
The field of view (FOV) in a given direction is given by

$$FOV = 2\pi / \gamma_e \tau \Delta G \qquad (30)$$

where, ΔG is the incremental gradient step. As can be seen, the finer the gradient steps, or higher the values of τ, the FOV would be correspondingly smaller. However, for the entire field of view to be properly encoded, the pulse should have optimal power and width (τ_p) so that it can provide a

uniform excitation spectrum for the entire frequency bandwidth $\Delta\nu$. In other words,

$$\Delta\nu \geq N / 2\tau \text{ and } \tau_p \leq 2\tau / N \quad (31)$$

If these requirements are not satisfied, then, the high k-space data will be attenuated, resulting in the blurring of sharp edges in the spatial image. For maximum SNR, the time point, τ could be as close to the pulse as possible, immediately following the dead time. Although the pure phase encoding method produces high-resolution images with minimal artifacts, the SPI sequence is time inefficient because it requires N^2 excitations for a 2D image of N^2 pixels. We determine the optimal N based on the viability of this technique for future *in vivo* studies. For a τ of 500 ns, the optimum value of N = 11, for a 2 mm resolution. Using 11X11 phase encoding steps, 2D SPI data image could be collected in 8 minutes with the existing data acquisition system. However, we are currently modifying the SPI acquisition with a commercial Gs/s digitizer with PCI bus and our preliminary results show that a 2D SPI with 121 phase encoding steps can be completed in less than a minute, and a 3D collection with 512 phase encoding steps could be accomplished in about 5 minutes.

6.2 Experimental Considerations for SPI

In SPI modality, phase modulation is monitored as a function of the gradient magnitude and sign. Therefore it is essential to retain the absolute sign of the phases and the consequent frequencies upon FT. This necessitates the collection of quadrature data (two receivers 90° out of phase with each other) for complex FT, as in MRI. To this effect, a quadrature detection scheme was implemented by using a quadrature mixer, and the real and imaginary parts were simultaneously collected using the high-speed digitizer. The schematics of the spectrometer operating in quadrature mode of data collection, used for EPR imaging in the SPI modality and the individual components such as the magnet/gradient assembly, etc., are essentially identical to that described previously. The phase cycling is implemented by storing the real and imaginary parts for the four transmitter phases in the computer memory, and later using software subtraction/addition. The parallel coil resonator tuned to 300 MHz with Q in the range of 20-25 was used. TAM derivatives Oxo63 and Oxo31were used in this study as well.

6.3 SPI Data Collection and Fourier Reconstruction

2-D SPI image data collection was carried out as follows: The transmitter frequency was set at 300 MHz, and excitation pulses (70 ns, 80 W) were repeated every 20 μs corresponding to 50,000 excitations and acquisitions per second. Since the custom-built digitizer is configured to collect 2k samples continuously, the entire FID was collected instead of a single data point. For 2D imaging, a total of 121 complex FIDs, each of 2k length, were collected at a sampling rate of 500 Ms/s. For 2-dimensional images in the XZ plane, the phase-encoding gradients in the X and Z directions were incremented in steps of 0.3 G/cm. For a typical 2-D image, a total of 121, (11 x 11) complex FIDs were collected.

The acquired FIDs in quadrature comprise the image data set from which several single point images can be constructed for different values of τ. Based on the SNR of the acquired signals, a single point in the time-domain at an appropriate time delay τ, was selected, from which the k-space data was constituted into a 11 x 11 square matrix. The matrix was taken first column-wise, each column zero-filled to 64 points and subjected to complex FT to yield 11 separate interferograms. The data were then reorganized to have the 'zero' frequency in the middle of the axis after which the matrix was transposed to give 64 columns of 11 points each. These were again zero-filled to 64 points, Fourier transformed and reorganized to give a 64 x 64 matrix of intensity data, which represents the spatial image. This was rendered in color or gray scale using Matlab® software. For 3D imaging, the gradients were incremented in steps of 0.3 G/cm in a looped fashion (X, Y and Z gradients looped inside one another from 1.5 G/cm to –1.5 G/cm in 11 steps) corresponding to 11 x 11 x 11 SPI data at each delay point τ. The resulting data were Fourier transformed consecutively in 3 dimensions after zero-filling the data sets to 64 points in each dimension, as outlined earlier. The final 3D image data of matrix size 64 x 64 x 64 was surface rendered in a Silicon Graphics Indigo2 workstation using the program Voxelview®.

For the sake of comparing FBP-FID and SPI data, projection data were acquired from the same phantom by rotating the gradient in the XZ plane in 180, 10° steps. The gradient magnitude was 0.8G /cm. For the reconstruction of the 2D image using back projection, spectral profiles were obtained in a single channel IF mode by mixing the transmit frequency of 300 MHz, with a local oscillator frequency of 320 MHz. The resulting signals, centered on 20 MHz, were sampled at 500 Ms/s. For each profile, 50,000 FIDs were averaged. The acquired FIDs were Fourier transformed after zero filling to 8 k points. A Shepp-Logan filter was used and the 2D image was reconstructed from 255 points centered on the zero-gradient frequency.

To verify the imaging capability of the SPI method, both 2D and 3D imaging of phantom objects, containing paramagnetic spin probes were carried out. Three different phantoms were considered to (i) investigate the line width dependent artifacts in the image, (ii) examine the image uniformity when long objects are imaged, and (iii) to evaluate the resolution in 3D imaging.

6.4 Representative Results from SPI EPR at RF

To examine the influence of the line widths on the EPR images obtained using the SPI or the filtered back projection (FBP) techniques, a three-tube phantom containing spin probe solutions of differing line widths was imaged. The three tubes contained air-saturated Oxo63, argon-saturated Oxo63, and argon-saturated Oxo31 solutions of differing spin count. The dimension of the phantom and the spin content and the line widths of the spin probe solutions are given in Figure 18. Transverse, 2D spin density images of the phantom, obtained by both the SPI and FBP techniques, given in Figure 18, show a general agreement with the physical dimensions of the phantom. The SPI image was obtained with 11 phase encoding steps along each direction with τ = 490 ns. This leads to an FOV of 2.4 cm and a resolution of 2 mm (equations 4 and 5). The gradient magnitude for the FBP image was 0.8 G/cm. The resolution expected for the frequency encoding, FBP method is given by,

$$\Delta Z = 2 / \gamma_e G_z T_2 \qquad (32)$$

for a Lorentzian line shape of width $1/\pi T_2$. Thus, the line width dependent resolution is one of the major limitations of the FBP method. It was observed that in the FBP the intensities of the images reconstructed from time-domain data do not faithfully represent the actual spin count in the samples. Highest intensity is observed for tube C that contains the spin probe solution (argon saturated, Oxo31) of narrowest line width, although its actual spin count is only one fifth of tube B. The tube with large line width shows the least intensity. This artifact is due to the significant loss of the exponentially decaying FID of the decay time-domain signals from the broader resonances, in comparison to the narrower ones, originating from the spectrometer dead time. To view all the three tubes in the figure, the overall intensity scale has to be enhanced significantly, due to the poor overall dynamic range of the image. This leads to a large contour for tube C, apparently larger than the physical dimension of the tube itself. In contrast, the pattern of the intensities of the three tubes in the SPI image shows a very uniform size and faithful representation of the spin count, almost independent of the line width.

Phantom Imaging: Imaging of a large object by FBP method poses many problems as discussed earlier. With current technical capability, we have optimized the resonator size to be 25 x 25 mm and the gradient magnitude to 0.5-0.6 G/cm. But even for this size, spectral and hence image distortion has been observed. In fact, this was one of the driving forces to look for an alternate imaging scheme.

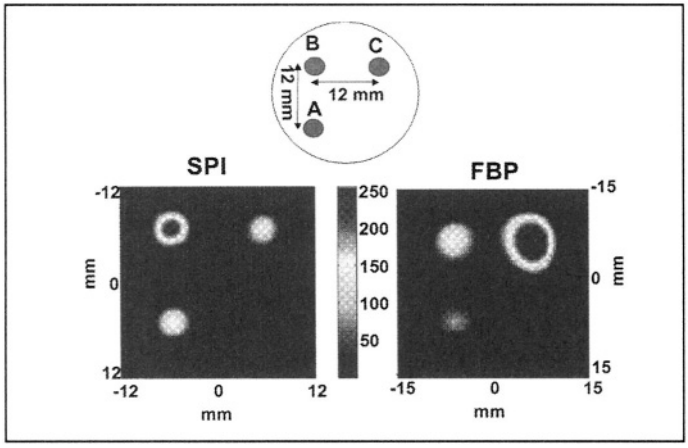

Figure 18. Arrangement of a three-tube phantom containing the spin probe Oxo63 (top) and the corresponding SPI (bottom left) and FBP images (bottom right). The tube A contained 2.5 mM fully aerated Oxo63 (line width 280 mG), B contained 5 mM de-aerated Oxo63 (line width: 180 mG) and C contained 1.25 mM de-aerated Oxo31(line width: 130 mG). The SPI images faithfully reproduce the dimensions of the tubes and the relative intensities are also proportional to the spin count. The FBP images have a much lower dynamic range, and in order to see the image of tube A (with the broadest line width probe), the contour levels are to be so lowered that the image of tube A (with the narrowest line width probe) gets over-emphasized with exaggerated dimension.

To compare the relative quality of FID-FBP and SPI images, we once again employed the X-phantom of Fig. 13. The holes were filled with deoxygenated 2 mM solution of Oxo31. The phantom was oriented in such a way that the plane of the X-shaped holes containing the spin probe was parallel to the Cartesian XZ plane (the Y-axis is perpendicular to the plane of the paper). A 2D SPI image of the X-phantom, generated from 11 x 11 phase encoding steps ($\tau = 450$, $G_{max} = 1.5$ G) is given in Figure 19B. From the Fourier reconstructed image, it was found that the measured dimensions of the spin distribution in the image matched well with the actual dimensions of the X-phantom. Projection data were acquired from the same phantom by rotating the gradient in the XZ plane in 10° steps. The gradient magnitude was 0.8 G /cm. The 2D FBP image reconstructed from 36 projections is shown in Fig. 19C. It can be seen that, although the image is reproduced well, there are some artifacts such as incompletely defined edges along the long axes of the X-phantom, as well

as some orientation of the gradient. Additionally, as pointed out earlier, the integrated intensity of each and every projection profile, which should remain constant for a given object, is not so when the objects are too oblong or asymmetric and the gradients are rather large. Though these artifacts can be reduced to a large extent by suitably scaling the integrated area of the projections, and modifying the filters, they cannot be eliminated entirely. Numerical treatment of the image data will also be an alternate way to reduce such artifacts. In the SPI procedure, the absence of spectral information in a given image, gives rise to well-defined images without any edge artifacts or distortion of the dimensions.

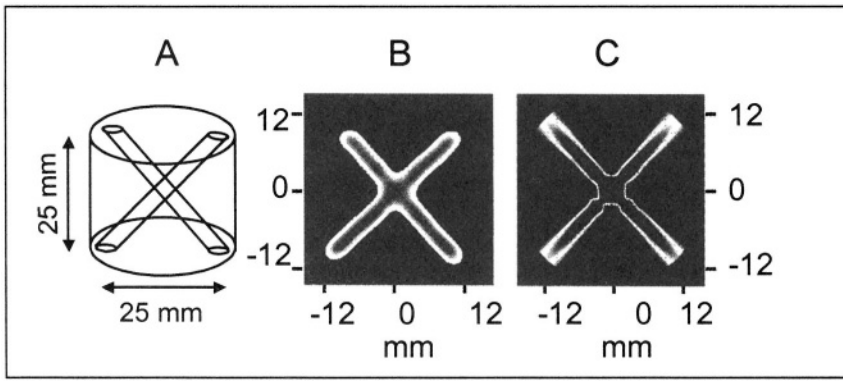

Figure 19. Comparison between SPI and FBP. A. Schematics of the X-phantom described in the text. B. The SPI image with 11 x 11 matrix size faithfully reproducing the 2D image of the phantom. C, The FBP image showing artifacts at the edges and the center of the X phantom. See text for explanation.

Three-dimensional imaging: In order to examine the 3-D EPR imaging capabilities of the SPI technique, a spiral phantom of outer diameter of 2.4 cm and length of 2.5 cm was used. The spiral, consisting of 5 turns of glass tubing of 1.4 mm bore, was filled with approximately 450 μl of 2 mM Oxo63 in saline. The spiral was loaded coaxially in a 2.5x2.5 cm, cylindrical parallel coil resonator. The schematics of the phantom and the 3D images (a few perspectives) are shown in Fig. 20. It can be seen that the images reproduce the shape of the spin distribution faithfully. As in 2-D imaging experiments, the 3-D images obtained from SPI were also of enhanced quality compared to the ones in the time-domain mode obtained from back-projection scheme with respect to resolution.

6.5 Spectroscopic Imaging with SPI

Although SPI produces well-resolved images with the spectral information completely deconvoluted from spatial information, it is possible to recover spectral information from a series of SPI images and examining the dependence of pixel-by-pixel intensity of a series of images as a function of the delay τ just as in the case of the oxymetric strategy outlined in section VI. The important point to note is that for a given set of gradient settings, the field of view is inversely proportional to the delay τ according to Eq.[29]. Fig. 21 shows the effect of systematically varying the single point acquisition delay τ, which leads to a gradual decrease in the field of view producing a 'zoom-in' effect. The phantom used for this purpose comprised of four tubes of Oxo63 (2 mM) with different line widths. The actual dimensions and distance between the four samples were reproduced accurately in all the images with the FOV decreasing in inverse proportion to the delay τ. In order to make the individual pixel intensities to correspond to identical spatial coordinates in a series of images with different τ values, it is necessary to digitally enlarge or diminish the image size appropriately such that the pixels in the modified images correspond to the same spatial coordinates, limited by the accuracy of numerical interpolation. Once this is done, we can look at the slope of the intensity as a function of τ and derive information on the spatial variation in T_2* and hence evaluate quantitative oxymetric information. Our preliminary results of SPI experiments on phantoms and mice to evaluate *in vivo* pO_2 are indeed quite promising.

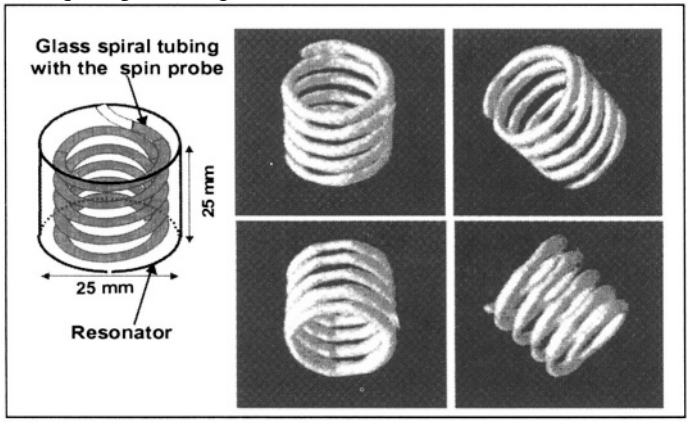

Figure 20. 3D SPI image of a spiral phantom. Schematics of the glass spiral tubing filled with 2 mM Oxo63 in saline. The inside diameter of the gals tube was 1.4 mm and the capacity of the spiral was around 450 μL. The gradient increment was 0.3 G/cm and the maximum gradient was 1.5 G/cm. The data matrix size was 11 x 11 x 11 (1331 single points) and the image matrix was 64 x 64 x 64. The 3D rendering at a few orientations shown on the left was carried out using the software Voxelview® in a silicon graphics Indigo2 workstation. The quality of the image is excellent and dimensions matched very well with those of the phantom.

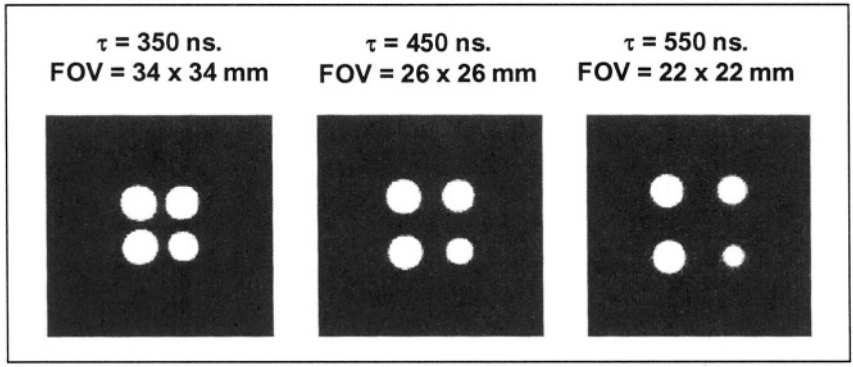

Figure 21 The effect of the progressive delay in gradually reducing the FOV. The sample consisted of four tubes of Oxo63 with different line widths. The 2D image data corresponded to 11 x 11 matrix size, and the final reconstructed image has a size of 64 x 64. The three images correspond to delays τ of 350, 450, and 550 ns. The corresponding FOVs calculated for a gradient step size of 0.3 G/cm are indicated in the figure. The 2D images of a four-tube phantom can be seen to show a gradual 'zoom-in' as τ increases.

7. SUMMARY AND FUTURE DIRECTIONS

As we have seen, very useful *in vivo* functional images, which can report on the physiological conditions such as tissue redox status, oxygen tension, etc. can be obtained through the use of EPR imaging employing non-toxic, implantable or water-soluble, biocompatible spin probes. As to what mode of approach, whether time-domain or CW, should be chosen will depend on the nature of the particular spin probe used and the kind of physiology interrogated. When temporal resolution (because of fast pharmacokinetics) is of paramount importance, time-domain methods would be the preferred choice. Added advantages of time-domain methods over CW methods are the availability of spectral information co-registered in time-domain data of the spatial image itself. The SPI mode of spatial encoding promises far superior quality of image data. With improved data collection strategies, SPI may in fact turn out to be the method of choice for small animal imaging in time-domain EPR. Time-domain EPR methods will be complementary to the CW modality and have the advantage of rapid data acquisition and reliable phramacokinetics.

There are several aspects of time-domain EPR that still need to be addressed, however, before practical human applications can be envisaged. Foremost among these is the availability of FDA approved narrow-line spin probes. Although the TAM derivatives are very promising, FDA approval is still awaited. Future directions should also address development of other

biocompatible oxygen-sensitive narrow-line paramagnetic compounds for use in both CW and time-domain *in vivo* spectroscopy and imaging.

In the pulsed mode of EPR imaging, we have to critically address the SAR problem since it involves the application of intense RF pulses of very short duration to larger biological objects. Stochastic or pseudo random pulsed excitation coupled with correlation techniques (such as Hadamard transform) have been developed for solid state deuteron NMR which employ RF powers reduced by at least two orders of magnitude, and yet achieve SNR comparable to the high power single pulse mode of excitation (Ernst, 1970; Ziessow and Bluemich, 1974). We have already carried out EPR experiments at 300 MHz on phantom objects with pseudo random excitation and Hadamard transform, and are able to reduce the power requirements by at least an order of magnitude without compromising the sensitivity (Pursley *et al.,* 2003). The use of the latest DSP (digital signal processing) techniques that have made a revolution in the cellular communication area, in improving EPR spectrometer sensitivity, will be of considerable importance. Sub-sampling techniques, that apparently defy the Nyquist theorem, are also being implemented in time-domain as well as CW techniques (Hyde *et al.,* 1998; see ch. 7 in volume 24) to take advantage of better bit-resolution achievable in low frequency digitizers. Development of high sensitivity resonators, especially for time-domain EPR for large volume applications is another important area. Pulse shaping (Freeman, 1998), which is a standard technique in accomplishing uniform selective excitation in NMR and slice selection in MRI, has not yet been explored in low-frequency time-domain EPR imaging, although it has been used at X-band (Crepeau *et al.,* 1989). The main bottleneck had been the non-availability of sub-nanosecond time-resolution required for constructing decent, tailored pulse shapes such as sinc or gaussian with total widths under 100 ns. These have now become available, and our laboratory is currently examining the use of shaped pulses in time-domain EPR.

ACKNOWLEDGEMENTS

We are grateful to Professors G. R. Eaton and S. S. Eaton for giving us the opportunity to contribute this Chapter to the Festschrift being brought out to felicitate Professor James Hyde. We also take this opportunity to thank our colleagues, J. B. Mitchell, A. Russo, J. A. Cook, R. Murugesan, N. Devasahayam, R. Tschudin and T. Pohida who have contributed immensely and continue to aid in the development of time-domain Radio frequency EPR imaging at the National Institutes of Health.

8. REFERENCES

Abragam, A.,1961, *The Principles of Nuclear Magnetism,* Oxford University Press, London .

Afeworki, M., Miller, N. R., Devasahayam, N., Cook, J., Mitchell, J. B., Subramanian, S. and Krishna, M. C., 1998, Preparation and EPR studies of lithium phthalocyanine radical as an oxymetric probe, *Free. Radical. Bio. Med.* **25**: 72-78.

Afeworki, M., van Dam, G. M., Devasahayam, N., Murugesan, R., Cook, J., Coffin, D., A-Larsen, J. H. A., Mitchell, J. B., Subramanian, S. and Krishna, M. C., 2000, Three-dimensional whole body imaging of spin probes in mice by time-domain radiofrequency electron paramagnetic resonance, *Magn. Reson. Med.* **43**: 375-382.

Alecci, M., Brivati, J. A., Placidi, G. and Sotgiu, A., 1998a, A radiofrequency (220-MHz) Fourier transform EPR spectrometer, *J. Magn. Reson.* **130**: 272-280.

Alecci, M., Brivati, J. A., Placidi, G., Testa, L., Lurie, D. J. and Sotgiu, A., 1998b, A submicrosecond resonator and receiver system for pulsed magnetic resonance with large samples, *J. Magn. Reson.* **132**: 162-166.

Alecci, M., Ferrari, M., Quaresima, V., Sotgiu, A. and Ursini, C. L., 1994, Simultaneous 280-MHz EPR Imaging of rat organs during nitroxide free-radical clearance, *Biophys. J.* **67**: 1274-1279.

Alecci, M., Gualtieri, G., Sotgiu, A., Testa, L. and Varoli, V., 1991, Multipolar Magnet for Low-Frequency Esr Imaging, *Meas. Sci. Technol.* **2**: 32-37.

Alecci, M., Nicholson, I. and Lurie, D. J., 1996, A novel multiple-tuned radiofrequency loop-gap resonator for use in PEDRI, *J Magn Reson B* **110**: 82-86.

Alecci, M., Penna, S. D., Sotgiu, A., Testa, L. and Vannucci, I., 1992, Electron paramagnetic resonance spectrometer for three-dimensional in vivo imaging at very low frequency, **63**: 4263-4270.

Ardenkjaer-Larsen, J. H., Laursen, I., Leunbach, I., Ehnholm, G., G., W. L., Petersson, J. S. and Golman, K., 1998, EPR and DNP properties of certain novel single electron contrast agents intended for oximetric imaging, *J. Magn. Reson.* **133**: 1-12.

Axelson, D. E., Kantzas, A. and Eads, T., 1995, Single point H-1 magnetic resonance imaging of rapid solids, *Can. J. Appl. Spectrosc.* **40**: 16-26.

Balcom, B., Beyea, S. D., Green, D. P., Armstrong, R. L. and Bremner, T. W., 1996, Single-Point Ramped Imaging with T1 Enhancement (SPRITE), *J. Magn. Reson.***123**: 131-134.

Bandettini, P. A.; Wong, E. C.; Hinks, R. S.; Tikofsky, R. S., and Hyde, J. S., 1992, Time course EPI of human brain function during task activation, *Magn. Reson. Med.* **25**: 390-397

Bendel, P., Davis, M., Berman, E. and Kabalka, G. W., 1990, A method for imaging nuclei with short T2 relaxation and its application to Boron-11 NMR imaging of a BNCT agent in an intact rat, *J. Magn. Reson.* **88**: 369-375.

Beyea, S. D., Balcom, B. J., Mastikhin, I. V., Bremner, T. W., Armstrong, R. L. and Grattan-Bellew, P. E., 2000, Imaging of heterogeneous materials with a turbo spin echo single-point imaging technique, *J. Magn. Reson.* **144**: 255-265.

Bloch, F., Hansen, W. W. and Packard, H. E., 1946, Nuclear Induction, *Phys. Rev.* **69**: 127-131.

Botto, R. E., Gody, G. D., Dieckman, S. L., French, D. C., Gopalsmai, N. and Rizo, P., 1996, Three-dimensional magnetic resonance microscopy of materials, *Solid. State. Nucl. Magn Reson.* **6**: 389-402.

Bourg, J., Krishna, M. C., Mitchell, J. B., Tschudin, R. G., Pohida, T. J., Friauf, W. S., Smith, P. D., Metcalfe, J., Harrington, F. and Subramanian, S., 1993, Radiofrequency FT EPR spectroscopy and imaging, *J. Magn. Reson. B* **102**: 112-115.

Bracewell, R. N., 1994, *Two dimensional imaging,* Prentice Hall, New York .

Brivati, J. A., Stevens, A. D. and Symons, M. C. R., 1991, A radiofrequency ESR spectrometer for in vivo imaging, *J. Magn. Reson.* **92**: 480-489.

Choi, S., Tang, X. W. and Cory, D. G., 1997, Constant time imaging approaches to NMR microscopy, *Int. J. Imag. Tech. Sys.* **8**: 263-276.

Crepeau, R. H., Dulcic, A., Gorchester, J., Saarinen, T. R., and Freed, J. H., 1989, Composite pulses in time-domain ESR, *J. Magn. Reson.* **84**: 184-190.

Devasahayam, N., Subramanian, S., Murugesan, R., Cook, J. A., Afeworki, M., Tschudin, R. G., Mitchell, J. B. and Krishna, M. C., 2000, Parallel coil resonators for time-domain radiofrequency electron paramagnetic resonance imaging of biological objects, *J. Magn. Reson.* **142**: 168-176.

Eaton, G. R., Eaton, S. E. and Ohno, K. ,ed., 1991, *EPR imaging and in vivo EPR,* CRC Press, Boca Raton.

Eaton, G. R., Eaton, S. S. and Maltempo, M. M., 1989, Three approaches to spectral spatial EPR imaging, *Appl. Radiat. Isotopes* **40**: 1227-1231.

Eaton, G. R., Eaton, S. S. and Rinard, G. A., 1998, Frequency dependence of EPR sensitivity, in *Spatially Resolved Magnetic Resonance: Methods, Materials, Medicine, Biology, Rheology, Geology, Ecology, Hardware,* P. Blümler, B. Blümich, R. Botto, R. Botto andE. Fukushima.ed.), Wiley-VCH. Weinheim

Eaton, S. S. and Eaton, G. R., 1986, EPR imaging, *Spectroscopy* **1**: 32-35.

Eaton, S. S. and Eaton, G. R., 2000, Relaxation times of organic radicals and transition metal ions. in *Biological Magnetic Resonance,* vol. 19 L. J. Berliner, S. S. Eaton andG. R. Eaton.eds.) pp. 29-154

Eaton, S. S., Maltempo, M. M., Stemp, E. D. A. and Eaton, G. R., 1987, Three-dimensional EPR imaging with one spectral and two spatial diemnsions, *Chem. Phys. Lett.* **142**: 567-569.

Edelstein, W. A., Hutchison, J. M. S., Johnson, G. and Redpath, T. W., 1980, Spin-warp NMR imaging and applications to human whole-body imaging, *Phys. Med. Biol.* **25**: 751-756.

Emid, S. and Creyghton, J. H. N., 1985, High-resolution NMR imaging in solids, *Physica B* **128**: 81-83.

Ernst, R. R., 1966, Sensitivity enhancement in magnetic resonance, *Adv. Magn. Reson.* **2**: 1-135.

Ernst, R. R., 1970, Magnetic resonance with stochastic excitation, *J. Magn. Reson.* **3**: 10-27.

Ernst, R. R. and Anderson, J. R., 1966, Application of Fourier spectroscopy to nuclear magnetic resonance, *Rev. Sci. Instrum.* **37**: 93-103.

Ewert, U. and Herrling, T., 1986, Spectrally resolved EPR tomography with stationary gradient, *Chem. Phys. Lett.* **129**: 516-520.

Farrar, T. C. and Becker, E. D.,1971, *Pulse and Fourier Transform NMR: Introduction to Theory and Methods,* Academic Press, New York .

Field, L. D., Sternhill, S. and Sternhill, L. S.,1989, *Analytical NMR* John Wiley & Son, New York.

Fowler, J. S., Volkow, N. D., Wang, G. J., Ding, Y. S. and Dewey, S. L., 1999, PET and drug research and development, *J. Nucl. Med.* **40**: 1154-1163.

Freeman, R., 1998, Shaped radiofrequency pulses in high resolution NMR, *Progress in NMR Spectroscopy* **32**: 59-106.

Froncisz, W. and Hyde, J. S., 1982, The Loop-Gap Resonator - a New Microwave Lumped Circuit Electron-Spin-Resonance Sample Structure, *J. Magn. Reson.* **47**: 515-521.

Fujii, H. and Berliner, L. J., 1985, One-dimensional and two-dimensional Electron-Paramagnetic-Resonance imaging studies on phantoms and plant specimens, *Magn. Reson. Med.* **2**: 275-282.

Gadian, D. G.,1995, *NMR and its Applications toLiving Systems,* Oxford University Press, Oxford.

Gallez, B., Debuyst, R., Dejehet, F., Liu, K. J., Walczak, T., Goda, F., Demeure, R., Taper, H. and Swartz, H. M., 1998, Small particles of fusinite and carbohydrate chars coated with aqueous soluble polymers: Preparation and applications for in vivo EPR oximetry, *Magn. Reson. Med.* **40**: 152-159.

Golman, K., Leunbach, I., Ardenkjaer-Larsen, J. H., Ehnholm, G. J., Wistrand, L. G., Petersson, J. S., Jarvi, A. and Vahasalo, S., 1998, Overhauser-enhanced MR imaging (OMRI), *Acta. Radiol.* **39**: 10-17.

Golman, K., Petersson, J. S., Ardenkjaer-Larsen, J. H., Leunbach, I., Wistrand, L. G., Ehnholm, G. and Liu, K. C., 2000, Dynamic in vivo oxymetry using Overhauser enhanced MR imaging, *J. Magn. Reson. Imaging.* **12**: 929-938.

Gravina, S. and Cory, D. G., 1994, Sensitivity and resolution of constant-time imaging, *J. Magn. Reson. B* **104**:53-61.

Griffiths, D. J.,1989, *Introduction to Electrodynamics* Prentice-Hall, Englewood Cliffs, NJ .

Haacke, E. M, Brown, R. W., Thompson, M. R. and Venkatesan, R.,1999, *Magnetic Resonance Imaging: Physical Principles and Sequence Design* John Wiley & Sons, New York .

Halpern, H. J. and Bowman, M. K., 1991, Low frequency EPR spectrometers: MHz range, in *EPR Imaging and in vivo EPR* G. R. Eaton, S. S. Eaton andK. Ohno.ed.), CRC Press. Boca Raton

Halpern, H. J., Spencer, D. P., van Polen, J., Bowman, M. K., Nelson, A. C., Dowey, E. M. and Teicher, B. A., 1989, Imaging radio frequency electron-spin-resonance spectrometer with high resolution and sensitivity for in vivo measurements, *Rev. Sci. Instrum.* **60**: 1040-1050.

Halpern, H. J., Yu, C., Peric, M., Barth, E., Grdina, D. J. and Teicher, B. A., 1994, Oximetry deep in tissues with low-frequency electron paramagnetic resonance, *Proc. Natl. Acad. Sci. USA* **91**: 13047-13051.

Halpern, H. J., Yu, C., Peric, M., Barth, E. D., Karczmar, G. S., River, J. N., Grdina, D. J. and Teicher, B. A., 1996, Measurement of differences in pO2 in response to perfluorocarbon carbogen in FSa and NFSa murine fibrosarcomas with low-frequency electron paramagnetic resonance oximetry, *Radiat. Res.* **145**: 610-618.

Herman, G. T.,1980, *Image Reconstruction from Projections: The Fundamentals of Computerized Tomography* Acadmic Press, New York .

Hirata, H., Walczak, T. and Swartz, H. M., 1997, An improved inductive coupler for suppressing a shift in the resonance frequency of electron paramagnetic resonance resonators, *Rev. Sci. Instrum.* **68**: 3187-3191.

Hyde, J. S., Froncisz, W. and Oles, T., 1989, Multipurpose loop gap resonator, *J. Magn. Reson.* **82**: 223-230.

Hyde, J. S., Mchaourab, H. S., Camenisch, T. G., Ratke, J. J., Cox, R. W. and Froncisz, W., 1998, Electron paramagnetic resonance detection by time-locked subsampling, *Rev. Sci. Instrum.* **69**: 2622-2628.

Ilangovan, G., Zweier, J. L. and Kuppusamy, P., 1999, Preparation and characterization of a highly sensitive EPR oximetry probe for biological application, *Free. Radical. Bio. Med.* **27**: S106-S106.

Ilangovan, G., Zweier, J. L. and Kuppusamy, P., 2000a, Electrochemical preparation and EPR studies of lithium phthalocyanine. Part 2: Particle-size-dependent line broadening by molecular oxygen and its implications as an oximetry probe, *J. Phys. Chem. B* **104**: 9404-9410.

Ilangovan, G., Zweier, J. L. and Kuppusamy, P., 2000b, Electrochemical preparation and EPR studies of lithium phthalocyanine: Evaluation of the nucleation and growth mechanism and evidence for potential-dependent phase formation, *J. Phys. Chem. B* **104**: 4047-4059.

Jiang, J. J., Nakashima, T., Liu, K. J., Goda, F., Shima, T. and Swartz, H. M., 1996, Measurement of pO_2 in liver using EPR oximetry, *J. Appl. Physiol.* **80**: 552-558.

Johnson, C. C. and Guy, A. W., 1972, Nonionizing electromagnetic wave effects in biological materials and systems, *Proc. I. E. E. E.* **60**: 6.

Kak, A. C. and Slaney, M.,1988, *Principles of Computerized Tomographic Imaging* IEEE Press, New York.

Kevan, L. and Bowman, M. K., ed., 1990, *Modern Pulsed and Continuous-wave Electron Spin Resonance* John Wiley & Sons, New York.

Krishna, M. C., Afeworki, M., Devasahayam, N., Cook, J., Subramanian, S. and Mitchell, J. B., 1999, In vivo free radical detection and imaging by EPR: Non-invasive mapping of tissue oxygen status., *Free. Radical, Bio. Med.* **27**: S154-S154.

Kumar, A., Welti, D. and Ernst, R. R., 1975, NMR Fourier zeugmatography, *J. Magn. Reson.* **18**: 69-83.

Kuppusamy, P., Afeworki, M., Shankar, R. A., Coffin, D., Krishna, M. C., Hahn, S. M, Mitchell, J. B. and Zweier, J. L., 1998, In vivo electron paramagnetic resonance imaging of tumor heterogeneity and oxygenation in a murine model, *Cancer. Res.* **58**: 1562-1568.

Kuppusamy, P., Chzhan, M., Vij, K., Shteynbuk, M., Lefer, D. J., Giannelia, E. and Zweier, J. L., 1994, Three-dimensional spectral-spatial EPR imaging of free radicals in the heart: A technique for imaging tissue metabolism and oxygenation, *Proc. Natl. Acad. Sci. USA* **91**: 3388-3392.

Kuppusamy, P., Chzhan, M., Wang, P. H. and Zweier, J. L., 1996, 3D gated EPR imaging of the beating heart, *Biophys. J.* **70**: Su409-Su409.

Kuppusamy, P., Li, H. Q., Ilangovan, G., Cardounel, A. J., Zweier, J. L., Yamada, K., Krishna, M. C. and Mitchell, J. B., 2002, Noninvasive imaging of tumor redox status and its modification by tissue glutathione levels, *Cancer. Res.* **62**: 307-312.

Kwong, K. K., Belliveau, J. W., Chesler, D. A., Goldberg, I. E., Weisskoff, R. M., Poncelet, B. P., Kennedy, D. N., Hoppel, B. E., Cohen, M. S., Turner, R., Cheng, H.-M., Brady, T. J., and Rosen, B. R., 1992, Dynamic magnetic resonance imaging of brain activity during primary sensory stimulation, *Proc. Natl. Acad. Sci. USA* **89**: 5675-5679.

Lauterbur, P. C., 1973, Image formation by induced local interactions: Examples employing nuclear magnetic resonance, *Nature* **242**: 190-191.

Lauterbur, P. C., Levin, D. N. and Marr, R. B., 1984, Theory and simulation of NMR spectroscopic imaging and field plotting by projection reconstruction involving an intrinsic frequency dimension, *J. Magn. Reson.* **59**: 536-541.

Liu, K. J., Gast, P., Moussavi, M., Norby, S. W., Vahidi, N., Walzak, T., Wu, M. and Swartz, H. M., 1993, Lithium phthalocyanine: a probe for electron paramagnetic resonance oximetry in viable biologic systems, *Proc. Natl. Acad. Sci. USA* **90**: 5438-5442.

Liu, K. J., Hoopes, P. J., Rolett, E. L., Beerle, B. J., Azzawi, A., Goda, F., Dunn, J. F. and Swartz, H. M., 1997, Effect of anesthesia on cerebral tissue oxygen and cardiopulmonary parameters in rats, *Adv. Exp. Med. Biol.* **411**: 33-39.

Lowe, I. J. and Norberg, R. E., 1957, Free-induction decays in solids, *Phys. Rev.* **107**: 46-61.

Lurie, D. J., Bussell, D. M., Bell, L. H. and Mallard, J. R., 1988, Proton-electron double magnetic resonance imaging of free radical solutions, *J. Magn. Reson.* **76**: 366-370.

Lurie, D. J., Hutchison, J. M. S., Bell, J. H., Nicholson, I., Bussell, D. M. and Mallard, J. R., 1989, Field cycled proton-electron double resonance imaging of free radicals in large aquous samples, *J. Magn. Reson.* **84**: 431-437.

Maltempo, M. M., 1986, Differentiation of spectral and spatial components in EPR imaging using 2-D image reconstruction algorithms, *J. Magn. Reson.* **69**: 156-163.

Maltempo, M. M., Eaton, S. S. and Eaton, G. R., 1987, Spectral-spatial two dimensional EPR imaging, *J. Magn. Reson.* **72**: 449-455.

Maltempo, M. M., Eaton, S. S. and Eaton, G. R., 1988, Reconstruction of spectral-spatial two dimensional images from incomplete sets of projections without prior knowledge of the component spectra, *J. Magn. Reson.* **77**: 75-83.

Maresch, G. G., Mehring, M. and Emid, S., 1986, High resolution ESR imaging, *Physica* **138B**: 261-263.

Marr, R. B., Chen, C.-N. and Lauterbur, P. C., 1981, *Mathematical Aspects of Computerized Tomography* Springer-verlag, New York .

Moonen, C. T. W., Bandettini, P. A., Aquirre, G. K. and Heilman, H. P., 1999, *Functional MRI* Springer Verlag, New York.

Murugesan, R., Afeworki, M., Cook, J. A., Devasahayam, N., Tschudin, R., Mitchell, J. B., Subramanian, S. and Krishna, M. C., 1998, A broadband pulsed radio frequency electron paramagnetic resonance spectrometer for biological applications, *Rev. Sci. Instrum.* **69**: 1869-1876.

Murugesan, R., Cook, J. A., Devasahayam, N., Afeworki, M., Subramanian, S., Tschudin, R., Larsen, J. A., Mitchell, J. B., Russo, A. and Krishna, M. C., 1997, In vivo imaging of a stable paramagnetic probe by pulsed-radiofrequency electron paramagnetic resonance spectroscopy, *Magnet. Reson. Med.* **38**: 409-414.

Natterer, F.,1986, *The Mathematics of Computerized Tomography* Wiley, Chichester.

Ogawa, S., Tank, D. W., Menon, R., Ellerman, J. M., Kim, S. G., Merkle, H. and Ugurbill, K., 1992, Intrinsic signal changes accompanying sensory stimulation - functional brain mapping with magnetic resonance imaging, *Proc. Natl. Acad. Sci. (USA)* **89**: 5951-5955.

Ohara, J. A., Goda, F., Liu, K. J., Bacic, G., Hoopes, P. J. and Swartz, H. M., 1995, The pO2 in a Murine Tumor after Irradiation - an in-vivo Electron-Paramagnetic-Resonance oximetry study, *Radiat. Res.* **144**: 222-229.

Ono, M., Ogata, T., Hsieh, K. C., Suzuki, M., Yoshida, E. and Kamada, H., 1986, L-band electron-spin-resonance spectrometer using a loop-gap resonator for in vivo analysis, *Chem. Lett.* : 491-494.

Panagiotelis, I., Nicholson, I., Foster, M. A. and Hutchison, J. M. S., 2001, T*(1e) and T*(2e) maps derived in vivo from the rat using longitudinally detected electron spin resonance phase imaging; Application to abdominal oxygen mapping. *Magnet. Reson. Med.* **46**:1223-1232.

Pfenninger, S., Forrer, J., Schweiger, A. and Weiland, T., 1988, Bridged loop gap resonator - a resonant structure for pulsed electron-spin-resonance transparent to high-frequency radiation, *Rev. Sci. Instrum.* **59**: 752-760.

Pfenninger, S., Froncisz, W., Forrer, J., Luglio, J. and Hyde, J. S., 1995, General-method for adjusting the quality factor of EPR resonators, *Rev. Sci. Instrum.* **66**: 4857-4865.

Placidi, G., Alecci, M., Colacicchi, S. and Sotgiu, A., 1998, Fourier reconstruction as a valid alternative to filtered back projection in iterative applications: Implementation of Fourier spectral spatial EPR imaging, *J. Magn. Reson.* **134**: 280-286.

Polk, C, and Postow, E., 1996, *Handbook of Biological Effects of Electromagnetic Fields, 2nd Edition* CRC Press, Boca Raton, FL.

Poole, C, P., 1997, *Electron Spin Resonance: A Comprehensive Treatise on Experimental Techniques* John Wiley & Sons, New York .

Purcell, E. H., Torrey, H. C. and Pound, R. V., 1946, Resonance absorption by nuclear moments in solid, *Phys. Rev.* **69**: 37-38.

Pursley, R., Kakareka, J., Salem, G., Devasahayam, N., Subramanian, S., Tschudin, R. G., Krishna, M. C. and Pohida, T. J., 2003, Stochastic excitation and Hadamard correlation spectroscopy with bandwidth extension in RF FT-EPR, *J. Magn. Reson.* **162**: 35-45.

Quine, R. W., Rinard, G. W., Eaton, S. S. and Eaton, G. R., 2002, A pulsed and continuous wave 250 MHz electron paramagnetic resonance spectrometer, *Conc. Magn. Reson. (Magn. Reson. Engineer.)* **15**: 59-91.

Ramachandran, G. N. and Lakshminarayanan, A. V., 1971, Three-dimensional reconstruction from radiographs and electron-micrographs: application of convolutions instead of Fourier transforms, *Proc. Natl. Acad. Sci. USA* **68**: 2236-2240.

Rinard, G. A., Quine, R. W., Eaton, S. S. and Eaton, G. R., 1993, Microwave coupling structures for spectroscopy, *J. Magn. Reson. A* **105**: 137-144.

Rinard, G. A., Quine, R. W., Eaton, S. S., Eaton, G. R. and Froncisz, W., 1994, Relative benefits of overcoupled resonators vs inherently low-Q resonators for pulsed magnetic resonance, *J. Magn. Reson.* **A. 108**: 71-81.

Rinard, G. A., Quine, R. W., Harbridge, J. R., Song, R. T., Eaton, G. R, and Eaton, S. S., 1999a, Frequency dependence of EPR signal-to-noise, *J. Magn. Reson.* **140**: 218-227.

Rinard, G. A., Quine, R. W., Song, R. T., Eaton, G. R. and Eaton, S. S., 1999b, Absolute EPR spin echo and noise intensities, *J. Magn. Reson.* **140**: 69-83.

Rinard, G. A., Eaton, S. S., Eaton, G. R., Poole, Jr., C. P. and Frach, H. A., 1999c, Electron spin resonance sensitivity, in *Handbook of Electronm Spin Resonance, vol. 2,* C. P. Poole, Jr., and H. A. Farach, eds., API Press.

Rinard, G. A., Quine, R. W., Eaton, S. and Eaton, G. R., 2002a, Frequency dependence of EPR signal intensity, 250 MHz to 9.1 GHz, *J. Magn. Reson.* **156**: 113-121.

Rinard, G. A., Quine, R. W., Eaton, G. R. and Eaton, S. S. 2002b, 250 MHz Crossed loop resonator for pulsed electron paramagnetic resonance, *Magn. Reson. Engineer.* **15**, 37-46.

Rinard, G. A., Quine, R. W., Eaton, S. S., G. R. Eaton, S. S., 2004, Frequency dependence of EPR sensitivity, *Biological Magnetic Resonance,* **21**, in press.

Rollett, J. S. and Higgs, L. S., 1962, Correction of spectroscopic line profiles for instrumental broadening by a Fourier analysis method, *Proc. Roy. Soc. Land.* **79**: 87-91.

Sakamoto, Y., Hirata, H. and Ono, M., 1995, Design of a Multicoupled Loop-Gap Resonator Used for Pulsed Electron-Paramagnetic-Resonance Measurements, *IEEET Microw. Theory* **43**: 1840-1847.

Savitzky, A. and Golay, M. J. E., 1964, Smoothing and differentiation of data by simplified least squares procedures, *Anal. Chem.* **36**: 1627–1639.

Shepp, L. A., 1980, Computerized tomography and nuclear magnetic resonance, *J. Comp. Assist. Tomogr.* **4**: 94-107.

Shepp, L. A. and Logan, B. F., 1974, The Fourier reconstruction of a head section, *IEEE Trans. Nuc. Sci.* **NS-21**: 21-43.

Subramanian, S., Murugesan, R., Devasahayam, N., Cook, J. A., Afeworki, M., Pohida, T., Tschudin, R. G., Mitchell, J. B. and Krishna, M. C., 1999, High-speed data acquisition system and receiver configurations for time-domain radiofrequency electron paramagnetic resonance spectroscopy and imaging, *J. Magn. Reson.* **137**: 379-388.

Subramanian, S., Yamada, K., Irie, A., Murugesan, R., Cook, J. A., Devasahayam, N., Van Dam, G. M., Mitchell, J. B. and Krishna, M. C., 2002, Noninvasive in vivo oximetric imaging by radiofrequency FT EPR, *Magn. Reson. Med.* **47**: 1001-1008.

Swartz, H. M. and Walczak, T., 1998, Developing in vivo EPR oximetry for clinical use, *Adv. Exp. Med. Biol.* **454**: 243-252.

Utsumi, H., Takeshita, K., Miura, Y., Masuda, S. and Hamada, A., 1993, In vivo EPR measurement of radical reaction in whole mice - influence of inspired oxygen and ischemia-reperfusion injury on nitroxide reduction, *Free Rad. Res. Comm.* **19**: S219-227.

Von Schulthess, G. K. ,ed., 2000, *Clinical Positron Emission Tomography (PET): Correlation with Morphological Cross-Sectional Imaging* Lippincott, Williams & Wilkins, Philadelphia.

Weil, J. A., Bolton, J. R. and Wertz, J. E.,1994, *Electron Paramagnetic Resonance - Elementary Theory and Practical Applications,* Wiley-Interscience, New York .

Wuthrich, K.,1995, *NMR in Structural Biology* World Scientific, London .

Yamada, K. I., Murugesan, R., Devasahayam, N., Cook, J. A., Mitchell, J. B., Subramanian, S. and Krishna, M. C., 2002, Evaluation and comparison of pulsed and continuous wave Radiofrequency electron paramagnetic resonance techniques for in vivo detection and imaging of free radicals, *J. Magn. Reson.* **154**: 287-297.

Yong, L., Harbridge, J., Quine, R. W., Rinard, G. A., Eaton, S. S., Eaton, G. R., Mailer, C., Barth, E. and Halpern, H. J., 2001, Electron spin relaxation of triarylmethyl radicals in fluid solution, *J. Magn. Reson.* **152**: 156-161.

Zavoisky, E., 1945, Spin-magnetic resonance in paramagnetics, *J. Phys. E* **9**: 245-249.

Ziessow, D. and Bluemich, B., 1974, Hadamard-NMR-spektroskopie, *Ber. Bunsenges. Phys. Chem.* **11**: 1168-1179.

Zweier, J. L., Wang, P. H. and Kuppusamy, P., 1995, Direct measurement of nitric-oxide generation in the ischemic heart using electron-paramagnetic-resonance spectroscopy, *J. Biol. Chem.* **270**: 304-307.

IV

Metals

Chapter 13

Copper Biomolecules in Solution

Riccardo Basosi, Giovanni Della Lunga, Rebecca Pogni
Department of Chemistry, University of Siena, Siena, Italy

Abstract: For copper(II) in biological systems, and even for small copper complexes in fluid solution at room temperature, the CW lineshapes are strongly influenced by molecular motion. The intermediate tumbling lineshapes for Cu(II) complexes have been analyzed using the stochastic Liouville equations. Various methods of analysing Cu(II) spectra are presented. Examples are given for complexes of peptides, phenanthroline plus glutathione, bleomycin, and β-casomorphins. The methods could be extended to other paramagnetic metal ions.

1. INTRODUCTION

1.1 Rationale for the ESR Spectra of Copper Complexes in Solution

Copper is an essential trace element. Copper-containing enzymes and proteins are widely distributed in both animals and plants. In the blood, copper (II)-albumin is the major transport form of Cu(II). However, only 5-10% of serum copper is bound to albumin; most of the rest is bound to ceruloplasmin, with the remainder being bound to peptides and amino acids like histidine. Knowledge of the metal binding sites in proteins like albumins has prompted the design of metal binding sites and their sequence-specific incorporation into proteins and peptides (Hellinga *et al.* 1991; Arnold and Haymore, 1991; Shullenberger, *et al.,* 1993). Copper complexes can interact with DNA, promoting its cleavage (Shullenberger, *et al.,* 1993; Hegg and Burstyn, 1996; Harford and Sarkar, 1997). Recently, Cu^{2+} binding sites in the N-terminal domain of the prion protein (Aronoff-Spencer *at al.,* 2000) and copper's role in Alzheimer's disease (Multhaup *et al.,* 1998) have been

identified, and represent examples of the prominent physiological role of copper (see also ch. 14 by W. Antholine).

Performing ESR experiments on copper biomolecules in solution is crucial to understanding the biological significance of the model, as sample conditions match the physiological reaction conditions during this process. Furthermore, performing ESR experiments in solution avoids undesirable effects due to changes in physical state at low temperature such as changes in coordination of ligand to metal, changes in local pH, induction of artificial aggregation and changes in temperature-dependent equilibria (Vänngård, 1972; Falk, *et al.,* 1970; Leigh and Reed, 1971; Orii and Morita, 1977).

As far as dynamic conditions are concerned, even at room temperature with an isotropic solvent of membrane-like viscosity, copper ESR spectra have to be analyzed using a Stochastic Liouville Equation-based (SLE) theory (Freed *et al.,* 1971; Freed, 1976; Meirovitch *et al.,* 1982) because of a large anisotropy in the hyperfine interaction of Cu(II) in these complexes. For most square planar copper complexes dissolved in an isotropic solvent, when the probe fulfills the fast-motion conditions, the rotational correlation time, τ_R, is less than 2×10^{-9} s, but for viscous solvents like paraffin oil, even at 45°C, τ_R is longer than 2×10^{-9} s. Furthermore, in anisotropic solvents (membranes or liquid crystals), the Cu(II) spectrum should be analyzed by the SLE theory at any temperature (Rao *et al.,* 1977; Korstanje *et al.,* 1989). The SLE theory for an ESR spectrum has been applied to paramagnetic metal ions in solution only in a limited number of cases. The first metal complex tested by this theory was a vanadyl complex in isotropic solvents (Bruno *et al.,* 1977).

Although we confine ourselves in this chapter to the field of copper(II)[1], the problems addressed here can be easily extended to other paramagnetic metal ions sharing similar electronic features (Maki and McGarvey, 1958).

1.2 Historical Background for Copper ESR in Solution

The relaxation mechanisms governing the ESR line width for Cu(II) in solution were first described by McConnell (McConnell, 1956), based on the early experimental work of McGarvey (McGarvey, 1956) on Cu(II) acetylacetonate. The McConnell theory related the broadening of the

[1] Copper sites have historically been divided into three classes based on their spectroscopic features (Reinhammar, 1984; Solomon *et al.,* 1992), which reflect the geometric and electronic structure of the active site: (1) Cu(II) type I: Absorption spectrum in the 600 nm range. ESR: $g_{\|} > g_{\perp} > 2$. Blue proteins. Geometry: distorted four-coordinate tetrahedron-like; (2) Cu(II) type II: Visible absorption and ESR spectral properties compatible with those of the simple Cu(II) amino acid and peptide chelates. Geometry: square-planar; (3) Cu(II) type III: Absorption spectrum at 330 nm. ESR inactive. Pairs of Cu(II) which are strongly antiferromagnetically coupled.

hyperfine lines to the tumbling of a microcrystalline species with an anisotropic *g* factor and anisotropic hyperfine coupling A. The line width could then be attributed to the incomplete averaging of the spin Hamiltonian parameters by the tumbling motion. Kivelson (Kivelson, 1960; 1972) refined the theory of the motionally narrowed limit. The central point of Kivelson's theory was his famous line width equation:

$$\delta B(G) = \frac{2\hbar}{\sqrt{3}g\beta_e}(\alpha + \alpha' + \alpha'' + \beta M_I + \gamma M_I^2 + \delta M_I^3) \qquad [1]$$

where α' is the residual line width including inhomogeneous contributions, α'' is the spin rotational contribution, and α, β, γ and δ are coefficients strongly dependent on the correlation time, τ_c, and on the anisotropies of the g tensor and the nuclear hyperfine interaction. After Kivelson's work, a number of papers were devoted to the study of the motional line-narrowing effect of copper complexes in organic or aqueous solution (Herring and Park, 1979; Keijzers *et al.,* 1975; Lewis *et al.,* 1966; Noack and Gordon, 1968). Difficulties have arisen in applying the theory to experimental data. The correlation times have usually been much shorter than those calculated by the Debye-Stokes formula. Furthermore, the theory failed to give an adequate description of the molecular dynamics in the slow-motional region. A significant refinement was inclusion of the spin-rotational mechanism as an M_I-independent contribution to the line width (Atkins and Kivelson, 1966; Hubbard, 1963).

General theories of magnetic resonance predict modification of the position of hyperfine lines in ESR spectra as a result of line broadening and relaxation (Abragam and Bleaney, 1970; Bloch, 1956; Redfield, 1957). Fraenkel (Fraenkel, 1965; 1967) discussed the equation of motion of the density matrix in terms of the relaxation matrix, found the form of the spectral densities (for the case of a free radical), and calculated the dynamic shifts using the Redfield-Abragam approach. Bruno and coworkers (Bruno *et al.,* 1977), using the stochastic-Liouville approach of Freed, analyzed VO^{2+} complexes in the slow tumbling limit both experimentally and theoretically. In the course of their analyses, they developed a complete expression for the dynamic second-order shift in the fast tumbling limit. Fraenkel and Bruno *et al.,* after developing the shift analysis, dismissed it as a negligible effect. Nevertheless, second-order shifts are quite significant at low microwave frequencies. These shifts have been properly discussed and exploited by Basosi *et al.* (Basosi *et al.,* 1984), who demonstrated that they can provide direct information on the magnetic parameters of the liquid phase at room temperature.

The slow tumbling region is that range of rotational reorientation times for which the ESR spectrum can no longer be described as a simple superposition of Lorentzian lines, characteristic of the fast-motional or motional narrowing region, for which the theory outlined in the previous paragraph applies. In the slow-motion region, ESR copper spectra are affected in a complicated way by both molecular motions and magnetic spin interactions. From a general point of view, the slow tumbling ESR line shape theory is based on a generalization of stochastic theories of jump models that reached their peak in the Stochastic Liouville Equation theory developed mainly by R. Kubo (Kubo, 1957; 1966; 1969a; 1969b). Freed solved this problem for the case of spin labels in which there is a single hyperfine interaction. We extended his approach in order to simulate copper complexes involving nitrogens and other heteroatoms. Due to the crucial role played by this theory for interpreting the ESR spectra of copper biomolecules, the subject will now be discussed in detail.

1.3 Line Shapes, Motional Conditions and Multifrequency

There is a strong connection among line shape, motional conditions and microwave frequency. In fact, line width variations can be ascribed, in most cases, to fluctuations in the anisotropic terms of the magnetic Hamiltonian parameters caused by molecular motions. These terms can be written as:

$$H_1 = \beta_e \vec{\vec{B}} \cdot \vec{g}^{(1)} \cdot \vec{S} + \vec{S} \cdot \vec{A}_{Cu}^{(1)} \cdot \vec{I}_{Cu} \qquad [2]$$

where $\vec{g}^{(1)}$ and $\vec{A}_{Cu}^{(1)}$ are traceless matrices. The importance of anisotropic terms in determining the line shape of ESR spectra of copper complexes in the fast-motion regime can be inferred from the Kivelson theory (Kivelson, 1972). In the liquid phase, molecular tumbling makes H_1 (given by Eq. [2]) a random function of time. As a consequence, there is random modulation of the energy levels and transition frequencies. The frequency fluctuations can be characterized by amplitude and coherence. Amplitude Δ_ω is defined by the mean square value of the anisotropic interactions, $\Delta_\omega = \langle H_1^2 \rangle$, and coherence is given by the correlation time τ_c of the random motion. A random process is considered fast if the product $\Delta_\omega \cdot \tau_c << 1$. Under these conditions, the anisotropic terms are averaged to zero and the spectrum is composed of sharp Lorentzian lines. For $\Delta_\omega \cdot \tau_c >> 1$, the SLE theory must be applied, since the line shape directly reflects the random frequency distribution, approaching the limiting case of polycrystalline spectra. As can be seen from Eq. [2], the value of H_1 is directly proportional to the value of the external magnetic field, and consequently, to the microwave frequency.

For this reason, the amplitude Δ_ω depends not only on the magnetic parameters but also on the microwave band at which the measurement is performed. This explains why for the fast-motion conditions (and therefore the Kivelson approach outlined in section 2.2) for ESR spectra obtained at a lower frequency (e.g. S-band instead of X-band) might still hold true, even when incipient slow motion dominates the higher frequency (e. g. X-band) spectra (Della Lunga *et al.,* 1994).

Conventional ESR spectroscopy is carried out at 9-10 GHz in the X-band microwave region, and employs 100 kHz field modulation. Since the resonance conditions can be fulfilled for a variety of frequency-field combinations, many other frequencies are possible. From an experimental point of view, many authors have demonstrated the advantages of recording ESR spectra at frequencies other than 9 GHz (Hyde and Froncisz, 1982). Higher frequencies, where spectral dispersion provides resolution of small g-value differences, permit accurate magnetic tensors to be obtained. Lower frequencies, typically 2-4 GHz (S-band), are important for determination of nitrogen-metal ligation. Analysis of the $M_I = -1/2$ transition in the parallel region of powder spectra, which has minimal line width at S-band, allows the number and type of nucleus coupled to the metal ion to be ascertained (Basosi *et al.,* 1993). A thorough treatment of the advantages of using low frequencies to analyze copper complexes in the rigid limit can be found in chapter 14 of this volume.

As far as determination of the spin Hamiltonian parameters is concerned, the main reason for multifrequency analysis in the liquid and solid states is that fitting ESR spectra at several frequencies (using the same spin Hamiltonian input parameters) is a stringent requirement. Thus, this strategy yields an unambiguous characterization of the system. There exist several levels at which multifrequency ESR of copper complexes can yield useful structural information. At one level, answers are sought to questions such as the number of nitrogen ligands, or perhaps an estimate of the degree of rhombicity. At another level, comparison with spectra of model compounds can permit statements of charge and ligation. Molecular weights can be estimated from liquid phase spectra and information on the anisotropy of rotational diffusion may be obtainable. At the highest level, one can hope for a proper molecular-orbital description of the complex. The use of good simulation programs is the key step to applying this strategy.

1.4 Solving Problems with a Standard Continuous Wave Instrument

ESR spectra of copper biomolecules in solution have been neglected for a long time due to lack of resolution. This problem was often exacerbated by

the occurrence of baseline drift. Introduction of microwave frequency as a "new" experimental parameter by Hyde and coworkers (Hyde and Froncisz, 1982; Basosi *et al.,* 1984), together with development of computers and the availability of powerful simulation programs, improved the information content of previously unappreciated ESR spectra with poor line shape. Furthermore, the study of biosystems for which retaining the physiological conditions was mandatory made it clear that in some cases, low temperature experiments were precluded by the possibility of undesirable modifications of the samples. The observation that magnetic parameters for copper are temperature dependent (Wilson and Kivelson, 1966), in some cases prevented direct extrapolation of data obtained from liquid nitrogen or helium measurements at room temperature. Three problems need to be considered when computer simulations are employed:

1. As computer simulation becomes a crucial method for extracting magnetic parameters from ESR spectra from complexes in solution, a further problem arises because it is difficult to minimize a function in a multidimensional space when the parameter space is very large. This task is made more difficult without an automatic optimization program because the possibility of finding secondary minima is very great.2. Another factor that makes the interpretation of ESR spectra in solution difficult is that slow-motion ESR spectra typical of biological molecules (high molecular weight) cannot be described as a superposition of Lorentzian lines, and are affected by both the molecular motion and magnetic spin interaction.

3. Furthermore, when nitrogens coordinate the paramagnetic metal ion – a typical event with biomolecules – direct inclusion of superhyperfine interaction terms is not easy due to a substantial increase in the size of the matrix associated with the operator, resulting in negative consequences for numerical stability and processing speed.

Nevertheless, as working at physiological conditions is so crucial, and considering that most laboratories are equipped with a standard continuous wave (CW) instrument, it is necessary to overcome these problems.

The first and third points above are addressed in Section 2. Problems arising in the slow-motion regime, and their solution, are the subject of Section 3. Applications to copper biomolecules in solution, where these problems occur, are discussed in Section 4.

2. EXPERIMENTAL PROCEDURES AND DATA PROCESSING

2.1 Signal Intensity and Sensitivity

Optimization of the signal-to-noise ratio of a spectrometer is always a prerequisite for successful performance of an ESR experiment (Poole, 1967). The classical paper on sensitivity and noise reduction of ESR spectrometers is that of Feher (1957), who analyzed the effect of paramagnetic resonance on cavity impedance and discussed a number of possible spectrometer arrangements. In a classic CW ESR spectrometer, good sensitivity for a small to moderate number of paramagnets in the sample is obtained by using a resonant cavity. The advantage of such a resonant structure is that the standing wave pattern generated leads to very large RF field values. In general, the signal ultimately observed is increased by a factor *Q,,* which is the quality factor of the cavity:

$$Q = \frac{2\pi(\text{stored energy})}{\text{cavity energy losses per cycle}} \qquad [3]$$

If we assume the presence of a sample of susceptibility χ occupying a fraction η of the effective resonator volume $(0 < \eta < 1)$ in the cavity, where η is usually termed the sample filling factor, we can demonstrate that the detected ESR signal is

$$S \propto \eta Q \chi'' \sqrt{P} \qquad [4]$$

where χ'' is the absorption component of susceptibility and P is the incident microwave power. From this formula, we can see why the standard resonant cavity with $Q \approx 2000\text{-}5000$ is attractive. In fact, the large Q value offsets the very small filling factors of these cavities (typically $\eta \approx 0.01$). In recent years, the center of attention in resonator design has shifted from high Q value cavities, for which η is limited to values << 1, toward structures such as loop-gap resonators (Hyde and Froncisz, 1986; 1989), where $\eta \approx 1$ and $Q \approx 500\text{-}1000$ provides a significantly larger ηQ value.

2.2 Resolution Enhancement

As far as data processing is concerned, the second derivative (or second harmonic) can be particularly useful for analyzing superhyperfine patterns. Shoulders in the spectrum become peaks that facilitate the estimation of coupling constants. Just as it is better to filter spectra after acquisition, it is also better to transform spectra after acquisition. The rationale for second-harmonic display is improved resolution. A variety of resolution-

enhancement algorithms can now be studied conveniently by computer (Hyde *et al.,* 1992). All of these algorithms are basically filters, and their improved resolution implies a reduction in low frequency components of the spectrum relative to high frequencies. There is a trade-off between resolution and noise. The lower the noise of the initial spectrum, the better the resolution that is possible using post-acquisition techniques. And, of course, the better the initial experimental resolution, the better the final results

From an experimental point of view, it can be useful to record ESR spectra at frequencies lower than X-Band. Canceling a term that is dependent on frequency with a term that is M_I-dependent improves the resolution of superhyperfine lines in low frequency spectra of immobilized cupric complexes in powders or frozen solution.

2.3 Pseudomodulation

Pseudomodulation is defined as computer simulation of the effect that would be obtained if a sinusoidal field modulation was applied followed by phase-sensitive detection at the fundamental frequency of an MR spectrum or at one of its harmonics (Hyde *et al.,* 1990). Since it is done by computer, it is not necessary that it actually be possible to modulate the field. This procedure has been successfully utilized for resolution enhancement (Hyde *et al.,* 1992).

The input parameter is the pseudo-field modulation amplitude and the outputs are harmonics of that modulation. The harmonics produced by Pseudomodulation become proportional to the corresponding derivatives as the modulation amplitude decreases. As the modulation amplitude increases, this proportionality begins to fail, but concomitantly, high-frequency noise present in a spectrum decreases. The pseudomodulation equations for the zero, first and second harmonics are

$$f_0(H_0, H_m) = \int F(s) J_0(H_m S/2) e^{iH_0 S} dS \qquad [5]$$

$$f_1(H_0, H_m, t) = 2i \sin(\omega_m t) \int F(s) J_1(H_m S/2) e^{iH_0 S} dS \qquad [6]$$

$$f_2(H_0, H_m, t) = 2 \cos(2\omega_m t) \int F(s) J_2(H_m S/2) e^{iH_0 S} dS \qquad [7]$$

In these equations, *F(s)* is the Fourier Transform (FT) of the spectrum *f(H).* The only input parameter is H_m, which is conveniently expressed as a fraction of the width of the spectrum. An effective application of pseudomodulation is for performing sensitivity analysis of the input parameters in the spin Hamiltonian. The motivation for this task is to determine the number of nitrogens in copper complexes, including the

possibility that all nitrogens are not equally coupled or that there might be a strongly-coupled proton. From the experimental side of this study, is now feasible to do this, thanks to the time-locked sub-sampling methods developed by Hyde (Hyde *et al.,* 1998).

2.4 Fourier Analysis of ESR Spectra of Copper Complexes

ESR spectra of cupric complexes provide useful information about the nitrogen donor atoms coordinating the metal ion. Hyperfine coupling constants can be reliably determined either by direct inspection of the spectra or by computer simulation of experimental data. Problems in determining the number of nitrogens arise when the hyperfine pattern consists of more lines than are resolved (Hyde *et al.,* 1986). Lack of resolution is common in ESR spectra in solution. In this case, algorithms for resolution enhancement based on FT can help distinguish hyperfine coupling constants. The improvement in resolution is usually achieved by convolution of the spectrum. A different procedure based on FT of ESR spectra has been proposed for a straightforward discrimination between different ligand coordinations around copper (Della Lunga *et al.,* 1995). The procedure, which is not based on resolution enhancement, is particularly useful whenever the involvement of an even or odd number of nitrogen nuclei is crucial for determining the structural arrangement in solution. The formal description of this procedure is given in a series of papers to which the reader can refer (Della Lunga *et al.,* 1995 and references therein), which is briefly summarized here:

The FT of the pattern function which describes the line pattern generated by the hyperfine interaction with a nucleus having spin I and coupling constant *A* is given by (Silsbee, 1966):

$$F(f_{pattern}) = \frac{1}{2I+1}\sum_{m=-I}^{+I} e^{-2\pi i m A\omega} = \frac{1}{2I+1}\sum_{m=-I}^{+I}\cos(2\pi m A\omega) \qquad [8]$$

where ω is the Fourier space variable. For copper (I = 3/2):

$$F(f_{pattern}) = \frac{1}{4}\sum_{m=-3/2}^{+3/2}\cos(2\pi mA\omega) = \frac{1}{2}(\cos(3\pi A\omega) + \cos(\pi A\omega)) \qquad [9]$$

whereas for *n* with magnetically equivalent nuclei of spin I = 1 such as ^{14}N or deuterium:

$$F(f_{pattern}) = \frac{1}{3^n}(1 + 2\cos(2\pi A\omega))^n \qquad [10]$$

As far as the line shape function is concerned, one can assume a Lorentzian function is a good approximation; the FT of the derivative of a Lorentzian is given by:

$$\phi(\omega) = -2\pi i\omega e^{-2\pi\Gamma\omega} \qquad [11]$$

in which Γ is the half-height width in Gauss. On the basis of the Convolution Theorem, assuming the nitrogen coupling constants are all the same, one can write the FT of an ESR spectrum of copper with n ^{14}N ligands in the form:

$$e^{2\pi i\sigma\omega}\ \phi(\omega)\frac{1}{2}(\cos(3\pi A_{Cu}\omega) + \cos(\pi A_{Cu}\omega))\frac{1}{3^n}(1 + 2\cos(2\pi A_N\omega))^n \qquad [12]$$

where n is the number of nitrogens bound to copper and the exponential function is due to the central resonance.

Fig. 1 shows the region of the FT that is sensitive to the parity of the number of nitrogens. In particular, Fig. 1a shows the trend of the function described by Eq. [11], Fig. 1b the trend of the function of Eq. [9] and Fig. 1c the trend of Eq. [10] for $n = 3$. Fig. 1d clarifies the effect of this sensitivity. This figure demonstrates the trend of the real part of the FT of two simulated spectra with different ligand coordinations, an even number in the first case and an odd number in the second. It can be observed that the phase of the region enlarged in the box is inverted by varying the number of bound nitrogens. The important thing to note is that the phase variation is confined to that region, while the phase of the neighboring regions is not altered by varying the number of nitrogens. This phase difference provides unequivocal information on the parity of the number of nitrogens involved.

2.5 Baseline Correction

Often the baselines of spectra obtained from ESR spectrometers are not good enough to permit correct interpretation or make comparisons with other curves (notably simulated spectra). Clearly, the best remedy for an unsatisfactory baseline is to detect its source and record the curve again. On the other hand, if the source of an unsatisfactory baseline cannot be traced to a routine cause (impurities, incorrect form of sample, wrong concentration, incorrect medium, wrong measurement parameters, etc.), baseline correction can be done numerically. Simple procedures to remove baseline artifacts from ESR spectra have been published (Della Lunga *et al.,* 1994b; Della Lunga and Basosi, 1995). In the first reference, the problem was addressed by simple polynomial interpolation of the baseline, while in the latter, cubic spline functions were used. In a typical implementation of these procedures, the user is asked to choose the type of interpolation (linear correction,

second- or third-order polynomial interpolation or interpolation with cubic splines) and to fix the points through which the interpolation curve is required to pass.

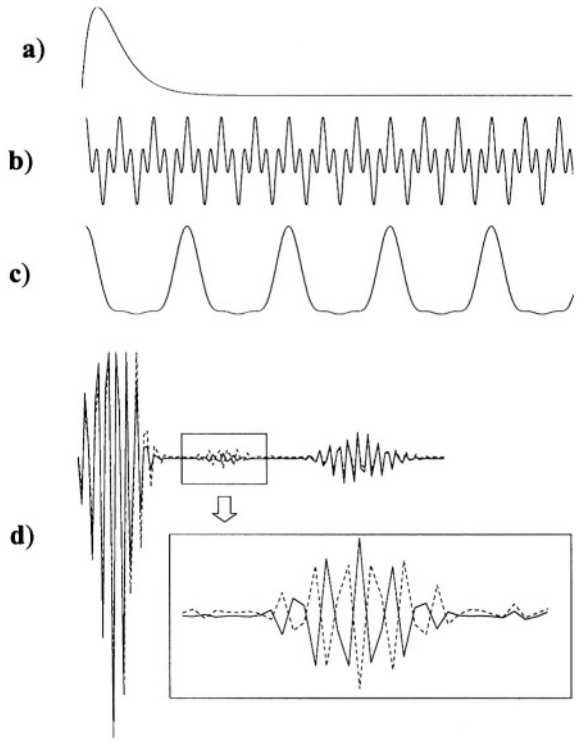

Figure 1. Trends of the functions reported in Equations (a) [11] (b) [9], (c) [10] for $n = 3$ and (d) trend of real part of FT for two simulated spectra with different ligand coordination (*Della Lunga et al., 1995b*).

2.6 Integrated Strategies for Best Fit

Given a function *F(x),* the general problem is to find the value of the variables *x,* for which the function takes on its smallest value. The method which finds the minimum variable (within a given tolerance) after the smallest number of F(x) evaluations is usually the preferred one. Nevertheless, other considerations may be important, for example, the amount of date storage required by the method or the amount of time required to implement it. Normally, however, the dominating factor will be the time spent in evaluating the function.

One of the most important procedures is the *simplex* method of Nelder and Mead (Nelder and Mead, 1965). This method requires only function evaluations, not derivatives. It is not very efficient in terms of the number of function evaluations that it requires, however, the downhill simplex method may frequently be the *best* method to use when there is little information about which feature of the function to minimize. The downhill simplex method takes a series of steps, most of which move the point of the simplex where the value of the function is largest ("highest point") through the opposite face to a lower point (Fig. 2). These steps are called reflections, and they are constructed to conserve the volume of the simplex (hence maintaining its non-degeneracy). When it can do so, the method expands the simplex in one or another direction to take larger steps. When it reaches a "valley floor," the method contracts itself in the transverse direction and tries to ooze down the valley. If there is a situation where the simplex tries to "pass through the eye of a needle," it contracts itself in all directions, pulling itself in around its lowest point. Termination criteria can be delicate in any multidimensional minimization routine. Generally, one can terminate when the vector distance moved in a particular step is fractionally smaller than some tolerance level. Alternatively, one could require that the decrease in the function value in the terminating step be fractionally smaller than some tolerance point. Either of the above criteria might be fooled by a single anomalous step that, for one reason or another, failed to get anywhere. Therefore, it is frequently good practice to restart a multidimensional minimization routine at a point where it claims to have found a minimum. When a high degree of precision in the determination of parameters is required, different methods should be used. Marquardt (Marquardt, 1963) presented an elegant method, related to an earlier suggestion by Levenberg, for varying smoothly between the extremes of the inverse-Hessian method and the steepest descent method. The latter method is used far from the minimum, switching continuously to the former as the minimum is approached. This *Levenberg-Marquardt method* works very well in practice and has become the standard non-linear least-squares routine. Much information about these classic minimization procedures is available in the literature (Press *et al.,* 1994).

Finally, the *Simulated Annealing* method (Kirkpatrick *et al.,* 1983; Kirkpatrick, 1984) has attracted significant attention as suitable for optimization problems where a desired global extremum is hidden among many poorer local extrema. This task is particularly important when spectra are being simulated at many frequencies. In this situation, the convergence to a single set of spin Hamiltonian parameter values that fit all frequencies is often elusive. In this case, it is important to avoid the use of best fit procedures that can become stuck in local minima of parameter space. The

essence of simulated annealing is *slow* cooling, allowing ample time for redistribution of the atoms as they lose mobility. This is the technical definition of *annealing,* and it is essential for ensuring that a low energy state will be achieved. Even at low temperatures, there is a chance, albeit very small, of a system being in a high energy state. Therefore, there is a corresponding chance for the system to leave a local energy minimum in favor of finding a better, more global one. In other words, the system sometimes goes *uphill* as well as *downhill;* but the lower the temperature, the lower the probability of any significant uphill excursion.

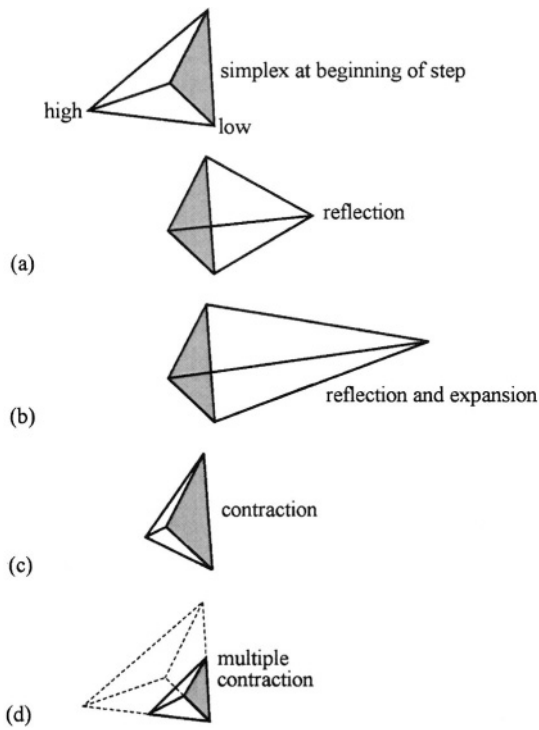

Figure 2. Possible outcomes for a step in the downhill simplex method. The simplex at the beginning of the step, here a tetrahedron, is shown, top. The simplex at the end of the step can be any one of (a) a reflection away from the high point, (b) a reflection and expansion away from the high point, (c) a contraction along one dimension from the high point, or (d) a contraction along all dimensions towards the low point. An appropriate sequence of such steps will always converge to a minimum of the function (Press *et al.,* 1994).

In 1953, Metropolis and coworkers (Metropolis *et al.,* 1953) first incorporated annealing principles into numerical calculations. This general scheme, of normally taking a downhill step while *sometimes* taking an uphill

step, has come to be known as the Metropolis algorithm. The algorithm was originally developed for problems of combinatorial minimization, but the basic ideas of simulated annealing are also applicable to optimization problems with continuous *N*-dimensional control spaces, e.g., finding the (ideally global) minimum of some function *f(x),* in the presence of many local minima, where *x* is an *N*-dimensional vector. The elements required by the Metropolis procedure are: the value of *f* is the objective function; a system state is described by point *x* and a control parameter, *T,* which is something like a temperature, and an annealing schedule by which the system is gradually reduced. The choice of annealing schedule can be difficult and interested readers are referred to the literature for an in-depth discussion (Press *et al.,* 1994). The problem with the method is one of efficiency: a generator of random changes is inefficient if *when locally downhill moves exist* it, nevertheless, almost always proposes an uphill move. A good generator should not become inefficient in narrow valleys, nor should it become more inefficient as convergence to a minimum is approached.

The importance of an integrated strategy using global minimization procedures is shown by Fig. 3, which shows the distribution of different values for which the best fit is obtained. As we can see, using only a strategy based on simulated annealing is a guarantee for reaching a global minimum (Della Lunga *et al.,* 1998).

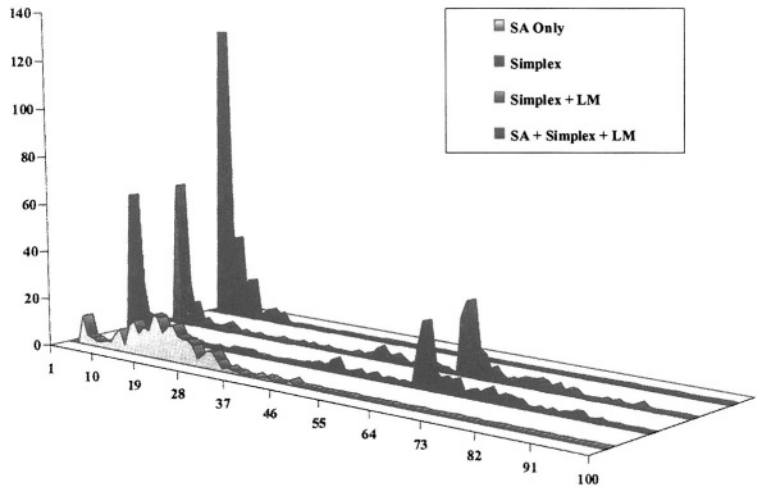

Figure 3. Distribution of the mean square error for 250 iterations using different minimization procedures. On the abscissa, the minimum chi-square value is reported while on the ordinate, the number of occurrences of that value in the course of 250 iterations is reported. In a significant number of cases, the simplex procedure without annealing converges on a chi-square value that is higher than the global minimum.

3. THE STOCHASTIC LIOUVILLE APPROACH TO SIMULATION

As previously noted, in the so-called slow-motion region, ESR spectra cannot be expressed as a sum of simple Lorentzian lines. The studies of Freed and co-workers on nitroxides in liquids (Freed and Fraenkel, 1963; Freed *et al.,* 1971; Moro and Freed, 1981; Schneider and Freed, 1989) increased information about the microscopic models of rotational dynamics, relying on computer programs for simulating ESR spectra based on the Stochastic Liouville Equation (SLE). However, application of Freed's method to copper systems of biological interest has been precluded for a long time by lack of programs that could simulate ESR spectra containing more than one hyperfine interaction. The direct extension of Freed's approach to include superhyperfine interaction is not difficult from a theoretical point of view, but the resulting algorithm is problematic because it leads to a substantial increase in the dimensions of the matrix related to the spin-Hamiltonian operator. The computer program requires a huge amount of memory and only recently has a feasible solution to this problem has become possible, thanks to the striking improvements in PC performance. In the following section, the theoretical bases of the application are discussed and some preliminary results presented.

3.1 Computation of Spectral Density with Superhyperfine Contribution

Using the SLE approach, absorption of energy from a microwave field by a spin system far from saturation can be written as (Moro, 1980; Meirovitch *et al.,* 1982):

$$I(\omega-\omega_0)=\frac{1}{\pi}\mathrm{Re}\left[\left\langle\left\langle v\left|\left[(\Gamma-iL)+i(\omega-\omega_0)I\right]^{-1}\right|v\right\rangle\right\rangle\right] \qquad [13]$$

where Γ is the symmetrized diffusion operator, L is the Liouville operator associated with the Hamiltonian parameter of the magnetic interactions, ω is the frequency of the microwave field and $|v\rangle$ is the so-called "starting vector" constructed from the spin transition moment averaged over the equilibrium ensemble. We assume the following Hamiltonian:

$$H=\mu\vec{S}\cdot\tilde{g}\cdot\vec{H}+\vec{I}\cdot\tilde{A}\cdot\vec{S}+\sum_{i=1}^{N}\vec{I}_i\cdot\tilde{A}_i\cdot S \qquad [14]$$

where $\tilde{A}_i$ is the tensors describing the superhyperfine coupling of the electronic spin with a set of N completely equivalent nuclei (Freed and Fraenkel, 1963). The Liouville operators Γ and L are defined in the Liouville

space of the direct product of the normalized Wigner rotation matrices and spin transitions. Using Dirac notation, the basis vector of this space is:

$$\sqrt{\frac{2L+1}{8\pi^2}}D^{L}_{M,K}(\Omega)\left|p^S,q^S;p^I,q^I;\prod_i\left(p^N,q^N\right)\right\rangle = \\ = \sqrt{\frac{2L+1}{8\pi^2}}D^{L}_{M,K}(\Omega)\left|S,m_S\right\rangle\left\langle S,m'_S\right|\otimes\left|I,m_I\right\rangle\left\langle I,m'_I\right|\otimes\prod_i\left(\left|N,m_N\right\rangle\left\langle N,m'_N\right|\right)_i \qquad [15]$$

where m_s and m_I are the eigenstates of the z components of the electronic spin operator S and the nuclear spin operator I, respectively, and m_N is the eigenstate of the z component of the nuclear spin operator of the completely equivalent nuclei.

In order to discuss the types of terms that are included in the Liouville and diffusion superoperators, several coordinate systems need to be introduced. This problem is discussed completely in Freed's papers, to which the reader should refer (Schneider and Freed, 1988; 1989). It is convenient to write the Hamiltonian in the spherical tensor notation:

$$H_0 = \sum_{\mu} F^{(0,0)}_{\mu,L}A^{(0,0)}_{\mu,L} \qquad [16]$$

$$H_1(\Omega) = \sum_{\mu,m',m'',m'''} d^2_{mm'}(\Psi)D^2_{m'm''}(\Omega)d^2_{m''m'''}(\Phi)F^{(2,m''')}_{\mu,L}A^{(2,m)}_{\mu,L} \qquad [17]$$

where μ specifies the kind of interaction (Zeeman, hyperfine, superhyperfine), $F^{(l,m)}_{\mu,L}$ is proportional to the standard Irreducible Spherical Tensor Operator (ISTO) components of the magnetic tensor of type μ in the reference frame L, and $A^{(l,m)}_{\mu,L}$ is the ISTO components of the tensors that arise from the coupling of spin and/or magnetic field operators. Since L is the superoperator associated with the Hamiltonian, we can write:

$$L = \sum_{l,\mu,m',m'',m'''} d^l_{mm'}(\Psi)D^l_{m'm''}(\Omega)d^l_{m''m'''}(\Phi)F^{(l,m''')}_{\mu,m}A^{\times(l,m)}_{\mu,m} \qquad [18]$$

Freed's approach to the solution of the SLE is based on the Lanczos algorithm, which can be applied only when the matrix associated with $\Gamma - iL$ is complex symmetric. In order to symmetrize the matrix, we must introduce a proper basis set (Moro, 1980; Meirovitch *et al.*,, 1982) defined as:

$$|\sigma_n\rangle = \left[2(1+\delta_{K_n,0})\right]^{-1/2} e^{i\frac{\pi}{4}(1-j^{K_n})} \times \left|p_n^S, q_n^S, p_n^I, q_n^I, \prod_i \left(p_n^N, q_n^N\right)_i\right\rangle \times \left\{ |L_n, M_n, K_n\rangle + j^{K_n}(-)^{L+K} |L_n, M_n, -K_n\rangle \right\}. \quad [19]$$

Using this basis, the matrix elements of the Liouville superoperator can be written as:

$$\langle\sigma_1|L|\sigma_2\rangle = \left\langle L_1, M_1, K_1, j^{K_1}, p_1^S, q_1^S, p_1^I, q_1^I, \prod_i \left(p_1^N, q_1^N\right)_i \middle| L \middle| L_2, M_2, K_2, j^{K_2}, p_2^S, q_2^S, p_2^I, q_2^I, \prod_i \left(p_2^N, q_2^N\right)_i \right\rangle =$$

$$\sum_{l,\mu,m',m'',m'''} d^l_{mm'}(\Psi) d^l_{m''m'''}(\Phi) F^{(l,m''')}_{\mu,m} \sqrt{(2L_1+1)(2L_2+1)}$$

$$\times \frac{1}{8\pi^2} \int d\Omega D^{L_1 *}_{M_1 K_1}(\Omega) D^l_{m'm''}(\Omega) D^{L_2}_{M_2 K_2}(\Omega) \quad [20]$$

$$\times \left\langle p_1^S, q_1^S, p_1^I, q_1^I, \prod_i \left(p_1^N, q_1^N\right)_i \middle| A^{\times(l,m)}_{\mu,m} \middle| p_2^S, q_2^S, p_2^I, q_2^I, \prod_i \left(p_2^N, q_2^N\right)_i \right\rangle.$$

In our approach, we assume an isotropic rotational diffusion operator. The corresponding matrix elements are:

$$\langle\sigma_1|\Gamma_{iso}|\sigma_2\rangle = \left\langle L_1, M_1, K_1, j^{K_1}, p_1^S, q_1^S, p_1^I, q_1^I, \prod_i \left(p_1^N, q_1^N\right)_i \middle| \Gamma_{iso} \middle| L_2, M_2, K_2, j^{K2}, p_2^S, q_2^S, p_2^I, q_2^I, \prod_i \left(p_2^N, q_2^N\right)_i \right\rangle. \quad [21]$$

No restoring potential has been introduced in order to describe anisotropic liquids.

The continued fractional representation of the spectral function holds a central position in Freed's approach, since it represents an efficient means of obtaining an entire sequence of approximations to the spectral function directly from the tridiagonal matrix obtained by applying the Lanczos algorithm (Lanczos, 1950) to the matrix described by [20] and [21]. The sequence of continued fractional approximations to the spectral function are defined in terms of the elements of this tridiagonal matrix. The derivation is quite straightforward; to begin, the spectral function can be written in the form:

$$I^{(N)}(\omega) = \vec{v}^T \left[\omega I_N + A\right]^{-1} \vec{v} \quad [22]$$

where the superscript and subscript N refer to the dimension of the matrix A. The sequence of approximants to be constructed is actually approximations of $I^{(N)}(\omega)$. The transformation matrix Q_N defined by the Lanczos vectors allows rewriting the equation [22] in terms of the tridiagonal matrix T_N.

$$I^{(N)}(\omega) = \vec{v}^{T} Q_N^{T} Q_N \left[\omega I_N + A\right]^{-1} Q_N^{T} Q_N \vec{v} = \left(Q_N \vec{v}\right)^{T} \left[\omega I_N + T_N\right]^{-1} \left(Q_N \vec{v}\right) \qquad [23]$$

Since the matrix Q_N is orthogonal, it must satisfy $Q_N^{tr} Q_N = I_N$. In addition, the matrix elements in the first row of Q_N are just the component of $\vec{v}$. Using these two components, it is possible to simplify the last term of equation [23]. In fact, we can prove that $I^{(N)}(\omega)$ is just the (1,1) matrix element of the inverse of $\left[\omega I_N + T_N\right]$, i.e.,

$$I^{(N)}(\omega) = \left[\omega I_N + T_N\right]^{-1}_{1,1} . \qquad [24]$$

The entire sequence of continued fractional approximations is obtained directly from equation [24]. This is accomplished by using the determinant-cofactor formulae for the elements of the inverse matrix and using Laplace's method to expand the determinants and cofactors. It is not difficult to demonstrate that equation [24] can be written as

$$I^{(N)}(\omega) = \frac{D^{N}_{2,N}(\omega)}{D^{N}_{1,N}(\omega)} \qquad [25]$$

where $D^{N}_{1,m}$ is the determinant of the diagonal blocks of $\left[\omega I_N + T_N\right]$. The continued fractional representation of $I^{(N)}(\omega)$ follows from equation [24] by using Laplace's method to derive a recurrence relation for the determinants:

$$I^{(N)}(\omega) = \cfrac{1}{\omega + \alpha_1 - \beta_1^2 \cfrac{D^{N}_{3,N}(\omega)}{D^{N}_{2,N}(\omega)}} \qquad [26]$$

Reapplication of the recurrence relation gives

$$I^{(N)}(\omega) = \cfrac{1}{\omega + \alpha_1 - \cfrac{\beta_1^2}{\omega + \alpha_2 - \beta_2^2 \cfrac{D^{N}_{4,N}(\omega)}{D^{N}_{3,N}(\omega)}}} \qquad [27]$$

and so on. The sequence is then truncated at an appropriate value, depending on the motional condition of the complex. In Fig. 4, the resulting spectra for different values of the anisotropic coupling constants of nitrogens are presented (note that all the spectra have the same isotropic value of the nitrogen coupling constant)

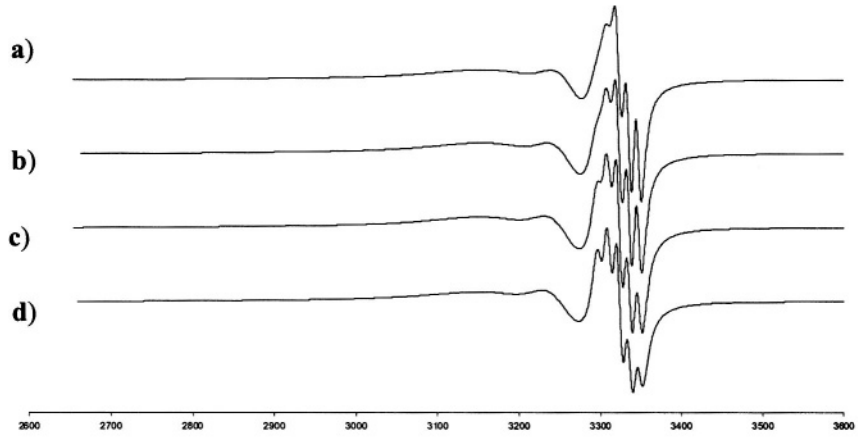

Figure 4. Simulated spectra for different values of the nitrogen anisotropic coupling constant where A_x, A_y and A_z are respectively equal to a) 1, 1, 34; b) 5, 5, 26; c) 9, 9, 18; d) 12, 12, 12 Gauss. The magnetic field axis extends from 2600 to 3600 gauss.

3.2 A Simplified Approach

If we can assume that the superhyperfine constant of equivalent bound nuclei is isotropic, it is possible to approach the problem of spectra simulation using a simplified algorithm. Specifically in the context of the SLE approach, the simplified solution is to simulate the spectrum of copper without nitrogens and then perform a convolution between the spectrum obtained and the pattern function of the nitrogens under the desired conditions (Della Lunga *et al.,* 1994). As previously noted, this procedure is valid only when the hyperfine coupling of nitrogens can be regarded as isotropic. The simplified procedure can be summarized as:

1. A solution of the SLE for copper only (without ligands) is obtained.
2. Fourier Transform of the resulting spectrum and of the function describing the stick diagram of nitrogens is performed.
3. The two FT's are multiplied and the results are reversed in order to obtain the desired results.

In Fig. 5, spectra obtained with the two procedures (the simplified approach and computation of spectral density with superhyperfine contribution described in Sec. 3.1) using the same set of parameters, are shown. As far as the superhyperfine transitions are concerned, the two spectra were computed using completely different approaches. This fact can represent an *a posteriori* validation of our previous simplified approach.

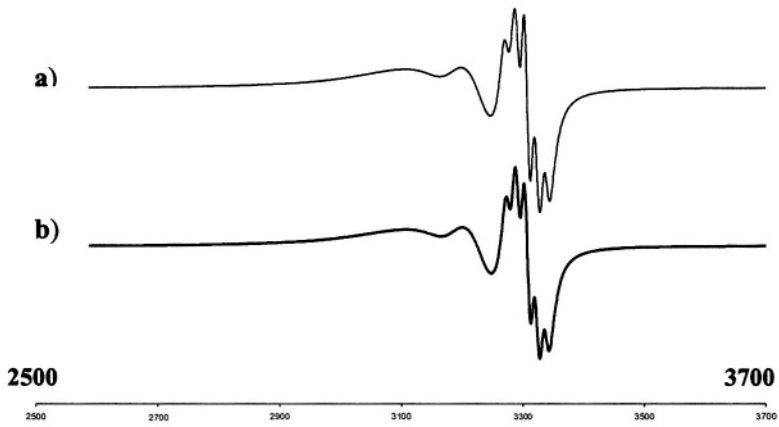

Figure 5. Resulting spectra obtained with the two procedures discussed in the text.

Copper complexes with peptides represent the first application of the computer program based on the SLE equation using the assumption of the isotropic nitrogen coupling constant (Della Lunga *et al.,* 1994). To our knowledge, only our own efforts and those of Bill Antholine's group at the National Biomedical ESR Center have utilized this method. Copper complexes with histidine-containing peptides were used almost incidentally by us to test the applicability of this approach, as the corresponding magnetic parameters were well known in both rigid and fast-motion limits (Pogni *et al.,* 1993) (see also Sec. 4.1).

Pasenkiewicz-Gierula (Pasenkiewicz-Gierula *et al.,* 1997) applied the simplified approach, to simulate square planar copper complexes of thiosemicarbazones in solution and phospholipid membranes. Fig. 6 shows X-band experimental (left) and corresponding simulated (right) ESR spectra for $CuKTSM_2$ in light paraffin oil over a range of temperatures. The authors confirmed that the procedure is valid and gives good results when the hyperfine coupling constant of nitrogens can be regarded as isotropic. This assumption holds when the anisotropy of the nitrogen superhyperfine tensor is effectively averaged out by rotational motion leading to a correlation time of less than 10^{-7} s. For correlation times longer than 10^{-7} s, a single value of N_{iso} can no longer be used to calculate the spectrum because the anisotropy of the nitrogen splitting becomes significant.

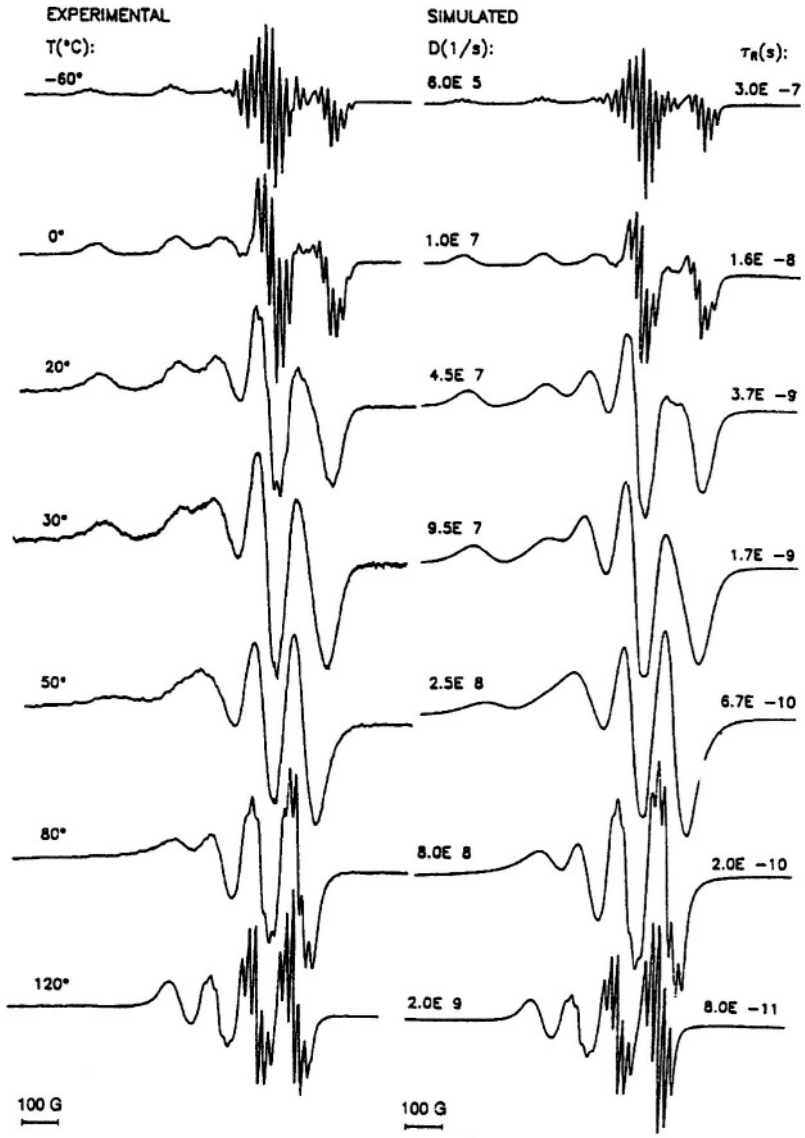

Figure 6. Comparison of X-band experimental (left) and corresponding simulated (right-) ESR spectra for **CuKTSM$_2$** in light paraffin oil over a range of temperature (Pasenkiewicz-Gierula *et al.,* 1997).

4. APPLICATIONS TO COPPER BIOMOLECULES IN SOLUTION

4.1 Copper Complexes with Peptides

Peptides often serve as effective ligands for a variety of metal ions. They contain a set of potential donor atoms, and the complexes formed exist in a variety of conformations (Pettit *et al.,* 1991; Bal *et al.,* 1997). Among metal ions, Cu(II) has interesting chemistry and has been widely studied (Kozlowski *et al.,* 1999).

Dipeptides formed from amino acids containing side chains with potential donor centers are important in biological systems. Among such dipeptides, those containing histidine are particularly interesting. The involvement of histidine imidazole nitrogens is a crucial step in the coordination of histidine to copper to form stable chelate complexes in solution (Basosi *et al.,* 1986; Pasenkiewicz-Gierula *et al.,* 1987; Romanelli and Basosi, 1988). This was established from chemical and dynamic information from room temperature ESR spectra. Multifrequency analysis of copper (II) dipeptide complexes (Cu-GlyHis versus Cu-HisGly) led to a unique set of spin Hamiltonian magnetic parameters for different arrangements in the first coordination sphere of copper for a 1:2 metal:ligand molar ratio. In the case of the Cu-GlyHis complex, the simultaneous presence of the monomer and the bis complex and their relative percentages were established. For the Cu-HisGly complex, histidine-like coordination was proposed (Pogni *et al.,* 1993). The possibility of investigating copper complexes in the slow-motion regime was then explored with the use of a program based on the SLE equation. Fig. 7 shows the S-band (left) and X-band (right) ESR spectra for the complex ^{63}Cu(GlyHis) in H_2O. Increasing amounts of glycerol were added to the solutions in order to approach the slow motion regime and to test the program for all cases in which the rotational correlation time (τ_c) of the complex was modified by an increase in the complex molecular weight or viscosity of the solution(Della Lunga *et al.,* 1994).

Coordination properties of a histidine residue within a peptide sequence depend enormously on the position of this residue in a peptide chain. Furthermore, many copper complexes with amino acids and peptides have been proposed as superoxide dismutase-like compounds (Amar, *et al.,* 1982; Bonomo, *et al.,* 1993). In this context, a structure-activity relationship study on the superoxide scavenger activity of histidine-containing peptides was attempted and the chemical arrangements determined from room temperature ESR spectra (Pogni *et al.,* 1999). Fig. 8 shows the room temperature ESR spectra of Cu-Glycyl-Glycyl-Histidyl-Glycine (Cu-GGHG), Cu- Glycyl-Histidyl-Glycine (Cu-GHG) and Cu-Histidyl-Glycyl-Glycine (Cu-HGG).

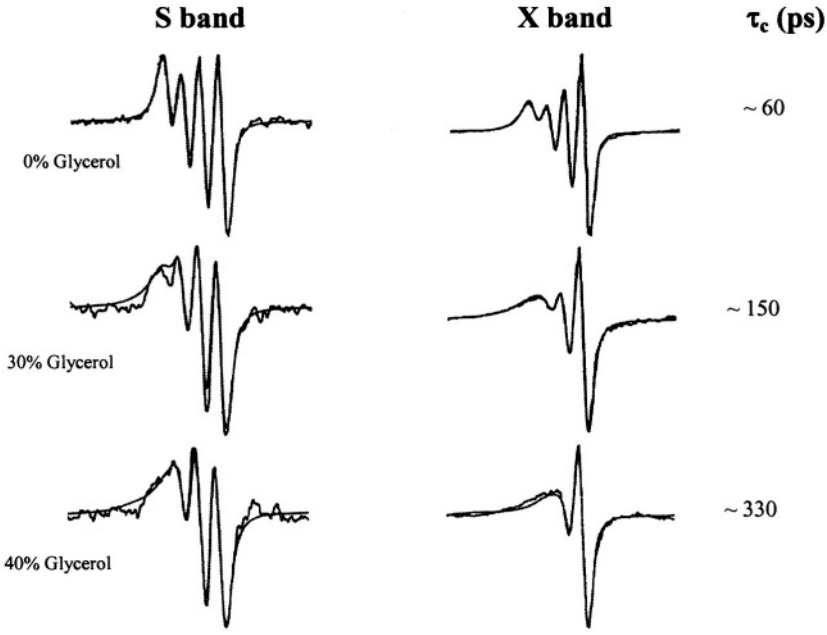

Figure 7. S-band (v = 4 GHz) and X-band (v = 9 GHz) ESR spectra for the complex ^{63}Cu(GlyHis) in H_2O recorded with increasing amounts of glycerol. Experimental ESR spectra are paired with their simulations. All spectra are recorded at 298K (Della Lunga *et al.*, 1994).

Spin Hamiltonian parameters determined for the copper complexes shown in Fig. 8 were compared with those of copper complexes with only glycine residues (GG, GGG and GGGG). ESR parameters were obtained from the simulations of the room temperature spectra. Different arrangements were defined and estimation of the scavenger activity of the complexes due to the particular environment created by the ligands around copper was discussed. When ESR spectroscopic data was compared with measurements of SOD-like activity, it suggested that a deviation from ring planarity of the copper complexes correlates with the most active compounds.

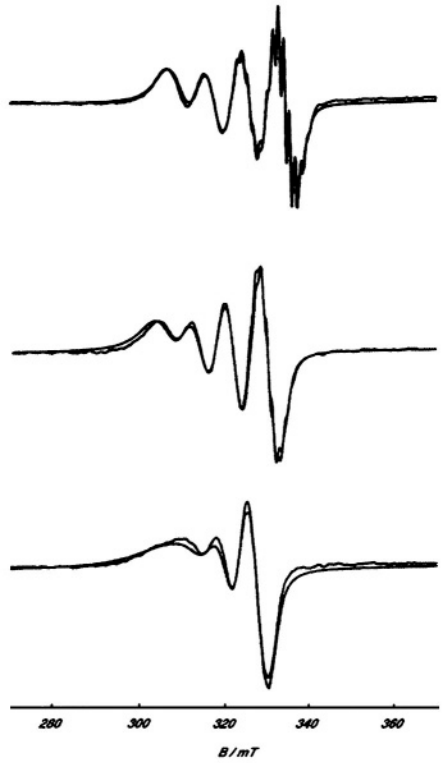

Figure 8. Room temperature ESR spectra (from top to bottom) of Cu-GGHG, Cu-GHG and Cu-HGG paired with simulations. 1:10 metal:ligand molar ratio and pH =7 (Pogni *et al.*, 1999a). The magnetic field (x) axis extends from 275 to 365 mT.

4.2 Copper Ternary Complex with Phenanthroline and Oxidized Glutathione

Because determination of bound nitrogens is always difficult, especially in the case of three nitrogens versus four nitrogens, an approach based on analysis of the FT of the ESR spectra was successfully applied. A study of the ternary complex Cu-Phen-GSSG addressed this problem (Della Lunga *et al.,* 1995).

The naturally occurring tripeptide glutathione (L-γ-glutamyl-L-cysteine-L-glycine) is one of the most abundant thiols. It is present in all living cells in a relatively high concentration, and is involved in a number of intracellular processes. The copper phenanthroline complex plays a role in cleavage of DNA in neoplastic cells. The ESR spectrum of the ternary Cu-Phen-GSSG

complex at room temperature is given in Fig. 9a along with the simulation that gave the best fit (Fig. 9a). Due to the multiplicity of potential metal-binding sites and the formation of complexes with many different stoichiometries (depending on the pH of the solution), the copper coordination assessment was difficult (Piu *et al.* 1995). Because the superhyperfine pattern from the interaction between the unpaired electron and nitrogen ligands is not well resolved, the second derivative expansion of the $M_I = +3/2$ component (solid line) (Fig. 9b) was eventually compared with a simulation for 2N + 1N (dotted line) and a simulation for 2N + 2N (dashed-dotted line).

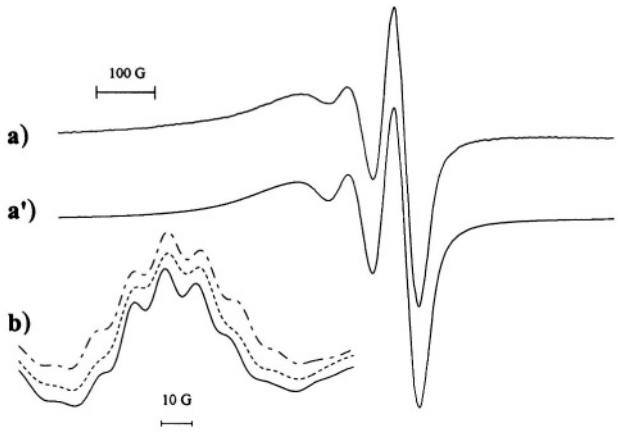

Figure 9. (a) ESR spectrum of the ternary complex Cu-phen-GSSG (T= 298K) together with its simulation (a), (b) second derivative expansion (110 G) of the experimental $M_I = +3/2$ component paired with a simulation for 2N + 1N (dotted line) and 2N + 2N (dashed-dotted line)(Della Lunga *et al.,* 1995b).

The second derivative display is customarily useful (see also Antholine chapter) for analyzing a complex superhyperfine pattern. It is often difficult to distinguish between three and four nitrogen atoms. The procedure described in Section 2.4, based on Fourier analysis of ESR spectra, was instrumental in overcoming this problem (Della Lunga *et al.,* 1995b). Fig. 10 was generated by this procedure and provides much information about the type of coordination. Fourier Transform of the second derivative room temperature ESR spectrum (solid line) is compared with those of the simulated spectra (dotted lines) of the cases 2N + 2N (Fig. 10a) and 2N + 1N (Fig. 10b). The similarity between the trends in the phase-sensitive section of the FT of the experimental ESR spectrum and the FT of the simulated one is clear proof of 2N + 1N coordination around the copper ion. The approach outlined in Sec. 2.4, based on FT analysis of the ESR spectra, eliminates any

residual uncertainties about ligand coordination around copper in solution. The method is simple and straightforward for deciding if the number of nitrogens involved is even or odd and is particularly useful for extracting information from poorly resolved patterns such as often occur in room temperature ESR spectra.

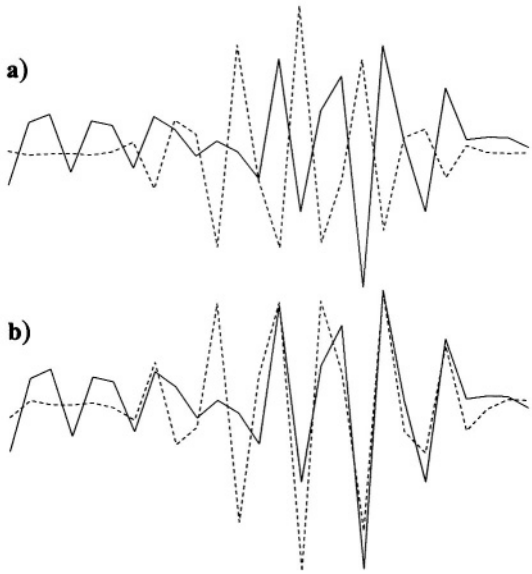

Figure 10. Pattern of the FT sensitive to nitrogen-number parity of the room temperature ESR experimental spectrum (solid line) and the corresponding section of the FT of the simulated spectrum (dotted line) for two different nitrogen ligand arrangements: (a) 2N + 2N (even parity) and (b) 2N + 1N (odd parity) (Della Lunga *et al.,* 1995b).

In this way it was established that the ternary complex $[Cu(GSSG)(Phen)]^-$ involves only one glutamyl moiety. The carboxyl groups that are not involved in the equatorial binding scheme are located far from the metal. The coordination of a metal by a carboxylic group in synergy with that of an amino group gives a five-membered stable ring – the other two positions in the plane being occupied by two nitrogen donor atoms from the phenanthroline ligand.

4.3 Copper Complex of Bleomycin

Metal-free bleomycin is a natural antitumor antibiotic that forms several metal complexes. *In vivo* bleomycin is activated by forming an iron complex in cells. Iron bleomycin (FeBlm) attacks DNA through the reactive species,

HO_2-Fe(III)Blm, causing single and double strand scission (Li *et al.,* 2001). Bleomycins bind copper, but Cu-Blm is inactive in the DNA strand scission reaction. Because the glycopeptide bleomycin is isolated as a copper complex from *Streptomyces Verticillus,* it has been the subject of many studies. The CuBlm complex has a molecular weight of 1700 and its ESR spectrum in solution shows a line shape consistent with incipient slow motion. For a long time, this prevented direct simulation of the ESR spectra, as explained in Sec. 3. Antholine *et al.* (1984) used S-band to extract magnetic parameters from the room temperature ESR spectrum at low frequency where fast conditions still hold, allowing for simulation of spectra with programs based on Kivelson's theory available at that time. Later, simulation of spectra at X band in the incipient slow-motion regime was successfully achieved by us following the simplified approach outlined in Sec. 3.2. Fig. 11 shows the ESR spectra of the Cu(II)Blm complex in aqueous solution from physiological temperature (310 K) to near freezing (260 K) (Pogni *et al.,* 1999). Spectra are paired with the simulations that gave the best fit. As can be inferred from line shape analysis of the ESR spectra at 310 K, the appearance of the spectrum is that of an incipient slow-motion spectrum consistent with the molecular weight of the complex (MW $\approx$ 1700). As the temperature decreases, the line shape of the spectrum varies continuously until at 277 K, the spectral anisotropy becomes evident. At 260 K, the ESR spectrum approaches a powder pattern-like species.

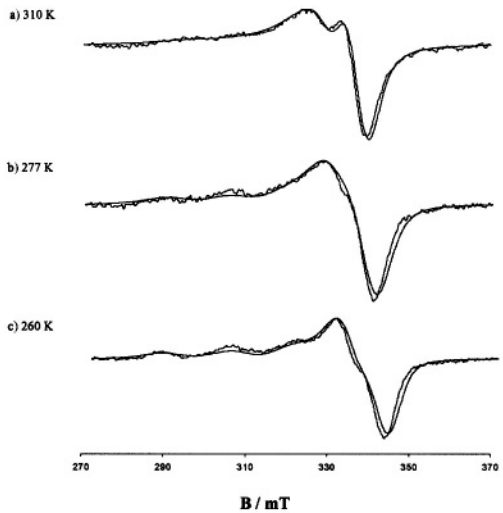

Figure 11. Experimental ESR spectra of the Cu(II)Blm complex in aqueous solution pH=7.4, recorded at: (a) 310K, (b) 277K, (c) 260K, paired with the simulations that eventually gave the best fit (Pogni *et al.,* 1999b).

From this result, it is evident that a square pyramidal coordination environment around copper involving four nitrogens can be confirmed with copper displaced out of the square plane. This is evident only by analysis of the room temperature ESR spectra of cupric bleomycin because the configuration of the complex may vary from the solid to the liquid state, to a greater extent than in low molecular weight square planar cupric complexes. Particular care should be taken when, for example, a "magnetopharmaceutical" compound is being analyzed. Living systems present a wide range of environments that can alter the dynamics of the nominally isotropically tumbling agents. The rotation of the complex plays an important role in determining proton relaxation enhancement (Chen *et al.,* 1994) and analysis of the copper complex structure at room temperature is necessary.

4.4 Copper Complex of β-Casomorphins

Room temperature simulations of the ESR spectra of copper complexes with β-casomorphin peptides (BCM-7, BCM-5, BCM-4) were useful in an integrated study based on ESR and NMR studies (Basosi et *al.,* 2001a). β-casomorphins are opioid peptides originally identified in enzymatic digests of the bovine milk protein β-casein. The presence of proline in the sequence imposes structural constraints that may determine secondary structure, even in the case of short chain peptides (Morris *et al.,* 1992; Basosi *et al.,* 2001b). Another important feature is that peptidyl-proline bonds yield both cis and trans conformations that are relatively stable at temperatures above 0°C (Fox *et al.,* 1986). The interaction of copper with opioid peptides, as well as neuro-transmitters and neuro-modulators, has also been thoroughly investigated. The metal is unevenly distributed in the body and is found in relatively high concentrations in the brain, although its function is still rather unclear. Fig. 12 shows the room temperature ESR spectrum of the copper complex of β-casomorphin 7 (BCM-7) (Tyr-Pro-Phe-Pro-Gly-Pro-Ile).

Computer simulations of ESR spectra allowed the number of coordinated nitrogens in the major species to be inferred (2 for BCM-4 and BCM-5, 4 for BCM-7), and the correlation time to be evaluated for all complexes. All isomers of BCM-4 and BCM-5 were shown to bind copper, but the resulting structures were strictly determined by the conformational state of ^{2}Pro. In the case of BCM-7, only the cis-cis-trans and/or the cis-cis-cis isomers did not bind copper. The conformational state of each Pro was shown to drive formation of the copper-nitrogen bond within the immediately adjacent residue, leading to the complex having four coordinated nitrogens in the case of the trans-trans-trans isomer for BCM-7 (Basosi *et al.,* 2001a).

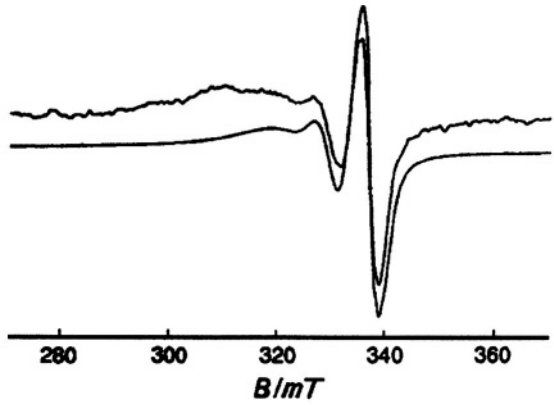

Figure 12. Room temperature ESR spectrum of the copper complex of BCM-7 paired with its simulation. (Basosi *et al.,* 2001a).

4.5 Perspectives

Hyde and Froncisz (Hyde and Froncisz, 1982), pointed out that 1000 isthe upper limit for molecular weight of copper complexes that can be analyzed using Kivelson's theory to obtain the rotational correlation time. This assumes that the magnetic parameters are known and a suitable choice of microwave frequency can be chosen. The question is important from a biological perspective, since many compounds of biological interest exceed this limit. Again, the region of 4 to 8 GHz is optimum for analyzing longer correlation times. Hyde and Froncisz estimated that the longest time that can be measured using fast tumbling models for copper complexes is 1 nsec, corresponding to a molecular weight of 3000 in aqueous solution. For slower motions, lines become non–Lorentzian and a slow-tumbling theory is required (see Sec. 3).

At this time, a computer program to simulate fluid-phase copper spectra is available in the form of a direct extension of Freed's approach with the inclusion of the superhyperfine interaction. In our opinion, the use of multifrequency ESR spectroscopy in combination with computer simulation programs will resolve a number of problems related to biological systems for which the room temperature information is needed (see Sec.1).

Study of the fragments that bind copper, either in prion proteins or in the protein involved in Alzheimer's disease, represent examples of where the programs may be effective for analysis of biologically interesting copper complexes. Furthermore, copper complexes can be used as molecular

probes for investigating the structure and dynamics of membranes and for obtaining information concerning metal transport in membranes.

Nevertheless, from a methodological point of view, this research might represent only a starting point for new contributions and new problems: for example, the restoring potential should be included in order to describe anisotropic liquids. Furthermore, dipolar coupling constants should be included and copper quadrupole coupling might be added. Future development may include motional averaging of forbidden transitions and slow-motion spectra with H1||H0 areas potential. These explorations could exploit the great synergy of computer science and ESR spectroscopy, to expand the investigation into biologically significant systems with higher molecular weights in solution.

5. REFERENCES

Abragam, A., Bleaney, B. (1970) *in* Electron Paramagnetic Resonance of Transition Ions, Oxford University Press: London.

Amar, C., Vilkas, E., Foos, J. (1982) *J. Inorg. Biochem.* **17**, 313.

Antholine, W.E., Riedy, G., Hyde, J.S., Basosi, R., Petering, D.H. (1984) *J. Biomol. Struct. Dyn.,* **2**, 469.

Arnold, F.H., Haymore, B.L. (1991) *Science,* **252**, 1796.

Aronoff-Spencer, E., Burns, C.S., Avdievich, N.I., Gerfen, G.J., Peisack, J., Antholine, W.E., Ball, H.L., Cohen, F.E., Prusiner, S.B., Millahuser, G.L. (2000) *Biochemistry,* **39**, 13760.

Atkins, D., Kivelson, D. (1966) *J. Chem. Phys.,* **44**, 169.

Bal, W., Dyba, H., Kozlowski, H. (1997) *Acta Biochim. Pol.,* **44**, 467.

Basosi, R., Valensin, G., Gaggelli, E., Froncisz, W., Pasenkiewicz-Gierula, M., Antholine, W.E., Hyde, J.S. (1986) *Inorg. Chem.,* **25**, 3006.

Basosi, R., D'Amelio, N., Gaggelli, E., Pogni, R., Valensin, G. (2001a) *J. Chem. Soc.,* Perkin Trans., **2**, 252.

Basosi, R., Antholine, W.E., Froncisz, W., Hyde, J.S. (1984) *J. Chem. Phys.,* **81**, 6869.

Basosi, R., Antholine, W.E., Hyde, J.S. (1993) *in* Biological Magnetic Resonance, (Berliner, J. R. and Reuben J. eds.) Plenum Press: New York and London, Vol. 13, pp. 103-147 and references therein.

Basosi, R., D'Amelio, N., Gaggelli, E., Gaggelli, N., Maccotta, A., Pogni, R., Valensin D., Valensin, G. (2001b), *Curr. Top. Peptide & Protein Research,* **4**, 17.

Bloch, F. (1956) *Phys. Rev.* **102**, 104.

Bonomo, R.P., Bonsignore, F., Conte, E., Impellizzeri, G.,; Pappalardo, G., Purrello, V., Rizzarelli, E. (1993) *J. Chem. Soc.* Dalton Trans., 1295.

Bruno, G.V., Harrington, J.K., Eastman, M.P. (1977) *J. Phys. Chem.,* **81**, 1111.

Chen, J.W., Auteri,F.P., Budil, D.E., Belford, R.L., Clarkson, R.B. (1994) *J. Phys. Chem.,* **98,** 13452.

Della Lunga, G., Pogni, R., Basosi, R. (1994a) *J. Phys. Chem.,* **98**, 3937.

Della Lunga, G., Pogni, R., Basosi, R. (1994b) *J. Magn. Reson.,* **108A,** 65.

Della Lunga, G., Basosi, R. (1995a) *J. Magn. Reson.,* **112A**, 102.

Della Lunga, G., Pogni, R., Basosi, R. (1995b) *J. Magn. Reson.,* **114A,** 174.

Della Lunga, G., Pogni, R., Basosi, R. (1998) *Mol. Phys.,* **95**, 6, 1275.

Falk, K.E., Ivanova, E., Roos, B., Vänngård, T. (1970) *Inorg. Chem.,* **9**, 556.
Feher, G. (1957) *Bell. Syst. Tech. J.,* **36**, 449.
Fox, R.O., Evans, P.A., Dobson, C.M. (1986) *Nature,* **320**, 192.
Fraenkel, G.K. (1965) *J. Chem. Phys,.* **62**, 6275.
Fraenkel, G.K. (1967) *J. Phys. Chem.,* **71**, 139.
Freed, J.H. (1976) *in* Theory of Slow Tumbling ESR Spectra of Nitroxides, *in* Spin Labeling: Theory and Application, (Berliner L. eds.) Academic Press: New York; Vol.1, Ch. 3, p. 53.
Freed, J.H. (1987) *in* Rotational Dynamics of Small Probes and Macromolecules in Liquids (T. Dorfmuller and R. Pecora, eds.) Springer-Verlach, New York; p. 89.
Freed, J.H., Bruno, G.V., Polnaszek, C.F. (1971) *J. Phys. Chem.,* **75**, 3385.
Freed, J.H., Fraenkel, G.K. (1963) *J. Chem. Phys.,* **39**, 2.
Froncisz, W., Hyde, J.S. (1980) *J. Chem. Phys.,* **73**, 3123.
Harford, C., Sarkar B. (1997), *Acc. Chem. Res.,* **30**, 123.
Hegg, E.L., Burstyn, J.N. (1996) *Inorg.Chem.,* **35**, 7474.
Hellinga, H.M., Caradonna, J.P., Richards, F.M. (1991) *J. Mol. Biol.,* **222**, 787.
Herring, F.G., Park, J.M. (1979) *J. Magn. Reson.,* **36**, 311.
Hubbard, P.S. (1963) *Phys. Rev.,* **131**, 1155.
Hyde, J.S., Froncisz, W. (1982) *Ann. Rev. Biophys. Bioeng.,* **11**, 391.
Hyde, J.S., Jesmanowicz, A., Ratke J.J., Antholine, W.E. (1992) *J. Magn. Reson.,* **96**, 1.
Hyde, J.S., Mchaourab, H.S., Camenisch, T.G., Ratke, J.J., Cox, R.W., Froncisz, W. (1998) *Rev. Sci. Instrum.,* **69**, 2622.
Hyde, J.S., Pasenkiewicz-Gierula, M., Jesmanowicz, A., Antholine, W.E. (1990) *Appl. Magn. Reson.,* **1**, 483.
Hyde, J.S., Antholine, W.E., Froncisz, W., Basosi, R. (1986) *in* Advanced Magnetic Resonance Techniques in Systems of High Molecular Complexity (Niccolai, N.; Valensin, G. eds.) Birkhäuser: Base.
Hyde, J.S., Froncisz, W. (1986) *Electron Spin Reson.,.***10A**, 175.
Hyde, J.S., Froncisz, W. (1989) *in* Advanced EPR: Applications in Biology and Biochemistry, (Hoff, A. J., eds.) Elsevier Science B.V: Amsterdam; pp. 277-306.
Hyde, J.S., Jesmanowicz, A., Ratke, J.J., Antholine, W.E. (1992) *J. Magn. Reson.,* **96**,1 and references therein.
Keijzers, C.P., Paulussen, F.G.M., de Boer, E. (1975) *Mol. Phys.,* **29**, 973.
Kirkpatrick, S. (1984) *J. Stat. Phys.,* **34**, 975.
Kirkpatrick, S., Gelatt, C.D. Jr., Vecchi, M.P. (1983) *Science,* **220**, 4598.
Kivelson, D. (1972) *in* Electron Spin Relaxation in Liquids (Muss, L.T.; Atkins, P.W., eds.); Plenum: New York, 213; and references therein.
Kivelson, D.J. (1960) *Chem. Phys.,* **33**, 1094.
Korstanje, L.J., van Faassen, E.E., Levine, Y.K. (1989) *Biochim. Biophys. Acta,* **982**, 196.
Kozlowski, H., Bal, W., Dyba, M., Kowalik-Jankowska, T. (1999) *Coord. Chem. Rev.,* **184**, 319.
Kubo, R. (1969b) *Adv. Chem. Phys..* **15**, 101.
Kubo, R. (1969a) *J. Phys. Soc. Jap. Suppl.,* **26**, 1.
Kubo, R. (1957) *J. Phys. Soc. Jap.,* **12**, 570.
Kubo, R. (1966) *Rep. Prog. Phys.,* **29**, 255.
Lanczos (1950) *Journal of Research of National Bureau of Standards* **45**, 255.
Leigh, J.S., Reed, G.H. (1971) *J. Phys. Chem.,* **75**, 1202.
Lewis, W.B., Alei, M. Jr., Morgna, L.O. (1966) *J. Chem. Phys.,* **44**, 2409.
Li, W., Zao, C., Xia, C., Antholine, W.E., Petering, D.H. (2001) *Biochemistry,* **40**, 7559.
Maki, A.H., McGarvey, B.R.(1958) *J. Chem. Phys.,* **29**, 31.
Marquardt, D.W. (1963) *J. Soc. Industrial Appl. Math.,* **11**, 431.

Mc Connell, H.M. (1956) *J. Chem. Phys.,* **25**, 709.
McGarvey, B.R. (1956) *J. Chem. Phys.,* **60**, 71.
Meirovitch, E., Igner, D., Igner, E., Moro, G., Freed, J.H. (1982) *J. Chem. Phys.,***77**, 3915.
Metropolis, N., Rosenbluth, A., Rosenbluth, M., Teller, A., Teller, E. (1953) *J. Chem. Phys.,* **21**, 1087.
Moro, G. (1980) *EPRLF and EPRLP Routines,* unpublished report, Cornell University, Ithaca, New York.
Moro, G., Freed J.H. (1981) *J. Chem. Phys.,* **74**, 3757.
Moro, G., Freed, J.H. (1986) *in* Large Scale Eigenvalue Problems (Cullum, J., Willough, R.A,, Eds.) Elsevier: Amsterdam, p. 143.
Morris, A.L., MacArthur, A.G., Hutchinson, A.G., Thornton, J.M. (1992) *Proteins,* **12**, 345.
Multhaup, G., Ruppert, T., Schlicksupp, A., Hesse, L., Bill, E., Pipkorn, R., Masters, C.L., Beyreuther, K. (1998) *Biochemistry,* **37**, 7224
Nelder, J.A., Mead, R. (1965) *Computer Journal,* **7**, 308.
Noack, M., Gordon, J. (1968) *J. Chem. Phys.,* **48**, 2689.
Orii, Y., Morita, M. (1977) *J. Biochem.,* **81**, 163.
Pasenkiewicz-Gierula, M., Froncisz, W., Basosi, R., Antholine, W.E,, Hyde, J.S. (1987) *Inorg. Chem.,* **26**, 801.
Pasenkiewicz-Gierula, M., Subczynski, W.K., Antholine, W.E. (1997) *J. Phys. Chem.* ***B*** **101**, 5596.
Pettit, L.D., Gregor, J.E., Kozlowski, H. (1991) *Perspectives in Bioinorganic Chemistry,* JAI Press, London, vol. **1**, p. 1.
Piu, P., Sanna, G., Zoroddu, M.A., Seeber, R., Basosi, R., Pogni, R. (1995) *J. Chem. Soc.* Dalton Trans.,.1267.
Pogni, R., Della Lunga, G., Basosi, R. (1993) *J. Am. Chem. Soc.,* **115**, 1546.
Pogni, R., Baratto, M.C., Busi, E., Basosi, R. (1999a) *J. Inorg. Biochem.,* **73**, 157.
Pogni, R., Busi, E., Della Lunga, G., Basosi, R. (1999b) *Ann. NYAcad. Sci.,* p. 276.
Poole, C. (1967) *Electron Spin Resonance,* John Wiley & Sons: New York; and references therein.
Press, W.H., Teukolsky, S.A., Vetterling, W.T., Flannery, B.P. (1994) *Numerical Recipes in C,* Cambridge University Press: Cambridge.
Rao, K.V.S., Polnaszek, C.F., Freed, J.H., (1977) *J..Phys..Chem.,* **81**, 449.
Redfield, A.G. (1957) *IBM J. Res. Develop.* **1**, 19.
Reinhammar, B. (1984) *in* Copper Proteins and Copper Enzymes (Lontie, R., eds.) Vol. 3, pp. 1-35.
Romanelli, M., Basosi, R. (1988) *Chem. Phys. Lett.,* **143**, 404.
Schneider, D.J., Freed, J.H. (1988) *Calculating Slow Motional Magnetic Resonance Spectra A User's Guide,* Cornell University, Ithaca, New York.
Schneider D.J.,; Freed, J.H. (1989) *Adv. Chem. Phys.,* **73**, 387.
Shullenberger, D.F., Eason, P.D., Long, E.C. (1993) *J. Am. Chem. Soc.,* **115**, 11038.
Silsbee, R.H. (1966) *J. Chem. Phys.* **45**, 1710.
Solomon E.I. (1984) *Commun. Inorg.Chem.* **3**, 225.
Solomon, E.I., Baldwin, M.J., Lowery, M.D. (1992) *Chem. Rev.,* **92**, 521.
Vänngård, T. (1972) in *Biological Applications of Electron Spin Resonance,* (Swartz, H.M., Bolton, J.R. and Borg, D.C., eds.) Wiley, New York, 423.
Vasavada, K.V., Schneider, D.J., Freed, J.,H. (1987) *J. Chem. Phys.,* **86**, 647.
Wilson, R., Kivelson, D. (1966) *J. Chem. Phys.,* **44**, 4445.

Chapter 14

Low Frequency EPR of Cu^{2+} in Proteins

William E. Antholine
National Biomedical ESR Center, Medical College of Wisconsin, 8701 Watertown Plank Road, Milwaukee, WI 53226

Abstract: Frequencies lower than X-band give better-resolved CW EPR spectra for copper(II) complexes. Use of S-band (2-4 GHz) revealed a new type of copper center in proteins. In the $g_{||}$ region of the spectrum there is narrowing of the linewidths for negative values of m_I, with minimum linewidths near 3 GHz. Examples of S-band spectra are given for particulate methane monooxygenase, Cu-substituted prions, azurin, laccase, mixed valence dinuclear copper sites in nitrous oxide reductase and Cytochrome c oxidase, and from Cu in clusters.

1. INTRODUCTION

1.1 Overview

This chapter reviews low frequency EPR studies completed since the one written by Riccardo Basosi, Bill Antholine and Jim Hyde, entitled "Multifrequency ESR of Copper" in *Biological Magnetic Resonance, Vol. 13,* 1993. A brief description of why low frequency EPR of cupric complexes is useful follows. Numerous applications over the last ten years have used the Froncisz-Hyde loop gap resonator to obtain better resolved spectra at microwave frequencies lower than 9 GHz for EPR detectable copper complexes. Not only were better-resolved spectra obtained, but a new type of copper complex in proteins was observed and studied. Using EPR and other methods, it was found to be a [$HisCu^{1.5+}(Cys)_2Cu^{1.5+}His$] site where the sulfurs of Cys are bridging ligands (see Sec. 3).

1.2 Parameters for Cu^{2+}

The EPR spectra of Cu^{2+} bound to acetylacetonate, a typical square planar complex, are shown in Fig. 1. In frozen solution, the axial direction of the powder pattern is identified by $g_{\|}$ and $A_{\|}$, the direction parallel to the perpendicular to the square plane. Every direction in the square plane has equivalent EPR parameters as measured by $g_{\perp}$ and $A_{\perp}$. This accounts for the greater intensity of the lines in the perpendicular region relative to the parallel region. The dashed lines in Fig. 1 mark the overshoot lines (sometimes referred to as hyperfine anomaly lines or extra absorption lines), which arise because a large number of orientations have almost identical EPR parameters. If the cupric molecule has a low molecular weight and is rapidly tumbling in solution, the rigid parameters obtained in frozen solution average to isotropic EPR parameters as indicated in spectrum B of Fig. 1.

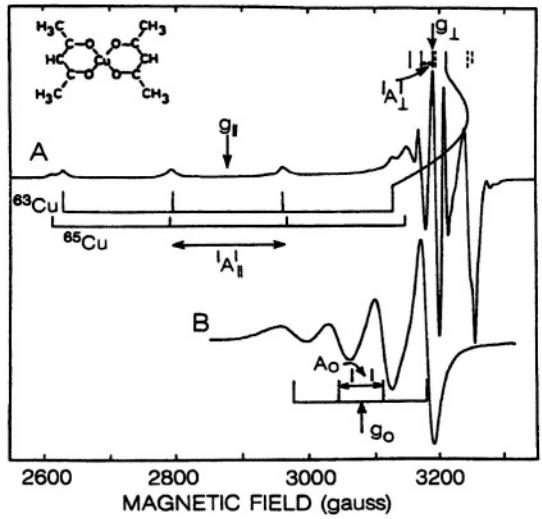

Figure 1. EPR spectra of a solution of a Cu^{2+} complex, (A) frozen at 77K and (B) at room temperature. The values of the g factors and hyperfine constants are $g_{\|} = 2.285$, $g_{\perp} = 2.060$, $g_0 = 2.135$, $A_{\|} = 167$ G, $A_{\perp} = 17$ G, and $A_0 = 67$ G. In (A) the dashed bars indicate the position of the overshoot lines, which occur from the angular dependence of the copper hyperfine lines as shown for one of them (the full curved line to the right). The small peaks at the highest field in (A) arise from a second complex existing in low concentration [*cf.* Fig. 3 in Gersmann and Swalen (1962)]. The sample is 5 mM in Cu^{2+} and 40 mM in acetylacetonate $(CH_3COCH_2COCH_3)$ in a 1:1 water:dioxane solvent at alkaline pH. The same tube was used for both spectra with five times higher spectrometer gain in (B). Other settings were microwave power, 2mW; frequency, 9.2 GHz; field modulation, 7 G; time constant, 0.3 s; and sweep time, 4 min. (*From Vänngård,* 1972).

Chapter 13 of this text, by Basosi, describes how to obtain EPR parameters like those in spectrum B. The EPR parameters for proteins are

usually not averaged in the liquid phase due to their high molecular weights. All the spectra shown in this chapter were obtained at 77 K or at colder temperatures. Fig. 2 diagrams the transitions for an S = ½ and $M_I = 3/2$ spin system like Cu^{2+}. For most cupric ions bound to proteins, copper is bound to nitrogen atoms, which have a nuclear spin of I = 1 for ^{14}N, which will split the lines further. From this additional splitting, termed superhyperfine structure, a coupling for nitrogen, A^N, is sometimes obtained. For example, if there are four equivalent nitrogen donor atoms, each line will be split into a 1:4:10:16:19:16:10:4:1 pattern. In the perpendicular region, there are four copper lines, plus overshoot lines and lines from nuclear quadrupolar interactions, giving more than 36 lines (4 Cu lines times 9 superhyperfine lines from the 4 equivalent nitrogens), which are superimposed, making analysis difficult. Much of the analysis of the superhyperfine structure in our studies relies on resolution of the superhyperfine structure in the $g_{||}$ region where the copper lines are spread out and the superhyperfine lines are not superimposed on other superhyperfine lines.

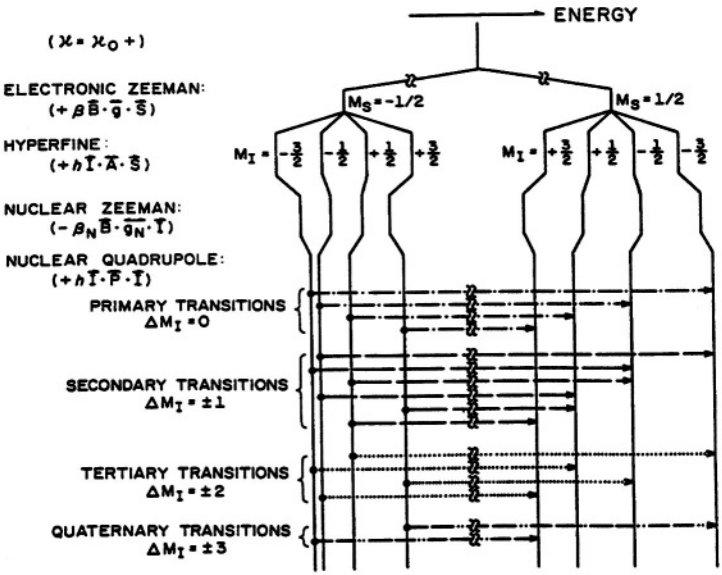

Figure 2. Schematic representation of energy levels and possible transitions for an $S = 1/2$, $M_I = 3/2$ system [such as $^{63}Cu(II)$] subject to an initial Hamiltonian H_0 plus four spin Hamiltonian terms. The M_I quantum numbers are assigned in the conventional way so that the selection rule would be $\Delta M_I = 0$ if there were no nuclear Zeeman or quadrupole terms. The primary transitions are the four allowed transitions normally described in textbooks; the secondary and tertiary transitions are usually ignored or referred to as "forbidden," often an inappropriate name. The quaternary transitions normally are so weak as to merit the name "forbidden." The relative transition frequencies and intensities are highly dependent on magnetic field orientation. *(From Belford and Duan, 1978).*

Examples of structures of the different types or classes of copper complexes will be given in later sections. The EPR detectable types are: (1) type 1 blue copper with trigonal or distorted tetrahedral symmetry, two ligands from nitrogens from two histidines and a sulfur from cysteine with $A_{\|} < 120$ G, usually ranging from 60 to 90 G; (2) type 2 copper with square planar or pyramidal square planar geometry with $A_{\|}$ ranging from > 120 G to around 200 G; (3) mixed valence dinuclear purple copper $[HisCu^{1.5+}(Cys)_2Cu^{1.5+}His]$ with nitrogen donor atoms from two histidines and donor atoms from two bridging sulfurs from cysteines, with $A_{\|}^{Cu}$ of about 40 G and the copper hyperfine lines in a seven-line pattern with relative intensities of 1:2:3:4:3:2:1; and (4) multinuclear copper clusters comprised of three or four copper ions.

Both $g_{\|}$ and $A_{\|}$ are used to suggest the donor atoms from the ligands. The lowest g values are for type 2 cupric model complexes with sulfur donor atoms, for example, a typical $g_{\|}$ value of 2.09 and $A_{\|}$ value of 130 G for 4-S donor atoms, and $g_{\|}$ of 2.14 and $A_{\|}$ value of 187 G for 2-S and 2-N donor atoms. The $g_{\|}$ value increases as nitrogen replaces sulfur and oxygen replaces either nitrogen or sulfur. $A_{\|}$ increases as nitrogen replaces a sulfur donor atom, but decreases when oxygen replaces a nitrogen donor atom. A typical $g_{\|}$ value is 2.21, and a typical $A_{\|}$ is 190 G for 4-N donor atoms, while $g_{\|}$ of 2.4 and $A_{\|}$ of about 130 G would be expected for 4-O donor atoms. Plots of $g_{\|}$ versus $A_{\|}$ are called Peisach-Blumberg plots, and suggest the nature of the donor atoms for a cupric complex (Peisach and Blumberg, 1974). One such plot by Vänngård (1972) nicely shows the separation of type 2 and type 1 complexes as well as the trend in $g_{\|}$ and $A_{\|}$ as the donor atoms to copper vary.

Table 1 lists compounds and EPR parameters $g_{\|}$ and $A_{\|}$ as a function of donor atoms. Our laboratory has published EPR parameters for all but one of these complexes. The examples are heavily weighted to complexes with nitrogen atoms and "purple" copper, i.e. the mixed valence $[HisCu^{1.5+}(Cys)_2Cu^{1.5+}His]$ Cu_A sites, rather than the "blue" type 1 cupric sites with trigonal or distorted tetrahedral configurations, because of the author's interest in these compounds. While there is overlap between, for example, four nitrogen donor atoms (N-N-N-N) and two nitrogen donor atoms plus a sulfur and an oxygen donor atom, determination of $g_{\|}$ and $A_{\|}$ will usually give a good indication of the donor atoms. Many more examples exist for type 1 Cu^{2+} than are listed in Table 1. While there is some overlap in EPR parameters between type 1 and mixed valence sites, the sites are usually easy to differentiate because of the color associated with the sites and because type 1 Cu^{2+} generates a four-line pattern with almost equal intensities while the mixed valence sites generate a seven-line pattern with relative intensities of 1:2:3:4:3:2:1.

Table 1. Parameters for Copper Complexes*

	$g_{\|}$	$A_{\|}$ (G)	Donor atoms
Type 2 Complexes (light blue)			
$Cu(dtc)_2$	2.09	130	S-S-S-S
CuKTS	2.14	187	S-S-N-N
CuPTS+GSH	2.14	180	S-S-N-N
CuPTS+ascites cells	2.13	178	S-S-N-N
Cu(PTS)(His)	2.19	169	S-N-N-N
CuPTS+en	2.19	169	S-N-N-N
CuPTS	2.20	186	S-N-N-O
$Cu(PTS)(OH_2)$	2.21	185	S-N-N-O
CuBLM	2.21	175	N-N-N-N
CuTPP	2.18	176	N-N-N-N
Cu-serum albumin	2.18	213	N-N-N-N
Cu-carnosine	2.20	190	N-N-N-N
Cu+excess histidine	2.22	183	N-N-N-N
Cu-pMMO	2.24	185	N-N-N-N
Cu^{2+}+ascites cells	2.25	180	N-N-N-N (possibly)
Cu-prion protein	2.23	158	N-N-N-O
CuEDTA(pH 6)	2.29	155	N-N-O-O
Cu^{2+} in excess acetylacetonate	2.28	167	O-O-O-O
$Cu(OH)_4$	2.40	113	O-O-O-O
$CuSO_4$ in DMF	2.40	128	O-O-O-O
Type 1 Complexes (dark blue)			
type 2-depleted fungal laccase	2.19	90	N-N-S
Laccase	2.30	40	N-N-S
Azurin	2.25	57	N-N-S
Mixed Valence Cu-Cu (purple)			
Cu_A-N_2OR	2.18	38	N-Cu-S_2-Cu-N
Cu_A-*Cc*O (bovine)	2.18	38	N-Cu-S_2-Cu-N
Cu_A-*Cc*O (*R. sphaeroides*)	2.19	30	N-Cu-S_2-Cu-N
Cu_A(engineered in *P. aeruginosa* azurin)	2.18	56	N-Cu-S_2-Cu-N
Cu_2L^{3+}	2.02($g_{\|}$<$g_{\perp}$)	~20	N_4-Cu-Cu-N_4

* Abbreviations: dtc, dithiocarbamate; KTS, oxobutyraldehyde bis(thiosemicarbazones); PTS, 2-formylpyridine monothiosemicarbazone; en, ethylenediamine; His, histidine; BLM, bleomycin; TPP, tetraphenylporphyrin; pMMO, particulate methanemonooxygenase; EDTA, ethylenedeaminetetraacetic acid; DMF, dimethylformamide; N_2OR, nitrous oxide reductase; *Cc*O, cytochrome *c* oxidase, L, $N[CH_2CH_2N(H)CH_2CH_2N(H)CH_2CH_2]_3N$.
NOTE: net charges of the cupric complexes are not indicated.

One of the best means of obtaining EPR parameters is through simulation of the spectrum. Most of our copper spectra were simulated using the program QPOW (Rakhit *et al.,* 1985). This program has a line width equation that results in narrowing of the $M_I = -½$ line in the $g_{\|}$ region at low microwave frequencies. Bruker Instruments, Inc., (Billerica, MA) offers two simulation programs. Of these, Simfonia, uses perturbation theory for superhyperfine structure for the signal from a cupric site. The other,

XSophe, allows choice between direct diagonalization and perturbation methods. XSophe has the line width equations to simulate low microwave frequency spectra, but the equations in Simfonia will not reduce the line width in the $g_{\|}$ region as the microwave frequency decreases. Using direct diagonalization with XSophe and including extensive superhyperfine structure increases the simulation time to many hours per spectrum. Two other simulation programs are readily available, from Frank Neese (Max Planck Institut, Germany) and Antal Rockenbauer (Department of Organic Chemistry, Vesprem University, Budapest, Hungary). Both programs are fast, but the line width equations needed for low frequency must be requested from the authors, as they are not available in all versions. The most accurate parameters are obtained from simulating the spectra from the same complex at several microwave frequencies, with one set of EPR parameters (Basosi *et al.,* 1984)

1.3 Line Width Reduced for the $M_I = -½$ in the $g_{\|}$ Region at Lower Frequencies

The basis for most of the low frequency work with cupric complexes is that the line widths in the $g_{\|}$ region are narrower at lower microwave frequencies. There exists a microwave frequency for negative values of M_I, where the width of the line is the residual width, $H^R_{1/2}$. Froncisz and Hyde (1980) expressed the line width for a type 2 cupric complex as follows:

$$\Delta H_{½} = [(H^R_{½})^2 + (M_I \sigma A_{\|})^2 + ((h\nu/g_{\|}^2\beta_0)(\sigma g_{\|}))^2 + (2M_I h\nu/ g_{\|}^2\beta_0)(\sigma g_{\|}\sigma A_{\|})]^{½} \quad (1)$$

If M_I is negative, i.e. $-½$ or $-^3/2$ for cupric complexes, the line width in the $g_{\|}$ region will reach a minimum at a microwave frequency lower than 9 GHz. The minimum line width for the $M_I = -½$ line in the $g_{\|}$ region for $Cu(catachol)_2$ is about 2 GHz. We generally work at about 3 or 4 GHz (S-band, Table 2), because the signal-to-noise ratio is better and the curve is somewhat flat in the low frequency region.

Table 2: Microwave Bands for Multifrequency ESR

Band	Frequency (GHz) $h\nu = g\beta H$
L	1
S	3
C	5
X	9
K	18
Q or *Ka*	35
W	95
F, D or *G*	140
Y, J or A_2	250

1.4 Froncisz-Hyde Loop Gap Resonator

A difficulty with working at lower frequencies is that the TE_{102} rectangular cavity is three times the size of the X-band cavity at 9 GHz. About 20 ml of sample must be used at low frequency to get comparable sensitivity to the 0.3 ml samples in 4 mm tubes at 9 GHz. This problem was solved by Froncisz and Hyde (1982), who developed a loop gap resonator (Fig. 3). This resonator was made to accommodate the standard 4 mm quartz sample tube used at 9 GHz. The entire assembly is placed in a dewar held between the magnet poles, and cold gas is used to chill the resonator. While this is not as stable as a resonator that allows a quartz insert, high quality spectra have been obtained over the years, and it gives a larger filling factor. Bruker sells a slotted tube resonator with a quartz insert to cool the sample and to hold a 4 mm standard quartz sample tube. More details on loop gap resonators can be found in the chapter of this text by George Rinard and Gareth Eaton (vol. 24, ch.2).

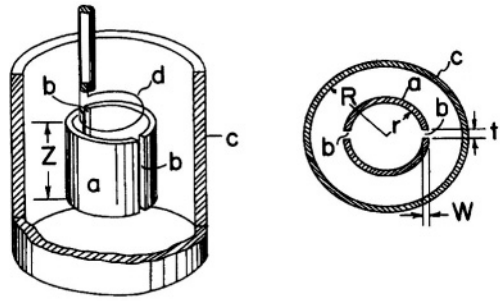

Figure 3. The loop gap resonator showing the principal components (*a*) loop; (*b*) gaps; *(c)* shield; *(d),* inductive coupler; and the critical dimensions *(Z,* resonator length, *r,* resonator radius; *R*, shield radius; *t,* gap separation; *W,* gap width). The sample is inserted into the loop *a* through the coupler, *d.* The microwave magnetic field in the loop is parallel to the axis of the loop (*Froncisz and Hyde, 1982*).

1.5 Effect of Isotopes: ^{63}Cu and ^{15}N

It has been our experience that the $M_I = -½$ line in the $g_{||}$ region for cupric complexes is resolved well enough at low microwave frequencies to determine the number of nitrogen donor atoms. In almost all cases, it is necessary to incorporate a single isotope of copper, usually ^{63}Cu (69% natural abundance), to obtain adequate resolution to determine the number of approximately equivalent nitrogen donor atoms. Sometimes the use of D_2O instead of H_2O is also necessary. Substitution of ^{15}N (I = ½) instead of ^{14}N (I = 1) not only reduces the number of superhyperfine lines from nitrogens, but

also gives lines that are well resolved because the nuclear moment of ^{15}N is 1.4 times the nuclear moment for ^{14}N. In several applications discussed in the following sections, cells were grown with $^{63}Cu(II)$ nitrate, and sometimes potassium ^{15}N-nitrate or D,L-[1,3-$^{15}N_2$] histidines in the medium to incorporate the isotopes into the EPR detectable cupric complex. In order to use $^{15}N_2$-histidine, His^- strains were required (Neese *et al.,* 1996).

2. EXAMPLES FROM TYPE 2 (SQUARE PLANAR) AND TYPE 1 (BLUE) Cu^{2+} SITES

2.1 Particulate Methane Monooxygenase, pMMO

Methanotrophs, cells that grow on methane as their sole source of carbon and energy, generate a type 2, square planar Cu^{2+} EPR signal (Fig. 4). Methane monooxygenases (MMOs) are enzymes that convert methane to methanol (Hanson, Netrusov and Tsuji, 1991; Hanson and Hanson, 1996; Anthony, 1986):

$$CH_4 + O_2 + NAD(P)H + H^+ \leftrightarrows CH_3OH + H_2O + NAD(P)^+ . \qquad (2)$$

Particulate methane monooxygenase, pMMO, is a copper enzyme that converts methane to methanol under most conditions. Under conditions where copper is limited, soluble methane monooxygenase, sMMO, with a dinuclear iron active center is turned on. Several years ago, our lab began to study the type 2 cupric signal in *Methylomicrobium album* BG8, which has two almost identical genes for pMMO, but no sMMO, and avoids the complications of sMMO. The EPR signal in *M. album* BG8 cells was compared to a Cu^{2+} standard, 1.0 mM cupric perchlorate, and the concentration of EPR detectable type 2 Cu^{2+} was about 500 μM. This concentration is at least 10 times the concentration of other enzymes in these cells. pMMO is the only enzyme in these cells and in membrane fractions expressed at such a high concentration. The same Cu^{2+} signal is found in several purifications, even though the activity is either down or lost (Nguyen *et al.,* 1998; Kamachi *et al.,* 2001), but the EPR signal was not found in one recent attempt to purify it (Lieberman *et al.,* 2001). While most investigators have concluded that the signal is from pMMO, it is still of interest to EPR spectroscopists if it is subsequently shown to be from another site, because it will help determine how cells can continue to survive after accumulating so much Cu^{2+}.

The X-band spectrum shown in the lower trace of Fig. 4 is enlightening. It shows there is often a free radical signal at g = 2.00 accompanying the Cu^{2+} signal. The well-resolved superhyperfine structure

in the $g_\perp$ region of the spectrum obtained with ^{63}Cu in the growth medium suggests nitrogen donor atoms with A^N of 13G. A $g_\parallel$ value of 2.24 and $A_\parallel$ value of about 185 G suggest, from consideration of Peisach Blumberg plots, that there are three or four nitrogen donor atoms (Yuan *et al.,* 1999). The S-band spectra at 3.4 GHz are also consistent with three or four nitrogen atoms (Figs. 5 and 6, Yuan *et al.,* 1997).

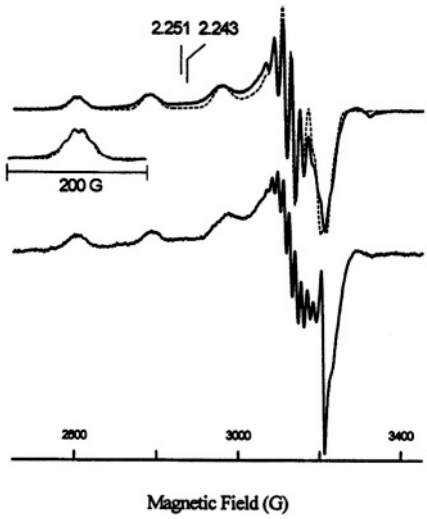

Figure 4. X-band EPR spectra *(upper trace)* of *M. album* BG8 cells grown with ^{15}N and $^{63}Cu^{2+}$. The upper spectrum is the average of four scans. The insert is the expansion of the –3/2 line in the $g_\parallel$ region after 15 scans. The dotted lines are simulations. Spectrometer conditions: microwave frequency, 9.089 GHz; modulation amplitude, 5 G; microwave power, 5 mW; temperature 77 K. Simulated spectra are the sum of two spectra. X-band EPR spectrum *(lower trace)* of *M. album* BG8 cells grown with ^{14}N and ^{63}Cu compounds *(Yuan et al., 1999).*

It was difficult to choose between a nine-line pattern with relative intensities of 1:4:10:16:19:16:10:4:1 for four equivalent nitrogens, and a seven-line pattern with relative intensities of 1:3:6:7:6:3:1 for three equivalent nitrogens – the outer line with an intensity of one could be buried in the noise. Fortunately, substitution of ^{15}N for ^{14}N was more informative (Fig. 4, upper trace). The number of superhyperfine lines in the $g_\perp$ region was reduced consistent with the change from I = 1 for ^{14}N to I = ½ for ^{15}N. In addition, the superhyperfine coupling increased from 13 G for ^{14}N, to 18 G for ^{15}N, consistent with $A(^{15}N)/A(^{14}N) = 1.4$. The lines in the $g_\parallel$ region were also better resolved due to substitution of ^{15}N for ^{14}N. An even line pattern of six lines on the $M_I = -3/2$ line in the $g_\parallel$ region was observed. Five lines with intensity 1:2:3:2:1 are expected for four equivalent nitrogens from ^{15}N with I = ½. Either another coupling, for example from a proton, was

observed or there was a superposition of two signals. Analysis of a low frequency S-band spectrum distinguished between these two situations. At S-band, the EPR signal in the $g_{||}$ region is a five-line, odd line pattern (Figs. 7 and 8, Lemos *et al.,* 2000). The two five-line patterns observed in the $g_{||}$ region collapsed at S-band to give two superimposed five-line patterns. (If an even line pattern had been observed, one would have to conclude that there was an extra coupling, possibly from a proton, to give an even, six-line pattern.) Obviously there are two very similar type 2 Cu^{2+} signals from *M. album* BG8 cells and each Cu^{2+} site has four nitrogen atoms.

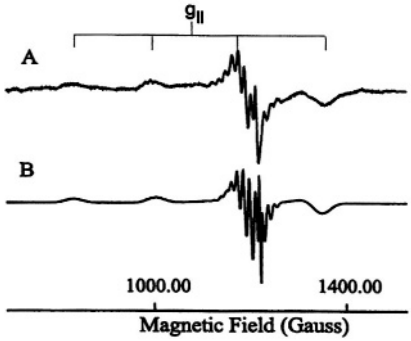

Figure 5. S-band (3.444 GHz) EPR spectra. (A) *M. albus* BG8 cells grown with ^{63}Cu. Experimental conditions: temperature 123 K; modulation amplitude 5 G. (B) Simulation with $g_{||} = 2.243$, $g_y = 2.061$, $g_x = 2.059$, and $A_Z = 194$ G plus a simulated free radical at g = 2.007 *(Yuan et al., 1997).*

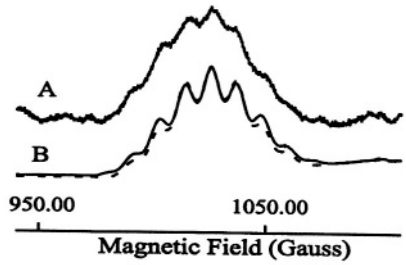

Figure 6. Expansion of $M_I = -½$ line in the $g_{||}$ region of the S-band spectrum. (A) Sample and experimental conditions are the same as in Figure 5A. (B) Simulation with four equivalent nitrogen atoms (solid line) and three equivalent nitrogen atoms (dashed line) *(Yuan et al., 1997).*

Although it is not a theme of this chapter, it is interesting to determine how many of the nitrogen donor atoms are nitrogens from imidazoles of histidines. Electron spin echo envelope modulation (ESEEM) is an EPR technique well suited for determining the histidines involved. The intensities of the quadrupolar combination bands indicate that there are three or four coordinated imidazoles, which form the Cu^{2+} site in pMMO (Lemos *et al.,* 2000). As will be discussed, one can then look for histidines in the amino acid sequence to suggest a Cu^{2+} binding site.

pMMO consists of three subunits – 47, 27 and 25 kDA – with a molecular weight of about 100 kDA (Zahn and DiSpirito, 1996). A recent study confirmed that the molecular weight was about 200 kDA with a dimer, $\alpha_2\beta_2\gamma_2$, with subunits of 45, 31 and 29 kDa (Lieberman *et al.,* 2001). Moreover, the isolated dimer was inactive and crystals resolving to 9 Å did not have a Cu^{2+} EPR signal. In contrast, pMMO from other purifications did have the type 2 Cu^{2+} signal (Kamachi *et al.,* 2001). It may be that the two

resolved signals for type 2 Cu^{2+} are small variations of a single site. Assuming that all three or four histidines originate from one subunit, the binding site for Cu^{2+} is probably not the 27 kDa subunit. This 27 kDa subunit is most likely the site of the active center because it covalently binds the suicide substrate acetylene (Prior and Dalton, 1985; Zahn and Dispirito, 1996; Tukhvatullin *et al.,* 2000). This subunit has three histidines, His 38, His 40 and His 168, that are conserved in both pMMO (GenBank #U94337, U31650, U81596) and AMO (GenBank #96611, AF047705, AF153344). If the active site involves Cu^{+} ions, and Cu^{+} binds to one or more histidines, possibly forming a cluster, three or four additional histidines are not found in the 27 kDa subunit. An interesting side note is that there are about three Cu^{+} ions per 100 kDa of pMMO. The best evidence for the Cu^{+} ions is the X-ray absorption data (Nguyen et al, 1996). This means that these methanotrophs have 0.5 mM of EPR detectable Cu^{2+} and 1.5 mM Cu^{+}, which is much more copper than in other cell types.

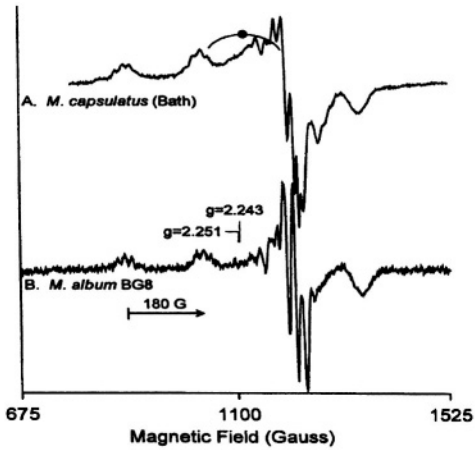

Figure 7. S-band EPR spectra of cells grown with ^{15}N and ^{63}Cu. (A) M. capsulatus (Bath) cells grown in 10 μM Cu and (B) M. album BG8 cells grown in 5μM Cu. A filled circle with an arc marks the broad underlying signal. Spectrometer conditions: microwave frequency 3.45 GHz; modulation amplitude 5 G; microwave power (A) 16 dB, and (B) 22 dB 0.0063 mW; temperature 133 K; four scans *(Lemos et al., 2000).*

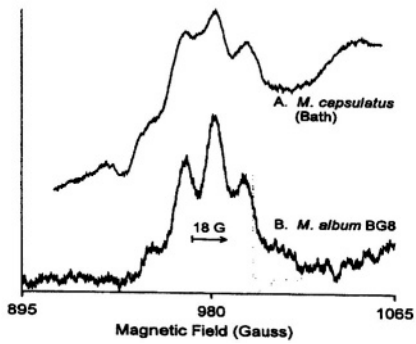

Figure 8. Expansion of M_I = -1/2 line in the $g_{||}$ region of the S-band spectrum. (A) M. capsulatus (Bath) cells grown in 10μM Cu and (B) M. album BG8 cells grown in 5 μM of Cu. Spectrometer conditions are as in Fig. 7, except that 16 scans were averaged. *(Lemos et al., 2000).*

There are four conserved histidines in both the 47 and 25 kDa subunits. Typical patterns for strong binding of Cu^{2+} such as ...HXXH... are absent from pMMO. The 47 and 27 kDa subunits both have the ...HXH...

sequence. This sequence is found in copper binding sites for amine oxidases, which add a third histidine and two water molecules to form a square pyramidal site (Wilce *et al.,* 1997). Assuming that the ...HXH... sequence helps form the active site and bind Cu^{+}, it is hypothesized that the EPR detectable site utilizes the .. .HXH.. .sequence in the 47 kDa subunit to form the type 2 square planar site. This site then utilizes one or two histidines to complete the site. If two or more subunits of pMMO supply histidines, or if the type 2 site is formed at the interface of the dimer, many more arrangements of histidines are possible. For these reasons, positive identification of the type 2 Cu^{2+} binding site has been elusive.

2.2 Prions

Different forms of copper seem to be involved in neurodegenerative diseases, including transmissible spongiform encephalopathies (Mad Cow disease) (Rajan and Surewicz, 2001), Alzheimer's disease and amyotrophic lateral sclerosis (Requena *et al.,* 2001). It is thought that reduced copper reacts with H_2O_2 to generate $^{\bullet}OH$, which oxidizes specific amino acids close to the binding site for copper (Requena *et al.,* 2001; McMahon *et al.,* 2001). Conversion of the prion protein (PrP^{C}) to the scrapie isoform (PrP^{Sc}) is a key pathogenic event resulting in a fatal neurodegenerative disorder (Aronoff-Spencer *et al.,* 2000). Copper binds to many sites in prion proteins, including the octarepeat N-terminal region (Aronoff-Spencer *et al.,* 2000) and the C-terminal domain (Van Doorshaer *et al.,* 2001). Low frequency EPR was used to study the N-terminal domain. Although spectroscopy determined most of the binding site before the crystal structure, it is instructive to begin with the structure before discussing the EPR spectra.

The crystal structure of the fundamental binding unit HGGW with the N-terminal amine blocked and with one Cu^{2+} bound has equatorial coordination of the nitrogen from the imidazole of the histidine, two deprotonated glycine amides, a glycine carbonyl to complete the equatorial plane, and a water in an axial position (Fig. 9, Burns *et al.,* 2002).

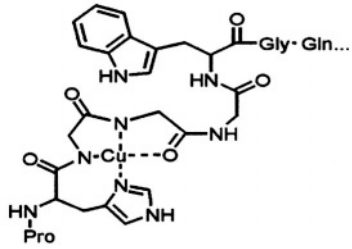

Figure 9. Structure of the HGGGW segment in complex with Cu^{2+} (*Burns et al.,* 2002).

X-band EPR spectra of amino acid fragments consist of a dominant EPR spectrum and a second minor species with g-values and A-values consistent with a type 2 Cu^{2+} site, for example, at pH 7.45, $g_{\|} = 2.23$ and $A_{\|} = 158$ G, with 3-N 1-O coordination (Aronoff-Spencer *et al.,* 2000). There are no resolved superhyperfine lines attributed to nitrogen coordination in the $g_{\perp}$ region. The S-band spectrum (3.5 GHz) is better resolved in the $g_{\perp}$ region, indicative of ^{14}N superhyperfine structure (Fig. 10). The $M_I = -½$ line in the $g_{\|}$ region is also resolved into an eight-line pattern, which was simulated using three equivalent nitrogen donor atoms with $A^N = 13$ G and one proton with $A^H = 10$ G (Fig. 11). The structure of the type 2 Cu^{2+} site was determined before the crystal structure was known, suggesting that the EPR method will likely be accurate for sites where the structure has not yet been determined by X-ray.

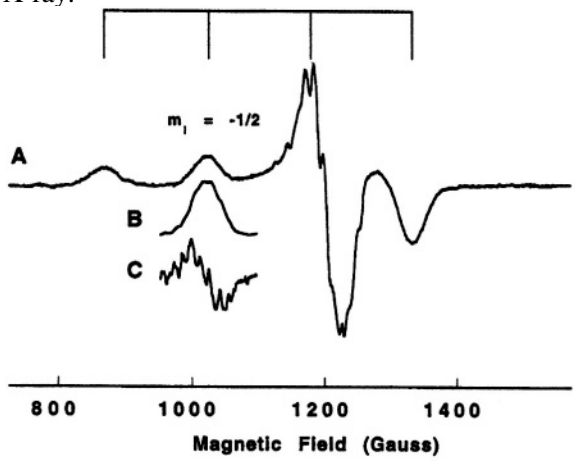

Figure 10. S-band EPR (3.5 GHz) of the octarepeat (PHGGGWGQ). The grid at the top shows the ^{63}Cu hyperfine splitting, and the $m_I = -1/2$ line is indicated. Trace (A) is the full field scan; trace (B) is the $m_I = -1/2$ line scanned with high resolution and signal averaging; trace (C) is the derivative of (B) emphasizing the multiplet structure *(Aronoff-Spencer et al., 2000).*

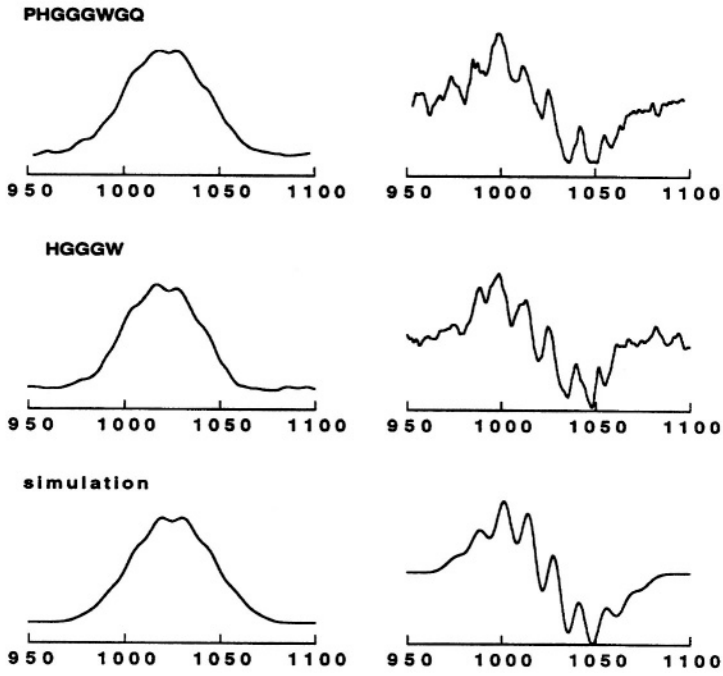

Figure 11. Expansion of the m_I = -½ lines of the S-band EPR spectra. The octarepeat (P**H**GGGWGQ) and **H**GGGW lines shown (left) along with their derivatives (right). The simulated spectrum is from a model of three equivalent nitrogens (a_N = 13 G) and one proton (a_H = 10 G) *(Aronoff-Spencer et al., 2000).*

The EPR spectra are the same for the single octarepeat fragment and the full octarepeat fragment (Fig. 12). The superhyperfine structure from the nitrogen donor atoms and a proton in the spectra of the M_I = -½ line in the $g_{||}$ region at 3.4 GHz are well resolved. Site specific ^{15}N labeling was used to identify the directly coordinated nitrogens by an observed change in multiplet structure. The spectra down each column in Fig. 12 are ^{15}N substituted for ^{14}N at a single site, i.e. the underlined glycine. The peptide nitrogens of the first and second glycines directly coordinate to the copper center, as indicated by a change in the superhyperfine structure. Using substitution of ^{15}N for ^{14}N is a sound method to determine the nitrogen donor atoms of the Cu^{2+} site.

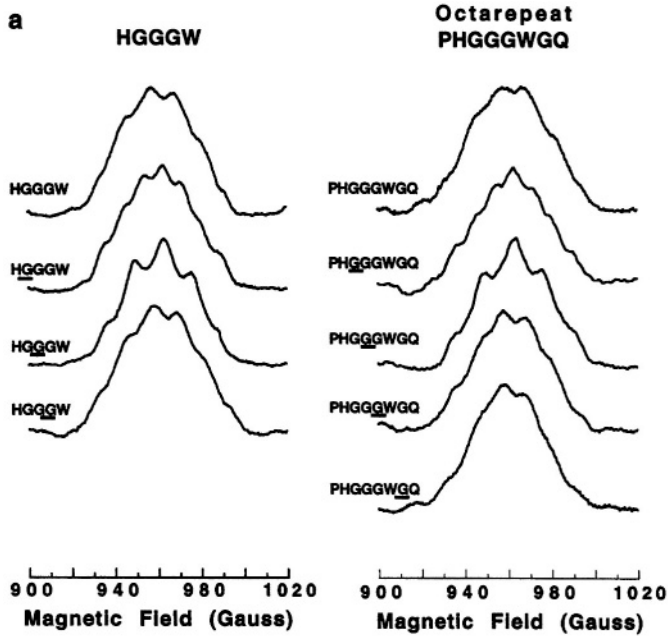

Figure 12. EPR spectroscopy demonstrates that the coordination environment identified remains intact in the octarepeat and full octarepeat domain. The m_I = -½ line of the low frequency S-band (3.4 GHz) EPR spectrum reveals superhyperfine couplings from nitrogens directly coordinated to Cu^{2+} centers. It was previously shown that the couplings seen here in the top spectra arise from three ^{14}N couplings, consistent with the equatorial coordination geometry of Fig. 9. Because ^{15}N possesses a different nuclear spin (I = ½) than ^{14}N (I=1), site specific ^{15}N labeling may be used to identify the directly coordinated nitrogens by an observed change in multiplet structure. The family of spectra down each column are ^{15}N substituted at the underlined glycines. A change in multiplet structure relative to the unlabeled species is seen only for the first and second glycines, demonstrating that the nitrogens of these residues directly coordinate to the copper center *(Burns et al. 2002).*

2.3 Azurin

Azurin is one of many blue copper proteins with a type 1 cupric site. The $A_{\|}$ value for type 1 cupric sites is about half the value of a type 2 cupric site, i.e. about 60 to 90 G. The name "blue copper site" arises from the intense blue color that comes from a strong band at about 600 nm, which has an extinction coefficient of about 5000 $M^{-1}cm^{-1}$. The molecular orbital of the unpaired electron in a type 1 site has d_{x2-y2} character, which is strongly π antibonding with the cysteinate and weakly antibonding with the two imidazolyl ligands (Fig. 13, Holm *et al.,* 1996). In addition to the equatorial plane, Cu(S-Cys, N-His, N-His), a weak axial ligand (S-Met) and an even

weaker ionic interaction with oxygen (O=C-Glu) completes the site. Little change in geometry occurs upon reduction of the type 1 site, which accounts for their function as electron transfer agents.

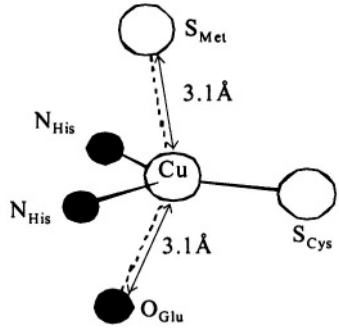

Figure 13. Axially-substituted blue copper sites *(adapted from Holm et al., 1996).*

Extensive studies including CW (continuous wave), electron nuclear double resonance (ENDOR) and electron spin echo envelope modulation (ESEEM) have determined the EPR parameters of azurin (van Gastel *et al.,* 1998; Coremans *et al.,* 1995 and refs. therein). The orientation of the principal axes of the g-tensor with respect to the bond axes were determined using high frequency, W-band (95GHz), electron spin echo detected EPR spectra (Coremans *et al.,* 1994). The g-values are $g_x = 2.0393$, $g_y = 2.0568$, and $g_z = 2.273$ with the x- and y-axes in the N_δ(His)S(Cys)N_δ(His) plane, and rotated by 24° with respect to the Cu-S(Cys) bond.

Some low frequency data have been reported for type 1 Cu^{2+} sites. We published spectra for a type 1 site from *Pseudomonas aeruginosa* azurin, and resolved superhyperfine structure. This was used as a sensitive reporter for obtaining refined EPR parameters from simulations (Antholine *et al.,* 1993). First derivative spectra at low frequencies show superhyperfine structure in the $g_\perp$ region (Fig. 14), which is emphasized in the second derivative spectra (Fig. 15). The fit between experimental and simulated data is sensitive to changes in the Euler angles, particularly α, which rotates the Cu_A tensor about the z-axis (Fig. 16). Simulations are usually consistent with, but not proof of, the EPR spectra and parameters because the EPR parameters, including line widths, are underdetermined. Nevertheless, the same parameters fit spectra at several frequencies.

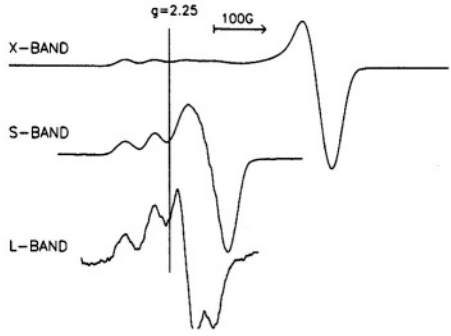

Figure 14. Multifrequency EPR spectra of the cupric site of azurin. Spectrometer conditions: X-band (9.13 GHz) 7.4 K; S-band (2.38 GHz) 120 K; L-band (1.14 GHz) 120 K; modulation amplitude 5 G; modulation frequency 100 kHz *(Antholine et al., 1993).*

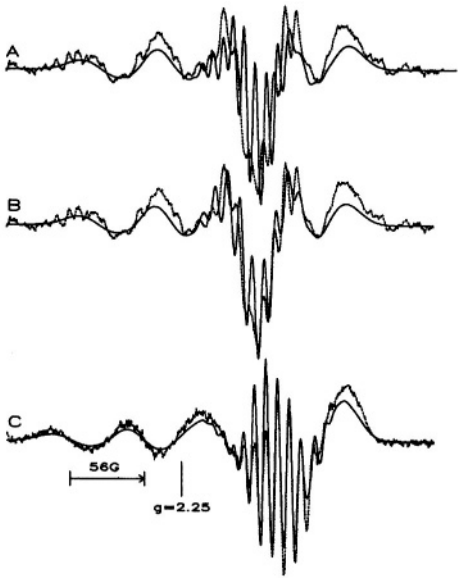

Figure 15. Second derivative L-band (1.64 GHz) spectra (dashed lines, A and B) at ~20 K for the cupric site from azurin *(Antholine et al., 1993).* Modulation frequencies 100 kHz and 270 Hz; time constant 0.1 s; scan time 1 min; microwave power 22 dB. The first harmonic (*dashed lines,* C) of the experimental S-band spectrum. Simulations with parameters from table in Antholine et al., 1993, except (A) $A_X = 46$ MHz; for (B) and (C) $A_X = 30$ MHz.

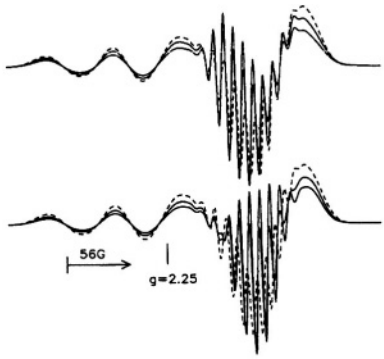

Figure 16. Second derivative simulated S-band spectra for the cupric site of azurin, in which the Euler angle, α, is varied from 0 to 20 to 40° *(top spectra)* and from 40 to 60 to 80° *(bottom spectra).* The dashed lines mark the 40° spectrum in both sets *(Antholine et al., 1993).*

2.4 Laccase

Laccase, which is isolated from the latex of an oriental lacquer tree, is an oxidase that mediates the four electron reduction of O_2 to H_2O. Laccase contains four copper atoms, of which one is a type 2 site, one is a type 1 site, and two are antiferromagnetically coupled, EPR silent, type 3 sites (Fig. 17 and Sundaraman *et al.,* 1997, and Messerschmidt *et al.,* 1992). The type 2 and type 3 sites form a trinuclear copper cluster. The EPR spectra of the type 2 and type 1 sites are superimposed. When mercury is substituted for copper at the type 1 site (type 1-Hg), only the type 2 EPR signal is observed. The type 2 Cu^{2+} site is three coordinate, comprised of two nitrogen donor atoms from imidazoles of histidines and an oxygen donor atom from H_2O as determined from the crystal structure of the oxidized trinuclear site (Nar *et al.,* 1992).

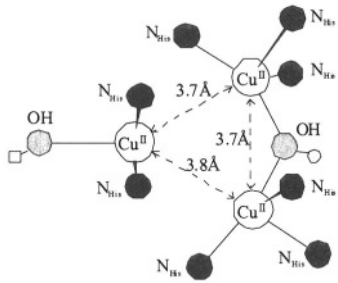

Figure 17. Active-site structure of the trinuclear copper cluster in oxidized ascorbate oxidase *(adapted from Holm et al., 1996).*

There are at least two imidazole nitrogens bound to Cu^{2+} at the type 2 binding site in the mercury derivative of laccase, as determined by pulsed EPR (Lu *et al.,* 1991). On the basis of $g_{\|} = 2.25$ and $A_{\|} = 575$ MHz (205 G), it was first suggested that the ligand coordination for the type 2 copper in the mercury derivative of laccase is probably of the type 3N1O (Morie-Bebel *et al.,* 1986). However, it is difficult to determine a difference in coordination between 2N2O and 3N1O based on $g_{\|}$ and $A_{\|}$ (Peisach-Blumberg plots) due to changes in ligand charge and site symmetry. On the basis of ESEEM of the protein, it was determined that two imidazoles are equatorially bound to copper (Lu *et al.,* 1992). In the CW spectrum at S-band, the nitrogen superhyperfine structure is resolved for the $M_I = -3/2$ line in the $g_{\|}$ region (Morie-Bebel *et al.,* 1986). If there are two almost equivalent nitrogens, the superhyperfine pattern is 1:2:3:2:1, and if there are three approximately equivalent nitrogens, the pattern is 1:3:6:7:6:3:1. A seven-line pattern is more reasonable for the $M_I = -½$ line in the $g_{\|}$ region of the low frequency S-band spectra (Fig. 18). There are four clearly resolved lines on the low field side of the peak, which is simulated with a 1:3:6:7:6:3:1 intensity, but the fit to the high field side is not as good, possibly because the intensities other

than the M_I = -½ line are pushing it above the simulated line. To my knowledge, this is the only example where there is a discrepancy between the number of nitrogens determined by low frequency EPR (3N1O) and the coordination determined from a structure (2N1O). It may be that this sample has an altered cupric site or that a second signal is superimposed on the first signal.

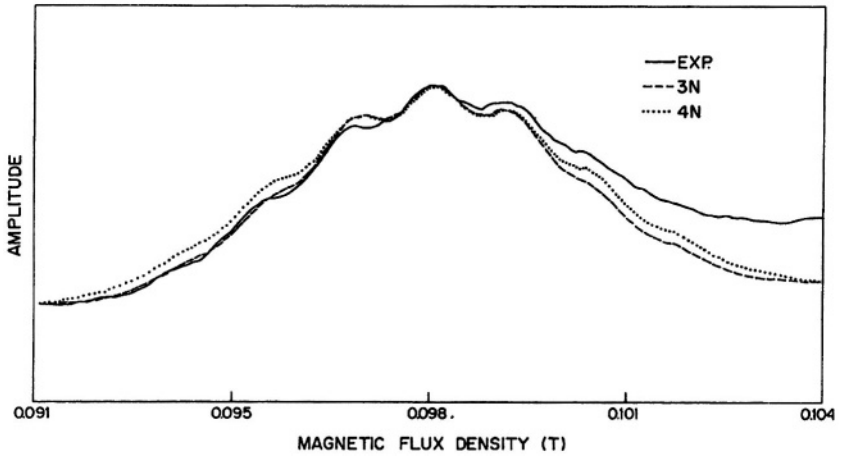

Figure 18. The m_I component of the S-band EPR spectrum of MDL (*Morie-Bebel et al., 1986*).

Laccase was isotopically enriched with, for example $^{65}Cu^{2+}$, depleted of the type 2 Cu^{2+}, and reconstituted with $^{63}Cu^{2+}$, or vice versa (Fig. 19, Li *et al.,* 1992). The Cu^{2+} that was removed and reinserted is not the same type 2 Cu^{2+} detected by EPR at 77 K. However, the same Cu^{2+} removed and inserted is detected at room temperature (Fig. 20). The microwave frequency used for room temperature data was S-band, because the lines were too broad to detect at X-band, and the S-band loop gap resonator was coupled with a greater volume of aqueous sample and a better signal-to-noise ratio than with the TE_{102} X-band cavity. These data were interpreted in terms of a temperature-dependent structural reorganization. Subsequently, a quantitative method was developed to denature laccase and sequester the copper in the form of the bis(acetylacetonato)Cu^{2+} complex (Miller *et al.,* 1995). It was found that reconstitution of the type 2 Cu^{2+} is possible under conditions where little or no exchange occurs between the type 1 or type 3 coppers and the external pool in an oxidizing environment. But under reducing conditions, exchange occurred. The type 2 site was depleted, i.e. T2D enzyme, and the type 1 site studied by EPR (Hanna *et al.,* 1988). The X-band spectrum was well resolved in the $g_\perp$ and the S-band spectrum was well resolved in both the $g_\perp$ and $g_\parallel$ regions. The spectra were simulated assuming two nitrogen donor atoms, presumably the nitrogens from two

histidines, and two H nuclei, presumably two H atoms on the β carbon of the covalently-bonded cysteine ligand.

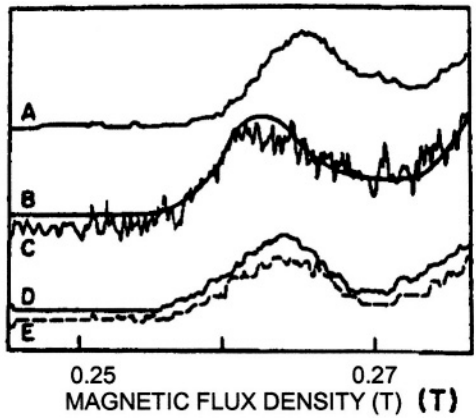

Figure 19. The $m_I = -3/2$ transition of type 2 copper in various laccase derivatives: (A) ^{63}Cu-enriched laccase; (B) ^{65}Cu-enriched laccase (smooth curve); (C) ^{65}Cu-enriched T2D laccase reconstituted with ^{63}Cu; (D) T2D laccase with natural-abundance copper reconstituted with excess ^{65}Cu; (E) native laccase (---). All samples are in phosphate buffer at -150°C. Microwave frequency 9.13 GHz *(Li et al., 1992).*

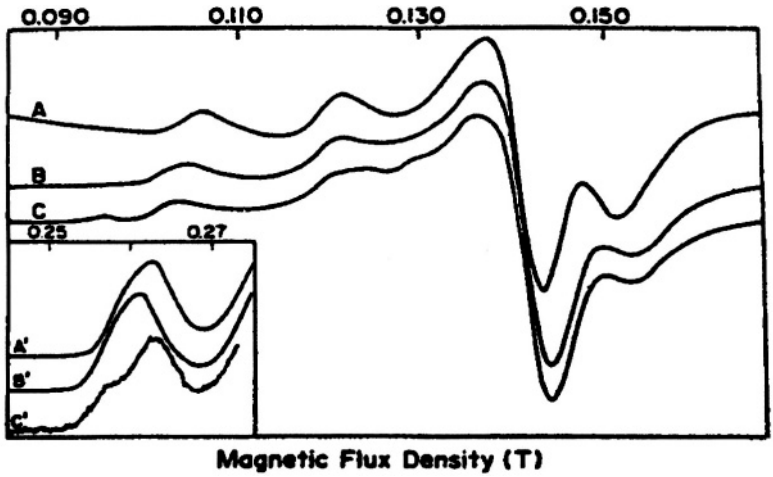

Figure 20. S-band EPR spectra of laccase derivatives recorded at room temperature in acetate buffer: (A) ^{63}Cu-enriched laccase; (B) ^{65}Cu-enriched laccase; (C) ^{63}Cu-enriched T2D laccase that has been reconstituted with ^{65}Cu. Microwave frequency 3.92 GHz. *Inset*: Lowest flux density peaks in the corresponding X-band EPR spectra measured at 9.13 GHz and at -150°C in acetate buffer *(Li et al., 1992).*

3. A MIXED VALENCE DINUCLEAR COPPER $[HISCu^{1.5+}(CYS)_2Cu^{1.5+}HIS]$ PURPLE Cu_A SITE

3.1 Nitrous Oxide Reductase, N_2OR

Nitrous oxide reductase, N_2OR, is the terminal enzyme in the denitrification chain converting N_2O to N_2 (Eq. 3), and will be discussed in greater detail in the chapter on metalloenzymes of the biological nitrogen cycle by Peter Kroneck.

$$N_2O + 2H^+ + 2e^- \rightleftharpoons N_2 + H_2O \qquad (3)$$

The $g_{\|}$ region of the X-band spectrum from N_2OR (Fig. 21, Kroneck *et al.,* 1988) is resolved into seven lines, indicative of one electron equally shared by two copper ions, i.e. $[HisCu^{1.5+}(Cys)_2Cu^{1.5+}His]$ mixed valence dimer (Robin and Day class IIIA dimer; Robin and Day, 1967). The resolution of the seven-line pattern improves as the microwave frequency is lowered, even though the lines from the seven-line pattern in the $g_{\|}$ region overlap substantially with the g_x and g_y regions (Fig. 21). The Q-band spectrum in Fig. 21 is an absorption spectrum, either because of adiabatic rapid passage or because it is out of phase. Still a $g_{\|}$ value of 2.18 is readily determined from the Q-band spectrum. In addition to better resolved lines in the $g_{\|}$ region, better resolved lines on the high field side are evident at lower microwave frequencies. The last spectrum in Fig. 21 is the second derivative spectrum, which proved to be invaluable in later studies because of its improved resolution. The resolved high field lines of the N_2OR S-band spectra and the similarity to resolved lines in the spectra for the EPR-detectable Cu of cytochrome *c* oxidase suggested that the S-band spectrum for cytochrome *c* oxidase measured below 30 K may also contain hyperfine splittings from two approximately equivalent Cu nuclei (Kroneck *et al.,* 1988). The idea of a mixed valence Cu_A site in cytochrome *c* oxidase has been both refuted (Li *et al.,* 1989) and defended (Kroneck *et al.,* 1989). Nevertheless, the S-band spectrum from N_2OR and its comparison to the S-band spectrum of cytochrome *c* oxidase, *CcO,* provided the first hint that the Cu_A site in *CcO* was a dinuclear copper site.

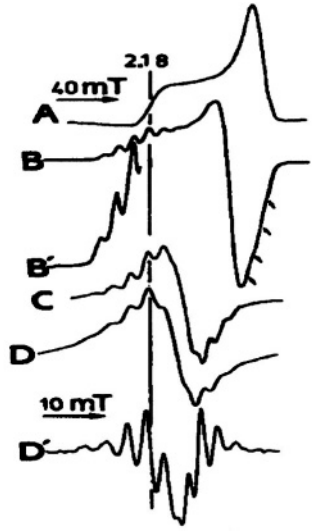

Figure 21. Multifrequency EPR spectra of nitrous oxide reductase from *Pseudomonas stutzeri* (form I), 0.25 mM in 25 mM Tris-HCl buffer, pH 7.5. Microwave frequency (A) 35.14 GHz, 10 K; (B) 9.315 GHz, 10 K; (B') 5-fold increase in gain; (C) 3.480 GHz, 20 K; (D) 2.393 GHz, 20 K; (D') second derivative spectrum *(Kroneck et al., 1988).*

3.2 Cytochrome *c* Oxidase, C*c*O

Cytochrome *c* oxidase, C*c*O, the terminal enzyme of the respiratory chain, catalyzes the four-electron reduction of oxygen to water and pumps four protons across the mitochondrial membrane (Eq. 4).

$$4H^+ + 4H^+_i + O_2 + 4\text{Cyt-c}^{2+} \rightleftharpoons 4\text{Cyt-c}^{3+} + 4H^+_o + 2H_2O \qquad (4)$$

The first crystal structures of C*c*O provided the ligand structure, whereas EPR only demonstrated that the Cu_A site was a dinuclear copper site (Tsukihara *et al.* 1995 and 1996; Iwata *et al.* 1995). The structure for Cu_A shown in Fig. 22 consists of dimeric copper bridged by two cysteine thiolates and a terminal nitrogen from the imidazole of histidine bound to each copper, i.e. N-Cu-S_2-Cu-N. Binding sites for Cu_B, $heme_{a3}$, $heme_a$, Mg, and Zn, as well as sites for adventitious Cu^{2+}, have been confirmed by spectroscopy (Fig. 23; Yuan *et al.,* 1998 and refs. therein). It was recently reported that a tyrosine is covalently cross-linked to a histidine, which is a ligand of Cu_B (Buse *et al.,* 1999), and this tyrosine forms a radical during reaction of C*c*O with H_2O_2 (MacMillan *et al.,* 1999). Clearly the role of low frequency EPR was most influential for unraveling the Cu_A site, but conventional EPR also played a major role in studies of C*c*O.

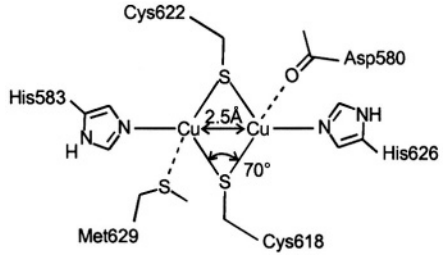

Figure 22. Spectroscopic model of the Cu_A center in N_2OR from *Pseudomonas stutzeri.* The ligand assignment was based primarily on the crystallographic data of Cu_A (*Kroneck, 2001*).

Proof that the Cu_A site in CcO is a dinuclear mixed valence Cu_A = $[HisCu^{1.5+}(Cys)_2Cu^{1.5+}His]$ site followed, once a second low frequency bridge, C-band (about 4.5 GHz), was built in Jim Hyde's National Biomedical ESR Center. At this point, the high field lines could be resolved at two low microwave frequencies (2.8 GHz and 4.5 GHz). It was found that the high field lines were invariant at g = 2.00 for a seven-line pattern, indicative of a single electron distributed equally over two coppers, but not for the four-line pattern indicative of a cupric monomer (Table 3; Kroneck *et al.,* 1990). A full paper and review followed (Antholine *et al.,* 1992, 1997). Clearly the dinuclear copper site was discovered because of the better resolution of the hyperfine structure at low frequency. At X-band, only $g_{\|}$ and $g_{\perp}$ were readily determined, but at low frequency, the hyperfine structure was resolved as best demonstrated by the comparison of the X-band spectrum with the first harmonic of the C-band spectrum (Fig. 24).

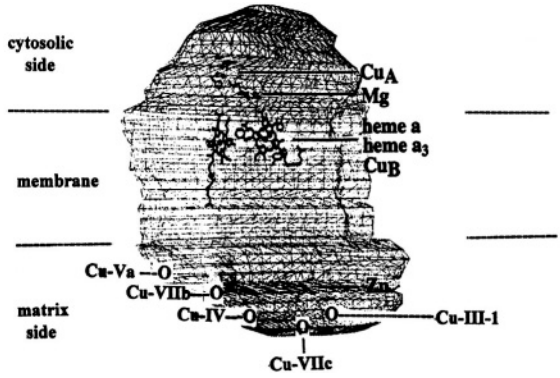

Figure 23. Hypothetical schematic from the five N-terminal binding sites from subunits III, IV, Va, VIIb and VIIc as adapted from Tsukihara *et al.,* 1995, 1996). Metal sites for the catalytic site ($heme_{a3}$-Cu_B), electron transfer site (Cu_A-Cu_A), $heme_a$, Mg, and Zn are identified as well as the membrane matrix side and cytosolic side. The approximate location of the N-terminal for the five sequences for which a His is the second or third amino acid are indicated by an O, and the dashed lines and Roman numerals on the matrix side identify the subunit. III denotes the first transmembrane helix for subunit III *(Yuan et al., 1998).*

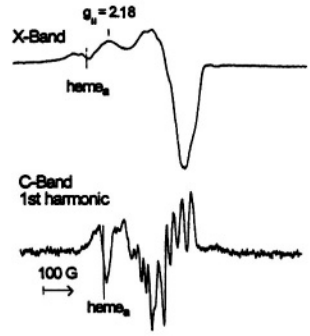

Figure 24. (Top spectrum) X-band spectrum of CcO with $g_{\parallel}$ indicated by the vertical marker. The middle line for the low spin Fe_A in $heme_a$, also indicated by the vertical marker, is superimposed on the $[Cu_A(1.5+)Cu_A(1.5+)]$ signal. *(Bottom spectrum)* First harmonic of the C-band spectrum of CcO. Note the multi-line pattern and improved resolution of the C-band spectrum *(Antholine, 1997).*

Table 3. g-values calculated from multifrequency EPR spectra assuming binuclear coppers, Cu-Cu (a seven-line pattern), or mononuclear copper, Cu (a four-line pattern) (Antholine *et al.*, 1997).

Sample	*Frequency (GHz)*	$g_z^{Cu\text{-}Cu}$	g_z^{Cu}	$g_x^{Cu\text{-}Cu}$	$g_x^{Cu\text{-}}$
CcO	9.130 (X-band)	—	—	2.00	—
CcO	4.530 (C-band)	—	—	2.00	1.96
CcO	2.760 (S-band)	—	—	2.00	1.94
N_2OR	9.130 (X-band)	2.18	2.22	2.02	1.98
N_2OR	4.670 (C-band)	2.18	2.26	2.02	1.97
N_2OR	3.480 (S-band)	2.18	2.29	2.02	1.95
N_2OR	2.397 (S-band)	2.18	2.34	2.02	1.92

3.3 Engineered Cu_A Sites and Mutants of CcO

Ligands to produce a mixed valence Cu_A unit were inserted into cytochrome *o* quinol oxidase in *E. coli* (van der Oost *et al.,* 1992). The mixed valence site was also engineered by replacing the loop for the type 1 Cu site in azurin with a loop,

CysSerGluLeu**Cys**GlyIleAsn**His**SerAlaLeu**Met**,

which together with another **His,** forms the $[NCu_AS_2Cu_AN]$ binding site (Hay *et al.,* 1996). The equatorial His 120 in the Cu_A site was changed to Asn or Gly to understand the role of His in the mixed valence site. Most spectral methods, including ENDOR with superhyperfine couplings from the

mutants similar to couplings of the wild type for His120Asn and His120Gly, predict a mixed valence structure. But CW multifrequency EPR with a four-line pattern in the $g_{||}$ region is consistent with a trapped valence structure following mutation (Fig. 25; Lukoyanov *et al.,* 2002). If the axial ligand methionine is changed to Gln or Glu, a mixed valence complex still forms, with $A_{||}$ increased to 42 G in the mutants, as compared to 31 G in the wild type soluble fragment (Slutter *et al.,* 1999). While it is suggested that stronger axial ligands shift spin from the sulfur ligands to the Cu, we found that an exchange of Met to Leu also increases $A_{||}$. The EPR spectrum for mutation Met263Leu in *Cc*O in *Rhodobacter sphaeroides,* formed with subunits II and III deleted and a plasmid-borne copy of the subunit II/III operon inserted, retained a mixed valence character as determined by multifrequency EPR of the high field lines. $A_{||}$ increased from 30 G and a seven-line pattern to a range of values with nonequivalent couplings centered about 65 G and 57 G, and more than seven lines for the two coppers (Fig. 26, Zhen *et al.,* 2002). A redox potential change and a slower $heme_a$ reduction results from the Met263Leu mutation.

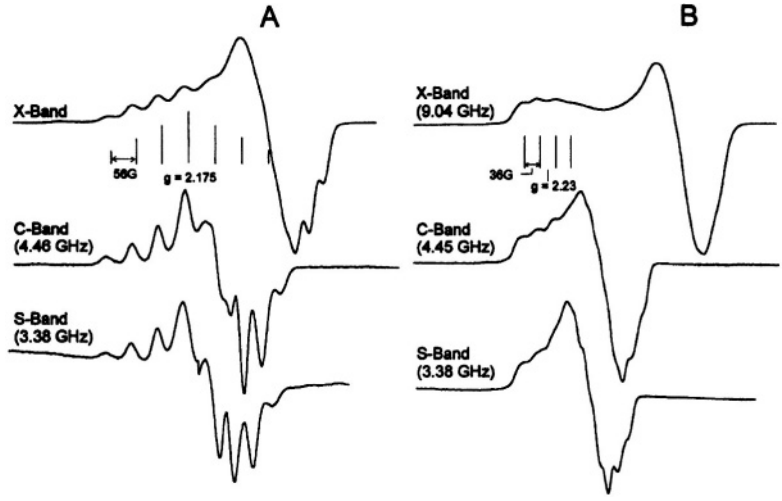

Figure 25. Comparison of S-band, C-band and X-band spectra of Cu_A-azurin (A) and H120N mutant (B). Experimental conditions: temperature 15 K; microwave power 23 dB down from an incident power of 7 mW, time constant 0.1 s; scan time 4 min.; modulation amplitude 5 G; gain 3.2×10^2; cavity loop gap resonator at S- and C-band. A standard TE102 resonator was used at X-band with a power of 5 mW (*Lukoyanov et al., 2002*).

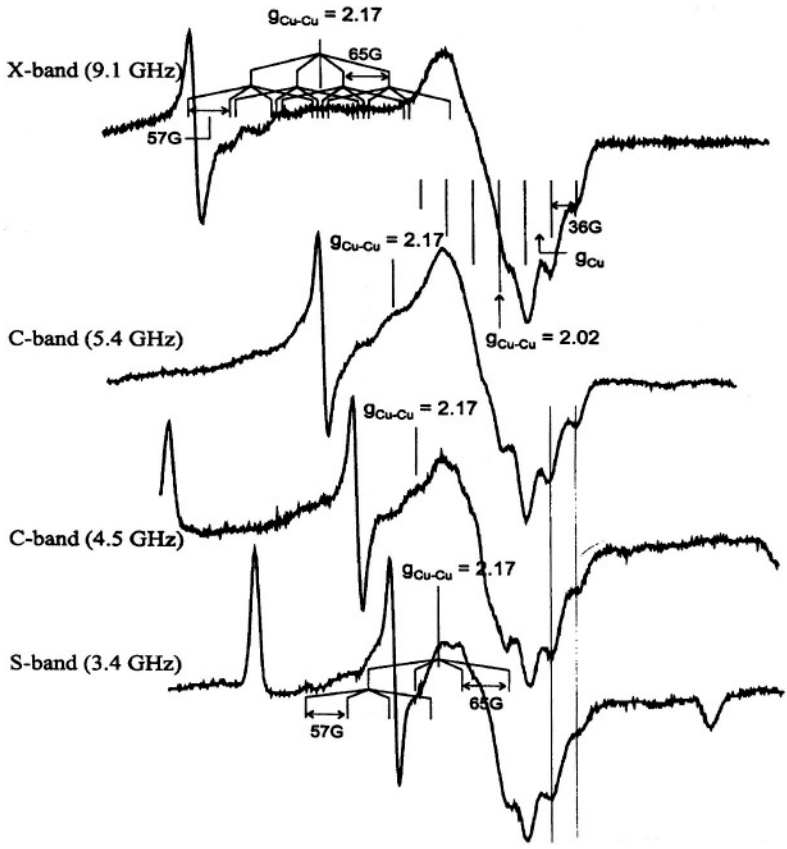

Figure 26. Multifrequency EPR spectra for M263L mutant in C_cO of *R. sphaeroides.* The microwave frequencies used in the experiments are S-band (3.4 GHz); C-band (4.5 and 5.4 GHz); X-band (9.2 GHz); temperature 15 K *(Zhen et al., 2002).*

4. EPR SIGNALS FROM A CLUSTER

4.1 Laccase

The type 2 and type 1 Cu^{2+} EPR signals of laccase are described in section 2.4. Laccase, which contains four coppers, catalyzes the four-electron reduction of oxygen to water. The remaining two coppers form a type 3 site, which has two antiferromagnetically coupled dinuclear copper atoms. The ground state for type 3 is EPR silent. The type 2 and type 3 coppers form a trinuclear cluster, which is the site for reduction of O_2 (Fig. 17). A broad EPR signal at < 20 K with g < 2 from the native intermediate

is observed during reduction of O_2 to H_2O (Aasa *et al.,* 1976). When the type 1 signal from type 2 depleted laccase is subtracted from the signals from the native intermediate, a broad signal with g values about 2.15, 1.86, and 1.65 is obtained (Fig. 27, Lee *et al.,* 1999, 2002). It is useful to obtain signals like this at a second frequency to determine whether the g-values are true g-values. One advantage of low frequency is that the spectral width is smaller; a disadvantage is that the signal decreases by a factor of three due to the Boltzman factor. The g-values from both X- and S- band spectra are similar. So far, we have not been able to detect this signal at Q-band for several reasons, one of which is that the already broad signal is spread over a larger range – about 3,500 G at Q-band – compared to about 850 G at X-band and about 340 G at S-band.

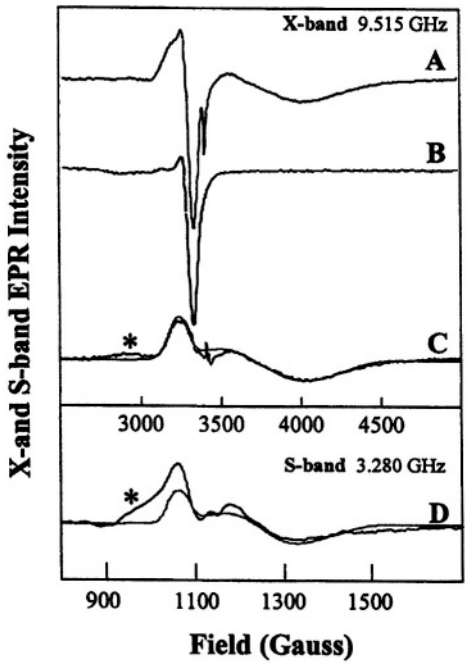

Figure 27. (A) X-band EPR spectrum of the native intermediate sample at 200 mW and 10 K. (B) EPR spectrum of the oxidized T2D under the same conditions. (C) The spectrum of the native intermediate after subtracting the T1 and a small radical signal (<1%) shows a broad rhombic signal with *g* values of 2.15, 186 and 1.65. (D) S-band EPR spectrum of the native intermediate after a similar subtraction. Simulation gives the same set of *g* values (2.15, 1.86 and 1.65) with different line widths. No hyperfine structure is resolved. * denotes subtraction residual of T1 Cu low-field feature *(Lee et al., 1999).*

4.2 Nitrous Oxide Reductase, N_2OR.

There is a second EPR active site in N_2OR, the Cu_Z site, in addition to the Cu_A center discussed in section 3.1. Resolution of the hyperfine structure at low frequency for this signal has not been as successful as for the mixed valence dinuclear site. High frequency, Q-band, established $g_{\|}$ equal to 2.16, and X-band indicated a value of about 61×10^{-4} cm^{-1} for $A_{\|}$ (Chen *et al.,* 2002). One reason low frequency S-band data are not well resolved is that the signal is composed of at least two centers, both EPR active, and overlap at S-band obscures the hyperfine structure. The Cu_Z center is a four-copper cluster with seven histidine ligands, a bridging sulfur and an oxygen as ligands (Fig. 28, adapted from Brown *et al.,* 2000). Thus N_2OR has two remarkable copper sites, a mixed valence dinuclear copper site and a four copper cluster, that serve as models for the two newest EPR active copper centers.

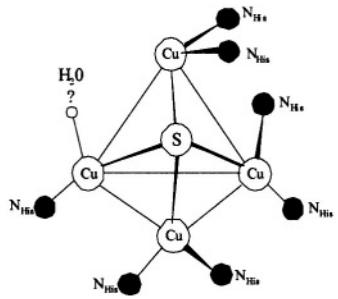

Figure 28. Schematic representation of the Cu_Z center with ligands from the crystal structure of N_2OR from Pn *(adapted from Brown et al., 2000 and Chen et al., 2002).*

4.3 Particulate Methane Monooxygenase, pMMO g = 2.1 Signal?

Another broad signal attributed to copper is the g = 2.1 signal observed in *M. capsulatus* (Bath) (Nguyen *et al.,* 1994; Lemos *et al.,* 2001, in press). One problem is that this signal has been observed only in *M. capsulatus* (Bath) and not in, for example, *M. album* BG8, which only has genes for pMMO and not sMMO. Nevertheless, the concentration of this EPR active center, which can be $100 \mu M$, is dependent on Cu in the growth medium and does not saturate easily, which is a characteristic of clusters. No resolution of structure is evident at low frequencies (Fig. 29), and the signal at g = 2.1 appears to be a true g-value. At best, this is a new type of copper signal from a cluster in pMMO (see section 2.4).

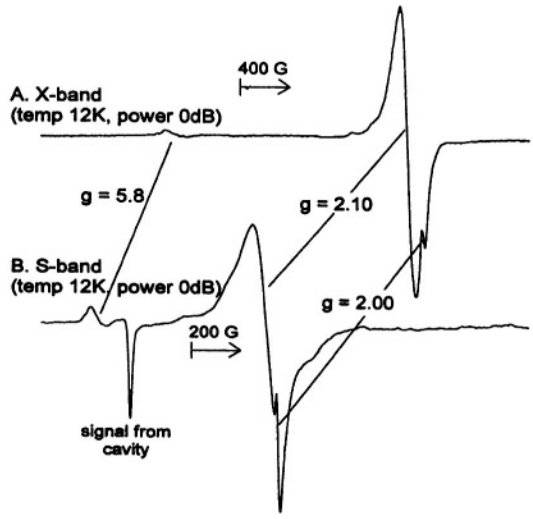

Figure 29. X-band (A) and S-band (B) spectra under conditions that emphasize the $g = 2.1$ signal *(Lemos et al., in press).*

5. PERSPECTIVES

5.1 Half Field Transitions from Cupric Dimers

Both $\Delta m_S = 1$ and $\Delta m_S = 2$ signals are detected from cupric dimers. Often the half field transitions are too weak to observe at X-band, and even more difficult to observe at higher frequencies because the transition probability is inversely proportional to the square of the microwave frequency, i.e. the transition probability should be about nine times more at 3 GHz. Froncisz, Hyde and co-workers built a loop gap resonator at 1.1 GHz with $\mathbf{B}_0$ parallel to $\mathbf{B}_1$ (unpublished). The sample tube and loop gap resonator are rotated 90° from the usual direction (Fig. 30, left). The signal intensity at 3 GHz is three times less than at 9 GHz from the Boltzman factor, so a net gain is expected. In a second configuration, a coil was wound to give magnetic fields of a few hundred Gauss in the vertical direction so that the loop gap resonator did not need to be rotated (Fig. 30, right). The decrease in sensitivity at S-band due to the Boltzman factor is less than the increase of the relative intensity of the half-field transition (Eaton *et al.,* 1983, 1985). I am not aware of published data using EPR half-field transitions to determine the interspin distance and orientation of the interspin vector at low frequencies. Scratches in the resonators often give signals from metals at $g = 4$, so the resonators have to be repeatedly replated.

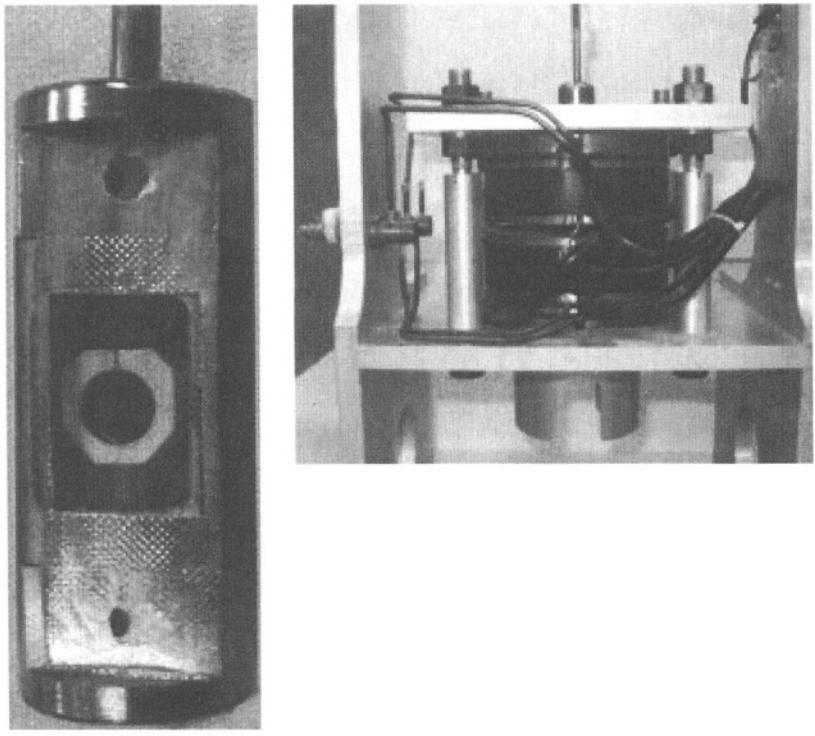

Figure 30. *(Left)* Loop gap resonator placed on its side in the housing so that B_1 is parallel to B_0. *(Above)* Loop gap resonator upright as in Fig. 3, and coils wound so that B_1 is parallel to B_0

5.2 Effect of ^{17}O on the EPR Spectrum of Intermediate X in the Dinuclear Cluster of Ribonucleotide Reductase

The effect of g-anisotropy on low frequency S-band spectra is less than at X- and Q-band. In addition to the S-band data with copper, other isotopes that broaden the spectrum can be used. One such novel use is the broadening of the spectrum for intermediate X at S-band by ^{17}O (Burdi *et al.,* 1998). ^{17}O has $I = {}^5/_2$ and a nuclear moment about one-half that of copper, so replacing oxygen with the oxygen isotope stands a good chance of broadening the EPR spectrum. Intermediate X is a spin-coupled Fe^{III}/Fe^{IV} center with $S = ½$ formed during the self-assembly reaction of the tyrosyl radical/μ-oxo-bridged diferric cofactor of *E. coli* ribonucleotide reductase. Ribonucleotide reductase converts ribonucleotides to deoxyribonucleotides, which can subsequently be used for the production of DNA. S-band spectroscopy helped to determine that the inorganic core, $[(H_xO)Fe^{III}OFe^{IV}]$, contains only one oxo bridge. The

S-band spectrum for intermediate X prepared with 85% $^{17}O_2$ and quenched at 4030 ms fits a single bridging oxygen better than two identical bridging oxygen atoms (Fig. 31, Burdi *et al.,* 1998). If the sample is quenched at 42 ms, the spectrum is comprised of contributions from four differently labeled core sites, i.e. one that has two labeled ^{17}O atoms per molecule (bridging ^{17}O and terminal $H_2{}^{17}O$), one with bridging O and $H_2{}^{17}O$, one with bridging ^{17}O and H_2O, and one with H_2O and bridging O. While difficult to interpret, S-band data with samples with spin density on ^{17}O atoms is clearly a valuable experiment, one that is better done at low frequency and that may not be possible at high frequency.

5.3 S = ½ or S> ½

S-band spectra may be used to distinguish whether the lines are at true g-values or whether spin-spin interaction is involved. One such example comes from a multifrequency study of hydrogenase (Albracht *et al.,* 1984). In Fig. 32 at X-band, four lines due to the interaction of Ni^{3+} with $[4Fe4S]^{3+}$ are observed along with the signal for [3Fe4S], but at S-band there are two broad bands at g = 2.06 and g = 1.935, and a shoulder, suggesting an exchange-coupled pair of dissimilar ions. In Fig. 33, the positions of the lines at the three frequencies remain the same with respect to g-value, but the width as plotted using a g-value axis is broader at S-band. This suggests unresolved hyperfine or spin-spin interaction.

5.4 Low frequency over high frequency

The general rule is that low microwave frequencies are better for resolution of hyperfine parameters and high frequencies are better for g-values. All frequencies can be used to study strain. For type 2 Cu^{2+}, g_x and g_y may be determined at high frequency if the strain broadening is not too large. For example, even the nitrogen hyperfine in W-band spectra for 1% Cu(pc) (phthalocyanine) in H_2PC are well resolved, although little strain is expected (P. Doan, personal communication). There have been at least two experiments published which demonstrate the use of high frequency to obtain EPR parameters for copper – one a pulsed ENDOR paper (Gromov *et al.,* 1999) and the other an ESEEM study (Coreman *et al.,* 1994). The best approach may be to use several frequencies. The ENDOR effect at S-band is enhanced by about a factor of 16 by going from 9.4 GHz to 2.35 GHz, i.e. as $(1/\nu)^2$ (Newton and Hyde, 1991). Clearly the utility of low frequency EPR has not been fully exploited.

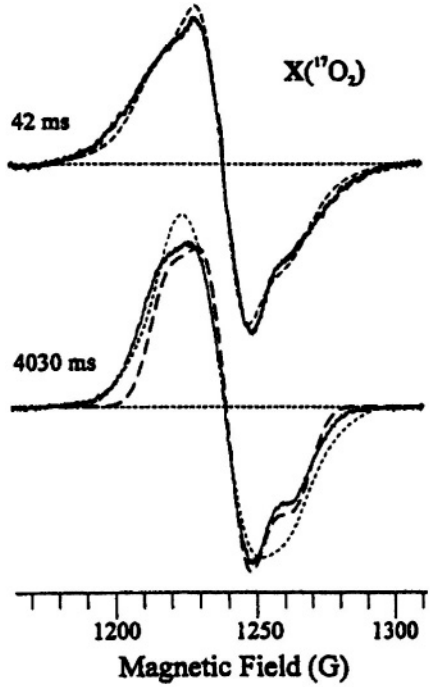

Figure 31. S-band spectra for mutant $X(^{17}O_2)$ quenched at 42 ms (upper) and 4030 ms (lower). Solid lines, experimental spectra; dashed lines, simulations. The displayed spectra have been shifted slightly as necessary to have the same zero-crossing, which corresponds to a microwave frequency of 3.470 GHz. Simulation parameters for 4030 ms: heavy-dashed line, one $^{17}O_{br}$ (85%) enrichment) having parameters listed in the table in Burdi *et al.,* 1998; short-dashed line, two $^{17}O_{br}$ (85% enrichment each), each with the $^{17}O_{br}$ parameters. For 42 ms: 40% occupancy of $^{17}O_t$, 85% of $^{17}O_{br}$ oxygens; three different conformers in a ratio of 0.2:1:0.2, where the A_3 values of $^{17}O_{br}$ in the two minority conformers are approximately 30% higher/lower than those listed in Burdi *et al.* For all: EPR line width for "terminal" oxygen, [20, 20, 40] MHz; EPR line width for bridging oxygen, [20, 20, 20] MHz. Experimental conditions: scan time 4 min, time constant 100 ms, modulation amplitude 5 G; microwave power 30 dB; incident microwave power 6.87 mW; microwave frequency 3.470 (4030 ms), 3.464 (42 ms) GHz, temperature 13 K (*Burdi et al., 1998*).

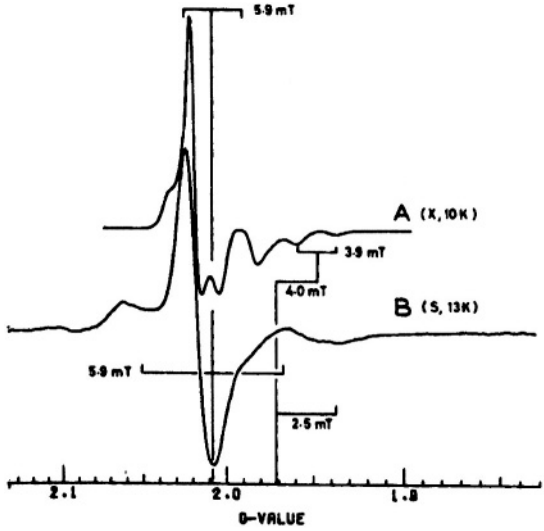

Figure 32. EPR spectra of the enzyme at X- and S-band. An X-band tube was used for both measurements. EPR conditions for X-band (A) are described in *Albracht et al., 1984.* Conditions for S-band (B): microwave frequency 3.953 GHz, temperature 13 K, microwave power 2 mW, modulation amplitude 0.4 mT.

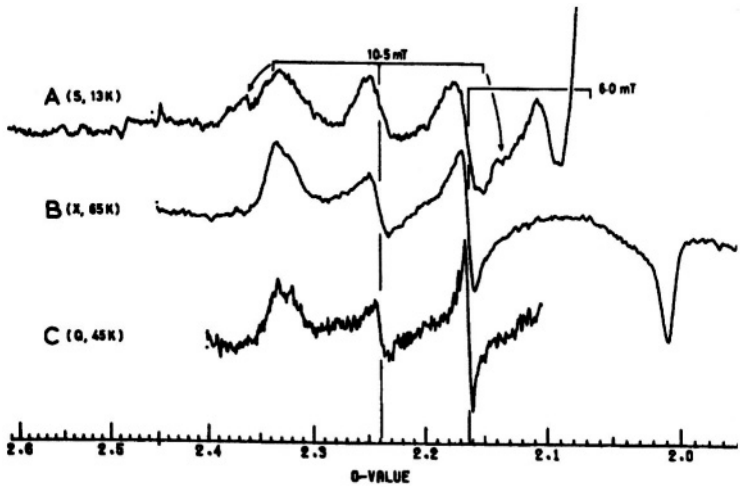

Figure 33. EPR spectra of hydrogenase in the g = 2.1-2.4 region at S- X- and Q-band. For X- and Q-band measurements (traces (B) and (C) respectively), the Q-band EPR tube is described by Albracht *et al,* 1984. For S-band, trace (A), the X-band tube of Fig. 4 was used. EPR conditions for S- X- and Q-band: microwave frequencies 3.953, 9.2695 and 34.360 GHz; temperatures 13, 65 and 45 K; microwave powers 2, 2 and 0.5 mW; modulation amplitudes, 0.9, 1.0 and 1.25 mT. Spectra were averages of six (S-band), nine (X-band) and nine (Q-band) scans *(Albracht et al., 1984).*

6. REFERENCES

Aasa, R., Branden, R., Malmstrom, B.G., Reinhammar, B. and Vänngård, T., 1976, A ^{17}O-Effect on the EPR Spectrum of the Intermediate in the Dioxygen-Laccase Reaction, *Biochem. Biophys. Res. Commun.* **70**:1204-1209.

Albracht, S.P.J., van der Zwaan, J.W. and Fontijn, R.D., 1984, EPR Spectra at 4, 9, and 35 GHz of Hydrogenase from *Chromatium vinosum:* Direct Evidence for Spin-Spin Interaction between Ni(III) and the Iron-Sulpher Cluster, *Biochim. Biophys. Acta* **766**:245-258.

Antholine, W.E., 1997, Evolution of Mononuclear to Binuclear Cu_A: An EPR Study, *Adv. In Biophys. Chem.,* **6**:217-246.

Antholine, W.E., Hanna, P.M. and McMillan, D.R., 1993, Low Frequency EPR of *Pseudomonas aeruginosa* Azurin: Analysis of Ligand Superhyperfine Structure fro a Type 1 copper Site, *Biophys. J.,* **64**:267-272.

Antholine, W.E., Kastrau, D.H.W., Steffens, G.C.M., Buse, G., Zumft, W.G. and Kroneck, P.M.H., 1992, A Comparative EPR Investigation of the Multicopper Proteins Nitrous-Oxide Reductase and Cytochrome *c* Oxidase, *Eur. J. Biochem.* **209**:875-88

Anthony, C., 1986, Bacterial oxidation of methane and methanol. *Adv. Microb. Physiol.* **27**:113-209.

Aronoff-Spencer, E, Burns, C. S., Avdievich, N.I., Gerfen, G. J., Peisach, J., Antholine, W.E., Ball, H.L., Cohen, F.E., Prusiner, S.B., Millhauser, G.L., 2000, Identification of the Cu^{2+} Binding Sites in the N-Terminal Domain of the Prion Protein by EPR and CD Spectroscopy. *Biochemistry,* **39**: 13760-71.

Basosi, R., Antholine, W.E. and Hyde, J.S., 1993, Multifrequency ESR of Copper: Biophysical Applications, in: *Biological Magnetic Resonance, Vol. 13,* L. J. Berliner and J. Reuben, eds. (Plenum Press, NY) pp. 103-150.

Basosi, R., Antholine, W.E., Froncisz, W. and Hyde, J.S., 1984, Spin-Hamiltonian Input Parameters in the EPR Analysis of Liquid Phase Copper Complexes, *J. Chem. Phys.* **81**:4849-4857.

Belford, R.L. and Duan, D.C., 1978, Determination of Nuclear Quadrupole Coupling by simulation of EPR spectra of Frozen Solutions, *J. Magn. Reson.* **29**:293.

Brown, K. Djinovic-Carugo, K., Haltia, T., Cabrito, I., Saraste, M., Moura, J.J.G., Moura, I., Tegoni, M. and Cambillau, C., 2000, Revisiting the Catalytic CuZ Cluster of Nitrous Oxide (N_2O) Reductase, *J. Biol. Chem.* **275**:41133-41136.

Burdi, D., Williems, J.,-P., Riggs-Gelasco, P., Antholine, W.E., Stubbe, J., Hoffman, B.M., 1998, The Core Structure of X Generated in the Assembly of the Diiron Cluster of Ribonucleotide Reductase: $^{17}O_2$ and $H_2{}^{17}O$ ENDOR, *J. Am. Chem. Soc.* **120**:12910-12919.

Burns, C.S., Aronoff-Spencer, E., Dunham, C.M., Lario, P., Avdievich, N.I., Antholine, W.E., Olmstead, M.M., Vrielink, A., 2002, Molecular Features of the Copper Binding Sites in the Octarepeat Domain of the Prion Protein, *Biochemistry,* **41**:3991-4001.

Buse, G., Soulimane, T., Dewor, M., Meyer, H.E. and Bluggel, M. 1999, Evidence for a Copper-Coordinated Histidine-Tyrosine Cross-Link in the Active Site of Cytochrome Oxidase, *Protein Sci.* **8**:985-990.

Chen, P., George, S.D., Cabrito, I., Antholine, W.E., Moura, J.J.G., Moura, I., Hedman, B., Hodgson, K.O. and Solomon, E.I., 2002, Electronic Structure Description of the μ_4-Sulfide Bridged Tetranuclear Cu_z Center in N_2O Reductase, *J. Am. Chem. Soc.,* **124**:744-745.

Coremans, J.W.A., Poluektov, O.G., Groenen, G.J.J., Canters, G.W., Nar, H. and Messerschmidt, A., 1994, A W-band Electron Paramagnetic Resonance Study of a Single Crystal of Azurin, *J. Am. Chem. Soc.* **116**:3097-3101.

Coremans, J.W.A., van Gastel, M., Poluektov, O.G., Groenen, G.J.J., den Blaauwen, T., van Pouderoyen, G., Canters, G.W., Nar, H., Hammann C. and Messerschmidt, A., 1995, An ENDOR and ESSEM Study of the Blue Copper Protein Azurin, *Chem. Phys. Letters* **235**:202-210.

Eaton, S.S., More, K.M., Sawant, B.M. and Eaton, G.R., 1983, *J. Am. Chem. Soc.* **105**, 6560-6567.

Eaton, S.S., Eaton, G.R. and Chang, C.K., 1985, J. *Am. Chem. Soc.* **107**, 3177-3184.

Froncisz, W. and Hyde, J.S., 1982, The Loop gap Resonator: A New Microwave Lumped Circuit ESR Sample Structure, *J. Magn. Reson.* **47**:515.

Froncisz, W. and Hyde, J.S., 1980, Broadening by Strains of Lines in the g-Parallel Region of Cu^{2+} EPR Spectra, *J. Chem. Phys.,* **73**:3123-3131.

Gromov, I, Krymov, V., Manikandan, P.; Arieli, D. and Goldfarb, D., 1999, A W-Band Pulsed ENDOR Spectrometer: Setup and Application to Transition Metal Centers, *J. Magn. Reson.,* **139**:8-17.

Hanna, P.M., McMillin, D.R., Pasenkiewicz-Gierula, M., Antholine, W.E. and Reinhammar, B., 1988, Type 2-Depleted Fungal Laccase, *Biochem. J.* **253**:561-568.

Hanson, R.S. and Hanson, T.E., 1996, Methanotrophic bacteria, *Microbiol. Rev.* **60**:439471.

Hanson, R.S., Netrusov, A.I and Tsuji, K., 1991, The obligate methanotropic bacteria *Methylococcus. Methylomonas,* and *Methylosinus,* in The Procaryotes. A. Bolows, H. G. Truper, M. Dworkin, and K. Schliefer, editors. Springer Verlag, New York, 2350-2364.

Hay, M., Richards, J.H. and Lu, Y., 1996, Construction and Characterization of an Azurin Analog for the Purple Copper Site in Cytochrome *c* Oxidase, *Proc. Natl. Acad. Sci. USA* **93**:461-464.

Holm R.H., Kennepohl, P. and Solomon, E.I., 1996, Structural and Functional Aspects of Metal Sites in Biology, *Chem. Rev.* **96**:2239-2314.

Iwata, J., Ostermeier, C., Ludwig, B. and Michel, H., 1995, Structure at 2.8A Resolution of Cytochrome *c* Oxidase from *Paracoccus denitrificans, Nature,* **376**:660-669.

Kamachi, T., Miyaji, A. and Okura, I., 2001, Effect of detergents on the purification of particulate methane monooxygenase from *Methylosinus trichosporium* OB3b, *J. Inorg., Biochem.* **86**:285.

Kroneck, P.M.H., in *Handbook of Metalloproteins* (editors, Albrecht Messerschmidt, Robert Huber, Thomas Poulos, Karl Wieghardt, Vol. 2, John Wiley and Sons, LTD, Chichester, New York, 2001.

Kroneck, P.M.H., Antholine, W.E., Riester, J. and Zumft, W.G., 1988, The Cupric Site in Nitrous Oxide Reductase Contains a Mixed-Valence [Cu(II),Cu(I)] Binuclear Center: A Multifrequency Electron Paramagnetic Resonance Investigation, *FEBS Lett.* **247**:70-74.

Kroneck, P.M.H., Antholine, W.E., Riester, J. and Zumft, W.G., 1989, The Nature of the Cupric Site in Nitrous Oxide Reductase of a CuA in Cytochrome C Oxidase, *FEBS Lett.* **248**:212-213.

Kroneck, P.M.H., Antholine, W.E., Kastrau, D.H., Buse, G., Steffens, G.C.M. and Zumft, W.G., 1990, Multifrequency EPR Evidence for a Bimetallic Center at the Cu_A Site in Cytochrome *c* Oxidase, *FEBS Lett.* **268**:274-276.

Kroneck, P.M.H., Riester, J., Zumft, W.G. and Antholine, W.E., 1990, The Copper Site in Nitrous Oxide Reductase, *Biol. Met.* **3**:103-109.

Lee, S-K., George, S.D., Antholine, W.E., Hedman, B., Hodgson, K.O. and Solomon, E.I., 2002, Nature of the Intermediate Formed in the Reduction of O_2 to H_2O at the Trinuclear Copper Cluster Active Site in Native Laccase, *J. Am. Chem. Soc.,* **124**:6180-6193.

Lee, S-K. and Solomon, E.I., 1999, Spectroscopic Analysis of Dioxygen Activation by the Trinuclear Copper cluster in Laccase, *J. Inorg. Biochem.* **74**:202.

Lemos, S.S., Collins, M.L.P., Eaton, S.S., Eaton, G.R. and Antholine, W.E., 2000, Comparison of EPR-visible Cu^{2+} Sites in pMMO from *M. capsulatus* (Bath) and *M. album* BG8, *Biophys. J.* **79**:1085-1094.

Lemos, S.S., Yuan, H., Collins, M.L.P. and Antholine, W.E., Review of Multifrequency EPR of Copper in Particulate Methane Monooxygenase, 2002, *Curr. Top. Biophys., in press.*

Lemos, S.S., Collins, M.L.P. and Antholine, W.E., 2001, A Search for a Cluster in pMMO: the Broad g = 2.1 Signal Revisited, 2001, *J. Inorg. Biochem.* **86**, Abstr. pg. 126.

Li, J., McMillin, D.R. and Antholine, W.E., 1992, Evidence for Temperature-Dependent Changes in the Coupling Within the Type 2/Type 3 Cluster of Laccase, *J. Am. Chem. Soc.* **114**:725-727.

Li, P.M., Malmstrom, B.G. and Chan, S.I., 1989, The Nature of Cu_A in Cytochrome *c* Oxidase, *FEBS Lett.* **248**:210-211.

Lieberman, R.L., Doan, P.E., Hoffman, B.M., and Rosenzweig, A. C., 2001, Characterization of the particulate form of methane monoxygenase (pMMO) from *Methyloccus capsulatus* (Bath) and *Methylosinus albus* BG8, *J. Inorg. Biochem.,* **86**:316.

Lu, J., Bender, C.J., McCracken, J., Peisach, J., Severns, J.C. and McMillin, D.R., 1992, Pulsed EPR Studies of the Type 2 Copper Binding Site in the Mercury Derivative of Laccase, *Biochemistry,* **31**:6265-6272.

Lukoyanov, D., Lu, Y., Berry, S.M., Antholine, W.E. and Scholes, C.P., 2002, Role of the Coordinating Histidine in Altering the Mixed-Valency of Cu_A: An ENDOR-EPR Investigation, *Biophys. J.,* **82**:2758-2766.

MacMillan, F., Kannt, A., Behr, J., Prisner, T. and Michel, H., 1999, Direct Evidence for a Tyrosine Radical in the Reaction of Cytochrome *c* Oxidase with Hydrogen Peroxide, *Biochemistry,* **38**:9179-9184.

McMahon, H.E., Mange, A., Nishida, N., Creminon, C., Casanova, D. and Lehmann, S., 2001, Cleavage of the amino terminus of the prion protein by reactive oxygen species, *J. Biol.Chem.,* **276**:2286-91.

Messerschmidt, A., Huber, R., van de Kamp, M. and Canters, G.W., 1992, Refined Crystal Structure of Ascorbate Oxidase at 1.9Å Resolution, *J. Mol. Biol.,* **224**:179-205.

Miller, C., Fajardo, J., Antholine, W.E. and McMillin, D. R. An Electron Paramagnetic Resonance Method for Quantification of Copper Isotopes in Proteins: Application to a Mixed-Isotope Derivative of Laccase, 1995, *Anal. Biochem.* **227**:69-72.

Morie-Bebel, M.M., McMillin, D.R. and Antholine, W.E., 1986, Multi-Frequency EPR Studies of a Mercury-Containing Mixed-Metal Derivative of Laccase, *Biochem. J.* **235**:415-420.

Nar, H., Messerschmidt, A., Huber, R., van de Kamp, M. and Canters, G.W., 1991, Crystal structure of oxidized *Pseudomonas aeruginosa* azurin at pH5.5 and pH 9.0: A pH-induced conformational transition involves a peptide bond flip, *J. Mol. Biol.* **221**:765-772.

Neese, F., Zumft, W.G., Antholine, W.E. and Kroneck, P.M.H., 1996, The Purple Mixed-Valence Cu_A Center in Nitrous-oxide Reductase: EPR of the Copper-63-, Copper-65-, and Both Copper-65- and [^{15}N] Histidine-Enriched Enzyme and a Molecular Orbital Interpretation. *J. Am. Chem. Soc.* **118**:8692-8699.

Newton, M. E. and Hyde, J.S., 1991, ENDOR at S-band (2-4 GHz) Microwave Frequencies, *J. Magn. Reson.,* **95**:80-87.

Nguyen, H-H.T., Elliott, S.J., Yip, J.H-H. and Chan, S.I., 1998, The particulate methane monooxygenase from *Methylococcus capsulatus* (Bath) is a novel copper-containing three-subunit enzyme, *J. Biol. Chem.,* **273**:7957-7966.

Nguyen, H-H. T., Nakagawa, K. H., Hedman, B., Elliott, S. J., Lidstrom, M. E., Hodgson, K. O., and Chan, S. I., 1996, X-ray Absorption and EPR Studies on the Copper Ions

Associated with Particulate Methane Monooxygenase from *Methylococcus capsulatus* (Bath). Cu(I) Ions and their Implications, *J. Am. Chem. Soc.,* **118**:12766-12776.

Nguyen, H-H.T., Shiemke, A.K., Jacobs, S.J., Hales, B., Lidstrom, M.E., and Chan, S.I., 1994, The Nature of the Copper Ions in the Membranes containing the Particulate Methane Monooxygenase from Methylococcus capsulatus (Bath), *J. Biol. Chem.* **269**:14995-15005.

Peisach, J. and Blumberg, W.E., 1974, Structural Implications Derived from the Analysis of Electron Paramagnetic Resonance Spectra of Natural and Artificial Copper Proteins, *Arch. Biochem. Biophys.* **165**:691-708.

Prior, S.D. and Dalton, H., 1985, The effect of copper ions on membrane content and methane monooxygenase activity in methanol-grown cells of *Methylococcus capsulatus* (Bath), *J. Gen. Microbiol.* **131**:155-163.

Ranjan, N. and Surewicz, W.K., 2001, The Role of a Disulfide Bridge in the Folding and Stability of the Recombinant Human Prion Protein, *J. Biol. Chem.,* **276**:2427-2431.

Rakhit, G., Antholine, W.E., Froncisz, W., Hyde, J.S., Pilbrow, J.R., Sinclair, G.R. and Sarkar, B., 1985, Direct Evidence of Nitrogen Coupling in the Copper(II) Complex of Bovine Serum Albumin by S-Band Electron Spin Resonance Technique, *J. Inorg. Biochem.* **25**:217-224.

Requena, J.R., Groth, D., Legname, G., Stadtman, E.R., Prusiner, S.B. and Levine, R., 2001, Copper-catalyzed oxidation of the recombinant Sha(29-231) prion protein, *Proc. Natl. Acad. Sci.* **98**:7170-7175.

Robin, M.B. and Day, P., 1967, *Adv. Inorg. Chem. Radiochem.,* **10**:247.

Slutter, C.E., Gromov, I., Richards, J.H., Pecht, I. and Goldfarb, D., 1999, Mutations of the Weak Axial Ligand in the Thermus Cu_A Center Modulates Its Electronic Structure, *J. Am. Chem. Soc.,* **121**:5077-5078.

Sundaram, U.M., Zhang, H.H., Hedman, B., Hodgson, K.O. and Solomon, E.I., 1997, Spectroscopic Investigation of Peroxide Binding to the Trinuclear Copper Cluster Site in Laccase: Correlation with the Peroxy-Level Intermediate and Relevance to Catalysis, *J. Am. Chem. Soc.* **119**:12525-12540.

Tsukihara, T., Aoyama, H., Yamashita, E., Tomizaki, T., Yamaguchi, H., Shimzawa-Itoh, K., Nakashima, R., Yaono, R., Yoshikawa, S., 1995, Structures of metal sites of oxidized bovine heart cytochrome ***c*** oxidase at 2.8 Å., *Science,* **269**:1069-1074.

Tsukihara, T., Aoyama, H., Yamashita, E., Tomizaki, T., Yamaguchi, H., Shimzawa-Itoh, K., Nakashima, R., Yaono, R., Yoshikawa, S., 1996, The Whole Structure of the 13-Subunit Oxidized Cytochrome ***c*** Oxidase at 2.8 Å, *Science,* **272**:1136-1144.

Tukhvatullin, I.A., Gvozdev, R.I. and Andersson, K.K., 2000, The structure of the active center of ***β*-peptide** membrane-bound methane monooxygenase (pMMO) from *Methylococcus capsulatus* (Bath), *Doklady Biochemistry,* **374**:177-182.

van der Oost, J., Lappapainen, P., Musacchio, A., Warne, A., Lemieux, L., Rumbley, J., Gennis, R.B., Aasa, R., Pascher, T., Malmstrom, B.G. and Saraste, M., 1991, Restoration of a Lost Metal-Binding: Construction of Two Different Copper Sites into a Subunit of the *E. coli* Cytochrome *o* Quinol Oxidase Complex, *EMBO J.,* **II**:3209-3217.

Van Doorshaer, S.V., Cereghetti, G.M., Glockshuber, R., Schweiger, A., 2001, Unraveling the Cu^{2+} Binding Sites in the C-Terminal Domain of the Murine Prion Protein: A Pulse EPR and ENDOR Study, *J. Phys. Chem. B.* **105**:1631-1639.

van Gastel, M., Coremans; J.W.A., Jeuken, L.J.C., Canters, G.W. and Groenen, E.J.J., 1998, Electron Spin-Echo Envelope Modulation Spectrum of Azurin at X-Band, *J. Phys. Chem. A* **102**:4462-4470.

Vänngård, T., 1972, Copper Proteins, in *Biological Applications of Electron Spin Resonance* (H. M. Swartz, J. R. Bolton, and D. C. Borg, eds.) Wiley-Interscience, New York, p. 411.

Wilce, M.C.J., Dooley, D.M., Freeman, H.C., Guss, J.M., Matsunami, H., McIntire, W.S., Ruggiero, C.E., Tanizawa, K. and Yamaguchi, H., 1997, Crystal Structures of the Copper-Containing Amine Oxidase from *Arthrobacter globiformis* in the Holo and Apo Forms: Implications for the Biogensis of Topaquinone, *Biochemistry* **36**:16116-16133.

Yuan, H., Antholine, W.E. and Kroneck, P.M.H., 1998, Complexation of Type 2 Copper by Cytochrome *c* Oxidase: Probing of Metal-Specific Binding Sites by Electron Paramagnetic Resonance, *J. Inorg. Biochem.* **71**:99-107.

Yuan, H., Collins, M.L.P. and Antholine, W.E., 1997, Low-Frequency EPR of the Copper in Particulate Methane Monooxygenase from *Methylmicrobium albus* BG8, *J. Am. Chem. Soc.* **119**:5073-5074.

Yuan, H., Collins, M.L.P. and Antholine, W.E., 1999, Type 2 Cu(2+) in pMMO from *Methylomicrobium album* BG8, *Biophys. J.* **76**:2223-2229.

Zahn, J.A. and DiSpirito, A.A., 1996, Membrane-associated methane monooxygenase from *Methylococcus capsulatus* (Bath). *J. Bacterial.* **178**:1018-1029.

Zhen, Y., Schmidt, B., Kang, U.G., Antholine, W.E., Ferguson-Miller, S., 2002, The Cu_A Site of Cytochrome *c* Oxidase of *Rhodobacter sphaerodes:* I. Spectral and Functional Properties of Ligand Mutants, *Biochemistry,* **41**:2288-2297.

Chapter 15

Electron Spin-Echo Envelope Modulation Studies Of ^{14}N In Biological Systems[1]

Michael J. Colaneri°† and Jack Peisach†
Department of Chemistry and Physics, State University of New York at Old Westbury, Old Westbury, New York 11568 and † Department of Physiology and Biophysics, Albert Einstein College of Medicine, 1300 Morris Park Avenue, Bronx, New York 10461

Abstract: Electron Spin-Echo Envelope Modulation Spectroscopy has provided great insight into the structure and function of many important biomolecules. Since its first application, this pulsed resonance technique has been found to be especially sensitive to those systems containing weak nuclear couplings. This chapter highlights representative Electron Spin-Echo Envelope Modulation investigations into protein systems containing paramagnetic transition ions and free radicals where geometric and electronic information was obtained through the detection and analysis of weak ^{14}N coupling interactions.

1. INTRODUCTION

The first biological application of Electron Spin-Echo Envelope Modulation (ESEEM) spectroscopy was the study by Mims and Peisach (1976) of metal coordination in the blue copper (or type 1) protein stellacyanin isolated from *Rhus vernicifern.* Modulations of the spin-echo amplitude were observed for frozen solution samples of both this and copper bound to bovine serum albumin (BSA) that differed from those seen for aquo-Cu^{2+}. Based on the similarity in their respective ESEEM patterns and combined with previous biochemical evidence showing that histidine-imidazole was bound to copper in BSA, stellacyanin was suggested to have the same coordinating ligand. Parallel studies involving copper models such

[1] Dedicated to the memory of Professor Larry Kevan, 1938 – 2002.

as hexaglycine-Cu^{2+} and glycylglycine-Cu^{2+} were used to exclude the possibility that the low frequency modulations observed for stellacyanin and BSA arose from ^{14}N nuclei directly bound to the metal ion and therefore, their origin was assigned to a weaker coupled ^{14}N, possibly from the remote nitrogen of coordinated histidine-imidazole (Figure 1). This assignment was soon verified through comparison of the Fourier transformed-ESEEM patterns (FT-ESEEM) obtained from stellacyanin (Mims and Peisach, 1979) and from diethylenetriamine-Cu^{2+}-imidazole prepared with ^{14}N and ^{15}N imidazole (Mims and Peisach, 1978, 1979). Later X-ray diffraction experiments confirmed histidine-imidazole ligation by determining the three-dimensional structure of the "blue copper" in stellacyanin (Hart et al., 1996) and other similar proteins (Baker, 1988, Messerschmidt et al., 1989), demonstrating two imidazoles bound to copper in all of them.

The major impetus of these early ESEEM investigations was to identify metal ligands in biological macromolecules where little prior structural information was available, And, as demonstrated by the recent study undertaken to ascertain whether His 332 (D1) binds the manganese cluster in photosystem II (Debus et al., 2001), the employment of ESEEM to address similar questions of protein structure remains equally important today.

ESEEM has emerged to become a valuable complement to the host of other Electron Magnetic Resonance (EMR) methods in the modern study of protein structure and function. Among these, ESEEM remains uniquely suited to detect and analyze weakly coupled nuclei, including ^{13}C (Zweier, et al., 1979, Tipton et al., 1989, Eaton et al., 1989, 1990), ^{17}O (Thomann et al., 1996), ^{15}N (Cornelius et al., 1990, Dikanov, et al., 1994, Coremans, et al., 1996) and ^{2}H (Mims et al., 1984, McCracken et al., 1987, 1988, Lee et al., 1992, Warncke et al., 1994), but particularly natural abundant ^{14}N (Peisach, 1995). Its advantage is in its capacity to measure both frequency and signal amplitudes from frozen solution specimens, which, when taken together, carry all the information required to determine complete coupling tensor parameters. ESEEM has consequently evolved into a powerful technique used to probe electronic features at active sites through analysis of weak magnetic couplings. This evolution has been guided largely by an increasing awareness that important mechanistic information can be gleaned from nuclear interactions at the outer fringes of the unpaired spin wavefunction.

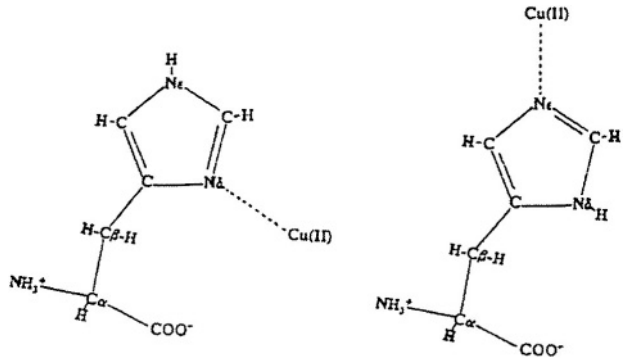

Figure 1. The remote nitrogen of coordinated histidine-imidazole to copper is either the amino Nε or Nδ, depending on the mode of metal binding to the imidazole moiety. The directly bound nitrogens have hyperfine couplings too large to be detected by ESEEM at X-band.

This review starts with a short experimental description of the technique, which is followed by discussions on selected ^{14}N ESEEM investigations into protein structure and function. As mentioned above, initial studies have focused on copper-imidazole complexes in proteins. However, the versatility of the technique can also be documented using examples where couplings from other types of nitrogen are analyzed. This report is therefore cast as a summary of ESEEM applications, organized according to the type of nitrogen commonly found in proteins. These include remote and directly metal-bound nitrogen of a coordinated histidine-imidazole, peptide nitrogen, nitrogen contained in other amino acid side chains and coupled nitrogens in substrates or chemical intermediates. Some general reviews on the physical basis and applications of ESEEM can be found in Mims (1972), Kevan and Schwartz (1979), Mims and Peisach (1981), Dikanov and Tsvetkov (1992), Peisach (1995) and more recently, Deligiannakis et al. (2000).

2. THE ESEEM EXPERIMENT

Figure 2 illustrates the basic ESEEM experiment (Mims, 1972, Kevan and Schwartz, 1979) consisting of a sequence of two or three microwave pulses, which, when applied to a sample, results in the emission of a burst of microwave energy called an electron spin-echo. The shortness of the microwave pulse produces coherent excitations of allowed and forbidden

EPR transitions associated with weak nuclear couplings. These excitations produce interference effects causing the amplitude of the spin-echo to depend on the inter-pulse time interval in a periodic fashion. The frequencies of the modulations in the spin-echo envelope pattern as a function of inter-pulse time are related to energy differences between nuclear spin states, i.e., the superhyperfine (shf) frequencies. It is important that the employed microwave field strength H_1 be large enough to ensure that $\gamma H_1/\hbar$ (where γ is the gyromagnetic ratio) is larger than the individual shf frequencies for the modulation phenomena to be fully developed. For typical X-band experiments $\gamma H_1/\hbar$ is usually less than ~25MHz (Kevan and Schwartz, 1979). This allows the detection and analysis of weak couplings from low magnetic moment nuclei, such as ^2H and ^{14}N, to distances from the paramagnetic center out to 4-6Å.

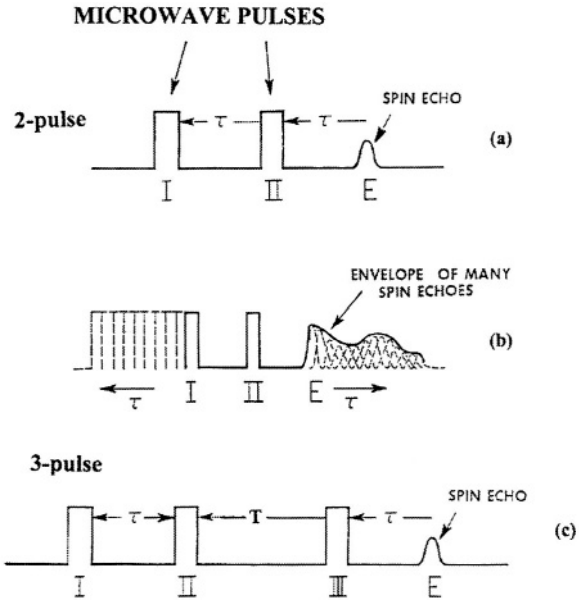

Figure 2. The basic two-pulse and three-pulse ESEEM experiment, (a) A sequence of resonant microwave pulses creates a burst of radiation from the sample called an electron spin-echo, (b) The envelope of spin-echo amplitudes as a function of incrementation of inter-pulse time is modulated by weak nuclear coupling interactions, (c) In a typical stimulated-echo experiment, the inter-pulse time τ is fixed and T is varied. Here the envelope of echo amplitude is measured as a function of $\tau + T$ and again is modulated by frequencies arising from weak couplings. Typical X-band ESEEM samples require a paramagnetic concentration ranging from 0.1-2mM in about 1-200μl of volume. Reproduced from Blumberg et al. (1973) with permission. Copyright 1973 American Institute of Physics.

Both two-pulse and three-pulse (or stimulated-echo) sequence experiments can show modulations from weak couplings. However, three-pulse experiments are more common because it offers two advantages (Mims, 1972, Kevan and Schwartz, 1979). First, the three-pulse modulation pattern contains only the individual shf frequencies, which makes it much easier to interpret than the two-pulse pattern, which contains modulations from the shf frequencies as well as their sums and differences. Second, the two-pulse echo envelope decay is generally faster than the stimulated-echo decay, and therefore the amount of useful modulation data is usually greater in the three-pulse experiment.

In the stimulated-echo experiment the first inter-pulse time, τ, is held constant while the second, T, is varied as the echo envelope is traced out. Mims (1972) showed that specific τ settings can cause the suppression or even the disappearance of certain frequency components of the three-pulse echo envelope modulation. This property turns out to be quite useful experimentally because it can discern whether two frequencies belong to the same or opposite electron spin manifolds and therefore help in the assignments of the observed shf frequencies.

Fourier transform (FT) of the ESEEM pattern converts the modulation time periods into a set of frequency lines which possess the same information as the Electron-Nuclear Double Resonance (ENDOR) frequencies of coupled nuclei (Blumberg et al., 1973, Merks and de Beer, 1980). Unlike ENDOR however, in ESEEM both the modulation frequencies and their amplitudes contain coupling tensor information (Mims and Peisach, 1978, 1979, Reijerse and Dikanov, 1991). This is because the intensity of a particular modulation is related to the extent at which allowed and forbidden EPR transitions are excited by the pulses. During the initial applications of ESEEM, it became apparent that for weak ^{14}N (I=1) couplings, the modulation pattern becomes deeper as a condition known as "exact cancellation" (Mims, 1972) is approached (Mims and Peisach, 1978). This happens when the signs of the hyperfine and nuclear Zeeman energies (ν_n) are opposite, causing them to cancel each other resulting in a nuclear alignment in one of the electron spin manifolds according to the pure nuclear quadrupole states. The other has nuclear eigenstates governed by nuclear Zeeman, hyperfine and quadrupole terms. At X-band (~9 GHz) microwave frequency and for an EPR resonant signal at $g \approx 2$, this is met when the ^{14}N hyperfine interaction is about 1.8 MHz.

Figure 3 shows a typical spin energy level diagram (a) and powder-averaged X-band 3-pulse FT-ESEEM spectrum (b) from a weakly coupled ^{14}N near the cancellation situation. Here the three "nuclear quadrupole interaction" (nqi) lines (ν_{1o}, ν_{1-} and ν_{1+}) arise from the manifold where cancellation occurs and one broad "double quantum" line (ν_{2o}) is from the

other electron spin manifold. The remaining two lines from the second manifold are broadened by anisotropy of the hyperfine and quadrupole couplings, and are not commonly observed in a disordered sample, but can be in oriented single crystals, as for example in Figure 4. The spectroscopic coupling parameters are usually partly determined using the FT-ESEEM modulation frequencies and then completed by adjustments that match theoretically simulated FT-ESEEM spectra with experimental line frequencies and amplitudes.

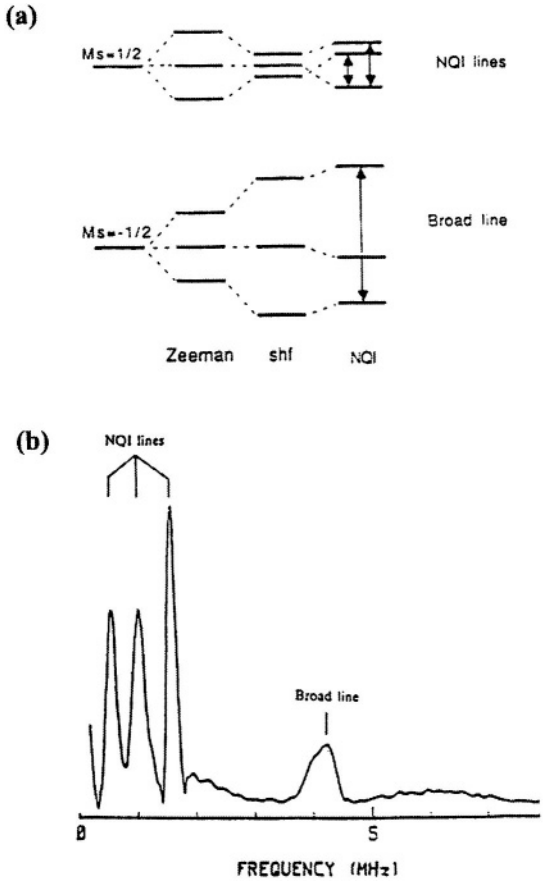

Figure 3. (a) Spin energy levels for S=½, I=1 (^{14}N) system near the exact cancellation condition displaying the assignments of the nqi and double quantum (broad) frequency lines. (b) Fourier transformed 3-pulse ESEEM spectra from a powder-averaged Cu^{2+} sample possessing a weak ^{14}N nuclear coupling. The low frequency nqi lines refer to ν_{1o}, ν_{1-} and ν_{1+} from one spin manifold and the higher frequency, broad line ν_{2o} arises from the opposite spin manifold. Reprinted from Jiang et al. (1990).

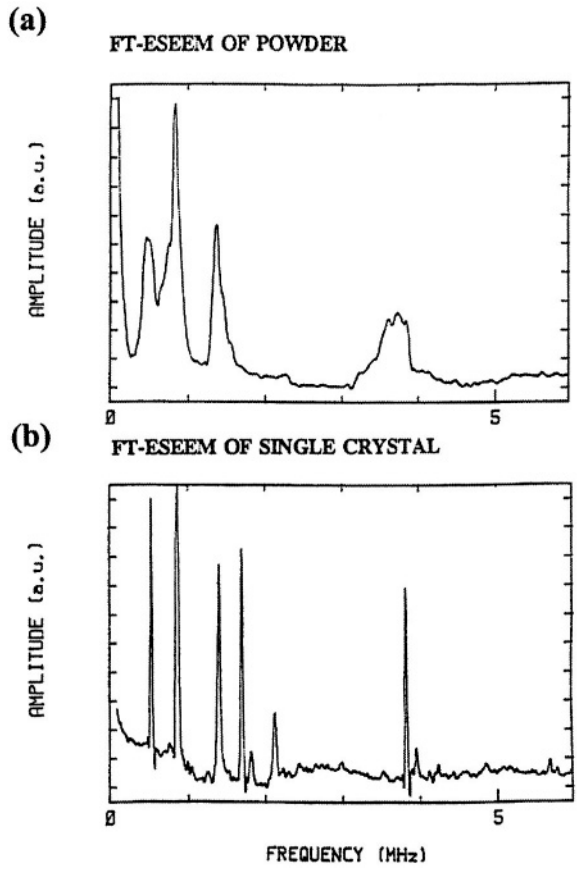

Figure 4. Fourier transforms of 3-pulse ESEEM patterns for a copper-remote nitrogen interaction in a crushed powder (a) and single crystal (b) of a Cu^{2+}-histidine complex. Four ^{14}N modulation frequency lines are observed in the powder-averaged spectra, the other two are absent because of broadening from orientation anisotropy. In contrast, all six lines are evident in the aligned crystal. Lines of smaller amplitude in the single crystal sample are due to a minor copper site.

The two sets of coupling parameters provided by the ESEEM experiment are the hyperfine coupling and the nuclear quadrupole interaction tensors (Mims and Peisach, 1978, 1979, Merks and de Beer, 1980). The hyperfine consists of isotropic and anisotropic components. The isotropic hyperfine (a_{iso}) provides a measure of the amount of electron spin in the s-orbital of the atom of the coupled nucleus, whereas the anisotropic hyperfine component reflects spin density distributed in a non-spherical fashion about the nucleus (Carrington and McLachlan, 1967). In frozen solution samples, this latter

component is usually interpreted in terms of a "classical dipolar" part involving the interaction between the metal based unpaired electron and coupling nucleus or a "pseudo-dipolar" interaction, which also encompasses interactions between the coupling nucleus and electron spin delocalized away from the paramagnetic center, here a metal ion (Rowan et al., 1965, Minis and Peisach, 1979). The hyperfine tensor therefore contains positional information on the nucleus as well as important insight into the nature of the electron spin wavefunction.

The nuclear quadrupole interaction represents the coupling energy between the nuclear quadrupole moment and the electric-field gradient (efg) it experiences (Carrington and McLachlan, 1967, Lucken, 1969). According to approximations developed by Townes and Dailey (1949), the valence orbitals of an atom in a molecule are largely responsible for the resulting efg at its nucleus. The local perturbations imparted on valence bonds of ^{14}N by differences in hydrogen bonding or by the coordination to metal ions cause a change in the efg at the nucleus, which is reflected in its nqi parameters. The derived nqi interaction consequently offers insight into local bonding affects at the nitrogen. The nqi parameters routinely cited in ESEEM are the maximum quadrupole coupling, e^2qQ, η the tensor asymmetry, and the direction that e^2qQ makes with respect to the g-tensor principal axes. The value of η varies between zero for an axially symmetric case to unity for complete rhombicity.

3. APPLICATIONS

Near the "cancellation" condition estimates for the 3-pulse FT-ESEEM frequencies in terms of the ^{14}N effective hyperfine (A') and nqi (e^2qQ and η) parameters can be obtained from first-order relationships listed below (Reijerse and Keijers, 1987). For conditions far from exact cancellation, a straightforward analysis of the FT- ESEEM pattern becomes more difficult and initial parameters may not be as well determined.

$$\nu_{1o} = e^2qQ\eta/2$$

$$\nu_{1\pm} = 3e^2qQ(1 \pm \eta/3)/4$$

$$(\nu_{2o})^2 \approx 2[(\nu_n + A'/2)^2 + (e^2qQ)^2(3 + \eta^2)]$$

The isotropic and anisotropic hyperfine components and three angles specifying each of the hyperfine and quadrupole tensor orientations are

usually determined by adjusting first-order parameters to match the Fourier transforms of electron spin-echo modulation patterns (FT-ESEEM spectra) simulated from equations derived by Mims (1972a, 1972b) with those experimentally obtained. These equations and similar sets of mathematical expressions are therefore commonly referred to as "Minis' formulas". When deriving these theoretical expressions, Mims also showed that when two or more nuclei weakly couple, the appearance of combination frequencies occurs from the product of modulations of the individual nuclear couplings (Mims, 1972a). The depth of the overall modulation pattern depends on the number of similarly coupled nuclei and therefore ESEEM can also be used to determine their number.

3.1 Couplings to the Remote Imidazole Nitrogen

That the first biological ESEEM study was conducted on stellacyanin (Mims and Peisach, 1976) was quite prophetic, given the now known ubiquitous histidine-imidazole ligation to copper in all Cu^{2+} proteins, many of which were initially assigned by ESEEM rather than by X-ray crystallography. It was also fortuitous that the hyperfine coupling ($\approx$1.8 MHz) of the remote nitrogen of coordinated histidine-imidazole was near the condition for "cancellation" as this study demonstrated the great spectral sensitivity of the technique. Figure 5 shows the close match between FT-ESEEM spectra taken from diethylenetriamine- Cu^{2+}-imidazole, stellacyanin and spectra simulated using the following nuclear coupling parameters; a_{iso} = 1.75 MHz, e^2qQ = 1.42 MHz and η = 0.99. The nqi parameters were obtained from earlier Nuclear Quadrupole Resonance (NQR) spectroscopic studies on the protonated nitrogen of imidazole (Hunt et al., 1975).

The first determination of the number of coupled nuclei in a protein using ESEEM was by McCracken et al. (1988) in their characterization of the coordination of copper-bound to dopamine β-hydroxylase, an enzyme that catalyzes the conversion of dopamine to norepinephrine. 3-pulse ESEEM decay patterns obtained from simulations of copper models containing 2, 3 and 4 bound imidazoles were compared to the pattern from the protein (Figure 6). This led to the conclusion that 3 or 4 histidine-imidazoles coordinate to copper in this protein. Four histidine-imidazoles were deemed most likely as this was also consistent with the lack of any deuterium modulation arising from equatorially bound water from samples made in D_2O, which placed the closest Cu-D distances to be greater than 5Å.

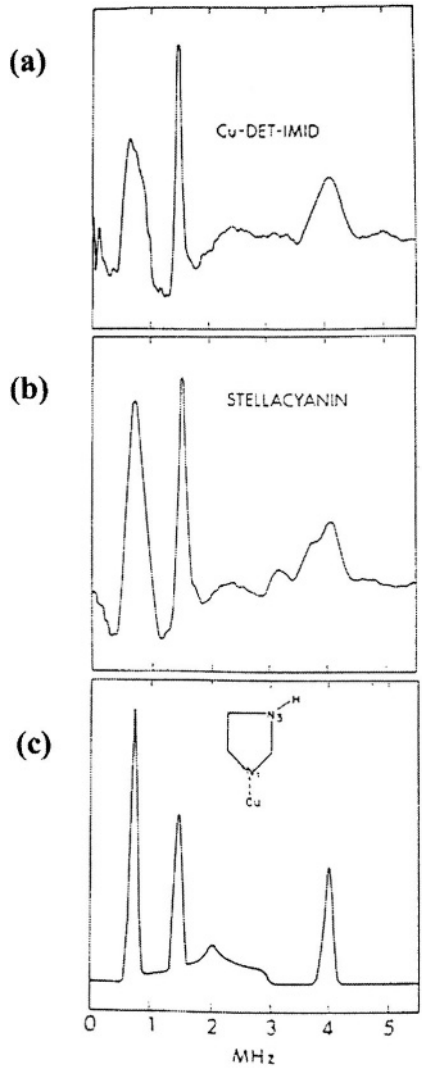

Figure 5. Fourier transformations of 3-pulse ESEEM patterns obtained from (a) a copper model, diethylenetriamine (dien)–Cu^{2+}-imidazole, (b) the blue copper protein, stellacyanin and (c) theoretical simulations based on parameters given in the text. The diethylenetriamine bound to copper makes no ESEEM spectral contribution. In the spectra shown, the lowest two nqi frequency lines are mostly overlapped indicating $\eta \approx 1$. The close similarity of these spectra confirms the assignment of the weak ^{14}N coupling to the remote amino nitrogen (N3) of coordinated imidazole. Taken from Mims and Peisach (1979).

The remote nitrogen hyperfine and nqi parameters found in the non-blue (or type 2) copper protein dopamine β-hydroxylase (e^2qQ = 1.44 MHz, η= 0.98), were similar to those in stellacyanin. In contrast, FT-ESEEM spectra obtained from another type 2 protein, galactose oxidase shown in Figure 7 have the two lowest frequency nqi lines (ν_{1o} and ν_{1-}) clearly resolved, which is indicative of η being smaller than 0.9. Indeed, results on this type 2 copper gave two equivalent ^{14}N couplings with parameters of a_{iso} = 1.8 MHz, e^2qQ = 1.7 MHz and a very significantly different η value, 0.65, than is found for the remote nitrogen of coordinated histidines in blue copper (or type 1) centers (Jiang et al., 1990, Kosman et al., 1980). It was suggested that this alteration of nqi compared to other studied copper proteins may be due to perturbations at the imidazole remote nitrogens in the galactose oxidase structure, perhaps a weak hydrogen bonding to some other part of the protein (Kosman et al., 1980).

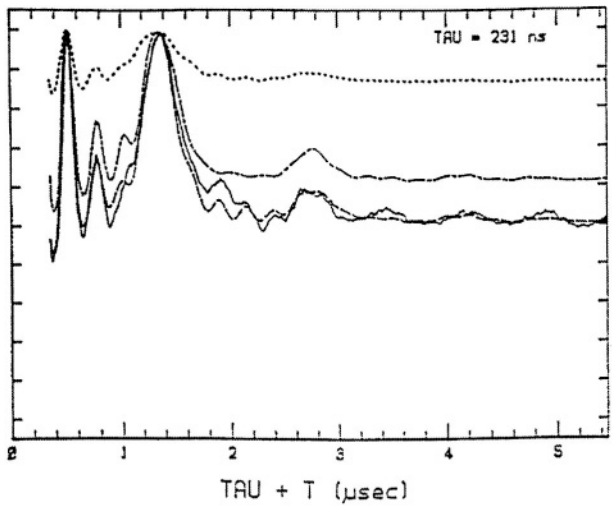

Figure 6. Comparison of 3-pulse ESEEM decay patterns obtained for dopamine β-hydroxylase (solid line) and theoretical simulations of copper-imidazole models containing 2(....), 3(-.-.-.) and 4(----) remotely coupled ^{14}N nuclei. Based on this comparison, 3 or 4 histidine-imidazoles were deduced to coordinate to the copper in the enzyme. Reprinted from McCracken et al. (1988).

ESEEM studies on copper bound in porcine kidney amine oxidase (McCracken et al., 1987) resolved different sets of parameters from two different magnetically independent remote nitrogens of histidine-imidazoles coordinated to copper, one normal with a_{iso} = 1.8 MHz, e^2qQ = 1.43 MHz

and $\eta = 0.91$ (like stellacyanin), and the other "strongly coupled" with parameters $a_{iso} = 2.3$ MHz, $e^2qQ = 1.7$ MHz, $\eta = 0.5$. The nqi for the latter is similar to that in galactose oxidase. Besides providing this evidence for multiple histidine-imidazole coordination, the ^2H ESEEM patterns from samples exchanged against D_2O indicated that both equatorial and axial waters are also bound to the metal ion. The proposed copper site was consistent with cyanide inhibition of the enzyme where CN^- replaces water and binds directly to copper. The observance of ^{14}N modulation frequencies for the CN bound protein was similar to those from a Cu^{2+}(*dien*)-$C^{14}N$ model complex and the simultaneous elimination of equatorial ^2H modulations upon CN^- binding lend support to this model.

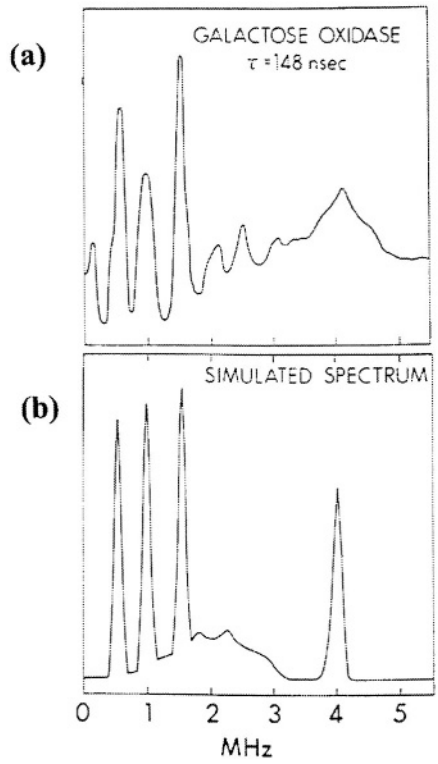

Figure 7. 3-pulse FT-ESEEM spectra from (a) galactose oxidase and a (b) computer simulation using parameters reported in the text. The large splitting in the lowest two modulation frequency lines (as compared to the spectra in Figure 5) reflect a η value significantly smaller than 1. Extra lines of low intensity in the 2-3 MHz range are known as "combination lines" (Mims, 1972) and arise because of the coupling of more than one ^{14}N nucleus. Reprinted from Kosman et al. (1980).

The variations in the nqi of the remote ^{14}N of copper-coordinated histidine-imidazole were becoming increasingly evident in many protein studies and this prompted an ESEEM investigation into a series of copper-imidazole model complexes (Jiang et al., 1990). Experimental observations revealed that the nqi of the remote nitrogen depends on chemical modifications on the imidazole ring (Figure 8a). However, copper-imidazole models prepared in the presence of D_2O and/or formate (Figure 8b) affect the amino nitrogen's hydrogen bonding environment and this too affects the nqi parameters. A Townes-Dailey analysis, similar to one carried out on a group of Zn^{2+}-imidazole compounds (Ashby et al., 1978), explained the dependencies of the e^2qQ and η parameters in terms of differences in the electron occupancy of the >N-H valance orbital. NQI parameters derived from copper proteins were accordingly interpreted according to a scheme where observed variations in nitrogen quadrupole couplings are due to differences in the hydrogen bond environment of the amino nitrogen of coordinated histidine-imidazole.

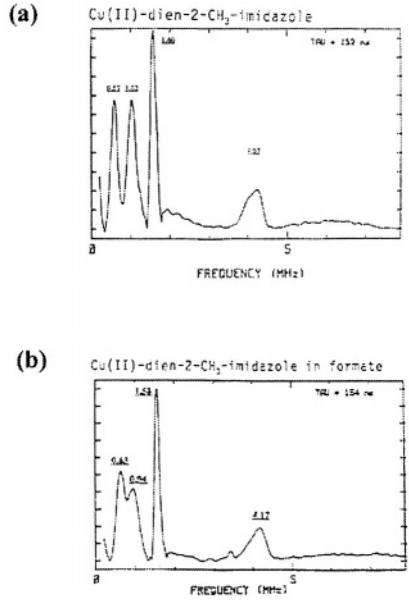

Figure 8. Fourier transforms of the 3-pulse ESEEM patterns for Cu^{2+}-diethylenetramine-2-methylimidazole model systems in (a) aqueous and (b) formate solutions. Compared with the FT-ESEEM of Cu^{2+}-diethylenetriamine-imidazole (Figure 5a), the lowest modulation frequency lines are resolved indicating an η value < 0.9. The presence of formate in the lower spectra causes a change in splitting of the low frequency nqi lines, and therefore η, to change. This is attributed to the stronger hydrogen bonding interaction at the remote amino nitrogen. Taken from Jiang et al. (1990).

Greater accuracy in ESEEM derived parameters was partly accomplished by the development of computational procedures for resonance-angle summation of the powdered averaged ESEEM patterns. In one such development by Cornelius et al. (1990), the ESEEM simulation program called **NANGSEL** (**N**itrogen **ANG**le **SEL**ection) was written to analyze weak axial nitrogen modulations arising from ^{14}N-pyridine coordinated axially to bis(benzoylacetonate)-Cu(II) for selected orientations brought into resonance across the EPR pattern. In this study, the use of ^{15}N-pyridine proved extremely useful as the ^{15}N nucleus has spin ½ with no quadrupole moment. Weak couplings to this nucleus produce a very different pattern of FT-ESEEM lines as compared to ^{14}N. From the ^{15}N-pyridine generated spectra, hyperfine parameters were deduced, consequently scaled for a similarly coupled ^{14}N nucleus, and then used in conjunction with **NANGSEL** to precisely determine the coordinated pyridine ^{14}N tensor couplings.

The first biological application of a similar orientation-selection strategy was by Goldfarb et al. (1992) in their investigation of copper coordination in two multi-copper containing proteins, ascorbate oxidase and laccase, both of which contains type 1 and type 2 copper. These enzymes are involved in the four-electron reduction of dioxygen to water and the one-electron oxidation of substrate. The study was undertaken to extend a previous ESEEM investigation (Avigliano et al., 1981) by comparing the type 1 and type 2 copper sites in laccase to those in ascorbate oxidase, whose 3-dimensional structure was known from diffraction studies (Messerschmidt et al., 1989). An ESEEM investigation of these proteins was challenging, given the extensive overlap in the EPR for the different copper species. This problem was circumvented by a clever substitution of the EPR silent Hg^{2+} for type 1 copper in laccase, which allowed for unobstructed ESEEM measurements for the type 2 copper. Using this approach, the coordinated histidine-imidazole remote ^{14}N coupling parameters for both sites could be adjusted to fit the variation of the FT-ESEEM frequencies on g(magnetic field) shown by Figure 9.

The remote ^{14}N parameters for the two type 1 copper-bound histidine-imidazoles in laccase (a_{iso} = 1.6 & 1.53 MHz, e^2qQ = 1.45 MHz, η = 0.92) and in ascorbate oxidase (a_{iso} = 0.76 & 1.27 MHz, e^2qQ = 1.45 MHz, η = 0.95) indicated similar ligands but different geometries (Goldfarb et al., 1992). A flattening of the coordination geometry was suggested to cause an increase in the isotropic hyperfme coupling, a_{iso} in laccase as compared to ascorbate oxidase. For the type 2 site in laccase, the η parameter for copper coordinated imidazole was also significantly lower than 0.9, similar to those found for other type 2 copper proteins. This led to the alternate explanation for the nqi variations observed in copper proteins, i.e., they originate from

the chemical inequivalence of the two ring nitrogens (Nδ and Nε) in histidine-imidazole (Goldfarb et al., 1992) (see Figure 1). As noted in their report, such a hypothesis is consistent with the finding that in all blue copper (or Type 1) proteins, histidine-imidazole coordinates to copper through Nδ, and have η very close to 0.9, whereas in non-blue (or type 2) copper proteins, histidine-imidazole normally ligates to Cu^{2+} through their Nε, and in all such characterized cases, η values were indeed found to exhibit values significantly smaller than 0.9.

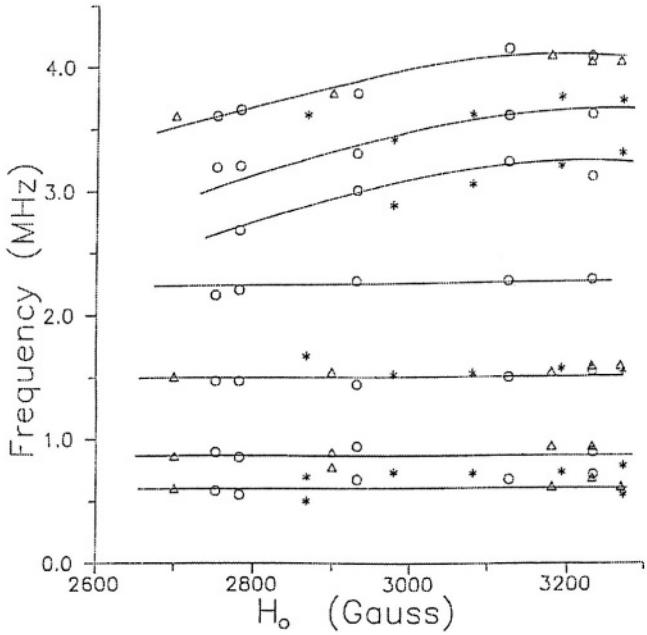

Figure 9. Magnetic field dependencies of the 3-pulse FT-ESEEM modulation frequencies arising from couplings to remote nitrogens in histidine-imidazoles coordinated to type 1 (T1) and 2 (T2) copper in laccase and ascorbate oxidase (0-laccase, Δ-laccase T1(Hg), *-ascorbate oxidase). These field dependencies were evaluated to fit ^{14}N coupling parameters for these sites. Reprinted from Goldfarb et al. (1992) with permission.

In contrast, results derived from ESEEM of Cu^{2+}-doped histidine single crystal models showed that similar ^{14}N nqi coupling parameters (a_{iso} = 1.35 MHz, 1.60 MHz, e^2qQ = 1.40 MHz, 1.56 MHz, η = 0.65, 0.66) can occur when either Nδ or Nε served as the remote nitrogen (Colaneri and Peisach, 1995). Additionally, these studies experimentally verified the presumed correlation between the ^{14}N quadrupole tensor orientation and the imidazole amino nitrogen bonding geometry. The quadrupole tensor orientation could

therefore be used to match observed couplings with remote nitrogens in metal-bound histidine-imidazole systems. Further results from these single crystals suggested that the z-axis, or the direction associated with the maximum quadrupole coupling, depended on the strength of the hydrogen bond at the remote nitrogen. An in-plane direction was observed in the case where a strong hydrogen bond was made to the remote nitrogen and a direction normal to the imidazole plane occurred for the situation of a weaker hydrogen bond.

Colaneri et al. (2000) adopted single-crystal derived ^{14}N tensor orientations to help interpret FT-ESEEM spectra of copper-substituted insulin in multi-crystalline samples. The ligand environment of the copper was presumed to be the same as for zinc in the native crystal structure, with three histidine-imidazoles (His B10) coordinated to the metal ion through $N\epsilon$, complemented by three bound water molecules (Baker et al., 1988). The imidazole remote nitrogen of each histidine makes a hydrogen bond to water, which in turn forms another hydrogen bond to the carboxyl oxygen of a glutamate (Glu B13) side chain. EPR measurements have suggested a Jahn-Teller distortion about the copper, resulting in two of the histidines and two waters forming an approximate equatorial plane about the copper (Brill and Venable, 1968, 1972). The remaining histidine-imidazole and water are presumed to be positioned axial to this plane (Brill and Venable, 1968, 1972). The FT-ESEEM spectral features in Figure 10a show that by soaking the Cu^{2+}-insulin samples in Cd^{2+}-acetate, the coupling parameters convert from those typically found for type 1 sites (a_{iso} = 1.33 MHz, e^2qQ = 1.54 MHz, η = 0.90) to those more representative of type 2 sites (a_{iso} = 1.68 MHz, e^2qQ = 1.67 MHz, 1.76 MHz, η = 0.77, 0.55). X-ray crystallographic studies on Cd^{2+}-insulin reveal cadmium binding to glutamate (Glu B13) carboxyl groups that neighbour the coordinated histidines (Hill et al., 1991). As illustrated in Figure 10b, modelling a conformational change of these nearby glutamic acid side chains to accommodate the binding of Cd^{2+} also allows the formation of hydrogen bonds from the carboxyl oxygen to the remote amino nitrogens of the histidine side chain. The observed change in η in the presence of Cd^{2+} is proposed to occur because of alterations in hydrogen bonding interactions at the remote nitrogen from water oxygen to glutamate oxygen. The nitrogen nqi was further interpreted according to a hypothesis that the η parameter value reflects the identity of the hydrogen bond donor to this nitrogen, irrespective of whether it is $N\varepsilon$ or $N\delta$. Were this donor water, η has a value of 0.9 or higher. For a donor other than water, η varies but always adopts values less than 0.9. A comparison of results from previous ESEEM investigations of copper proteins with known crystal structures appears to support this contention (Colaneri et al., 2000).

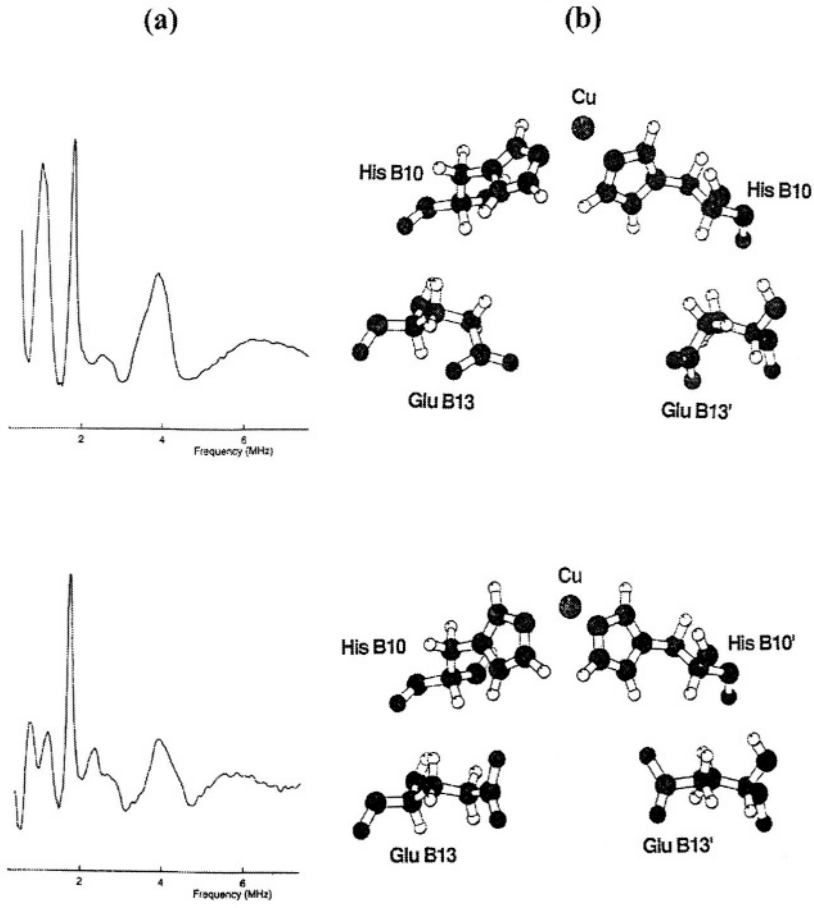

Figure 10. (a) 3-pulse FT-ESEEM spectra for multicrystalline samples of Cu^{2+}-insulin soaked in (top) 0.12 M citrate buffer and (bottom) 5 mM Cd^{2+}-acetate and then washed with 0.12 M citrate, (b) (top) Conformation of histidine (His B10) and glutamic acids (Glu B13) residues near copper in the native zinc-insulin structure. The imidazole remote nitrogen of each coordinated histidine forms a hydrogen bond to water (not shown in figure), (bottom) Postulated changed conformations of these residues showing hydrogen bonding from the histidine (His B10) remote amino nitrogens to the glutamate (Glu B13) carboxylate oxygens in the Cd^{2+}-acetate soaked crystals. Reproduced from Colaneri et al. (2000).

Stellacyanin was revisited by ESEEM spectroscopy some 22 years after its initial study. In an extensive graphical analysis of the dependencies shown by ESEEM patterns on both magnetic field strength and microwave operating frequency, Bender and Peisach (1998) were able to resolve accurate parameters for the two slightly inequivalent coupled nitrogens (a_{iso}

= 2.0 MHz & 1.5 MHz, e^2qQ = 1.45 & 1.50 MHz, η = 0.9) from coordinated histidine-imidazoles. No evidence, however, was seen for a third, weak nitrogen coupling from either the peptide backbone or a predicted glutamine Nε ligand (Bender and Peisach, 1998).

3.2 Couplings to the Directly Coordinated Imidazole Nitrogen

Adjusting the resonant magnetic field by operating at different microwave frequencies can shift the window of opportunity for the ESEEM experiment. Microwaves at W-band (95 GHz), for example, place more strongly coupled nuclei at the condition of "cancellation" and therefore make their hyperfine and quadrupole interactions amenable for study. In order to characterize the unpaired wavefunction in blue copper proteins in more detail, Coremans et al. (1997) carried out W-band ESEEM studies on single crystals of the blue copper protein, azurin. This impressive accomplishment provided complete and accurate coupling parameters for the two histidine-imidazole Nδ nitrogens directly ligated to Cu^{2+} (a_{iso} = 18.1 MHz & 25.1 MHz, e^2qQ = 2.9 MHz & 2.5 MHz, η = 0.5 & 0.6). X-ray diffraction experiments have characterized the coordination, of the copper, which consists of two histidine-imidazoles, His-117 and His-46, and two sulfurs from cysteine and methionine (Baker, 1988) (Figure 11). The directly bound imidazole ^{14}N quadrupole axes were aligned with each of the coordinating imidazole geometries. However, the authors found it necessary to use correspondence between the maximum hyperfine and Cu-N bond directions to corroborate the larger coupling with His-117 and the smaller to His-46. The inequivalent hyperfine couplings exhibited by the two different histidine ligands reflects the relative orientations, and therefore overlap, of the postulated copper d_{xy} unpaired orbital lobes with respect to each of the N-Cu directed lone pairs. A theoretical evaluation of the ^{14}N hyperfine tensors estimated the unpaired spin density involved with the Cu-N coordinate bond and were in agreement with the experimental parameters. These results further demonstrated that the imidazole-copper bond was predominantly sigma in nature.

In an ESEEM study of xylose isomerase, an enzyme requiring divalent cations to catalyze the isomerization of α-D-xylose to α-D-xylulose, Dikanov et al. (1995) demonstrated that vanadyl ion ($V{=}O^{2+}$) substituted in the high affinity cation binding site is a good paramagnetic probe of histidine-divalent metal coordination in this enzyme. Here, 2-pulse ESEEM was used to determine the coupling parameters for the directly bound ^{14}N of a lone histidine-imidazole coordinated to the vanadyl ion. Hyperfine parameters for nitrogens directly coordinated to vanadyl generally range

from 4-7 MHz and because these are relatively far from the cancellation condition at X-band frequencies, the authors derived second-order formulae in order to extract precise parameters from the 2-pulse ESEEM experiment. These formulae were applied to single-crystal-like FT-ESEEM spectra obtained at the turning points of the EPR spectrum as well as to magnetic field and orientation dependencies exhibited by the modulation frequencies. Calculated parameters produced excellent correspondence between simulated and experimental 2-pulse and 3-pulse FT-ESEEM spectra. The nqi quantities ($e^2qQ \approx 2.0$ MHz, $\eta \leq 0.5$) were similar in value to those found from NQR studies on other metal-coordinated imidazole compounds. In addition, the orientation of the quadrupole tensor axes, because these closely match the imidazole ring geometry, revealed that the imidazole had the same orientation as when bound to Mn^{2+}, the catalytically active cation, in the protein structure (Figure 12). Other ESEEM experiments determined proton couplings that were consistent with this structural model since these could be assigned to hydrogens on the imidazole ring. This geometric consistency assured the validity and future use of $V{=}O^{2+}$ as a good structural surrogate for divalent cations in protein systems.

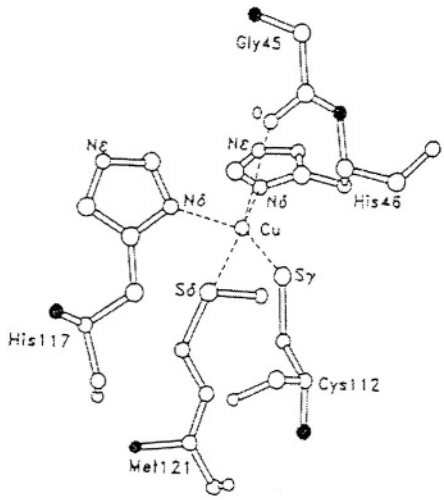

Figure 11. Illustration of the copper coordination site in azurin. The copper ligands are imidazole from His46 and His117, and sulfur from Cys112 and Met121. The carbonyl of Gly45, at a larger distance to copper, contributes a weaker interaction. Reprinted from Coremans et al. (1996) with permission. Copyright 1996 American Chemical Society.

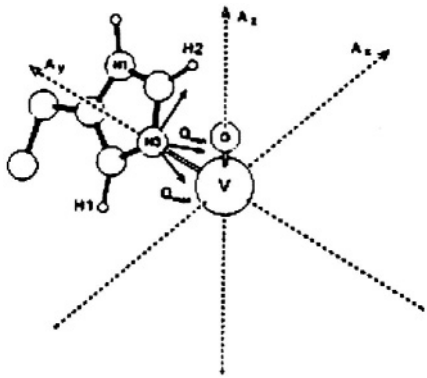

Figure 12. Model for histidine binding to vanadate in xylose isomerase. The Ax, Ay and Az refer to the vanadyl hyperfine components. The directly bound imidazole N3 quadrupole tensor (Q) components and directions are consistent with the rotational orientation of the imidazole ring found in the Mn^{2+} bound protein crystal structure. Reprinted from Dikanov et al. (1995) with permission. Copyright 1995 American Chemical Society.

Geometric and electronic features were the focus of Magliozzo and Peisach (1993) in their ESEEM investigation on the weak bond between proximal histidine-imidazole and low-spin heme-iron in ferric myoglobin (Mb). Differing exogenous ligands on the distal side were discovered to alter the couplings of the proximal histidine-imidazole nitrogen coordinated directly to iron. For MbCN (cyanometmyoglogin) and MbRS (metmyoglobin-metcaptoethanol) complexes, $e^2qQ = 2.2$ MHz, but increased to 3.2 MHz for MbN_3 (azidometmyoglobin). The isotropic hyperfine coupling (a_{iso}), on the other hand, was 4.4 MHz for MbN_3 but decreased to 2.2 MHz for both MbCN and MbRS. A decrease in the maximum nqi for directly coordinated imidazole nitrogen corresponds to a decrease in its lone pair electron occupancy in the sp^2 hybrid orbital, which means a stronger nitrogen-metal interaction. The hyperfine coupling in this system arises from spin polarization into the nitrogen-metal σ-bond and is therefore dependent on the amount of unpaired electron delocalized away from the metal. Possible reasons for a weaker hyperfine coupling of the proximal imidazole nitrogen in MbN_3 compared to MbCN and MbRS included a redistribution of spin density such that more delocalization from iron orbitals into the azide. In addition, the difference in e^2qQ for the various myoglobin derivatives was analyzed in the context of relative overlap between the unpaired electron orbital plane and the p-π orbital of the imidazole. A larger overlap causes a smaller nqi. This leads to the suggestion that the proximal

imidazole may act as a σ-acceptor in low-spin heme complexes in order to cause a strong π electron donation from the lone pair on the proximal imidazole nitrogen to iron.

An ESEEM study of oxycobalt-substituted human wild-type myoglobin (Figure 13a) and a series of distal mutants for the E7 (His64) residue were determined in order to probe the affect these changes have on the cobalt-nitrogen bond of the proximal histidine-imidazole, and in turn how these may be related to the affinity of the protein for oxygen (Lee et al., 1994). The presence of hydrogen bonding to the dioxygen ligand of $Co(II)\text{-}O_2$ was also inferred through the detection of modulations that reveal ^2H hyperfine couplings in some of the ESEEM patterns. Comparing ESEEM results for the wild type and four His64 mutants, a correlation was observed such that as the polarity of the mutated residue decreased, both the hyperfine and quadrupole ^{14}N couplings for the proximal imidazole increased. The FT-ESEEM of the wild type H64 (polar) compared to H64L (non-polar) mutant shown in Figure 13b clearly demonstrate the affect of residue polarity on the modulation frequency line positions, and with them, a change in nuclear couplings. For example, analysis of the two spectra shown provided proximal histidine ^{14}N parameters of $a_{iso} = 2.63$ MHz, $e^2qQ = 2.13$ MHz, $\eta = 0.37$ for the wild-type protein and by replacing His64 with leucine (H64L) these changed to $a_{iso} = 3.79$ MHz, $e^2qQ = 2.62$ MHz, $\eta = 0.59$. This trend was interpreted with an orbital model where a more polar E7 distal residue added stability to an ionic $Co(III)\text{-}O_2^{\bullet -}$ valence form of the complex. As a polar distal site or a hydrogen bond to the dioxygen stabilizes this ionic description, spin density is shifted towards the dioxygen moiety and away from the cobalt. A smaller unpaired density in the cobalt dz^2 orbital results in a weaker hyperfine coupling to the distal imidazole nitrogen. Additionally, more Co(III) ionic character in the $Co\text{-}O_2$ bond helps to explain the decrease in the quadrupole coupling, since an increased lone pair donation from the proximal imidazole nitrogen to cobalt is expected for a more positively charged metal. The trend shown by the axial nitrogen nuclear coupling opposes the H64 site polarity. Since polarity of the E7 residue was also found to positively affect oxygen affinity in oxyCoMb and parallels the oxygen affinity shown by polar mutants of iron-containing myoglobin, a connection between nuclear spectroscopic parameters and an important biological characteristic of myoglobin was uncovered by ESEEM.

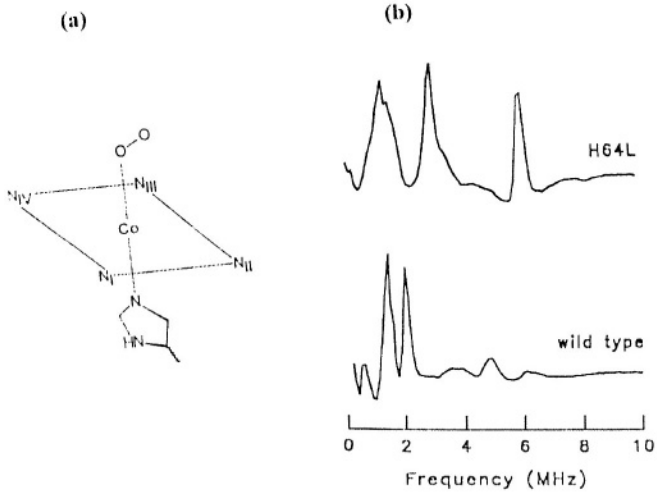

Figure 13. (a) Diagram of the O_2 binding site in Co substituted myoglobin. $N_{I\text{-}IV}$ refer to the heme nitrogens. The z-axis is defined perpendicular to the heme plane. The nuclear coupling parameters of the directly bound proximal histidine-imidazole ^{14}N, trans to bound O_2, are affected by interactions between the distal E7 His 64 residue (not shown) and the dioxygen moiety. (b) A comparison of the 3-pulse FT-ESEEM spectra for the H64L mutant and the wild-type protein showing the changes to the spectra afforded by the replacement of the E7 residue from the polar histidine in the native to a hydrophobic leucine in the mutant. Reproduced from Lee et al. (1994).

3.3 Couplings to Peptide Nitrogen

The first ESEEM report of electron-nuclear couplings to nitrogens other than imidazole was by LoBrutto et al (1986) on studies of reduced 2Fe-2S clusters in succinate dehydrogenase and in two ferrodoxins. Weak couplings had also been previously attributed to peptide nitrogens by ESEEM experiments on a series of 2Fe and 4Fe ferrodoxins (Peisach, 2003), and this type of interaction was later fully analyzed in similar studies on fumarate reductase (Cammack et al., 1988). Since then, a variety of similar metalloenzymes studied by EMR techniques have yielded weak couplings to nitrogens that have been assigned to the polypeptide backbone. A recent review on hyperfine interactions in 2Fe-2S proteins discusses ESEEM results from both plant ferrodoxins and Rieske 2Fe-2S clusters (Figure 14) (Cammack et al., 1999). In these systems, ESEEM-detected peptide ^{14}N hyperfine couplings ranged from 0.4 to about 1.2 MHz, reflecting the weak nature of these interactions. The unique feature that allows an assignment of these interactions to peptide nitrogens is the similarity of their nqi

parameters ($e^2qQ = 3.2$ MHz, $\eta = 0.5$) with those found for amide nitrogens using NQR. The exact mechanism of coupling is not known but two explanations appear viable. One is that the interaction occurs through a N-H···S hydrogen bond, which is inferred in plant ferrodoxins, based on X-ray crystal models of the peptide backbone to the bridging and terminal ligands in the 2Fe-2S cluster. Or that a weak coupling could arise from spin density finding its way to the amide nitrogen of the ligating cysteine residues (see Figure 14). In either case, the biological relevance of such weak couplings has not been established although recent evidence has indicated a correspondence between amide nitrogen contact couplings and the reduction potential of the iron-sulfur sites in native and mutated rubredoxins (Lin et al., 2003). In any case, these interactions indicate a path of communication between Fe-S sites and the rest of the protein, which may have bearing on processes of these enzymes involving electron transfer.

Molecular features of the copper binding site in prion protein (PrP) were investigated using a combination of EMR techniques that included X and S-band (~3.5GHz) EPR, X-band ESEEM and a 2-dimensional ESE technique developed by Höfer (1986) called Hyperfine Sublevel Correlation (HYSCORE) (Burns et al., 2002). Knowledge of the structural aspects of prion protein is biologically important because of the implication of the misfolded form of this copper-binding protein in the human neurological disorders as in Creutzfeldt-Jakob disease. The N-terminal region of the prion protein from humans and other species are distinguished by a region (residues 57-91) containing multi-repeated octa-sequences containing histidine and glycines (PHGGGWGQ), whose disposition lends itself to tight copper binding.

Comparing the magnitudes of $A_{\parallel}$ and $g_{\parallel}$ from X-band EPR measurements in a "Peisach and Blumberg analysis" (Peisach and Blumberg, 1974) suggested a 3N1O equatorial coordination to Cu^{2+}. Further evidence of this coordination was achieved by S-band studies, where the superhyperfine pattern clearly showed that three nitrogens are bound, one of these from imidazole, as shown by the ESEEM for the remote ^{14}N of the bound ligand. Comparison with the Cu^{2+} complex of HGGGW shows indistinguishable spectra from that of the Cu^{2+} complex of the N-terminal region of the protein. From an S-band study of Cu^{2+} HGGGW prepared with specifically labelled ^{15}N glycine, it is concluded that Gly1 and Gly2 are bound to copper. The ^{14}N of Gly3, although not directly bound to Cu^{2+}, makes a spectral contribution observed in the ESEEM, which can no longer be seen when Gly3 is prepared with ^{15}N. This finding suggests that the oxygen equatorially bound to Cu^{2+} is peptidic. The structure derived by EMR for the peptide model was confirmed by X-ray diffraction.

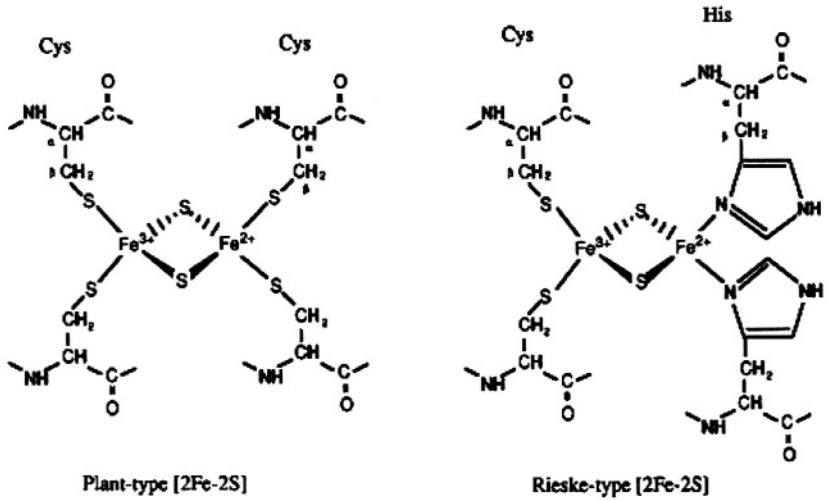

Figure 14. Covalent structures of plant ferrodoxins and Rieske iron-sulfur clusters showing bound cysteine residues. Weak ^{14}N couplings observed by EMR methods have been attributed to either peptide nitrogens of the bound cysteines or peptide nitrogens involved in hydrogen bonding interactions with sulfurs of the cluster (not shown). Reprinted from Cammack et al. (1999) with permission from Elsevier.

Comparative FT-ESEEM spectra in HGG^{14}NGW and HGG^{15}NGW as depicted in Figure 15 proved that the modulation pattern is a composite of couplings from the remote imidazole nitrogen and the amide nitrogen of the third glycine. This substitution was used to disentangle the $^{14}N/^{15}N$-peptidyl coupling contribution to the HYSCORE spectra and led to a ^{14}N hyperflne coupling (a_{iso} = 1.41 MHz). The FT-ESEEM spectra of HGGGW was subsequently used to derive the remote peptide nitrogen nqi parameters (e^2qQ = 3.2 MHz, η = 0.5). FT-ESEEM of the full octa-repeat and the N-terminal region were identical and thus provided important evidence used to confirm identical coordination for bound copper in HGGGW, PHGGGWGQ and the N-terminal region, which in turn has led to a postulation concerning the pH dependent modulation of copper binding to PrP.

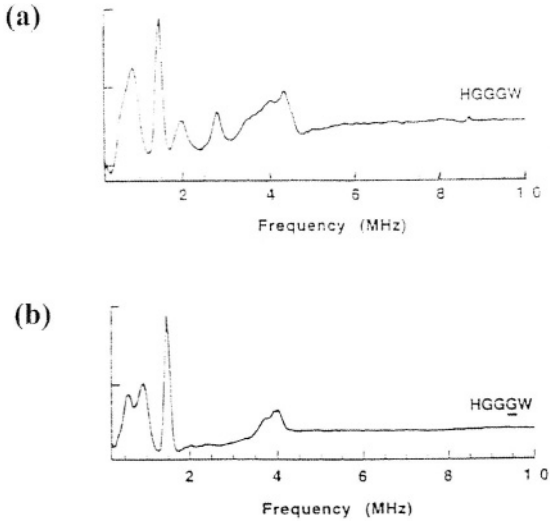

Figure 15. Comparison of 3-pulse FT-ESEEM spectra for copper bound to (a) HGGGW and (b) HGGGW with ^{15}N substitution at G3. The frequency lines in (b) arise from the remote nitrogen of the coordinated histidine-imidazole. The extra lines in (a) that are absent in (b) therefore arise from the remote peptide nitrogen of G3, which coordinates to Cu^{2+} through its carboxyl oxygen. Reproduced from Burns et al. (2002).

3.4 Couplings to Side Chain Nitrogen (non-imidazole)

The positions of peptide side chain nitrogens near paramagnetic centers have lead to insight into the workings and related structural changes that occur at an active site. For example, ESEEM studies using $V{=}O^{2+}$ as a surrogate for a divalent ion cofactor in adenosyl methionine synthetase demonstrated that nitrogen couplings arise from direct coordination of lysine Nε in the enzyme-substrate, E ·VO^{2+} ·ATP ·Methionine ·K^+ (a_{iso} = 4.3 MHz, e^2qQ = 3.7 MHz, η = 0.3) and the enzyme-intermediate E ·VO2+ ·AdenosylMethionine ·PPP_i ·K^+ (a_{iso} = 4.8 MHz, e^2qQ = 2.9 MHz, η = 0.4) (Zhang et al., 1993). These assignments were verified by the disappearance of the ^{14}N modulation frequency lines when the protein was either fully ^{15}N labelled or selectively ^{15}N labelled at the Nε of all the lysine residues. The hyperfine couplings are in the range normally observed for nitrogens coordinated equatorially to vanadyl. In the subsequent product complex, E ·VO^{2+} ·AdenosylMethionine ·K^+, the use of ^{15}Nε-adenosylmethionine showed that lysine modulation frequencies are replaced by those from the Nε nitrogen of methionine. Couplings to this nitrogen (a_{iso} = 5.3 MHz, e^2qQ = 2.9 MHz, η = 0.4) display a slightly higher hyperfine interaction. In conjunction with other studies, these results inferred a possible scheme for

metal coordination changes whereby a switch of ligand from lysine to methionine upon substrate binding and loss of PP_i, respectively, occurs, during the course of the reaction.

ESEEM analysis on and a series of mutations at residues that surround the S=3/2 iron-molybdate-sulfur cluster in FeMo nitrogenase were performed to determine the origin of a weak coupling interactions. labelled as N1 and N2 (Lee et al., 1998, DeRose et al., 1995). The major interaction evident in the ESEEM of the native enzyme had been previously assigned to the histidine-imidazole nitrogen of α-195-histidine (Thomann et al., 1991). A later X-ray determined structure of this protein (Kim and Rees, 1992) (Figure 16a) revealed six candidates for these couplings, either via hydrogen bonding or through a covalent bond with the cluster (DeRose et al., 1995). Various mutants were enlisted to assign possible sources of nitrogen couplings by the process of elimination but these were also of interest because of the possibility of correlating differences in activity with their perturbations on the metal cluster structure as reflected in change of coupling. Because of high anisotropy in g and nitrogen coupling tensors, a field-selected 2-dimensional ESEEM analysis was employed to extract accurate parameters. The success of this approach is evident from the excellent comparison between experimental and simulated FT-ESEEM patterns as a function of g-value (field) based on final parameters (a_{iso} = 1.05 MHz, e^2qQ = 2.17 MHz, η = 0.59) as reproduced in Figure 16b. Substitutions of residues α-96-arginine, α-195-histidine and α-359-arginine could all eliminate the ESE modulations from the stronger coupling, denoted as N1. However, the replacement of α-195-histidine with glutamine and of α-96-arginine with either glutamine or lysine retained the N1 pattern in the ESEEM. The possibility that His442, covalently bound to Mo, was responsible for N1 was discounted based on the unlikely situation that mutations at either α-96-arginine, α-195-histidine or α-359-arginine cause the Mo-His442 bond to break, leading to loss of the N1 modulations. In addition, Mo in the complex has been suggested to exist in a diamagnetic state, which greatly reduces the possibility for a His442 coupling interaction. The terminal nitrogen of α-359-arginine, through hydrogen bonding to the S2B sulfur of the complex, was therefore concluded to be the origin of the weak nitrogen coupling-observed in the native enzyme. However, a recently reported high resolution crystal structure of this FeMo nitrogenase gave a surprising result; that a light atom, possibly a nitrogen, was located inside the cofactor, at the center of the cluster, and equidistant from the six "trigonal prismatic" irons and sulphurs (Einsle et al., 2002). A subsequent ESEEM and ENDOR study using ^{14}N and ^{15}N-enriched N_2 showed that this uncovered atom is not an exchangeable nitrogen from enzymatic turnover, which raises the possibility that one of the previously reported nitrogenous

couplings could be from this very interesting, interstitial atom (Lee at al., 2003).

3.5 Nitrogen Couplings from an Intermediate or Substrate

Direct biochemical information can be obtained by measuring the interaction between a metal and a distant nitrogen nucleus in ESEEM studies involving intermediate states or substrate binding. For example, in a study of ethanolamine deaminase, a vitamin B12 dependent enzyme, nitrogen couplings to Cob(II)alamin in the poised Cobalt(II)-radical intermediate state were detected and analyzed using ESEEM spectroscopy (Ke et al., 1999).

Comparison of FT-ESEEM spectra of the enzyme and an activated Cob(II)alamin-dimethylbenzimide model system coupled with theoretical calculations of nqi parameters suggest that part of the observed ESEEM patterns arise from couplings to the remote nitrogen (N1) of axially bound dimethybenzimide (Figure 17). The directly bound N2 possesses too large a coupling to be observed in the ESEEM. This is consistent with measurements on models where couplings to this nitrogen can be resolved in the EPR spectra. In addition, the similarity of patterns found in the model and protein allowed other lines in the FT-ESEEM to be assigned to couplings from nitrogens in the corrin ring. It was thus concluded that the intermediate state in ethanolamine deaminase is a pentacoordinate Co(II), with an intact α-axial, dimethylimidazole ligand.

Obtained coupling parameters for the N1 nitrogen in enzyme bound Cob(II)alamin (a_{iso} = 2.15 MHz, e^2qQ = 3.2, η = 0.12) showed a modest increase (14%) in hyperfine coupling compared to that found in the model system. This was interpreted to mean that there is an enhanced delocalization of spin density from Co(II) onto the axial ligand in the enzyme.

ESEEM also allowed estimates of spin density delocalized on the tryptophan tryptophyl-semiquinone (TTQ) catalytic intermediate in methylamine dehydrogenase (Singh et al., 2000). Using ^{15}N isotopic substitution of the methylamine substrate, Singh et al. were able to assign the FT-ESEEM frequency lines arising from bound substrate and the tryptophan tryptophyl-semiquinone cofactor. Subsequent analysis of the ^{14}N ESEEM patterns resulted in coupling parameters for nitrogens of the methylamine (a_{iso} = 2.4 MHz, e^2qQ= 1.7 MHz, η = 0.5) and the heteroatoms of TTQ (N1; a_{iso} = MHz, e^2qQ= 3.0 MHz, η = 0.3, N2; a_{iso} = 1.9 MHz, e^2qQ= 2.1 MHz, η = 0.7). Methylamine nitrogen hyperfine parameters were comparable to those for the TTQ nitrogens and the small nqi, along with previous ENDOR and ESEEM results on amine oxidase (Warncke et al., 1994), provided definitive evidence for covalent substrate binding to the TTQ in an imine-

like state (N-form). Using these findings and results from earlier pulsed-EPR work (Warncke et al., 1993), the catalytic pathway proposed for this enzyme is shown in Figure 18. In addition, substrate bound TTQ produced ring nitrogen couplings significantly different than found by chemical reduction using dithionite. This indicates a change in the electronic structure of the intermediate in the substrate bound N-form of TTQ which may be related to electron transfer properties of the site.

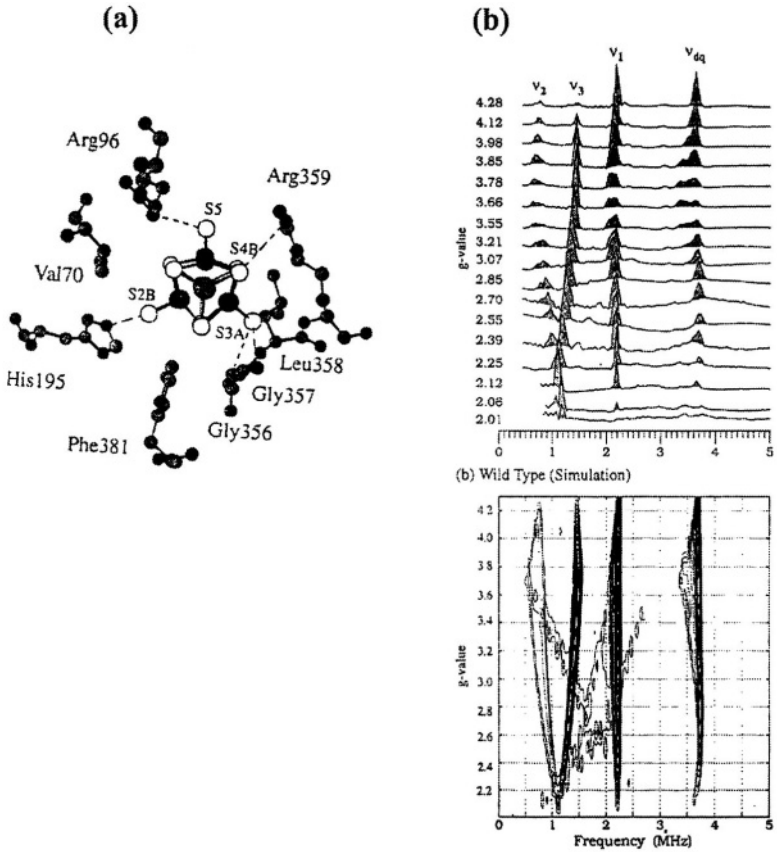

Figure 16. (a) Diagram of the FeMo site in FeMo nitrogenase. The origin of the N1 coupling in the FT-ESEEM spectra is assigned to the Arg359 side chain nitrogen that hydrogen bonds to the S4B sulfur atom. This assignment was based on changes in the ESEEM patterns and enzymatic activity induced by mutations at various residues that surround the FeMo cluster. (b) Two-dimensional plot of 3-pulse FT-ESEEM spectra as a function of g-value obtained from (upper) FeMo nitrogenase and (lower) simulations based on parameters reported in the text. The coupling producing these frequency lines has been designated as N1. Reprinted from Lee et al. (1998) with permission. Copyright 1998 American Chemical Society.

4. CONCLUDING THOUGHTS

Since its earliest application, the ESEEM technique has demonstrated its unique ability to analyze weakly coupled nuclei in proteins possessing a paramagnetic center. Study of these subtle couplings, invisible in almost all other EMR techniques, gives important information on metal ligands, substrate binding, intermediate states and structural changes, all of which lead to an increased knowledge on the function of this important class of biomolecules. The wide array of nitrogens that exist in enzyme systems represents a large opportunity for the use of ESEEM as a primary or complementary tool for the study of metalloproteins. ESEEM will continue therefore to have an increased presence as an important component among many EMR techniques used in modern approaches to the study of metalloproteins.

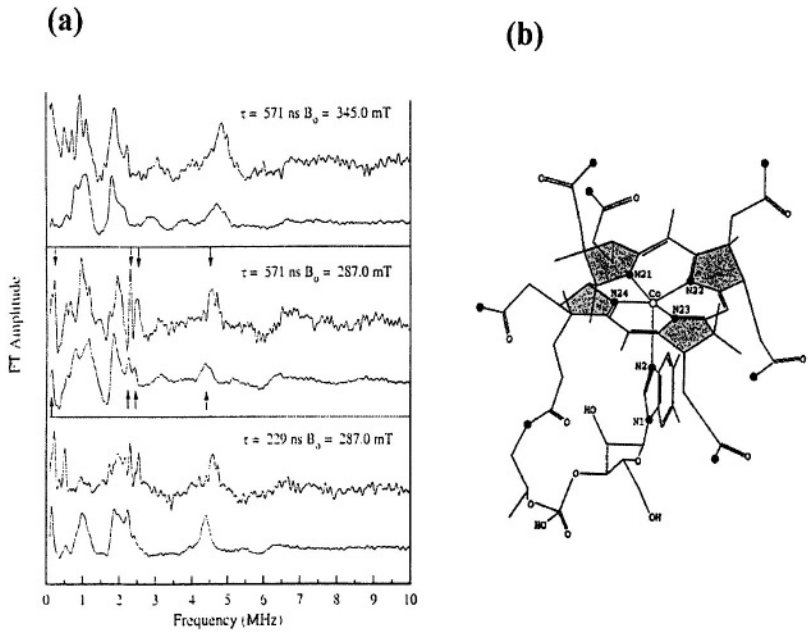

Figure 17. (a) 3-pulse FT-ESEEM spectra for cob(II)alamin in the (upper in each panel) poised cobalt(II)-radical intermediate state in ethanolamine deaminase and in the (lower in each panel) model free base-on form in glycerol-water glass. Arrows designate frequency lines identified with the remote nitrogen (N1) coupling of the axial dimethylimidazole ligand. The spectra were obtained at the indicated τ and magnetic field settings. (b) Structure of cob(II)alamin depicting the positions of the corrin ring and dimethylimidazole axial ligand. Couplings from ^{14}N from N21-N24 of the corrin ring also contribute to the modulation frequency pattern in the FT-ESEEM. Reprinted from Ke et al. (1999) with permission. Copyright 1999 American Chemical Society.

Advancement in the method is due to the great technological improvements over the years. These have resulted in the advent of multi-pulse ESE (e.g., 4-pulse from Gemberle et al., 1990), HYSCORE (Höfer et al., 1986), nuclear Zeeman-resolved ESEEM (Willer et al., 1998) and the biological applications of high-field (Coremans et al., 1997) and low-field (Dikanov et al., 1995) resonance that can shift sensitivity of ESEEM to higher and lower nuclear hyperfine interactions and to other types of nuclei. Add these to the greater array of computational advances that allow a time-practical evaluation and analysis of the above as well as field and frequency dependencies of spectral lines, all of which result in the unravelling of accurate nuclear coupling parameters from increasingly complex patterns.

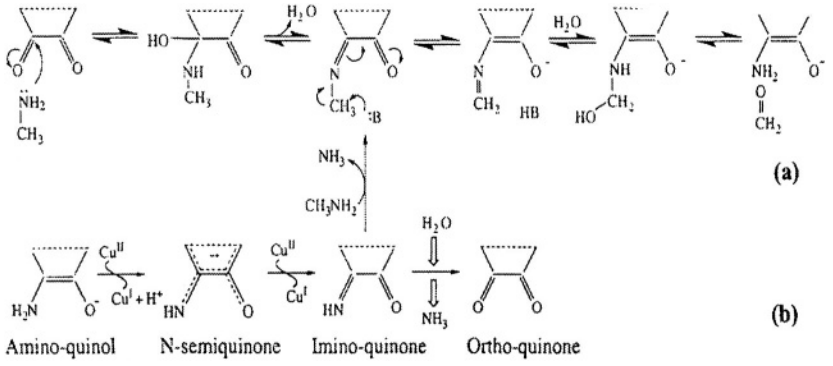

Figure 18. Postulated reaction mechanism for methylamine dehydrogenase separated in (a) reductive and (b) oxidative steps. ESEEM observations confirm the imino form of the methylamine-TTQ intermediate in this reaction by detecting and analyzing the ^{14}N couplings from nitrogens in covalently bound methylamine and in the TTQ rings (not shown completely in figure). Reprinted from Singh et al. (2000) with permission. Copyright 2000 American Chemical Society.

The weak interactions from remote nitrogen nuclei summarized in Table 1 provide information on structural aspects of metal sites, alterations caused by mutations, substrate and cofactor binding and important electronic characteristics at the outer limits of the active site. Some of these have been shown to have relation to the biological activity in proteins. In others, the relevance of such small and distant interactions has been difficult to assess. The experimental interpretation of these results once depended solely on model systems but has since evolved into more powerful approaches employing mutant proteins and isotopic substitutions, in particular to residues, substrates, products or intermediates. Both hyperfine and nqi coupling parameters remain complementary and, taken together, are used to

identify and probe the unpaired spin and local electronic environments at the coupled nitrogen. Influences from nearby substitutions or hydrogen bonding have been shown to significantly change the nqi parameters but these affects have not been fully characterized for all types of nitrogens. An understanding of these factors will undoubtedly increase as more studies are completed. In the meantime, the use of theoretically calculated nqi parameters has been necessary to guide some conclusions.

Table 1. Representative ^{14}N couplings in proteins, analyzed by ESEEM.

Nitrogen/ Protein	Paramagnetic Center	Coupling Constants (MHz) a_{iso}	e^2qQ	η	Ref.
Histidine-Imidazole Remote ^{14}N					
Stellacyanin	Type 1 Cu(II)	1.5	1.50	0.9	(a)
		2.0	1.45	0.9	
Dopamine β-Hydroxylase	Type 2 Cu(II)	1.3-1.8	1.44	0.98	(b)
Galactose Oxidase	Type 2 Cu(II)	1.8	1.7	0.65	(c)
Amine Oxidase	Type 2 Cu(II)	2.3	1.7	0.5	(d)
		1.8	1.43	0.91	
Ascorbate Oxidase	Type 1 Cu(II)	0.76	1.45	0.95	(e)
		1.27	1.45	0.95	
Laccase	Type 2 Cu(II)	1.55	1.55	0.82	(e)
Cu^{+2}-Insulin	Type 2 Cu(II)	1.33	1.54	0.90	(f)
Cu^{+2}-Insulin + Cd^{2+}-acetate	Type 2 Cu(II)	1.86	1.67	0.77	(f)
		1.86	1.76	0.55	
Histidine-Imidazole Directly - Coordinated ^{14}N					
Azurin W-band	Type 1 Cu(II)	18.1	2.9	0.5	(g)
		23.6	2.5	0.6	
Xylose Isomerase	V=O	5.7	≈2.0	<0.5	(h)
Myoglobin MbN_3	Low spin heme	4.4	3.2	0.1	(i)
Myoglobin MbCN	Low spin heme	2.2	2.5	0.3	
Myoglobin MbRS	Low spin heme	2.2	2.5	0.3	
OxyCo Myoglobin					
H64	Co-O-O	2.62	2.13	0.45	(j)
H64L	Co-O-O	3.79	2.62	0.59	

Nitrogen/ Protein	Paramagnetic Center	Coupling Constants (MHz) a_{iso}	e^2qQ	η	Ref.
Peptide ^{14}N					
[2Fe-2S] proteins	2Fe-2S	0.6-1.1	≈3.2	≈0.5	(k)
Prion	Cu(II)	1.41	3.20	0.50	(l)
^{14}N of Side Chain					
S-Adenosyl-	V=O				
Methionine	(Lysine)	4.3	3.7	0.3	(m)
Synthetase	(Lysine)	4.8	2.9	0.4	
	(AdoMet)	5.3	3.0	0.3	
MoFe Nitrogenase	MoFe (Arginine)	1.05	2.17	0.59	(n)
^{14}N in Substrate or Intermediate					
Ethanol Deaminase	Cob(II)alamin- (N1) Dimethyl- Benzimidazole	2.15	3.20	0.12	(o)
Methylamine	Tryptophyl- (N1)	2.8	3.0	0.3	(p)
Dehydrogenase	Semiquinone (N2)	1.9	2.1	0.7	
	Methylamine	2.4	1.7	0.5	

(a) Bender and Peisach (1998), (b) McCracken et al. (1988), (c) Kosman et al. (1980), (d) Jiang et al. (1990), McCracken et al. (1988), (e) Goldfarb et al. (1992), (f) Colaneri et al. (2000), (g) Coremans et al. (1997), (h) Dikanov et al. (1995), (i) Magliozzo and Peisach (1993), (j) Lee et al. (1994), (k) Cammack et al. (1999), (l) Burns et al. (2002), (m) Zhang et al. (1993), (n) Lee et al. (1998), (o) Ke et al. (1999), (p) Singh et al. (2000).

In summary, the future concerning application of ESEEM techniques to biochemical questions looks bright. The information obtained by this technique cannot be obtained easily by other methods and leads to a more complete and detailed understanding of coordination chemistry and unpaired electron distribution in many important biological systems. Recent employment of multi-pulse, multi-dimensional and multi-field ESEEM techniques will, at the very least, extend our knowledge of the bonding characteristics about paramagnetic sites in a wider variety of proteins, leading to unique insight into how they operate.

ACKNOWLEGEMENTS

We acknowledge grant NIH GM-40168 (to J.P.) and a Cottrell College Science Award (CC4518) from Research Corporation (to M.J.C.). We also thank Dr. Jacqueline Vitali for helpful discussions.

5. REFERENCES

Ashby, C.I.H., Cheng, C.P., and Brown, T.L. (1978) ^{14}N Nuclear Quadrupole Resonance Spectra of Coordinated Imidazole. *J. Amer. Chem. Soc.* **100**, 6057-6063.

Avigliano, L., Davis, J.L., Graziani, M.T., Marchesini Cherries, A., Mims, W.B., Mondovi, B., and Peisach, J. (1981) Electron Spin Echo Spectroscopic Studies of Type 1 and Type 2 Copper in *Rhus Vernicifera* and in *Cucurbita Pepo Medullosa* Ascorbate Oxidase. *FEBS Letters* **136**, 80-84.

Baker, E.N., Blundell, F.R.S., T.L, Cutfield, J.F., Cutfield, S.M., Dodson, E.J., Dodson, G.G., Hodgkin, F.R.S., D.M.C., Hubbard, R.E., Issacs, N.W., Reynolds, C.D., Sakabe, K., Sakabe N., and Vijayan N.M. (1988) The Structure of 2Zn Pig Insulin Crystals at 1.5Å Resolution. *Philos. Trans. R. Soc. London* **B319**, 369-456.

Baker, E.N. (1988) Structure of Azurin from *Alicaligenes denitrificans. J. Mol. Biol.* **203**, 1071-1095.

Bender, C.J. and Peisach, J. (1998) Electron Spin-Echo Modulation Spectroscopic Study Of The Type I Copper Center Associated With Stellacyanin from *Rhus vernicifera. J. Chem. Soc. Faraday Trans.* **94**, 375-386.

Blumberg, W.E., Mims, W.B., and Zuckerman, D. (1973) Electron Spin Echo Envelope Spectrometry. *Rev. Sci. Instruments 44,* 546-554.

Brill, A.S. and Venable, Jr., J.H. (1968) The Binding of Transition Metal Ions in Insulin Crystals. *J. Mol. Biol.* **36**, 343-353.

Brill, A.S. and Venable, Jr., J.H. (1972) Water Co-ordination in Insulin. *J. Mol. Biol.* **66**, 169-180.

Burns, C.S., Aronoff-Spencer, E., Dunham, C.M., Lario, P., Avdievich, N.I., Antholine, W.E., Olmstead, M..M., Vrielink, A., Gerfen, G.J., Peisach, J., Scott, W.G., and Millhauser, G.L. (2002) Molecular Features of the Copper Binding Sites in the Octarepeat Domain of the Prion Protein. *Biochemistry* **41**, 3991-4001.

Cammack, R., Chapman, A., McCracken, J., Cornelius, J.B., Peisach, J., and Weiner, J.H. (1988) Electron Spin-Echo Spectroscopic Studies Of *Eschericia Coli* Fumarate Reductase. *Biochim.et Biophys. Acta* **956**, 307-312.

Cammack, R., Gay, E., and Shergill, J.K. (1999) Studies Of Hyperfine Interactions In [2Fe-2S] Proteins By EPR And Double Resonance Spectroscopy. *Coordination Chemistry Reviews,* **190-192,** 1003-1022.

Carrington, A. and McLachlan, A.D. (1967) Chapter 7, *Introduction to Magnetic Resonance,* Harper and Row, New York.

Colaneri, M.J. and Peisach, J. (1992) An Electron Spin-Echo Envelope Modulation Study of Cu(II)-Doped Single Crystals of L-Histidine Hydrochloride Monohydrate. *J. Amer. Chem. Soc.* **114**, 5335-5341.

Colaneri, M.J. and Peisach, J. (1995) A Single Crystal EPR and ESEEM Analysis of Cu(II)-Doped Bis(L-histidinato)cadmium Dihydrate. *J. Amer. Chem. Soc.* **117**, 6308-6315.

Colaneri, M.J., Vitali, J., and Peisach, J. (2000) Electron Spin-Echo Envelope Modulation Study of Multicrystalline Cu^{2+}-Insulin: Effects of Cd^{2+} on the Nuclear Quadrupole Interaction of the Cu^{2+}-Coordinated Imidazole Remote Nitrogen. *Biochemistry* **39**, 584-591.

Coremans, J.W.A., Poluektov, O.G., Groenen, E.J.J., Canters, G.W., Nar, H., and Messerschmidt, A. (1996) A W-band Electron Nuclear Double Resonance Study of Single Crystals of ^{14}N and ^{15}N Azurin. *J. Amer. Chem. Soc.* **118**, 12141-12153.

Coremans, J.W.A., Poluektov, O.G., Groenen, E.J.J., Canters, G.W., Nar, H., and Messerschmidt, A. (1997) A W-band Electron Spin Echo Envelope Modulation Study of a Single Crystal of Azurin.. *J. Amer. Chem. Soc.* **119**, 4726-4731.

Cornelius, J.B., McCracken, J., Clarkson, R.B., Belford, R.L., and Peisach, J. (1990) Electron Spin Echo Envelope Modulation Angle Selection Studies of Axial Pyridine Coordination to Copper(II) Benzoylacetonate. *J. Phys. Chem.* **94**, 6977-6982.

Debus, R.J., Campbell, K.A, Gregor, W., Li, Z.L., Burnap, R.L., and Britt, R.D. (2001) Does histidine 332 of the D1 polypeptide ligate the manganese cluster in photosystem II? An electron spin echo envelope modulation study. *Biochemistry* **40**, 3690-3699.

Deligiannakis, Y., Louloudi, M., and Hadjiliadis, N. (2000) Electron Spin Echo Envelope Modulation (ESEEM) Spectroscopy As A Tool To Investigate The Coordination Environment Of Metal Centers. *Coordination Chemistry Reviews,* **204**, 1-112.

DeRose, V.J., Kim, C.H., Newton, W.E., Dean, D.R., and Hoffman, B.M. (1995) Electron Spin Echo Envelope Modulation Spectroscopic Analysis of Altered Nitrogenase MoFe Proteins from *Azotobacter vinelandii. Biochemistry* **34**, 2809-2814.

Dikanov, S.A, and Tsvetkov, Y.D. eds., (1992) *Electron Spin Echo Envelope Modulation (ESEEM) Spectroscopy,* CRC Press, Boca Raton, Florida.

Dikanov, S.A., Felli, I., Viezzoli, M-S., Spoyalov, A., and Hüttermann, J. (1994) X-Band ESEEM Spectroscopy Of ^{15}N Substituted Native And Inhibitor-Bound Superoxide Dismutase. *FEBS Letters* **345**, 55-60.

Dikanov, S.A., Tyryshkin, A.M., Hüttermann, J., Bogumil, R., and Witzel, H. (1995) Characterization of Histidine Coordination in VO^{2+}-Substituted D-Xylose Isomerase by Orientationally-Selected Electron Spin-Echo Envelope Modulation Spectroscopy. *J. Amer. Chem. Soc.* **117**, 4976-4986

Dikanov, S.A., Tyryshkin, A.M., Felli, I., Reijerse, E.J., and Hüttermann, J. (1995) C-band ESEEM of Strongly Coupled Peptide Nitrogens in Reduced Two-Iron Ferredoxin. *J. Magn. Res.* **B108**, 99-102.

Eaton, S.S., Dubach, J., More, K.M., Eaton, G.R., Thurman, G., and Ambruso, D.R. (1989) Comparison of the Electron Spin Echo Envelope Modulation (ESEEM) for Human Lactoferrin and Transferrin Complexes of Copper(II) and Vanadyl Ion. *J. Biol. Chem.* **264**, 4776-4781.

Eaton, S.S., Dubach, J., Thurman, G., and Ambruso, D.R. (1990) Electron Spin Echo Envelope Modulation (ESEEM) Evidence for Carbonate Binding to Iron(III) and Copper(II) Transferrin and Lactoferrin. *J. Biol. Chem.* **265**, 7138-7141.

Einsle O., Tezcan F.A., Andrade S.L., Schmid B., Yoshida M., Howard J.B., and Rees D.C. Nitrogenase Mofe-Protein At 1.16 Å Resolution: A Central Ligand In The Femo-Cofactor. (2002) *Science* **297**, 1696-1700.

Gemberle, C., Aebli, G., Schweiger, A., and Ernst, R.R. (1990) Phase Cycling in pulse EPR. *J. Magn. Res.* **88**, 241-244.

Goldfarb, D., Fauth, J.-M., Farver, O., and Pecht, I. (1992) Orientation Selective ESEEM Studies on the Blue Oxidases Laccase and Ascorbate Oxidase. *Appl.Magn.Reson.* **3**, 333-343.

Hart, P.J., Nersissian, A.M., Herrmann, R.G., Nalbandyan, R.M., Valentine, J.S., and Eisenberg, D. (1996) A Missing Link In Cupredoxins: Crystal Structure Of Cucumber Stellacyanin At 1.6 Å Resolution. *Protein Sci.* **5**, 2175-2183.

Hill, C.P., Dauter, Z., Dodson, E.J., Dodson, G.G., and Dunn, M.F. (1991) X-Ray Structure Of An Unusual Ca^{2+} Site And The Roles Of Zn^{2+} And Ca^{2+} In The Assembly, Stability, And Storage Of The Insulin Hexamer. *Biochemistry* **30**, 917-924.

Höfer, P, Grupp, A., Nebenfuehr, H., and Mehring, M. Hyperfine Sublevel Correlation (HYSCORE) Spectroscopy, a 2D ESR investigation of the squaric acid radical. (1986) *Chem. Phys. Lett.* **132**, 279-286.

Hunt, M.J., Mackay, A.L., and Edmonds, D.T. (1975) Nuclear Quadrupole Resonance of ^{14}N in Imidazole and Related Compounds. *Chem. Phys. Lett.* **34**, 473-475.

Jiang, F., McCracken, J., and Peisach, J. (1990) Nuclear Quadrupole Interactions in Copper(II)-Diethylenetriamine-Substituted Imidazole Complexes and in Copper(II) Proteins. *J. Amer. Chem. Soc.* **112**, 9035-9044.

Ke, M. Torrent, D.G. Museav, K. Morokuma and K. Warncke (1999) Identification of Dimethylbenzimidazole Axial Coordination and Characterization of ^{14}N Superhyperfine and Nuclear Quadrupole Coupling in Cob(II)alamin Bound to Ethanolamine Deaminase in a Catalytically-Engaged Substrate Radical-Cobalt(II) Biradical Site. *Biochemistry* **38**, 12681-12689.

Kevan, L. (1979) Modulation of Electron Spin-Echo Decay in Solids., Chapter 8 in Kevan, L. and Schwartz, R.N., eds., *Time Domain Electron Spin Resonance,* Wiley, New York.

Kim, J. and Rees, D.C. (1992) Crystallographic Structure And Functional Implications Of The Nitrogenase Molybdenum-Iron Protein From Azotobacter Vinelandii. *Nature* **360**, 553-560.

Kosman, D.J., Peisach, J., and Mims, W.B. (1980) Pulsed Electron Paramagnetic Resonance Studies of the Copper(II) Site in Galactose Oxidase. *Biochemistry* **19**, 1304-1308.

Lee, H-I., Thrasher, K.S., Dean, D.R., Newton, W.E., and Hoffman, B.M. ^{14}N Electron Spin-Echo Envelope Modulation of the S=3/2 Spin System of the *Azotobacter vinelendii* Nitrogenase Iron-Molybdenum Cofactor. (1998) *Biochemistry* **37**, 13370-13378.

Lee, H-I., Benton, P.M.C., Laryukhin, M. Igarashi, R.Y., Dean, D.R., Seefeldt, L.C., and Hoffman, B.M. The Interstitial Atom of the Nitrogenase FeMo-Cofactor: ENDOR and ESEEM Show It Is Not an Exchangeable Nitrogen. (2003) *J. Am. Chem. Soc.* **125**, 5604 - 5605.

Lee, H.C., Ikeda-Saito, M., Yonetani, T., Magliozzo, R.S., and Peisach, J. (1994) Hydrogen Bonding to the Bound Dioxygen in Oxy Cobaltous Myoglobin Reduces the Superhyperfine Coupling to the Proximal Histidine. *Biochemistry* **31**, 7274-7281.

Lee, H.C., Peisach, J., Dou, Y., and Ikeda-Saito, M. (1994) Electron-Nuclear Coupling to the Proximal Histidine in Oxy Cobalt-Substituted Distal Histidine Mutants of Human Myoglobin. *Biochemistry* **33**, 7609-7618, 12000.

Lin, I-J., Gebel, E.B., Machonkin, T.E., Westler, W.M., and Markley, J.L. (2003) Correlation between Hydrogen Bond Lengths and Reduction Potentials in *Clostridium pasteurianum* Rubredoxin. *J. Amer. Chem. Soc.* **125**, 1464-1465.

LoBrutto, R., Haley, P.E., Yu, C.-A,, Ohnishi, I., and Leigh, J.S. (1986) EPR and Electron Spin Echo Studies of Iron-Sulfur Clusters S-1 and S-2 in Beef Heart Succinate Dehydrogenase. *Biophysical Journal* **40**, 327a.

Lucken, E.A.C. (1969) *Nuclear Quadrupole Coupling Constants,* Academic Press, New York., pp.217-248.

Magliozzo, R.S. and Peisach, J. (1993) Evaluation of Nitrogen Nuclear Hyperfine and Quadrupole Coupling Parameters for the Proximal Imidazole in Myoglobin-Azide, -

Cyanide, and –Mecaptoethanol Complexes by Electron Spin Echo Envelope Modulation Spectroscopy. *Biochemistry* **32**, 8446-8456.

Messerschmidt, A., Rossi, A., Ladenstein, R., Huber, R., Bolognesi, M., Gatti, G., Marchesini, A., Petruzzelli, R., and Finazzi-Agro, A. (1989) X-ray Crystal Structure of the Blue Oxidase Ascorbate Oxidase from Zucchini. *J. Mol. Biol.* **206**, 513-529.

McCracken, J., Desai, P.R., Papadopoulos, N.J., Villafranca, J.J., and Peisach, J. (1988) Electron Spin-Echo Studies Of The Copper(II) Binding Sites In Dopamine B-Hydroxylase. *Biochemistry* **27**, 4133-4137.

McCracken, J., Peisach, J., and Dooley, D.M. (1987) Cu(II) Coordination Chemistry of Amine Oxidases: Pulsed EPR Studies of Histidine Imidazole, Water, and Exogenous Ligand Coordination. *J. Amer. Chem. Soc.* **109**, 4064-4072.

Merks, R.P.J. and de Beer, R. (1980) Fourier Transform of the ^{133}Cs Modulation of the Electron Spin-echo Envelope of $Cs_2ZnCl_4:Cu^{2+}$. *J. Mag. Res.* **37**, 305-319.

Mims, W.B. (1972) Electron Spin Echoes, Chapter 4 in Geschwind, S., ed., *Electron Paramagnetic Resonance,* Plenum Press, New York.

Mims, W.B. (1972a) Envelope Modulation in Spin-Echo Experiments. *Phys. Rev.* **B5**, 2409-2418.

Mims, W.B. (1972b) Amplitudes of Superhyperfine Frequencies Displayed in the Electron-Spin-Echo Envelope. *Phys. Rev.* **B6**, 3543-3545.

Mims, W.B. and Peisach, J. (1976) Assignment of a Ligand in Stellacyanin by a Pulsed Electron Paramagnetic Resonance Method. *Biochemistry* **15**, 3863-3869.

Mims, W.B. and Peisach, J. (1978) The Nuclear Modulation Effect In Electron Spin Echoes For Complexes Of Cu^{2+} And Imidazole With ^{14}N And ^{15}N. *J. Chem. Phys.* **69**, 4921-4930.

Mims, W.B. and Peisach, J. (1979) Measurement of ^{14}N Superhyperfine Frequencies in Stellacyanin by an Electron Spin Echo Method. *J. Biol. Chem.* **254**, 4321-4323.

Mims, W.B., Davis, J.L., and Peisach, J. (1984) The Accessibility of Type I Cu(II) Centers in Laccase, Azurin, and Stellacyanin to Exchangeable Hydrogen and Ambient Water. *Biophys. J.* **45**, 755-766.

Mims, W.B. and Peisach, J. (1981) Electron Spin Echo Spectroscopy And The Study Of Metalloproteins, 213-263 In Berliner, L.J., Reuben, J., eds., *Biological Magnetic Resonance,* Plenum Press, New York.

Peisach, J. and Blumberg, W.E. (1974) Structural Implications Derived from the Analysis of Electron Paramagnetic Resonance Spectra of Natural and Artificial Copper Proteins. *Arch. Biochem. Biophys.* **165**, 691-708.

Peisach, J. (1995) ESEEM Spectroscopy – Probing Active Site Structures Of Metalloproteins. In Oliva-Nishiguchi, H., Packer, L., eds., *Bioradicals Detected by ESR Spectroscopy,* Birkhauser Verlag, Basil, Switzerland.

Peisach, J. (2003) An Appreciation of William H. Orme-Johnson III. *J. Inorg. Biochem.* **93.** 6-10.

Reijerse, E.J. and Keijers, C.P. (1987) Model Calculations Of Frequency Domain ESEEM Spectra Of Disordered Systems. *J. Magn. Res.* **71**, 83-88.

Reijerse, E.J. and Dikanov, S.A. (1991) Electron Spin Echo Envelope Modulation Spectroscopy on Orientationally Disordered Systems – LineShape Singularities in S=1/2, 1=1/2 Spin Systems. *J. Chem. Phys.* **95**, 836-845.

Rowan L.G., Hahn, E.L., and Mims, W.B. (1965) Electron-Spin-Echo Envelope Modulation. *Physical Review* **137**, A61-71.

Singh, V., Zhu, Z., Davidson, V.L., and McCracken, J. (2000) Characterization of the Tryptophan Tryptophyl-Semiquinone Catalytic Intermediate of Methylamine Dehydrogenase by Electron Spin-Echo Envelope Modulation Spectroscopy. *J. Amer. Chem. Soc.* **122**, 931-938.

Thomann, H., Bernardo, M., Newton, W.E., and Dean, D.R. (1991) N Coordination of FeMo Cofactor Requires His-195 of the MoFe Protein α Subunit and is Essential for Biological Nitrogen Fixation. *Proc. Natl. Acad. Sci. U.S.A.* **88**, 6620-6623.

Tipton, P.A., McCracken, J., Cornelius, J.B., and Peisach, J. (1989) Electron Spin Echo Envelope Modulation Studies of Pyruvate Kinase Active-Site Complexes. *Biochemistry,* **28**, 5720-5728.

Townes, C.H. and Dailey, B.P. (1949) Determination of Electronic Structure of Molecules from Nuclear Quadrupole Effects. *J. Chem. Phys.* **17**, 782-796.

Warncke, K, Brooks, H.B., Babcock, G.T., Davidson, V.L., and McCracken, J. (1993) The Nitrogen Atom of Substrate Methylamine is Incorporated into the Tryptophan Tryptophyl-Semiquinone Catalytic Intermediate in Methylamine Dehydrogenase. *J. Amer. Chem. Soc.* **115**, 6464-6465.

Warncke, K, Babcock, G.T., McGuirl, M.A., Dooley, D.M., and McCracken, J. (1994) Structure of the Topa-semiquinone Catalytic Intermediate of Amine Oxidase as Revealed by Magnetic Interactions with Exchangeable ^{2}H and ^{1}H Nuclei. *J. Amer. Chem. Soc.* **116**, 4028-4037.

Willer, M., Granwehr, J., Forrer, J., and Schweiger, A. (1998) Two-Dimensional Nuclear-Zeeman-Resolved Electron Spin Echo Envelope Modulation (NZ-ESEEM) Spectroscopy. *J. Magn. Reson.* **133**, 46-52.

Zhang, C., Markham, G.D., and. LoBrutto, R. (1993) Coordination of Vanadyl(IV) Cation in Complexes of S-Adenosylmethionine Synthetase: Multifrequency Electron Spin Echo Envelope Modulation Study. *Biochemistry* **32**, 9866-9873.

Zweier, J., Aisen, P., Peisach, J., and Mims, W.B. (1979) Pulsed Electron Paramagnetic Resonance Studies of the Copper Complexes of Transferrin. J. Biol. Chem. 254, 3512-3515.

Contents of Previous Volumes

VOLUME 2

VOLUME 3

VOLUME 5

VOLUME 6

VOLUME 9

VOLUME 15

VOLUME 18

VOLUME 19

VOLUME 21

VOLUME 22

Index